

The reconstitution of visual cortical feature selectivity *in vitro*

Dissertation
(Cumulative Dissertation)

for the award of the degree
“Doctor rerum naturalium”

Division of Mathematics and Natural Sciences of the
Georg August University Göttingen within the doctoral program GGNB
of the Georg August University School of Science (GAUSS) submitted by

Manuel Schottdorf
from Bad Kissingen

Göttingen 2017

Thesis committee:

- Prof. Dr. Fred Wolf (Thesis supervisor and 1st reviewer)
Max Planck Institute for Dynamics and Self-Organization
- Prof. Dr. Jörg Enderlein (2nd reviewer)
Third Institute of Physics, University of Göttingen
- Prof. Dr. Walter Stühmer (Thesis cosupervisor)
Max Planck Institute for Experimental Medicine

Further members of the examination board:

- Dr. Andreas Neef,
Max Planck Institute for Dynamics and Self-Organization
- Prof. Dr. Siegrid Löwel,
Faculty of Biology, University of Göttingen
- Prof. Dr. Alexander Gail,
German Primate Center, Göttingen

Date of oral examination: August 22nd, 2017

Contents

Contents	1
1 Introduction	3
1.1 Synthetic neurobiology	4
1.2 Content	5
2 Fundamentals	7
2.1 Content	7
2.2 Eye and retina	8
2.3 The LGN	9
2.4 The primary visual cortex	11
2.5 Interfacing neurons	19
2.6 Reconstituting visual cortical feature selectivity	21
3 Feed-forward orientation selectivity	23
3.1 Content	23
3.2 Manuscript	23
4 Which surrogate cortex?	67
4.1 Content	67
4.2 Method I: μ -Contact printing of neuronal circuits	68
4.3 Manuscript	68
4.4 Closing the loop	88
4.5 Method II: Realistic local circuits	89
5 A synthetic orientation selective hybrid neural network	105
5.1 Content	105
5.2 Introduction	106
5.3 Results	108
5.4 Discussion	123
5.5 Supplemental	127
5.6 Materials and Methods	127
6 Developmental manipulation of the surrogate cortex	131
6.1 Content	131
6.2 Introduction	132
6.3 Results	134
6.4 Discussion	141
6.5 Materials and Methods	143
7 Challenges to the common design	147
7.1 Content	147
7.2 The random wiring hypothesis revisited	148
7.3 Manuscript	148

7.4	Primate color vision and V1 functional architecture	166
8	Gender bias in peer review	187
8.1	Content	187
8.2	Manuscript	187
9	Summary and outlook	207
9.1	Summary	208
9.2	Outlook	212
10	Materials and Methods	213
10.1	Experimental protocols	214
10.2	Agents	218
	Bibliography	221
	Acknowledgements and CV	249
	Acknowledgements	249
	Curriculum Vitæ	251

Introduction

“What I cannot create, I do not understand.”

Richard Feynman¹⁴¹, 1988

1.1 Towards a synthetic neurobiology

Understanding system level functions, realized by the coordinated activity of large numbers of biological elements, constitutes one of the greatest challenges to science in the 21st century. Prime examples are the information processing functions of nervous systems, which typically require the coordinated activity of nerve cells interacting in complicated networks called neuronal circuits. Despite massive effort, the design principles underlying neuronal circuits in most animal brains remain poorly understood because we can not control all contributing circuit elements in the brain simultaneously. I aim to explore and possibly lay the foundation for a new strategy to address this challenge.

While the physiology of individual neurons is important for circuit function it is probably its wiring diagram, its connectome, that determines the function of neuronal circuits as information processing device. If connectomes are in fact decisive, then thorough testing of the relationship between circuit structure and function will be key for understanding neuronal circuit design. For genes and proteins *engineering* approaches enable biological researchers to modify their biological structure and assess the resulting loss and gain of function. Historically, studies on proteins like hemoglobin showed that structural variations can lead to impaired function and disease and these studies were key for the understanding of its molecular function^{210,381}. Similarly, manipulating the structure of various ion channels and monitoring the associated functional changes lead to novel insights into their working mechanisms^{71,460}. These early structure-function studies evolved into synthetic biology, a “rigorous engineering discipline to create, control and program cellular behavior [...] poised to transform biotechnology and medicine.”⁶⁴ by providing the biological engineer with specific genetic tools like toggle switches, oscillators and even logic gates. In the case of living neuronal circuits, however, our capabilities of redesigning connectomes at present are very limited. My aim is to develop a *synthetic neurobiology* approach to this problem to create, control and program neuronal circuits, with the ultimate goal of performing a first connectomic structure-function study.

The key to this novel approach is the incorporation of artificial components into a neuronal circuit formed by living cells. I will use the reliability of engineered neuronal networks *in silico* to specifically replace key elements of the connectome. The control over the artificial circuit then allows me to design, switch and manipulate the connectome on the fly. The total network is thus a synthetic hybrid circuit composed of simulated and living nerve cells in which key features of its wiring diagram can be digitally manipulated. Taken together, the merged *in silico* and *in vitro* components of this system can realize a recurrent and functional circuit of neurons which is flexible enough for specific structure-function studies. Recent advances in optogenetics together with digital phase-only holography and electrophysiology allow me to construct such a hybrid circuit. This is what I call synthetic neurobiology of hybrid neuronal circuits.

I will focus on one fundamental and enigmatic neuronal circuit motive common to many brain areas: a recurrently connected layer of neurons processing information arriving through a feed-forward neuronal pathway. This large-scale circuit motive predominates in the cerebral cortex, which is the seat of our conscious experience and our recognition, memory, and executive control capabilities. The response properties of neurons in many regions of the cerebral cortex have been extensively described. For most of them, however, it is still unclear which aspects of circuit structure are critical to their function. In particular, it is a long-standing and highly controversial question, what feed-forward inputs arriving from e.g. a sensory pathway and recurrent connections within the target circuit specifically contribute to cortical information processing.

Let us consider the early visual system: after half a century of extensive study we have gained substantial insights into its functional organization and its cellular composition. Yet, we are far away from a deep understanding of the computational goals, the underlying algorithms and the hardware implementation^{309,310}. A landmark component of the visual system is the primary visual cortex. Its constituting nerve cells are feature selective; they respond to specific aspects of visual scenes. Feature selectivity has been studied for more than 50 years¹⁹⁶ and most V1 scientists agree that feature selectivity is a key property of cortical neurons, going so far as to refer to it as “giant squid axon of cortical neurophysiology”⁶⁶ to which both feed-forward and recurrent circuits contribute. The interplay of both, however, is enigmatic because both circuits are hard to selectively and specifically manipulate *in vivo*⁴³⁴. Here, I use synthetic neurobiology of hybrid neuronal circuits as a novel research avenue for structure-function studies of neuronal circuit design in the visual pathway which I hope might lead to genuine insights into the underlying logic of neuronal circuits.

Synthetic neurobiology enables a new and systematic approach to dissect the contributions of feed-forward and recurrent connectomes to the generation of cortical feature selectivity, because: (1) The *in vitro* component realizes a dense medium scale recurrent circuit, composed of thousands of neurons, so that collective processing functions can spontaneously emerge. (2) The wiring diagram of the feed-forward input connectome can be freely designed and thus varied from highly specific to completely random. (3) The system can be rapidly and reversibly switched between different pathway connectomes. (4) Different pathway connectomes can be connected to the same target circuit of living neurons, providing for an internal control. (5) High quality optical access to the recurrent circuit for all-optical interfacing and optical monitoring of activity can be achieved with relative ease.

1.2 Content

In the first part of this thesis, **chapter 2**, we review the mammalian visual system and the technologies for interfacing living neuronal networks.

In **chapter 3** we study a state-of-the-art model of the early visual pathway to both develop a framework for the virtual connectome and to answer the question whether random wiring of the afferent visual pathway alone suffices to generate (i) feature selectivity and (ii) determine the functional architecture of the primary visual cortex. We find that weak orientation selectivity can be generated in the random wiring scheme, but to obtain the specific layout observed across various mammalian species, the common design²⁴², random wiring is insufficient. Self-organization of recurrent connections during development determining the preferred orientations remains the most likely candidate.

Next, in **chapter 4**, we will develop and assess two distinct approaches to construct an *in vitro* surrogate cortex. We first assess the viability of what we call *virtual networks*, realized by closed loop optogenetic connections^{162,348} between islands of individual neurons grown on multielectrode arrays (MEAs). Virtual networks are artificial neural networks with biological neurons as nodes. This approach seems promising because it allows in principle to construct arbitrary networks. We develop a protocol to yield $\approx 60\%$ populated islands on glass electrode arrays, but find that recording electrical activity is partially impaired by the required surface treatment of the glass chips. In the end, we observe only few islands with active electrodes. Next, we design a system in which the local neuronal circuits are as realistic as possible. We find that cortical cultures can be set up with the same cell density and cellular content as the

input layer of sensory cortex. As these cultures are easier to produce on a large scale and show rich spontaneous activity, resembling the spontaneous activity in the young neocortex, our second strategy was to wire this surrogate cortex to a virtual sensory pathway. We implemented the virtual sensory pathway *in silico* and interfaced the living neurons by a custom build digital phase-only holographic projection system.

In **chapter 5**, we show details of the *in silico* visual pathway and its interface to the surrogate cortex. We also find a generic scaling law for the layout of the early visual system which allows us to transform the visual pathway of a cat into that of a mouse. We connect these different pathways to the same target circuit of living neurons, providing for an internal control, and find that shrinking the visual system leads to a substantial loss of orientation selectivity in the afferent input, while surprisingly the total fraction of tuned cells changes little. The orientation bias of neurons in the limit of homogeneous inputs is generated by the recurrent network alone. These cells are mostly simple cells with a small fraction of complex and direction tuned cells. We also find cells with receptive fields composed of excitatory and inhibitory subregions, and these receptive fields have a typical spatial scale of ≈ 1 mm, consistent with the generic scaling laws which we extracted earlier. Consistent with simple cells, the tuning can be predicted from the receptive field. The spatial arrangement of spontaneously tuned cells resembles a sparse salt and pepper pattern. This diversity of responses suggests that even in this most generic case, a recurrent circuit is sufficient to spontaneously generate a basic level of orientation selectivity.

In **chapter 6** we will present a new method to manipulate the circuits in the surrogate cortex. The surrogate cortex is based on neuronal circuits generated in the absence of any input and the processes by which neurons wire into circuits are most likely partially activity dependent. One way to manipulate the circuit's connectome is thus by controlling the prevalent activity patterns during the course of circuit formation. In this chapter, we therefore ask whether the local circuits can be configured differently by supplying external inputs during development. We discover that external inputs during development change the collective dynamics of the surrogate cortex massively. This chapter concludes the synthetic neurobiology part of this thesis.

In **chapter 7** we further test the random wiring hypothesis using experimental data from cat and primate retinal ganglion cell mosaics. We compare it with an ensemble of bespoke ganglion cell mosaics that can theoretically seed iso-orientation domains in the visual cortex and find that the currently available data puts a strong quantitative constraint on the random wiring hypothesis and the idea that the layouts of domains are already encoded in the geometry of the retina. Considering the specificity and ubiquity of the common design, we next ask where the selective forces that favor the common design can break down. Using the reinvention of color-vision among primates as natural experiment, we find a virtually identical layout of orientation domains in trichromatic macaque and color-blind owl monkeys, highlighting that orientation selectivity is truly a key player of functional cortical architecture, and likely orchestrates other functional aspects of the cortex.

In **chapter 8** we reveal distortions in the peer review process, specifically showing that a scientist's personal attributes matter. This chapter was originally motivated by personal observations, and made rigorous by web-crawling the publicly available article web pages from the Frontiers Journal Series to obtain one of the largest datasets for the sociology of science available today including more than 175,000 individuals.

Finally, we review the content of this thesis in **chapter 9** together with an assessment of the merits of a synthetic neurobiology approach for the reconstitution of living neuronal circuits.

Fundamentals

“Felix, qui potuit rerum cognoscere causas.”

Publius Vergilius Maro³⁸⁹: “Georgica”, Liber II, 490.

2.1 Content

Here, we review the building blocks of the early visual system and the currently available technologies for interfacing living neuronal circuits. Its content serves as the foundation of the work in the following chapters. Reviewing these elements is critical to (1) construct the *in vitro* model of the visual pathway, (2) interpret our subsequent findings and (3) assess the potential merits of constructing a synthetic hybrid system of this specific sensory pathway.

The visual system is the paradigm of a sensory pathway and it is sequentially organized: A recurrently connected layer of neurons in the brain is processing the information arriving through the feed-forward neuronal pathway of retina and lateral geniculate nucleus, a thalamic processing station. Most importantly, we will introduce orientation selectivity, a key element of what is called the functional architecture of the visual cortex. It has recently been discovered that this functional architecture exhibits a set of quantitative layout rules, called the common design, that is likely to have been invented independently several times during mammalian evolution.

2.2 Eye and retina

The optical machinery of the eye projects an image of the visual world on the retina, a light-sensitive layer of tissue, see **Fig. 2.1A**. On the retina, the two dimensional light pattern is translated into variations of the membrane potential of rod and cone cells. These light detectors, in humans on the order of 100 million, densely convert an image into electrochemical signals. The signals are subsequently processed by a cascade of neurons, **Fig. 2.1B** and provide input to retinal ganglion cells (RGCs). These cells generate complex sequences of action potentials that provide input to the brain.

Ganglion cells

Every single RGC responds to specific aspects of a stimulus, located within a small region in the visual field, the neuron's so-called receptive field²⁵⁸. For many RGC types, the receptive field is radially symmetric. Stimulation in the center of this receptive field increases the firing whereas stimulation of the surround suppresses it. Such a cell is called an ON center cell, **Fig. 2.1C**. Cells for which the activity increases upon presentation of a dark center are called OFF center cells. The response of RGCs in the frequency domain reflects this behavior, **Fig. 2.1D**. For small spatial frequencies that illuminate the entire receptive field, the response is suppressed compared to intermediate spatial frequencies.

Ganglion cell mosaics

In the primate retina, there are several types of ganglion cells, most notably Parasol (10%-20%), Midget (60%-80%) and Bistratified cells (10%-20%). Parasol and Midget cells have a center-surround receptive field. Midget cells are color selective, often sampling from a single cone only. They also have very small receptive fields. In the cat, nomenclature is different^{454,478}. There exists a ganglion cell type with a small and linearly summing receptive field, similar to the primate midget cell, which is referred to as X-cell³¹⁸. There is another type with larger receptive field, resembling to some extent the primate parasol cell, and is called a Y-cell¹⁰⁶. Midget and parasol cells are distinguished according to their response properties, as are X- and Y-cells. However, the cells are also different histologically and morphologically. Y-cells in the cat correspond to α -cells in morphology, and X-cells correspond to β -cells^{318,465}.

The mammalian retina contains so-called mosaics of retinal ganglion cells which tile the entire surface^{100,101}. This was found in rabbits¹¹⁴, rats^{13,421}, cats^{378,506,508}, primates^{99,142} including humans¹⁰⁰, and is illustrated in **Fig. 2.2**. Both the position of RGC somata, and of the receptive fields, form an aperiodic pattern with a typical scale⁴²⁷. A cat's α -cell mosaic is shown in **Fig. 2.2A**. Notably, there are different types of RGCs that coexist, and that convey different signals to the brain.

Ganglion cell projections

The ganglion cell's axons form the optic nerve. The two optic nerves meet in the optic chiasm where the nasal sides of the image are interchanged. The optic tract projects to a region in the thalamus, the *lateral geniculate nucleus* (LGN). This is one of the key region of the brain where retinal input arrives (the other being the superior colliculus and the pretectum). Thalamic nuclei are thought to modulate the signal transduction depending on attention and sleep. This selection is influenced by cortical projections that terminate in the thalamus. Neurons receiving retinal input are termed relay cells as their response properties resemble retinal cells^{85,193,235,467}.

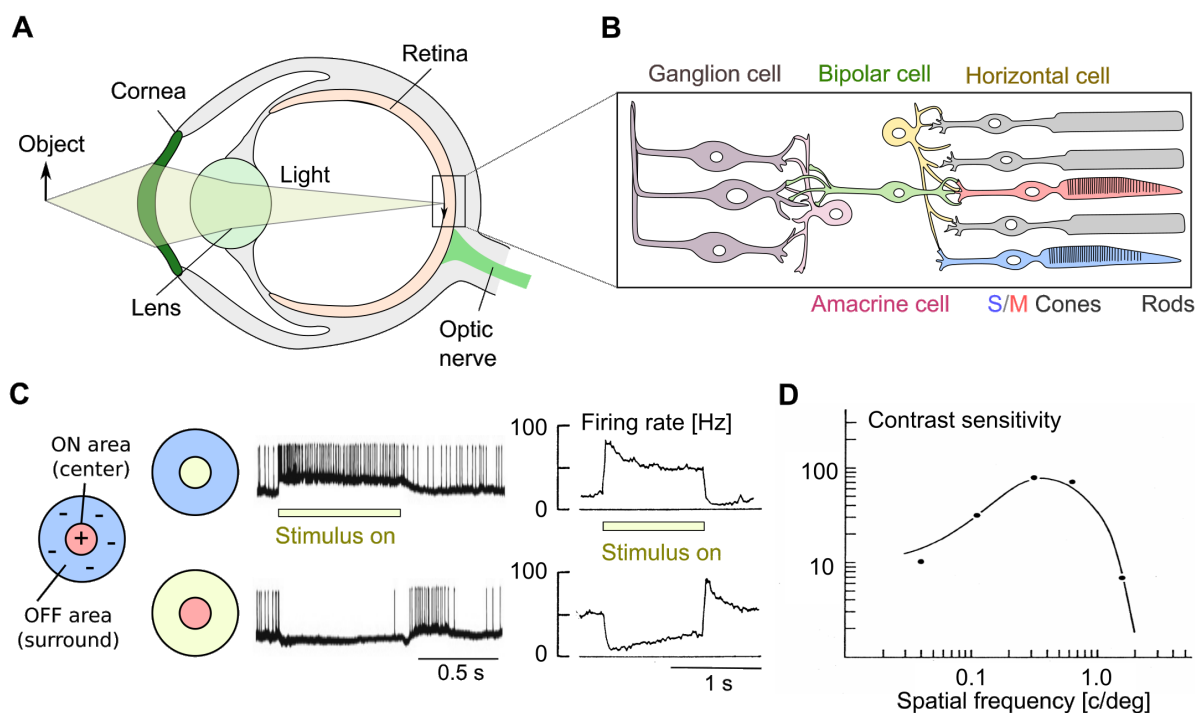


Figure 2.1: **Visual processing in the retina.** **A** A sagittal cut through the eye of a cat. **B** The cellular inventory of the primate retina. Light enters from the left. **C** Receptive field of an ON center X-type retinal ganglion cell. An illumination pattern (left) creates a certain response (center and right). The bar corresponds to the time span when the stimulus is presented (spike data reprinted with permission from⁵¹⁸. Firing rates reprinted with permission from¹³⁰). **D** Response of a ganglion cell to different spatial frequencies. The decrease at small spatial frequencies is the effect of surround suppression (reprinted with permission from¹³⁰).

2.3 The LGN

Fig. 2.3A shows the location of the LGN within the early visual pathway of a primate. A staining for cell bodies, **Fig. 2.3B**, shows a distinct six-layered structure, characteristic for primates. LGN neurons are the target of a subset of retinal projections, and these retinal projections are ordered with clear ocular dominance layering¹⁹⁹. Layers 1,4,6 are contra-lateral, and 2,3,4 ipsi-lateral. In the primate, parasol cells are part of the *magnocellular pathway* and midget cells part of the *parvocellular pathway*, two distinct parallel pathways to the visual cortex. In the literature, geniculate neurons of the parvocellular pathway are called P-cells and neurons of the magnocellular pathway are called M-cells. Of the six histologically distinct layers of the LGN, four belong to the parvocellular, and two belong to the magnocellular pathway. The thalamic neurons respond similarly as retinal cells. M-cells of the magnocellular pathway are not color sensitive and respond well to low luminance contrast. P-cells are color sensitive and require a great luminance contrast. A loss of P-cells leads to a complete loss of color vision. LGN neurons have center-surround receptive fields. This similarity is the main reason for modeling the LGN as relay station, despite the fact that anatomically, only 10%-20% of the synaptic connections to LGN neurons originate in the retina. The vast majority originate in different brain regions²³³. Axons leaving the LGN follow the optic radiation to primary visual cortex.

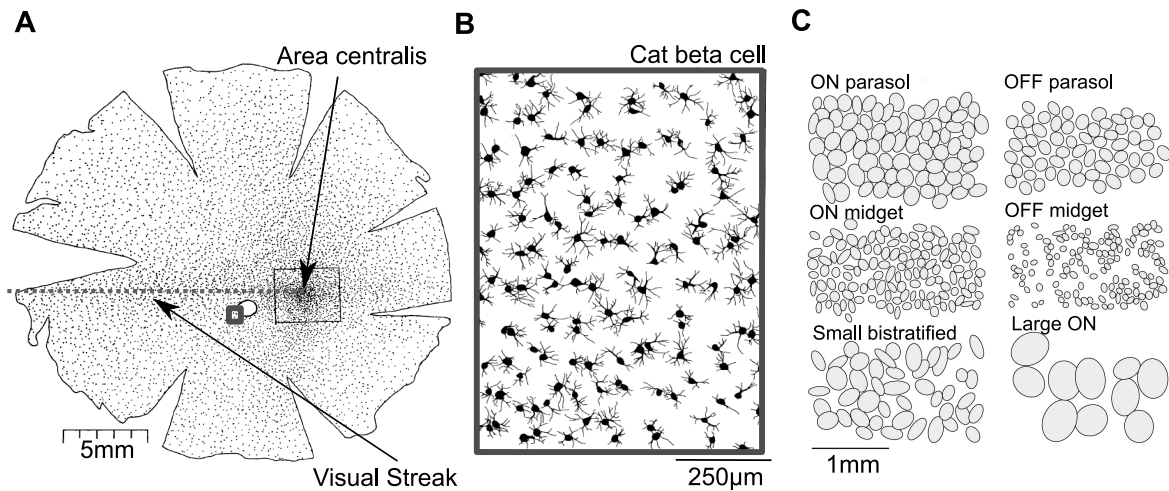


Figure 2.2: **Ganglion cell mosaics cover the retinal surface.** **A** A full mount of a cat retina, with visual streak and the fovea indicated (reprinted with permission from⁵⁰⁷). **B** Section of the β -cell mosaic of a cat (reprinted with permission from⁵⁰⁶). The retinal position of this mosaic is indicated in A. **C** Receptive field mosaic of a primate retina. Shown are contours of Gaussian fits to the receptive fields at 1.3σ (reprinted with permission from¹⁴²).

Expansion and convergence from RGCs to relay cells

Independent of retinal topography all α - and β -cells in the cat retina project through the optic nerve to the thalamus. 70% of the fibers terminate in the LGN. In the A lamina of dLGN, there are 240,000 X-cells (Retinal X-ganglion cells project mainly into the A-lamina of the LGN. Of the approximately 450,000 cells in the LGN⁴¹⁹, two-thirds are located in the A and A1 layers, and two-thirds of these are X-type). These receive input from at least around 90,000 β -cells in the retina^{203,209,406}. Therefore, each retinal X ON center ganglion cell from one eye projects to ≈ 3 geniculate relay cells. This is consistent with the estimate by⁴⁸⁷. Others estimate an expansion of around 1.5-2.0 from X-cells in the retina to X-relay cells in the LGN^{209,382}. Moreover, geniculate neurons can receive input from several retinal afferents and these multiple retinal inputs have mostly overlapping receptive-field centers⁴⁸⁷. Input is typically provided by one or at most a few RGCs, RGC input drives LGN neurons effectively⁸⁴ and ON and OFF channels remain separated in the LGN¹⁹¹.

Functional considerations

Such divergence from the retina might be important in the light of synchronous activity in the LGN which in turn might be particularly effective in driving layer IV cells in the visual cortex (see below). Another hypothesis was recently brought forward by Martinez³¹⁶ et al. In their study, they inferred the mapping between RGC inputs and LGN relay cells using a statistical connectivity approach: ON and OFF cell types were homogeneously distributed and their polarity (ON or OFF) was inherited from the nearest retinal input. Connection probability between RGCs and LGN neurons was modeled as an isotropic Gaussian function of the relative distance between the RF centers of the presynaptic and postsynaptic partners. With this simple wiring scheme, together with similar connectivity rules for the population of inhibitory interneurons, several spatiotemporal properties of LGN RFs robustly agreed with the experimental data. They deduce that the retinthalamic convergence provides an interpolated map with improved coverage of visual space. Their model suggests that a typical relay cells gets

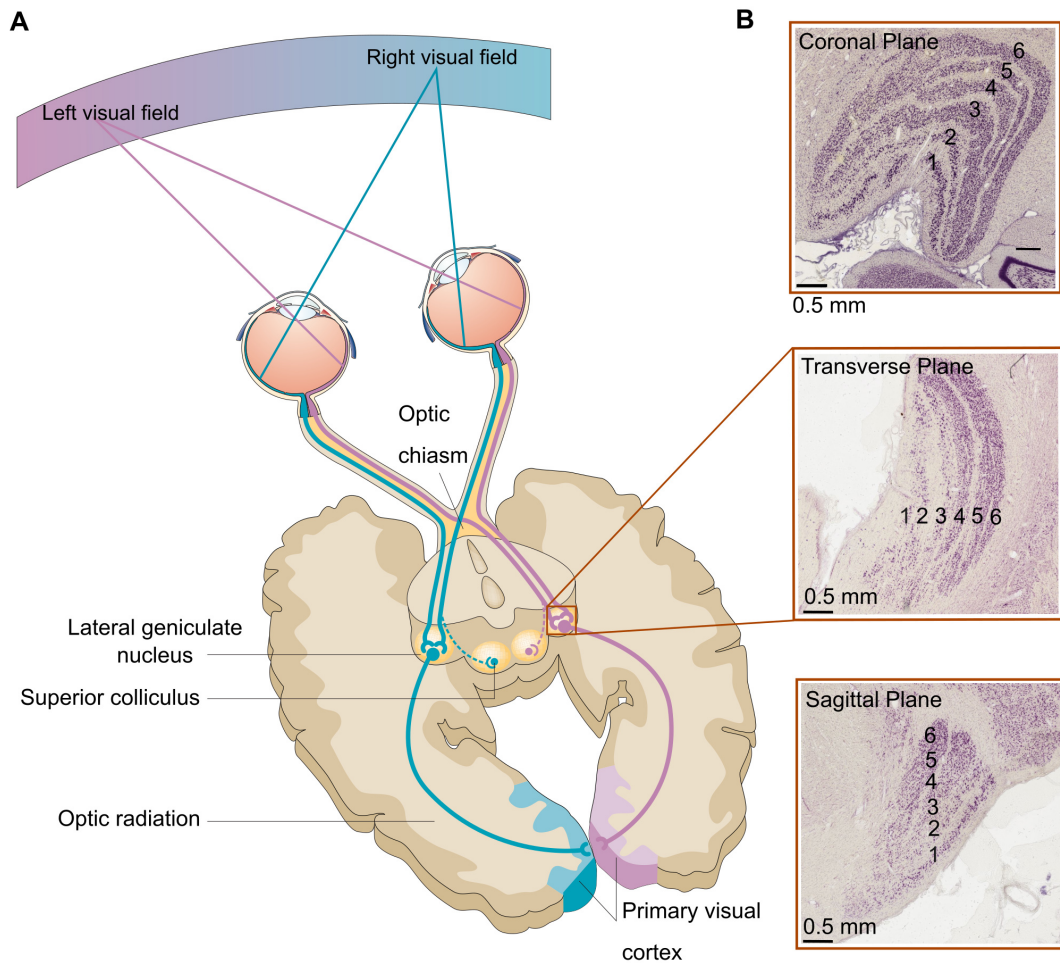


Figure 2.3: **Position and anatomy of the LGN in the primate brain.** **A** A transverse sketch of the visual system (reprinted with permission from¹⁷²). **B** Three Nissl stained adult *Macaca mulatta* brain sections of the lateral geniculate nucleus (adapted from³²⁸). The characteristic six layers in primates are numbered.

input from three to four RGCs.

The spike output of LGN relay cells is basically monotonic with contrast⁴. Notably, between 5% and 100% contrast, spike rates can change about 40% and the signal transmitted from the LGN rides on a maintained spontaneous discharge. This is consistent with earlier reports³⁶¹, who found that “relay cells do not adapt to any significant degree, the signals they carry may convey information about absolute contrast levels.”

2.4 The primary visual cortex

From the LGN, projection to the visual cortex are made through the optic radiation. Along these fibers visual signals are sent to the primary visual cortex in the occipital lobe. This is the first cortical processing station.

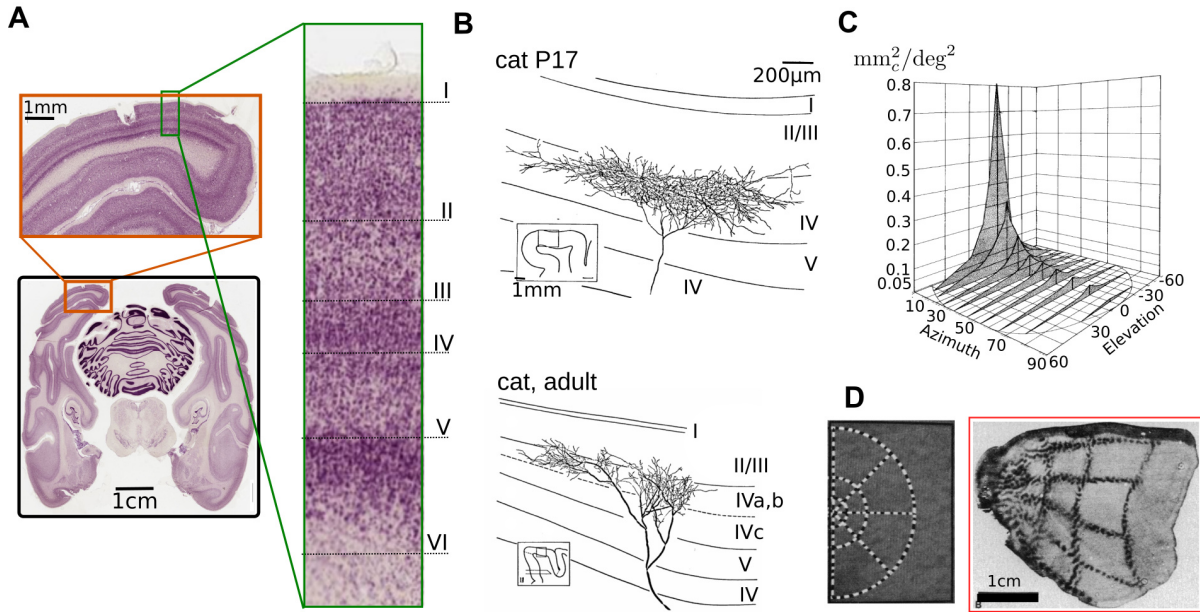


Figure 2.4: **Anatomy of the neocortex and retinotopic projections.** **A** A transverse cut through a nissl stained macaque monkey brain (adapted from³²⁸). The inset indicates the six cortical layers. **B** Two LGN afferents to the visual cortex of a kitten (top) and an adult cat (bottom) (adapted from²⁶⁷). **C** There exists a topographic map from the visual world to the visual cortex, of which the magnification depends on the position in visual space (reprinted with permission from⁴⁸⁴). **D** This is, for instance, directly visible by studying activity patterns generated by geometric shapes (reprinted with permission from⁴⁷⁵).

Anatomy and inputs of the visual cortex

The mammalian cerebral cortex is a superficial layer of tissue and contains most of the neurons of the Cerebrum, see **Fig. 2.4A**. The occipital lobe of the brain contains the primary visual cortex, the first cortical area concerned with processing of visual information. The primary visual cortex, sometimes referred to as the striate cortex, is a sheet of tissue with six layers, each of which with substantial differences in cell density and cell composition³⁹¹. Through history and for other regions, other numbering schemes have been used. However, the division into six layers is the most common one²³³. Layer IV receives thalamic input. In primates, it is further subdivided into layer $\text{IVC}\alpha$, to which the magnocellular pathway projects and $\text{IVC}\beta$, target of the parvocellular pathway. **Fig. 2.4B** shows two LGN projections into the cortex in a cat's brain, terminating in layer IV. In cat "virtually all" relay cells of X-type in the A lamina project to area 17²⁰⁴. Thalamic X-cell axons terminate in single irregular clumps of size 0.6 mm^2 to 0.9 mm^2 in the primary visual cortex²⁰⁴. In young cats, thalamic projections are isotropic and cover about 0.5 mm^2 . In adult cats, the geometry is similar but more patchy. The density of binocular layer IV neurons is about 14000 mm^{-2} in layer IVC ²⁹. The projections from the thalamus into the cortex preserve the topography of the visual world. Neighboring projections, and neighboring neurons in the cortex respond to neighboring points of the visual world. This is called retinotopy^{104,304,526}. In mice, this mapping is rather uniform^{115,429}, in contrast to cats^{304,484}, macaque⁴⁷⁶ or human⁴¹². The linear magnification factor in units mm_c/deg is the conversion factor between angle in the visual world and mm on the cortical surface. For most animals, it depends on the position in visual space, **Fig. 2.4C**. Thus, any object in the real world generates a distorted, but topographically identical activity pattern on the cortex⁵²⁶. This is visualized with an autoradiograph from the metabolization of radioactive glucose in **Fig. 2.4D**.

The retinotopic thalamic inputs into the visual cortex are excitatory^{10,329} and specifically target stellate neurons in layer IV^{137,157,268}. As most of the stellate cells are spiny, excitatory spiny stellate neurons are the major target of thalamic inputs^{152,294,314,322,382,459}.

Thalamic synapses are neither special nor particularly strong^{4,35} and only $\approx 5\%$ of spiny stellate cell synapses come from thalamic axons. In numbers, about 100-200 from 5000 connections come from the thalamus⁹³ and do not dominate the activity of a particular cortical neuron³⁸². In the words of Kevan Martin: “We are connected to reality only through a tiny thread; the cortex is spending a lot of time talking to itself”¹. The median size of the synapses is slightly larger than that of other synapses on the dendrites of spiny stellate cells, but they are not located particularly proximal to the soma, nor cluster on the dendrites. A theoretical study with a biologically realistic model spiny stellate cell of layer IV revealed that a large number of thalamocortical synapses have to be activated roughly simultaneously to elicit a spike in this cell²¹. This might imply that input alone cannot drive the stellate cells and lead researchers to speculate about alternative mechanisms, such as synchronous activation of the sparse thalamic synapses to boost the efficacy, or as intracortical inputs provide most of the excitation to spiny stellate cells in layer IV, recurrent intracortical circuits may amplify the initial feed-forward thalamic signal^{21,93,252,459}.

The number of inputs

With this qualitative understanding, how many RGCs provide input to a single layer IV stellate cell through the LGN? Quantitatively, it has been subject of ongoing debate for the past 30 years^{11,466}. In the following few lines, we will try to estimate the number using several independent ways.

(1) One can estimate it directly, for instance by analyzing published β -cell mosaics^{506,540}. For these mosaics, using known relations between visual angle^{25,37} and cortical magnification⁴⁸⁴, we estimate the cortical magnification⁴²⁷ as $\xi = 1.7 \frac{\text{mm}_c}{\text{mm}_r}$. The mosaic w81s1^{427,506}, shown in **Fig. 2.2B**, measures $0.75 \times 1.0 \text{ mm}_r^2$ and consists of 65 ON and 70 OFF cells. With perfect retinotopy, it would provide input to a cortical area of about $1.3 \times 1.7 \text{ mm}_c^2$. X-cell input into layer IVC is typically restricted to single clumps¹³⁷ with a radial extend of $\approx 500 \mu\text{m}_c$. This is roughly consistent with the presumably more precise findings by Humphrey and colleagues²⁰⁴, who specifically studied X- and Y-cell projections, by anatomically identification of the cell and subsequent intracellular injection of horseradish peroxidase. They report that thalamic X-cell axons terminate in single irregular clumps of size 0.6 mm_c^2 to 0.9 mm_c^2 in the primary visual cortex. The number of projections accessible to a layer IV stellate cell is therefore $N = \frac{(65+70) \times (0.75 \pm 0.15) \text{ mm}_r^2}{1.3 \times 1.7 \text{ mm}_c^2} \simeq 45 \pm 10$. The other mosaic, m623^{427,540}, measures $1.0 \times 1.1 \text{ mm}_r^2$ and consists of 74 ON and 82 OFF cells, providing input to an area of about $1.7 \times 1.9 \text{ mm}_c^2$. It follows for this mosaic that $N = \frac{(74+82) \times (0.75 \pm 0.15) \text{ mm}_r^2}{1.7 \times 1.9 \text{ mm}_c^2} \simeq 36 \pm 7$.

(2) A different approach would be anatomical. Peters and Payne measured the synaptic connectivity between thalamus and cortex and from there estimated the number of inputs into a cortical cell. They found that there are 115 ± 15 genicocortical synapses per layer IV stellate cell³⁸². Freund et al. measured the number of synapses that stellate cells form with thalamic projections. They found typically 1 synapse per projecting X-cell axon, with a mean of 1.27 and a maximum of 8^{147,382}, so that one layer IV cell receives 15-125 different inputs. As the LGN expands the number of retinal inputs by a factor of 2 to 3 (with some estimates¹¹ going as high as 3-6), there are effectively between 5 and 60 RGCs that could provide input into one layer IV cell.

(3) Some researchers estimated the number of inputs using a random wiring hypothesis. The

¹Comment at 113th International Titisee Conference 2016, in Titisee, Germany.

first such estimation⁴⁴⁶ comes from Robert Soodak in 1987. Assuming a Gaussian distance function (which he defined as wiring strength as function of distance in retinotopic space between RGC position, and cortical target), with a width of $\sigma=150\ \mu\text{m}$ (estimated from Ferster's¹³⁷ and Humphrey's²⁰⁴ work), and counting connections only if the distance function > 0.01 , he estimated that a cortical neuron receives input from typically 27 RGCs through LGN relay cells. In 2004, Dario Ringach⁴⁰⁶ estimated the number of LGN inputs to a simple cell to be around 10, and Troyer estimates it to 61 ± 5 ⁴⁷⁹.

(4) The number of effective geniculate inputs onto a simple cell can also be estimated from the size of simple cell and geniculate receptive fields, the coverage and the wiring probability¹¹, $N = A \cdot C \cdot p$, where A is ratio of the visual space covered by a geniculate receptive fields over a simple receptive field, C is the number of geniculate centers per point of visual space (i.e. the Coverage of visual space), and p is the probability of connection between a geniculate cell and a simple cell with overlapping receptive fields. A typical layer IV simple cell has two to three subregions, each with a length/width ratio of ≈ 2.5 . Therefore, six geniculate receptive fields would suffice to cover a simple receptive field. The coverage factor for both, ON and OFF center X-cells is ≈ 6 in the retina⁵⁰⁶ and $2.5\times$ larger in the LGN^{209,382}, therefore, $C \approx 15$. The probability of finding a monosynaptic connection between a geniculate cell and a simple cell with overlapping receptive fields is approximately $p = 0.33$. Thus, $N = 6 \cdot 15 \cdot 0.33 \approx 30$ geniculate cells would converge onto a simple cell¹¹.

(5) From the relation of visually stimuli, thalamic activity and LFPs in area 17, Jin et al. estimated the number of strong X inputs into one cortical column²²⁵. They found on average 26 strong inputs, with a range from 12-47, indicating in turn 4-25 RGCs

Taken together, these estimations point to at least 10, but probably much less than 100 RGCs that effectively provide visual input to a layer IV cell. If there are in fact so few inputs with which a given cell can construct a receptive field, would this not generate substantial receptive field scatter on local scales?

It turns out that there is very small scatter of receptive field position. Hetherington and Swindale found that typical scatter was half an average RF size (tetrode recordings in cat area 17)¹⁸⁴. This seems consistent with²²⁵ who found about 2.5 geniculate centers and³⁴⁶ who found typically 10%-20% of RF size. More recent studies using either electrode penetrations²⁵⁶ or calcium imaging^{272,346} revealed that retinotopy is very precise, in the words of Ian Nauhaus: "close to perfect on a microscale"². Specifically in cats and treeshrews, OFF retinotopy is very precise and the scatter is larger for the ON subregion. The relative displacement of the ON subregion is consistent with the cell's orientation preference^{225,256,272,393}.

Feature selectivity in V1

Recording from neurons in the primary visual cortex, **Fig. 2.5A**, reveals a remarkable phenomenon: orientation selectivity. Neurons in the primary visual cortex respond preferably to edge-like stimuli or contours of a particular orientation^{194,197} (they also show spatial frequency preference²¹², ocular dominance^{238,289} and others⁴⁶³). This feature preference distinguishes primary cortical neurons from cells in the retina and the thalamus⁴⁶⁷ and is reflected by both receptive fields from reverse correlation measurements^{107,487} with specific ON and OFF regions³⁹⁸ and the response to an elongated bar³³⁵, **Fig. 2.5B**. Measuring the response of a cell as function of the stimulus orientation yields a tuning curve, **Fig. 2.5C**. Notably, the tuning of cortical cells prevails even after silencing the cortex, for instance by cooling¹³⁶ or pharmacological innervation⁷⁷, indicating that the convergence of multiple thalamic projections on the target cortical neuron has a substantial contribution to its tuning. These results have been confirmed more

²Comment at Cosyne 2015 in Salt Lake City, USA.

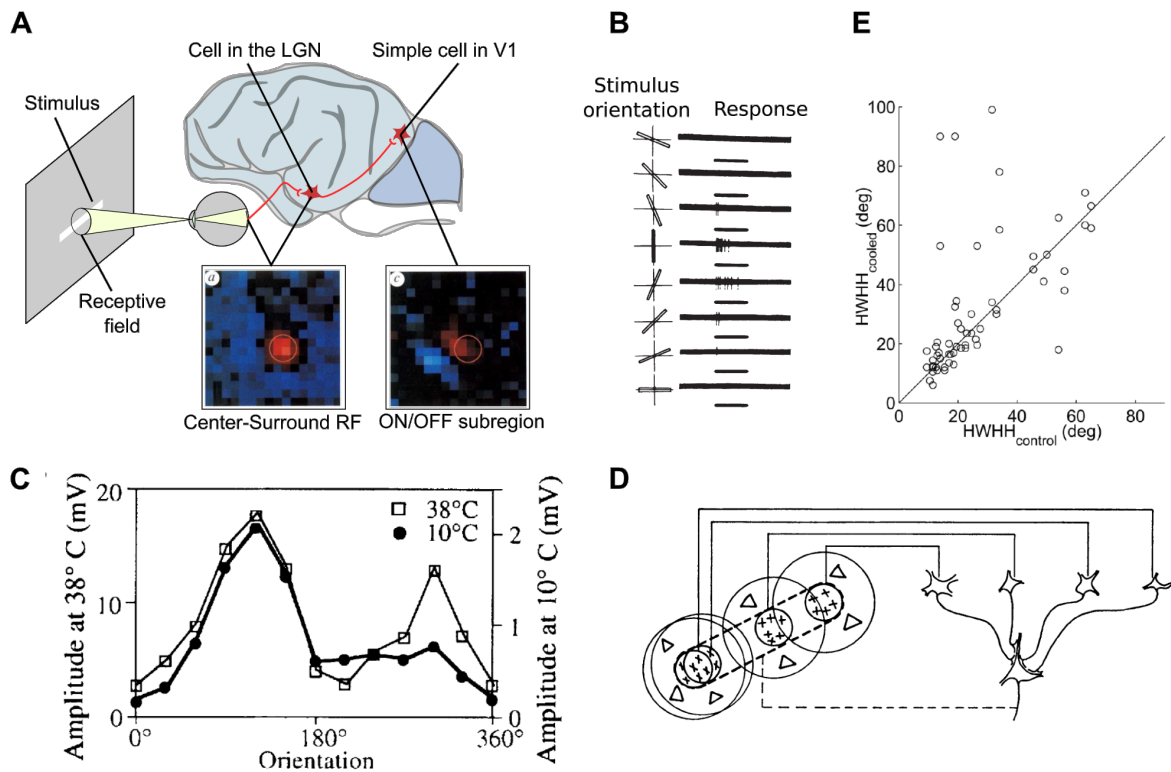


Figure 2.5: **Orientation selectivity in the visual cortex.** **A** Retinal and LGN receptive fields have a center surround structure. Cortical receptive fields are elongated (reprinted with permission from³⁹⁸). **B** The presentation of an elongated stimulus at different angles elicits different responses (reprinted with permission from¹⁹⁶). **C** Orientation tuning in the cortex persists even at low temperatures (reprinted with permission from¹³⁶), consistent with **D**, the Hubel and Wiesel scheme for the generation of orientation selectivity (reprinted with permission from¹⁹⁴). **E** In an independent study, the half width half height of various cells also remained invariant under cooling (reprinted with permission from¹⁵⁸).

recently with optogenetic inhibition in mice²⁷⁹. Furthermore, the receptive fields of the afferents to some extent predicted the preferred orientation of the cortical cells²²⁵. These findings are consistent with the first model of orientation selective responses that David Hubel and Torsten Wiesel proposed¹⁹⁴. They suggested that the convergence of several center-surround receptive fields at different positions in the visual world can produce an elongated receptive field with distinct ON and OFF subregions, as observed in the cortex, **Fig. 2.5D**. The half-width-half-height of the afferent tuning, scattering around the mean value of ≈ 35 deg¹³⁶, is similar to the tuning of cortical cells within the active cortex, **Fig. 2.5E**. Most cells in layer IV, the thalamic input region, are simple cells^{315,329} with small receptive field³⁷⁶ and similar for various stimuli⁵³³.

The spatial organization of orientation selectivity

In the primary visual cortex of primates and carnivora, orientation selectivity is arranged in a pattern across the cortical sheet. Electrode penetration experiments revealed a smooth progression tangentially to the cortex^{39,194,196,197}, see **Fig. 2.6A**. Later, the advent of various imaging techniques, most notably voltage sensitive dyes⁴¹, intrinsic signals^{39,46,50,51,166}, and recently calcium imaging^{207,360,442,519}, revealed a remarkably complex layout, **Fig. 2.6B,C**: Tangentially to the cortex, orientation preference changes smoothly^{194,195}, except for so-called pinwheels,

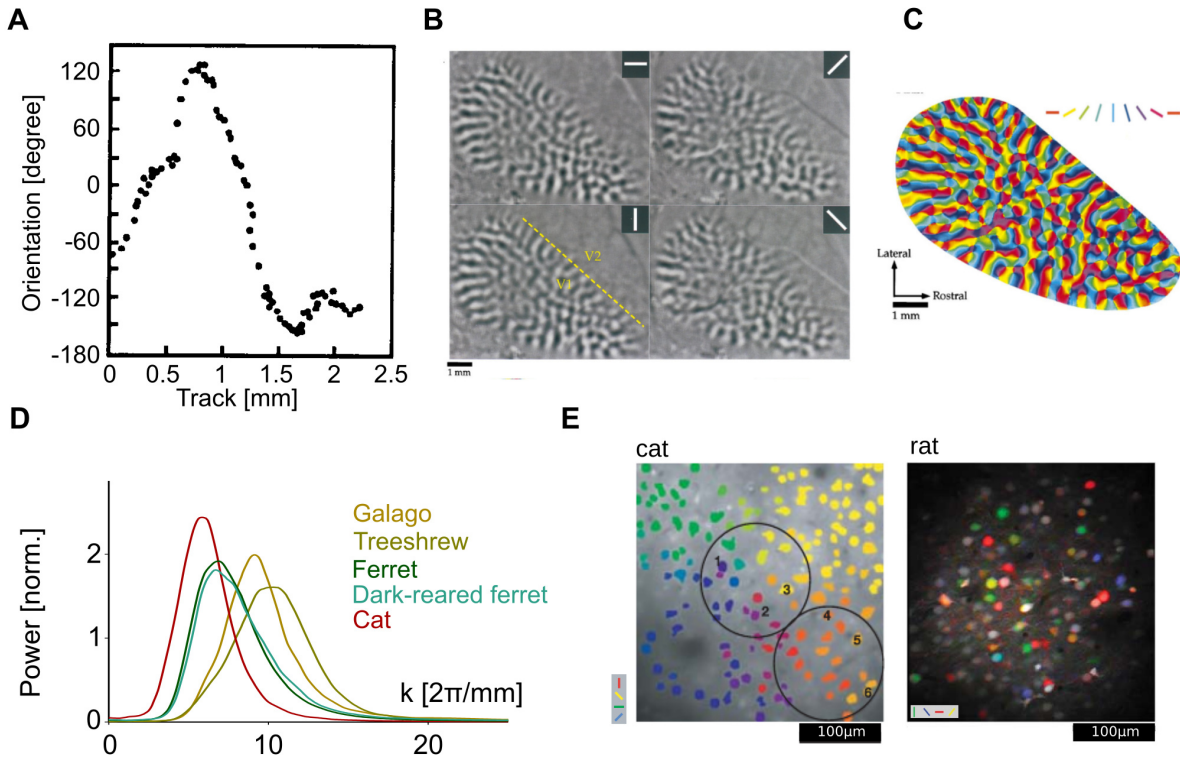


Figure 2.6: **The spatial organization of orientation selectivity.** **A** The preferred orientation of neurons along an electrode penetration (adapted from³⁹). **B** Intrinsic signal imaging reveals a modulation of activity from stimulation with gratings of various orientations (adapted from⁵⁰). Darker regions are more active. **C** Color coded layout of the preferred orientations from the measurement in B (adapted from⁵⁰). **D** The averaged marginal powerspectra for several different species extracted from the data in **chapter 3**. The inverse of the evident length scale is called the column spacing. **E** The smooth progression of preferred orientations including the pinwheels have cellular precision. In rodents, as the rat, the layout of preferred orientations is disorganized (reprinted with permission from^{359,360}).

around which the preferred orientations are arranged radially^{41,46,166,199}. Pinwheels exist in two chiralities, with either clockwise or counterclockwise progression of the preferred orientations. Notably, pinwheels around which every possible orientation is represented more than once have never been reported experimentally and are structurally not stable⁴²⁸. These layouts, interrupted by discrete pinwheels, exist in a variety of mammals as monkeys, cats, ferrets, sheep, treeshrews and humans^{41,76,77,83,190,242,360,482}. Another property of the layout of orientation domains is a typical scale^{41,46,47,50,166,241} that separates regions of neurons preferring similar orientations. Their power spectra are dominated by a typical spatial frequency which sets a natural length scale^{40,356}, **Fig. 2.6D**.

In the primary visual cortex of rodents, electrode penetration experiments since the 1970s suggested a disorganized layout of orientation preference. These experiments were conducted in the visual cortices of various rodents as rat^{159,359,374}, gray squirrel⁴⁸⁹, mouse^{327,349} and rabbits³³⁹. More advanced imaging techniques^{112,458} revealed a true dichotomy in the layouts of visual cortical architecture, **Fig. 2.6E**, between orientation domains and a salt and pepper pattern.

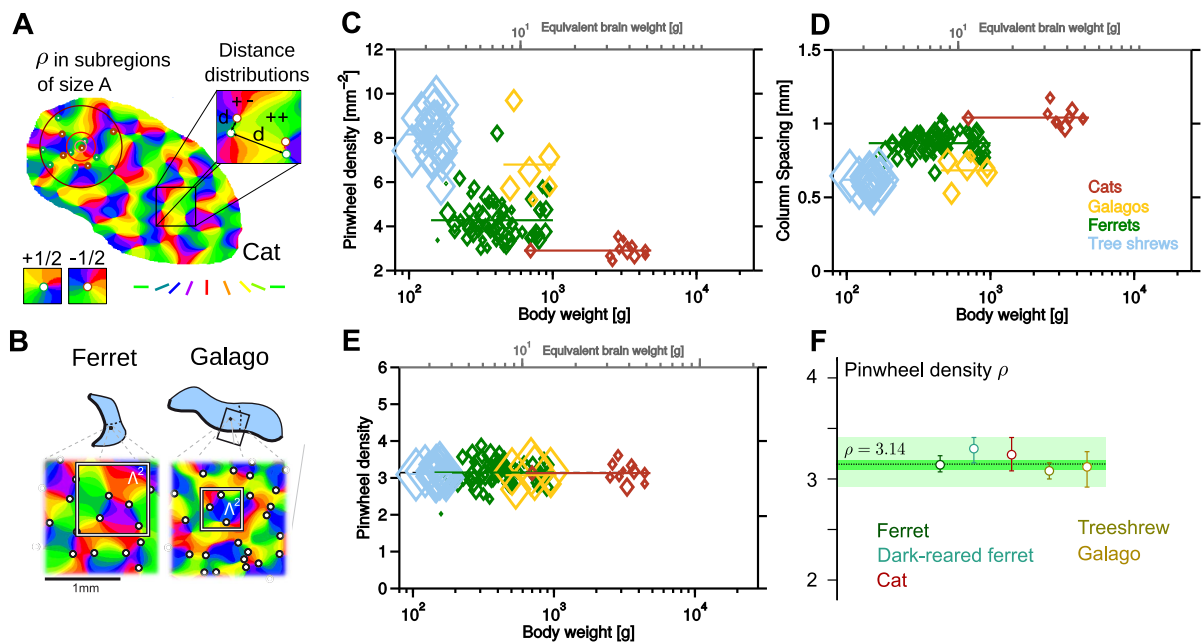


Figure 2.7: **Orientation domains and the common design.** **A** The layout of orientation domains in a cat. Insets illustrate various measures of the spatial arrangement of pinwheels: variability in a subregion of various size and nearest neighbor statistics for pinwheels of different charges. **B** Two more examples for layouts of orientation domains in a ferret and a galago (reprinted with permission from²⁴⁵). **C** The pinwheel density for different individuals of four species: symbol size corresponds to the size of the dataset. **D** The column spacing for the same animals as in C. Note that substantial variations cross individuals and across species. **E** The pinwheel density in natural units (see text) is very similar. **F** The pinwheel density averaged across individuals with bootstrapped 95% confidence intervals for the four species.

The common design

The layout of orientation domains in cats, galagos, ferrets, **Fig. 2.7A,B**, and others is qualitatively similar^{40,41,47,50,166,242,516}. The layout, as described, consists of a smooth progression of domains, interrupted by an irregular array of pinwheel positions. The number of pinwheels per mm², **Fig. 2.7C**, can be very different in various animals. Similarly, the columns spacing, the typical distance separating columns of similar orientation preference, varies substantially, **Fig. 2.7D**. It turns out that expressing the density of pinwheels in natural units, i.e. per column spacing squared, shows a common quantitative layout rule, **Fig. 2.7E,F**. At least for the studied species, belonging to very different clades, there exists a *common design*, characterized by the statistical identity of (i) pinwheel density, (ii) pinwheel density fluctuations as a function of subregion size, and (iii) nearest neighbor distance distributions notably distinct from a random process with the same spatial correlations^{132,242,423,528}. The large degree of phylogenetic separation highlights that these species in all likelihood evolved a layout of orientation domains that adheres to the common design independently. A fundamental question for visual cortical architecture is whether there are constraints that lead to this particular set of spatial layout. This question is at the core of **chapters 3** and **7**.

Orientation domains in the visual world

Convergent evolution of the common design suggests a potential functional benefit of layout of orientation domains with specific layout rules including pinwheels. To assess whether pinwheels could potentially be relevant, we have to address two points: how many pinwheels exist in a typical field of view and how large is the cortical point spread function? (1) For macaques and humans, cortical magnification horizontally follows $M = \frac{\lambda}{\epsilon + \epsilon_0}$ where $\lambda \approx 12$ mm and $\epsilon_0 \approx 1$ deg. For macaque, the column spacing is roughly 0.7 mm, thus the pinwheel density in visual space is

$$\rho \simeq \frac{3.14}{(0.7 \text{ mm})^2} \times M^2 \quad (2.1)$$

$$\simeq \frac{3.14}{(0.7 \text{ mm})^2} \frac{(12 \text{ mm})^2}{(\epsilon + 1 \text{ deg})^2} \simeq \begin{cases} 920/\text{deg}^2, & \text{for center of vision } \epsilon \leq 1 \text{ deg} \\ 920/\epsilon^2, & \text{otherwise} \end{cases} \quad (2.2)$$

(2) In humans, the numbers are slightly different^{12,58,154,205,412,492}, $\lambda = 17.3$ mm and $\epsilon_0 = 0.71$ deg. Close to the fovea, using the equation and column spacing above, there are 1900 pinwheels per deg². In a typical reading distance, there are ≈ 200 pinwheels in the letter o and every pinwheel is responsible for processing a circular region of radius 0.8' (minutes of arc). This number falls exactly in the range of visual acuities of healthy humans, 0.4' – 2.0'. It should be noted that this range is determined geometrically. An aperture with diameter 5 mm at a wavelength of 500 nm has a Rayleigh resolution limit of 0.4', implying that pinwheels might possibly help to sample the visual world at geometrically optimal resolution. (3) In cats (and ferrets²⁶⁶), the situation is more complicated, because their cortical magnification is not a complex logarithmic map³⁰⁴. Along the horizontal meridian, the cortical magnification follows roughly a powerlaw, $M = 2.9\epsilon^{-0.6}$ where the eccentricity along the horizontal meridian is measured in degree (numbers extracted from the figure in⁴⁸⁴), and the cortical magnification in mm_c/deg. Then for cats,

$$\rho = \frac{3.14}{1 \text{ mm}^2} \times M^2 \approx 26.4\epsilon^{-1}, \quad (2.3)$$

so at $\epsilon \approx 10$ deg, the cat has a pinwheel density of about 2.6/deg⁻².

Next, how large is the cortical point-spread function? To answer this question, Ian Nauhaus and colleagues³⁴⁶ measured receptive field size, receptive field scatter and cortical magnification, using 2p-microscopy in layer II/III in a macaque. Independent of the region, around 6 deg to 10 deg of eccentricity they found 1.1 ± 0.2 mm, close to the column spacing. If this measurement is correct, any point in space provides *direct* input to at least 1 mm² of cortex, thereby potentially hiding orientation scotomas associated with the discretization of the pinwheel mosaic and the layout of orientation domains.

The formation of orientation selective circuits

David Hubel and Torsten Wiesel proposed genetic predetermination of the circuits that generate orientation selectivity¹⁹⁵, but this view has several “disadvantages” as Christoph von der Malsburg phrased it³⁰⁵. Notably, it would require an extraordinary amount of genetic information, and the genetically defined circuits would not necessarily be very plastic. Proposing an alternative mechanism, he showed the self-organized emergence of orientation selectivity without depending on a genetically predetermined connectome³⁰⁵.

Experimental studies have shown that visual experience has a crucial influence on cortical circuits^{95,278} and these circuits develop substantially after birth. Notably, the number and density of synapses per volume of tissue increase massively^{94,522}. In cats and ferrets, columnar layouts

emerge around eye opening^{75,76,95,96} and the emergence of ordered layouts coincides with the formation and development of horizontal connections^{50,63,121,516,517}, originating from a diffuse pattern^{63,292}. Activity dependent mechanisms further specify the layout^{62,290}. Without visual input, visual cortical neurons show spontaneous activity, resembling to some extent evoked patterns of activity^{15,483}. The presence thereof seems plausible as major contributor for shaping the structure of neocortical circuits⁴³¹. For instance, the emergence of early horizontal clusters occurs even with dark rearing, or intra-ocular injection of Tetrodotoxin. This lead Katz and Callaway to speculate that spontaneous activity in the cortex might be sufficient to generate the crude clusters, which are then refined by visual inputs²⁴³. Experimental evidence for the robustness of the emergence of orientation selectivity is the emergence of ordered layouts of orientation domains in the rewired ferret auditory cortex⁴³⁴ and their reappearance in the damaged visual cortex⁵³⁹. Orientation selectivity in visual cortical neurons can be observed as soon as kittens open their eyes¹⁹⁵. Its basic spatial organization is innate, but visual input is necessary for maintaining the layout and normal development^{74,95,96}. Once a pattern of orientation preference is formed, its overall organization changes little^{76,160}.

2.5 Interfacing neurons

To construct neuronal circuits *in vitro* we have to communicate effectively, specifically and reliably with populations of living neurons. In other words, we have to use an interface that can couple the domain of digital computers with living circuits of neurons. The combination of tools required for this task became available only recently and is still under active development. We use a state-of-the-art combination of electrical recordings with light sensitive ion channels and genetically encoded calcium indicators to construct such an interface.

Evoking activity

More than 15 years ago, Francis Crick speculated about the ideal way to communicate with neuronal circuits⁹⁷. He wrote that “The ideal signal would be light, probably at an infrared wavelength to allow the light to penetrate far enough. This seems rather far-fetched but it is conceivable that molecular biologists could engineer a particular cell type to be sensitive to light in this way.”. Today, his words appear almost prophetic, but one should note that light sensitive proteins that allow the movement of charges across the membrane were discovered already in 1971 in the purple membrane of *Halobacterium halobium*³⁵⁸. Unfortunately, the potential of this discovery was largely overlooked. The first light controlled activation of neurons was accomplished in 2002 using *Drosophila* photoreceptor genes⁵³⁸, but the use of genetically encoded light sensitive channels remained a technical challenge. A game changer was the discovery of Channelrhodopsins, proteins expressed in the eyespot of the green algae *Chlamydomonas reinhardtii* by Georg Nagel and colleagues³⁴³ and the subsequent transfer of this protein into neurons with a viral vector⁵⁴. Channelrhodopsins can be expressed with a single gene and allowed to screen for mutants with reduced inactivation level and a stronger sustained response in comparison the wildtype, most notably the H134R mutant of ChR2^{282,283} and their biophysics become increasingly well understood⁴²⁴. Today, optogenetics with all its facets became a useful and established tool box for the dissection of neuronal circuits *in vitro* and *in vivo*, in health and disease, and in awake organisms^{248,485}.

With the availability of light sensitized cells, the next challenge is the design of an optical system to generate arbitrary light patterns in a narrow range of wavelength. Various techniques are known and used, most notably sequential scanning and digital micro-mirror devices, however, they are known to be “horribly inefficient”¹⁶¹. We therefore use digital phase-only holography

because it combines several advantages: high spatial resolution, high intensity, efficiency, the correction of distortions in the optical system and the ability for simultaneous parallel illumination in two and even three dimensions^{129,161,317,532,537}. Holographic projection systems have been used in a variety of applications, most notably manipulations in an optical trap^{36,98,269,530}. The first studies using holography in a neuroscientific context appeared less than 10 years ago^{161,295,350,401,537} and holography is currently on the rise as a method to provide precision input into neural circuits^{129,317}.

Recording activity

Arguably, the most established method to record neuronal activity is via extracellular electrodes⁴⁰⁷ with which electrical activity of electrogenic cells can be monitored. While charge is transported electronically in metals, in liquids this transport is typically ionic. Thus, the metal-liquid interface forms an obstacle for charge transport and without electrochemistry, a metal electrode submerged in a liquid behaves like a constant phase element for which $Z \propto \omega^{-n}$ where Z is the impedance and ω is the frequency. For gold and many other metals^{43,324,408,426}, $n \approx 0.9$. The alleged reason for this power-law behavior is a non-smooth and fractal surface topology of the electrode material^{28,234,286}. In the approximation of a capacitive coupling between electrode and liquid, many of the interface properties can be calculated in closed form and the cell-sensor interface for dish electrodes has been studied in one dimension³⁹⁴ as well as in two dimensions^{511,512}. Common models to calculate the electrical properties of a given cell-sensor interface are the point-contact and the area-contact model^{149,228,368,394,512}. Both models represent elements of the membrane, the electrode and the chip either as resistors or capacitors and many properties follow essentially the cable equation. Notably, Weis and Fromherz coined the term “sandwich cable”⁵¹² for the membrane-liquid-metal interface. While recording from electrogenic cells is not a principle problem, one of the key limitations of the type of model is the spatial anisotropy of many cell types, specifically neurons. Most notably, these cells generate substantial longitudinal currents of $\mathcal{O}(\text{nA})$ along the axon during the action potential, and the extracellular waveform of neurons can be dominated by this lateral displacement of charges³. For a recent review on microelectrodes, see⁴⁴⁹.

A more recent technique to record activity of neurons is via calcium indicators. The first recordings of intracellular calcium dynamics were done with a calcium-sensitive bioluminescent protein from the jellyfish *Aequoria victoria*⁴³⁸. Aequorin injected into cells allowed for the first time to record calcium dynamics by measuring changes in bioluminescence¹⁷⁴. Such proteins together with organic dyes like Arzenazo III were used, but turned out to be unstable with respect to the chemical environment, and constrained by very limited accessibility. Pioneering work in the lab of Roger Tsien in 1980s yielded new classes of organic dyes with vastly improved properties^{168,481} that are now used for various studies (for a review see³⁷³). Starting in the 1990s, several different genetically encoded calcium indicator proteins were described and studied³¹¹, some based on fluorescent proteins³³³ and some on luminescent proteins like Aequorin³¹² and also Obelin²⁰⁸. More recently, genetically encoded calcium indicators were engineered using fluorescent proteins like GFP, fused to calmodulin (CaM) and the CaM-interacting M13 peptide³⁴⁴. Specifically constructs derived from circularly permuted green fluorescent protein were the founding fathers of the famous GCaMP family of genetically encoded calcium indicators^{6,81}. To combine optical excitation in the blue light channel, appropriate for Channelrhodopsins, we use a red-shifted calcium indicator, originally derived from mRuby²⁵⁵, fused to calmodulin (CaM) and the CaM-interacting M13 peptide in the construct RCaMP⁷. A recent large-scale structure-guided mutagenesis and neuron-based screening study¹⁰³ optimized this class of constructs and discovered a protein, jRCaMP1a, that is well suited for combination with Chr2.

2.6 Reconstituting visual cortical feature selectivity

In the introduction, I wrote that synthetic neurobiology enables a new and systematic approach to dissect the contributions of feed-forward and recurrent connectomes. What does that mean specifically? We saw that a key component of cortical computations, which have been extensively described, are feature selective responses. For the visual cortex and in the words of David Hubel, they “were the first indication from a single-cell recording that the cortex might be doing something interesting, something that transcended what the geniculate could do.”¹⁹⁸. In particular orientation selectivity, i.e. the selective response to edge-like stimuli of a particular orientation, is a property shared by many mammalian species. We also saw that in carnivores, primates and their close relatives, orientation selectivity is arranged in patterns of iso-orientation domains that exhibit a continuous, roughly repetitive arrangement of preferred orientations^{41,46,50,76,166} and that orientation specificity is at least in part generated by orientation selective feed-forward projections. In the primary visual cortex of rodents, electrode penetration experiments since the 1970s suggested a lack of orderly layouts of orientation domains^{159,327,339}. More advanced imaging techniques^{112,458} revealed a true dichotomy in the layouts of visual cortical architecture between orientation domains and a salt and pepper pattern^{359,360}. The nature of this transition is not understood and might be related to constraints imposed by a small brain^{239,242,245}. To better understand the connection between visual pathway structure and function, specifically the constraints invoked by finite brain size, we first re-engineered the early visual system of the cat and then study how miniaturizing this circuit to the scale of a small animal like a mouse or a eutherian common ancestor, would affect its functionality. The first critical step in this agenda is the engineering of an *in vitro* model of the early visual pathway. We will develop the necessary elements in **chapter 3** before setting up any experiment. The wiring diagram of the feed-forward input connectome can be freely configured and thus varied from highly specific to completely random. In fact, we aim to replicate the evolutionary change of brain size which in the living animal required tens of millions of years within a few hours in the same neural network. Different pathway connectomes can be connected to the same target circuit of living neurons, providing for an internal control. We will discover that shrinking the pathway leads to a loss of orientation specificity of the afferents, and the only possible source of tuning are the recurrent connections. In **chapter 4**, we will construct a *in vitro* surrogate cortex set up with the same cell density and cellular content as the input layer of sensory cortex. We subsequently implement the virtual sensory pathway *in silico* and interface the living neurons *in vitro* with a custom build digital phase-only holographic projection system. Our work culminates in **chapter 5**, where we show the results of our structure-function experiments.

Feed-forward orientation selectivity

“I would remind you that in other data intensive, phenomenological areas—astrophysics and cosmology, for example—when you go off to spend ~\$100 million to collect data, there are theorists on the team for the design of the instruments and observations. You think about what you’re looking for and what framework you’re planning on analyzing it with *before* you collect the data, not after.”

William Bialek³³: “Perspectives on theory at the interface of physics and biology”.

3.1 Content

In this chapter we quantitatively study a state of the art biological model of the afferent visual pathway. This chapter serves two purposes: (1) To develop the framework for the simulation of the afferent visual pathway, (2) to elucidate the relative contributions of feed-forward seeding and activity-dependent refinement in shaping feature selectivity in neuronal circuits.

It has long been controversial whether and how the emergence of ordered layouts of orientation domains can be explained by self-organized activity-dependent development of cortical circuits and to what degree their development is influenced or dominated by subcortical feed-forward constraints. One of the most important hypotheses was recently rearticulated in several prominent studies fostering this controversy and we derive predictions from this model analytically and with mathematical rigor. We confirm these predictions numerically and show that while weak orientation selectivity can emerge, its spatial arrangement is incompatible with experimental data. We find that the layout of visual cortical orientation domains cannot be explained by generic random feed-forward wiring models, and that recurrent connections in the target circuits must have an essential contribution.

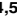

3.2 Citation and original contribution

Manuel Schottdorf*, Wolfgang Keil*, David Coppola, Leonhard E. White, and Fred Wolf: “*Random Wiring, Ganglion Cell Mosaics, and the Functional Architecture of the Visual Cortex*”, PLoS Comput Biol 11(11): e1004602 (2015) [* eq. contribution]⁴²⁸

I conceived and designed the study together with W. Keil and F. Wolf. I analyzed the data, performed the analytical study and the simulations and I generated all figures and all tables. I wrote the manuscript as well as the supplemental information together with all authors.

RESEARCH ARTICLE

Random Wiring, Ganglion Cell Mosaics, and the Functional Architecture of the Visual Cortex

Manuel Schottdorf^{1,2,3,4,5} , Wolfgang Keil^{1,2,3,4,6} * , David Coppola⁷, Leonard E. White⁸, Fred Wolf^{1,2,3,4,9}

1 Max Planck Institute for Dynamics and Self-Organization, Göttingen, Germany, **2** Bernstein Center for Computational Neuroscience, Göttingen, Germany, **3** Bernstein Focus for Neurotechnology, Göttingen, Germany, **4** Faculty of Physics, University of Göttingen, Göttingen, Germany, **5** Institute for Theoretical Physics, University of Würzburg, Würzburg, Germany, **6** Center for Studies in Physics and Biology, The Rockefeller University, New York, New York, United States of America, **7** Department of Biology, Randolph-Macon College, Ashland, Virginia, United States of America, **8** Department of Orthopaedic Surgery, Duke Institute for Brain Sciences, Duke University, Durham, North Carolina, United States of America, **9** Kavli Institute for Theoretical Physics, Santa Barbara, California, United States of America

 These authors contributed equally to this work.

* wkeil@rockefeller.edu



 OPEN ACCESS

Citation: Schottdorf M, Keil W, Coppola D, White LE, Wolf F (2015) Random Wiring, Ganglion Cell Mosaics, and the Functional Architecture of the Visual Cortex. *PLoS Comput Biol* 11(11): e1004602. doi:10.1371/journal.pcbi.1004602

Editor: Geoffrey J Goodhill, The University of Queensland, AUSTRALIA

Received: March 19, 2015

Accepted: October 14, 2015

Published: November 17, 2015

Copyright: © 2015 Schottdorf et al. This is an open access article distributed under the terms of the [Creative Commons Attribution License](https://creativecommons.org/licenses/by/4.0/), which permits unrestricted use, distribution, and reproduction in any medium, provided the original author and source are credited.

Data Availability Statement: A subset of the data is available as Supplemental Material. The full data set used in the present study is available on the neural data sharing platform <http://www.g-node.org/>.

Funding: This work was supported by the Human Frontier Science Program, the German Federal Ministry of Education and Research (BMBF), the German Research Foundation (DFG), the Max Planck Society (MPG), and the Volkswagen Foundation. Grant nos.: CRC 889, BFL 01GQ0921, 01GQ0922, BCCN 01GQ0430, 01GQ1005B, 01GQ07113 and BFNT 01GQ0811. This work was supported in part by the National Science

Abstract

The architecture of iso-orientation domains in the primary visual cortex (V1) of placental carnivores and primates apparently follows species invariant quantitative laws. Dynamical optimization models assuming that neurons coordinate their stimulus preferences throughout cortical circuits linking millions of cells specifically predict these invariants. This might indicate that V1's intrinsic connectome and its functional architecture adhere to a single optimization principle with high precision and robustness. To validate this hypothesis, it is critical to closely examine the quantitative predictions of alternative candidate theories. Random feedforward wiring within the retino-cortical pathway represents a conceptually appealing alternative to dynamical circuit optimization because random dimension-expanding projections are believed to generically exhibit computationally favorable properties for stimulus representations. Here, we ask whether the quantitative invariants of V1 architecture can be explained as a generic emergent property of random wiring. We generalize and examine the stochastic wiring model proposed by Ringach and coworkers, in which iso-orientation domains in the visual cortex arise through random feedforward connections between semi-regular mosaics of retinal ganglion cells (RGCs) and visual cortical neurons. We derive closed-form expressions for cortical receptive fields and domain layouts predicted by the model for perfectly hexagonal RGC mosaics. Including spatial disorder in the RGC positions considerably changes the domain layout properties as a function of disorder parameters such as position scatter and its correlations across the retina. However, independent of parameter choice, we find that the model predictions substantially deviate from the layout laws of iso-orientation domains observed experimentally. Considering random wiring with the currently most realistic model of RGC mosaic layouts, a pairwise interacting point process, the predicted layouts remain distinct from experimental observations and resemble

Foundation, Grant no. NSF PHY11-25915. A Boehringer Ingelheim Fonds PhD fellowship to MS is gratefully acknowledged. The funders had no role in study design, data collection and analysis, decision to publish, or preparation of the manuscript.

Competing Interests: The authors have declared that no competing interests exist.

Gaussian random fields. We conclude that V1 layout invariants are specific quantitative signatures of visual cortical optimization, which cannot be explained by generic random feed-forward-wiring models.

Author Summary

In the primary visual cortex of primates and carnivores, local visual stimulus features such as edge orientation are processed by neurons arranged in arrays of iso-orientation domains. Large-scale comparative studies have uncovered that the spatial layout of these domains and their topological defects follows species-invariant quantitative laws, predicted by models of large-scale circuit self-organization. Here, we ask whether the experimentally observed layout invariants might alternatively emerge as a consequence of random connectivity rules for feedforward projections from a small number of retinal cells to a much larger number of cortical target neurons. In this random wiring framework, the semi-regular and spatially granular arrangement of retinal ganglion cells determines the spatial layout of visual cortical iso-orientation domains—a hypothesis diametrically opposed to cortical large-scale circuit self-organization. Generalizing a prominent model of the early visual pathway, we find that the random wiring framework does not reproduce the experimentally determined layout invariants. Our results demonstrate how comparison between theory and quantitative phenomenological laws obtained from large-scale experimental data can successfully discriminate between competing hypotheses about the design principles of cortical circuits.

Introduction

Processing high-dimensional external stimuli and efficiently communicating their essential features to higher brain areas is a fundamental function of any sensory system. For many sensory modalities, this task is implemented via convergent and divergent neural pathways in which information from a large number of sensors is compressed into a smaller layer of neurons, transmitted, and then re-expanded into a larger neuronal layer. When sensory inputs are sparse, compression of the inputs through random convergent feedforward projections has been shown to retain much of the information present in the stimuli [1–3]. On the other hand, random expanding projections can lead to computationally powerful high-dimensional representations of such compressed signals, which combine separability of the inputs with high signal-to-noise ratio to facilitate downstream readouts [4]. Given these computational benefits, one might expect randomness to be a fundamental wiring principle employed by different sensory systems. The most striking example of a random expansion so far has been observed in the olfactory system of *Drosophila melanogaster*. Kenyon cells in the fly brain’s mushroom body were shown to integrate input from various olfactory glomeruli in combinations that are consistent with purely random choices from the overall distribution of glomerular projections to the mushroom body [5].

What is the role of random projections between neural layers in mammalian sensory systems? Sompolinsky and others have argued that the human visual system, for instance, implements a compression-transmission-expansion strategy [3, 4]. In fact, visual stimulus information is transmitted from about 5 million cone photoreceptors [6, 7] to 1 million retinal ganglion cells (RGCs) [7] and then via the optic nerve to about 1 million lateral geniculate relay cells [8] to on the order

of 100 million neurons in the primary visual cortex (V1) [9, 10]. We note that, while the overall connectivity indeed suggests compression for peripheral retinal regions [11], close to the fovea RGC density is higher than the density of photoreceptors [12, 13].

How much does randomness contribute to shaping the functional architecture of early visual cortical areas? Projections between individual layers of the early mammalian visual pathway are clearly not entirely random. Visual information is mapped visuotopically from the retina to V1 such that neighboring groups of V1 neurons process information from neighboring regions in visual space. Yet, it has long been realized that many features of the spatial progression of receptive fields across V1 layer IV naturally emerge if random feedforward connections from groups of RGC cells to layer IV neurons (via the lateral geniculate nucleus (LGN)) are assumed (see [14] for an early example). The most important of such features is orientation selectivity, i.e. the selective response to edge-like stimuli of a particular orientation. In carnivores, primates and their close relatives, orientation selectivity is arranged in patterns of iso-orientation domains. Iso-orientation domains (orientation domains for short) in V1 exhibit a continuous, roughly repetitive arrangement. A distance in the millimeter range, called the column spacing, separates close-by domains preferring the same orientation. The continuous progression of preferred orientations is interrupted by a system of topological defects, called pinwheel centers, at which neurons selective to the whole complement of stimulus orientations are located in close vicinity [15–20]. These topological defects exhibit two distinct topological charges, indicating that preferred orientations change clockwise or counterclockwise around the defect center [15, 18, 21–23].

More than 25 years ago, Soodak [24, 25] (see also [26]) proposed random wiring between irregularly positioned retinal ganglion cells (RGCs) and layer IV neurons in V1 via the thalamus as a candidate mechanism defining the pattern of iso-orientation domains. According to this statistical wiring hypothesis, a V1 neuron randomly samples feedforward inputs from geniculate projections in the immediate vicinity of its receptive field center (see e.g. [27]). The neuron then is likely to receive the strongest inputs from a central pair of ON/OFF RGCs, forming a so-called RGC dipole [28–30]. In this scheme, one ON and one OFF subregion dominate the receptive field (RF) of the V1 neuron and its response is tuned to the orientation perpendicular to the dipole axis. Thus, the preferred orientation of the neuron in this case is determined by the orientation of the RGC dipole. Consequently, the key prediction of the statistical wiring hypothesis is that the spatial arrangement of ON/OFF RGC cells in the retina essentially determines the spatial layout of orientation preference domains in V1.

Recently, Paik & Ringach showed that the statistical wiring hypothesis—when constructed with a hexagonal grid of RGCs—predicts a periodic orientation domain layout with a hexagonal autocorrelation function [28]. Moreover, it predicts that orientation preference is differently linked to the visuotopic map around pinwheels of positive or negative topological charge [29]. Qualitative signatures of both predictions were reported to be present in experimentally measured patterns [28, 29]. Thus the statistical wiring model has conceptual appeal and is a mechanistically particularly transparent candidate explanation for V1 functional architecture (see however [31, 32]). Does the predictive power of the random wiring hypothesis for the early visual pathway reach beyond this qualitative agreement?

The recent discovery of species-invariant quantitative layout laws for the arrangement of pinwheel centers in tree shrews, galagos and ferrets [23] provides a unique opportunity to address this question. Kaschube et al. demonstrated that in these species, the statistics of pinwheel defect layouts is quantitatively invariant, with potential deviations in geometrical layout parameters of at most a few percent [23]. Specifically, the overall pinwheel density, defined as the average number of defects within the area of one square column spacing Λ^2 was found to be virtually identical. Subsequently, orientation domain layouts from cat V1 were shown to

exhibit pinwheel densities very close to those of the three species previously studied [33]. Additionally, Kaschube et al. found an entire set of local and non-local quantitative pinwheel layout features to be species-invariant (see below). Following [23], we refer to this overall layout of orientation domains as the *common design*.

During mammalian evolution, the common design most likely arose independently in carnivores and euarchontans and potentially even in scandentia [23, 34]. This is suggested by two lines of evidence: (i) The four species in which the common design has been observed so far are widely separated in terms of evolutionary descent, belonging to distinct supra-ordinal clades that split already during basal radiation of placentals [35–42] (Fig 1A, see also [23, 33]). Their last common ancestor was a small shrew-like mammal [40–42] that is unlikely to have possessed a columnar V1 architecture [23, 34]. (ii) Distinct neuronal circuits underlie the generation of orientation selectivity in galago, ferret, tree shrew, and cat (Fig 1B). Tree shrews, for instance, lack orientation selectivity in the input layer IV of V1 [43, 44] and use intracortical circuits to compute contour orientation. In contrast, cats exhibit both, orientation selectivity and organization of selectivity into orientation domains already in layer IV and thus first generate orientation selectivity by thalamo-cortical circuits [45, 46] (see Fig 1B for further differences).

Kaschube et al. used a dynamical self-organization model with long-range suppressive interactions, the long-range interaction model, to explain all features of the common design [23]. The hypothesis that randomness of feedforward connections between the retina/LGN and V1 could explain the common design is conceptually diametrically opposed to large-scale self-organization. In the long-range interaction model, the orientation preference of a neuron is chosen from an, in principle, unlimited afferent repertoire of potential receptive fields. Single neurons dynamically select a particular preferred orientation as a result of large-scale circuit interactions involving millions of other cortical neurons. In the statistical connectivity model, to the contrary, the preferred orientation of a cortical neuron is essentially imposed by the alignment of only one pair of neighboring ON-OFF RGCs, a local process involving in principle not more than 5 cells. Can the invariant layout laws of iso-orientation domains and pinwheels be explained as the generic outcome of a locally stochastic feedforward wiring of the early visual pathway? More generally, do iso-orientation domains and pinwheels in different species adhere to identical layout laws because any mechanism that generates a retinotopic random feedforward circuit will automatically set up a layout that adheres to the common design?

Here, we systemically investigate the arrangements of iso-orientation domains generated by the statistical connectivity model and assess their consistency with the experimentally observed common design invariants. First, we consider the statistical wiring model with perfectly hexagonal mosaics of RGCs, its most tractable form. We derive closed-form expressions for cortical neuron receptive fields and orientation domain layouts resulting from the Moiré interference effect of hexagonal ON and OFF ganglion cell mosaics [28, 29]. The pinwheel density of these pinwheel layouts is $\rho = 2\sqrt{3} \approx 3.46$, substantially larger than experimentally observed. We then characterize the orientation domain layouts resulting from spatially disordered hexagonal mosaics. We find that parameters of RGC position disorder can not be tuned such that the statistical wiring model's layouts match the quantitative invariants of the common design. Next, we examine a generalized class of noisy hexagonal mosaics that allows for spatially correlated disorder of RGC positions. This correlated retinal disorder induces local variations in column spacing, mimicking column spacing heterogeneity in the visual cortex [47, 48]. With these mosaics, Moiré interference persists to larger disorder strength. Pinwheel densities, however, are unaffected by low and intermediate levels of disorder and increase from a lower bound of 3.5 for stronger disorder. Finally, we characterize the statistical connectivity model with RGC

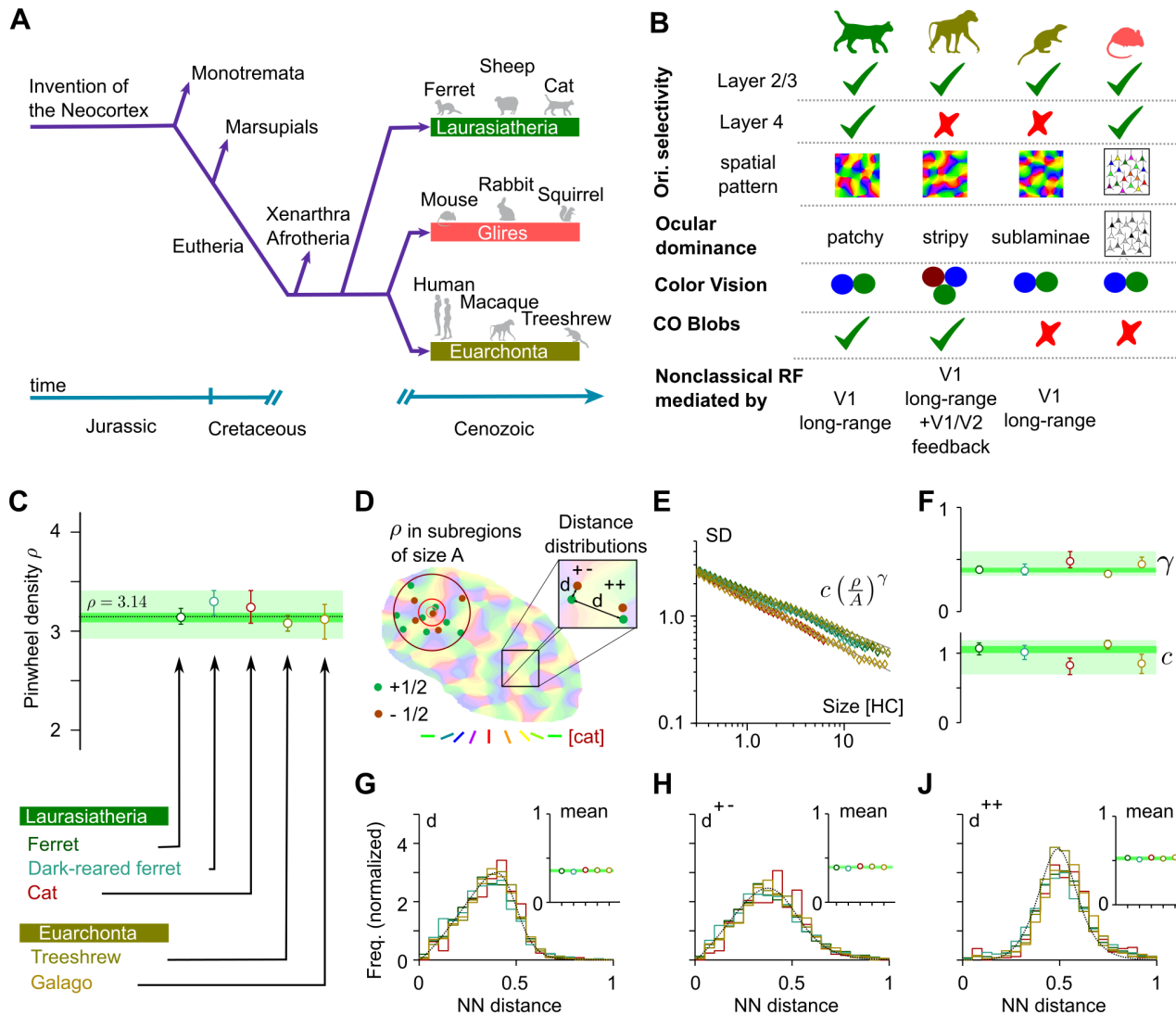


Fig 1. Common laws for the layout of iso-orientation domains in different mammalian species. **A** Phylogenetic relationships and macroevolution of laurasiatheria, euarchonta and glires [33–36, 52, 53]. **B** Key features of the thalamo-cortical pathway for cat [27, 45, 46, 54–65], macaque [66–73], treeshrew [19, 43, 44, 74–76] and mouse [77–81] at the level of retina/LGN and layer IV and II/III of V1. All species show orientation selective neurons in layer II/III, but only cat, ferret, and mouse exhibit orientation selectivity in input layer IV. Ocular dominance domain layouts differs greatly between all four species, macaque is the only species listed possessing trichromatic color vision. Only cat and macaque V1 display cytochrome oxidase blobs. Non-classical receptive fields are mediated by different circuits in cat, tree shrew and macaque. **C** Pinwheel density ρ in ferret (N = 82), dark-reared ferret (N = 21), cat (N = 13), tree shrew (N = 26), and galago (N = 9). Light green shading indicates one-species consistency range, dark green shading indicates common design consistency range (see text). **D** Illustration of the common design layout features, nearest neighbor (NN) distances, and pinwheel density in subregions of varying size. **E, F** Standard deviations (SD) of pinwheel densities as a function of the area A of randomly selected subregions. $SD(A)$ is well described by a power law with variability exponent γ (F, top) and variability coefficient c (F, bottom). **(G–J)** Nearest neighbor distance distributions for pinwheels of arbitrary (G), opposite (H) and equal (J) topological charge in units of the column spacing. Insets indicate species means. All error bars represent 95% confidence intervals of the bootstrap distributions.

doi:10.1371/journal.pcbi.1004602.g001

mosaics generated by Eglen’s pairwise interaction point process (PIPP), the most realistic model for RGC mosaics currently available [31, 32, 49]. The resulting arrangements of iso-orientation domains and pinwheels are identical to those predicted by Gaussian random field models [22, 50, 51]. Their pinwheel densities can be tuned by applying band pass filters of

different bandwidths. However, for all plausible filter shapes, pinwheel densities are substantially larger than experimentally observed.

Our findings demonstrate that the mechanism for seeding patterns of iso-orientation domains described by the stochastic wiring model predicts column arrangements substantially different from the long-range interaction model and distinct from the experimentally observed invariant common design.

Results

A benchmark for models of orientation domains in V1

Our overall goal was to assess whether the layout of orientation domains predicted by the statistical wiring model are consistent with the observed common design invariants. To achieve this, we first sought to establish a benchmark for models of orientation domain layouts in general, to which predicted layouts can then be compared. To this end, we re-analyzed the data set used in [23] using the fully automated method described in the same study. The data set contains optical imaging of intrinsic signal experiments from tree shrew ($N = 26$), ferrets ($N = 82$), dark-reared ferrets ($N = 21$) and galagos ($N = 9$). Because many previous studies used the statistical wiring model with parameters optimized to mimic the early visual pathway of the cat, e.g. [82], we additionally analyzed data from 13 cat V1 hemispheres.

Following [23], we first computed the average pinwheel densities (Fig 1C). Pinwheel densities of all four species, including cat were statistically indistinguishable from each other and statistically indistinguishable from π (dark-reared ferrets excluded)—the value predicted for the average pinwheel density by the long-range interaction model [23]. As a measure of pinwheel position variability, spanning all scales from single hypercolumn to the entire imaged region, we calculated the standard deviation, SD, of pinwheel density estimates in circular subregions of area A (see Fig 1D for an illustration). For all species, the function $SD(A)$ was well described by

$$SD(A) = c \left(\frac{\rho}{A} \right)^\gamma \quad (1)$$

(Fig 1E) with ρ denoting the average pinwheel density. The variability exponents γ and variability coefficients c were similar in all four species (Fig 1F). As a measure of relative pinwheel positioning on the hypercolumn scale, we computed the nearest neighbor (NN) distance statistics for pinwheels of same or opposite topological charge as well as independent of their topological charge (see Fig 1D for an illustration). Distance distributions were unimodal and very similar (Fig 1G–1J). Importantly, the distributions obtained from cat V1 were indistinguishable from the other three species. Mean NN distances, when measured in units of hypercolumns, were statistically indistinguishable (Fig 1G–1J, insets). These findings confirm the results of [23, 33] and show that cat primary visual cortex follows the same quantitative layout laws as in tree shrew, galago and ferret.

From the above results, we extracted two types of consistency ranges that can be used as a benchmark for models of orientation domains in V1. To be consistent with an observed layout of orientation domains, a model's predictions should not be significantly different from experimental observations in at least one species. We thus defined one species consistency ranges spanned by the minimal lower and maximal upper margin of the single species confidence intervals for each parameter. If a model's predicted layout parameters are located outside one or more of the one species consistency ranges, data from every species rejects this model at 5% significance level. This criterion is thus conservative in nature and does not assume that there is in fact one species invariant common design. If such a truly universal common design for orientation domains in fact exists, it would be appropriate to pool data from different species

Table 1. The six orientation domain layout parameters characterizing the common design. Values were calculated with the code provided in the supplemental material and intervals indicate 95% bootstrap confidence intervals. Also shown is the grand average and the associated one species and common design consistency ranges (CR).

	Pinwheel density ρ	NN distance ind. charge	NN distance same charge	NN distance opp. charge	Variab. exp. γ	Variab. coeff. c
Ferret	3.14 [3.06, 3.23]	0.355 [0.347, 0.363]	0.523 [0.521, 0.539]	0.393 [0.383, 0.403]	0.40 [0.37, 0.44]	1.07 [0.97, 1.15]
Dark-reared Ferret	3.30 [3.16, 3.42]	0.346 [0.334, 0.361]	0.511 [0.499, 0.528]	0.381 [0.366, 0.401]	0.39 [0.35, 0.46]	1.02 [0.90, 1.12]
Cat	3.24 [3.06, 3.42]	0.366 [0.352, 0.381]	0.534 [0.519, 0.551]	0.407 [0.388, 0.428]	0.48 [0.41, 0.58]	0.83 [0.68, 0.95]
Treeshrews	3.08 [2.99, 3.16]	0.364 [0.359, 0.370]	0.521 [0.514, 0.528]	0.404 [0.396, 0.411]	0.36 [0.34, 0.39]	1.13 [1.05, 1.19]
Galago	3.12 [2.93, 3.27]	0.363 [0.345, 0.381]	0.536 [0.522, 0.556]	0.396 [0.375, 0.417]	0.45 [0.42, 0.52]	0.85 [0.71, 0.99]
Ensemble Average	3.14	0.359	0.525	0.396	0.40	1.05
Common Design—CR	[3.09, 3.19]	[0.344, 0.357]	[0.506, 0.522]	[0.387, 0.399]	[0.37, 0.42]	[0.99, 1.11]
One Species—CR	[2.93, 3.42]	[0.334, 0.381]	[0.499, 0.556]	[0.366, 0.428]	[0.34, 0.58]	[0.68, 1.19]

doi:10.1371/journal.pcbi.1004602.t001

and to consider the more precisely defined confidence intervals of the grand average statistics as the relevant benchmark. To perform this more demanding test of model viability, we also defined common design consistency ranges as the 95% bootstrap confidence intervals obtained from the whole data set. If the layout parameters predicted by a model are within all of the common design consistency ranges, the model offers a quantitative account of the bona fide universal common design. If one or more layout parameters have predicted values outside the common design consistency ranges the model is inconsistent with the common design. With the current data set, if a model is common design consistent, it is also one species consistent. One species (common design) consistency ranges are shaded in light (dark) green in Fig 1C, 1E–1J and summarized in Table 1. The tests of model viability defined above are most simply performed if the parameter values predicted by a model are determined exactly or with a numerical error that is much smaller than the empirical uncertainties. For models that can be solved accurately numerically, this can in principle always be achieved by a sufficiently large sample size of simulations. In the following, through analytical and numerical calculations, we will perform a comprehensive search through the statistical wiring model’s parameter space to identify regimes in which the model is one species consistent or common design consistent.

The statistical wiring model

The statistical wiring model formalizes the hypothesis that the spatial progression of orientation preference domains arises from the spatial distribution of RGC receptive fields on the retina via feedforward wiring. Fig 2A shows a simplified schematics of the early visual pathway in the cat [27, 45, 46, 54–65], from the retina to layer IV of V1. A stimulus is focussed onto the retina through the cornea and lens, is sampled by RGC RFs and transmitted to the LGN. LGN neurons project to stellate cells in layer IV of V1, whose responses are orientation tuned. Orientation tuning varies smoothly across the cortical surface.

In the model, RGCs are assumed to be mono-synaptically connected one-to-one to relay cells in the LGN. Thus, the receptive fields of LGN neurons are similar to those of RGCs and the spatial arrangement of ON/OFF receptive fields of relay cells in the LGN mirrors the RGC receptive field mosaic. Neurons in the model visual cortex linearly sum inputs of LGN neurons

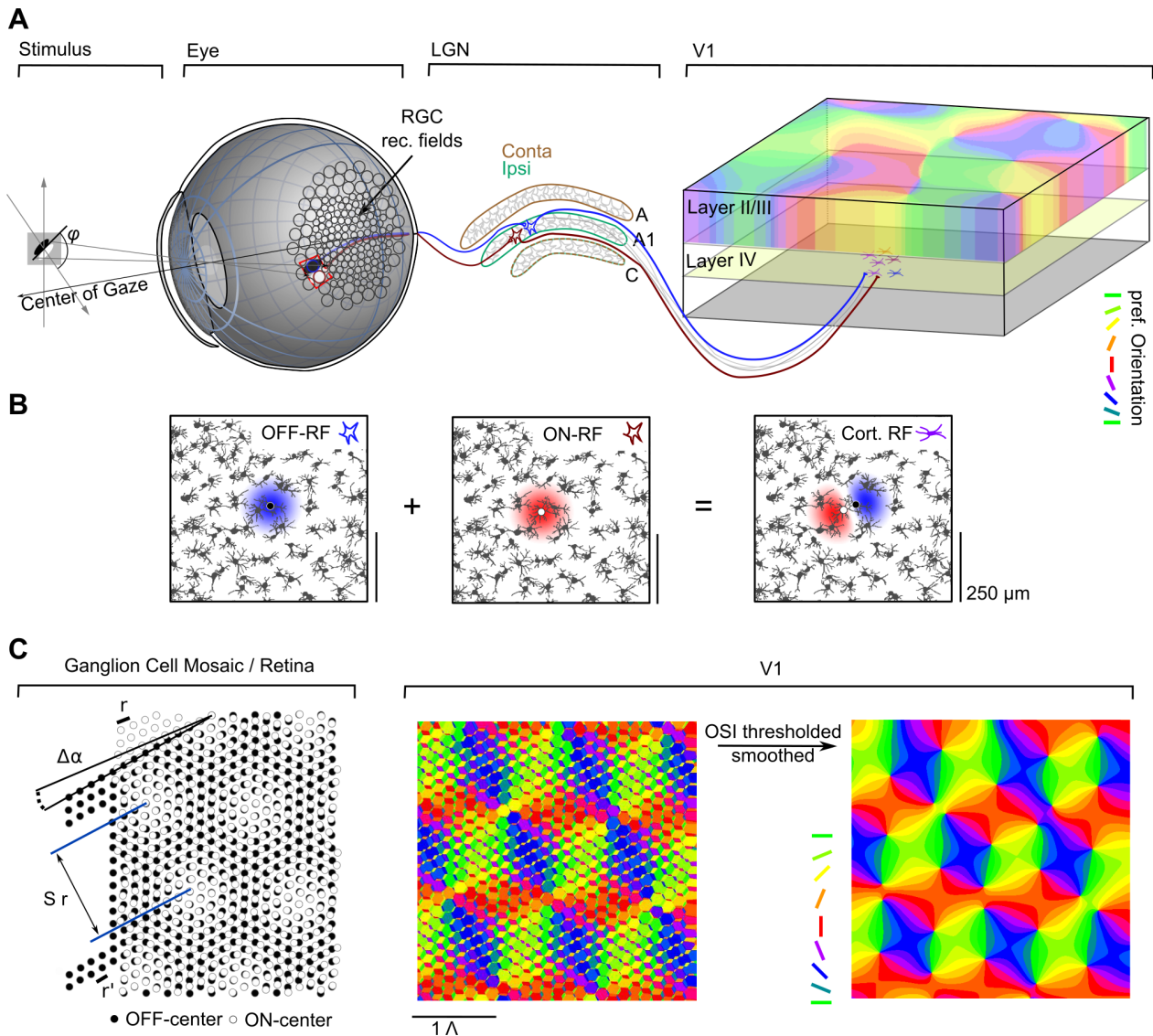


Fig 2. Early visual pathway, RGC dipoles, and Moiré interference of RGC mosaics. **A** Schematic illustration of the early visual pathway following the organization in the cat (see text for details). **B** Orientation selective receptive fields can arise through summation of two adjacent rotationally symmetric retinal/LGN receptive fields (RGC dipole). Shown are ON and OFF center mosaics from cat retina [26]. Colors indicate ON (red) and OFF (blue) regions of a receptive field in the LGN (left and middle) and V1 (right). For illustration, the RGC mosaic is overlaid and the two RGCs whose RFs are summed are shown as black and white dots. **C** Left: Moiré interference between a hexagonal ON (white dots) and OFF (black dots) RGC lattice with relative orientation $\Delta\alpha$ and lattice constants r and r' (black bars) creates a Moiré pattern with lattice constant $S \cdot r$. Middle: sampling from this RGC mosaic as described in B (and text) yields a periodic orientation preference pattern through Moiré interference. Right: Model layout predicted by the statistical wiring model, obtained by thresholding and smoothing the pattern in the middle (see text).

doi:10.1371/journal.pcbi.1004602.g002

(Fig 2B). Their spatial receptive fields and orientation preferences are assumed to solely depend on the spatial arrangement of their afferent inputs. V1 neurons are assumed to receive dominant inputs from a small number of geniculocortical axons. Most of them sample from a single pair of ON/OFF RGCs, a so-called RGC dipole (Fig 2B). The neuron's receptive field then consists of one ON and one OFF subregion and its response to edge-like stimuli is tuned to an edge orientation orthogonal to the RGC-dipole vector (Fig 2B). Within a mosaic of ON and OFF center RGCs, many such dipoles are present and the spatial arrangement of dipoles on the

retina determines how tuning properties, e.g. the preferred orientation, change along a two-dimensional sheet parallel to the layers of the visual cortex. If ON and OFF RGCs are positioned on hexagonal lattices, the model predicts that a hexagonal pattern of orientation preference can arise through Moiré interference (MI) between the two lattices (Fig 2C).

Following [28, 83], we model RGC receptive fields using a Gaussian function $\text{GRF}_j(\mathbf{x})$ of width σ_r , localized at the center position \mathbf{x}_j :

$$\text{GRF}_j(\mathbf{x}) = \pm \exp\left(-\frac{(\mathbf{x}_j - \mathbf{x})^2}{2\sigma_r^2}\right), \tag{2}$$

where \mathbf{x} indicates position in retinal space. All subsequent results remain qualitatively unchanged if a biologically more realistic difference-of-Gaussians (see [84]) is used. A plus or minus sign in Eq (2) indicates an ON or OFF center cell, respectively. The receptive field RF_y of a visual cortical neuron at position \mathbf{y} in the two-dimensional cortical sheet is obtained by summing several ganglion cell receptive fields with positive synaptic weights w_j :

$$\text{RF}_y(\mathbf{x}) = \sum_j w_j(\mathbf{y}) \text{GRF}_j(\mathbf{x}). \tag{3}$$

The synaptic weights are chosen as

$$w_j(\mathbf{y}) = \exp\left(-\frac{(\mathbf{x}_j - \mathbf{y})^2}{2\sigma_s^2}\right). \tag{4}$$

The parameter σ_s sets the range from which a V1 neuron receives retino-thalamic inputs, \mathbf{x}_j denotes the center of an RGC receptive field. According to Eq (3) the spatial distribution of RGC locations determines how response properties change across cortex. For σ_s smaller than the lattice spacing, each cortical cell receives substantial input only from a very small number of ganglion cells. Inputs received by most cortical cells are dominated by one ON and one OFF center RGCs (see inset in Fig 2A), forming an RGC dipole. The small σ_s regime is thus generally referred to as the dipole approximation of the model. While the dipole approximation leads to the robust emergence of simple-cell receptive fields with one (ON, OFF) or two (ON-OFF) subfields in the model V1 layer, it is worth mentioning that simple cells in cat and macaque monkey sometimes have more than two aligned, regularly spaced subfields (e.g. ON-OFF-ON or OFF-ON-OFF) (see [85, 86]). In the dipole approximation of the statistical wiring model, such simple-cell RFs almost never occur. While the model as defined above implements a deterministic wiring scheme, it represents a simplification of a more detailed formulation of the statistical connectivity model proposed in [83]. In the more detailed formulation, the synaptic weights between the cortical units and the retina/LGN are chosen at random from a Gaussian distribution with the shape given in Eq (4). Ringach established in [83] that the spatial structure of the resulting domain layouts for the detailed and simplified model are nearly identical. We therefore refer to the model as statistical connectivity model.

We used the linear response assumption [87, 88] to determine cortical stimulus responses. A response R of a cortical neuron is modeled by the inner product between its receptive field $\text{RF}_y(\mathbf{x})$ and the stimulus, in our case an illumination pattern $L(\mathbf{x})$:

$$R_y = \int d^2\mathbf{x} \text{RF}_y(\mathbf{x}) L(\mathbf{x}). \tag{5}$$

Because R_y can become negative, a firing rate f of the cortical neuron is then defined through a static nonlinearity, e.g. half-wave rectification [87]. For the purposes of the present study, this

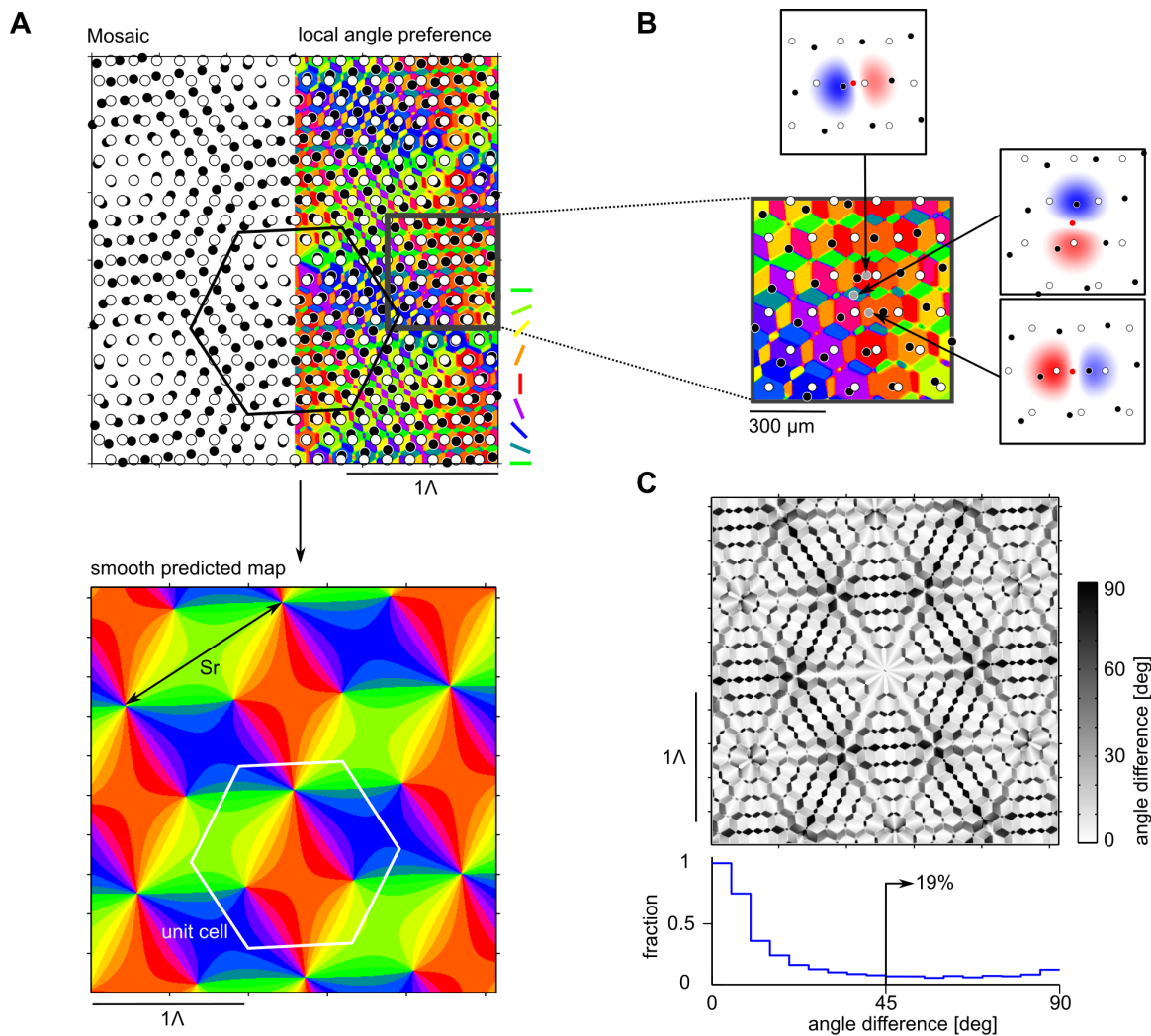


Fig 3. Receptive fields and iso-orientation domains in the Moiré interference model. **A** Top: Moiré interference between two RGC mosaic (left) with ON and OFF center RGCs illustrated as white and black dots. The corresponding orientation domain layout (Eq (52) in Methods) is shown on the right with the mosaic overlaid. Bottom: low frequency contribution of the domain layout. Black arrows indicate the lattice constant $S \cdot r$ of the Moiré pattern, white hexagon indicates the unit cell of the domain layout. **B** Inset of the layout shown in A with RFs of three closely spaced neurons. Scale bar indicates distance on the retina. **C** Circular distance (see text) between the preferred angles of unfiltered and low-pass filtered domain layouts shown in A top and bottom. Bottom: Histogram of differences in preferred angles. Model parameters: $\sigma_r = 70 \mu\text{m}$, $\sigma_s = 20 \mu\text{m}$, lattice constants $r = r' = 170 \mu\text{m}$, and a relative angle $\Delta\alpha = 7^\circ$ leading to a scaling factor of $S = 8.2$ (Eq (10)), as proposed in [28, 29].

doi:10.1371/journal.pcbi.1004602.g003

nonlinearity can be neglected assuming that it does not alter core properties of the receptive field such as orientation preference and spatial frequency preference [82, 83].

We derived close-form expressions for the pattern of cortical receptive fields across V1 that arises through Moiré interference in the case that ON and OFF center cells are localized on perfectly hexagonal lattices with different lattice constants r and r' and relative angle α between the lattices (see Fig 2C). Detailed derivations are provided in Methods, along with closed-form expressions for receptive fields, the frequency response of orientation selective neurons, and their spatial organization.

Fig 3A depicts the analytically calculated orientation preference pattern generated through Moiré interference between two hexagonal ON/OFF RGC mosaics. Iso-orientation domains

are organized in fine-grained parcellations on small scales and repeat in a hexagonal pattern on a larger scale Λ . The larger scale is the predicted column spacing of the orientation domain layout (see [Methods](#)), and model parameters are chosen such that $\Lambda \approx 1\text{mm}$ as experimentally measured (see [Methods](#) and [28, 29] for details). The scale of the small parcels therefore is $< 200\mu\text{m}$. A magnified view of a small region of the domain layout is provided in [Fig 3B](#) along with three analytically determined cortical receptive fields at closely spaced locations roughly $100\mu\text{m}$ apart from each other. These receptive fields highlight that individual parcels contain highly tuned units with vastly different preferred orientations. This means that orientation preference changes abruptly on scales $< 200\mu\text{m}$ in the predicted patterns. Clearly, these features distinguish the obtained pattern of orientation preferences from the experimentally observed domain layouts. While orientation selectivity in V1 exhibits some small scale scatter within orientation domains [89, 90], two-photon imaging suggests that orientation preferences progresses rather smoothly across the cortical surface [65, 78].

Orientation preference maps from crystalline RGC mosaics

Paik & Ringach implicitly assumed that random feedforward wiring from the retina/LGN to V1 effectively results in a *smoothed* version of the dipole layout (see [Fig 2C](#)). To extract this smooth pattern of orientation preferences from the statistical connectivity model, they adopted a two-step procedure to suppress the small-scale variation in the Moiré interference pattern: First, locations with orientation selectivity index (OSI) larger than a threshold value are determined [28, 29, 82, 83]. Second, the orientation selectivity of all other location is set to zero. The resulting layout is then filtered with a Gaussian lowpass filter resulting in continuous and smooth array of iso-orientation domains [28, 29, 82].

We find that the thresholding/smoothing procedure effectively extracts the dominant lowest spatial frequency Fourier components of the Moiré interference pattern. As derived in [Methods](#), the lowest spatial frequency contribution to the Moiré interference pattern consists of six Fourier modes with identical amplitude and wave number

$$k_c = \frac{4\pi}{\sqrt{3}rr'} \sqrt{r^2 + r'^2 - 2rr' \cos(\Delta\alpha)}, \tag{6}$$

Here, r, r' denote to the lattice constants and $\Delta\alpha$ the angle between the hexagonal ON/OFF lattices ([Fig 2C](#)). The smooth orientation domain layout resulting from Moiré interference can therefore be summarized in a complex-valued field $z(\mathbf{y})$ composed of six planar waves with wave numbers \mathbf{k}_j and fixed phase factors u_j ,

$$z(\mathbf{y}) = \sum_{j=1}^6 \exp(i\mathbf{k}_j \cdot \mathbf{y}) \cdot u_j. \tag{7}$$

The pattern of preferred orientations across the cortical coordinate \mathbf{y} is given by the phase of this complex-valued field as,

$$\vartheta_{\text{pref}}(\mathbf{y}) = \frac{1}{2} \arg(z(\mathbf{y})). \tag{8}$$

[Fig 3A](#) (bottom) depicts $\vartheta_{\text{pref}}(\mathbf{y})$ as analytically determined. The pattern of pinwheels and iso-orientation domains is organized into a smooth hexagonal crystalline array. Interestingly, an identical layout of iso-orientation domains was constructed by Braitenberg et al. [91] based on an the idea that orientation preference is generated by discrete centers of inhibition in V1. It was also found by Reich et al. to solve a symmetry defined class of models for the self-organization of iso-orientation domains [92, 93]. [Fig 3C](#) shows the differences in preferred angle

between the unfiltered domain layout of the Moiré interference pattern and its low frequency contribution, together with a histogram of the differences. With $\Delta(\mathbf{x}) = \vartheta_1(\mathbf{x}) - \vartheta_{\text{pref}}(\mathbf{x})$, the difference $d(\mathbf{x})$ between the two preferred angles is defined as $d(\mathbf{x}) = \frac{1}{2} \text{abs}(\arg(e^{2i\Delta(\mathbf{x})}))$. The bimodal shape of the histogram indicates that the orientation preference of a large fraction of cortical locations differs substantially between unfiltered and smoothed layout. Roughly one fifth of all locations exhibit differences of orientation preferences of more than 45° .

To compare our mathematical expression for the column spacing of the orientation domain layout to previous results, Eq (6) can be rewritten by introducing a parameter β representing the detuning between the two lattice constants in units of the lattice constant $r' \rightarrow (1 + \beta)r$. The expression for the column spacing becomes

$$\Lambda_c \equiv \frac{2\pi}{k_c} = \frac{\sqrt{3}}{2} \cdot S \cdot r, \tag{9}$$

where S is the distance between two vertices of the Moiré pattern in units of r , called the scaling factor [94–96]

$$S = \frac{1 + \beta}{\sqrt{\beta^2 + 2(1 - \cos(\Delta\alpha))(1 + \beta)}}. \tag{10}$$

The difference between $S \cdot r$ and Λ_c is displayed in Fig 3A (bottom). Eqs (9) and (10) are identical to previous results for the spacing of hexagonal Moiré patterns derived via geometrical considerations [95, 96].

Using these explicit expressions for the iso-orientation domain layout and its column spacing Λ_c , we first evaluated the central quantity of the common design—the pinwheel density, i.e. the number of pinwheels per unit area Λ_c^2 . Within each unit cell of area $A = \frac{\sqrt{3}}{2} (S \cdot r)^2$, there is one “double pinwheel” of topological charge 1, around which each orientation is represented twice, and two pinwheels of topological charge $\pm \frac{1}{2}$. With $\Lambda_c^2 = \frac{3}{4} (S \cdot r)^2$ and counting the pinwheel with charge 1 as two pinwheels (see below), the pinwheel density is

$$\rho = (2 + 2 \cdot 1) \cdot \frac{\Lambda_c^2}{A} = 2\sqrt{3} \approx 3.46. \tag{11}$$

Notably, this value is outside of both, the common design consistency range and the single species consistency range for the experimentally measured pinwheel densities (cf. Table 1). Since the statistical connectivity model for perfectly hexagonal RGC mosaics results in a periodic array of pinwheels, all three nearest neighbor distance distributions of pinwheels are sharply peaked (see also Supplementary Material of [23]) and, thus, in disagreement with the distributions experimentally observed (cf. Fig 1).

We compared these analytical results to numerically evaluated Moiré interference patterns (Fig 4). The fine-grained layouts of numerically and analytically obtained unfiltered layouts are almost indistinguishable (cross-correlation coeff. 0.9, Fig 4A top). This confirms the analytical treatment and indicates accuracy of the numerical implementation. A hierarchy of discrete spatial frequency contributions is apparent in amplitude spectra of both domain layouts (Fig 4A (bottom)). The peaks at larger spatial frequencies in Fig 4A and 4B are localized at $\sqrt{3}k_c$ as analytically predicted (see Methods).

To numerically generate the smoothed array of orientation domains, the layout in Fig 4A (top) was thresholded ($\text{OSI} > 0.25$, see Methods) and subsequently smoothed with a Gaussian lowpass filter (Fig 4B top) [28, 82]. In general, strongly tuned locations are those exactly between ON-OFF RGC pairs (Fig 4B, inset). Fig 4C depicts the crystalline pinwheel

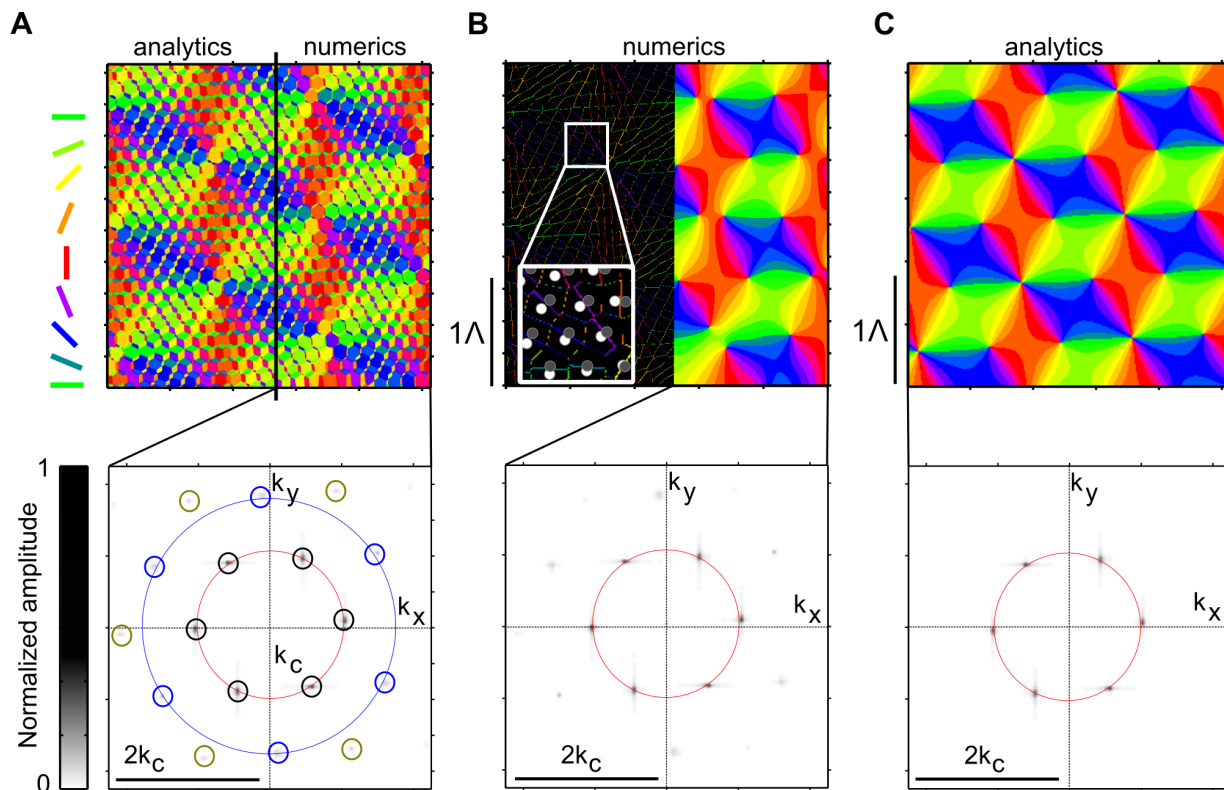


Fig 4. Comparison of analytically and numerically obtained solutions of the Moiré interference model. **A** Top: unfiltered Moiré interference patterns. Black line separates analytical (left, see Eq (52)) from numerical result (right). Bottom: amplitude spectrum of numerically obtained Moiré interference patterns. Red circle marks k_c (cf. Eq (6)), blue circle indicates $\sqrt{3}k_c$. Note the high frequency contributions, indicated by the small yellow circles. **B** Top: Numerically obtained Moiré interference pattern after thresholding for cells with OSI > 0.25 (left, see Methods for the OSI definition used) and subsequent smoothing (right, see text). Inset shows a magnified region of the OSI-filtered domain layout together with the RGC mosaic from which the neurons sample. Bottom: amplitude spectrum of the numerically obtained thresholded and smoothed layout. Red circle indicates k_c (cf. Eq (6)). **C** Orientation domain layout (top) and amplitude spectrum (bottom) obtained by calculating the lowest spatial frequency contributions of the layout in A (Eq (8)). All model parameters as in Fig 3.

doi:10.1371/journal.pcbi.1004602.g004

arrangement of the analytically calculated smoothed layout (Eq (8)) as well as the six dominant low frequency Moiré modes in the amplitude spectrum. While the numerically obtained layouts and its analytical approximation are similar (cross-correlation coeff. 0.6), one major difference can be observed: the pinwheel of topological charge 1 is replaced by two pinwheels of topological charge $\frac{1}{2}$ in the numerically obtained layouts, along with subtle deformations of adjacent orientation domains (compare Fig 4B and 4C). To see why this is the case, we note that the pinwheel with charge 1 in the analytically calculated pattern (Eq (8)) arises from a zero of the field $z(\mathbf{x})$ (Eq (7)) with multiplicity two. A phase singularity of a complex-valued field arising from a zero with multiplicity $N > 1$ is structurally unstable and unfolds upon generic infinitesimal perturbations into N closely spaced singularities of multiplicity one [97]. The numerical procedure of discretizing V1 unit positions on a numerical grid, OSI thresholding, and smoothing realizes such a perturbation and this explains why in the numerical solutions the pinwheel of charge 1 unfolds into two adjacent pinwheels of charge $\frac{1}{2}$.

The impact of spatially uncorrelated disorder in RGC position

So far, we have studied the idealized situation of iso-orientation domains induced by perfectly ordered hexagonal RGC mosaics. RGC mosaics in the eye, however, are not perfectly hexagonal

but exhibit substantial spatial irregularity [26, 98]. Therefore, we next turned to numerically investigate the statistical connectivity model with hexagonal RGC mosaics subject to Gaussian disorder in RGC position as previously described [28, 29]. The effect of ganglion cells displaced by Gaussian distributed offsets with standard deviation $\sigma = \eta \cdot r$ is illustrated in Fig 5. The parameter r is the lattice constant and η is the disorder strength. Fig 5 shows the unfiltered orientation domain layout (far left), the layout thresholded for cells with an OSI > 0.25 (left), the smoothed thresholded layout (right) as well as its amplitude spectrum (far right), numerically obtained for $\eta = 0.12$. As in the perfectly ordered case, the unfiltered layout of the noisy Moiré interference model exhibits a substantial scatter of orientation preferences across small scales. For a disorder strength of $\eta = 0.12$ (Fig 5A), the domain layout is still dominated by the six lowest spatial frequency Moiré modes also present in the perfectly ordered system. For a disorder strength of $\eta = 0.3$ (Fig 5B), the amplitude spectrum (Fig 5B, far right) lacks any indication of these Moiré modes indicating that Moiré interference no longer takes place. As a consequence the resulting layouts of iso-orientation domains lack a typical column spacing.

To characterize the model orientation domain arrangements, we first calculate amplitude spectra for both, unfiltered and smoothed layouts (Fig 5A and 5B),

$$|\mathcal{R}(\mathbf{k})| = \left| \int d^2\mathbf{x} z(\mathbf{x}) e^{i\mathbf{k}\mathbf{x}} \right| \text{ where } z(\mathbf{x}) = e^{2i\vartheta_{\text{pref}}(\mathbf{x})}. \quad (12)$$

Normalizing and radially averaging yields the so-called marginal amplitude spectrum (Fig 5C and 5D),

$$f(k) = \frac{\int_0^{2\pi} d\vartheta |\mathcal{R}(k \cos(\vartheta), k \sin(\vartheta))|}{\max_k \int_0^{2\pi} d\vartheta |\mathcal{R}(k \cos(\vartheta), k \sin(\vartheta))|}. \quad (13)$$

The sharp peak at k_c corresponds to the dominant Moiré mode indicating that orientation domain layouts exhibit a typical column spacing. For increasing disorder, the relative levels of peak height to background decreases while the peak width remains small. As expected, marginal amplitude spectra of unfiltered and the smoothed layout mainly differ in the strength of background components. The flat amplitude spectrum of the unfiltered iso-orientation domain layouts for large disorder strength is transformed into a Gaussian amplitude spectrum by the lowpass filtering. Based on this assessment, the disorder strength η has to be smaller than 0.3 to ensure that layouts exhibit a typical spacing between adjacent iso-orientation domains.

We next systematically evaluated the core layout parameters of the common design—pinwheel density and pinwheel nearest neighbor distance distributions for the statistical wiring model with disordered hexagonal RGC mosaics. To compare the model predictions with experiments, we estimated the column spacing of the model orientation domain layouts as well as pinwheel layout parameters using the exact same methods that we applied to the experimental data (see Methods). For weak disorder, column spacing estimates closely match the theoretical prediction Λ_c (Fig 6A), confirming the accuracy of the wavelet method. For disorder strengths larger than 0.12, Moiré modes are no longer the dominant spatial frequency contribution in the model layouts and the estimated column spacing increases with disorder strength.

Having estimated the column spacing, we analyzed model orientation domain layouts with respect to the common design parameters (Fig 6B–6D). As expected, pinwheel densities approach the analytical predicted value of $2\sqrt{3}$ for weak disorder (Fig 6B) and increase with increasing disorder strength. This increase is largely caused by the increase in the estimated column spacing (Fig 6A) and does not involve a massive generation of additional pinwheels for larger disorder strength. We next calculated the standard deviation of pinwheel densities as a function of the area A of randomly selected subregions of the iso-orientation domain layouts.

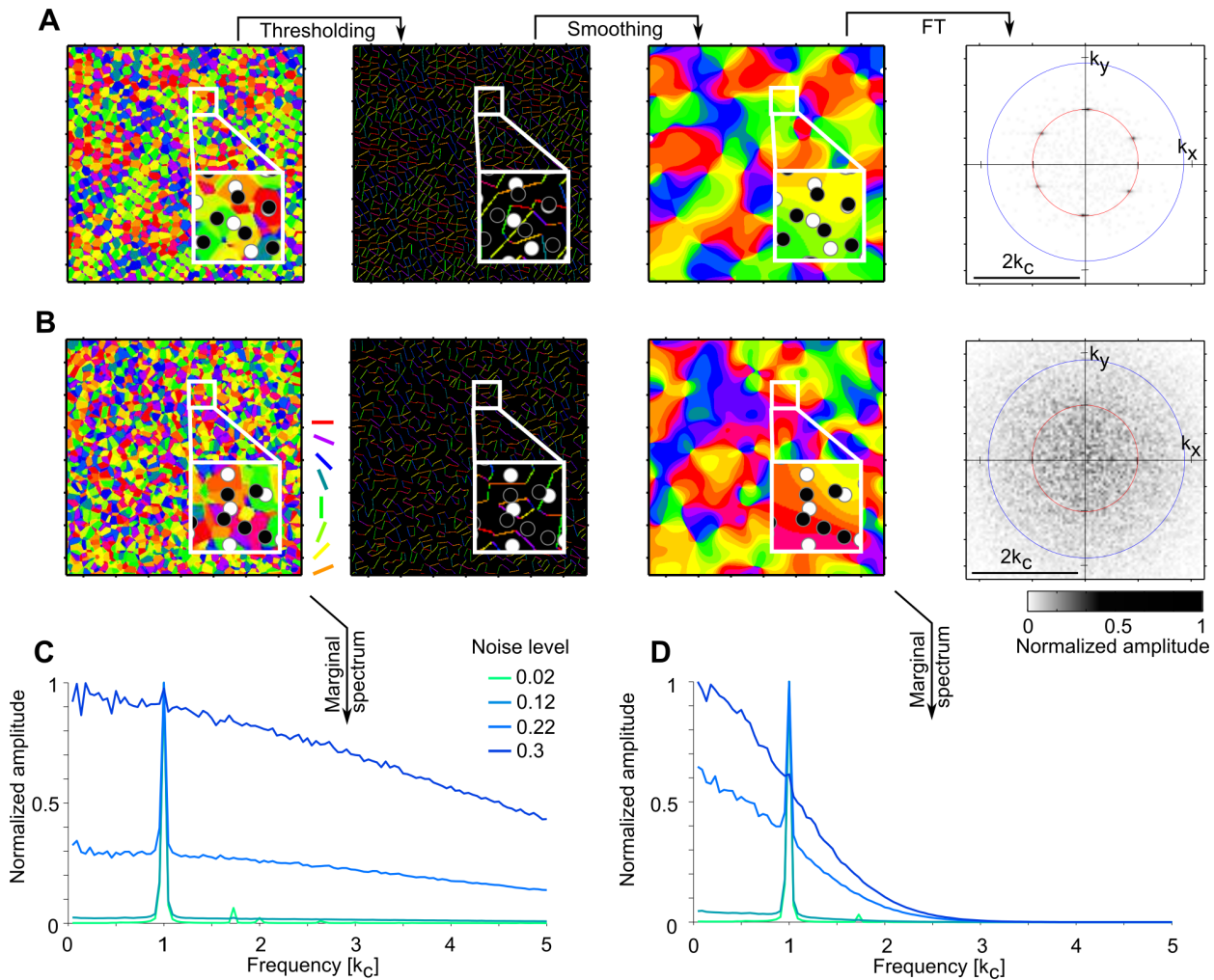


Fig 5. Spatially uncorrelated position disorder in hexagonal RGC mosaics induce broadband noise in iso-orientation domain layouts. A Numerically calculated orientation domain layouts with disorder strength $\eta = 0.12$. From left to right: Moiré interference pattern, filtered Moiré interference pattern ($OSI > 0.25$), smooth layout and the smoothed layout's amplitude spectrum. Insets show magnified regions. Circles in the amplitude spectrum mark k_c (red) and $\sqrt{3}k_c$ (blue) (cf. Eq (6)). **B** As A but for a higher disorder strength $\eta = 0.30$. **C** Radially averaged normalized amplitude spectra of the orientation domain layouts for different disorder strengths. The fluctuation strength is color coded (legend). x-axis is given in units of k_c (cf. Eq (6)). **D** As C but for the smoothed layouts. All other model parameters as in Fig 3.

doi:10.1371/journal.pcbi.1004602.g005

Generally, the standard deviation's decay with subregion size followed a power law with increasing area size, with larger exponents for weak disorder (Fig 6D).

Fig 6E and 6F show a complete characterization of pinwheel nearest neighbor (NN) distance distributions of the noisy Moiré interference model. Histograms for NN distances for arbitrary charge are bimodal for weak disorder (Fig 6E). The peak at smaller NN distances results from the unfolding of pinwheels with topological charge 1 into two adjacent pinwheels of topological charge 1/2 for finite disorder strength (see above and Figs 3 and 4). For the same reason, the NN distance histogram for pinwheels of identical topological charge is also bimodal (Fig 6F). With increasing disorder strength, both distributions become unimodal (Fig 6E and 6F left). The NN distance distribution for pinwheels of opposite sign is unimodal for all parameter values, indicating that only very few additional pinwheel pairs are added to the pinwheels of the

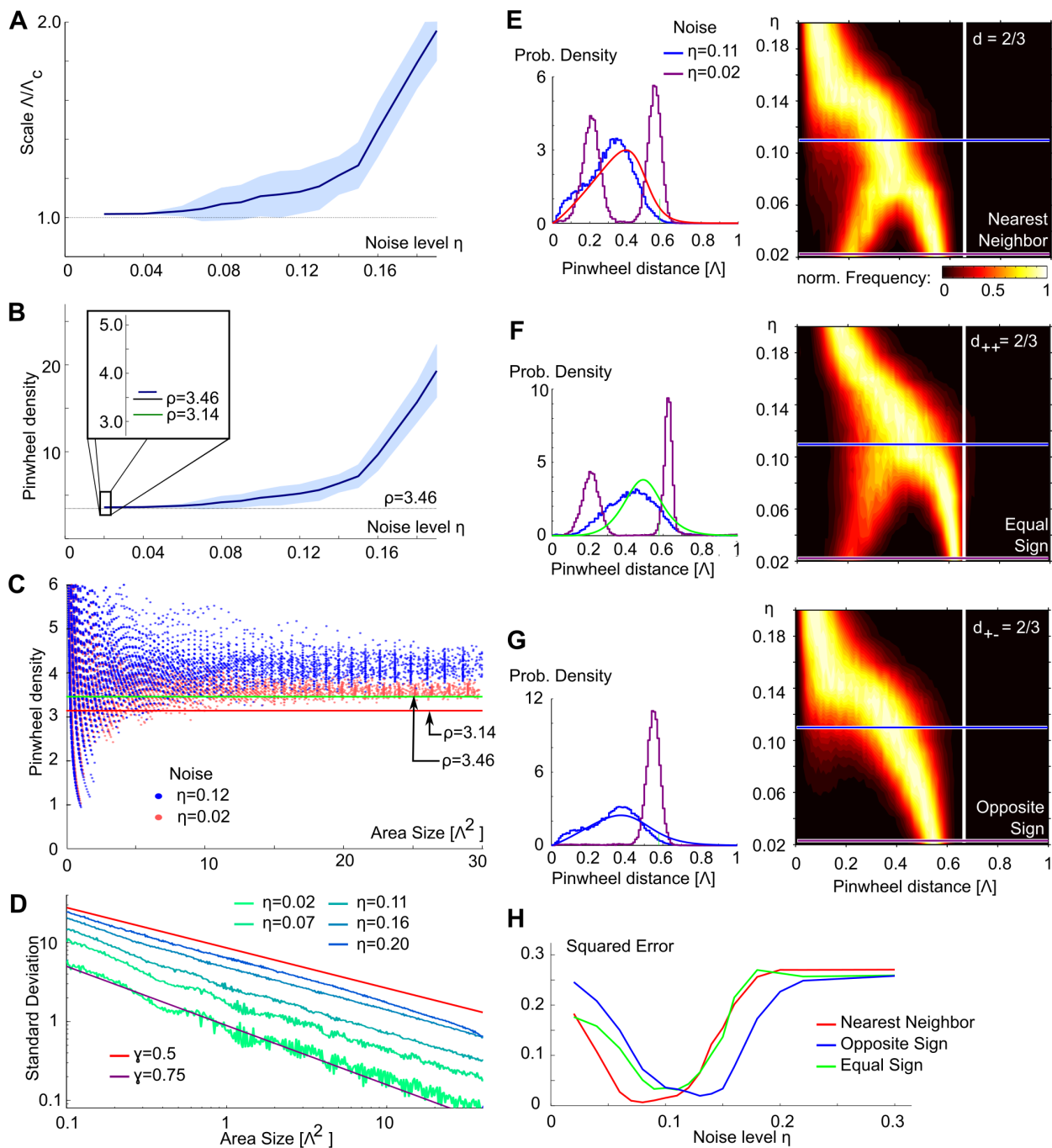


Fig 6. Pinwheel statistics in the Moiré interference model. **A** Column spacing Λ estimated by the wavelet method compared to the Moiré scale Λ_c for different disorder strength. **B** The pinwheel density ρ as function of disorder strength. Dashed line shows theoretically predicted value $\rho = 2\sqrt{3}$. Dark green line in inset shows experimentally observed mean value $\rho = 3.14$. **C** Pinwheel density in circular regions of increasing area for $\eta = 0.12$ (blue) and $\eta = 0.02$ (red). Lines show theoretically predicted and experimentally observed values as in B inset. **D** The standard deviation of pinwheel density estimates for increasing subregion size. Red line shows a power law fit to the experimental data ($\gamma = 0.5$, [23]), purple line indicates a fit to the perfectly ordered hexagonal pinwheel arrangement ($\gamma = 0.75$, [23, 92, 93]). **E** Nearest neighbor (NN) distances for pinwheels irrespective of topological charge. Left: distributions for two disorder strengths ($\eta = 0.11$, blue; $\eta = 0.02$, purple) and the experimental data (red). Right: Distributions for different disorder strengths. Color encodes the (normalized) fraction of pinwheels at this distance. Blue and purple lines indicate disorder strengths shown on the left. The white line marks the theoretically predicted distance of NN pinwheels ($2/3\Lambda_c$) for vanishing disorder [92, 93]. **F** same as E for pinwheels of equal charge, data green curve. **G** same as E for pinwheels of opposite charge, data blue curve. **H** squared deviation of NN distance distributions to the experimental estimates (shown in E-G, left) as function of disorder strength. All other model parameters as in Fig 3.

doi:10.1371/journal.pcbi.1004602.g006

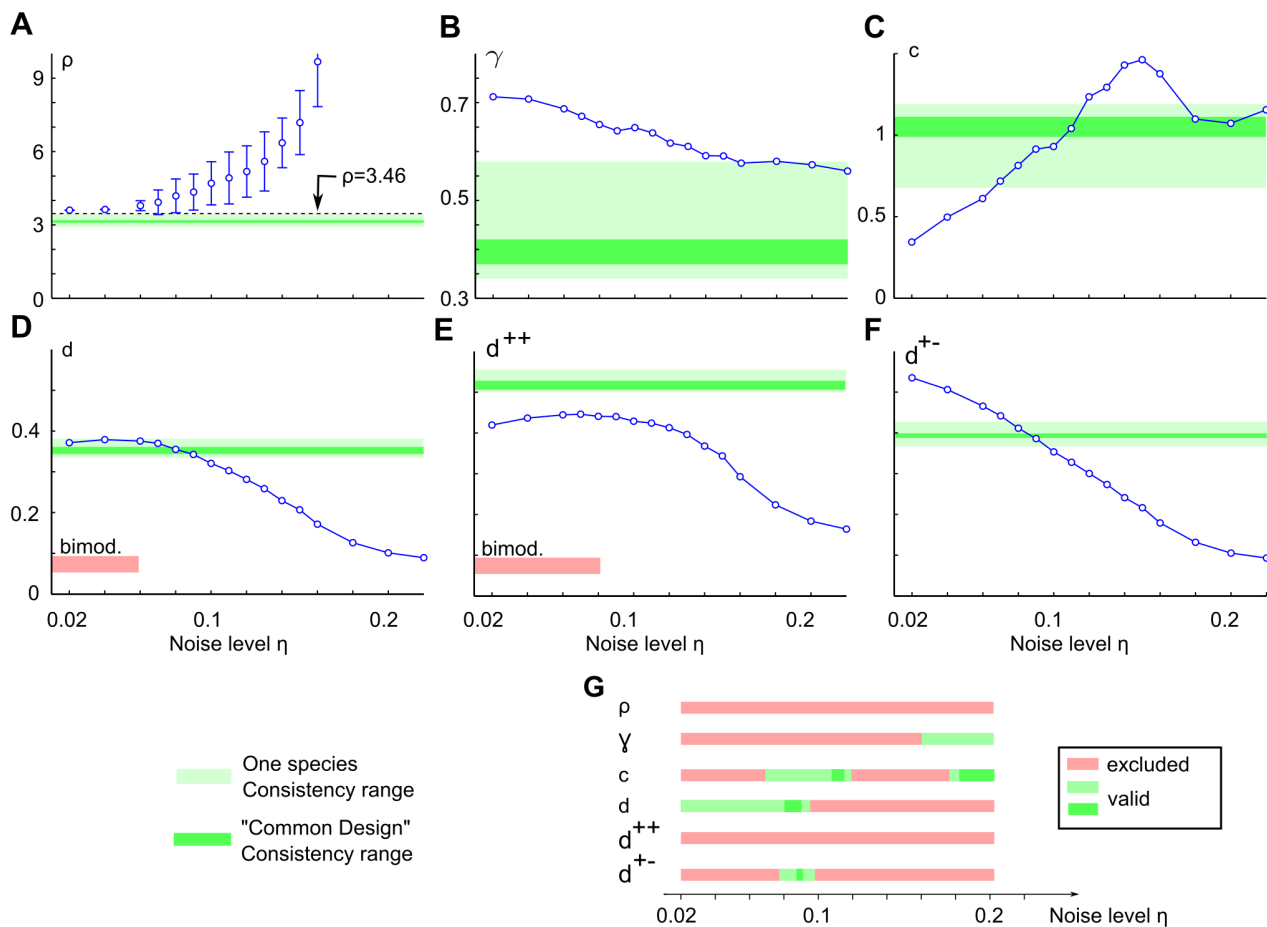


Fig 7. Pinwheel statistics of the disordered Moiré interference model fail to match V1 functional architecture. **A** Pinwheel density as a function of disorder strength in the statistical connectivity model with noisy hexagonal mosaics. Error bars indicate standard deviation around the mean for 20 model realizations, circles indicate the mean. Green shaded areas indicate the range consistent with the experiments (see Fig 1). **B** The variability exponent as function of disorder strength in comparison to the common design. **C** As B for the variability constant. **D** Mean nearest neighbor distance for pinwheels independent of topological charge in comparison to common design. **E** As D but for pinwheels of equal charge. **F** As D for pinwheels of opposite charge. **G** Summary of ranges of disorder parameters consistent with the common design. Disorder strengths larger than 0.3 can be excluded by the lack of typical column spacing in the domain layouts (cf. Fig 5). Note that there is no disorder strengths for which all features of the common design are reproduced.

doi:10.1371/journal.pcbi.1004602.g007

Moiré layout for small and intermediate disorder strengths (Fig 6G). The overall decay in mean NN distance for strong disorder in all three histograms mostly reflects the increase in measured column spacing (see Fig 6A).

Based on these results, we attempted to identify a disorder strength for which all NN pinwheel distance distributions resembled the experimental data. To this end, we calculated the squared error between the calculated histograms and the experimental data as a function of disorder strength (Fig 6H). Smallest deviations from experimental data were obtained around $\eta \approx 0.11$ for all three NN distance distributions.

Fig 7 summarizes all common design features determined for disordered Moiré interference model layouts as a function of disorder parameter and compares them to the experimentally observed values in tree shrew, galago, ferret, dark-reared ferrets, and cats. Light (dark) green shaded areas indicate the single species (common design) consistency ranges (see Fig 1, cf. Table 1). With increasing disorder, pinwheel density of model layouts steadily increases from

$\rho = 2\sqrt{3} \approx 3.46$ (Fig 7A) and always lies above the single species consistency range. Thus, the pinwheel density of model orientation domain layouts is inconsistent with pinwheel densities observed in all species. Next, we fitted the empirically observed power law, Eq (1), to the standard deviation of the pinwheel density estimate in increasing subregions of area A (see Fig 6D) [23]. The variability exponent γ is consistent with experiments for disorder levels exceeding $\eta = 0.15$. The variability constant c is monotonically increasing up to $\eta \approx 0.15$ at which point the model domain layouts lose their typical column spacing (cf. Fig 5) and the increasing pinwheel density ρ causes a drop (Fig 7C). Fig 7D–7F displays the mean pinwheel NN distances as function of the disorder strength, all of which substantially decrease with increasing disorder strength. This can be attributed to the increasing mean column spacing of the domain layouts under increasing disorder (see Fig 6A). Mean NN distances for weak disorder strength are close to the experimental data, but NN distance distributions for pinwheels of different topological charge and independent of topological charge are bimodal for weak disorder (Fig 6E and 6F). The latter is clearly distinct from the experimental data (cf. Fig 1, [23]). Fig 7G shows an overview of the consistency of model orientation domain layout parameters with the data for various disorder strengths. As can be seen, no strength of disorder results in layouts that are consistent with the common design for all layout parameters. Perhaps, even more surprising, pinwheel density and NN distance for pinwheels of the same sign are inconsistent with the individual values obtained for each species, no matter how the strength of disorder is chosen.

Iso-orientation domain layouts from hexagonal RGC mosaics with spatially correlated disorder

The above results show that the statistical connectivity model with hexagonal mosaics is unable to reproduce all features of the common design, even if spatially uncorrelated position disorder is imposed on the RGC positions. Whatever the source of disorder that causes the irregularity in the RGCs' positions, it is plausible to assume that it is correlated on scales spanning several RGCs. Such spatial correlations would preserve the Moiré effect locally, yet generate spatial irregularity in orientation domain layouts.

To test whether correlated positional disorder can produce model arrangements of orientation domains that match experimental observations, we generalized the noisy hexagonal mosaics proposed in [28, 83] to include spatial correlations. To obtain noisy hexagonal RGC mosaics with spatial correlations, we started with a hexagonal array of RGC positions. The position of each lattice point \mathbf{x}_i was then shifted depending on its position according to $\mathbf{x}_i \rightarrow \mathbf{x}_i + \eta \mathbf{y}(\mathbf{x}_i)$. The shift $\eta \mathbf{y}(\mathbf{x})$ with amplitude η for $\mathbf{y}(\mathbf{x}) = (y_1(x), y_2(x))$ was chosen from a Gaussian random field with vanishing mean $\langle y_1(\mathbf{x}) \rangle = \langle y_2(\mathbf{x}) \rangle = 0$, fixed standard deviation $\text{std}(y_1(\mathbf{x})) = \text{std}(y_2(\mathbf{x})) = 1$ and correlation function $\langle \mathbf{y}(\mathbf{x}_1) \mathbf{y}(\mathbf{x}_2) \rangle = 2 \exp\left(-\frac{|\mathbf{x}_1 - \mathbf{x}_2|^2}{2\sigma^2}\right)$ with correlation length σ (see Methods) where y_1 and y_2 are statistically independent. The two parameters, correlation length σ and amplitude η were expressed in units of the lattice constant r .

Fig 8A and 8B illustrates this procedure. RGCs are shifted in a coordinated manner across the plane, correlated in both direction and magnitude of the shift. The determinant of the Jacobian

$$\det J(\mathbf{x}) = \det \begin{pmatrix} \frac{\partial y_1(\mathbf{x})}{\partial x_1} & \frac{\partial y_1(\mathbf{x})}{\partial x_2} \\ \frac{\partial y_2(\mathbf{x})}{\partial x_1} & \frac{\partial y_2(\mathbf{x})}{\partial x_2} \end{pmatrix}, \tag{14}$$

measures the local change of RGC lattice constant. In regions of negative $\det J$, RGCs are closer

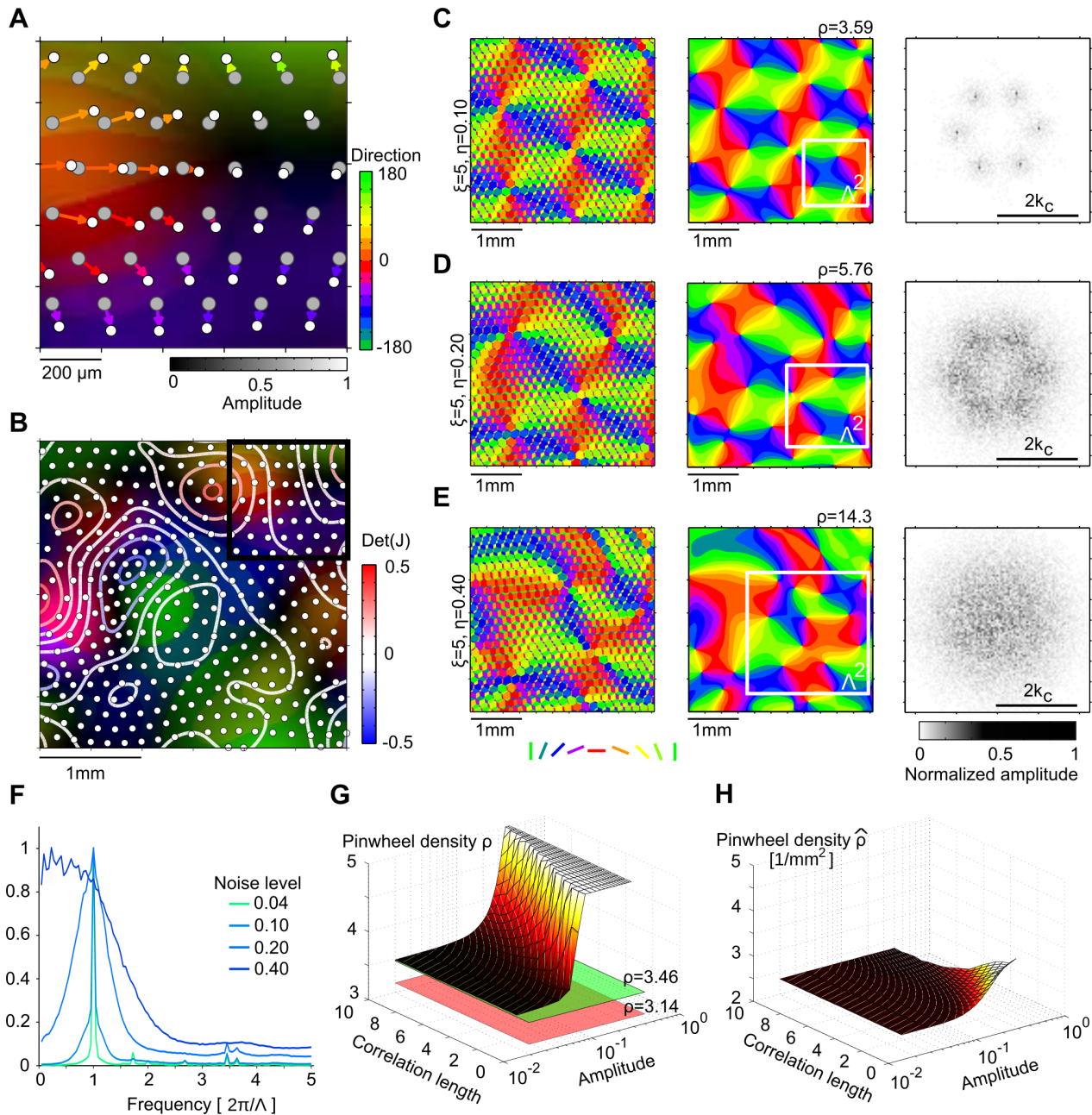


Fig 8. Impact of spatially correlated positional disorder in hexagonal RGC mosaics on iso-orientation domain layouts. **A** Generation of spatially correlated disorder in hexagonal RGC mosaics (see text and Methods). White dots mark ON RGC cells, gray dots marks the perfectly hexagonal ON RGC lattice before distortion. Colors of the arrows and underlay indicate direction of RGC displacements (right colorbar). Magnitude of displacement is indicated by color saturation (bottom colorbar). Note that nearby RGCs move into similar directions and with similar magnitude. Scale bar indicates retinal distances, assuming ON/OFF lattice constant of $170\mu\text{m}$. **B** Larger region of the mosaic shown in A (black square). Colors as in A. Contour lines mark lines of constant $\det(J(\mathbf{x}))$ (see text). Scale bar indicates retinal distances. **C-E** Unfiltered model domain layout (left), thresholded and smoothed layout (middle) its amplitude spectrum (right) for noise correlation length $\xi = 5$ and different noise amplitudes ($\eta = 0.1$ (C), $\eta = 0.2$ (D), $\eta = 0.4$ (E)). White squares in middle panels indicate wavelength of pattern as measured by wavelet analysis (see Methods). Scale bars indicate cortical distance with parameter choices as in Fig 2 and cortical magnification factor ≈ 1 (see [32]). **F** Marginal amplitude spectra of smoothed domain layouts for $\xi = 5$ and different disorder strengths. **G** Pinwheel density of model layouts as a function of disorder amplitude and correlation length. Red surface indicates experimentally determined value ($\rho = 3.14$), green surface indicates pinwheel density in the disorder-free case ($\rho = 2\sqrt{3}$). Values for $\rho \geq 5$ are drawn as a plane at $\rho = 5$. **H** As G, but pinwheels per square millimeter $\hat{\rho}$. Note that the absolute number of pinwheels is largely constant. All other model parameters as in Fig 2.

doi:10.1371/journal.pcbi.1004602.g008

together than average, in regions of positive $\det J$, RGCs are further apart (contour lines in Fig 8B). In primates, regions of higher density are predicted to have higher cortical magnification and vice versa [12]. The RGC mosaics with correlated positional noise therefore imply local fluctuations in the cortical magnification factor on the scale of the noise correlation length.

Fig 8C–8E display unfiltered and smoothed model layouts obtained with spatially correlated noisy hexagonal mosaics as well as their amplitude spectra. As expected, orientation domain layouts exhibit a typical column spacing up to higher disorder strengths, when the position disorder was correlated (compare Fig 8F with Fig 5D). Locally, Moiré interference leads to a roughly hexagonal layout of columns that is distorted on larger scales. Both, the orientation of the hexagons as well as column spacings change continuously across the layout. For weak disorder, the amplitude spectrum still exhibits six peaks, indicating a globally hexagonal layout (Fig 8C, right). For intermediate disorder local column spacing and direction of the hexagons varies to the extent that peaks can hardly be identified in the amplitude spectrum of the resulting domain layout. In particular, the spatially varying local column spacing leads to a broader peak in the radially averaged amplitude spectrum with increasing disorder strength (Fig 8F). This is in contrast to the case of uncorrelated disorder (cf. Fig 5D). Note that experimental iso-orientation domain layouts exhibit a similarly broad peak in their marginal amplitude spectra [99]. We quantified the pinwheel density of orientation domain layouts obtained with correlated noisy hexagonal RGCs (Fig 8G) as a function of disorder correlation length and disorder strengths. Independent of the disorder correlation length, pinwheel densities plateau around $2\sqrt{3}$ for weak disorder and monotonically increase above a critical disorder strength. This critical disorder strength is higher, the larger the correlation length. Thus, model pinwheel densities are inconsistent with the individual values obtained for each species, no matter what the strength of disorder or correlation length is. Fig 8H illustrates that the pinwheel density increases with increasing disorder strength largely because the overall measured column spacing increases, not because additional pinwheels appear in the layouts. In fact, the number of pinwheels per mm^2 is almost independent of either correlation length or disorder strength.

Pinwheel densities of iso-orientation domain layouts derived from PIPP mosaics

Finally, we examined whether the statistical connectivity model could reproduce the common design invariants with RGCs distributed in space according to a pairwise interacting point process (PIPP). The PIPP developed by Eglen et al. [49] is currently the experimentally best supported model for RGCs mosaics and was shown by several studies to generate RGC positions which accurately reproduce a variety of spatial statistics of RGC mosaics [31, 32, 49, 82]. The PIPP model generates samples from a statistical ensemble of RGC mosaics by iteratively updating RGC positions to maximize a target joint probability density, specified by pairwise interactions between neighboring RGCs (for details see [Materials & Methods](#)). Each PIPP mosaic represents a random realization of a regularly-spaced RGC mosaic with radially isotropic autocorrelograms [31] and lacks long-range positional order. Fig 9A depicts a realization of a PIPP with parameters chosen to reproduce cat RGC mosaics (for details see [Materials & Methods](#)). We generated thresholded and smoothed iso-orientation domain layouts from PIPP RGC mosaics as from the ordered mosaics (Fig 9A and 9B left). The lack of long-range positional order in ON and OFF mosaics prevents any Moiré interference between them. Thus, no typical spacing between adjacent columns preferring the same orientation is set in the model layouts (Fig 9B, right, see also [31, 32]). Spectral power in these layouts is broadly distributed and monotonically decays with increasing spatial frequency. As a consequence, one needs to apply bandpass filtering to obtain orientation domain layouts that are at least qualitatively

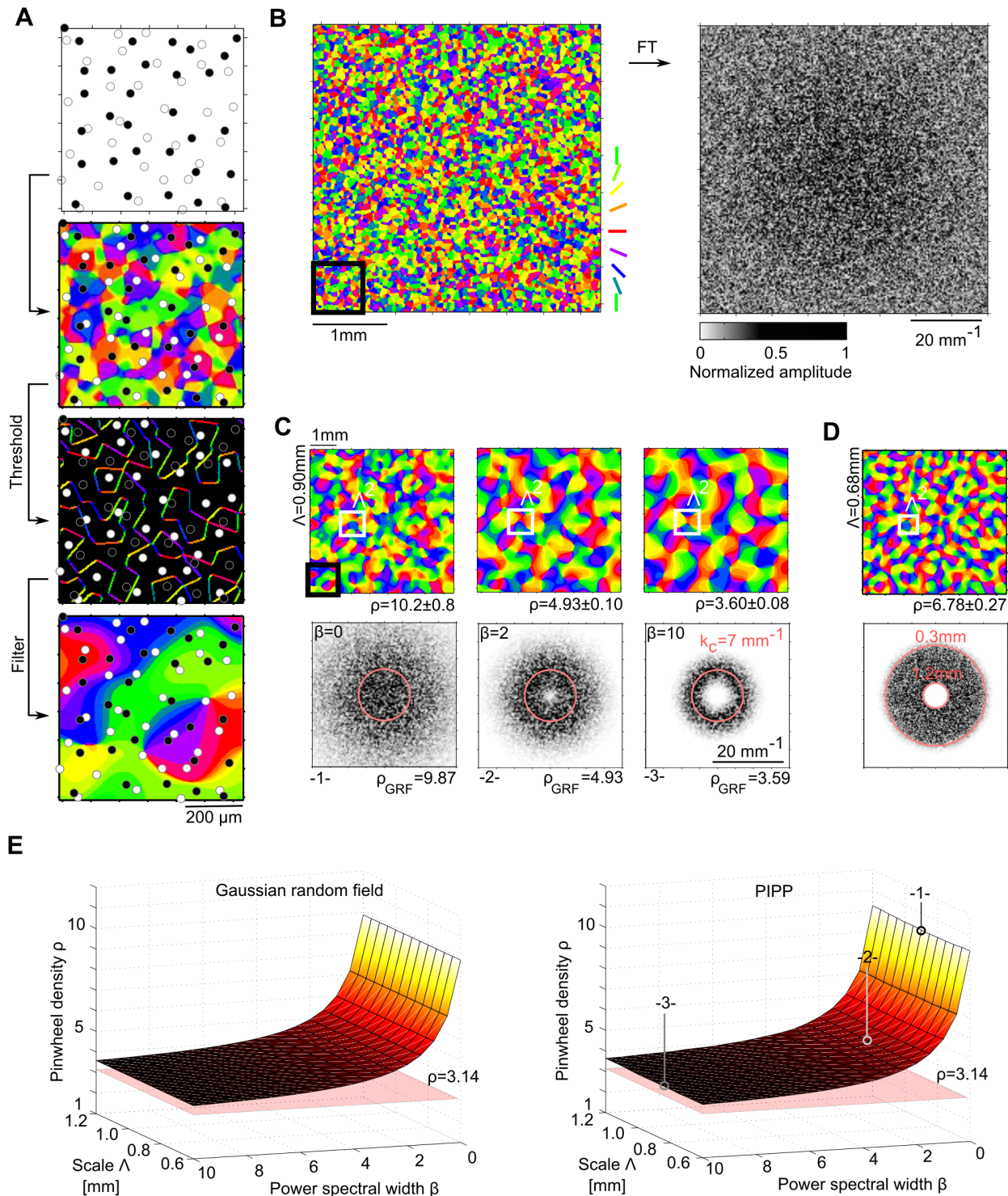


Fig 9. Iso-orientation domain layouts obtained from PIPP RGCs with the statistical connectivity model. **A** Generating orientation domain layouts from PIPP RGCs in the statistical connectivity model [83]. Top: Inset of a PIPP RGC mosaic (see [Methods](#)). Black (white) dots represent OFF (ON) cells. Middle top: unfiltered layout with RGC mosaics overlaid. Middle bottom: thresholded layout with RGC mosaics overlaid. Bottom: thresholded and smoothed layout ($\beta = 0$) with RGC mosaics overlaid. Scale bar indicates retinal distances, assuming PIPP parameters as in [49]. **B** Left: larger region of the unfiltered layout shown in **A** (black square). Scale bar indicates retinal distances. Right: normalized amplitude spectrum of unfiltered layout shown on the left. **C** Thresholded and smoothed layout (top) and corresponding amplitude spectrum (bottom) for filter function parameters (see [Eq \(15\)](#)) $\beta = 0$ (left), $\beta = 2$ (middle), and $\beta = 10$

(right). Scale bar indicates cortical distances, assuming cortical magnification factor ≈ 1 , and $\Lambda = 0.9\text{mm}$ (see Eq (17) and text). Red circles indicate $k_c = 2\pi/\Lambda$. Black square indicates inset in A, white square indicates Λ^2 . D As C but filtered with Fermi band pass filters [23]. White square (top) indicates $\Lambda = 0.68\text{mm}$, the column spacing as measured by wavelet analysis. Red circles (bottom) indicate low pass (1.2 mm) and high pass (0.3 mm) position. Pinwheel densities are stated with standard error of the mean. E Left: Analytically predicted pinwheel density of orientation domain layouts derived from Gaussian random fields [51] as a function of filter parameter β and spatial scale (see text). Right: Pinwheel density of orientation domain layouts obtained from PIPP mosaics with the statistical connectivity model as a function of filter parameter β and spatial scale. Numbers 1–3 indicate parameter choices displayed in C.

doi:10.1371/journal.pcbi.1004602.g009

resembling the experimental data. We used a flexible band-pass filtering function $f(\mathbf{k})$ of the following form to the amplitude spectrum:

$$f(\mathbf{k}) = a|\mathbf{k}|^\beta \exp(-|\mathbf{k}|^2 b), \quad (15)$$

with $a, b, \beta > 0$. The filter function was normalized such that

$$\int d^2\mathbf{k} f(\mathbf{k}) = 2\pi. \quad (16)$$

With this normalization, one can define the mean column spacing of the resulting layout via $\Lambda = 2\pi/\bar{k}$ with

$$\bar{k} = \int_0^\infty dk 2\pi k f(k) = 1. \quad (17)$$

By increasing the parameter β , the shape of the filter can be changed from Gaussian lowpass ($\beta = 0$, Fig 9C, left) to wide bandpass ($\beta = 2$, Fig 9C, middle) and to narrow bandpass ($\beta = 10$, Fig 9C, right). There is an additional degree of freedom in this filter definition, namely how the filter is scaled relative to the absolute physical units mm^{-1} of the amplitude spectrum. To scan a wide range of filter shapes and column spacings, we varied β between 0 and 10 and choose the scaling such that Λ varied between 0.6 mm and 1.2 mm, i.e. covering the entire range of experimentally observed mean column spacings in tree shrew, galago, cat, and ferret [23, 33]. We then measured the pinwheel densities of the resulting statistical connectivity model layouts (Fig 9E, right), where pinwheel density was defined as the number of pinwheels within an area Λ^2 . Pinwheel densities were independent of the scale Λ and increased monotonically with increasing spectral width (decreasing β). They are in general substantially larger than the experimentally observed value of 3.14 (see also Fig 9C) and outside of the single-species/common-design consistency range.

Qualitatively, iso-orientation domain layouts generated with the PIPP RGC mosaics resembled those generated from Gaussian random field (GRF) [22, 50, 51] (Fig 9C). In fact, we find that this resemblance is quantitative. Fig 9E depicts the analytical prediction [51] for the pinwheel density of orientation domains obtained with GRFs with a marginal amplitude spectrum corresponding to the filter function in Eq (15) (Fig 9E, left). Pinwheel densities for GRF layouts and layouts obtained from PIPP mosaics with the statistical connectivity model are indistinguishable. For the pinwheel density to be consistent with at least the single-species consistency range ($\rho < 3.42$), amplitude spectra had to be much more peaked ($\beta \geq 17$) than experimentally observed [99]. Finally, we filtered statistical connectivity model layouts with the Fermi-Filter function as used in [23, 33] with cut-off wavelengths of 0.3 mm and 1.2 mm (Fig 9D). Again, pinwheel densities were much larger than those observed in the experimental data and outside of the single-species and common-design consistency range.

In summary, iso-orientation domain layouts generated by the statistical connectivity model using PIPP RGC mosaics quantitatively resemble layouts derived from Gaussian random fields. Their statistics is distinct from the statistics of experimentally measured layouts.

Discussion

In this study, we examined whether the statistical connectivity model—a biologically plausible scheme of circuit disorder—is able to explain the common design of spatially aperiodic arrangements of orientation domains and pinwheels in the primary visual cortex. As an analytically tractable limiting case, we first considered the model with perfectly ordered hexagonal RGC mosaics (Moiré interference model). For this model we derived exact expressions for receptive fields and tuning curves as well as for unfiltered and filtered layouts. We found that unfiltered orientation domain layouts generated by Moiré-interference exhibited a fine-grained structure of subdomains with substantial and systematic variation in orientation preference on scales much smaller than the typical size of orientation domains. After smoothing, the resulting Moiré interference pattern could mathematically be expressed as the phase of a complex-valued field composed of six planar waves. The pinwheel density of this perfectly hexagonal pattern of orientation domains is $\rho = 2\sqrt{3} \approx 3.46$. Next, we studied the layout of numerically obtained domain layouts derived from hexagonal mosaics that are randomly distorted by spatially uncorrelated disorder. We found that pinwheel density and pinwheel nearest neighbor statistics vary substantially with the degree of randomness. Nevertheless, there was no parameter regime in which all of the common design parameters matched experimental observations. Most prominently, the pinwheel density increased monotonically with increasing disorder strength. To examine the effect of noisy RGC mosaics more broadly, we introduced a more general class of noisy hexagonal mosaics, which allows for the inclusion of spatial correlations in RGC positional disorder. We found that, while RGC dipole patterns for such mosaics are inherently aperiodic, the model still predicts domain layouts that substantially deviate from experimentally observed pinwheel layouts. Finally, we studied the model with RGC mosaics derived from Eglen's random pairwise interacting point process. The resulting layouts lacked a typical spacing between neighboring orientation domains and, after bandpass filtering, pinwheel densities were inconsistent with the values observed for any of the four species investigated.

Alternative random wiring models

The statistical wiring model analyzed in the present study is only one representative of possible random wiring schemes. One could argue that alternative, perhaps more realistic, schemes might do a better job at reproducing the experimentally observed pinwheel layouts. There is good evidence that the spatial statistics of RGC mosaics is well approximated by Eglen's PIPP [31, 32, 49], and, hence, there is little freedom of choice at the retinal level. In contrast, at the next network layer, two main modifications or extensions of the statistical wiring model could be considered: (i) adding an additional layer to the feedforward network implementing the transformation of the retinal input structure by the lateral geniculate nucleus (LGN) (ii) choosing different probabilistic connectivity rules between the retinal/LGN layer and the primary visual cortex. We argue that both modifications of the random wiring approach are unlikely to improve the consistency of the model with experimental data.

Regarding (i), Martinez et al. [100] have recently tried to infer the mapping between RGC inputs and LGN relay cells using a statistical connectivity approach. In their model, ON and OFF cell types were homogeneously distributed and their polarity (ON or OFF) was inherited from the nearest retinal input. Connection probability between RGCs and LGN neurons was modeled as an isotropic Gaussian function of the relative distance between the RF centers of the presynaptic and postsynaptic partners. With this simple wiring scheme, together with similar connectivity rules for the population of inhibitory interneurons, several spatiotemporal properties of LGN RFs robustly agreed with the experimental data. In the architecture between the retina and the LGN proposed by these authors, the dipoles of ON- and OFF-center cells

that characterize the retinal mosaic are transformed into small clusters of same-sign relay cells. The LGN ON-OFF dipoles occur at the boundaries of these clusters with LGN dipole orientations strongly correlating but not necessarily matching dipole orientations in the retina. Notably, dipole density and dipole angle correlation length in the LGN is not increased compared to the retina. The data and modeling by Martinez et al. suggest that the LGN mosaics do not systematically alter the spatial structure of RGC inputs beyond providing an additional source of dipole disorder. Additional disorder imposed by the LGN mosaics would likely add a uniform level of disorder to all spatial frequency components in the unfiltered orientation domain layouts predicted by RGC dipole structure. When hexagonal mosaics are considered, the disorder strength that has to be assumed to match the spatial distribution of RGC cells found in experiment is already rather high [28, 29, 31, 32, 83]. Additional noise is likely to obstruct any remaining Moiré interference. We therefore speculate that when considering an additional LGN layer, after smoothing, domain layouts for both, the noisy Moiré interference model and the model with PIPP mosaics would be similar to those obtained with PIPP mosaics [31, 32, 82]. As we have shown in the present study, the spatial statistics of these layouts resembles those derived from Gaussian random fields and is inconsistent with the data obtained for any of the four species analyzed (cf. Fig 9, see also [23, 50]).

A similar argument can be made for alternative probabilistic connectivity rules between the retinal/LGN layer and V1. As our analysis shows, the dipole structure emerging from “realistic” RGC mosaics (be it very noisy hexagonal mosaics or PIPP mosaics) is spatially fine-grained because dipole angles vary over short distances in cortical space relative to the typical size of an iso-orientation domain. For this reason, the statistical connectivity model requires an additional smoothing step (cf. Figs 4, 5 and 9) to yield smooth orientation domain layouts as observed in experiment [65, 78]. Unless the connectivity rule is assumed to specifically select dipoles with a similar angle from a larger spatial region of the retina, or neurons within an iso-orientation domain are assumed to choose one particular dipole to receive the input from and ignore all other dipoles in the vicinity, such spatial averaging within the cortical layer will always be required no matter what the actual probabilistic connectivity rule is. Domain layouts resulting from such spatial averaging of weakly correlated dipole angles (see also [32]) are likely to follow layout statistics that resemble those of Gaussian random fields, independently of the connectivity rule assumed. If neurons are assumed to select specific dipoles out of the repertoire of “available” ones, then the overall spatial layout of RGC dipoles is not informative about the resulting domain layout, which contradicts the main hypothesis of the statistical wiring model.

Ultimately, the key experiment to provide support for the random wiring approach consists of determining both, the orientation domain layout and the retinotopic map in a single animal and, in a second step, correlate these with the spatial arrangement of RGCs in the same animal. This challenging experimental task is still awaiting its completion.

Spatial irregularity by disorder or optimization

So far, the only model class able to robustly reproduce all common design parameters, describes the formation of orientation domain layouts as a deterministic optimization process converging to quasi-periodic pinwheel-rich orientation domain patterns associated with and stabilized by a matching system of intrinsic horizontal connections [23, 101, 102]. Irregular layouts of orientation domains dynamically emerge as a consequence of large-scale circuit optimization of domain patterns and intrinsic circuits. Is this agreement between model and data good evidence for global circuit optimization or are there simple alternative explanations such as the random feedforward wiring hypothesis that can explain the invariant statistical properties of orientation domains? Qualitatively, it is in fact tempting to attribute the spatial

irregularity and apparent randomness of pinwheel layouts in V1 to some general kind of “biological noise”. In this view, the quantitative laws of pinwheel organization that Kaschube et al. found [23] would then be conceived as outcome of a largely random process underlying the emergence of orientation domains. By now, however, all proposals based on the assumption of disorder as the determinant of spatial irregularity have failed to reproduce the common design parameters and laws that have now been observed in four divergent species.

Orientation domain layouts obtained from statistical ensembles of Gaussian random fields [22, 50, 51] as well as phase randomized layouts derived from experimental data [23], exhibit pinwheel densities that are substantially higher than experimentally observed. Importantly, most dynamical models for the development of orientation domains produce such Gaussian random domain layouts during the initial emergence of orientation selectivity [22, 50]. Therefore approaches based on “frozen” early states of such models are also ruled out by the existing data (see [103]). The present study shows that a mechanistic and biologically plausible feedforward model of the early visual pathway based on (i) noisy hexagonal placement of RGCs or (ii) a more realistic semi-regular positioning of RGCs generated by the PIPP also generates layouts distinct from experimental observations. These findings illustrate that orientation domains and pinwheels positions, although spatially non-periodic and irregular, follow a rather distinct set of layout laws. These laws cannot easily be accounted for by a spatial irregularity or randomness in the structure of afferent projections to visual cortical neurons.

A further conceivable and potentially critical source of stochasticity that is often overlooked is randomness within intracortical circuits. The field approach employed in various models for orientation domain layouts, such as the long-range interaction model, represents an idealization of a complex network, in which every neuron is characterized by its own set of inputs and outputs. These inputs and outputs may, at least to some extent, be stochastic. How and to what extent randomness in intracortical connections can affect and shape orientation domain layouts is not well understood. In that respect, it is interesting to note that model networks for largely stochastic intracortical circuits are able to generate and robustly maintain orientation selective responses to afferent inputs and can lead to highly coherent orientation domains [104, 105].

Hexagonal order of orientation domains

Paik & Ringach reported indications of hexagonal order in visual cortical orientation domain patterns of tree shrew, ferret, cat, and macaque monkey [28, 29]. Two recent studies have casted doubt on the hypothesis that this hexagonal order echoes hexagonal or quasi-hexagonal arrangements of ganglion cell mosaics in the retina [31, 32]. Hore et al. showed that noisy hexagonal lattices do not capture the spatial statistics of RGC mosaic. Moreover, the positional correlations in measured mosaics extends to only 200–350 μm , far less than required for generating Moiré interference [31]. More generally, Schottdorf et al. studied the spatial arrangement of RGC dipole angles in cat beta cell and primate parasol RF mosaics [32]. According to the statistical wiring hypothesis, dipole angle correlations should follow the spatial correlations of preferred orientations in the primary visual cortex, i.e. be positively correlated on short scales (0–300 μm) and negatively correlated on larger scales (300–600 μm) in the retina. By introducing a positive control point process that (i) reproduces both, the nearest neighbor spatial statistics and the spatial autocorrelation structure of parasol cell mosaics and (ii) exhibits a tunable degree of spatial correlations of dipole angles, they were able to show that, given the size of available data sets, the presence of even weak angular correlations in the data is very unlikely.

If not from the structure of RGC mosaics, where does the apparent hexagonal organization in orientation domains come from? A variety of self-organization models on all levels of

biological detail have been shown to generate orientation domains with hexagonal arrangements, e.g. [14, 92, 93, 103, 104, 106, 107] (notably including the earliest theory for the self-organization of orientation preference by von der Malsburg in 1973). Thus, hexagonal order, even if present, would not provide specific evidence in favor of Moiré interference between RGCs. Future work will have to elucidate whether the long-range interaction model for orientation domains [23, 101, 102] can not only explain the common design statistics, but at the same time account for the observed hexagonal order in the visual cortex.

The impact of retinal orientation biases on visual cortical architecture

Compared to the dense sampling of stimulus space by cortical neurons, the repertoire of detectors on the retina that input into a given cortical area is limited. For the cat visual pathway, Alonso et al. estimated the number of LGN X-relay cells converging onto a single simple cell in V1 to be ~ 20 – 40 [27], based on measuring the probability of finding a connection between individual geniculate and cortical neurons with overlapping receptive fields. This estimate was later confirmed by directly measuring population receptive fields of ON and OFF thalamic inputs to a single orientation column [108]. With an expansion of around 1.5–2.0 from X-cells in the retina to X-relay cells in the LGN [109, 110], each simple cell in V1 receives on average input from only ~ 10 – 25 RGCs. This not only implies that random afferent inputs to cortical neurons might seed groups of V1 neurons with similar orientation preferences but also that they might in fact impose substantial *biases* on the preferred orientation that can be adopted by the cortical neurons. The postnatal development of orientation columns could then be imagined as a dynamical activity-dependent process which refines and remodels an initial set of small biases provided by the RGC mosaic model through Hebbian learning rules and other mechanisms of synaptic plasticity. The up to now most striking experimental evidence that retinal organization can impose local biases in V1 function architecture was revealed by the finding that the pattern of retinal blood vessels can specifically determine the layout of ocular dominance columns in squirrel monkey [111] (for a modeling study see [112]).

Dynamical models of orientation column formation generally assume no a priori constraints or biases as to which preferred orientation a given position in the cortical surface can acquire. Usually random initial conditions determine which instance from the large intrinsic repertoire of stable potential domain layouts is adopted. Including seeds and biases derived from RGC mosaics in such models for the dynamical formation of V1 orientation domain layouts may elucidate the potentially complex interplay between a sparse set of subcortical feed-forward constraints and self-organization in a dense almost continuum-like intracortical network. The present study provides a detailed description of a candidate set of such subcortical biases and, therefore, can serve as a foundation for such future investigations.

The common design as benchmark for models of visual cortical development and function

The common design invariants comprise four distinct functions in addition to the apparently invariant pinwheel density. As such, they represent a rather specific quantitative characterization of orientation domain layouts. It is, thus, not surprising that entire model classes have been rejected based on whether their predictions match these invariants.

Since the discovery of visual cortical functional architecture more than fifty years ago, a large number of models based on a variety of circuit mechanisms has been proposed to account for their postnatal formation (see [113–115] for reviews). Many of these models are explicitly or implicitly based on optimization principles and attribute a functional advantage

to the intriguing spatial arrangement of orientation domains. Because many, even mutually exclusive, models could qualitatively account for main features of orientation domain layouts such as the presence of pinwheels or the roughly periodic arrangement of columns, theory could not provide decisive evidence on whether to favor one hypothesis over another. It is only in recent years that the large available data sets have started to allow for a rigorous quantitative analysis of visual cortical architecture and its design principles in distinct evolutionary lineages.

To date, abstract optimization models have been analyzed most comprehensively, providing in many cases the complete phase diagram. For instance, Reichl et al. systematically evaluated energy-minimization-based models for the coordinated optimization of orientation preference and ocular dominance layouts [92, 93]. By quantitatively comparing model solutions to the common design, they were able to rule out a whole variety of otherwise intuitive and plausible principles for their emergence. It is desirable to obtain a similarly quantitative understanding of more detailed models for the formation of orientation domains. In this regard, the analysis of abstract models is informative because there is a many-to-one relationship between detailed models of the visual cortical pathway and those abstract formulations. Abstract models often can be shown to be representative of an entire universality class and, once comprehensively characterized, the questions become whether more complex modeling schemes are simply complicated instantiations of such a class.

For models of an intermediate degree of realism, semi-analytical perturbation methods can be employed to explicitly provide this mapping. Using this approach, Keil & Wolf studied orientation domain layouts predicted by a widely used representative of a general optimization framework [103]. According to this framework, the primary visual cortex is optimized for achieving an optimal tradeoff between the representation of all combinations of local edge-like stimuli, i.e. all positions in the visual field and all orientations, and the overall continuity of this representation across the cortical surface [116]. While this framework has successfully explained a variety of qualitative aspects of orientation domain design, e.g. [116–118], the authors found quantitative disagreement with the common design in all physiologically realistic parameter regimes of the representative model [103]. Their analysis enabled an unbiased comprehensive search of the model's parameter space for a match to the experimental data and indicated alternative more promising optimization hypotheses to explain the experimentally observed V1 functional architecture.

Although the statistical wiring model is still rather simplistic, it is hard to make analytical or semi-analytical progress as soon as RGC mosaics with the necessary degree of realism are considered. In this case, the question of whether models account for the cortical architecture can only be answered with the approach we have pursued here, i.e. by systematic comparison between their solutions, experimental data, as well as predictions from minimal approaches.

The results presented here show that this approach can indeed be successfully applied to rule out candidate mechanisms as sufficient explanations for the emergence of V1 functional architectures. We expect a re-examination of the quantitative predictions of other modeling approaches to be highly informative about candidate mechanisms for the formation of V1 functional architecture.

This present study provides the first systematic assessment as to whether the common design of orientation domains could result from an inherently random process, as realized through the local feedforward structure of the early visual pathway rather than an optimization process coordinated on large scales. Given the disagreement between the layouts predicted by the statistical wiring model and the data, global circuit optimization as proposed by the long-range interaction model currently is the only theory known to be capable of explaining the common design of orientation domains in the primary visual cortex.

Methods

Analysis of model and experimentally obtained orientation domain layouts

Column spacing and pinwheel statistics of both data and simulation were analyzed using the wavelet method introduced in [47, 119]. This method specifically takes into account that experimentally measured domain layouts often exhibit local variations in column spacing (as opposed to most model layouts) and is thus well-suited to unbiasedly compare the pinwheel layouts of model layouts and experimental data. Matlab source code for preprocessing of experimentally obtained layouts, column spacing analysis, and the analysis of pinwheel layouts can be found in the Supplemental Material, along with four example cases from ferret V1 to test the code. The full data set used in the present study is available on the neural data sharing platform <http://www.g-node.org/>.

For comparison between model orientation domain layouts and experimentally obtained layouts, both were analyzed with the exact same wavelet parameters settings. Raw difference images obtained in the experiments were Fermi bandpass filtered as described in [23]. Filter parameters were adapted to the column spacings of the different species such that structures on the relevant scales were only weakly attenuated (see [23]).

To determine the local column spacing of the layouts, we first calculated wavelet coefficients of an image $I(\mathbf{x})$, averaged over all orientations

$$\Psi(\mathbf{y}, \Lambda) = \int \frac{d\varphi}{\pi} \left| \int d^2\mathbf{x} I(\mathbf{x}) \cdot \phi_{\mathbf{y}}(\mathbf{x}, \Lambda, \varphi) \right| \quad (18)$$

where \mathbf{y} is the position, φ the orientation and Λ the scale of the wavelet $\phi_{\mathbf{y}}(\mathbf{x}, \Lambda, \varphi)$. We used complex-valued Morlet wavelets composed of a Gaussian envelope and a plane wave

$$\phi(\mathbf{x}) = \frac{1}{\sigma} \exp\left(-\frac{\mathbf{x}^2}{2\sigma^2}\right) \cdot \exp(i\mathbf{k}_{\varphi}\mathbf{x}) \quad (19)$$

and

$$\phi_{\mathbf{y}}(\mathbf{x}, \Lambda, \varphi) = \phi(\Omega^{-1}(\varphi)(\mathbf{y} - \mathbf{x})). \quad (20)$$

The matrix $\Omega(\varphi)$ is the two dimensional rotation matrix (Eq (25)). To compute the wavelet orientation average in Eq (18), 16 equally spaced wavelet orientations were used. For a given Λ , the parameters of the Morlet wavelet were chosen as

$$\mathbf{k}_{\varphi} = \frac{2\pi}{\Lambda} \begin{pmatrix} 1 \\ 0 \end{pmatrix} \quad (21)$$

$$\sigma = \frac{\xi\Lambda}{2\pi}. \quad (22)$$

ξ determines the size of the wavelet and was chosen to be $\xi = 7$, as in [23]. This captures column spacing variations on scales larger than 4 hypercolumns while at the same time enabling robust column spacing estimation. To obtain the map of local column spacing $\Lambda_{\text{local}}(\mathbf{y})$, we calculated the scale Λ with the largest wavelet coefficient

$$\Lambda_{\text{local}}(\mathbf{y}) = \operatorname{argmax}_{\Lambda}(\Psi(\mathbf{y}, \Lambda)) \quad (23)$$

for every position \mathbf{y} .

To estimate the pinwheel density and other pinwheel layout parameters, we used a fully automated procedure proposed in [23]. We refer to the Supplemental Material accompanying [23] for further details.

A mathematical treatment of the Moiré-interference model

Here, we examine the analytically most tractable variant of the statistical wiring model, in which ON and OFF center cells are localized on perfectly hexagonal lattices \mathcal{L} , (Fig 2B), that may exhibit different lattice constants r and r' ,

$$\mathcal{L} = \left(\begin{pmatrix} 1 \\ 0 \end{pmatrix} k + \frac{1}{2} \begin{pmatrix} 1 \\ \sqrt{3} \end{pmatrix} l \right) f \quad \forall k, l \in \mathbb{Z}, \tag{24}$$

where $f = r, r'$ is the lattice constant. Describing a rotation of the lattice vectors by the rotation matrix

$$\Omega(\alpha) = \begin{pmatrix} \cos(\alpha) & -\sin(\alpha) \\ \sin(\alpha) & \cos(\alpha) \end{pmatrix}, \tag{25}$$

the ON mosaic is rotated by an angle α , the OFF lattice by an angle α' (Fig 2B). Paik & Ringach found in numerical simulations that in this case, Moiré interference between two hexagonal RGC mosaics results in a hexagonal layout of orientation domains [28, 29, 83]. We now first derive an explicit expression for cortical receptive fields RF_y , spatially varying with y predicted by the model. Calculating the preferred orientation of these receptive fields then provides an explicit expression for the hexagonal domain layouts.

The sum in Eq (3) can be evaluated analytically for *rectangular* lattices using Jacobi Theta functions [120]. To solve the Moiré interference model, we used the fact that every hexagonal lattice can be written as sum $\mathcal{L} = \mathcal{L}_1 + \mathcal{L}_2$ of two rectangular lattices with orthogonal base vectors by separating even and odd numbers in l and shifting the l -sum so that the x-component is equal to zero. The two rectangular lattices are

$$\begin{aligned} \mathcal{L}_1 &= \left(\begin{pmatrix} 1 \\ 0 \end{pmatrix} k + \begin{pmatrix} 0 \\ \sqrt{3} \end{pmatrix} l \right) f \quad \forall k, l \in \mathbb{Z}, \\ \mathcal{L}_2 &= \left(\begin{pmatrix} 1 \\ 0 \end{pmatrix} k + \begin{pmatrix} 0 \\ \sqrt{3} \end{pmatrix} l + \frac{1}{2} \begin{pmatrix} 1 \\ \sqrt{3} \end{pmatrix} \right) f \quad \forall k, l \in \mathbb{Z}. \end{aligned} \tag{26}$$

Evaluating the infinite Gaussian sum (Eq (3)) yields the result for a single sub lattice (either ON or OFF)

$$RF_{\alpha,r,y}^{ON/OFF}(\mathbf{x}) = T \left(\Theta_3(\mathbf{b} \mathbf{e}_\phi, \tau) \Theta_3(\mathbf{b} \mathbf{e}_r, \kappa) + \Theta_4(\mathbf{b} \mathbf{e}_\phi, \tau) \Theta_4(\mathbf{b} \mathbf{e}_r, \kappa) \right) \tag{27}$$

where

$$\mathbf{b} = \frac{\mathbf{x}\sigma_s^2 + \mathbf{y}\sigma_r^2}{\sigma_s^2 + \sigma_r^2} \tag{28}$$

$$\mathbf{e}_r = -\frac{\pi}{r} \begin{pmatrix} \cos(\alpha) \\ \sin(\alpha) \end{pmatrix} \tag{29}$$

$$\mathbf{e}_\phi = -\frac{\pi}{\sqrt{3}r} \begin{pmatrix} -\sin(\alpha) \\ \cos(\alpha) \end{pmatrix} \quad (30)$$

$$\tau = e^{-\frac{2\pi^2\sigma_r^2\sigma_s^2}{3r^2(\sigma_r^2+\sigma_s^2)}} \quad (31)$$

$$\kappa = e^{-\frac{2\pi^2\sigma_r^2\sigma_s^2}{r^2(\sigma_r^2+\sigma_s^2)}} \quad (32)$$

$$T = \frac{2\pi\sigma_r^2\sigma_s^2}{\sqrt{3}r^2(\sigma_r^2+\sigma_s^2)} \exp\left(-\frac{(\mathbf{x}-\mathbf{y})^2}{2(\sigma_s^2+\sigma_r^2)}\right) \quad (33)$$

and Θ_3 and Θ_4 are the third and fourth Jacobi theta functions [120]. The cortical receptive fields $RF_y(\mathbf{x})$ are obtained by summing the ON and OFF sublattices

$$RF_y(\mathbf{x}) = RF_{x,r,y}^{\text{ON}}(\mathbf{x}) - RF_{x',r',y}^{\text{OFF}}(\mathbf{x}), \quad (34)$$

where α (α') and r (r') are the angle and the lattice spacing of the ON (OFF) lattice. The inset of a receptive field in Fig 3B shows a plot of Eq (34). These receptive fields resemble simple cell receptive fields in V1 with a size of about 1° for our choice of parameters [121, 122]. An implementation/visualization of the equations for receptive fields can be found in the Supplemental Material.

Tuning curves from receptive fields

The response R_y of a neuron with receptive field $RF(\mathbf{x})$ to a sine wave grating can be calculated using $L(\mathbf{x}) = \exp(-i\mathbf{k} \cdot \mathbf{x})$ as a stimulus in Eq (5). Evaluating the integral then corresponds to Fourier transforming the receptive field $RF(\mathbf{x})$. Denoting the Fourier transform of the receptive field as

$$\mathcal{R}_y(\mathbf{k}) = \frac{1}{2\pi} \int d^2\mathbf{x} RF_y(\mathbf{x}) e^{-i\mathbf{k}\cdot\mathbf{x}}, \quad (35)$$

we refer to the absolute value $|\mathcal{R}_y(\mathbf{k})|$ as the amplitude spectrum of the receptive field. Given the above definition, the amplitude spectrum represents the response to a sine wave grating with wave vector $\mathbf{k} = (k \cos(\vartheta), k \sin(\vartheta))$, where ϑ is the grating orientation and k its spatial frequency. A *tuning curve* for spatial frequencies k and orientations ϑ is given by

$$TC(\vartheta, k) = |\mathcal{R}_y(k \cos(\vartheta), k \sin(\vartheta))|. \quad (36)$$

We calculated the Fourier transform of Eq (34) by transforming Eq (2) and subsequently summing over the two rectangular lattices \mathcal{L}_1 and \mathcal{L}_2 in Eq (26). Interchanging summation and integration is valid because all infinite sums are uniformly convergent. The result is

$$\mathcal{R}(\mathbf{k})_{x,r,y}^{\text{ON/OFF}} = U (\Theta_3(\mathbf{c}\mathbf{e}_\phi, \nu)\Theta_3(\mathbf{c}\mathbf{e}_r, \zeta) + \Theta_4(\mathbf{c}\mathbf{e}_\phi, \nu)\Theta_4(\mathbf{c}\mathbf{e}_r, \zeta)), \quad (37)$$

where

$$U = \frac{2\pi\sigma_r^2\sigma_s^2}{\sqrt{3}r^2} \exp\left(-i\mathbf{k}\cdot\mathbf{y} - \frac{1}{2}\mathbf{k}^2(\sigma_s^2 + \sigma_r^2)\right) \quad (38)$$

$$\mathbf{c} = (\mathbf{y} - i\sigma_s^2\mathbf{k}) \quad (39)$$

$$v = \exp\left(\frac{-2\pi^2\sigma_s^2}{3r^2}\right) \tag{40}$$

$$\zeta = \exp\left(\frac{-2\pi^2\sigma_s^2}{r^2}\right). \tag{41}$$

The Fourier transform of cortical receptive fields is given by the sum of the ON and OFF sublattice Fourier transforms

$$\mathcal{R}_y(\mathbf{k}) = \mathcal{R}(\mathbf{k})_{z,r,y}^{\text{ON}} - \mathcal{R}(\mathbf{k})_{z',r',y}^{\text{OFF}}, \tag{42}$$

where we suppressed the dependencies on α, α', r, r' on the left hand side. Receptive fields depend on the two scales σ_r and σ_s . With increasing σ_s , more RGCs are pooled to form the cortical receptive field. If the cortical receptive field is dominated by more than two RGCs, it can exhibit multiple ON and OFF subregions. The spatial arrangement of these ON and OFF subregion mirrors the hexagonal lattices of the ON and OFF center RGCs. The parameter σ_s must be of a minimal size since for very small values of many cortical cells are connected with only a single, dominant RGC input and exhibit no orientation selectivity. Varying σ_r does not qualitatively change the shape of cortical receptive fields.

Extracting preferred orientation and spatial frequency from amplitude spectra of receptive fields

For simple cell receptive fields with one ON and one OFF subregion, the amplitude spectrum $|\mathcal{R}(\mathbf{k})|$ will typically look as in Fig 10A. We follow [28, 82] and define the preferred angle as $\vartheta_{\text{pref}} = \arg(\mu)/2$, where

$$\mu = \frac{\int d^2\mathbf{k} |\mathcal{R}(\mathbf{k})| \cdot e^{2i \arg(\mathbf{k})} \mathbf{k}}{\int d^2\mathbf{k} |\mathcal{R}(\mathbf{k})|}. \tag{43}$$

While there is consensus about the definition of the preferred orientation, methods for extracting the preferred spatial frequency differ within the literature. Ringach proposed to use $k_{\text{pref}} = |\mu|$ [82], referred to as *Center-of-Mass Method*. More commonly, the circular variance

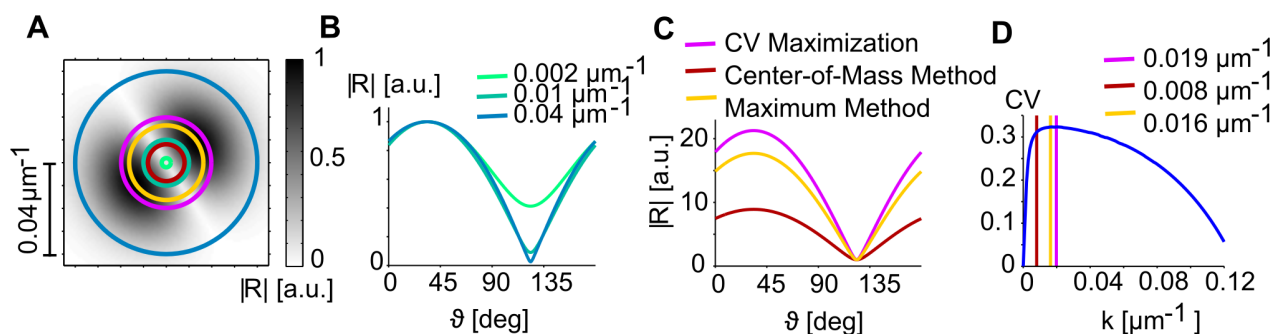


Fig 10. A comparison of different methods for extracting RF parameters from their amplitude spectrum. **A** Amplitude spectrum $|\mathcal{R}(\mathbf{k})|$ of a simple cell receptive field calculated with Eq (42) in the manuscript. Circles indicate the preferred spatial frequency as extracted by maximizing the CV (yellow), by the Center-of-Mass Method (brown), and the Maximum Method (pink). **B** The Tuning curves corresponding to the green, cyan and blue circles in A, normalized relative to their maximum. **C** The Tuning curves corresponding to the brown, the yellow and the pink circles in A, normalized relative to their minimum. **D** Circular variance of the various tuning curves calculated via Eq (44) as function of spatial frequency. The brown, the yellow and the pink line correspond to the preferred spatial frequency as extracted by the three methods.

doi:10.1371/journal.pcbi.1004602.g010

CV(k) [123–125]

$$CV(k) = \frac{\left| \int_0^{2\pi} d\vartheta TC(\vartheta, k) e^{2i\vartheta} \right|}{\int_0^{2\pi} d\vartheta TC(\vartheta, k)}, \quad (44)$$

is first computed as a measure of orientation selectivity at a given spatial frequency k . Maximizing the circular variance across all spatial frequencies is then performed to obtain an estimate of preferred spatial frequency:

$$k_{\text{pref}} = \underset{\{k\}}{\operatorname{argmax}} (CV(k)). \quad (45)$$

We refer to this method as *CV maximization*. Finally, one can use the maximum of the amplitude spectrum

$$k_{\text{pref}} = \underset{\{k\}}{\operatorname{argmax}} (|\mathcal{R}(\mathbf{k})|), \quad (46)$$

as an estimate of the preferred spatial frequency (*Maximum method*). We argue that Maximum method and CV maximization in most cases yield similar results. They extract preferred spatial frequencies that one would obtain when searching for the “strongest response” by presenting a set of gratings of varying orientation and spatial frequency to a subject [125–127]. In contrast, estimates made with the center-of-mass method are usually substantially smaller than this intuitive measure (Fig 10C and 10D). As a consequence, the orientation selectivity index defined as

$$OSI = \frac{\left| \int_0^{2\pi} d\vartheta TC(\vartheta, k_{\text{pref}}) e^{2i\vartheta} \right|}{\int_0^{2\pi} d\vartheta TC(\vartheta, k_{\text{pref}})} \quad (47)$$

for all three methods, will usually be substantially smaller, when estimated with the Center-of-Mass method compared to the other two methods. Among all three methods, the Maximum method has the advantage that its estimates are unaffected by monotonic nonlinearities applied to R commonly used to convert it to a firing rate of a neuron. For this reason, the Maximum method is our method of choice for extracting the preferred spatial frequency from amplitude spectra of receptive fields.

Extracting the spatial progression of preferred orientation

Using the equations for the receptive fields of cortical neurons in the Moiré interference model, we extracted the spatial progression preferred orientation and spatial frequency from their squared amplitude spectrum:

$$|\mathcal{R}_y(\mathbf{k})|^2 \propto \exp(-\mathbf{k}^2(\sigma_s^2 + \sigma_r^2)) \cdot \underbrace{\left(\Theta_3^{z,r} \Theta_3^{z,r} + \Theta_4^{z,r} \Theta_4^{z,r} - \Theta_3^{z',r'} \Theta_3^{z',r'} - \Theta_4^{z',r'} \Theta_4^{z',r'} \right)}_{G_y(\mathbf{k})}, \quad (48)$$

with abbreviation $\Theta_i^{z,r} \Theta_i^{z,r} = \Theta_i(\mathbf{c}_{\phi}(\alpha, r), \tau) \Theta_i(\mathbf{c}_r(\alpha, r), \zeta)$. $|\mathcal{R}(\mathbf{k})|^2$ is composed of a rotationally symmetric Gaussian envelope and a non-rotationally symmetric part $G_y(\mathbf{k})$ varying in space \mathbf{y} . To calculate the preferred orientation ϑ_{pref} and spatial frequency k_{pref} we expanded

the non-rotationally symmetric part $|G_y(\mathbf{k})|^2$ to quadratic order in \mathbf{k} :

$$|\mathcal{R}_y(\mathbf{k})|^2 \approx \exp(-\mathbf{k}^2(\sigma_s^2 + \sigma_r^2)) \left(|G_y^0|^2 + \frac{1}{2} \begin{pmatrix} k_1 & k_2 \end{pmatrix} \mathcal{H}_y \begin{pmatrix} k_1 \\ k_2 \end{pmatrix} \right), \quad (49)$$

where \mathcal{H}_y is the Hessian matrix

$$\mathcal{H}_y = \left. \begin{pmatrix} \frac{\partial^2 |G_y|^2}{\partial k_1^2} & \frac{\partial^2 |G_y|^2}{\partial k_1 \partial k_2} \\ \frac{\partial^2 |G_y|^2}{\partial k_2 \partial k_1} & \frac{\partial^2 |G_y|^2}{\partial k_2^2} \end{pmatrix} \right|_{\mathbf{k}=\mathbf{0}} \equiv \begin{pmatrix} a_y & b_y \\ b_y & c_y \end{pmatrix} \quad (50)$$

and $G_y^0 = G_y(\mathbf{k} = 0)$. Since $G_y(\mathbf{k}) = G_y(-\mathbf{k})$, this Taylor expansion only contains terms of even power in \mathbf{k} .

Using the fact that

$$h(\theta) = \begin{pmatrix} \cos \theta & \sin \theta \end{pmatrix} \mathcal{H}_y \begin{pmatrix} \cos \theta \\ \sin \theta \end{pmatrix} = a_y \cos^2 \theta + 2b_y \cos \theta \sin \theta + c_y \sin^2 \theta \quad (51)$$

yields the second directional derivative in the direction of $(\cos \theta, \sin \theta)$, ϑ_{pref} can be found as the maximum of $h(\theta)$, i.e. the direction of largest increase in amplitude spectrum,

$$\vartheta_{\text{pref}}(\mathbf{y}) = \text{atan} \left(\frac{\sqrt{(a_y - c_y)^2 + 4b_y^2} - a_y + c_y}{2b_y} \right). \quad (52)$$

This formula for $\vartheta_{\text{pref}}(\mathbf{y})$ represents an expression for the orientation domain layouts produced by the Moiré interference model for hexagonal RGC lattices.

To calculate the smoothed domain layout of the Moiré interference model analytically, we identified the low frequency components of our analytical solution. To this end, we expanded the Jacobi theta functions in Eq (42) [120]

$$|\mathcal{R}_y(\mathbf{k})|^2 = \sum_j \left(C_y^j \exp \left(-\frac{1}{2\sigma^2} (\mathbf{k} - \boldsymbol{\alpha}_y^j)^2 \right) + C_y^j \exp \left(-\frac{1}{2\sigma^2} (\mathbf{k} + \boldsymbol{\alpha}_y^j)^2 \right) \right) \quad (53)$$

where C_y^j and $\boldsymbol{\alpha}_y^j$ are determined by Eq (42). According to this equation, the power spectra of receptive fields in the Moiré interference model is represented by an infinite sum of Gaussians, each mirrored at the origin $(0, 0)$ of Fourier space. The preferred orientation of a receptive field represented by such an infinite sum is set by the direction in which the “center-of-mass” of the Gaussians is located. Due to the symmetry of the power under spatial inversion, there are two peaks located at $\vartheta(\mathbf{y})$ and $\pi + \vartheta(\mathbf{y})$. The direction towards the center-of-mass of the peak is obtained through the complex number

$$\mu(\mathbf{y}) = \sum_j C_y^j \cdot |\boldsymbol{\alpha}_y^j| \exp(2i \arg(\boldsymbol{\alpha}_y^j)) \quad (54)$$

with C_y^j and $\boldsymbol{\alpha}_y^j$ defined as in Eq (53). The preferred orientation then is $\arg(\mu(\mathbf{y}))/2$. Rewriting this sum and substituting the respective expressions for C_y^j and $\boldsymbol{\alpha}_y^j$, we obtained

$$\mu(\mathbf{y}) = \sum_{m,n,o,p} f(m, n, o, p) \exp(2iy(ne_\phi + me_r - oe'_r - pe'_\phi)), \quad (55)$$

Table 2. Lowest frequency contributions of the orientation domain layout predicted by the Moiré interference model. The vectors \mathbf{k}_i are the wave vectors and $|\mathbf{k}_i|$ their absolute values. u_i denotes the phase factors of the complex-valued coefficient $f(m, n, o, p)$ in Eq (55) (see also Eq (7)). The constant phase factor u_0 is given by Eq (56). n.d. means not determined.

m	n	o	p	\mathbf{k}_i	$ \mathbf{k}_i $	Phase factor u_i
1	1	1	1	$2((\mathbf{e}_r - \mathbf{e}'_r) + (\mathbf{e}_\phi - \mathbf{e}'_\phi))$	k_c	$u_0 e^{i4\pi/3}$
-1	-1	-1	-1	$-2((\mathbf{e}_r - \mathbf{e}'_r) + (\mathbf{e}_\phi - \mathbf{e}'_\phi))$	k_c	$u_0 e^{i4\pi/3}$
1	-1	1	-1	$2((\mathbf{e}_r - \mathbf{e}'_r) - (\mathbf{e}_\phi - \mathbf{e}'_\phi))$	k_c	$u_0 e^{i2\pi/3}$
-1	1	-1	1	$-2((\mathbf{e}_r - \mathbf{e}'_r) - (\mathbf{e}_\phi - \mathbf{e}'_\phi))$	k_c	$u_0 e^{i2\pi/3}$
0	2	0	2	$4(\mathbf{e}_\phi - \mathbf{e}'_\phi)$	k_c	u_0
0	-2	0	-2	$-4(\mathbf{e}_\phi - \mathbf{e}'_\phi)$	k_c	u_0
2	0	2	0	$4(\mathbf{e}_r - \mathbf{e}'_r)$	$\sqrt{3}k_c$	n.d.
-2	0	-2	0	$-4(\mathbf{e}_r - \mathbf{e}'_r)$	$\sqrt{3}k_c$	n.d.

doi:10.1371/journal.pcbi.1004602.t002

with coefficients $f(m, n, o, p)$. This is a decomposition of the orientation domain layout of the Moiré interference model into Fourier modes, indexed by four numbers $m, n, o, p = 0, \pm 1, \pm 2, \dots$ Table 2 lists the first terms of this series in ascending spatial frequency order. By rewriting $\mu \rightarrow z$ and selecting only the lowest contributing spatial frequencies, we obtain Eq (7). The phase factor

$$u_0 = \frac{e^{i(x+x')}(e^{iz'r} + e^{iz'r'})}{e^{iz'r} + e^{iz'r'}} \tag{56}$$

is associated with an overall shift of all preferred orientations. Note that $|u_0|^2 = 1$.

Correlated noise on hexagonal RGC mosaics

Realization of a random distortion field $\mathbf{y}(\mathbf{x})$ were generated by finding a complex-valued field $z(\mathbf{x})$ of which real and imaginary part correspond to dislocations in x and y direction, respectively. We constructed such a field using established methods (e.g. [51]) in the Fourier domain. In short, we drew complex-valued amplitudes $a(\mathbf{k})$ from a Gaussian distribution satisfying $\langle a(\mathbf{k})a(\mathbf{k}') \rangle = \tilde{f}(\mathbf{k}) \cdot \delta_{\mathbf{k},\mathbf{k}'}$, where $\tilde{f}(\mathbf{k})$ was a chosen power spectrum, in our case a Gaussian with width $1/\sigma$, σ being the desired correlation length. The corresponding amplitude spectrum was then inversely Fourier transformed to obtain a complex-valued field $z(\mathbf{x})$. Real and imaginary part of this field constitute two independent real-valued Gaussian random fields, both with the desired spatial statistics. We then transformed the coordinates of the hexagonal ON/OFF lattice points $\mathbf{r}_i = (x_i, y_i)$ according to $x_i \rightarrow x_i + \eta \Re(z(\mathbf{r}_i))$ and $y_i \rightarrow y_i + \eta \Im(z(\mathbf{r}_i))$. For the displacements of ON and OFF lattices, we used two independent complex-valued Gaussian random field realizations. Source code to generate hexagonal RGC mosaics with correlated spatial noise along with Matlab code for visualization is part of the supplementary material to this manuscript.

Generating PIPP RGCs mosaics

We generated RGC mosaics with a pairwise interacting point process using the code published by Schottdorf et al. [32] derived from the method developed in [49, 82].

Supporting Information

S1 Code. Source code for pinwheel statistics analysis and simulating statistical connectivity model layouts with a variety of RGC mosaics. Numerical implementation of the statistical

wiring model. We provide all necessary code to calculate single neuron properties and orientation domain layouts along with a Mathematica program which contains the analytical solution for both, an example single neuron and the domain layout obtained from a perfect and infinite lattice. The C-program ‘calculate_single_neuron.cpp’ calculates the same for a single neuron numerically. The C-program is provided to illustrate the use of the rfanalyzer class. The c-program ‘calculate_map.cpp’ calculates the same properties as ‘calculate_single_neuron.cpp’ but for a whole array of cells. After finishing a run, this program generates a set of ascii files in which the output is stored. These files are read in and analyzed by the Matlab program ‘plot_results.m’. It calculates the pinwheel density, pinwheel distance distributions, mean pinwheel distance and pinwheel density fluctuations as a function of subregion size. We compiled the code with gcc [g++ (Ubuntu 4.8.2-19ubuntu1) 4.8.2] and the gsl:

```
g++ ./calculate_single_neuron.cpp -lgsl -lgslcblas -O3 -march = native
g++ ./calculate_map.cpp -lgsl -lgslcblas -O3 -march = native
```

For this article, we have calculated orientation domain layouts with aspect ratio $22 \times 22 \Lambda$, sampled with 4096×4096 pixels. This corresponds to $\approx 6.5 \mu\text{m}$ per cortical unit for our standard combination of parameters ($r = r' = 170 \mu\text{m}$ and $\Delta\alpha = 7^\circ$). **Experimental data** The folder ‘map_data’ contains a data folder with single condition layouts and various ROIs for four ferrets cases. It also contains two Matlab files, ‘run_analysis.m’ and ‘plot_results.m’ to run the analysis and display the results. The full data set used in the present study is available on the neural data sharing platform <http://www.g-node.org/>. (ZIP)

Acknowledgments

We are grateful to Z. Kisvárdy (University of Debrecen, Debrecen, Hungary) for sharing optical imaging data. We thank Matthias Kaschube (Institute for Advanced Studies & Johann Wolfgang Goethe University, Frankfurt am Main, Germany) for providing his original PV-WAVE routines for the pinwheel statistics analysis and numerous stimulating discussions.

We thank Tim Gollisch, Ian Nauhaus, Kristina Nielsen, Joscha Liedtke, Conor Dempsey, and Lars Reichl for fruitful discussions and Bettina Hein, Markus Helmer and Juan Daniel Florez-Weidinger for comments on earlier versions of the manuscript.

Author Contributions

Performed the experiments: LEW DC. Analyzed the data: MS WK. Contributed reagents/materials/analysis tools: WK. Wrote the paper: MS WK LEW DC FW. Performed analytical study: MS. Performed and analyzed simulations: MS. Conceived and designed the study: FW WK.

References

1. Bruckstein AM, Donoho DL, Elad M. From sparse solutions of systems of equations to sparse modeling of signals and images. *SIAM Review*. 2009; 51(1):34–81. doi: [10.1137/060657704](https://doi.org/10.1137/060657704)
2. Ganguli S, Sompolinsky H. Statistical mechanics of compressed sensing. *Phys Rev Lett*. 2010; 104(18):188701–04. doi: [10.1103/PhysRevLett.104.188701](https://doi.org/10.1103/PhysRevLett.104.188701) PMID: [20482215](https://pubmed.ncbi.nlm.nih.gov/20482215/)
3. Ganguli S, Sompolinsky H. Compressed sensing, sparsity, and dimensionality in neuronal information processing and data analysis. *Ann Rev Neurosci*. 2012; 35:485–508. doi: [10.1146/annurev-neuro-062111-150410](https://doi.org/10.1146/annurev-neuro-062111-150410) PMID: [22483042](https://pubmed.ncbi.nlm.nih.gov/22483042/)
4. Babadi B, Sompolinsky H. Sparseness and expansion in sensory representations. *Neuron*. 2014; 83(5):1213–1226. doi: [10.1016/j.neuron.2014.07.035](https://doi.org/10.1016/j.neuron.2014.07.035) PMID: [25155954](https://pubmed.ncbi.nlm.nih.gov/25155954/)

5. Caron SJ, Ruta V, Abbott LF, Axel R. Random convergence of olfactory inputs in the *Drosophila* mushroom body. *Nature*. 2013; 497:113–117. doi: [10.1038/nature12063](https://doi.org/10.1038/nature12063) PMID: [23615618](https://pubmed.ncbi.nlm.nih.gov/23615618/)
6. Jonas JB, Schneider U, Naumann G. Count and density of human retinal photoreceptors. *Graef Arch Clin Exp Ophthalmol*. 1992; 230(6):505–10. doi: [10.1007/BF00181769](https://doi.org/10.1007/BF00181769)
7. Curcio CA, Allen KA. Topography of ganglion-cells in human retina. *J Comp Neurol*. 1990; 300(1):5–25. doi: [10.1002/cne.903000103](https://doi.org/10.1002/cne.903000103) PMID: [2229487](https://pubmed.ncbi.nlm.nih.gov/2229487/)
8. Selemon LD, Begovic A. Stereologic analysis of the lateral geniculate nucleus of the thalamus in normal and schizophrenic subjects. *Psychiat Res*. 2007; 151(1–2):1–10. doi: [10.1016/j.psychres.2006.11.003](https://doi.org/10.1016/j.psychres.2006.11.003)
9. Klekamp J, Riedel AA, Harper C, Kretschmann HJ. Quantitative changes during the postnatal maturation of the human visual cortex. *J Neurol Sci*. 1991; 103(2):136–43. doi: [10.1016/0022-510X\(91\)90156-2](https://doi.org/10.1016/0022-510X(91)90156-2) PMID: [1880530](https://pubmed.ncbi.nlm.nih.gov/1880530/)
10. Leuba G, Kraftsik R. Changes in volume, surface estimate, 3-dimensional shape and total number of neurons of the human primary visual cortex from midgestation until old-age. *Anat Embryol*. 1994; 190(4):351–366. doi: [10.1007/BF00187293](https://doi.org/10.1007/BF00187293) PMID: [7840422](https://pubmed.ncbi.nlm.nih.gov/7840422/)
11. Field GD, Gauthier JL, Sher A, Greschner M, Machado TA, Jepson LH, et al. Functional connectivity in the retina at the resolution of photoreceptors. *Nature*. 2010; 467(7316):673–677. doi: [10.1038/nature09424](https://doi.org/10.1038/nature09424) PMID: [20930838](https://pubmed.ncbi.nlm.nih.gov/20930838/)
12. Wässle H, Grünert U, J R, Boycott BB. Cortical magnification factor and the ganglion cell density of the primate retina. *Nature*. 1989; 347:643–646.
13. Wässle H, Grünert U, J R, Boycott BB. Retinal ganglion cell density and cortical magnification factor in the primate. *Vision Res*. 1989; 30(1):1897–1911.
14. von der Malsburg C. Self-organization of orientation sensitive cells in the striate cortex. *Kybernetik*. 1973; 14(2):85–100. doi: [10.1007/BF00288907](https://doi.org/10.1007/BF00288907) PMID: [4786750](https://pubmed.ncbi.nlm.nih.gov/4786750/)
15. Grinvald A, Lieke E, Frostig RD, Gilbert CD, Wiesel TN. Functional architecture of cortex revealed by optical imaging of intrinsic signals. *Nature*. 1986; 324(6095):361–64. doi: [10.1038/324361a0](https://doi.org/10.1038/324361a0) PMID: [3785405](https://pubmed.ncbi.nlm.nih.gov/3785405/)
16. Blasdel GG, Salama G. Voltage-sensitive dyes reveal a modular organization in monkey striate cortex. *Nature*. 1986; 321(6070):579–585. doi: [10.1038/321579a0](https://doi.org/10.1038/321579a0) PMID: [3713842](https://pubmed.ncbi.nlm.nih.gov/3713842/)
17. Swindale NV, Matsubara JA, Cynader MS. Surface organization of orientation and direction selectivity in cat area 18. *J Neurosci*. 1987; 7(5):1414–27. PMID: [3572486](https://pubmed.ncbi.nlm.nih.gov/3572486/)
18. Bonhoeffer T, Grinvald A. Iso-orientation domains in cat visual cortex are arranged in pinwheel-like patterns. *Nature*. 1991; 353:429–431. doi: [10.1038/353429a0](https://doi.org/10.1038/353429a0) PMID: [1896085](https://pubmed.ncbi.nlm.nih.gov/1896085/)
19. Bosking WH, Zhang Y, Schofield B, Fitzpatrick D. Orientation selectivity and the arrangement of horizontal connections in tree shrew striate cortex. *J Neurosci*. 1997; 17(6):2112–2127. PMID: [9045738](https://pubmed.ncbi.nlm.nih.gov/9045738/)
20. Chapman B, Stryker MP, Bonhoeffer T. Development of orientation preference maps in ferret primary visual cortex. *J Neurosci*. 1996; 16(20):6443–6453. PMID: [8815923](https://pubmed.ncbi.nlm.nih.gov/8815923/)
21. Swindale NV. A model for the formation of orientation columns. *Proc Roy Soc B-Biol Sci*. 1982; 215(1199):211–30. doi: [10.1098/rspb.1982.0038](https://doi.org/10.1098/rspb.1982.0038)
22. Wolf F, Geisel T. Spontaneous pinwheel annihilation during visual development. *Nature*. 1998; 395:73–78. doi: [10.1038/25736](https://doi.org/10.1038/25736) PMID: [9738500](https://pubmed.ncbi.nlm.nih.gov/9738500/)
23. Kaschube M, Schnabel M, Löwel S, Coppola DM, White LE, Wolf F. Universality in the evolution of orientation columns in the visual cortex. *Science*. 2010; 330(6007):1113–6. doi: [10.1126/science.1194869](https://doi.org/10.1126/science.1194869) PMID: [21051599](https://pubmed.ncbi.nlm.nih.gov/21051599/)
24. Soodak RE. Two-dimensional modeling of visual receptive fields using Gaussian subunits. *Proc Natl Acad Sci, USA*. 1986; 83(23):9259–9263. doi: [10.1073/pnas.83.23.9259](https://doi.org/10.1073/pnas.83.23.9259)
25. Soodak RE. The retinal ganglion cell mosaic defines orientation columns in striate cortex. *Proc Natl Acad Sci, USA*. 1987; 84(11):3936–3940. doi: [10.1073/pnas.84.11.3936](https://doi.org/10.1073/pnas.84.11.3936)
26. Wässle H, Boycott BB, Illing RB. Morphology and mosaic of on- and off-beta cells in the cat retina and some functional considerations. *Proc Roy Soc B-Biol Sci*. 1981; 212(1187):177–195. doi: [10.1098/rspb.1981.0033](https://doi.org/10.1098/rspb.1981.0033)
27. Alonso JM, Usrey WM, Reid RC. Rules of connectivity between geniculate cells and simple cells in cat primary visual cortex. *J Neurosci*. 2001; 21(11):4002–4015. PMID: [11356887](https://pubmed.ncbi.nlm.nih.gov/11356887/)
28. Paik SB, Ringach DL. Retinal origin of orientation maps in visual cortex. *Nat Neurosci*. 2011; 14(7):919–925. doi: [10.1038/nn.2824](https://doi.org/10.1038/nn.2824) PMID: [21623365](https://pubmed.ncbi.nlm.nih.gov/21623365/)
29. Paik SB, Ringach DL. Link between orientation and retinotopic maps in primary visual cortex. *Proc Natl Acad Sci, USA*. 2012; 109:7091–7096. doi: [10.1073/pnas.1118926109](https://doi.org/10.1073/pnas.1118926109)

30. Paik SB. Developmental models of functional maps in cortex. *Biomed Eng Lett*. 2014; 4(3):223–225.
31. Hore VRA, Troy JB, Eglén SJ. Parasol cell mosaics are unlikely to drive the formation of structured orientation maps in primary visual cortex. *Vis Neurosci*. 2012; 33:859–871.
32. Schottdorf M, Eglén SJ, Wolf F, Keil W. Can retinal ganglion cell dipoles seed iso-orientation domains in the visual cortex? *PLoS ONE*. 2014; e86139. doi: [10.1371/journal.pone.0086139](https://doi.org/10.1371/journal.pone.0086139) PMID: [24475081](https://pubmed.ncbi.nlm.nih.gov/24475081/)
33. Keil W, Kaschube M, Schnabel M, Kisvarday ZF, Löwel S, Coppola DM, et al. Response to comment on “Universality in the evolution of orientation columns in the visual cortex”. *Science*. 2012; 336(6080):413–413. doi: [10.1126/science.1206416](https://doi.org/10.1126/science.1206416)
34. Kaas J. Evolution of columns, modules, and domains in the neocortex of primates. *Proc Natl Acad Sci, USA*. 2012; 109:10655–10660. doi: [10.1073/pnas.1201892109](https://doi.org/10.1073/pnas.1201892109)
35. Murphy WJ, Eizirik E, O’Brien SJ, Madsen O, Scally M, Douady CJ, et al. Resolution of the early placental mammal radiation using Bayesian phylogenetics. *Science*. 2001; 294(5550):2348–2351. doi: [10.1126/science.1067179](https://doi.org/10.1126/science.1067179) PMID: [11743200](https://pubmed.ncbi.nlm.nih.gov/11743200/)
36. Kriegs JO, Churakov G, Kieffmann M, Jordan U, Brosius J, Schmitz J. Retroposed elements as archives for the evolutionary history of placental mammals. *PLoS Biol*. 2006; 4(4):e91. doi: [10.1371/journal.pbio.0040091](https://doi.org/10.1371/journal.pbio.0040091) PMID: [16515367](https://pubmed.ncbi.nlm.nih.gov/16515367/)
37. Kriegs JO, Churakov G, Jurka J, Brosius J, Schmitz J. Evolutionary history of 7SL RNA-derived SINEs in Supraprimates. *Trends Genet*. 2007; 4(23):158–161. doi: [10.1016/j.tig.2007.02.002](https://doi.org/10.1016/j.tig.2007.02.002)
38. Bininda-Emonds ORP, Cardillo M, Jones KE, MacPhee RDE, Beck RMD, Grenyer R, et al. The delayed rise of present-day mammals. *Nature*. 2007; 7135(446):507–12. doi: [10.1038/nature05634](https://doi.org/10.1038/nature05634)
39. Meredith RW, Janečka JE, Gatesy J, Ryder OA, Fisher CA, Teeling EC, et al. Impacts of the Cretaceous Terrestrial Revolution and KPg extinction on mammal diversification. *Science*. 2011; 334(6055):521–24. doi: [10.1126/science.1211028](https://doi.org/10.1126/science.1211028) PMID: [21940861](https://pubmed.ncbi.nlm.nih.gov/21940861/)
40. O’Leary MA, Bloch JL, Flynn JJ, Gaudin TJ, Giallombardo A, Giannini NP, et al. The placental mammal ancestor and the post-K-Pg radiation of placentals. *Science*. 2013; 339(6120):662–67. doi: [10.1126/science.1229237](https://doi.org/10.1126/science.1229237) PMID: [23393258](https://pubmed.ncbi.nlm.nih.gov/23393258/)
41. Springer MS, Meredith RW, Teeling EC, Murphy WJ. Technical comment on “The placental mammal ancestor and the post-K-Pg radiation of placentals”. *Science*. 2013; 6146(341):613. doi: [10.1126/science.1238025](https://doi.org/10.1126/science.1238025)
42. O’Leary MA, Bloch JL, Flynn JJ, Gaudin TJ, Giallombardo A, Giannini NP, et al. Response to comment on “The placental mammal ancestor and the post-K-Pg radiation of placentals”. *Science*. 2013; 341(6146):613. doi: [10.1126/science.1238162](https://doi.org/10.1126/science.1238162) PMID: [23929968](https://pubmed.ncbi.nlm.nih.gov/23929968/)
43. Chisum HJ, Mooser F, Fitzpatrick D. Emergent properties of layer 2/3 neurons reflect the collinear arrangement of horizontal connections in tree shrew visual cortex. *J Neurosci*. 2003; 23(7):2947–2960. PMID: [12684482](https://pubmed.ncbi.nlm.nih.gov/12684482/)
44. Van Hooser SD, Roy A, Rhodes HJ, Culp JH, Fitzpatrick D. Transformation of receptive field properties from lateral geniculate nucleus to superficial V1 in the Tree Shrew. *J Neurosci*. 2013; 33:11494–11505. doi: [10.1523/JNEUROSCI.1464-13.2013](https://doi.org/10.1523/JNEUROSCI.1464-13.2013) PMID: [23843520](https://pubmed.ncbi.nlm.nih.gov/23843520/)
45. Hubel D, Wiesel T. Receptive fields, binocular interaction and functional architecture in the cat’s visual cortex. *J Physiol*. 1962; 160:106–154. doi: [10.1113/jphysiol.1962.sp006837](https://doi.org/10.1113/jphysiol.1962.sp006837) PMID: [14449617](https://pubmed.ncbi.nlm.nih.gov/14449617/)
46. Hubel D, Wiesel T. Shape and arrangement of columns in cat’s striate cortex. *J Physiol*. 1963; 165:559–568. doi: [10.1113/jphysiol.1963.sp007079](https://doi.org/10.1113/jphysiol.1963.sp007079) PMID: [13955384](https://pubmed.ncbi.nlm.nih.gov/13955384/)
47. Kaschube M, Wolf F, Geisel T, Löwel S. Genetic influence on quantitative features of neocortical architecture. *J Neurosci*. 2002; 22(16):7206–7217. PMID: [12177215](https://pubmed.ncbi.nlm.nih.gov/12177215/)
48. Kaschube M, Schnabel M, Wolf F, Löwel S. Interareal coordination of columnar architectures during visual cortical development. *Proc Natl Acad Sci, USA*. 2009; 40(106):17205–17210. doi: [10.1073/pnas.0901615106](https://doi.org/10.1073/pnas.0901615106)
49. Eglén SJ, Diggie PJ, Troy JB. Homotropic constraints dominate positioning of on- and off-center beta retinal ganglion cells. *Vis Neurosci*. 2005; 22(6):859–871. doi: [10.1017/S0952523805226147](https://doi.org/10.1017/S0952523805226147) PMID: [16469193](https://pubmed.ncbi.nlm.nih.gov/16469193/)
50. Wolf F, Geisel T. Universality in visual cortical pattern formation. *J Physiol*. 2003; 97(2–3):253–264.
51. Schnabel M, Kaschube M, Löwel S, Wolf F. Random waves in the brain: Symmetries and defect generation in the visual cortex. *Eur Phys J, Special Topics*. 2007; 145(1):137–157. doi: [10.1140/epjst/e2007-00152-5](https://doi.org/10.1140/epjst/e2007-00152-5)
52. Kaas JH. The evolution of the complex sensory and motor systems of the human brain. *Brain Res Bull*. 2008; 75(2–4):384–390. doi: [10.1016/j.brainresbull.2007.10.009](https://doi.org/10.1016/j.brainresbull.2007.10.009) PMID: [18331903](https://pubmed.ncbi.nlm.nih.gov/18331903/)
53. Kaschube M. Neural maps versus salt-and-pepper organization in visual cortex. *Curr Opin Neurobiol*. 2014; 24:95–102. doi: [10.1016/j.conb.2013.08.017](https://doi.org/10.1016/j.conb.2013.08.017) PMID: [24492085](https://pubmed.ncbi.nlm.nih.gov/24492085/)

54. Usrey WM, Reppas JB, Reid RC. Specificity and strength of retinogeniculate connections. *J Neurophysiol.* 1999; 82(6):3527–3540. PMID: [10601479](#)
55. Ferster D, Chung S, Wheat H. Orientation selectivity of thalamic input to simple cells of cat visual cortex. *Nature.* 1996; 380:249–252. doi: [10.1038/380249a0](#) PMID: [8637573](#)
56. Reid RC, Alonso JM. Specificity of monosynaptic connections from thalamus to visual cortex. *Nature.* 1995; 378(6554):281–284. doi: [10.1038/378281a0](#) PMID: [7477347](#)
57. Thompson KG, Zhou Y, Leventhal AG. Direction-sensitive X and Y cells within the A laminae of the cat's LGNd. *Vis Neurosci.* 1994; 11(5):927–938. doi: [10.1017/S095252380003886](#) PMID: [7947406](#)
58. Shou T, Leventhal AG. Organized arrangement of orientation-sensitive cat's dorsal lateral geniculate nucleus. *J Neurosci.* 1989; 9(12):4287–4302. PMID: [2593002](#)
59. Levick WR, Thibos LN. Orientation bias of cat retinal ganglion cells. *Nature.* 1980; 286:389–390. doi: [10.1038/286389a0](#) PMID: [7402319](#)
60. Levay S, Gilbert CD. Laminar patterns of geniculocortical projections in the cat. *Brain Res.* 1976; 113:1–19. doi: [10.1016/0006-8993\(76\)90002-0](#) PMID: [953720](#)
61. Hammond P. Cat retinal ganglion cells: size and shape of receptive field centres. *J Physiol.* 1974; 242(1):99–118. doi: [10.1113/jphysiol.1974.sp010696](#) PMID: [4436829](#)
62. Boycott BB, Wässle H. The morphological types of ganglion cells of the domestic cat's retina. *J Physiol.* 1974; 240:397–419. doi: [10.1113/jphysiol.1974.sp010616](#) PMID: [4422168](#)
63. Hubel D, Wiesel T. Integrative action in the cat's lateral geniculate body. *J Physiol.* 1961; 155:385–398. doi: [10.1113/jphysiol.1961.sp006635](#) PMID: [13716436](#)
64. Hubel D, Wiesel T. Receptive fields of single neurones in the cat's striate cortex. *J Physiol.* 1959; 148:574–591. doi: [10.1113/jphysiol.1959.sp006308](#) PMID: [14403679](#)
65. Ohki K, Chung S, Kara P, Hübener M, Bonhoeffer T, Reid RC. Highly ordered arrangement of single neurons in orientation pinwheels. *Nature.* 2006; 442:925–928. doi: [10.1038/nature05019](#) PMID: [16906137](#)
66. Blasdel G, Fitzpatrick D. Physiological organization of layer 4 in macaque striate cortex. *J Neurosci.* 1984; 4(3):880–895. PMID: [6200586](#)
67. Ringach DL, Shapley RM, Hawken MJ. Orientation selectivity in macaque V1: diversity and laminar dependence. *J Neurosci.* 2002; 22(13):5639–5651. PMID: [12097515](#)
68. Gur M, Kagan I, Snodderly DM. Orientation and direction selectivity of neurons in V1 of alert monkeys: functional relationships and laminar distributions. *Cereb Cortex.* 2005; 15(8):1207–1221. doi: [10.1093/cercor/bhi003](#) PMID: [15616136](#)
69. Smith EL, Chino YM, Ridder WH, Kitagawa K, Langston A. Orientation bias of neurons in the lateral geniculate nucleus of macaque monkeys. *Vis Neurosci.* 1990; 5(6):525–545. doi: [10.1017/S095252380000699](#) PMID: [2085469](#)
70. van Essen DC, Zeki SM. The topographic organization of rhesus monkey prestriate cortex. *J Physiol.* 1978; 277:193–226. doi: [10.1113/jphysiol.1978.sp012269](#)
71. Schall JD, Perry VH, Leventhal AG. Retinal ganglion cell dendritic fields in old-world monkeys are oriented radially. *Brain Res.* 1986; 368(1):18–23. doi: [10.1016/0006-8993\(86\)91037-1](#) PMID: [3955359](#)
72. Obermayer K, Blasdel GG. Geometry of orientation and ocular dominance columns in monkey striate cortex. *J Neurosci.* 1993; 13(10):4114–4129. PMID: [8410181](#)
73. Irvin GE, Casagrande VA, Norton TT. Center/surround relationships of magnocellular, parvocellular, and koniocellular relay cells in primate lateral geniculate nucleus. *Vis Neurosci.* 1993; 10(2):363–373. doi: [10.1017/S0952523800003758](#) PMID: [8485098](#)
74. Humphrey AL, Albano JE, Norton TT. Organization of ocular dominance in tree shrew striate cortex. *Brain Res.* 1977; 134(2):159–89. doi: [10.1016/0006-8993\(77\)91069-1](#)
75. Kretz R, Rager G, Norton TT. Laminar organization of ON and OFF regions and ocular dominance in the striate cortex of the tree shrew (*Tupaia belangeri*). *J Comp Neurol.* 1986; 251(1):135–145. doi: [10.1002/cne.902510110](#) PMID: [3760256](#)
76. Fitzpatrick D. The functional organization of local circuits in visual cortex: insights from the study of tree shrew striate cortex. *Cereb Cortex.* 1996; 6(3):329–41. doi: [10.1093/cercor/6.3.329](#) PMID: [8670661](#)
77. Dräger UC. Receptive fields of single cells and topography in mouse visual cortex. *J Comp Neurol.* 1975; 160(3):269–290. doi: [10.1002/cne.901600302](#) PMID: [1112925](#)
78. Ohki K, Chung S, Ch'ng YH, Kara P, Reid RC. Functional imaging with cellular resolution reveals precise micro-architecture in visual cortex. *Nature.* 2005; 433:597–603. doi: [10.1038/nature03274](#) PMID: [15660108](#)

79. Niell CM, Stryker MP. Highly selective receptive fields in mouse visual cortex. *J Neurosci*. 2008; 28(30):7520–7536. doi: [10.1523/JNEUROSCI.0623-08.2008](https://doi.org/10.1523/JNEUROSCI.0623-08.2008) PMID: [18650330](https://pubmed.ncbi.nlm.nih.gov/18650330/)
80. Elstrott J, Anishchenko A, Greschner M, Sher A, Litke AM, Chichilnisky EJ, et al. Direction selectivity in the retina is established independent of visual experience and cholinergic retinal waves. *Neuron*. 2008; 58(4):499–506. doi: [10.1016/j.neuron.2008.03.013](https://doi.org/10.1016/j.neuron.2008.03.013) PMID: [18498732](https://pubmed.ncbi.nlm.nih.gov/18498732/)
81. Marshel JH, Kaye AP, Nauhaus I, Callaway EM. Anterior-posterior direction opponency in the superficial mouse lateral geniculate nucleus. *Neuron*. 2012; 76(4):713–720. doi: [10.1016/j.neuron.2012.09.021](https://doi.org/10.1016/j.neuron.2012.09.021) PMID: [23177957](https://pubmed.ncbi.nlm.nih.gov/23177957/)
82. Ringach DL. On the origin of the functional architecture of the cortex. *PLoS ONE*. 2007; 2(2):e251. doi: [10.1371/journal.pone.0000251](https://doi.org/10.1371/journal.pone.0000251) PMID: [17330140](https://pubmed.ncbi.nlm.nih.gov/17330140/)
83. Ringach DL. Haphazard wiring of simple receptive fields and orientation columns in visual cortex. *J Neurophysiol*. 2004; 92(1):468–476. doi: [10.1152/jn.01202.2003](https://doi.org/10.1152/jn.01202.2003) PMID: [14999045](https://pubmed.ncbi.nlm.nih.gov/14999045/)
84. Enroth-Cugell C, Robson JG. The contrast sensitivity of retinal ganglion cells of the cat. *J Physiol*. 1966; 187:517–552. doi: [10.1113/jphysiol.1966.sp008107](https://doi.org/10.1113/jphysiol.1966.sp008107) PMID: [16783910](https://pubmed.ncbi.nlm.nih.gov/16783910/)
85. Jones JP, Palmer LA. The two-dimensional spatial structure of simple receptive fields in cat striate cortex. *J Neurophysiol*. 1987; 58(6):1187–1211. PMID: [3437330](https://pubmed.ncbi.nlm.nih.gov/3437330/)
86. Ringach DL. Spatial Structure and Symmetry of Simple-Cell Receptive Fields in Macaque Primary Visual Cortex. *J Neurophysiol*. 2002; 88(1):455–463. PMID: [12091567](https://pubmed.ncbi.nlm.nih.gov/12091567/)
87. Heeger DJ. Nonlinear model of neural responses in cat visual cortex. In: Landy M, Movshon JA, Editors. *Computational Models of Visual Processing*. The MIT Press; 1991. p. 406.
88. Ferster D. Linearity of synaptic interactions in the assembly of receptive fields in cat visual cortex. *Curr Op Neurobiol*. 1994; 4:563–568. doi: [10.1016/0959-4388\(94\)90058-2](https://doi.org/10.1016/0959-4388(94)90058-2) PMID: [7812146](https://pubmed.ncbi.nlm.nih.gov/7812146/)
89. Hetherington P, Swindale NV. Receptive field and orientation scatter studied by tetrode recordings in cat area 17. *Vis Neurosci*. 1999; 16:637–652. doi: [10.1017/S0952523899164046](https://doi.org/10.1017/S0952523899164046) PMID: [10431913](https://pubmed.ncbi.nlm.nih.gov/10431913/)
90. Nauhaus I, Benucci A, Carandini M, Ringach DL. Neuronal selectivity and local map structure in visual cortex. *Neuron*. 2008; 57:673–679. doi: [10.1016/j.neuron.2008.01.020](https://doi.org/10.1016/j.neuron.2008.01.020) PMID: [18341988](https://pubmed.ncbi.nlm.nih.gov/18341988/)
91. Braitenberg V, Braitenberg C. Geometry of orientation columns in the visual cortex. *Biol Cybern*. 1979; 33:179–186. doi: [10.1007/BF00337296](https://doi.org/10.1007/BF00337296) PMID: [497262](https://pubmed.ncbi.nlm.nih.gov/497262/)
92. Reichl L, Heide D, Löwel S, Crowley JC, Kaschube M, Wolf F. Coordinated optimization of visual cortical maps (I) Symmetry-based analysis. *PLoS Comp Biol*. 2012; 8(11):e1002466. doi: [10.1371/journal.pcbi.1002466](https://doi.org/10.1371/journal.pcbi.1002466)
93. Reichl L, Heide D, Löwel S, Crowley JC, Kaschube M, Wolf F. Coordinated optimization of visual cortical maps (II) Numerical studies. *PLoS Comp Biol*. 2012; 8(11):e1002756. doi: [10.1371/journal.pcbi.1002756](https://doi.org/10.1371/journal.pcbi.1002756)
94. Blair HT, Welday AC, Zhang K. Scale-invariant memory representations emerge from moiré interference between grid fields that produce theta oscillations: a computational model. *J Neurosci*. 2007; 27(12):3211–3229. doi: [10.1523/JNEUROSCI.4724-06.2007](https://doi.org/10.1523/JNEUROSCI.4724-06.2007) PMID: [17376982](https://pubmed.ncbi.nlm.nih.gov/17376982/)
95. Amidror I. *The Theory of the Moiré Phenomenon, Volume I*. 2nd ed. Springer; 2009.
96. Nishijima Y, Oster G. Moiré patterns: Their application to refractive index and refractive index gradient measurements. *J Opt Soc Am*. 1964; 54:1–5. doi: [10.1364/JOSA.54.000001](https://doi.org/10.1364/JOSA.54.000001)
97. Berry MV, Dennis MR. Knotted and linked phase singularities in monochromatic waves. *Proc R Soc Lond A*. 2001; 457(3):2251–2263. doi: [10.1098/rspa.2001.0826](https://doi.org/10.1098/rspa.2001.0826)
98. Field GD, Chichilnisky EJ. Information processing in the primate retina: circuitry and coding. *Ann Rev Neurosci*. 2007; 30:1–30. doi: [10.1146/annurev.neuro.30.051606.094252](https://doi.org/10.1146/annurev.neuro.30.051606.094252) PMID: [17335403](https://pubmed.ncbi.nlm.nih.gov/17335403/)
99. Miller KD. A model for the development of simple cell receptive fields and the ordered arrangement of orientation columns through activity-dependent competition between ON- and OFF-center inputs. *J Neurosci*. 1994; 14(1):409–441. PMID: [8283248](https://pubmed.ncbi.nlm.nih.gov/8283248/)
100. Martinez LM, Molano-Mazón M, Wang X, Sommer FT, Hirsch JA. Statistical wiring of thalamic receptive fields optimizes spatial sampling of the retinal image. *Neuron*. 2014; 4(81):943–956. doi: [10.1016/j.neuron.2013.12.014](https://doi.org/10.1016/j.neuron.2013.12.014)
101. Wolf F. Symmetry, multistability, and long-range interactions in brain development. *Phys Rev Lett*. 2005 Nov; 95(20):208701. doi: [10.1103/PhysRevLett.95.208701](https://doi.org/10.1103/PhysRevLett.95.208701) PMID: [16384113](https://pubmed.ncbi.nlm.nih.gov/16384113/)
102. Kaschube M, Schnabel M, Wolf F. Self-organization and the selection of pinwheel density in visual cortical development. *New J Phys*. 2008; 10(1):015009. doi: [10.1088/1367-2630/10/1/015009](https://doi.org/10.1088/1367-2630/10/1/015009)
103. Keil W, Wolf F. Coverage, continuity, and visual cortical architecture. *Neural Syst & Circ*. 2011; 1(1):17. doi: [10.1186/2042-1001-1-17](https://doi.org/10.1186/2042-1001-1-17)

104. Ernst UA, Pawelzik KR, Sahar-Pikielny C, Tsodyks MV. Intracortical origin of visual maps. *Nat Neurosci.* 2001; 4:431–436. doi: [10.1038/86089](https://doi.org/10.1038/86089) PMID: [11276235](https://pubmed.ncbi.nlm.nih.gov/11276235/)
105. Hein B, Kaschube M. Weakly coherent neuronal interactions are sufficient to explain highly coherent orientation preference maps. *Society for Neuroscience Abstracts.* 2014; 155.02(CC34).
106. Grabska-Barwinska A, von der Malsburg C. Establishment of a scaffold for orientation maps in primary visual cortex of higher mammals. *J Neurosci.* 2008; 28(1):249–257. doi: [10.1523/JNEUROSCI.5514-06.2008](https://doi.org/10.1523/JNEUROSCI.5514-06.2008) PMID: [18171942](https://pubmed.ncbi.nlm.nih.gov/18171942/)
107. Reichl L, Löwel S, Wolf F. Pinwheel stabilization by ocular dominance segregation. *Phys Rev Lett.* 2009; 102(20):208101. doi: [10.1103/PhysRevLett.102.208101](https://doi.org/10.1103/PhysRevLett.102.208101) PMID: [19519077](https://pubmed.ncbi.nlm.nih.gov/19519077/)
108. Jin J, Wang Y, Swadlow HA, Alonso JM. Population receptive fields of ON and OFF thalamic inputs to an orientation column in visual cortex. *Nat Neurosci.* 2011; 2(14):232–238. doi: [10.1038/nn.2729](https://doi.org/10.1038/nn.2729)
109. Illing RB, Wässle H. The retinal projection to the thalamus in the cat—a quantitative investigation and a comparison with the retinotectal pathway. *J Comp Neurol.* 1981; 2(202):265–285. doi: [10.1002/cne.902020211](https://doi.org/10.1002/cne.902020211)
110. Peters A, Payne BR. Numerical relationships between geniculocortical afferents and pyramidal cell modules in cat primary visual cortex. *Cereb Cortex.* 1993; 1(3):69–78. doi: [10.1093/cercor/3.1.69](https://doi.org/10.1093/cercor/3.1.69)
111. Adams DL, Horton JC. Shadows cast by retinal blood vessels mapped in primary visual cortex. *Science.* 2002; 298(5593):572–576. doi: [10.1126/science.1074887](https://doi.org/10.1126/science.1074887) PMID: [12386328](https://pubmed.ncbi.nlm.nih.gov/12386328/)
112. Giacomantonio CE, Goodhill GJ. The effect of angioscotomas on map structure in primary visual cortex. *J Neurosci.* 2007; 18(27):4935–4946. doi: [10.1523/JNEUROSCI.1261-06.2007](https://doi.org/10.1523/JNEUROSCI.1261-06.2007)
113. Erwin E, Obermayer K, Schulten K. Models of orientation and ocular dominance columns in the visual cortex: A critical comparison. *Neural Comp.* 1995; 7:425–468. doi: [10.1162/neco.1995.7.3.425](https://doi.org/10.1162/neco.1995.7.3.425)
114. Swindale NV. The development of topography in the visual cortex: a review of models. *Network.* 1996; 7(2):161–247. PMID: [16754382](https://pubmed.ncbi.nlm.nih.gov/16754382/)
115. Goodhill GJ. Contributions of theoretical modeling to the understanding of neural map development. *Neuron.* 2007; 2(56):301–311. doi: [10.1016/j.neuron.2007.09.027](https://doi.org/10.1016/j.neuron.2007.09.027)
116. Durbin R, Mitchison G. A dimension reduction framework for understanding cortical maps. *Nature.* 1990; 343:644–647. doi: [10.1038/343644a0](https://doi.org/10.1038/343644a0) PMID: [2304536](https://pubmed.ncbi.nlm.nih.gov/2304536/)
117. Cimponeriu A, Goodhill GJ. Dynamics of cortical map development in the elastic net model. *Neurocomputing.* 2000; 32–33:83–90. doi: [10.1016/S0925-2312\(00\)00147-8](https://doi.org/10.1016/S0925-2312(00)00147-8)
118. Carreira-Perpinán M, Goodhill GJ. Influence of lateral connections on the structure of cortical maps. *J Neurophysiol.* 2004; 92(5):2947–2959. doi: [10.1152/jn.00281.2004](https://doi.org/10.1152/jn.00281.2004) PMID: [15190092](https://pubmed.ncbi.nlm.nih.gov/15190092/)
119. Kaschube M, Wolf F, Puhlmann M, Rathjen S, Schmidt KF, Geisel T, et al. The pattern of ocular dominance columns in cat primary visual cortex: intra- and interindividual variability of column spacing and its dependence on genetic background. *Eur J Neurosci.* 2003; 18:3251–3266. doi: [10.1111/j.1460-9568.2003.02979.x](https://doi.org/10.1111/j.1460-9568.2003.02979.x) PMID: [14686899](https://pubmed.ncbi.nlm.nih.gov/14686899/)
120. Weisstein EW. Jacobi Theta Functions; Available from: <http://mathworld.wolfram.com/JacobiThetaFunctions.html>.
121. Jones JP, Palmer LA. An evaluation of the two-dimensional Gabor filter model of simple receptive fields in cat striate cortex. *J Neurophysiol.* 1987; 58(6):1233–1258. PMID: [3437332](https://pubmed.ncbi.nlm.nih.gov/3437332/)
122. Mazer JA, Vinje WE, McDermott J, Schiller PH, Gallant JL. Spatial frequency and orientation tuning dynamics in area V1. *Proc Nat'l Acad Sci, USA.* 2002; 99(3):1645–1650. doi: [10.1073/pnas.022638499](https://doi.org/10.1073/pnas.022638499)
123. Wörgötter F, Eysel UT. Quantitative determination of orientational and directional components in the response of visual cortical cells to moving stimuli. *Biol Cybern.* 1987; 355:349–355.
124. Swindale NV. Orientation tuning curves: empirical description and estimation of parameters. *Biol Cybern.* 1998; 78:45–56. doi: [10.1007/s004220050411](https://doi.org/10.1007/s004220050411) PMID: [9518026](https://pubmed.ncbi.nlm.nih.gov/9518026/)
125. Bredfeldt CE, Ringach DL. Dynamics of spatial frequency tuning in macaque V1. *J Neurosci.* 2002; 22(5):1976–1984. PMID: [11880528](https://pubmed.ncbi.nlm.nih.gov/11880528/)
126. Issa NP, Trepel C, Stryker MP. Spatial frequency maps in cat visual cortex. *J Neurosci.* 2000; 20(22):8504–8514.
127. Movshon JA, Thompson ID, Tolhurst DJ. Spatial and temporal contrast sensitivity of neurones in areas 17 and 18 of the cat's visual cortex. *J Physiol.* 1978; 283:101–120. doi: [10.1113/jphysiol.1978.sp012490](https://doi.org/10.1113/jphysiol.1978.sp012490) PMID: [722570](https://pubmed.ncbi.nlm.nih.gov/722570/)

CORRECTION

Correction: Random Wiring, Ganglion Cell Mosaics, and the Functional Architecture of the Visual Cortex

The *PLOS Computational Biology* Staff

There are several errors in [Table 1](#). The authors confirm that the errors do not affect their conclusions in any way. Please view the correct version of [Table 1](#) here:



OPEN ACCESS

Citation: The *PLOS Computational Biology* Staff (2016) Correction: Random Wiring, Ganglion Cell Mosaics, and the Functional Architecture of the Visual Cortex. *PLoS Comput Biol* 12(2): e1004758. doi:10.1371/journal.pcbi.1004758

Published: February 3, 2016

Copyright: © 2016 The PLOS Computational Biology Staff. This is an open access article distributed under the terms of the [Creative Commons Attribution License](#), which permits unrestricted use, distribution, and reproduction in any medium, provided the original author and source are credited.

Table 1. The six orientation domain layout parameters characterizing the common design.

	Pinwheel density ρ	NN distance ind. charge	NN distance same charge	NN distance opp. charge	Variab. Exponent γ	Variab. coeff. c
Ferret	3.14 [3.06, 3.23]	0.355 [0.347, 0.363]	0.530 [0.521, 0.539]	0.394 [0.383, 0.403]	0.40 [0.37, 0.44]	1.07 [0.97, 1.15]
Dark-reared Ferret	3.30 [3.16, 3.42]	0.346 [0.334, 0.361]	0.511 [0.499, 0.528]	0.381 [0.366, 0.401]	0.39 [0.35, 0.46]	1.02 [0.90, 1.12]
Cat	3.24 [3.06, 3.42]	0.366 [0.352, 0.381]	0.534 [0.519, 0.551]	0.407 [0.388, 0.428]	0.48 [0.41, 0.58]	0.83 [0.68, 0.95]
Treeshrew	3.08 [2.99, 3.16]	0.364 [0.359, 0.370]	0.521 [0.514, 0.528]	0.404 [0.396, 0.411]	0.36 [0.34, 0.39]	1.13 [1.05, 1.19]
Galago	3.12 [2.93, 3.27]	0.363 [0.345, 0.381]	0.536 [0.522, 0.556]	0.396 [0.375, 0.417]	0.45 [0.42, 0.52]	0.85 [0.71, 0.95]
Ensemble Average	3.13	0.359	0.525	0.397	0.40	1.05
Common Design–CR	[3.09, 3.19]	[0.354, 0.363]	[0.520, 0.530]	[0.391, 0.403]	[0.37, 0.42]	[0.99, 1.11]
One Species–CR	[2.93, 3.42]	[0.334, 0.381]	[0.499, 0.556]	[0.366, 0.428]	[0.34, 0.58]	[0.68, 1.19]

doi:10.1371/journal.pcbi.1004758.t001

Values were calculated with the code provided in the supplemental material and intervals indicate 95% bootstrap confidence intervals. Also shown is the grand average and the associated one species and common design consistency ranges (CR).

doi:[10.1371/journal.pcbi.1004602.t001](https://doi.org/10.1371/journal.pcbi.1004602.t001)

Reference

- Schottdorf M, Keil W, Coppola D, White LE, Wolf F (2015) Random Wiring, Ganglion Cell Mosaics, and the Functional Architecture of the Visual Cortex. *PLoS Comput Biol* 11(11): e1004602. doi:[10.1371/journal.pcbi.1004602](https://doi.org/10.1371/journal.pcbi.1004602) PMID: [26575467](https://pubmed.ncbi.nlm.nih.gov/26575467/)

Which surrogate cortex?

“The way to understand a complicated system is to build it step by step, and each step of building is a step of understanding.”

Idan Segev cited in⁴⁶⁸.

4.1 Content

In this chapter, we develop the surrogate cortex, the target circuit of the afferent pathway.

We first assessed the viability of what we call *virtual networks*, realized by closed loop optogenetic connections^{162,348} between islands of individual neurons grown on multielectrode arrays. Virtual networks are artificial neural networks with biological neurons as nodes. This approach seemed promising because it allows in principle to construct arbitrary networks. To generate such islands, we developed a patterning technique to constrain the growth of cells to individual electrodes of a MEA. This patterning technique will provide a platform to predesign arbitrary networks with high reproducibility, where the network itself can be manipulated on the fly. We made substantial progress in designing the neuronal island system, the key contribution of optogenetic closed loop virtual networks. However, we found that this is not the way to go: Considering the finite yield of populated islands together with only a fraction of active electrodes generates substantial variability and we would need to adapt the circuit to the culture.

A second path that we followed, was to design a neuronal circuit from dissociated neurons in which the local neuronal circuits are as realistic as possible. We designed cultures with the same cell density and cellular content as the neocortical input layer IV and let them develop naturally. These cultures are easy to produce on a large scale and show rich spontaneous activity, resembling the spontaneous activity in the young neocortex. To interface this surrogate cortex with the virtual sensory pathway, we next constructed a digital phase-only holographic projection system. Digital holography was used, because it is the most flexible technique to generate spatially structured light pattern at specific wavelengths, and surpasses micromirror arrays in terms of light-efficiency by orders of magnitude¹⁶¹.

4.2 Method I: μ -Contact printing of neuronal circuits

The first method is published. It should be noted that in this published part of the project, we left out the idea of virtual networks. This topic will be covered in section 4.4.

4.3 Citation and original contribution

Robert Samhaber*, Manuel Schottdorf*, Ahmed El Hady*, Kai Bröking, Andreas Daus, Christiane Thielemann, Walter Stühmer, and Fred Wolf: “*Growing neuronal islands on multi-electrode arrays using an accurate positioning- μ CP device*”, J Neurosci Methods 257(1): 194-203 (2016) [* eq. contribution]⁴¹⁸

I assembled the construction sheets and generated the overview figure (Fig. 1); I measured the reproducibility of the patterning procedure by quantifying the PLL deposition on each stamping site (Fig. 3) and I produced patterned cultures and performed the electrophysiological measurements (Fig. 6). In addition, I designed the website for the supplemental online information, wrote the text together with all authors and I am corresponding author.



Basic neuroscience

Growing neuronal islands on multi-electrode arrays using an accurate positioning- μ CP device



Robert Samhaber^{a,b,d,e,f,1}, Manuel Schottdorf^{a,b,d,e,*,1}, Ahmed El Hady^{a,b,d,e,f,1}, Kai Bröking^{a,b,d,e}, Andreas Daus^c, Christiane Thielemann^c, Walter Stühmer^{a,e}, Fred Wolf^{b,d,e,f,g,*}

^a Max-Planck-Institute for Experimental Medicine, Dept. Molecular Biology of Neuronal Signals, Hermann-Rein-Str. 3, 37075 Göttingen, Germany

^b Max Planck Institute for Dynamics and Self-Organization, Dept. Nonlinear Dynamics, Am Faßberg 17, 37077 Göttingen, Germany

^c Faculty of Engineering, University of Applied Science, Würzburger Straße 45, 63743 Aschaffenburg, Germany

^d Bernstein Center for Computational Neuroscience, Göttingen, Germany

^e Bernstein Focus Neurotechnology, Göttingen, Germany

^f SFB-889 Cellular Mechanisms of Sensory Processing, Göttingen, Germany

^g Faculty of Physics, Georg-August-Universität Göttingen, Göttingen, Germany

H I G H L I G H T S

- A precision patterning protocol for hippocampal neurons on Multielectrode arrays (MEAs) using simple and widely available equipment.
- A scalable prototype for a versatile mechanical pattern aligner.
- Increased yield of electrical activity recording in patterned neuronal culture.

A R T I C L E I N F O

Article history:

Received 6 August 2015

Accepted 23 September 2015

Available online 1 October 2015

Keywords:

μ CP

MEA

Patterning

A B S T R A C T

Background: Multi-electrode arrays (MEAs) allow non-invasive multi-unit recording *in-vitro* from cultured neuronal networks. For sufficient neuronal growth and adhesion on such MEAs, substrate preparation is required. Plating of dissociated neurons on a uniformly prepared MEA's surface results in the formation of spatially extended random networks with substantial inter-sample variability. Such cultures are not optimally suited to study the relationship between defined structure and dynamics in neuronal networks. To overcome these shortcomings, neurons can be cultured with pre-defined topology by spatially structured surface modification. Spatially structuring a MEA surface accurately and reproducibly with the equipment of a typical cell-culture laboratory is challenging.

New method: In this paper, we present a novel approach utilizing micro-contact printing (μ CP) combined with a custom-made device to accurately position patterns on MEAs with high precision. We call this technique AP- μ CP (accurate positioning micro-contact printing).

Comparison with existing methods: Other approaches presented in the literature using μ CP for patterning either relied on facilities or techniques not readily available in a standard cell culture laboratory, or they did not specify means of precise pattern positioning.

Conclusion: Here we present a relatively simple device for reproducible and precise patterning in a standard cell-culture laboratory setting. The patterned neuronal islands on MEAs provide a basis for high throughput electrophysiology to study the dynamics of single neurons and neuronal networks.

© 2015 Elsevier B.V. All rights reserved.

* Corresponding authors at: Theoretical Neurophysics Research Group, Non Linear Dynamics Department, Max Planck Institute for Dynamics and Self-Organization, Am Fassberg 17, 37077 Göttingen, Germany. Tel.: +49 0 551 5176 423; fax: +49 0 551 5176 409.

E-mail addresses: manuel@nld.ds.mpg.de (M. Schottdorf), fred@nld.ds.mpg.de (F. Wolf).

¹ These authors contributed equally to this work.

1. Introduction

The culturing and survival of living cells *in vitro* requires the preparation of suitable conditions in an artificial environment. In particular, in order to study the electrophysiological properties of dissociated neurons, a close contact between the cells and the recording electrodes has to be established. The negative surface charge and hydrophobic nature of unmodified glass surfaces are known to counteract attachment and growth of neurons. One way to modify the surface properties in a favourable way is by coating with growth and adhesion promoting molecules to allow attachment, development and cell survival. Multi-electrode arrays (MEAs) offer a versatile and well-established tool for both, non-invasively studying activity patterns in neuronal networks on a wide range of spatial scales (Gross et al., 1977, 1995, 1997; Stett et al., 2003; Hofmann and Bading, 2006; Hofmann et al., 2011; Schottdorf et al., 2012) and biosensor applications (Keefer et al., 2001; Chiappalone et al., 2003; Selinger et al., 2004; Martinoia et al., 2005; Xiang et al., 2007).

MEAs are devices in which a thin layer of a conducting material in the form of an electrode array is embedded onto the surface of a glass substrate, allowing for non-invasive parallel recording and stimulation of electrical activity at multiple sites from a cell culture. Plating dissociated neurons on a uniformly coated culture substrate results in random network formation that are highly variable in their detailed topology. A way to align the growth of cell processes with the predefined topology of the MEA and to reduce inter-culture variability is to apply patterned substrate modifications that are aligned with the predefined topology of the MEA layout.

Culturing neurons on MEAs for extracellular stimulation and signal recording, together with the ability to precisely and reliably pattern neuronal networks, is thus a crucial step in the development of neuroelectronic hybrids such as biosensors, neuronal prostheses and neuroelectronic circuits.

Patterning neurons in a predefined topology requires that geometric parameters like pattern layout, dimension and alignment to a substrate can be adjusted reproducibly and precisely. Several methods to achieve a predefined topology in cultured neuronal networks have been proposed in the past: topographical-patterning and chemical-patterning. Pioneered in the 1960s, different topographical patterning techniques included etching grooves on a substrate and lithographic procedures to directly model three dimensional features on a culture substrate (Niemeyer and Mirkin, 2004). Chemical patterning methods include patterned deposition of adhesion promoting proteins (Wheeler et al., 1999; Scholl et al., 2000; Nam et al., 2004a,b). Using the cell repelling properties of polyethylenglycol (PEG) through a photo-lithographic process was also shown to effectively direct cell growth (Kumar and Whitesides, 1994). All of these methods, however, require specialised equipment not readily available in a standard cell-culture laboratory setting. Additionally, the alignment of the pattern to be cultured with a given substrate layout requires additional high-precision equipment.

More recently, seminal work on patterning using carbon nanotubes has been performed by the group of Yael Hanein (Shein-Idelson et al., 2011) where islands of carbon nanotubes were deposited on the electrodes leading to the preferential growth of clusters of neurons over the electrodes. One-dimensional neuronal cultures, which provide a platform to study the propagation speed of neuronal signals, have been realized on multielectrode array using a combination of adhesive and protein repelling coating (Jacobi and Moses, 2007). Glial islands on which monolayers of neurons or single neurons are grown have been widely used in electrophysiological studies (Lau and Bi, 2005; Burgalossi et al., 2012) and have provided a means to pattern neuronal cultures.

Micro-contact printing (μ CP) through patterned Polydimethylsiloxan (PDMS) micro stamps allows for a relatively simple approach to transfer adhesion promoting molecules such as Laminin or poly-D-lysine to substrate surfaces at high spatial resolution (Wheeler et al., 1999; Lauer et al., 2001a,b; James et al., 2004; Chang et al., 2006; Jun et al., 2007). While this method does not require a photo-lithography laboratory in order to produce a positive template for the stamps, continued access is not required once the stamp has been produced.

In the current method paper we present a simple positioning device and micro-contact printing technique (accurate positioning micro-contact printing, AP- μ CP).

To characterize the utility of the AP- μ CP procedure, we designed an island-pattern fitting the electrode layout of a MEA. Circular patterns were established by micro-contact printing the adhesion promoter on the MEA. The islands were aligned to the electrodes, allowing for the growth of isolated populations of neurons. We show that the AP- μ CP technique yields reproducible and topologically defined neuronal islands arbitrarily aligned with the electrodes of a MEA. We also patterned neurons in a one dimensional geometry allowing electrophysiological measurement of activity propagation through a one dimensional neuronal culture.

Our study thus presents a simple, precise and reliable patterning technique that can serve as an elementary but crucial component for throughput electrophysiology of single neurons and neuronal networks.

2. Materials and methods

2.1. Master production through photo-lithography

According to the designed pattern, a chrome coated soda-lime mask was produced by electron beam lithography (ML&C, Jena). Photoresist layers (AZ 9260; Microchemicals, Ulm, Germany) of 20 μ m were spin-coated on glass wafers and subsequently soft-baked at 100 °C for 12 min. Structuring of the photoresist-layer was obtained by exposure to UV irradiation for 12 min in close contact with the mask carrying the negative pattern. With proper care and handling, no wear on the masters could be observed during the course of this study. In this study, we used three pre-designed patterns, two which realized “Islands” patterns of 64 islands of either 90 μ m or 60 μ m diameter each separated by 200 μ m (Fig. 2A). The second pattern was designed as a “Highway” pattern (Fig. 6A) of 100 μ m in width and 2 mm in length (Fig. 6A).

2.2. PDMS preparation

PDMS preparation was performed by mixing the PDMS Silicone Elastomer Base and Curing Agent (Sylgard® 184; Dow Corning, Wiesbaden Germany) in a proportion of 10:1. The prepared volume was stirred vigorously by hand and subsequently degassed under a vacuum bell jar: The lidless volume containing the mixed PDMS agents was placed in the bell jar and evacuated with a vacuum pump. After 3 min, the pump was turned off and the bell jar left in low pressure (100–300 hPa) for 20 min to allow all air bubbles to escape. The PDMS exhibits effervescence during evacuation. Slower application of low pressure prevented this.

2.3. The mould

The stamps were cast from PDMS into a stainless steel mould, the interior surfaces of which had been turned to a smooth finish. The mould was bored through, so that it could be placed onto the negative pattern for the stamp that had been prepared by the photolithographic process described above. The mould was then

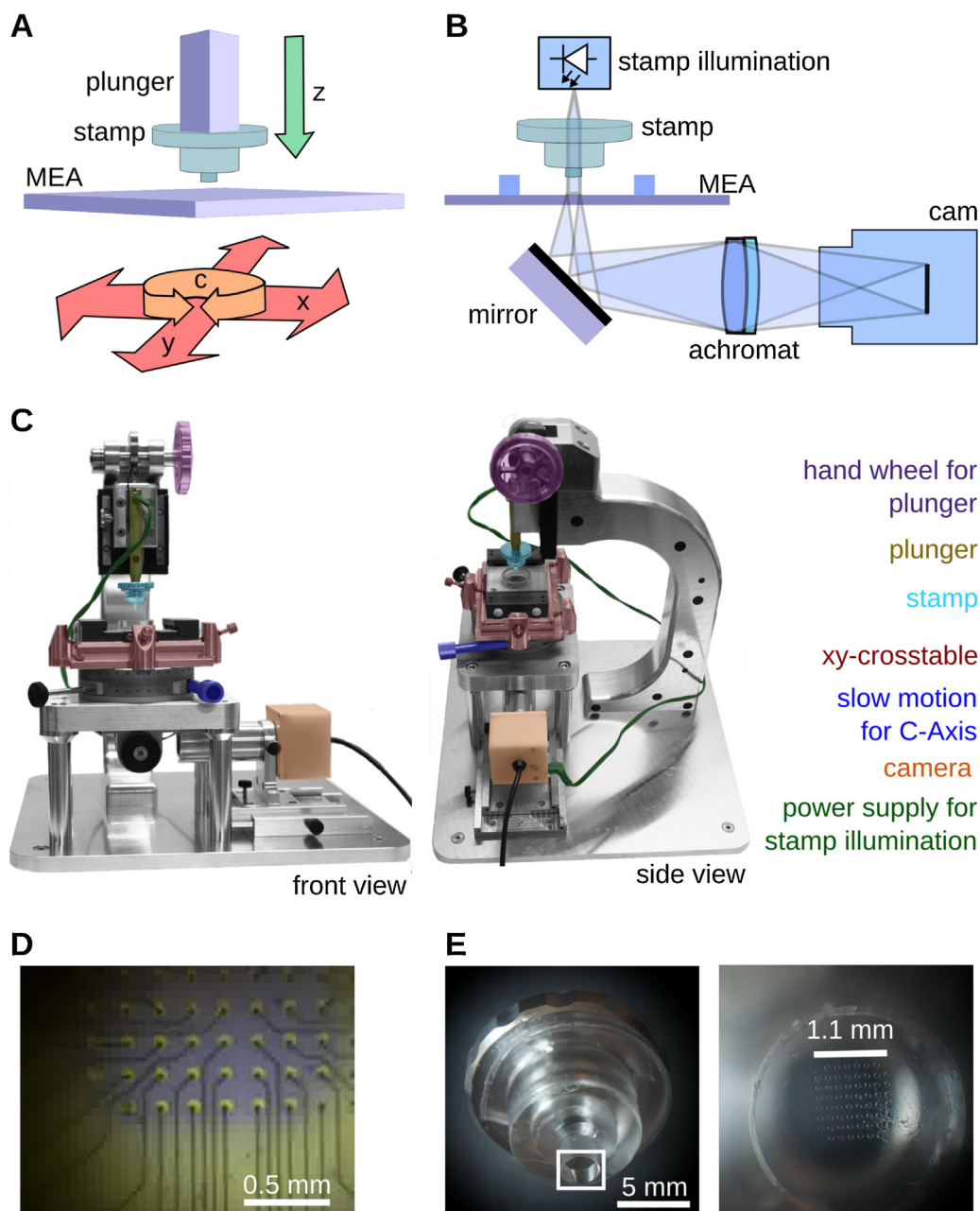


Fig. 1. Mechanical and optical setup of the stamping device. The degrees of freedom of the device are distributed as follows: (A) The stamp can be moved in z -direction, whereas the MEA (Multi-electrode array) can be translated in the xy -plane, and rotated around the C -axis (B) Optical setup: The transparent stamp is illuminated from above. The positioning of the stamp can be controlled by means of a webcam, onto which the MEA is imaged by means of an achromatic lens. (C) Photograph of the stamping device. (D) The stamp, as seen from below through a MEA by the webcam. For clarity, a drop of blue ink has been placed on the electrodes. The stamp pattern is in even contact over all sites (E) Micrograph of the stamps and the mould.

filled to its upper edge with PDMS and the threaded holding fixture pressed into the liquid polymer (Fig. 1E). Brushing the inside of the mould with a small amount of 10% SDS facilitated removing the stamps after the PDMS was fully cured. The masters bearing the PDMS filled moulds were kept at room temperature for 48 h to allow the mixture to polymerize. Faster curing at higher temperatures resulted in distortion of the pattern (Wu et al. 2003). The cured stamps were removed from the moulds and stored in double distilled water until needed.

2.4. Mechanical setup

The stamp is cast in an aluminium mould that allows for maintaining parallelism of the micro stamp surfaces and the locating

face of an aluminium holder moulded into the stamp. This face presses against the contact surface machined onto the plunger. Provided the abutment is kept clean, the surface of the stamps can be kept normal to the axis of the plunger within several seconds of arc. Therefore, it is unnecessary to provide rotational degrees of freedom around the A , and B axes in the stamping mechanism for adjustment.

The stamping press, however, must provide adjustments for the remaining four degrees of freedom: First, the MEA must be rotated around the C -axis, so that the electrode field can be brought into the same orientation as the grid of micro stamps. Then, the MEA must be movable in the x - y -plane to align the electrode field with the stamps (Fig. 1A). The stamp must be depressed by the plunger far enough for the micro stamps to have uniform contact all over

the electrode field of the MEA but only so far as not to squash the pattern. This means that the end position of the stamp has to be adjusted to an accuracy of $\pm 10 \mu\text{m}$. Otherwise, the pattern will be depressed so far that the micro stamps undergo an elastic deformation, similar to Eulerian buckling, which results in instantaneous contact between the MEA and the stamp substrate. To this end, a stopping screw of suitably fine pitch was used to regulate the final position of the stamp relative to the MEA surface. The mechanical setup thus consists of a micrometric cross-table, allowing for positioning of the MEA within a few μm in the x - y -plane. This stage is mounted on a rotary stage with fine movement, providing a rotary degree of freedom along the C axis.

The stamp is fixed to another linear stage with cross-roller bearings, allowing for precise movement in the z -axis. The stamp consists of a clear block of Sylgard 184, cast onto a threaded stamp-holder, the back of which is threaded to allow fixing it to the stamp plunger. The back of this holder also has an accurate locating face matching a similar face on the plunger. The stamp piston is actuated by an eccentric acting against a roller-bearing, fixed to the slide of a vertical stage. The plunger is held in a dovetail fixed to this slide. It is being held there by a small magnet and can be clamped by means of a small screw. This arrangement allows for some limited travel between the slide and the actual plunger, at the same time ensuring that the orientation of the plunger is kept as vertical as possible. All adjustments can be monitored by an inverted microscope built into the apparatus, consisting of an achromat ($f = 18.5 \text{ mm}$, $f/1.5$) below the MEA, and a webcam fixed to the side of the mechanism (see Fig. 1B). Since the stamp material is transparent, the stamp piston and the aluminium have been bored out and an LED has been fixed into the body of the plunger, providing enough light for the contact of the stamp with the MEA surface to be easily recognized (Fig. 1D). A computer rendering of the stamping machine is included along with the exact design of all parts of the setup and a list of components on the following website: <http://www.nld.ds.mpg.de/~manuel/website/index.html>.

The cost of the setup is small in terms of materials used as many of the elements can be harvested from available old machines or components. Here, we used a cheap commercial webcam for the inverted microscope and the C -axis manipulator has been taken from a microscopy stage. It is important to note that the specific choice of the manipulators, the webcam or the dichroic is not important as long as the other machine components are modified accordingly. Publishing the construction sheets along with this paper should allow adjusting our setup according to the materials available.

2.5. Substrate & stamp surface preparation

Sterile MEAs (60MEA200/30iR-Ti; Multi Channel Systems, Reutlingen, Germany) were incubated in purified foetal calf serum (FCS; Gibco) for 30 min and washed once with double distilled water and left to dry. A solution of 1% 3-glycidoxypropyltrimethoxysilane (3-GPS Nam et al., 2004a,b; Sigma Aldrich, Taufkirchen, Germany) in Toluene was added to the culture chamber of the MEA for 20 min and subsequently washed three times with Toluene. MEAs were then baked at 100°C for 1 h and left to cool down to room temperature under a laminar flow hood prior to stamping. Subsequently the prepared PDMS stamps were taken out of the double distilled water and any remaining water was removed by suction. Stamps were sterilized by dipping in 70% EtOH for 10 s. Excess EtOH was removed by suction and stamps were left to dry for 5 min.

A drop of the anionic detergent sodium dodecyl sulphate (SDS; 10% w/v; Sigma Aldrich-Aldrich, Taufkirchen, Germany) was added for 20 min on top of the patterned side of the stamp. This adds a release layer between the PDMS & the adhesion promoters to improve transfer to the glass surface, leading to enhanced cellular

growth on micro-stamped substrates and increasing the durability of the PDMS stamp (Chang et al., 2003). The SDS was dried under a nitrogen stream, washed with double distilled water and dried with nitrogen again. Aliquots of a 0.1 mg/ml solution of poly-L-lysine conjugated with the fluorescent label fluorescein isothiocyanate (PLL-FITC) (70,000–150,000 MW; Sigma Aldrich, Taufkirchen, Germany) in phosphate-buffered saline (pH 7.4) were thawed for 1 h at 37°C in a water bath and vigorously shaken by hand every 15 min to dissolve clusters of coagulated PLL-FITC (Wu et al. 2003). $50 \mu\text{l}$ droplets of the solution were added to the patterned side of the stamps and incubated in the dark for 1 h. Excess liquid was removed and the stamps were left to dry for 10 min to allow all moisture to evaporate. It was critical to the stamping process not to allow the PLL-FITC droplet to evaporate before removing it by suction. The stainless steel moulds containing the stamps were then placed into the plunger of the mechanical stamping device, aligned with the MEA and stamped onto the substrate.

2.6. Cell culture

Cell cultures were prepared according to Brewer et al. (1993). Hippocampal neurons were obtained from Wistar WU rat embryos at 18 days of gestation (E18). The pregnant rat was anaesthetized by CO_2 . The embryos were removed by a caesarean section, decapitated and transferred to cooled petri dishes. The skull cavity was opened and the brain removed. Hippocampi were surgically extracted and transferred to a HEPES (Invitrogen, Germany) buffer. The supernatant was removed and the extracted hippocampi were trypsinized in a Trypsin/Ethylenediaminetetraacetic acid (EDTA) (trypsin: 0.05%; EDTA: 0.02%; Sigma Aldrich, Taufkirchen, Germany) buffer for 15 min at 37°C . Trypsinized cells were then transferred to a 10% Foetal calf serum (FCS) solution. Thorough trituration using a syringe and a needle with a diameter of 1 mm followed. The cell suspension was then centrifuged at 1200 rpm for 2 min. The pellet was re-suspended in 2 ml of serum-free B27/Neurobasal (B27:5%; Gibco) medium supplemented with 0.5 mM glutamine and Basic Fibroblast Growth Factor (bFGF). Cells were counted with a Neubauer improved counting chamber. A droplet of $\sim 100 \mu\text{l}$ cell suspension containing 50,000 cells/ml was added on top of the electrode field of the MEAs. This density was chosen to prevent the formation of neuronal cell clusters, as deterioration of the pattern was observed at higher densities. Lower densities led to lower survivability of neurons after more than 7 days *in vitro*. The MEAs were then kept in an incubator providing a humidified atmosphere containing 5% CO_2 at 37°C for 4 h to allow the cells to settle. 1 ml of the B27/Neurobasal medium was then added to the cell chamber. Medium was changed every seven days.

All animals were kept and bred in the animal house of the Max-Planck-Institute of Experimental Medicine according to European and German guidelines for experimental animals. Animal experiments were carried out with authorization of the responsible federal state authority.

2.7. Immunocytochemistry

Patterned cultures on MEAs were used for immunocytochemistry after 14 days *in vitro*. Cultures were fixed with 4% paraformaldehyde in phosphate buffer (pH 7.4) for 3 min at 4°C and subsequently washed three times with phosphate-buffered saline (PBS). Unspecific binding sites were blocked by incubation with 3% Albumin PBS for 30 min at room temperature before cells were permeabilized with Triton X-100 (0.5% in PBS, 5 min, 4°C). Primary antibodies (mouse monoclonal anti-Neurofilament (Abcam, 1:100), rabbit monoclonal anti-GFAP (Abcam, 1:100)) were diluted in 3% bovine serum albumin (BSA) and 0.1% Tween-20 in PBS and

Table 1
Percentage of populated islands on the 60-island pattern.

No. populated islands	(%)
37	62
36	60
35	58
38	63
34	57

Percentage of populated islands of the island pattern consisting of 60 islands aligned to a standard MEA layout (60 electrodes) after 7 days *in vitro* ($n=5$; mean = 60%; standard deviation = $\pm 3.9\%$).

then applied overnight at 4 °C. After rinsing with PBS, secondary antibodies from donkey were applied for 2 h with a dilution of 1:1000 (alexa 647 anti-mouse IgG, alexa 488 anti-rabbit (Abcam)). MEAs were sealed with round coverslips (15 mm diameter) and mounting medium (ProLong Gold, Invitrogen, Carlsbad, USA), and samples were imaged by fluorescence microscopy using a Zeiss Axiovert 200 (Zeiss, Göttingen, Germany) with a 20 \times objective.

2.8. Statistics

Cultures growing on patterned islands were assessed by phase contrast microscopy after 7 days *in vitro*. Every island populated by at least 1 neuron was counted as populated. Interconnected islands showing more than one interconnection were omitted from the dataset. Mean and standard deviation of the percentage of patterned islands populated by neurons in a sample of X cultures are shown in Table 1.

2.9. Multielectrode array recording

Recordings were made on a 60 channel MEA amplifier (MEA-1060 Inv, Multichannel Systems, Reutlingen, Germany). Data from MEAs were registered at 25 kHz using a 64-channel A/D converter and MC.Rack software (Multichannel Systems, Reutlingen, Germany). After high pass filtering (Butterworth second order, 100 Hz) events were detected in a cutout recorded 1 ms before and 2 ms after crossing a threshold of -4 sigma of the filtered electrode signal. The threshold was evaluated for every channel individually and typically around -16 μ V. The identified events were then aligned at threshold-crossing and averaged. All data analysis was performed in Python.

3. Results

3.1. Island pattern requirements

To demonstrate our technique and the functionality of the mechanical patterning device we chose an island pattern (Fig. 2A). Sixtyfour circles with a diameter of 90 μ m were designed to fit on the electrodes of a 60-Channel MEA layout. This pattern allows for easy alignment and quick assessment of cell growth. The diameter and spacing of the islands/electrodes was chosen in order to minimize overlap of the populated islands, while simultaneously allowing growth and adhesion of several neurons per island. The quality of the produced masters was assessed by means of Scanning electron microscopy (SEM) (Fig. 2B and C). The negative pattern produced by the photo-lithographic process was checked for accuracy of island diameter and freedom from distortion. The structures seen in the figures represent holes in the photo resist layer. During stamp casting, the PDMS flows into these holes and forms micro-pillars. As printing the coated micro-pillars on the prepared substrate forms the island pattern, it is crucial to assess the quality of photoresist development before using the master as a mould for stamp casting. The steepness of the edges translates into structural integrity of

the PDMS micro pillars. This, in turn, affects the amount of pressure the pattern field can tolerate before collapsing during stamping. At the basis of the structures seen in Fig. 2B and C, the exposed surface of the soda-lime substrate has no apparent residues of photo resist. This is important, because incomplete development of the photo resist layer leads to an uneven stamp surface and also uneven printing of the adhesion promoting molecules to the MEA substrate.

After stamp casting and substrate preparation according to the protocol described above, the PLL-FITC coated stamps were printed on a MEA substrate and assessed for complete application of the islands pattern on the substrate (Fig. 2D and F). The patterning and alignment made possible by the mechanical patterning device described here lead to faithful, reproducible and highly controllable patterning of the desired topology. Fluorescence imaging showed that all sixty islands were printed on the electrodes without visible distortions or deformations of the pattern. The coating was smooth and relatively homogeneous over all islands. The variability between islands seems not to be affected by stamping rounds and is most likely a related to inhomogeneity of the protein coating on the PDMS columns or inhomogeneity of the chemical modification of the glass surface (Figs. 2D, 2E and 3). Fig. 3 shows that islands were coated with a variable degree of coating as measured by the fluorescence intensity.

Fig. 4 illustrates that cells prefer to grow on PLL-FITC covered regions over uncoated electrodes.

3.2. Neuronal cultures on patterned islands

Hippocampal neurons populated the Islands and showed normal neurite outgrowth (Fig. 2F and G). Cell bodies and processes generally avoided uncoated areas, though some axons reached neighbouring islands (Fig. 3A). Using the AP- μ CP technique, the pattern on the stamp can easily be aligned to any feature of the substrate, as shown in Fig. 3B, in which hippocampal neurons are located on islands patterned exactly between the electrodes. Five MEAs were AP- μ CP treated with the 64-islands pattern. The percentage of populated islands on the printed and aligned 60-island layout shows that after 7 days *in vitro* on average 36 out of 60 (60%, $n=5$; standard deviation = $\pm 3.9\%$) islands were populated by one or more neuronal cell bodies and their neurites (Table 1). These results show that the presented patterning method, together with the custom made mechanical stamping device (AP- μ CP) is well suited for patterning neurons in an accurate and reproducible manner.

3.3. Characterization of patterned neuronal cultures by immunocytochemical staining

To determine whether the neuronal cultures populating the islands patterns showed characteristics of typical neuronal networks grown *in vitro*, neurite structure and astroglial growth were assessed by immunocytochemical staining after 14 days *in vitro* (see Fig. 5).

Staining against neurofilament, a protein found in intermediate filaments in the axons of neurons, labels axonal processes indicating, that neuronal wiring occurs (Fig. 2A and B). Single neurons growing on the patterned islands enable using the island pattern in studies of autaptic neurons (Bekkers and Stevens, 1991; Pyott and Rosenmund, 2002).

Astrocytes are known to play a substantial role in neuronal development *i.e.*, in metabolic support of neurons, synaptic efficiency and long-term potentiation (Tsacopoulos and Magistretti, 1996; Pfrieger and Barres, 1997; Henneberger et al., 2010). Islands were stained after 14 days *in vitro* against glial fibrillary acidic protein (GFAP), an intermediate filament of the astroglial cytoskeleton. Each island populated by neurons as marked by staining against

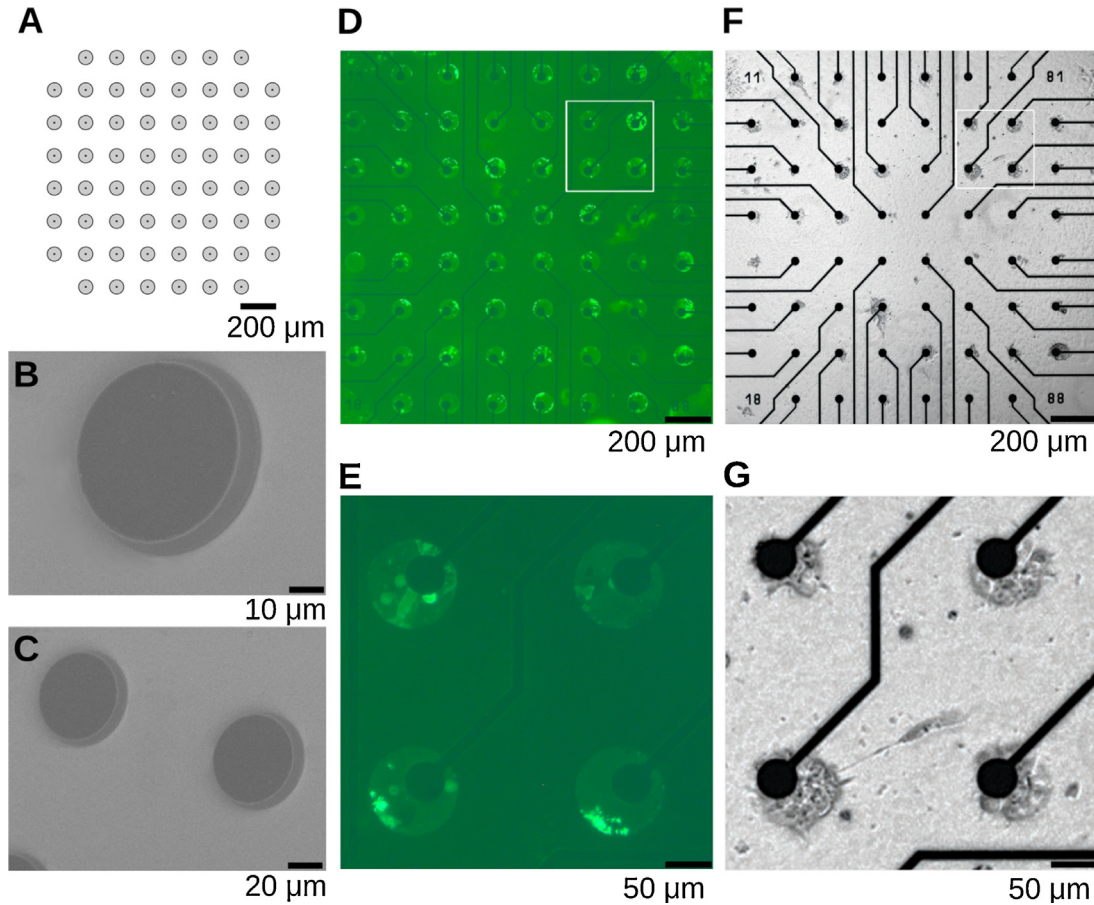


Fig. 2. Patterning procedure validation. (A) CAD schematic of the Island pattern: 60 Islands cover the same number of electrodes. Diameter of Islands: 90 μm . Dots represent electrodes. Scale bar: 200 μm . (B and C) Quality of produced masters was assessed through scanning electron microscopy (SEM). Examination focused on the steepness of the edges, indicating a thorough development of the exposed photoresist. The Islands in this image are dissolved photo resist holes, showing the soda-lime surface of the substrate at its bottom surrounded by an intact layer of photo resist. Scale bars: (B) 10 μm (C) 20 μm . (D) Fluorescence of PLL-FITC on aligned and stamped MEA substrate. (E) Higher magnification of (D), the part magnified is marked with a square. Scale bar: 50 μm . (F) Neuronal islands on MEA after 21 DIV. Scale bar: 200 μm (D). (G) Higher magnification of (F), the magnified part is marked with a square. Scale bar: 50 μm .

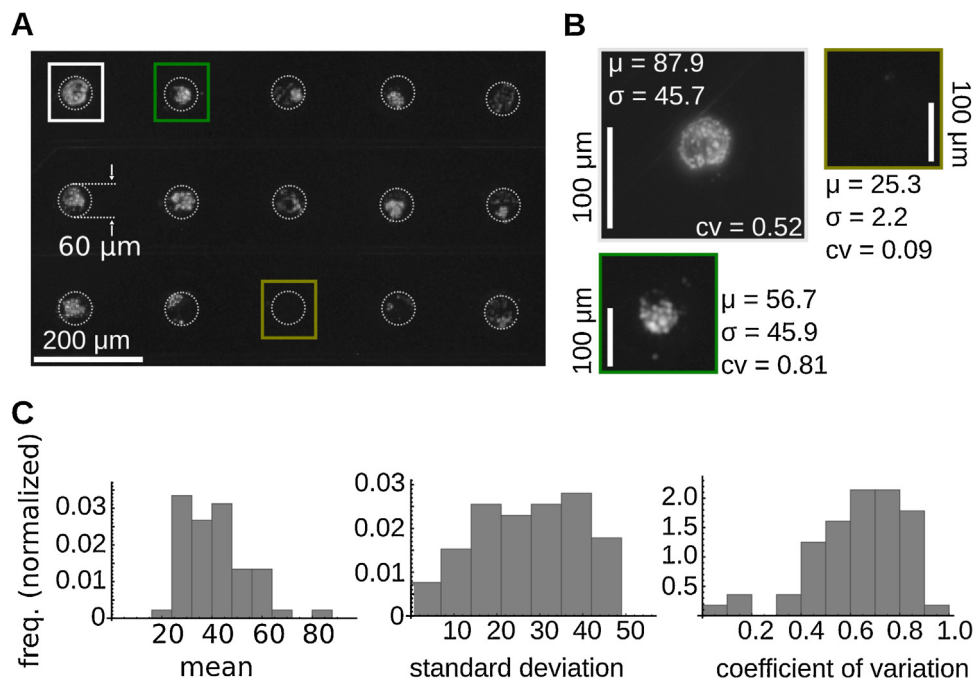


Fig. 3. Reproducibility of the patterning procedure. (A) PLL-FITC coated islands stamped on a substrate. The islands have 60 μm diameter. Scale bar: 200 μm . (B) Magnified PLL-FITC coated islands from (A) along with the mean, standard deviation and coefficient of variation of the fluorescence intensity of the FITC. Scale bar: 100 μm . (C) The histogram of distributions of the mean, standard deviation and coefficient of variation of fluorescence intensity.

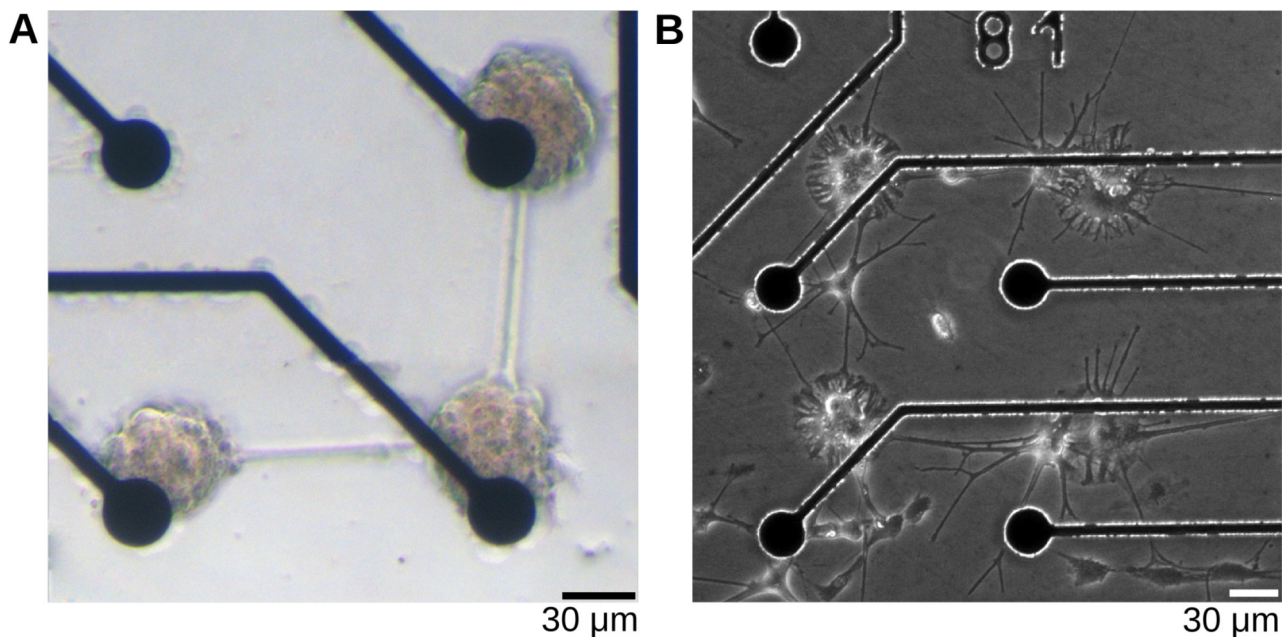


Fig. 4. Patterned neuronal cultures. (A) Neuronal islands on the electrodes of the MEA after 14 DIV. Scale bar: 30 μm (B) Neuronal islands growing beside the MEA electrodes. Patterns were slightly displaced to the electrodes to show that neurons prefer to grow on patterned PLL-FITC over unpatterned electrodes. Scale bar: 30 μm .

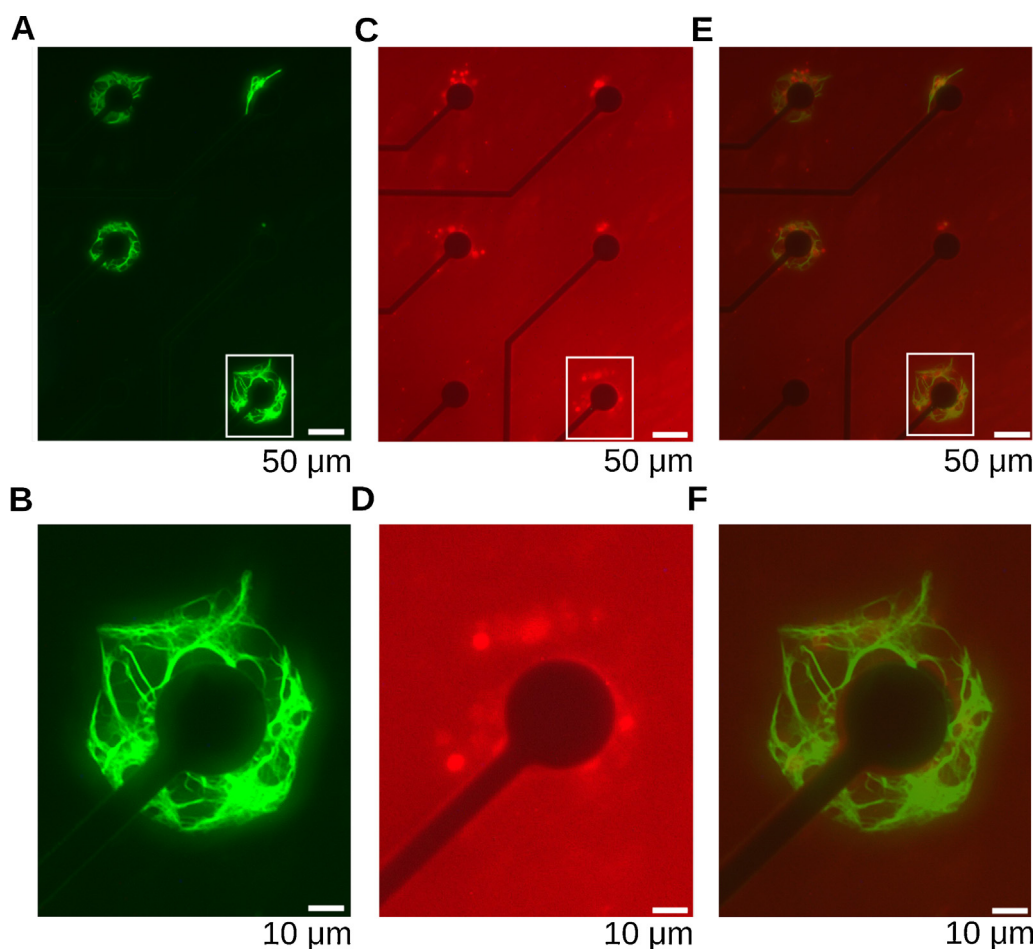


Fig. 5. Immunocytochemical staining of patterned neuronal cultures. (A) Neurofilament staining of neuronal islands on MEA. Scale bar: 50 μm . (B) Enlarged from the white frame in (A) Scale bar: 10 μm . (C) GFAP staining of neuronal islands on MEA. Scale bar: 50 μm . (D) Enlarged from the white frame in (C) Scale bar: 10 μm . (E) Overlay showing Neurofilament and GFAP staining of neuronal islands on MEA. Scale bar: 50 μm . (F) Enlarged from the white frame in (E) Scale bar: 10 μm .

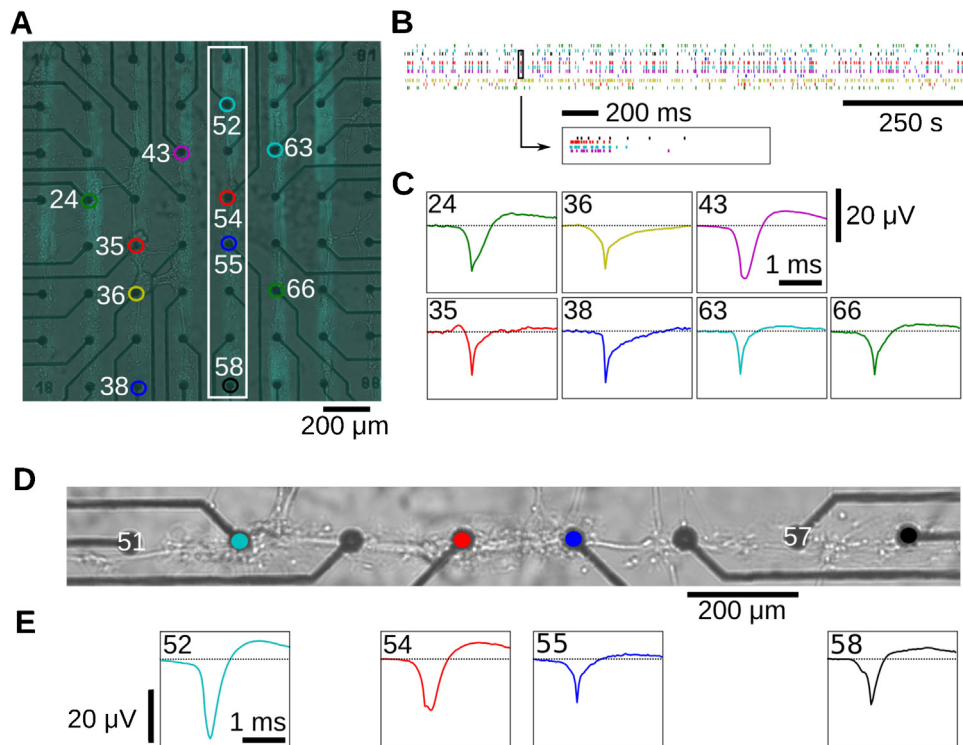


Fig. 6. Electrical activity propagation in patterned cultures. (A) The “Highway” pattern of a one dimensional neuronal culture on a multi-electrode array. Scale bar: 200 μm . (B) The spike trains of neurons spanning several electrodes. Scale bar: 250 s with an inset showing the bursting activity on a shorter time scale. Scale bar: 200 μm . (C) The waveform shapes recorded at electrodes 24, 36, 43, 35, 38, 63, 66. Scale bar: 20 μV . (D) Magnified neuronal line from (A) Scale bar: 200 μm (E). The waveforms from electrodes 52, 54, 55, 58.

neurofilament and thus was accompanied by supporting astrocytes (Fig. 2E and F).

3.4. Electrical activity in patterned cultures

In order to check the usability of these patterned neuronal cultures for electrophysiological studies, we measured the electrical activity in patterned cultures (Fig. 6A). We found that cultures were showing the stereotypical bursting behaviour observed in *in-vitro* neuronal cultures (Fig. 6B). The recorded voltage wave forms had relatively large amplitudes on multiple channel along the patterned one dimensional culture. The recorded electrical activity confirms the usability of these patterned cultures for electrophysiological measurements as it demonstrates that the substrate modification did not affect the electrode impedance.

4. Discussion

We presented a novel technique (AP- μCP) that enables reproducible, precise patterning of neurones on MEAs. We have shown that it can produce patterns of high reproducibility while neuronal growth remains intact. AP- μCP achieved a marked and significant increase in pattern coverage, compared to other already established methods. The percentage of populated islands on the printed and aligned 60-island layout in our study shows that after 7 days *in vitro*, on average 36 out of 60 (60%, $n=5$; standard deviation= $\pm 3.9\%$) islands are populated by one or more neuronal body and its processes. To compare these numbers with the literature, previous studies applying micro-contact printing techniques on MEAs were taken into consideration (James et al., 2000, 2004; Chang et al., 2003; Heller et al., 2005; Boehler et al., 2012). Few studies (Jungblut et al., 2009; Jun et al., 2007) explicitly state the percentage of pattern coverage over the standard MEA layout: $\sim 47\%$ and $\sim 25\%$ of electrodes covered in average respectively. The average coverage

of 60% achieved by AP- μCP thus suggests a significant improvement upon previous methods. The coating is placed on all islands and despite the variability in the coating homogeneity, the neurons seem insensitive to the homogeneity and occupy the majority of islands (60%). Nevertheless, we expect that the method can be further improved by increasing the homogeneity & reproducibility of the coating.

The electrode impedance did not change substantially as evidenced by the recorded electrical activity that showed the hallmarks of *in-vitro* spontaneous activity highlighting the feasibility of using these patterned cultures for electrophysiological recording. We also reproduced the observation of propagating activity in one dimensional cultures that have been demonstrated previously by Ca imaging (Feinerman et al., 2005).

Patterning of neuronal cultures is regarded as a promising tool to address questions concerning network dynamics and signal propagation. First devised in the 1960s and 1970s, topographical patterning methods on planar substrates were achieved by etched or scribed grooves. These first patterning experiments were hard to reproduce, lacking exact means and specifications for placement and alignment. Since then, lithographic procedures have been continuously refined during the past decade (Niemeyer and Mirkin, 2004). Micron-sized arrays of silicon pillars were used to guide the growth of neurones and astrocytes (Turner et al., 2000). Electron beam lithography has been used to define features in the nanometre scale for neuronal cell patterning (St John et al., 1997; Curtis and Wilkinson, 1998), requiring highly specialized equipment. Another way to direct cell growth along topographical substrate modification is by immobilizing cells in well-like structures. Lithographic methods developed for the production of Micro-Electro-Mechanical Systems (MEMS) enable the realization of these features with a good spatial-resolution. Neuronal cells were grown at the bottom of deep pits on a silicon substrate and recorded through metal micro-electrodes

(Maher et al., 1999). Three-dimensional (3D) microfluidic arrays of poly-dimethylsiloxane (PDMS) were also used to confine cell topology to a certain pattern and were directly structured on silicon wafers using a negative photo resist (Degenaar et al., 2001). Building on the results of these experiments, defined networks of cultured neurons from the pond snail *Lymnaea stagnalis* have been grown in micro-structured polyester photo resist on a silicon substrate to study interconnected nerve cell pairs using electrophysiological methods (Jenkner et al., 2001). All of these photo-lithographic approaches for physical cell patterning require the continued availability of photo-lithographic facilities and other techniques not generally available in standard cell-culture laboratories.

An alternative approach, chemical patterning methods were introduced in 1965 by adhering fibroblasts to palladium islands evaporated onto a poly-acetate surface (Carter, 1965). Adhesion promoting molecules then can be transferred to the pattern (Kleinfeld et al., 1988). Due to the techniques involved, organic solvents and alkaline solutions may interfere with the stability of the adhesion promoters. Another method is the patterned deposition of adhesion promoting proteins through silane- or alkanethiol based surface chemistry (Wheeler et al., 1999; Scholl et al., 2000; Nam et al., 2004a,b). Here, the properties of alkanethiolate monolayers on a substrate are altered through UV-Light exposition, which causes the oxidization to alkanesulfonate, thus altering its solubility. In a second step the exposed area can be linked to a second molecular layer by immersion, creating another monolayer on top of the first (Dulcey et al., 1991). These self-assembled monolayers (SAM) have been used to grow dissociated rat hippocampal neurons on circuit-like patterns (Stenger et al., 1998). SAMs of silanethioles have been used likewise to direct cell growth *in vitro* (Ma et al., 1998a,b). However, this method requires that the photo-lithographic process is run every time a pattern is created, limiting routine applicability for many biological laboratories. Uniformly coated MEA culture chambers with poly(L-lysine)-grafted-poly(ethylene glycol) (PLL-g-PEG), a polymer that has cell repelling properties, were locally freed from the polymer by electrical programmable desorption and in a multi process step subsequently coated with poly-L-lysine to establish a pattern of cell adhesive molecules. This method was developed for printing patterns of alkanethiolates on a gold substrate (Kumar and Whitesides, 1994), and has been used afterwards to topographically confine cell growth of neurons on a glass substrate (James et al., 2000; Lauer et al., 2001a,b; Chang et al., 2006; Jun et al., 2007; Jungblut et al., 2009). Previous work focused on confining cells to uniform patterns of rectangular, striped or triangular shape (Ma et al., 1998a,b; Branch et al., 2000; Liu et al., 2000; Thiebaud et al., 2002; Vogt et al., 2003, 2005; James et al., 2004; Heller et al., 2005; Jungblut et al., 2009).

Previous work describing micro-contact printing techniques on MEAs utilizing alignment of the pattern to a given substrate structure either required expensive microscopy precision placers (Jungblut et al., 2009) or used unspecified custom-made devices (Boehler et al., 2012). The mechanical stamping device presented here relies on few components and a small number of optimized parameters, enabling quick and reproducible alignment of a patterned micro-contact stamp to a substrate layout. With AP- μ CP, we present a technique, which can be used in any standard cell-culture laboratory, without expensive equipment and continued access to photo-lithography laboratories.

Author contributions

The project was conceived by Fred Wolf, Walter Stühmer, and Christiane Thielemann and co-supervised by Fred Wolf and Walter

Stühmer. Robert Samhaber, Ahmed El Hady, Manuel Schottdorf performed the experiments with the help of Andreas Daus and Kai Bröking. All authors examined and discussed the results. The manuscript was written by Robert Samhaber, Ahmed El Hady, Manuel Schottdorf, Kai Bröking, Walter Stühmer and Fred Wolf.

Acknowledgements

The authors would like to thank Markus Krohn and his team at the workshop of the Max Planck Institute of Experimental Medicine, Sabine Stolpe and Sabine Klöppner for help with the cell culture, Tureiti Keith for comments on the data analysis and Elisha Moses for discussions. The authors acknowledge the BMBF for funding (Grant numbers 01GQ0811, 01GQ01005B, 01GQ0922), ZIM grant (KF2710201 DF0), the DFG (SFB 889 and Cluster of Excellence “Nanoscale Microscopy and Molecular Physiology of the Brain”), and VolkswagenStiftung (ZN2632). A Boehringer Ingelheim Fonds PhD fellowship to Manuel Schottdorf is gratefully acknowledged.

References

- Bekkers JM, Stevens CF. Excitatory and inhibitory autaptic currents in isolated hippocampal neurons maintained in cell culture. *Proc Natl Acad Sci USA* 1991;88:7834–8.
- Boehler MD, Leondopulos SS, Wheeler BC, Brewer GJ. Hippocampal networks on reliable patterned substrates. *J Neurosci Methods* 2012;203:344–53.
- Branch DW, Wheeler BC, Brewer GJ, Leckband DE. Long-term maintenance of patterns of hippocampal pyramidal cells on substrates of polyethylene glycol and microstamped polylysine. *IEEE Trans Biomed Eng* 2000;47:290–300.
- Brewer GJ, Torricelli JR, Evege EK, Price PJ. Optimized survival of hippocampal neurons in B27-supplemented Neurobasal, a new serum-free medium combination. *J Neurosci Res* 1993;35:567–76.
- Burgalossi A, Jung S, Man KN, Nair R, Jockusch WJ, Wojcik SM, et al. Analysis of neurotransmitter release mechanisms by photolysis of caged Ca²⁺ in an autaptic neuron culture system. *Nat Protoc* 2012;7(7):1351–65.
- Carter SB. Principles of cell motility: the direction of cell movement and cancer invasion. *Nature* 1965;208:1183–7.
- Chang JC, Brewer GJ, Wheeler BC. A modified microstamping technique enhances polylysine transfer and neuronal cell patterning. *Biomaterials* 2003;24:2863–70.
- Chang JC, Brewer GJ, Wheeler BC. Neuronal network structuring induces greater neuronal activity through enhanced astroglial development. *J Neural Eng* 2006;3:217–26.
- Chiappalone M, Vato A, Tedesco M, Marcoli M, Davide FA, Marinoa S. Network of neurons coupled to microelectrode arrays: a neuronal sensory system for pharmacological applications. *Biosens Bioelectron* 2003;18:627–34.
- Curtis AS, Wilkinson CD. Reactions of cells to topography. *J Biomater Sci Polym Ed* 1998;9:1313–29.
- Degenaar P, Pioufle BL, Griscum L, Tixier A, Akagi Y, Morita Y, et al. A method for micrometer resolution patterning of primary culture neurons for SPM analysis. *J Biochem* 2001;130:367–76.
- Dulcey CS, Georger JH Jr, Krauthamer V, Stenger DA, Fare TL, Calvert JM. Deep UV photochemistry of chemisorbed monolayers: patterned coplanar molecular assemblies. *Science* 1991;252:551–4.
- Feinerman O, Segal M, Moses E. Signal propagation along unidimensional neuronal networks. *J Neurophysiol* 2005;94:3406–16.
- Gross GW, Harsch A, Rhoades BK, Gopel W. Odor, drug and toxin analysis with neuronal networks in vitro: extracellular array recording of network responses. *Biosens Bioelectron* 1997;12:373–93.
- Gross GW, Rhoades BK, Azzazy HM, Wu MC. The use of neuronal networks on multi-electrode arrays as biosensors. *Biosens Bioelectron* 1995;10:553–67.
- Gross GW, Rieske E, Kreutzberg GW, Meyer A. A new fixed-array multi-microelectrode system designed for long-term monitoring of extracellular single unit neuronal activity in vitro. *Neurosci Lett* 1977;6:101–5.
- Heller DA, Garga V, Kelleher KJ, Lee TC, Mahbubani S, Sigworth LA, et al. Patterned networks of mouse hippocampal neurons on peptide-coated gold surfaces. *Biomaterials* 2005;26:883–9.
- Henneberger C, Papouin T, Oliet SH, Rusakov DA. Long-term potentiation depends on release of D-serine from astrocytes. *Nature* 2010;463:232–6.
- Hofmann B, Katelhon E, Schottdorf M, Offenhausser A, Wolfrum B. Nanocavity electrode array for recording from electrogenic cells. *Lab Chip* 2011;11:1054–8.
- Hofmann F, Bading H. Long term recordings with microelectrode arrays: studies of transcription-dependent neuronal plasticity and axonal regeneration. *J Physiol Paris* 2006;99:125–32.
- Jacobi S, Moses E. Variability and corresponding amplitude-velocity relation of activity propagating in one-dimensional neural cultures. *J Neurophysiol* 2007;97(5):3597–606.
- James CD, Davis R, Meyer M, Turner A, Turner S, Withers G, et al. Aligned microcontact printing of micrometer-scale poly-L-lysine structures for controlled growth

- of cultured neurons on planar microelectrode arrays. *IEEE Trans Biomed Eng* 2000;47:17–21.
- James CD, Spence AJ, Dowell-Mesfin NM, Hussain RJ, Smith KL, Craighead HG, et al. Extracellular recordings from patterned neuronal networks using planar microelectrode arrays. *IEEE Trans Biomed Eng* 2004;51:1640–8.
- Jenkner M, Muller B, Fromherz P. Interfacing a silicon chip to pairs of snail neurons connected by electrical synapses. *Biol Cybern* 2001;84:239–49.
- Jun SB, Hynd MR, Dowell-Mesfin N, Smith KL, Turner JN, Shain W, et al. Low-density neuronal networks cultured using patterned poly-L-lysine on microelectrode arrays. *J Neurosci Methods* 2007;160:317–26.
- Jungblut M, Knoll W, Thielemann C, Pottek M. Triangular neuronal networks on microelectrode arrays: an approach to improve the properties of low-density networks for extracellular recording. *Biomed Microdevices* 2009;11:1269–78.
- Keefer EW, Gramowski A, Stenger DA, Pancrazio JJ, Gross GW. Characterization of acute neurotoxic effects of trimethylolpropane phosphate via neuronal network biosensors. *Biosens Bioelectron* 2001;16:513–25.
- Kleinfeld D, Kahler KH, Hockberger PE. Controlled outgrowth of dissociated neurons on patterned substrates. *J Neurosci* 1988;8:4098–120.
- Kumar A, Whitesides GM. Patterned condensation figures as optical diffraction gratings. *Science* 1994;263:60–2.
- Lau P-M, Bi G-Q. Synaptic mechanisms of persistent reverberatory activity in neuronal networks. *Proc Natl Acad Sci USA* 2005;102:10333–1033.
- Lauer L, Ingebrandt S, Scholl M, Offenhausser A. Aligned microcontact printing of biomolecules on microelectronic device surfaces. *IEEE Trans Biomed Eng* 2001a;48:838–42.
- Lauer L, Klein C, Offenhausser A. Spot compliant neuronal networks by structure optimized micro-contact printing. *Biomaterials* 2001b;22:1925–32.
- Liu QY, Coulombe M, Dumm J, Shaffer KM, Schaffner AE, Barker JL, et al. Synaptic connectivity in hippocampal neuronal networks cultured on micropatterned surfaces. *Brain Res Dev Brain Res* 2000;120:223–31.
- Ma W, Liu QY, Jung D, Manos P, Pancrazio JJ, Schaffner AE, et al. Central neuronal synapse formation on micropatterned surfaces. *Brain Res Dev Brain Res* 1998a;111:231–43.
- Ma W, Liu QY, Jung D, Manos P, Pancrazio JJ, Schaffner AE, et al. Central neuronal synapse formation on micropatterned surfaces. *Brain Res Dev Brain Res* 1998b;111:231–43.
- Maher MP, Dvorak-Carbone H, Pine J, Wright JA, Tai YC. Microstructures for studies of cultured neural networks. *Med Biol Eng Comput* 1999;37:110–8.
- Martinoia S, Bonzano L, Chiappalano M, Tedesco M, Marcoli M, Maura G. In vitro cortical neuronal networks as a new high-sensitive system for biosensing applications. *Biosens Biomed* 2005;20:2071.
- Nam Y, Chang J, Khatami D, Brewer GJ, Wheeler BC. Patterning to enhance activity of cultured neuronal networks. *IEE Proc Nanobiotechnol* 2004a;151:109–15.
- Nam Y, Chang JC, Wheeler BC, Brewer GJ. Gold-coated microelectrode array with thiol linked self-assembled monolayers for engineering neuronal cultures. *IEEE Trans Biomed Eng* 2004b;51:158–65.
- Niemeyer CM, Mirkin CA. *Nanobiotechnology*. first ed. Weinheim: Wiley; 2004. p. 54.
- Pfrierger FW, Barres BA. Synaptic efficacy enhanced by glial cells in vitro. *Science* 1997;277:1684–7.
- Pyott SJ, Rosenmund C. The effects of temperature on vesicular supply and release in autaptic cultures of rat and mouse hippocampal neurons. *J Physiol* 2002;539:523–35.
- Scholl M, Sprossler C, Denyer M, Krause M, Nakajima K, Maelicke A, et al. Ordered networks of rat hippocampal neurons attached to silicon oxide surfaces. *J Neurosci Methods* 2000;104:65–75.
- Schottdorf M, Hofmann B, Katelhon E, Offenhausser A, Wolfrum B. Frequency-dependent signal transfer at the interface between electrogenic cells and nanocavity electrodes. *Phys Rev E: Stat Nonlin Soft Matter Phys* 2012;85:031917.
- Selinger JV, Pancrazio JJ, Gross GW. Sensitivity of the neuronal network biosensor to environmental threats. *Biosens Biomed* 2004;15:675.
- Shein-Idelson M, Ben-Jacob E, Hanein Y. Engineered neuronal circuits: a new platform for studying the role of modular topology. *Front Neuroeng* 2011;4:10.
- St John PM, Kam L, Turner SW, Craighead HG, Isaacson M, Turner JN, et al. Preferential glial cell attachment to microcontact printed surfaces. *J Neurosci Methods* 1997;75:171–7.
- Stenger DA, Hickman JJ, Bateman KE, Ravenscroft MS, Ma W, Pancrazio JJ, et al. Microlithographic determination of axonal/dendritic polarity in cultured hippocampal neurons. *J Neurosci Methods* 1998;82:167–73.
- Stett A, Egert U, Guenther E, Hofmann F, Meyer T, Nisch W, et al. Biological application of microelectrode arrays in drug discovery and basic research. *Anal Bioanal Chem* 2003;377:486–95.
- Thiebaud P, Lauer L, Knoll W, Offenhausser A. PDMS device for patterned application of microfluids to neuronal cells arranged by microcontact printing. *Biosens Bioelectron* 2002;17:87–93.
- Tsacopoulos M, Magistretti PJ. Metabolic coupling between glia and neurons. *J Neurosci* 1996;16:877–85.
- Turner AM, Dowell N, Turner SW, Kam L, Isaacson M, Turner JN, et al. Attachment of astroglial cells to microfabricated pillar arrays of different geometries. *J Biomed Mater Res* 2000;51:430–41.
- Vogt AK, Brewer GJ, Offenhausser A. Connectivity patterns in neuronal networks of experimentally defined geometry. *Tissue Eng* 2005;11:1757–67.
- Vogt AK, Lauer L, Knoll W, Offenhausser A. Micropatterned substrates for the growth of functional neuronal networks of defined geometry. *Biotechnol Prog* 2003;19:1562–8.
- Wheeler BC, Corey JM, Brewer GJ, Branch DW. Microcontact printing for precise control of nerve cell growth in culture. *J Biomech Eng* 1999;121:73–8.
- Wu H, Odom TW, Chiu DT, Whitesides GM. Fabrication of complex three-dimensional microchannel in PDMS. *J Am Chem Soc* 2003;125:554–9.
- Xiang G, Pan L, Huang Z, Yu X, Song J, Cheng W, et al. Microelectrode array-based system for neuropharmacological applications with cortical neurons cultured in vitro. *Biosens Bioelectron* 2007;22:2478.

Supplemental Online Material

to

Growing neuronal islands on multi-electrode arrays using an accurate positioning- μ CP device

by R. Samhaber, M. Schottdorf, A. El Hady, K. Bröking, A. Daus, C. Thielemann, W. Stühmer, and F. Wolf

Introduction

On this website, you can find detailed instructions for building a micro contact printing (μ CP) machine and for using it to spatially structure neuronal cultures. Its purpose is to allow any lab without access to a lithography facility to structure cultures of neurons with the method developed in our group.

You can find a detailed description as to the preparation of neuronal cultures, the protocols used, and the construction of the μ CP machine including all CAD files (for Autodesk Inventor) to build your own!

This project has been carried out at the Max Planck Institute for Experimental Medicine in the department of Molecular Biology of Neuronal Signals, headed by Prof. Dr. Walter Stühmer. On the following pages, one can find a detailed and illustrated protocol of the stamping process. In the downloads section, all construction sheets for the stamping machine and the molds are available.

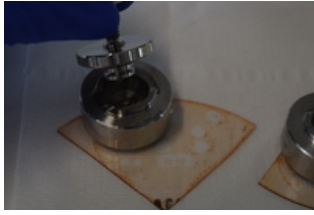


Fig. 1

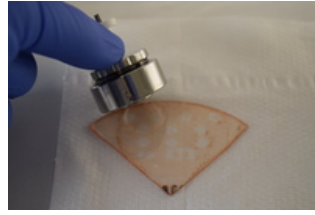


Fig. 2

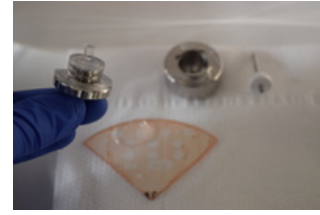


Fig. 3



Fig. 4

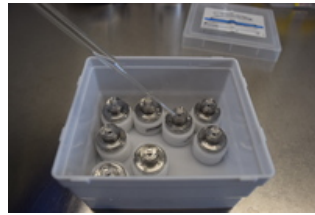


Fig. 5

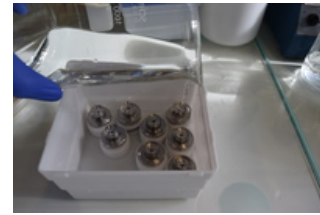


Fig. 6

Stamp and MEA preparation

Fabrication of the stamps

The stamps are fabricated by applying freshly prepared and degassed PDMS to molds which are placed on a photolithographically prepared mask. The molds are covered from the inside with a thin film of SDS. This is done by placing a drop of SDS solution in the inside and by spreading it evenly with the finger. The molds are then placed onto the masks and filled with freshly prepared and degassed PDMS. We add enough PDMS to fill the entire mold with the viscous liquid. Then a stamp-holder is inserted into the liquid. This assembly is left for 48h to cure (see **Fig. 1**). After two days, the stamps are removed from the mold by pulling at the stamp holder which is now embedded into solid PDMS (see **Fig. 2**) and (see **Fig. 3**). In one run, we usually prepare 8 stamps. After removal of the stamps they are placed for 30s in 70% Ethanol for both removal of excess SDS and sterilization. Then, the pin is removed and they are placed in Teflon holders. Next, a single drop of SDS is placed on each mold (see **Fig. 4**). It is left there for 20min, sucked off by vacuum (see **Fig. 5**), the stamp is rinsed in ddH₂O (see **Fig. 6**) and thoroughly dried with dry nitrogen (see **Fig. 7**). This procedure should create a thin layer of SDS to facilitate later stamping. Then, a drop of



Fig. 7



Fig. 8

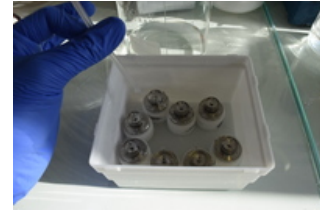


Fig. 9

FITC-PLL is placed on the stamps and left there for an hour (see **Fig. 8**). Subsequently, the drop of PLL is sucked off and the stamps are ready for use (see **Fig. 9**)



Fig. 10

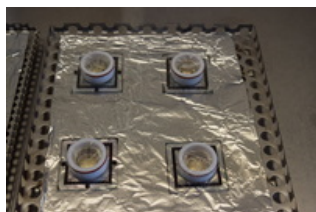


Fig. 11

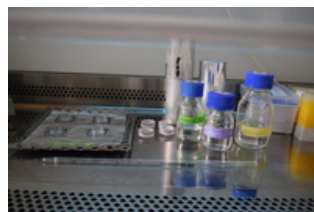


Fig. 12

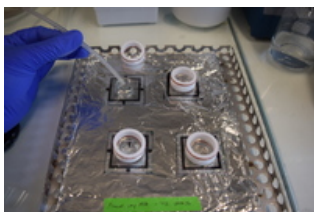


Fig. 13



Fig. 14



Fig. 15

Preparation of the MEAs

First, used MEAs are cleaned for 12h to 24h in a 1% Terg-A-Zyme solution in ddH₂O (for instance as described by Multichannel Systems). They are then thoroughly cleaned from any left Terg-A-Zyme, filled with ddH₂O and sterilized in an autoclave. After the autoclaving cycle has completed, they are rinsed with sterile ddH₂O (see **Fig. 10**) and filled with fetal calf serum (see **Fig. 11**) to hydrophilize the surface. The FCS is left in there for at least 30 min. Then, the FCS is sucked off, the MEA rinsed in ddH₂O again and left to dry (see **Fig. 12**). MEAs are conveniently dried in the air stream of the bench under UV light to prevent contamination. After making sure that all water residues have evaporated, the MEAs are filled with a 3-GPS solution in Toluene. This solution is left in the MEAs for 20 min, removed and the MEA quickly rinsed 3 times with pure toluene. After sucking off all excess toluene, the MEAs are dried with a dry nitrogen stream (see **Fig. 13**) and placed in an oven at 100° for 1 h to remove any remaining toluene (see **Fig. 14** and **Fig. 15**) After this procedure, the silanized surface is ready for the stamping. The prepared MEAs and the stamps are kept on the bench, in a sterile environment and the stamping process is immediately started.

Chemicals & Tools

The tools and molds are available as CAD sheets in the download section and to follow this protocol, you will need the following chemicals:

Chemical	Supplier
Tergazyme	Sigma-Aldrich
PDMS Sylgard 184	Dow Corning
10% w/v sodium dodecyl sulfate in ddH ₂ O	Sigma Aldrich
1% (3-glycidoxypropyl)trimethoxysilane	Sigma Aldrich
Toluene	Sigma Aldrich
Poly-L-lysine FITC labeled 1 mg/ml in PBS 70,000-150,000 MW	Sigma Aldrich
Fetal Calf Serum (FCS)	Biochrom
Trypsin/Ethylenediaminetetraacetic acid (EDTA) Trypsin: 0.05%; EDTA: 0.02%	Biochrom

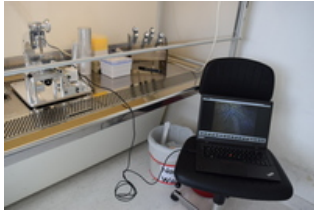


Fig. 16

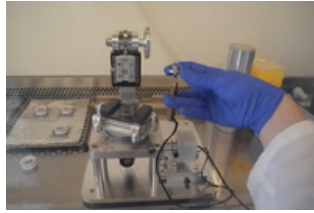


Fig. 17

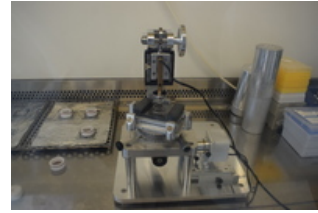


Fig. 18

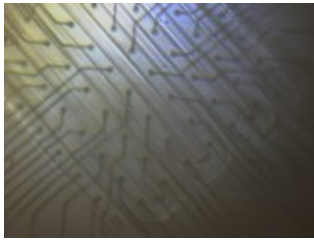


Fig. 19



Fig. 20

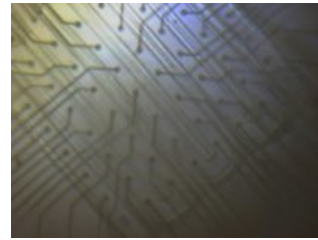


Fig. 21

Stamping

Stamping – How to?

For the stamping, we first spray the stamping apparatus with plenty of 70% ethanol and put it on the bench. We leave it to dry and connect it to a computer for readout of the images (**Fig. 16**). Next, we place one stamp into the stamp holder and place the stamp holder into its slot (**Fig. 17**). Then we put one of the prepared MEAs onto the MEA holder of the stamping machine (**Fig. 18**).

The built-in inverted microscope with the webcam allows for inspection of the position of the MEA. Next, the stamp is carefully lowered in such a manner that it stops above the MEA without touching its surface. This can be monitored by observing how the stamp comes into focus of the microscope. After lowering the stamp, the stage is adjusted such that the stamp's pattern matches the adjusted orientation of the MEA (**Fig. 19**). After both, the stamp and the MEA have been aligned, the stamp is lowered until it touches the surface of the MEA (**Fig. 20**). Touching the MEA can easily be seen by a change of color (**Fig. 21**). The stamp is left on the surface of the MEA for 2min, removed, and the MEA is finished. Next, 50.000 E18 neurons in 100

μ l NB medium are placed onto the electrode field. The neurons are allowed to settle for 4h and then the MEA is filled with 1ml of fresh medium. The medium needs to be changed once a week. Every MEA is stamped with its own PDMS stamp and every stamp is used only once.

CAD Sheets & Download

Comments

The machine has several main components. The base plate is connected to a column. On its top there is an eccentric which moves a linear guide with the stamp. With this linear guide, the stamp is lowered onto a MEA which is clamped into place on a table with x, y and C-axis manipulators. The C-Axis manipulator of our machine is taken from a microscope and therefore in the construction sheets, it is referred to as 'dummy'. The table assembly is held in place with four pillars. Under the table assembly, there is an inverted microscope consisting of a prism, an achromatic lens and a CCD Chip which allows monitoring the position. The achromatic lens with $f=18.5\text{mm}$ focal length is roughly $2f$ away from the MEA and projects the MEA's image in $2f$ distance onto a $1/4''$ CCD (Sony ICX098BQ) of a commercial webcam (Philips ToUCam Pro II). The type and size of the CCD chip is not important, but the focal length of the lens and the position of the CCD needs to be adjusted accordingly.

Downloads

We have prepared a collection of the CAD construction sheets, see **Fig. 8** of the stamping machine and its components as Autodesk Inventor Part and Assembly files, a few more pictures and a Microsoft Excel list of its components. You can find it for download online. Also, we have prepared a collection of construction sheets for the stamps. You can find them online, too.

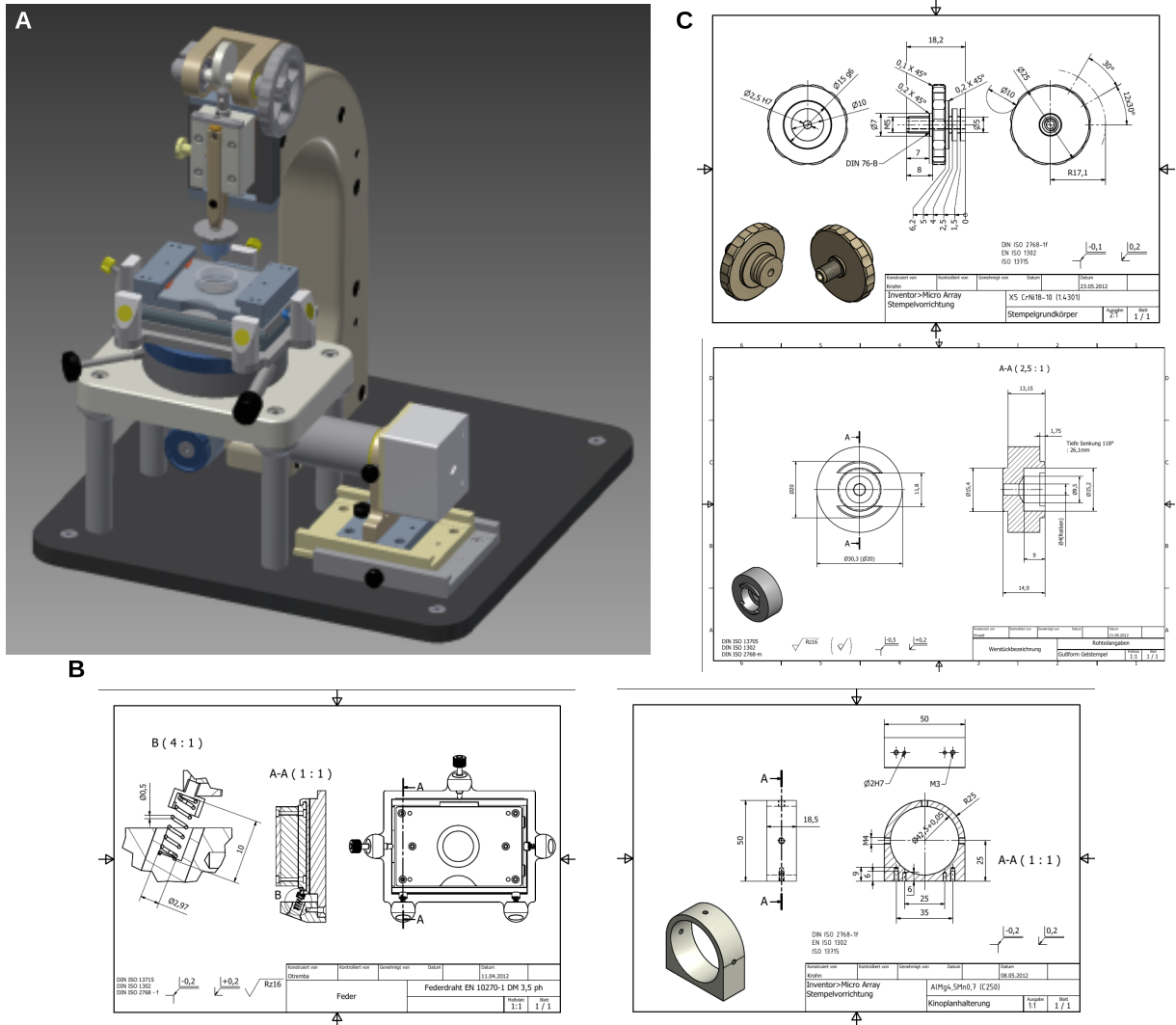


Fig. 8: Examples of the online supplemental material. **A** A rendering of the CAD construction sheets. **B** A few example construction sheets of the stamping machine. **C** A few example construction sheets of the stamp holders.

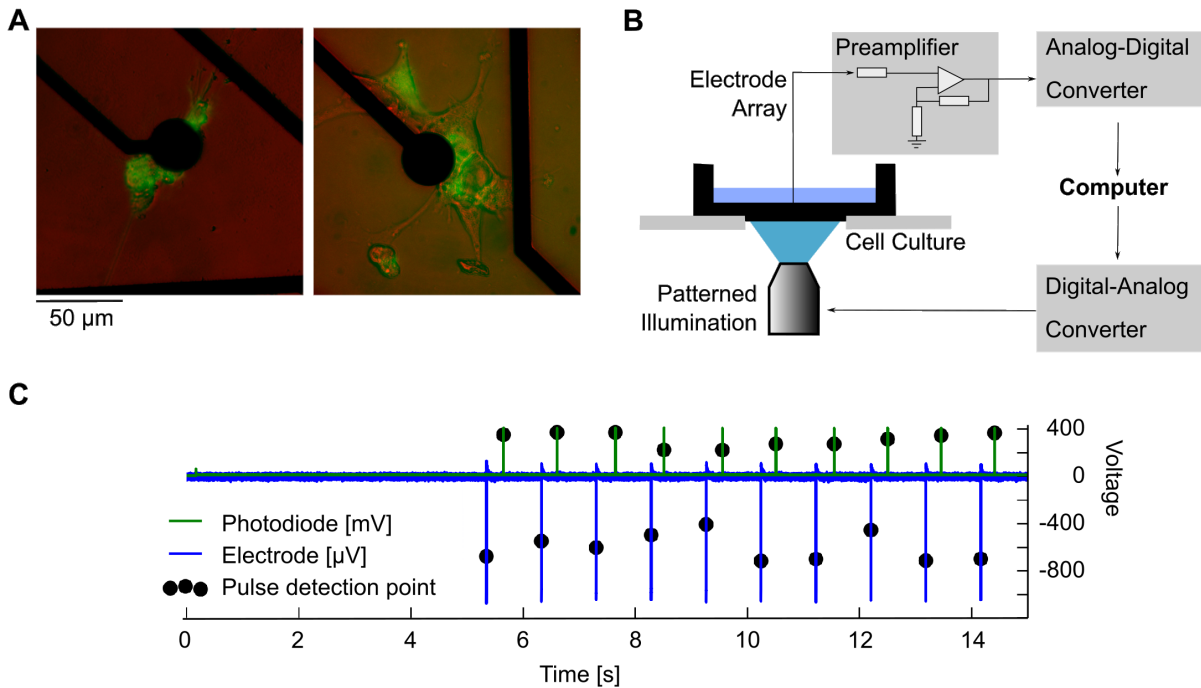


Figure 4.1: **The assembled elements of a closed loop system.** **A** Individual cells at the stamping sites express the light sensitive ionchannel ChR2. Shown is a DIC image (red) together with fluorescence of the YFP label of ChR2. **B** Neuronal signals can be recorded, processed, and fed back to the cells using light. **C** An example of such an experiment, data courtesy of Tūreiti Keith.

4.4 Closing the loop

Fig. 4.1A shows the elements of the closed loop system assembled. Islands of individual neurons are grown on multielectrode arrays. They are made light sensitive using a viral vector to express the construct ChR2-YFP under control of a Synapsin promoter. Using the electrodes, one can record from the neurons. This system provides a platform to predesign arbitrary virtual networks of biological neurons as nodes, while the connections are made digitally with a patterned illumination system, **Fig. 4.1B**. **Fig. 4.1C** shows first results with our current hardware; the close loop time on the order of 100 ms is too long for passing single spikes to the nodes, but with faster hardware we assembled all essential elements of an optogenetic closed loop virtual network.

We next design a system in which the local neuronal circuits are as realistic as possible. We use primary cortical cultures designed to have the same cell density and cellular content as the neocortex. These cultures are easy to produce on a large scale and show rich spontaneous activity, resembling the spontaneous activity in the young neocortex. To wire this surrogate cortex to the virtual sensory pathway, we construct a digital phase-only holographic projection system, because is the most flexible technique to generate spatially structured light pattern at specific wavelengths, and surpasses micromirror arrays that are known to be “horribly inefficient”¹⁶¹. Note that the holographic system could also be used to add virtual connections to the surrogate cortex.

4.5 Method II: Realistic local circuits

Introduction

μ -Contact printing of neuronal circuits is a complex technique and it is not clear at all how to implement a realistic cortical circuit within a virtual network. Therefore we developed a system in which the local neuronal circuits are as realistic as possible. We designed cultures with the same cell density and cellular content as the neocortex. These cultures are easy to produce on a large scale and show rich spontaneous activity, resembling the spontaneous activity in the young neocortex. To wire this surrogate cortex to the virtual sensory pathway, we then construct a digital phase-only holographic projection system, because it is the most flexible technique to generate spatially structured light pattern at specific wavelengths.

Designing the surrogate cortex

The target of thalamic projections in the mammalian brain is the primary visual cortex. Thalamic inputs *in vivo* are excitatory^{10,329} and target stellate neurons in layer IV^{157,268}. We therefore use optogenetics^{54,110,135,343} to express ChR2, an excitatory light sensitive excitatory algal ion channel² under the control of a neuron specific promoter in a recurrent network of living cortical neurons. Next, we designed a photostimulation setup to connect electronic and biological components, based on phase-only digital holography^{161,295,369,401}, see **Fig. 5.3A**. Here, we discuss the cell culture and the neuroelectronic interface.

A primary cell culture of neurons can resemble *in vivo* neural tissue in structural features²⁰², activity^{88,366}, development²⁷⁵ and composition²⁶. We achieved cellular content and the cell density corresponding to layer IV in area 17 of the cat, the primary target for projections from the LGN. In the lower part of layer IV, the average cell density of binocular neurons, is 56,000 mm⁻³ in a layer about 250 μ m thick^{29,150}. 75% of these cells are excitatory^{150,473,523}. Primary cultures from dissociated rat E18 cortical neurons form circuits spontaneously. In cortical cultures, periodic bursts of action potentials emerged after typically 10 days *in vitro* in 2D^{79,497,498} and also 3D cultures^{102,146} and increase in complexity with time^{308,498}. Notably these bursts resemble to some extent the spontaneous activity in the visual cortex before eye opening^{82,409}. We designed the surrogate cortex to a cell density of $\approx 60,000$ mm⁻³ with 75% excitatory cells (see Chapter 10). The surrogate cortex expresses the light sensitive ion channel ChR2(H134R)²⁸³ and the red-shifted calcium indicator jRCaMP1a¹⁰³, to combine the optical excitation with calcium imaging and use an all-optical interface¹²⁹, see **Fig. 5.3B**. **Fig. 5.3C** shows that the culture contains excitatory cells and inhibitory cells, expresses light sensitive ion channels and calcium dependent fluorescent indicators, and contains neurons suspended in a matrix of glial filaments. To count cell densities, we seed neurons on Poly-D-Lysine coated Marienfeld Superior cover slips, $\varnothing 12$ mm, # 1.5. We seed 1 million primary cells, after Tryptan blue stain identified as membrane-intact, in typically around 100 μ l medium. The cover slip preparations are identical to the preparation on MEAs, but we resort to this technique, as MEAs are too thick for confocal imaging, and for the higher throughput of coverslips in well plates. As with MEAs, on DIV2, we transduced neurons with $6.6 \cdot 10^{10}$ GC (genome copies) of the viruses AAV9.CamKII0.4.eGFP and AAV9.hSyn.TurboRFP. We then take images (Progres MF firewire camera, Jenoptik, Jena, Germany) in epifluorescence mode, at a low magnification of 10x, for a large field-of-view, see **Fig. 4.2A** with standard GFP and RFP filter cubes (Zeiss, Jena, Germany). From these images, we count the number of cells positive for GFP, RFP and both respectively, see **Fig. 4.2B**. The cell counting was done in Ilastik, Version 1.1.9 for Linux, and the pre and post processing was performed in Python. First, every fluorescence microscopy image, recorded with 12 bit, was normalized by cutting the 0.5% brightest, and the 10% darkest pixel, and rescaling of pixel

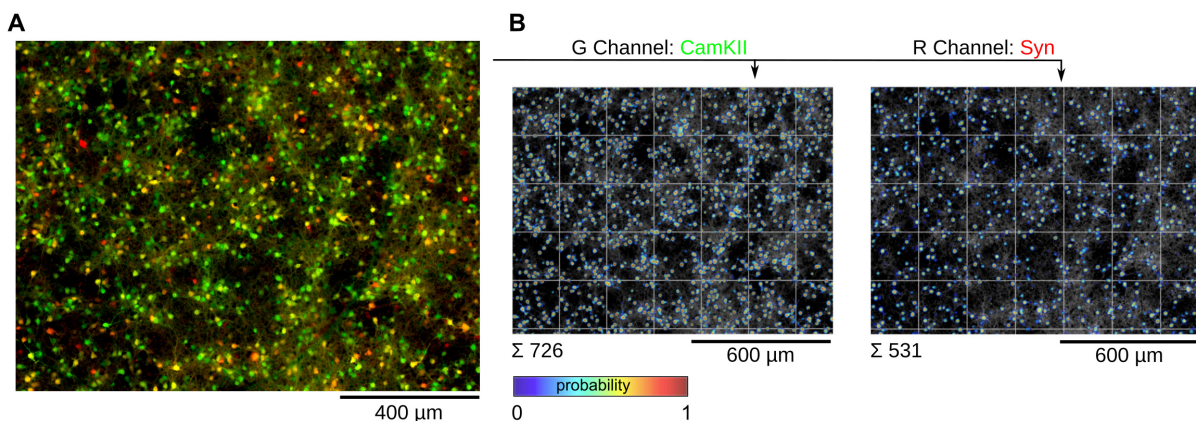


Figure 4.2: **Raw data and analysis of Synapsin and CamKII positive cells.** **A** Fluorescence image of neurons, transduced with $6.6 \cdot 10^{10}$ GC of each, AAV9.hSyn.TurboRFP and AAV9.CamKII0.4.eGFP. **B** Using Ilastik for image classification (see text), we extract probabilities for cells in each image. Integrating these probabilities gives an estimate of the total cell count.

values into an 8 bit range for faster processing. Next, the image was projected into a high dimensional space by (1) Gaussian smoothing, (2) calculating the Laplacian of the Gaussian, (3) calculating the magnitude of the Gaussian gradient, (4) performing an edge detection with a difference of Gaussians, (5) calculating the structure tensor Eigenvalues, and (6) calculating the Hessian of Gaussian Eigenvalues. We then used Ilastik to train a Random Forest classifier (on a sample of $\mathcal{O}(5)$ images), to estimate cell probabilities for every image. Finally, that density was integrated to yield the total cell count. The obtained raw data is a time resolved portrait of CamKII/Syn/both positive cells, see **Fig. 4.3 (top)**. These numbers depend on the relative number of excitatory and inhibitory cells, N_{ex} and N_{in} , the transduction efficiency of the viruses with Synapsin promoter α , and the transduction efficiency of the virus with CamKII promoter β .

$$\text{RFP positive} = \alpha(N_{\text{ex}} + N_{\text{in}}) \quad (4.1)$$

$$\text{GFP positive} = \beta N_{\text{ex}} \quad (4.2)$$

$$\text{GFP/RFP positive} = \alpha\beta N_{\text{ex}} \quad (4.3)$$

From these numbers, we can directly estimate the Synapsin transduction rate and the total number of neurons

$$\alpha = \frac{\text{GFP/RFP positive}}{\text{GFP positive}} \quad (4.4)$$

$$N_{\text{ex}} + N_{\text{in}} = \frac{\text{RFP positive} \times \text{GFP positive}}{\text{GFP/RFP positive}} \quad (4.5)$$

The relative number of excitatory cells depends on the CamKII transduction rate β ,

$$\gamma = \frac{N_{\text{ex}}}{N_{\text{ex}} + N_{\text{in}}} = \frac{\text{GFP/RFP positive}}{\text{RFP positive}} \times \frac{1}{\beta}. \quad (4.6)$$

With the constraint of $\gamma \leq 100\%$ across all experiments, we find that $\beta \geq 93\%$. The expression of the fluorescent construct after the CamKII promoter is substantially stronger than the expression after the synapsin promoter even though we kept the number of genome copies constant. For

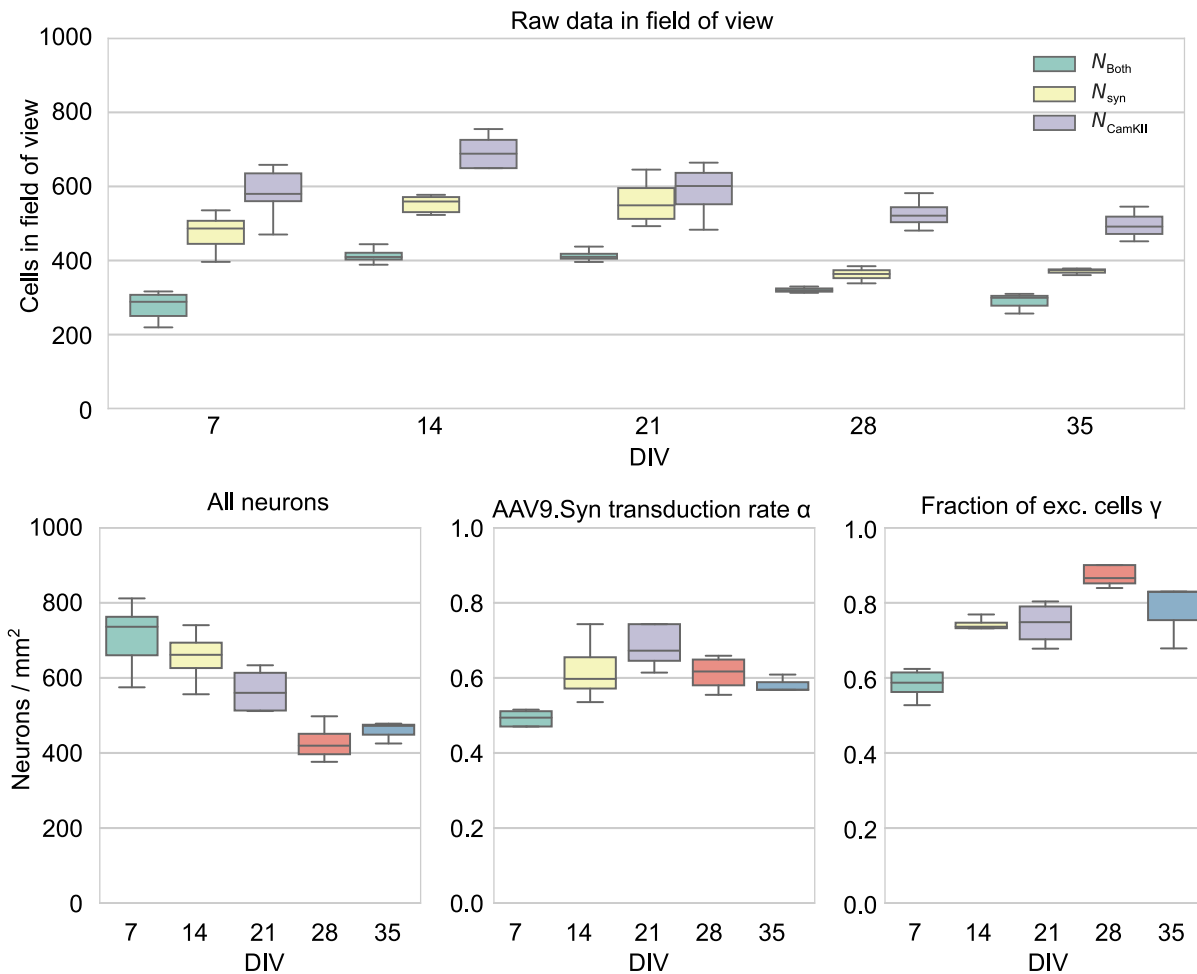


Figure 4.3: **Quantitative assessment of the neuron content, transduction efficiency and fraction of excitatory cells.** (top) Raw data of Synapsin, CamKII, and both positive cells. (bottom) From that data, we can estimate the total number of neurons, the viral transduction rate, and the fraction of excitatory cells (see text).

further analysis we assumed $\beta = 1$. Note that the error from this approximation is substantially smaller than the variability across measurements. This allows for a time resolved portrait of cell densities, **Fig. 4.3 (bottom)**.

Next, we performed the same experiment with $2.2 \cdot 10^{10}$ GC of the virus AAV5.GFAP.eGFP and AAV5.hSyn.TurboRFP, to estimate the fraction of GFAP positive glial cells, see **Fig. 4.4**. As expected with the lower viral count, the fraction of transduced cells is lower. Note the cells that are positive for both fluorescent dyes: cultured astrocytes are known to express a whole array of synaptic proteins, including Synapsin-1³⁰² and the cultures might contain neuronal progenitors of various lineages and we might see an intermediate, non-fully differentiated stage between glia and neuron, in which both genes are expressed. Assuming the same total number of neurons, as derived from the measurement in **Fig. 4.3**, i.e. about 600 mm^{-2} , we can estimate the transduction rate of the virus, and in turn the total number of glial cells. These results are shown in **Fig. 4.5A**. We should note that counting of GFAP positive cells with this methods will give a lower bound, because only a small fraction of AAV genomes is integrated into the host cell genome. These nonintegrated vector genomes would be lost in cell division⁴⁴¹, consistent with the drop in cell numbers. From the two experiments, with two different viral dosages, we

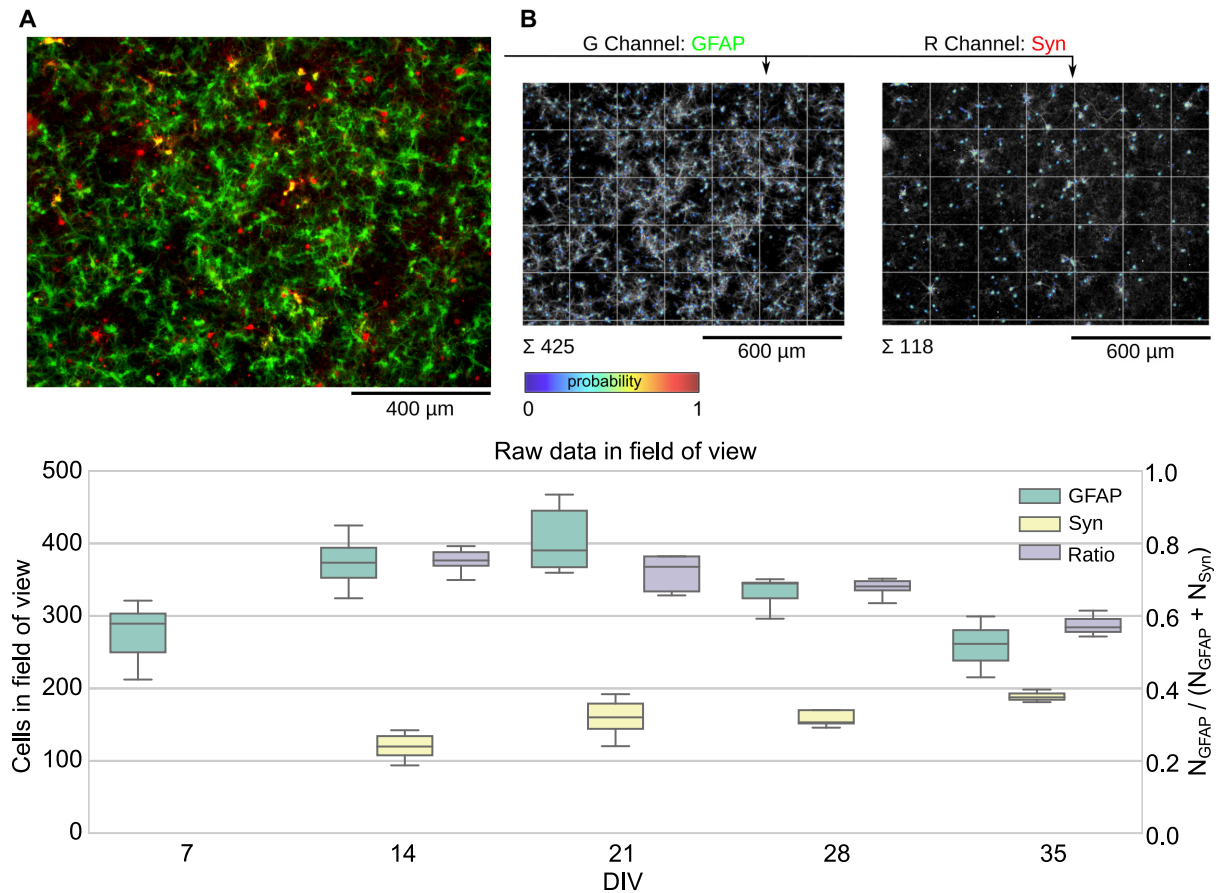


Figure 4.4: **Raw data and analysis of GFAP and Synapsin positive cells.** (top) **A** Example dataset of GFAP-positive glia and Synapsin-positive neurons, **B** sorted with Ilastik (see text). (bottom) From the images we can extract the raw counts of GFAP and Synapsin positive cells. Note that with at DIV7 no RFP label was detectable.

can estimate the transduction density, **Fig. 4.5B**. The two blue datapoints correspond to the two experiments, where the error in transduction rate is the scatter across experiments, and the error in viral dose is the pipetting error of $\pm 0.1 \mu\text{l}$. Fitting the datapoints with a line through the origin, we get a transduction efficiency of the Synapsin promoter as $10.5 \cdot 10^{-10} \times \text{GC}$. The red cross is the dose of AAV9.hSyn.hChr2(H134R) that we used for our experiments. The default transduction on cultures on MEAs, prepared the same way, was done with $1 \mu\text{l}$ virus per ml of medium. Notably, this is 25% more than in other studies.³⁷¹ The viral stock solution had a concentration of a $3.39 \cdot 10^{13}$ GC/ml solution, yielding $3.39 \cdot 10^{10}$ GC. These dosages are at least an order of magnitude below what would elicit cytotoxic effects^{192,413}.

To verify the measurements above with an independent method, we also studied the content of primary cortical cultures with immunostained samples on a confocal microscope (Olympus Fluoview FV1000), see **Fig. 4.6**. First, we compared the viral estimates of cell density with immunostainings. To this end, we used a stain for NeuN. NeuN antibodies specifically recognize the DNA-binding and neuron-specific protein NeuN (MAB377). As the NeuN protein is confined to neuronal nuclei, this makes counting easy. Other classical stainings as Tau as axonal marker and MAB2 as dendrite marker would have made counting very hard. We combined this stain with an antibody against GFAP (ab33922). GFAP, glial fibrillary acidic protein, is a cell-specific marker that reliably distinguishes astrocytes from other glial cells. **Fig. 4.6A** shows a

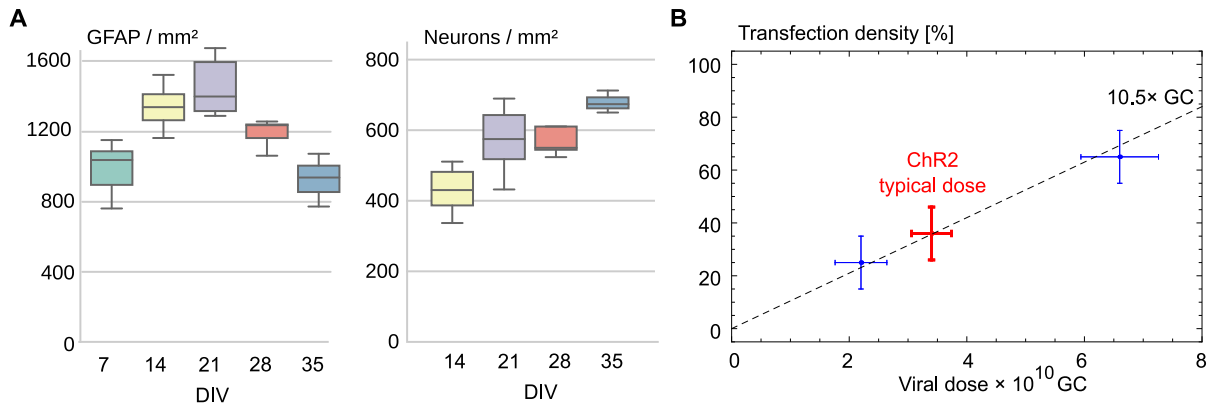


Figure 4.5: **Cellular content and transduction density in cortical cultures.** **A** Shown are the number of GFAP positive glia cells and neurons per area. **B** The transduction efficiency as function of the viral dose in units GC (genome copies), pooled from the measurements above.

z-projection through the entire volume of cells and reveals how the neurons are surrounded by dense glial fibers. In this field of view, there are 40 NeuN positive cells, corresponding to 890 Neurons/mm², consistent with the measurements above. **Fig. 4.6B** shows why it is hard in such dense cultures to directly count the number of hChR2(H134R)-eYFP positive cells. The dense expression, resembling a membrane stain, shows ubiquitous expression of hChR2(H134R)-eYFP, notably excluding the nuclei and regions that might be occupied by glial fibers. **Fig. 4.6C** shows an entire z-stack from a cortical culture, the dimensions are 212 μm \times 212 μm \times 15 μm . From this stack, we can calculate the z-profile, **Fig. 4.6D** that demonstrates that neurons grow mostly on top of a glia layer. There are various classical staining techniques for excitation, as VGlut, and a zoo of techniques for inhibition as Anti-GAD65, Anti-GAD67, Anti-GABA and Anti-Gephyrin. Unfortunately, they are not very reliable. For instance, a direct staining revealed only $\approx 5\%$ of neurons with anti-GABA immunoreactivity⁵⁰⁰, other studies arguably found Glutamate and GABA release from a single nerve terminal⁵², or clouds of synapses with challenging cell assignment²¹⁴. In this study they found a saturation of antibody labeled terminals after 3-4 weeks of development but a quantitative measurement of excitatory versus inhibitory cells is generally hard.

It is also possible to stain for synapses. Presynaptic terminals, or synaptic buttons, can be labeled with antibodies against the synaptic vesicle protein synaptotagmin-1³³¹. Only labeling for presynapses does not necessarily highlight viable synaptic connections. Postsynaptically, one can label the scaffold protein PSD-95. In addition to antibodies, this can be done elegantly with PSD-95:GFP and a lentiviral transmission system³³¹.

Designing the interface of the surrogate cortex

We will use optogenetics and digital phase-only holography to connect a virtual sensory pathway to a dense network of cortical neurons cultured on a multi-electrode array. **Technical description** We use a 473 nm diode laser (DL-473, Rapp OptoElectronic) which is coupled via a single mode fiber (Thorlabs P1-405B-FC-2) to the holographic projection system on an optical table (see **Fig. 4.7**). The beam leaving the fiber is collimated (2x PCX, d=6 mm, f=12 mm, ARC 350-700 nm, Thorlabs) and polarization restored with a Glan Laser Prism 10 mm (350-600 nm AR, NT47-256, Edmund Optics). Only vertically polarized light continues, the rest is sent to a beam dump. The beam is expanded through a Kepler telescope from two PCX lenses, (PCX f=20.0 mm LA1859-A, Thorlabs and PCX f=125.0 mm, LA1986-A, Thorlabs). It is then pro-

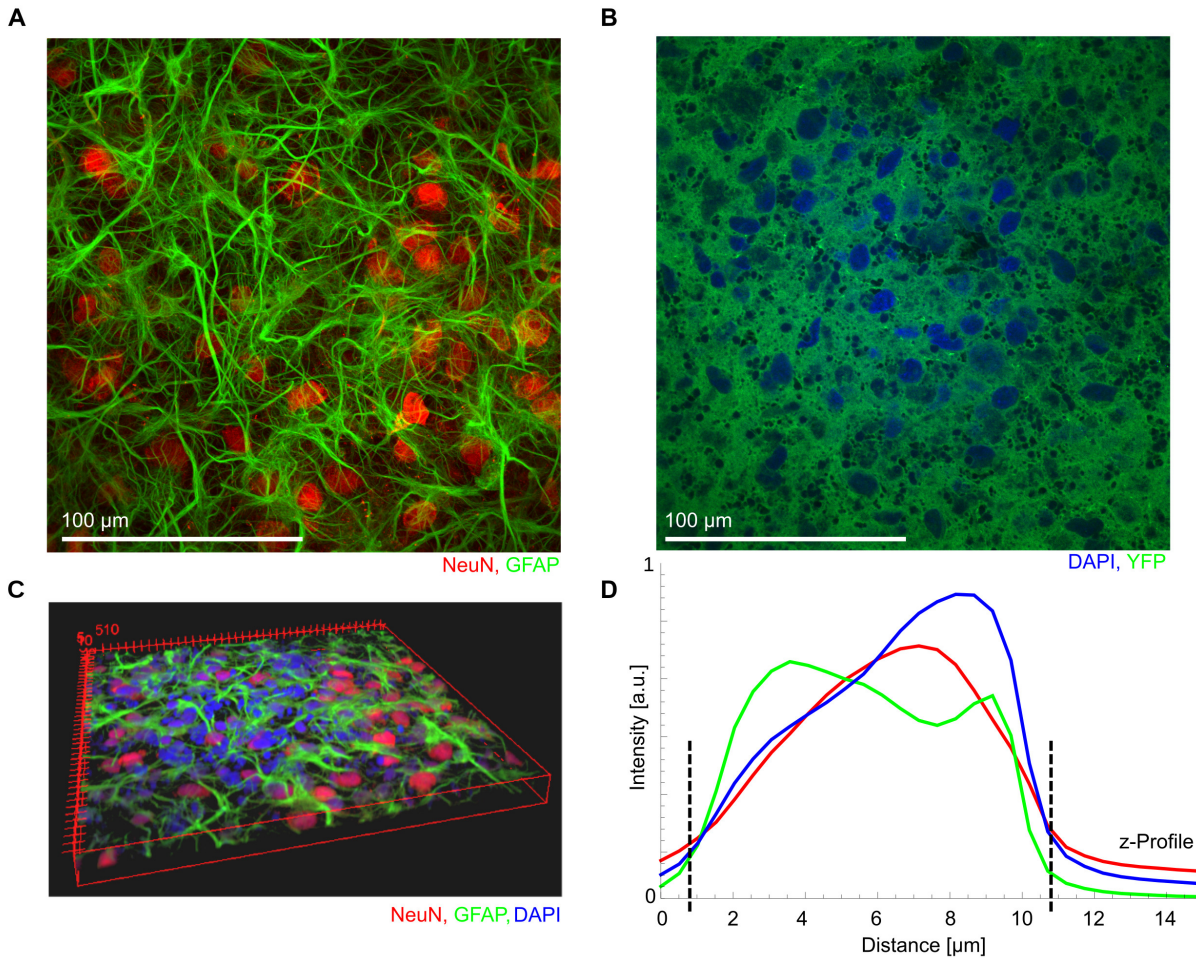


Figure 4.6: **The cellular composition in confocal microscopy.** **A** Immunostaining for NeuN and GFAP; this picture contains about 40 NeuN positive nuclei. **B** YFP fluorescence reveals the dense expression of the hChR2(H134R)-eYFP construct. From these images, we cannot just count transduction efficiency. Note the holes, filled by the DAPI positive nuclei, and *empty* holes, presumably filled by glia. **C** An entire z-stack shows a substantial fraction of dead nuclei from the culture preparation process. **D** From the data in C we can calculate the z-profile. It reveals that the primary cultures are very thin, the dashed lines have a distance of 10 μm , and that neurons sit on a glia layer.

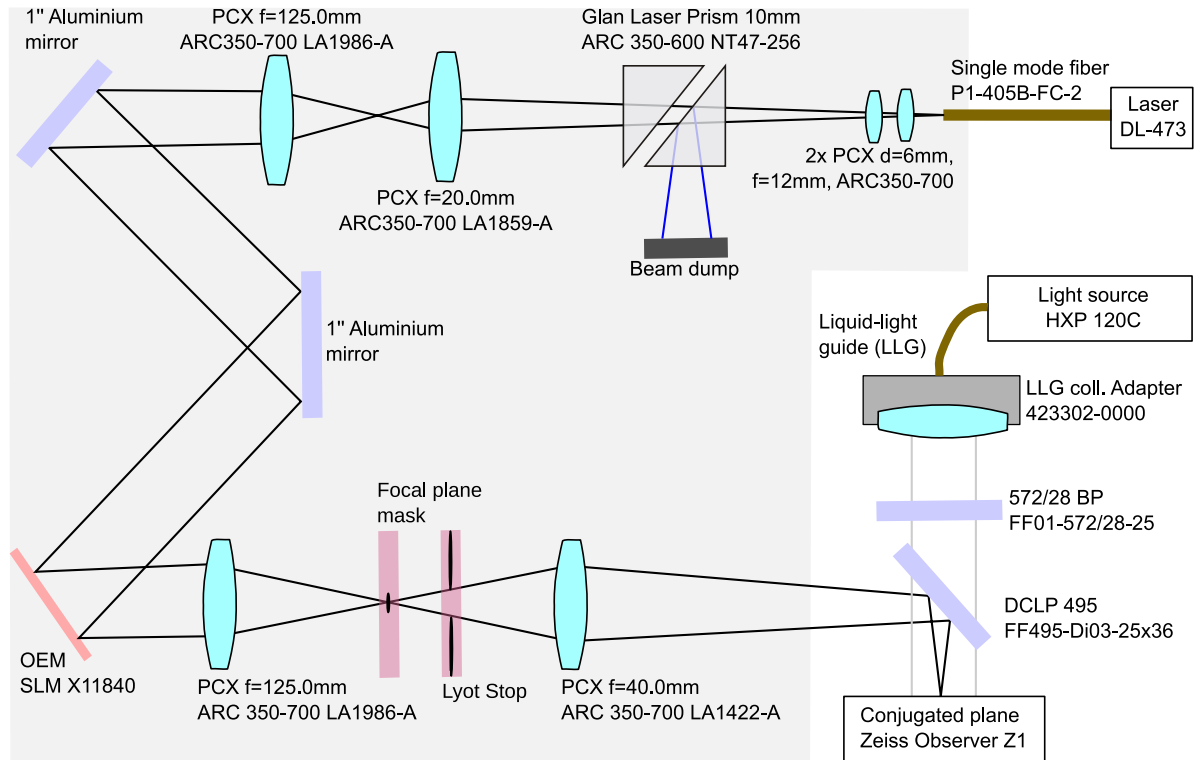


Figure 4.7: **Sketch of the holographic setup.** The single mode fiber is connected to a DL-473 100 mW Laser from Rapp OptoElectronic. The beam path is set up on an optical table and projecting to the conjugated plane at the epifluorescence port of a commercial Zeiss Observer.Z1 microscope.

jected with a periscope from two aluminum mirrors onto the spatial light modulator (SLM). Our SLM is a liquid crystal on silicon spatial light modulator, (OEM SLM X11840, Hamamatsu). This SLM has a resolution of $600 \text{ px} \times 800 \text{ px}$, a $12.5 \text{ }\mu\text{m}$ pixel pitch and a fill factor of 95%. Following the SLM, a Fourierlens (PCX $f=125.0 \text{ mm}$, LA1986-A, Thorlabs) generates an image, where a focal plane mask blocks the maximum of zeroth order. This aperture is custom made by evaporation of a $d=500 \text{ }\mu\text{m}$ aluminum dot, through a bronze mask, onto a glass plate. For protection it is covered with MgF_2 . The light then passes through a *Lyot aperture*, used to trap scattered light that impairs contrast. This is a technique first used by Bernhard Lyot to study the solar corona²⁹⁶. Finally, the light is projected (PCX $f=40.0 \text{ mm}$, LA1422-A, Thorlabs) to the conjugated plane of a Zeiss Axio Observer.Z1 inverted microscope.

Generation of Holograms This spatial light modulator is operated by a controller which allows us to control the phase shift on each pixel via a standard DVI interface. To remove the maximum of zeroth order, we employ an axial displacement of the hologram by a superimposed Fresnel lens with a focal length of $\approx 2 \text{ mm}$. Thus, the hologram is spatially separated from the focal point of the maximum of zeroth order. At the focal point of the maximum of zeroth order, it is blocked with a mask. The axial displacement leaves the hologram intact, except for a small loss of contrast and slight distortions. In comparison to other techniques to remove the maximum of zeroth order as a shift of the holographic pattern in x/y direction and a beam dump for the maximum, our setup's advantage is keeping the pattern close to the optic axis, i.e. where optics and the laser are most homogeneous. To create a hologram, we start with a target matrix of size $2050 \text{ px} \times 2722 \text{ px}$, corresponding to $2050 \text{ }\mu\text{m} \times 2722 \text{ }\mu\text{m}$. We then multiply the target intensity distribution with a correction mask, the simplest form of open-loop adaptive

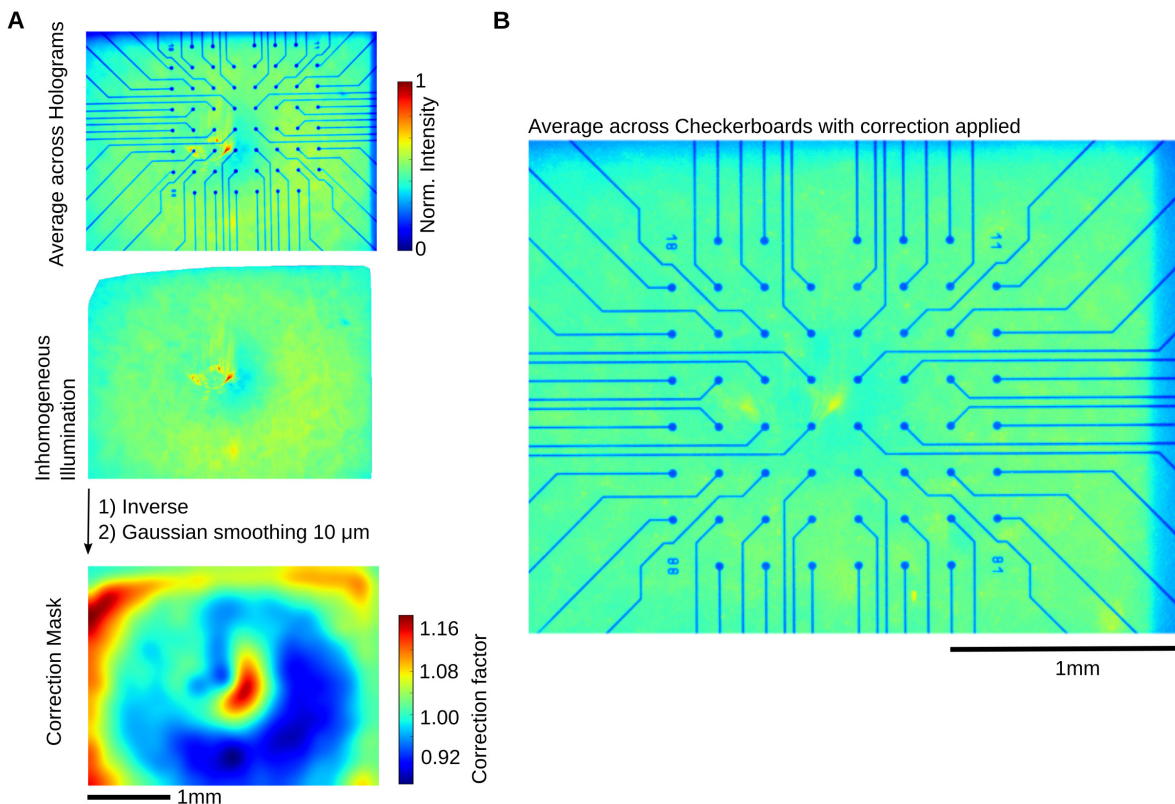


Figure 4.8: **Intensity correction for the holographic system.** **A** The procedure how the correction mask was calculated. Without correction, the holograms are anisotropic, due to inhomogeneities along the optic path. We extracted anisotropies from the holograms, inverted the result and smoothed it with a Gaussian kernel. In all subsequent holograms, we first multiply the goal with this correction mask. **B** The averaged hologram intensity in the entire field of view reveals a relatively flat intensity profile. All images were taken with a Zeiss EC Plan-Neofluar 5x/0.16, that generates an approximate $2\text{ mm} \times 3\text{ mm}$ field of view.

optics^{36,530}, see **Fig. 4.8A**, that incorporates anisotropies of our particular experimental setup and then rescale the pattern in (x,y) coordinates to SLM pixel coordinates (u,v) with an affine transformation, i.e.

$$\begin{pmatrix} u \\ v \end{pmatrix} = \begin{pmatrix} c_1 & c_2 & c_3 \\ c_4 & c_5 & c_6 \end{pmatrix} \begin{pmatrix} x \\ y \\ 1 \end{pmatrix} \quad (4.7)$$

where we obtained the parameters c_i from a fit to $\mathcal{O}(10 - 20)$ control points. Next we calculate phase fields for the rescaled patterns with the Gerchberg-Saxon method; $N=20$ iterations¹⁵⁶, implemented in Matlab. This recursive optimization method is a robust tool to solve the phase-only holography problem. After calculating the phase field, it is adjusted with a SLM specific flatness correction at 470 nm, provided by Hamamatsu. **Fig. 4.8B** illustrates the overall smoothness of the holographic field of view. The images were taken with fluorescence in a Fluorescein solution and a Jenoptik ProgRes 1.4 Megapixel CCD (monochrom, $2/3''$, firewire).

Measuring absolute intensities To measure absolute intensities, we used a calibrated photodiode (Hamamatsu S2386-8K), see **Fig. 4.9A,C,D**. This specific diode yields 274 mA/W at 473 nm illumination. We measure currents with a Keithley 2100 short-circuiting the diode. We use this method rather than a transimpedance amplifier and clamping the diode to 0 V, because

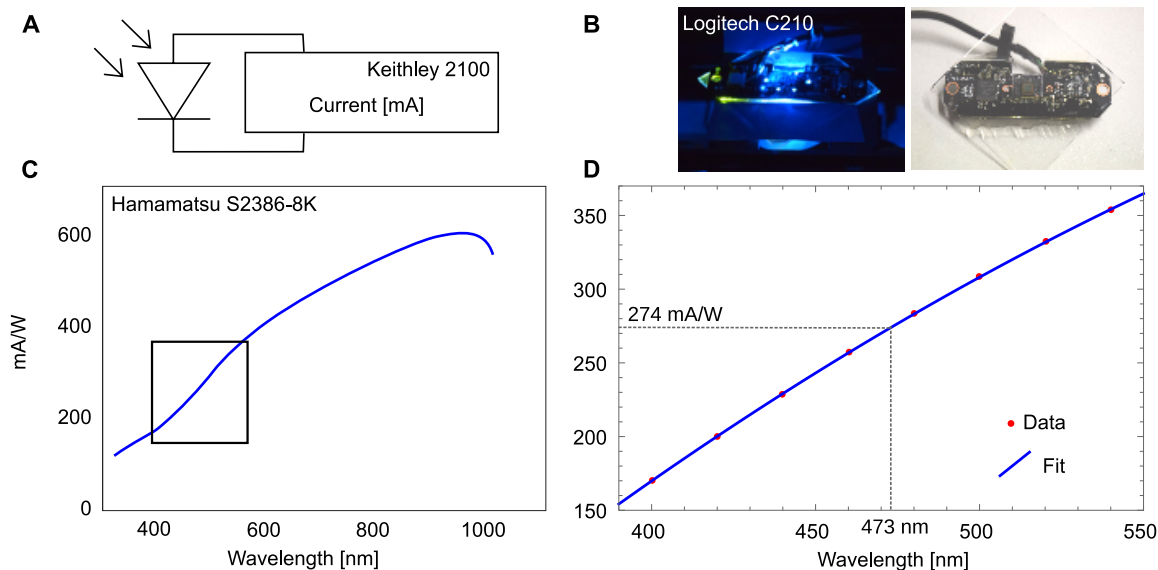


Figure 4.9: **Measurement of absolute light intensities I.** **A** Currents from the photodiode are measured with a Keithley 2100. **B** The spatial distribution of light is measured with a SIV100B CMOS sensor on a Logitech C210 circuit board, glued to a piece of glass. The sensor is exposed on the glass side. **C** The calibration curve of the Hamamatsu S2386-8K photodiode. **D** The relevant section of the calibration data with a parabolic fit. At 473 nm illumination, the photodiode produces 274 mA/W.

this is how the diode was calibrated by Hamamatsu. First, we measure the laser power at maximum output leaving the FC/PC fiber coupler of the DL-473 laser. This turned out to be 87 mW (consistent with the measurement from Rapp in the documentation of the DL-473. They measured 90 mW). Leaving the 2 m long single mode fiber, after calibration, we measured 55 mW (again consistent with their measurement of 56 mW). We next placed the photodiode above the objective (either a Zeiss Plan-Apochromat 10x/0.45 M27 or a Zeiss EC Plan-Neofluar 5x/0.16 M27), with either a dichroic longpass at 495 nm or at 593 nm (FF593-Di03-25x36, Semrock) reflecting the holograms into the optic path of the microscope, and measured the light intensity leaving the microscope. We obtain the curves shown in **Fig. 4.10A,B**, illustrating the total power in the object plane as function of the laser's power setting. In total, about 2.0 mW make it through the system, notably $\approx 2\%$ of the light from the DL-473. Finally, we checked how strongly the light power varies across holograms. Using the DCLP 593 with the 5x objective, we checked gratings and checkerboards of various spatial extend with $N = 10$ samples. For the checkerboards, we observed intensities of 2.08 ± 0.02 mW, and for the gratings, we observed 2.06 ± 0.06 mW (mean + standard deviation) total intensity across area.

Measuring spatial organization We analyze the spatial organization of the holograms with the sensor of a commercial webcam, a Logitech C210, glued on a piece of glass with the size of a MEA, that can be placed in the objectplane and mimics a MEA, see **Fig. 4.9B**. The sensor is a SIV100B, a 1/7" VGA/ISP CMOS chip with an integrated RGB color filter, 8 bit output, a pixel size of $3.2 \mu\text{m} \times 3.2 \mu\text{m}$ and a resolution of 640×480 pixels. Notably, every pixel has only one type of color filter on it, and color information is interpolated from that. Throughout the measurement, we fixed the exposure time and the gain of the CMOS with v4l2 to the smallest possible value. In addition, we analyzed only the Red-Channel, as a substantial fraction of the 473 nm light is absorbed by the R-color-filter, preventing an early saturation of the CMOS. Despite these precautions, the CMOS was already saturated at a power-setting of about 20%.

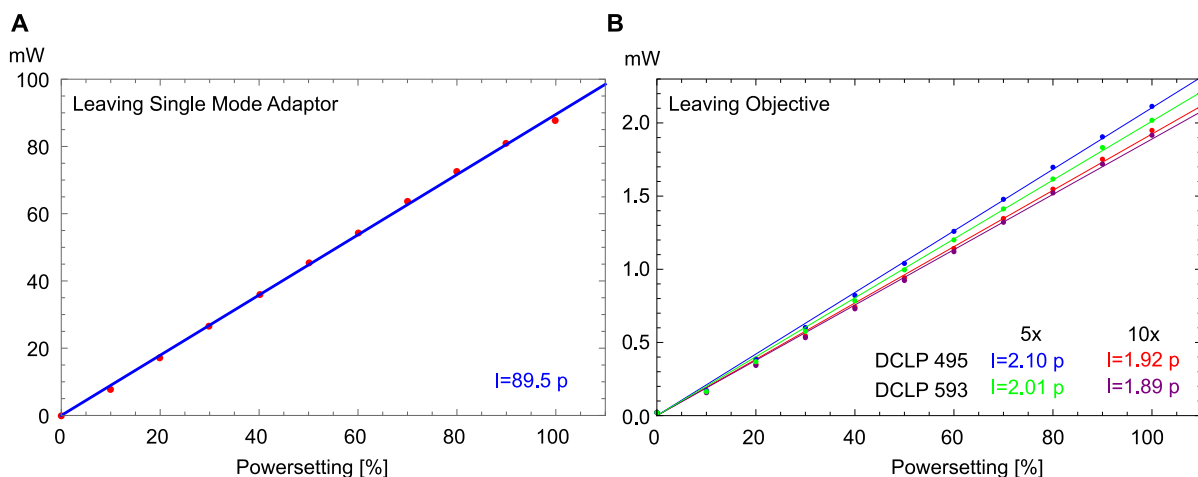


Figure 4.10: **Measurement of absolute light intensities II.** **A** Measurements of light intensities leaving the single mode adaptor at the DL-473 laser as a function of the laser’s powersetting. The drawn line is a linear fit. **B** Same as A but measured above the Axio Observer.Z1 objective, as function of the powersetting of the laser. The lines are best fits. We selected two dichroics and two objectives (see text).

To calibrate the CMOS of the Logitech C210, we first replaced the objective of the microscope with a brass holder. In this holder, about 40 mm below the CMOS, a bright LED was glowing. We choose the LED, a Luxeon rebel color from Philips Lumileds type “blue”, because it emits light centered around 470 nm with a spectral half-width of ≈ 20 nm. On the small spatial scale of the CMOS sensor, 2.6 mm diagonal, the illumination field should be roughly constant. This way we obtain a flat frame, shown in **Fig. 4.11A**. We also record a dark frame, **Fig. 4.11B**, by switching off the light source. Throughout our measurements, we kept the room lights off. The corrected image, **Fig. 4.11C** vs. **Fig. 4.11D**, is then

$$I(x, y) = \frac{I_{\text{CMOS}}(x, y) - \text{darkframe}(x, y)}{\text{flatframe}(x, y) - \text{darkframe}(x, y)} \quad (4.8)$$

Given the corrected image, the intensity field in proper units is

$$I(x, y) = \frac{I(x, y)}{\sum_{x, y} I(x, y)} \times \frac{P}{A} \quad (4.9)$$

where P is the measured total intensity in mW and A is the area of the CMOS in mm^2 . **Maximum light intensities in the system** After the calibration of the Logitech camera’s SIV100B, we look at actual light intensities, shown in **Fig. 4.12A,B**. With the DL-473 delivering maximum output, we can reach light-intensities up to $\approx 2 \text{ mW}/\text{mm}^2$ (which is more than sufficient to drive ChR2^{282,283}). Speckles, and the distortions from the mask to remove the maximum of zero-order notably distort the image. With the measured intensity distributions, we can estimate the contrast of the system,

$$C = \frac{I_{\text{bright}} - I_{\text{dark}}}{I_{\text{bright}} + I_{\text{dark}}} \quad (4.10)$$

The minimum of the sinusoidal pattern was $\approx 0.1 \text{ mW}/\text{mm}^2$, the maximum at $\approx 1.6 \text{ mW}/\text{mm}^2$. This yields a holographic contrast of $C \approx 90\%$. Note that in the experiments shown, we additionally applied a correction mask, shown in **Fig. 4.8**, to correct anisotropies along the beam

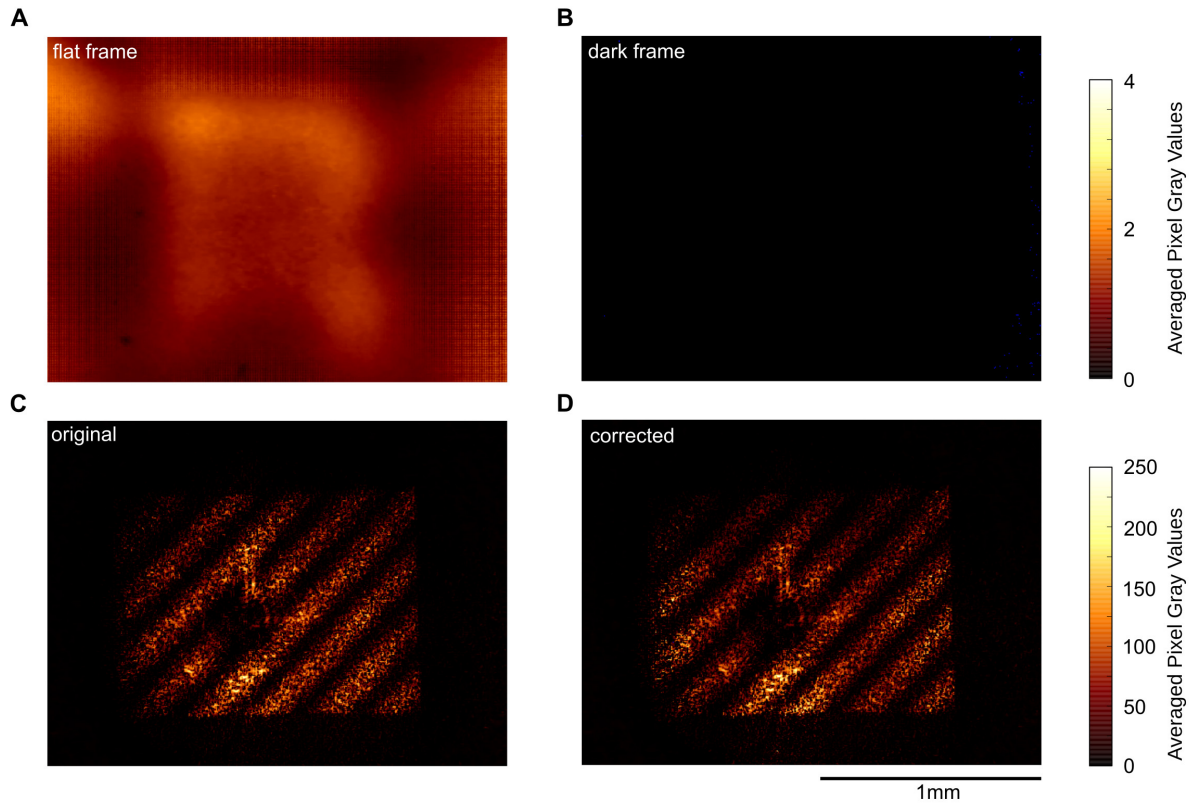


Figure 4.11: **Calibration of the CMOS Sensor.** **A** The flat frame and **B** the dark frame for the sensor of the Logitech C210. Both have been averaged from 50 individual measurements. **C** The original picture from a holographic grating with wavelength $200\ \mu\text{m}$. **D** The intensity-corrected picture. The scale corresponds to the size of the SIV100B CMOS.

path.

3D organization of holograms With the CMOS Chip in place, we can also measure the 3D distribution of light intensities of the holograms. To do this, we move the objective of the inverted microscope and keep the sensor fixed on the microscopy table. We take an image every $250\ \mu\text{m}$ in the range of $\pm 3\ \text{mm}$. We monitor the position of the objective with the build-in tool of the microscope. The result is shown in **Fig. 4.13**, to the left, **Fig. 4.13A**, as intensity plot, to the right, **Fig. 4.13B**, with five example planes. What we can see is that indeed $\approx 1.5\ \text{mm}$ after the hologram is in focus, we find the image of the mask. Also, the light intensities are highest in the focal plane, visible on the left in the central region (arrow).

Triggering. The holographic frame transitions were recorded from a screen receiving the same signal as the SLM after a DVI splitter. We measured the screen signal with a OPT101 photodiode and transimpedance amplifier (Texas Instruments) and recorded it with the electrophysiology setup. We made sure that this signal is within 2 ms synchronous to the SLM, see **Fig. 4.14A**. **Fig. 4.14B** shows the signal on the screen in comparison to a recording from blue light leaving the objective. We first note that even at 30 frames per second, individual frames can be lost. This is a problem for reverse correlation with uncorrelated stimuli. Therefore, we operated the system at 10 frames per second, at which the reliability is higher than 1 missed frame in 10.000 frames. For this configuration we also plotted the automatically detected frame transitions.

Optical recordings For imaging, we used a microscope camera (ProgRes MF 1.4 Megapixel CCD monochrom, $2/3''$, firewire, Jenoptik, Germany) connected to the same PC that provided the phase field. It sends trigger pulses to the MEA amplifier, that we recorded digitally. For

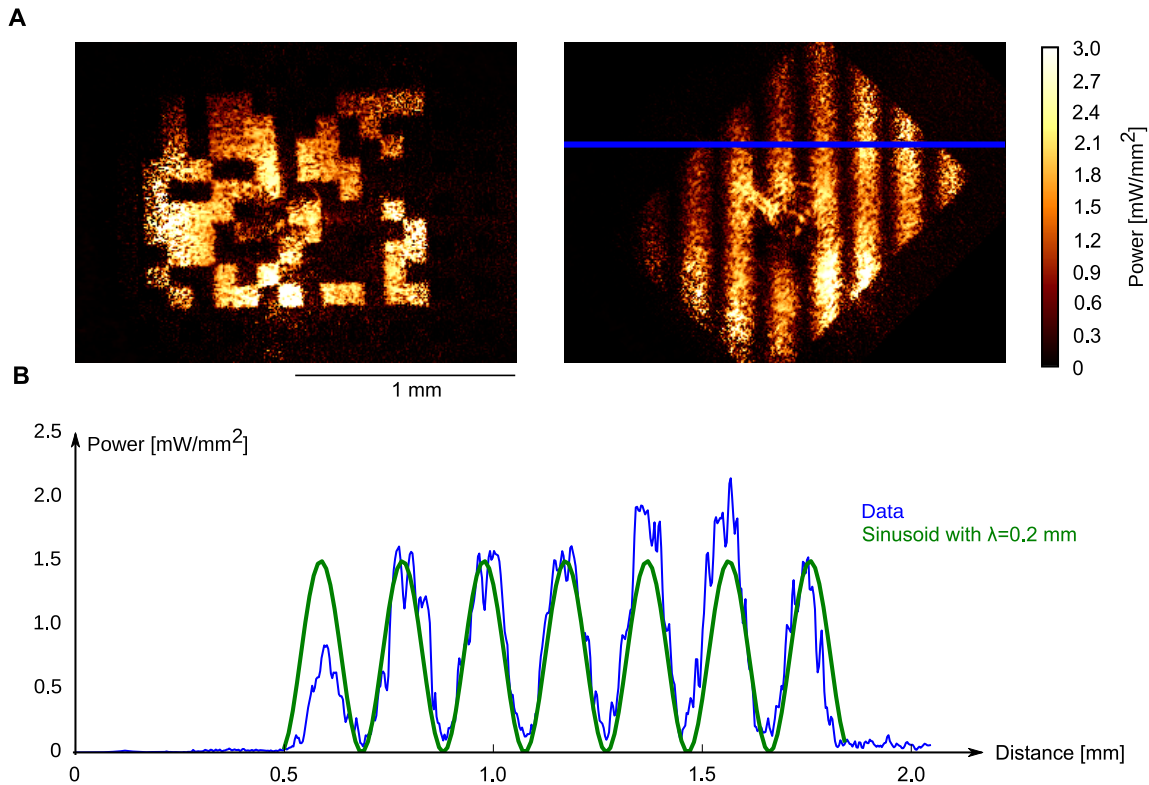


Figure 4.12: **Patterns measured with the CMOS sensor.** **A** Shown are two example patterns, a checkerboard pattern with box size $100\ \mu\text{m}$, and a grating with wavelength $200\ \mu\text{m}$ at maximum laser power. **B** The intensity along the blue line together with the sinusoid target pattern. Note that these holograms were generated before application of the correction mask, **Fig. 4.8**.

recordings of calcium dynamics, we use a red-shifted calcium indicator, jRCaMP1a, to combine the optical excitation with calcium imaging¹⁰³ and use an all-optical interface^{129,369}. A genetically encoded calcium indicator has the advantage of chronic imaging with low cytotoxicity in comparison with organic calcium dyes. To specifically target neurons, we express jRCaMP1a under the control of a Synapsin promoter. ChR2 produces no photocurrent between $550\ \text{nm}$ and $650\ \text{nm}$ ³⁷¹, therefore we can excite jRCaMP1a in this window, while stimulating the ChR2(H134R) channel at $473\ \text{nm}$ without cross-talk, see **Fig. 4.15A**. Please note that the ChR2(H134R) variant is slightly blue shifted in comparison to wildtype ChR2 with a excitation maximum around $450\ \text{nm}$ ²⁸³, and jRCaMP1a is even more red shifted than typical organic dyes, as Rhod-2. For comparison, we include the Rhod-2 excitation and emission spectra in the figure, too³⁷¹. Another notable dye that received some attention recently for deep optical imaging is Cal-590⁴⁷². The excitation filter for the jRCaMP1a fluorescence is a $572/28$ bandpass (FF01-572/28-25, Semrock), operated after a Zeiss HXP-120C metal halide light source. For calcium fluorescence we targeted light intensities well below $0.5\ \text{mW}/\text{mm}^2$, to avoid excessive bleaching³⁷¹. Using a calibrated photodiode (Hamamatsu S2386-8K), we measured light intensities at our setup to $0.10 \pm 0.01\ \text{mW}/\text{mm}^2$. The excitation light is combined with the holographic light through a $495\ \text{nm}$ dichroic longpass (FF495-Di03-25x36, Semrock). The beam then enters the microscope through the epifluorescence port. To record fluorescence, we project the beam with a $593\ \text{nm}$ dichroic longpass (FF593-Di03-25x36, Semrock) through the objective (a Zeiss Plan-Apochromat $10\times/0.45\ \text{M27}$ or a Zeiss EC Plan-Neofluar $5\times/0.16\ \text{M27}$), and collect fluorescence

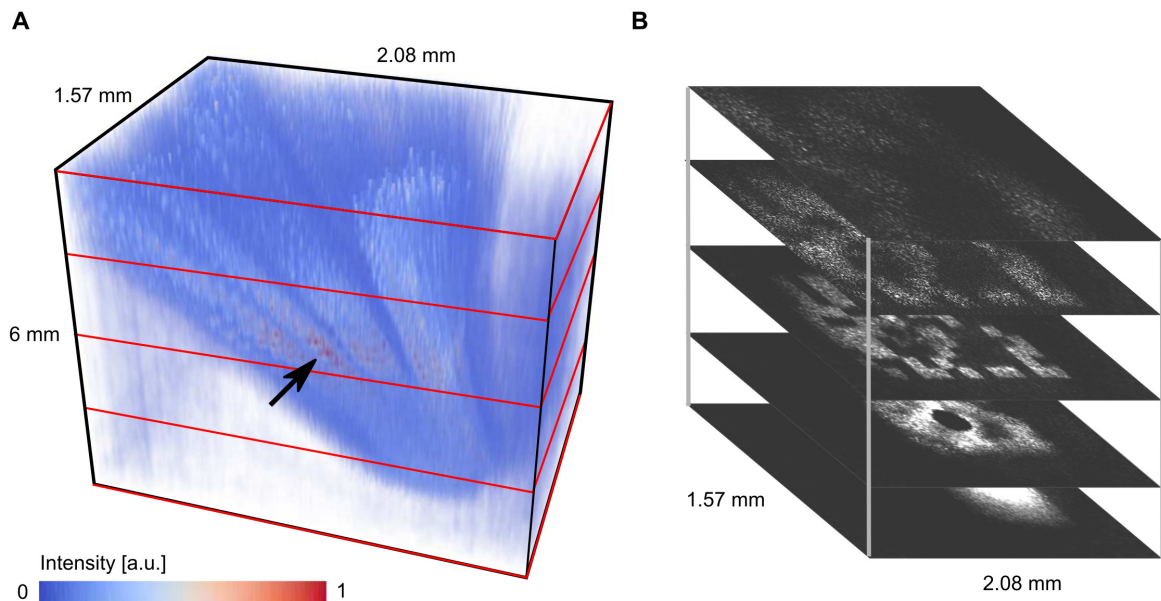


Figure 4.13: **The 3D distribution of intensities.** **A** A density plot of light intensities. The arrow indicates the highest intensities, reached in the focal plane. **B** A few selected example planes. Note the shadow of the beam block that is used to remove the maximum of 0th order, in focus about 1.5 mm below the focal plane of the holograms.

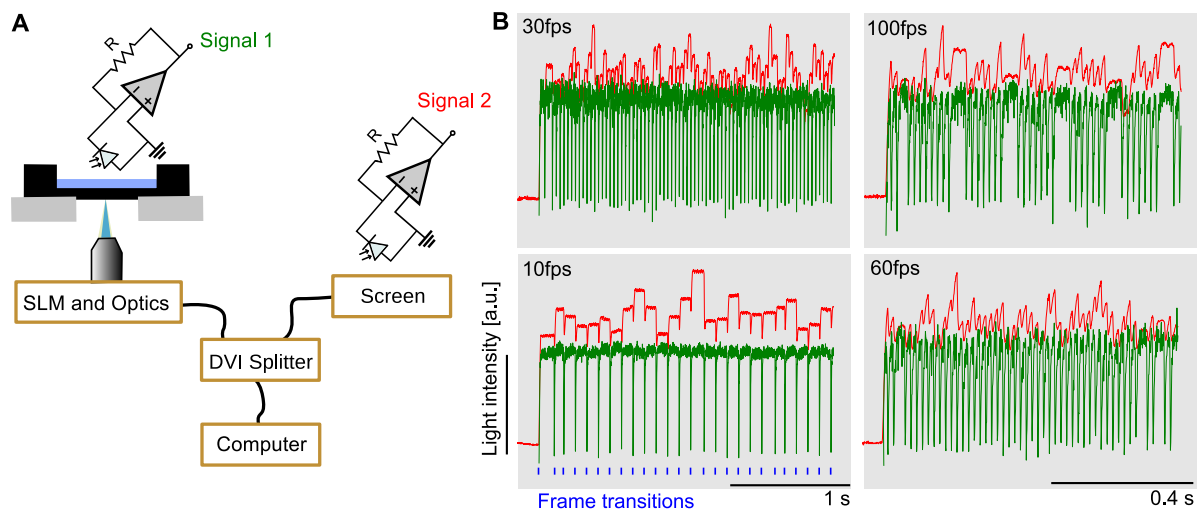


Figure 4.14: **Precision of the trigger system.** **A** We first recorded whether the signal after the beam splitter to a second screen and the holographic projections are in synchrony with two photodiodes. **B** The result of A, both signals are in synchrony to < 2 ms. We typically used a framerate of 10 Hz, the inset shows the identified frame transitions.

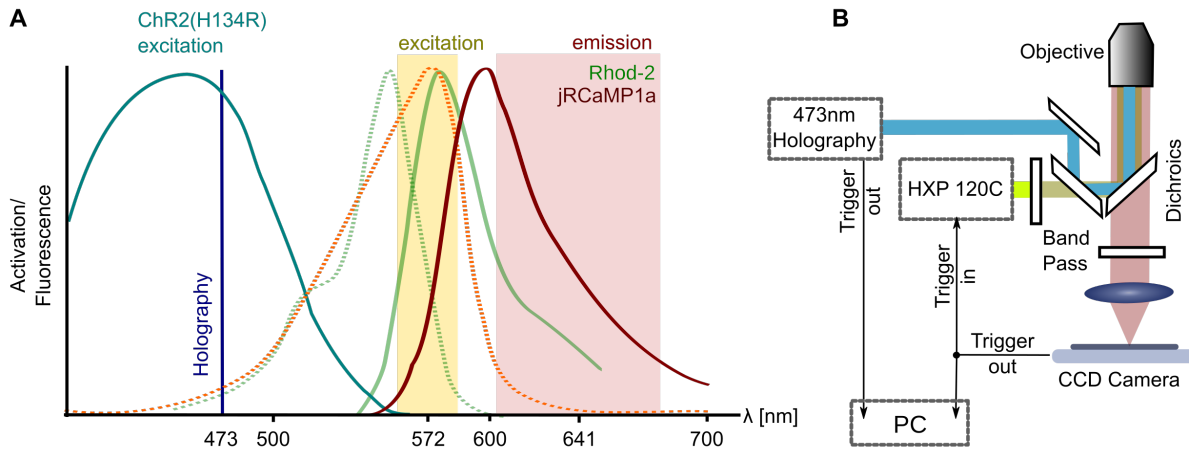


Figure 4.15: **Spectral separation of ChR2 and jRCaMP1a.** **A** Shown is the excitation spectrum of ChR2(H134R) together with the excitation (dashed lines) and emission (drawn lines) spectra of the genetically encoded calcium indicator jRCaMP1a and the organic calcium dye Rhod-2. Indicated are our filter positions, optimized for jRCaMP1a. Note the shoulder of the calcium indicators towards smaller wavelength, and the relative shift towards larger wavelengths of the jRCaMP1a excitation spectrum in comparison to Rhod-2. **B** The entire assembly with all trigger signals. PC indicates the electrophysiology Computer; we record the trigger signals together with the electrode raw data to have both in sync.

after filtering with a 641/75 emission filter (# 67036, Edmund Optics) with the microscope's camera. The camera's trigger pulses are used to open and close the shutter of the metal halide lamp, to avoid excessive photobleaching. The trigger was set to level-up during exposure, and is recorded together with the holography trigger with the MEA amplifier, see **Fig. 4.15B**. Note that such light sources, despite being very bright, are notoriously unreliable and a major source of noise in fluorescence recordings⁴⁹⁶.

Recordings

The electrophysiological activity of individual cells is generally observed using the patch clamp technique. This technique and related methods yield very high signal-to-noise ratios and are ideally suited to study the activity of ion channels. However, these techniques are limited with regard to long-term measurements and the number of recording units in a single experiment. Extracellular electrophysiological methods, on the other hand, yield weaker signals but allow long-term and multisite recordings of cellular networks due to reduced interference with cell viability. A well-established method for extracellular measurements relies on microelectrode arrays (MEAs). MEAs are devices in which a thin layer of a conducting material in the form of an electrode array is embedded onto the surface of a glass substrate, allowing for non-invasive parallel recording (and stimulation) of electrical activity from a cell culture in a wide range of spatial and temporal scales. In our study, we will not perform any stimulation through electrodes. In order to study the electrophysiological properties of dissociated neurons, a close contact between the cells and the recording electrodes has to be established. We use a homogeneous coating of the MEA surface with Poly-D-Lysine. An electrode immersed into an aqueous solution is an interface, which separates electron charge carriers from ionic charge carriers. Given that applied voltages are small enough to avoid electrochemical processes at the electrode, the coupling resembles a capacitive coupling⁴²⁶ and one can measure action potentials from electrically active cells. The electrode arrays are clamped into place by spring loaded contacts which connect the

electrode leads to the amplifier. Spring loaded gold contacts are versatile and robust even at extreme environmental conditions¹⁷⁶.

Here, recordings were made on a 60 channel MEA amplifier (MEA-1060 Inv, Multichannel Systems, Reutlingen, Germany). Data from MEAs were registered at 25 kHz using a 64-channel A/D converter and MC_Rack software (Multichannel Systems, Reutlingen, Germany). After high pass filtering (Butterworth second order, 100 Hz) events were detected in a cutout recorded 2 ms before and 4 ms after crossing a threshold of -5σ of the filtered electrode signal²⁷⁷, see **Fig. 4.16**. The threshold was evaluated for every channel individually. The identified N events were then sorted to remove false positives. This was done as follows: Every event is a point in a 150 dimensional voltage space, corresponding to the temporal length of the waveform. All N events are a cloud of points in this 150 dimensional space. To reduce the dimensionality of this cloud, we first perform a principal component analysis and only keep the first two coefficients. Subsequently we identify clusters using the mean-shift algorithm at a quartile of 0.3⁹⁰. For the identified clusters, typically one or two, we calculate averaged waveforms. If the averaged waveform within a cluster has a standard deviation larger than 5 μV and a maximum larger than +4 μV , we accept this cluster as action potentials; if not, we label the cluster as noise cluster. Please note that we only sort related to the rough shape of the waveform. The unit activity might still be taken as multiunit activity.

4. WHICH SURROGATE CORTEX?

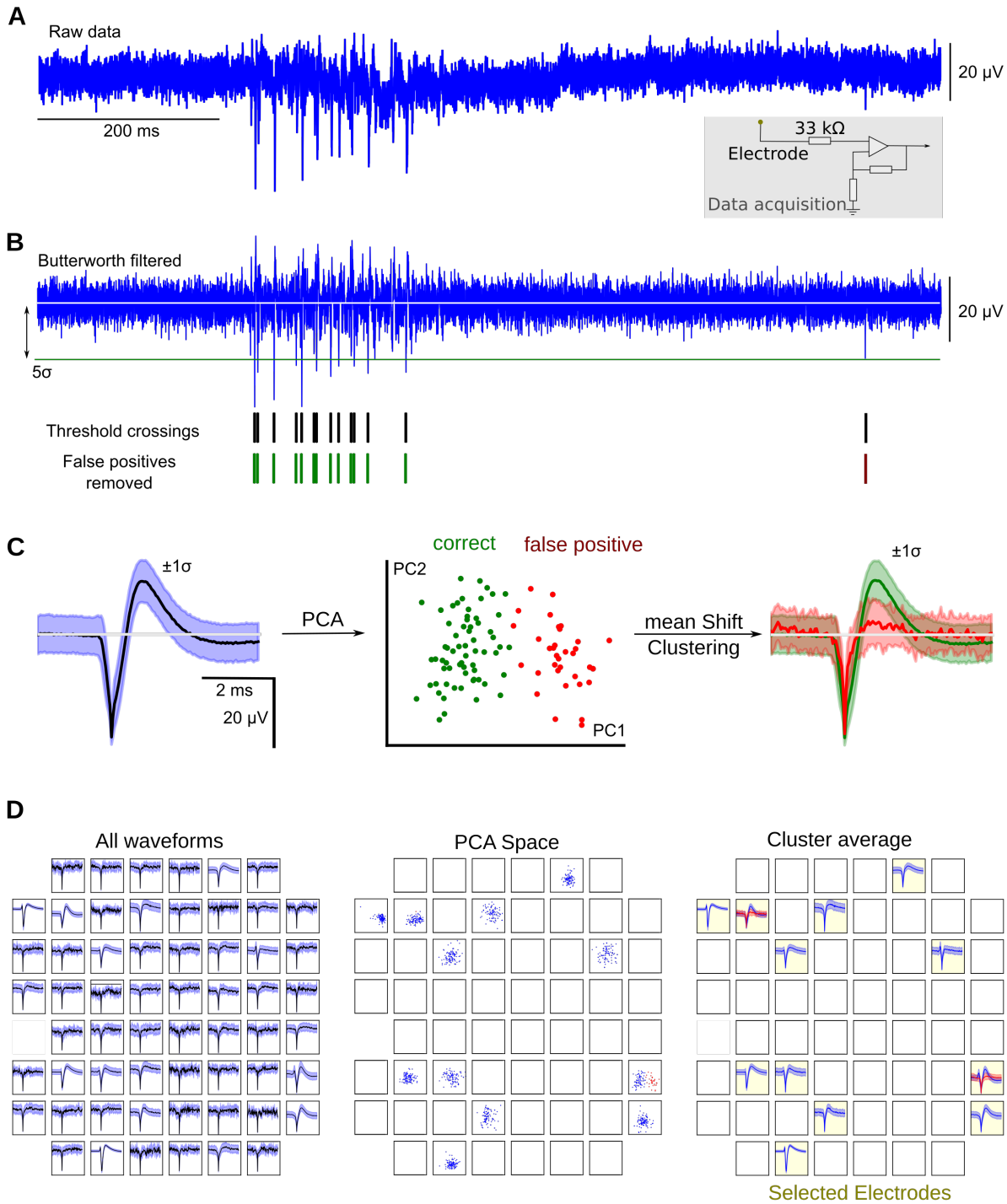


Figure 4.16: **Extraction of spike times from the raw data.** **A** The raw data is voltages, amplified from each of the 59 electrodes and sampled at 25 kHz. **B** The data is highpass filtered at 100 Hz, and thresholded at 5σ . From the threshold-crossings, we remove false positives to obtain spike times. **C** Sketch of the sorting scheme. To remove false positives, we take all individual threshold crossings (average shown left), cut a window of 2 ms before and 4 ms after the spike, and calculate the principle components of the cloud of waveforms in their 150 dimensional space. The first two principle components reveal a noise and a signal cluster, identified with mean-shift clustering at a quantile of 0.3 (middle). After averaging we obtain spike, and noise waveform (right). **D** The automatic analysis, done for the culture in **Fig. 6.3A**. Two electrodes required the removal of false positives.

A synthetic orientation selective hybrid neural network

“Our brains are plugged, so to speak, into the external world, by means of sensory receptors – the eyes, ears, nose, skin, and so on. However, these [machines] have their own ‘external world’, inside. [They] have receptor organs that function analogously to our sight, smell, hearing, touch, and so on. And the wires from these receptors are connected like nerves, but not to the external world, as our nerves are; they are connected to the drum there in the corner.”

Prof. Corcoran in²⁷⁴.

5.1 Content

In this chapter we construct the *in silico* visual pathway and connect it to the surrogate cortex. We use a generic scaling law for the layout of the early visual system to transform the visual pathway of a cat to that of a mouse. These different pathway connectomes can be connected to the same target circuit of living neurons, providing for an internal control.

We find that shrinking the visual system leads to a loss of orientation selectivity in the afferent input. Surprisingly, we discovered that a number of neurons exhibited orientation biased responses in the limit of homogeneous and unselective input and these orientation biased responses are generated by the recurrent network alone. These cells are simple cells with a small number of complex and direction tuned cells. We also find cells with receptive fields composed of excitatory and inhibitory subregions, and these receptive fields have a typical spatial scale of ≈ 1 mm, consistent with the generic scaling laws which we extracted from already available data. Consistent with simple cells, the tuning can be predicted from the receptive field. The spatial arrangement of spontaneously tuned cells resembles a sparse salt and pepper pattern. Finally, we show indications of contrast invariance.

This diversity of responses suggests that even in this most generic case, a recurrent circuit is sufficient to spontaneously generate a basic level of orientation selectivity. This phenomenon, already present in recurrent networks as disorganized as a primary culture, might provide a robust and generic scaffold for input classification, potentially the first workpiece refined by the selective forces of natural selection to form the basis of functional organization of neuronal circuits across many species of mammals.

5.2 Introduction

The visual system operates close to the limits of what is physically possible³² and it shows evidence for convergent evolution of optical elements^{261,351} and the neuronal processing machinery^{219,242}. A well established approach to better understand the selective forces that govern this evolution is by direct comparison of phylogenetically diverse model species^{180,242,245}, but this approach is fundamentally limited by the choice of model species that might have adapted a complex visual system to their specific environmental needs⁴²⁸. A more general approach for understanding visual system design would be based on thorough testing of the relationship between visual pathway structure and function. For genes and proteins *engineering* approaches enable biological researchers to modify their biological structure and assess the resulting loss and gain of function^{64,128}. Here, we pursue this idea and design a neuronal sensory system re-engineering the layout of the mammalian early visual pathway with a hybrid of biological and technological elements.

We focus on one fundamental and enigmatic large-scale neuronal circuit motive, common to the early visual and many other sensory systems: a recurrently connected layer of neurons processing information arriving through a feed-forward neuronal pathway, see **Fig. 5.1**. For this circuit motive, it is a long-standing and highly controversial question what feed-forward inputs from the sensory pathway and recurrent connections within the target circuit specifically contribute to cortical information processing. A key component of these computations, that has been extensively described, are feature selective responses. For the visual cortex and in the words of David Hubel, they “were the first indication from a single-cell recording that the cortex might be doing something interesting, something that transcended what the geniculate could do.”¹⁹⁸. In particular orientation selectivity, i.e. the selective response to edge-like stimuli of a particular orientation, is a property shared by many mammalian species.

In carnivores, primates and their close relatives, orientation selectivity is arranged in patterns of iso-orientation domains that exhibit a continuous, roughly repetitive arrangement of preferred orientations^{41,46,50,76,166}. In the primary visual cortex of rodents, electrode penetration experiments since the 1970s suggested a lack of orderly layouts of orientation domains^{159,327,339}. More advanced imaging techniques^{112,458} revealed a true dichotomy in the layouts of visual cortical architecture between orientation domains and a salt and pepper pattern^{359,360}. The nature of this transition is not understood and might be related to constraints imposed by a small brain^{239,242,245}. To better understand the connection between visual pathway structure and function, specifically the constraints invoked by finite brain size, we first re-engineered the early visual system of the cat, **Fig. 5.1A**, and then study how miniaturizing this circuit to the scale of a small animal, **Fig. 5.1B**, like a mouse or a eutherian common ancestor, would affect its functionality. We emulate this evolutionary transition by providing the same piece of tissue with input following the same rules. As neither the miniaturization nor experiments with the common ancestor can be done in a living animal, we use a hybrid system of biological and electronic components, **Fig. 5.1C**. We simulate the visual pathway by generating visual stimuli and then processing these patterns digitally, building on earlier work^{21,45,299,428,445,479,529}. The simulated LGN relay cells projected to a dense recurrent network of living cortical neurons *in vitro*, a *surrogate cortex*. The recurrent network of cortical neurons is a primary cell culture from embryonic rats, expressing the light sensitive ion channel ChR2(H134R) after viral transduction^{282,283}, so that projections can be made optically using high spatial resolution phase-only digital holography^{161,295,369,401}, connecting the electronic and the biological components.

We established a system with arguably the most classical sensory cortical connectivity motive, the Hubel&Wiesel connectome¹⁹⁴ for the generation of orientation selectivity in the primary visual cortex of cat, one of the model animals of visual neuroscience. Taking this connectivity motive seriously, we then miniaturize the pathway, shrinking eye size, cranium and the cortical

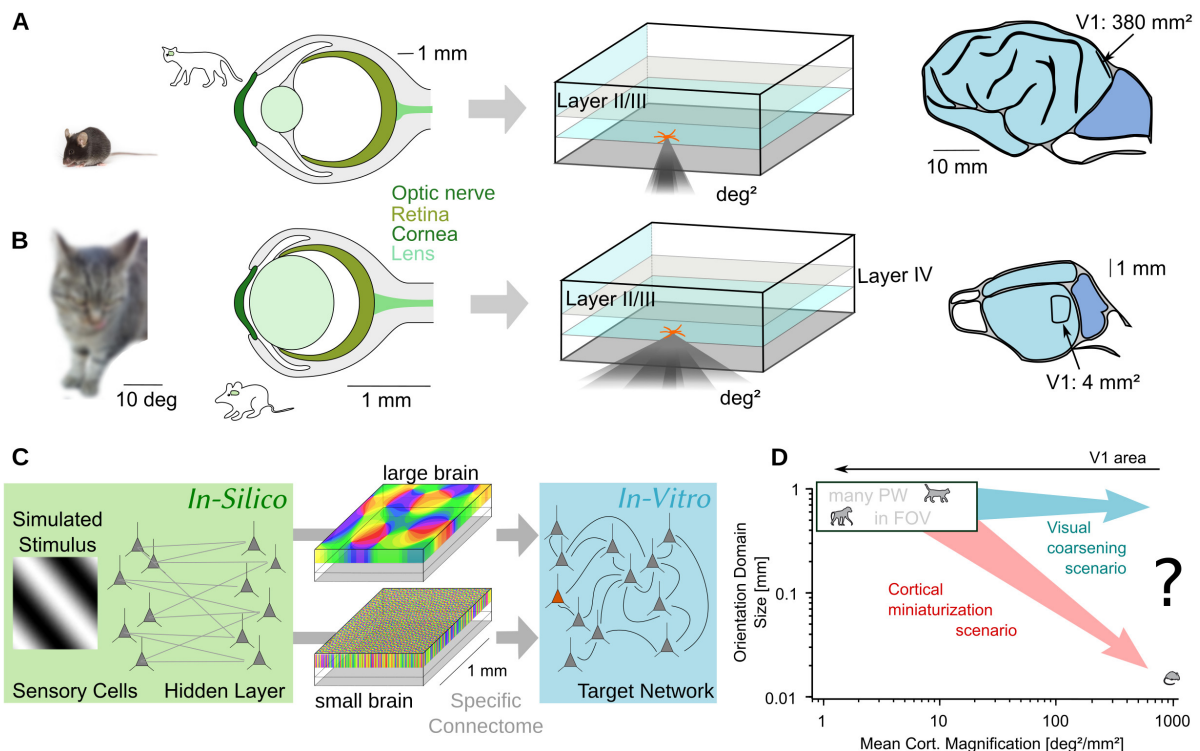


Figure 5.1: **Construction of a hybrid neuronal circuit.** **A** Visual system of a cat with high visual acuity. **B** Visual system of a mouse with poor sight and a very small visual cortex. **C** Schematic structure of a neuronal sensory system and how we re-engineer this layout with a hybrid system of biological and artificial elements such that the pathway connectome can be experimentally controlled. **D** In the *cortical miniaturization scenario*, the total number of hypercolumns is independent of cortex size; there exist many pinwheels (PW) in the field of view (FOV). In the *visual coarsening scenario* the column spacing is constant while the visual cortex shrinks. This leads to orientation scotomas at specific locations in the field of view.

target area, but preserving the total number of hypercolumns and therefore arguably the number of processing units to process natural scenes, see **Fig. 5.1D**. We refer to these changes as the cortical miniaturization scenario. The visual coarsening scenario in which the column scaling is conserved while the cranium shrinks would lead to orientation scotomas at some locations in the field of view. In the limit of a small brain in the visual coarsening scenario, the synthetic visual system resembles a mouse visual pathway, or the layout of late cretaceous eutherians, like *Asioryctes*, closely related to the eutherian common ancestor. We found that shrinking the visual system leads to a massive loss of visual acuity, to a loss of the orientation specificity of the afferent connectome and to a larger point spread function. Surprisingly, we also found that a number of neurons exhibited orientation biased responses in the limit of homogeneous and unselective input, that are generated by the recurrent network alone. We find that these cells are mostly simple cells. In addition, we also find a small number of complex and direction tuned cells while the majority of cells responds with irregular firing upon stimulation. This diversity of responses suggests that even in this most generic case, a recurrent circuit is sufficient to spontaneously generate a basic level of orientation selectivity.

5.3 Results

The visual pathway

The visual world is sampled by various types of ganglion cells that form mosaics on the retina. β -RGCs/X-cells in cats and midget cells in the monkey are thought to be the main vehicle of acute vision due to their high density and the small dendritic field, dominating central V1 physiology^{140,479}. X-cells and midget cells are characterized by a typically circular receptive field with a simple center (ON or OFF), linear summation of stimuli presented within the center and a more or less sustained responses to light³⁷⁸. In cats, they account for 50% and in primates 75% of all retinal ganglion cells^{203,505}¹. To implement the sensory pathway from the retina to the visual cortex in the cat, we choose ≈ 5 deg of eccentricity and focus on the β -RGCs/X-cell pathway, as other theoretical model studies^{479,529}. At this position, 1 mm_r^2 corresponds to $5 \text{ deg} \times 5 \text{ deg}$ of visual field³⁷ and this region is covered by 1000 mm_r^{-2} ON and OFF X-cells³⁷⁸.

In **Fig. 5.2** we illustrate the pathway. The grating shown in **Fig. 5.2A** has a spatial frequency of 0.7 deg^{-1} , a good stimulus across all eccentricities to drive visual cortical neurons in the cat^{212,336}. We model X-cell receptive fields with a difference of Gaussians model. This is a common model for the receptive field of ganglion cells^{107,130,410,529}. Linsenmeier and colleagues²⁸⁴ quantitatively tested the accuracy of the difference of Gaussians model in fitting spatial tuning data and concluded that it is “difficult to imagine any model fitting the X-cell data better”²⁸⁴, even though more recent work showed that on a fine scale, receptive fields are neither as regular, nor as linear¹⁵⁵. The difference of Gaussian model has been used for a series of modeling studies^{21,299,447,479,529}, and became a paradigms of a receptive field. It reads

$$R_{\text{ret/LGN}}(\mathbf{y}, t) = \left[R_0 + A(C) \int d^2\mathbf{x} \int d\tau (\text{RF}_c(\mathbf{y} - \mathbf{x}, \tau) - \text{RF}_s(\mathbf{y} - \mathbf{x}, \tau)) \cdot I(\mathbf{x}, t - \tau) \right]_+ \quad (5.1)$$

where R is an estimate for the firing rate of a retinal ganglion cell, or the corresponding LGN relay cell. \mathbf{y} is position in space, t is time, I is the stimulus, $A(C)$ is the contrast response function with contrast C and R_0 is the background firing rate. $[\dots]_+$ is a rectifier and $\text{RF}_{c/s}$ is the center/surround receptive field,

$$\text{RF}_{c/s}(\mathbf{s}, \tau) = K_{c/s} \exp\left(-\frac{\mathbf{s}^2}{2\sigma_{c/s}^2}\right) \quad (5.2)$$

with spatial scale σ , and temporal scale τ . These parameters generally depend on the eccentricity. For 5 deg eccentricity, we choose a center size of 0.25 deg, and a surround size of 1 deg. The coefficients at this eccentricity are $K_c = 17/\sigma_c^2$ and $K_s = 16/\sigma_s^2$, similar to the values in^{21,479,529} and taken from^{170,284,378}. Temporal frequency preference depends only weakly on eccentricity^{402,477,529} and we will neglect this aspect.

These receptive fields cover the retina, but to this date, no retinal mosaic with the spatial extend required for our model has been sampled; therefore we approximate the ganglion cell distribution using a pairwise interacting point process (PIPP)^{125,188}. The PIPP is a method for the generation of a spatial distribution of points specifying only pairwise interaction between individual points. It has been shown to accurately reproduce the spatial statistics of experimentally measured RGC mosaics^{125,188,427}. The model mosaics are shown in **Fig. 5.2B** for ON and OFF

¹One can identify cells with similar functional properties in the mouse retina^{417,457}, however little is known about them⁴²⁰. The mouse optic nerve contains only about 30% of the fibers of a cat optic nerve¹⁸⁷, notably only slightly less than the ferret¹⁸¹. The remarkable diversity of RGCs in mouse¹⁸ and uncommon distribution patterns of particular RGCs highlight the possibility that mice sample the visual world differently than other mammals⁴².

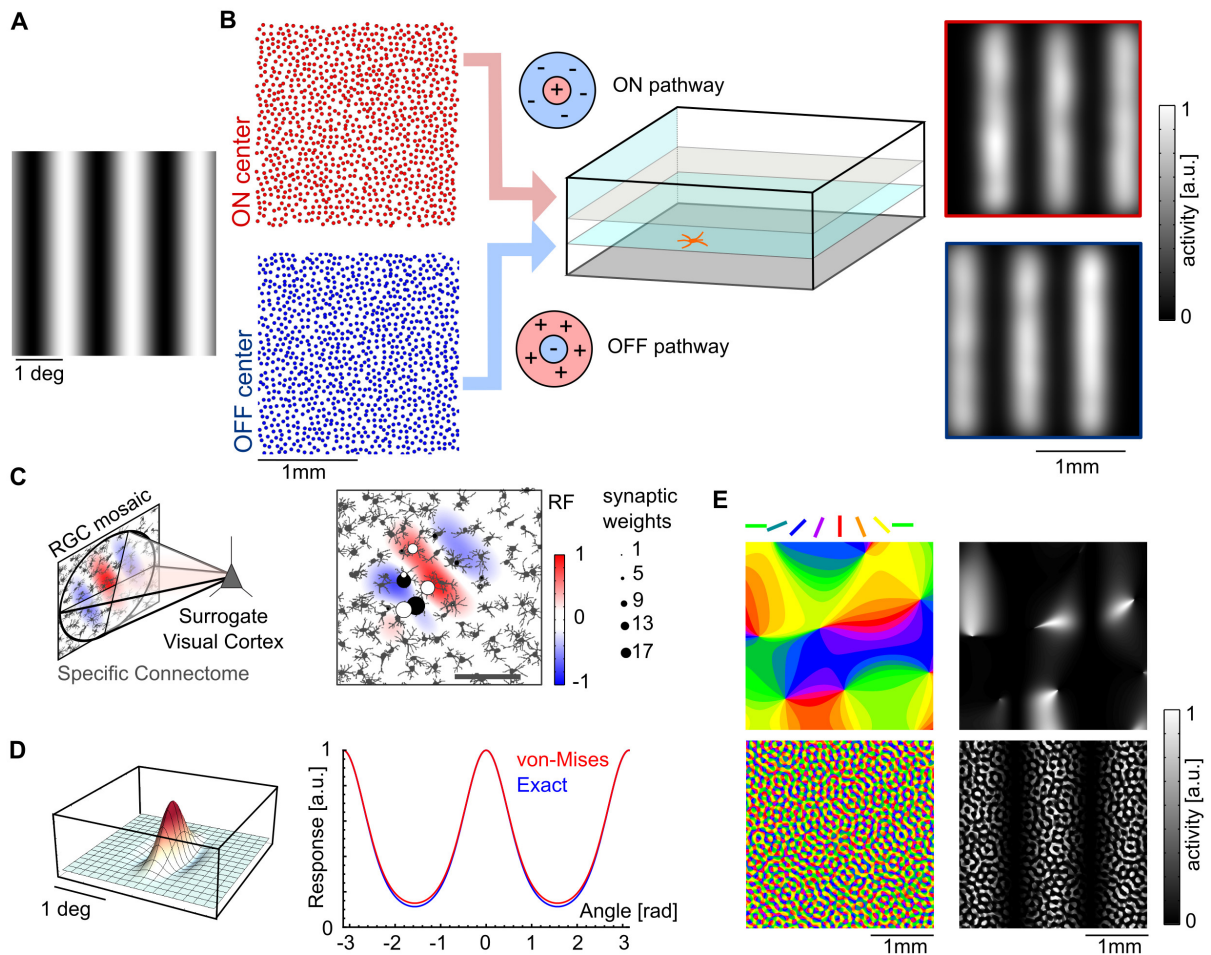


Figure 5.2: **The computational model used for the hybrid neuronal circuit.** **A** The typical stimulus for a visual neuroscience experiment: a grating of spatial frequency 0.7 cyc/deg. **B** It is processed by the ON and the OFF center pathways, that stay separate through the LGN¹⁹¹ and terminate in layer IV of the visual cortex. At 5 deg eccentricity, there are about 1000 mm^{-2} RGCs, leading to a dense representation. **C** A specific connectome of the thalamic afferents into V1 neurons makes the input orientation selective. Shown here is a simple cell receptive field, generated from fibers with Gaussian receptive fields. **D** A typical cortical cell receptive field with a tuning width of $\approx 35 \text{ deg}$ ^{136,227}. **E** In cat (top) the orientation of the filters follows the layout of orientation domains; effectively modulating the gratings in A. In mice, the layout of columns needs to be compressed into a small brain, effectively generating moving gratings as an input (bottom).

ϵ [deg]	k_{pref} [cyc/deg]	M [mm _c /deg]	k_{pref} [cyc/mm _c]	λ [mm _c]
0 - 5	1.3	1.2	1.1	0.9
5 - 10	0.6	0.5	1.2	0.8
23 [m623]	0.7	0.4	1.8	0.6

Table 5.1: The preferred spatial frequency k_{pref} and the cortical magnification M depend on the eccentricity. Here, we calculate the scale of a corresponding grating in cortical coordinates.

pathway. The contrast response function of cat geniculate relay neurons extends over the entire contrast range and there are substantial shifts in contrast-responses^{4,361}. The contrast response function (CRF) $A(C)$ of the cat LGN (building upon earlier work by⁸) proposed by Ahmed et al.⁴ is

$$A(C) = K \cdot \frac{C^p}{C_{50}^p + C^p}, \quad (5.3)$$

with parameters slightly different for ON and OFF pathway⁴⁷⁹. C is the contrast between 0 and 1, K can reach rates up to 100 Hz. The exponent $p \approx 1.2$ and $C_{50} = 0.3 \pm 0.1$ leading to a continuous increase of firing with contrast^{4,21,430,479}, as shown in many experiments^{113,276,534}. Due to the monotonic dependency in contrast, some studies do not incorporate this aspect^{113,276,529,534}. The LGN firing rate increase from typically 10/sec spontaneous discharge up to typically 50/sec-100/sec at 100% contrast^{5,21,361,416}, and firing rates for some cells can reach as much as 150 Hz⁴⁸. Depending on the choice of these numbers, there are two qualitatively different regimes. At low contrast, the modulation of the firing rates does not exceed the DC component, and the mean input into the cortex does not increase with contrast. Once the stimulus-evoked modulation is larger than the background firing rate, the nonlinearity becomes important and the input current scales with contrast. This transition occurs at about 5% contrast^{21,479,480}.

For our model, we assume that each X-LGN cell receives input from a single X-RGC and that there is no active processing. Therefore, we use the retinal receptive field properties together with the LGN CRF. The LGN relay cells, in turn, project to the visual cortex where their axons terminate in single irregular clumps^{147,148,204} of size 0.6 mm² to 0.9 mm². We assume circular patches of radius $r = 0.48$ mm, corresponding to an area of $A = 0.72$ mm². With random projections of the thalamic afferents, this would produce a Gaussian smoothing with a window of that size, $2\sigma_t = 0.48$ mm, so that

$$R_{\text{IV}}(\mathbf{x}, t) = \sum_i^N \exp\left(-\frac{(\mathbf{x} - \mathbf{y}_i)^2}{2\sigma_t^2}\right) R_{\text{LGN}}(\mathbf{y}_i, t) \quad (5.4)$$

where \mathbf{x} is the layer IV cell's position in space and \mathbf{y}_i is the LGN fiber's position, **Fig. 5.2B**. In principle, this input is scaled with the local cortical magnification^{9,304,484}, **Fig. 5.2B** (right). Cortical magnification depends on eccentricity, but across all eccentricities, a good stimulus for the cat is about 0.7 deg⁻¹ and consistent for electrical recordings of individual units at small eccentricities^{336,520} with optical imaging experiments²¹². To which scales does such a grating, shown in **Fig. 5.2A**, project? **Tab. 5.1** summarizes the relevant cortical scales as a function of eccentricity, specifically considering variations in preferred spatial frequency and cortical magnification.

How specific are these considerations to the cat? In mouse, another common animal for the study of visual circuits,³⁴⁹ receptive fields are big, the cortical magnification in units deg/mm_c is large, and to drive the system, one needs gratings with a substantially smaller spatial frequency. The inputs are projected to a very small V1, ≈ 4 mm_c² (as opposed to the ≈ 380 mm_c² of

the cat), covering about 5000 deg^{2153} . A grating that drives the mouse visual system well has a spatial frequency of 0.04 deg^{-1349} . The cortical magnification is rather uniform and about $32 \text{ deg/mm}_c^{153}$. Thus, such a grating would elicit a wave of $\lambda = 0.8 \text{ mm}_c$. Across the cells samples by Neill and Stryker, preferred spatial frequencies can be found in the range of 0.02 deg^{-1} and 0.08 deg^{-1} , corresponding to cortical scales of $\lambda = 0.4 \text{ mm}_c \dots 1.6 \text{ mm}_c$. The effective stimuli on a cortical scale for both cat and mouse are remarkably similar.

Next, we have to consider that convergent input from the thalamus is more complex than just a single center-surround receptive field. Layer IV cells receive input from $N = \mathcal{O}(10)$ Thalamic inputs (see chapter 2), constructing orientation tuned receptive fields. With specific connections,

$$R_{\text{IV}}(\mathbf{x}, t) = \sum_i^N w_i R_{\text{LGN}}(\mathbf{y}_i, t) \quad (5.5)$$

where the w_i are the specific weights of thalamic fibers, converging on a neuron in layer IV. The contribution of this convergent input to tuning is apparent in several experimental studies. Tuning in cortical neurons is robust against inactivation of the cortical circuits by cooling¹³⁶. In this study by David Ferster and others, the cortex was deactivated by cooling and using patch clamp recordings the sub-threshold responses of layer IV simple cells were tested with oriented drifting gratings. They showed that the orientation tuning curves of the sub-threshold response under cooled and normal conditions have the same width. The tuning curves differed in amplitude, because the cells responded much less in a cooled cortex. Some researchers commented that considering the technical challenges of cooling, Fersters interpretation should be treated with caution¹⁵⁸, but the experimental evidence of convergent tuning grew considerably. Silencing the cortex of ferrets with Muscimol or Kainic acid⁷⁷ and optogenetic silencing of cortical circuits in mice^{279,399} does not impair orientation selectivity. These experiments are consistent with the first model of orientation selective responses: the Hubel&Wiesel connectome for the generation of orientation selectivity in the primary visual cortex by the convergence of feed-forward inputs into layer IV¹⁹⁴. To effectively model this specific component of converging thalamic inputs, we use Gabor receptive fields. These orientation selective receptive fields can be constructed from simple Gaussian receptive fields, see **Fig. 6.3C**. For the example in **Fig. 6.3C** we constructed an error function,

$$E = \int d^2\mathbf{x} \left(\sum_i j_i w_i \exp\left(-\frac{(\mathbf{x} - \mathbf{x}_i)^2}{2\sigma_r^2}\right) + \exp\left(-\frac{\mathbf{x}^2}{2\sigma_G^2}\right) \cos(\mathbf{k}_g \mathbf{x} + \phi) \right)^2 \quad (5.6)$$

$$= \sum_{k,l} w_k w_l A_{kl} + \sum_k w_k B_k + C \quad (5.7)$$

where j_i is the sign, corresponding to ON and OFF receptive field respectively, and w_i are positive synaptic weights and A, B are used as abbreviations. We find these weights solving the constrained optimization problem

$$w_{\min} = \operatorname{argmin} \left(\sum_{i,j} w_i w_j A_{ij} + \sum_i w_i B_i \right) \text{ with } w_i \geq 0. \quad (5.8)$$

The quadratic problem can be solved analytically, but the nonholonomic constraint $w \geq 0$ makes the problem only numerically tractable. Thus, we solve it by simulated annealing in matlab. In addition, we set the phase to zero, $\phi = 0$, so that the receptive field is anchored by the OFF pathway^{225,272,393}, preserving perfect OFF retinotopy of the center. To simplify our model further, we will only consider perfect Gabor receptive field and we assume the input through

the thalamus to be simple moving gratings,

$$\mathcal{L}(\mathbf{x}, t) = I_0(1 + C \cos(\mathbf{k}_s \mathbf{x} - \omega t)), \quad (5.9)$$

where C is the contrast, I_0 is the mean luminance and

$$\mathbf{k}_s = \frac{2\pi}{\lambda} \begin{pmatrix} \cos(\theta) \\ \sin(\theta) \end{pmatrix}, \quad \mathbf{x} = \begin{pmatrix} x \\ y \end{pmatrix}. \quad (5.10)$$

where λ is a spatial scale, and θ the direction in which the gratings move. Most of the principal cells in layer IV have roughly Gabor like, elongated receptive fields²²⁷, that can be constructed by the sum in Eq. (5.5), realizing the Hubel&Wiesel connectome^{479,529}

$$\phi(x, y) = \frac{1}{2\pi\beta_1\beta_2\lambda^2} \exp\left(-\frac{x^2}{2(\beta_1\lambda)^2} - \frac{y^2}{2(\beta_2\lambda)^2}\right) \times \cos\left(\frac{2\pi}{\alpha\lambda}x + \psi\right) \quad (5.11)$$

with numerical constants α, β_1, β_2 . Locally, these filters are rotated

$$\phi_{\mathbf{y}}(\mathbf{x}) = \phi(\Omega_{\vartheta(\mathbf{y})}(\mathbf{y} - \mathbf{x})). \quad (5.12)$$

where Ω is the two dimensional rotation matrix

$$\Omega_{\vartheta} = \begin{pmatrix} \cos(\vartheta) & -\sin(\vartheta) \\ \sin(\vartheta) & \cos(\vartheta) \end{pmatrix}. \quad (5.13)$$

Then we can estimate the effective input currents into the neurons, here for $\psi = 0$

$$I(\mathbf{y}) = \int d^2\mathbf{x} \phi_{\mathbf{y}}(\mathbf{x}) \times \mathcal{L}(\mathbf{x}, t) \quad (5.14)$$

$$= \frac{1}{2} \left(e^{\frac{8\pi^2\beta_1^2}{\alpha} \cos(\vartheta(\mathbf{y}))} + 1 \right) e^{-\frac{2\pi^2}{\alpha^2} (\alpha^2\beta_2^2 \sin^2(\vartheta(\mathbf{y})) + (\alpha\beta_1 \cos(\vartheta(\mathbf{y})) + \beta_1)^2)} \times \mathcal{L}_s + c. \quad (5.15)$$

where \mathcal{L}_s is the stimulus without the DC component and c is a constant. This result is well approximated by a von-Mises function modulating the moving grating, see **Fig. 5.2D**.

$$I(\mathbf{y}) \approx \frac{\exp(\kappa(\cos(2\vartheta(\mathbf{y})) - 1)) \times \mathcal{L}_s}{\alpha} \quad (5.16)$$

$$\kappa = \frac{1}{\pi^2 \left(\beta_1^2 \tanh\left(\frac{4\pi^2\beta_1^2}{\alpha}\right) - \alpha(\beta_1 - \beta_2)(\beta_1 + \beta_2) \right)} \quad (5.17)$$

For the case of non-vanishing ψ , the response is phase shifted by this value. For our model of the visual pathway, we use receptive field parameters from the literature²²⁷, i.e. moving gratings matched to the Gabor preferred spatial frequency $\alpha = 1$ at a stimulus wavelength of $\lambda = 1.25$ deg, the typical preferred spatial frequency at 5 deg eccentricity. We chose an elongation of the Gaussians of $\beta_1 = 0.189$ and $\beta_2 = 0.325$, so that the 5% envelop has a width of 2.0 deg and 1.2 deg respectively with phase $\psi = 0$ ⁴⁷⁹. With these values $\kappa = 1.0$, and we obtain a Tuning curve with 35 deg HWHM (half-width-half-maximum) and $1 - CV \approx 0.45$, close to the experimental values¹³⁶.

Looking at the membrane fluctuations of a simple cell in V1, the membrane potential approximates a full sine wave with dominant contribution of the frequency of the stimulating grating, with clear presence of the negative-going part. Kevan Martin and colleagues⁴ speculate that this might be generated via a push-pull interaction of excitation and inhibition^{67,138,139,185,191,370,440,503}. They also found that the membrane potential of a cortical cell only weakly adapts to contrast, resembling the pattern for the LGN relay cells' spike discharge, but the entire contrast range is compressed into membrane fluctuations in the range of 5-10 mV and reflects the LGN contrast

response function. They conclude that the cortical neurons use cortical circuits to amplify the small input from the thalamus⁴. The spatial receptive field is a very good predictor of the preferred orientation measured with moving gratings, but typically underestimates the orientation selectivity³³⁵.

Looking at these differences between a mouse and a cat visual system, can we scale one into the other? The cat cortex covers 8000 deg² of visual space⁴⁸⁴. The spatial scale of a cat hypercolumn is $\Lambda \approx 1.0$ mm^{236,245}, so that the visual world is processed with ≈ 18 deg²/ Λ^2 . Assuming the mouse would have the same cortical processing requirements to process its visual space, its cortex should contain about $280\Lambda^2$, corresponding to $\Lambda = 120$ μm_c , see **Fig. 5.2E**. We call this the cortical miniaturization scenario, see **Fig. 5.1D**.

The surrogate cortex

Next, we designed a photostimulation setup to connect electronic and biological components, based on phase-only digital holography^{161,295,369,401}, see **Fig. 5.3A** and also chapter 4. The target of thalamic projections in the mammalian brain is the primary visual cortex. Thalamic inputs *in vivo* are excitatory^{10,329} and target stellate neurons in layer IV^{157,268}. We therefore use optogenetics^{54,110,135,343} to express Channelrhodopsin 2, an excitatory light sensitive ion channel² under the control of a neuron specific promoter in a recurrent network of living cortical neurons. A primary cell culture of neurons can resemble *in vivo* neural tissue in structural features²⁰², activity^{88,366}, development²⁷⁵ and composition²⁶. We can achieved cellular content and the cell density corresponding to layer IV in area 17 of the cat, the primary target for projections from the LGN. In the lower part of layer IV, the average cell density of binocular neurons, is 56000 mm⁻³ in a layer about 250 μm thick^{29,150}. 75% of these cells are excitatory^{150,473,523}. Primary cultures from dissociated rat E18 cortical neurons form circuits spontaneously. In cortical cultures, periodic bursts of action potentials emerged after typically 10 days *in vitro* in 2D^{79,497,498} and also 3D cultures^{102,146} and increase in complexity with time^{308,498}. Notably these bursts resemble to some extent the spontaneous activity in the visual cortex prior to eye opening^{82,175,177,409}. We designed the surrogate cortex to a cell density of $\approx 60,000$ mm⁻³ with 75% excitatory cells (see Chapter 10). The surrogate cortex expresses the light sensitive ion channel ChR2(H134R)²⁸³ and the red-shifted calcium indicator jRCaMP1a¹⁰³, to combine the optical excitation with calcium imaging and use an all-optical interface¹²⁹, see **Fig. 5.3B**. **Fig. 5.3C** shows that the culture contains excitatory cells and inhibitory cells, expresses light sensitive ion channels and calcium dependent fluorescent indicators, and contains neurons suspended in a matrix of glial filaments. The light patterns are generated with the *in silico* model of the visual pathway, see **Fig. 5.3D**, and there exists a quantitative relationship between thalamic inputs at different contrast levels in the model visual pathway and light intensities in the setup. As discussed above, starting from contrast values of $\approx 5\%$, the mean LGN input increases, attributable to the rectification (and also the amplitude of the first harmonic⁴⁷⁹). Kevan Martin et al.⁴ suggest for the geniculate-cortical synaptic efficacy ≈ 500 pA somatic current at 100 events/s synaptic excitation. Assuming 5-10 active fibers provide input into a layer IV simple cell, each would fire with about 10 Hz - 20 Hz at contrast values of $\approx 10\% - 20\%$ ³⁶¹ to generate this input current. Wang and colleagues⁵⁰² studied how the light intensity changes the photocurrent to neurons in brain slices of transgenic mice and found that it is well approximated by a Hill equation,

$$I = I_{\max} \frac{l^n}{k^n + l^n} \quad (5.18)$$

where currents are measured in pA, l is the luminance in mW/mm². For the peak response of the photocurrent, they measured $I_{\max} = 642 \pm 38$ pA, $n = 0.76 \pm 0.1$ and the half-maximal light sensitivity is $k = 0.84 \pm 0.2$ mW/mm². These numbers are comparable to other studies which

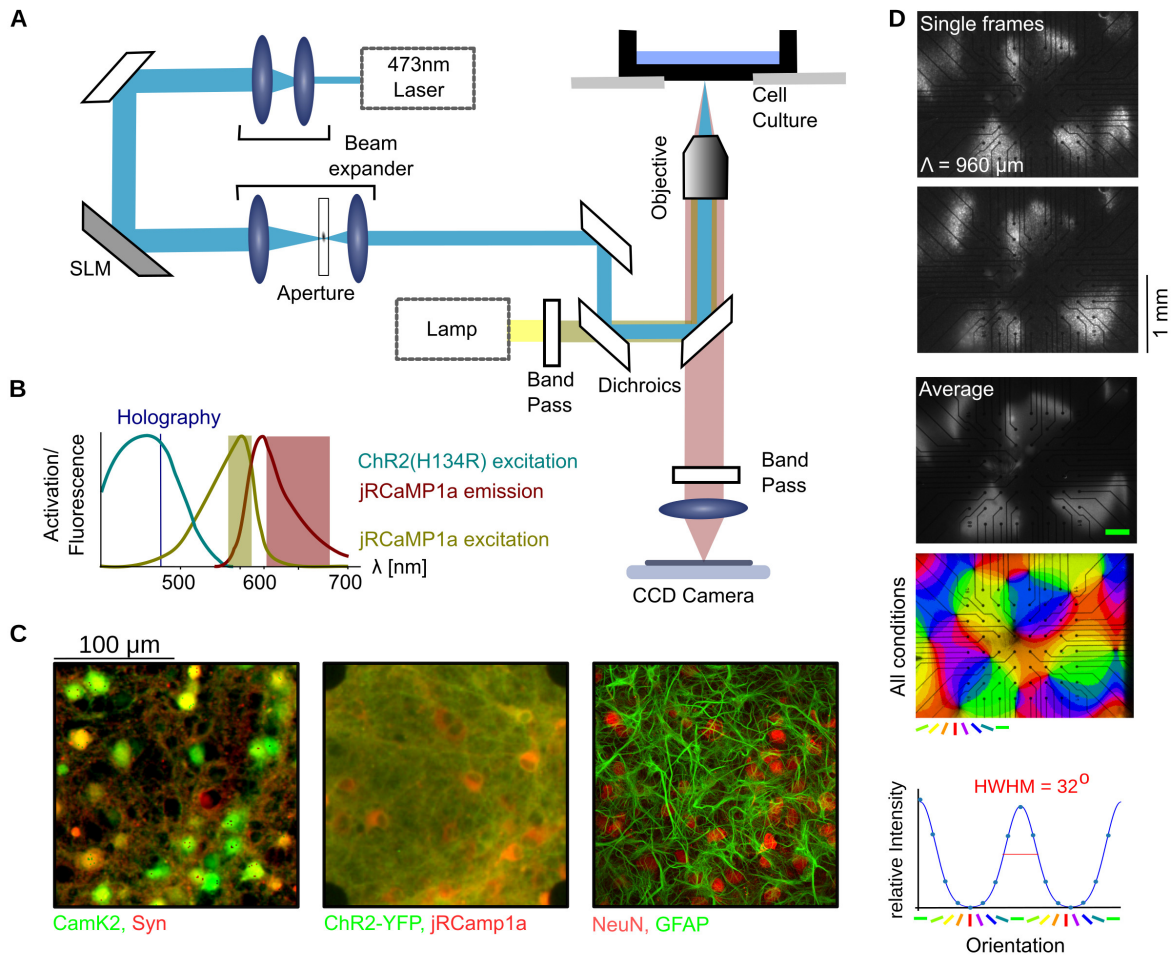


Figure 5.3: **The experimental setup.** **A** The holographic setup, integrated into a commercial inverted microscope. **B** The excitation spectrum of the light sensitive ion channel, together with the fluorescent probe jRCaMP1a. **C** The surrogate cortex consists of excitatory and inhibitory cells, expresses ChR2 and jRCaMP1a, and is composed of neurons and glial cells (Images are contrast adjusted). Note the typical donut-shape of the jRCaMP1a/calcium signal localized to the cytoplasm surrounding a dark nucleus. **D** An example for a holographic stimulus, measured with Fluorescein in water: Top three are three examples for single frames generated with moving horizontal gratings. Below: the averaged frame, reflecting domains that prefer horizontal orientations. Below that: the preferred orientations of the input for all conditions.

reported maximum peak currents of $I_{\max} \approx 700$ pA and EC50 of ≈ 1 mW/mm², for instance in^{250,283,524}. With our setup, we can reach light intensities of ≈ 2 mW/mm². This corresponds to 400 pA – 500 pA as peak current. The sustained component of the ChR2(H134R) light response is about 40% of the transient peak²⁸³, such that the sustained induced current with our setup can reach 160 pA – 200 pA, corresponding to $\approx 10\%$ contrast. Note that increasing the contrast is equivalent to increasing the light intensity, because beyond $\approx 5\%$ contrast, both the DC and F1 component of LGN inputs increase proportionally⁴⁷⁹.

Imposed tuning in synthetic circuits

We first realized the Hubel&Wiesel connectome¹⁹⁴ for the generation of orientation selectivity. Specifically we used moving gratings, filtered with Gabor filters, see **Fig. 5.4A**, whose preferred orientation changed in space, following the layout of an essentially complex planform, a solution of the long-range interaction model⁵²⁵. **Fig. 5.4B-F** show the responses of several units in the same culture as polar plots on top of the imposed layout of domains and a YFP fluorescence image of the electrode array. We used three different domain sizes, following the cortical miniaturization scenario. The scales are 0.96 mm/Λ, 0.48 mm/Λ, 0.24 mm/Λ, 0.12 mm/Λ and 0.06 mm/Λ. For most of the cases, the preferred orientation is consistent with the stimulation. **Fig. 5.4G** shows an example tuning curves together with its 95% bootstrapped consistency intervals. Note that this specific neuron retains its orientation selectivity down to the smallest domain size studied here. To study the fraction of orientation biased cells, we next calculate a measure for orientation selectivity, derived from the circular variance (CV),

$$1 - \text{CV} = \frac{|\int d\theta r(\theta) e^{2i\theta}|}{\int d\theta r(\theta)} \quad (5.19)$$

for the observed tuning curve $r(\theta)$. The results are summarized in **Fig. 5.5**. **Fig. 5.5A** shows all units collected from 15 experiments together with the shuffled control. For the shuffled controls, we use the observed spike time, and randomize the grating assignment. The shuffled controls allow to identify a significance threshold above which we consider units significantly tuned. This is illustrated in **Fig. 5.5B** for a specific tuning curve. For a significance level of 5%, the fraction of tuned cells are shown in **Fig. 5.5C**. We find that the fraction of tuned cells as well as the tuning strength decreases with decreasing column size, but even though the overall tuning strength decreases substantially, the overall fraction of tuned cells changes little. Note that the selectivity of the input is $1 - \text{CV} \approx 0.5$, and only few cells reach this tuning strength. A cell at position \mathbf{y} of size A receives the averaged input across its soma and dendrite,

$$I(\mathbf{y}) = \frac{1}{A} \int_A dp \int d^2\mathbf{x} \phi_{\mathbf{y}+\mathbf{p}}(\mathbf{x}) \times \mathcal{L}(\mathbf{x}, t) \quad (5.20)$$

$$= \int d^2\mathbf{x} \langle \phi_{\mathbf{y}}(\mathbf{x}) \rangle_A \times \mathcal{L}(\mathbf{x}, t) \quad (5.21)$$

where $\phi_{\mathbf{y}+\mathbf{p}}(\mathbf{x})$ is the Gabor receptive field at position $\mathbf{y} + \mathbf{p}$ and $\langle \phi_{\mathbf{y}}(\mathbf{x}) \rangle_A$ is the area average. In the limit of large domains,

$$\langle \phi_{\mathbf{y}}(\mathbf{x}) \rangle_A \approx \phi_{\mathbf{y}}(\mathbf{x}) \quad (5.22)$$

because the gabor filters within area A are all identical. In the limit of small domains,

$$\langle \phi_{\mathbf{y}}(\mathbf{x}) \rangle_A \approx \exp\left(-\frac{(\mathbf{x} - \mathbf{y})^2}{2\sigma^2}\right) \quad (5.23)$$

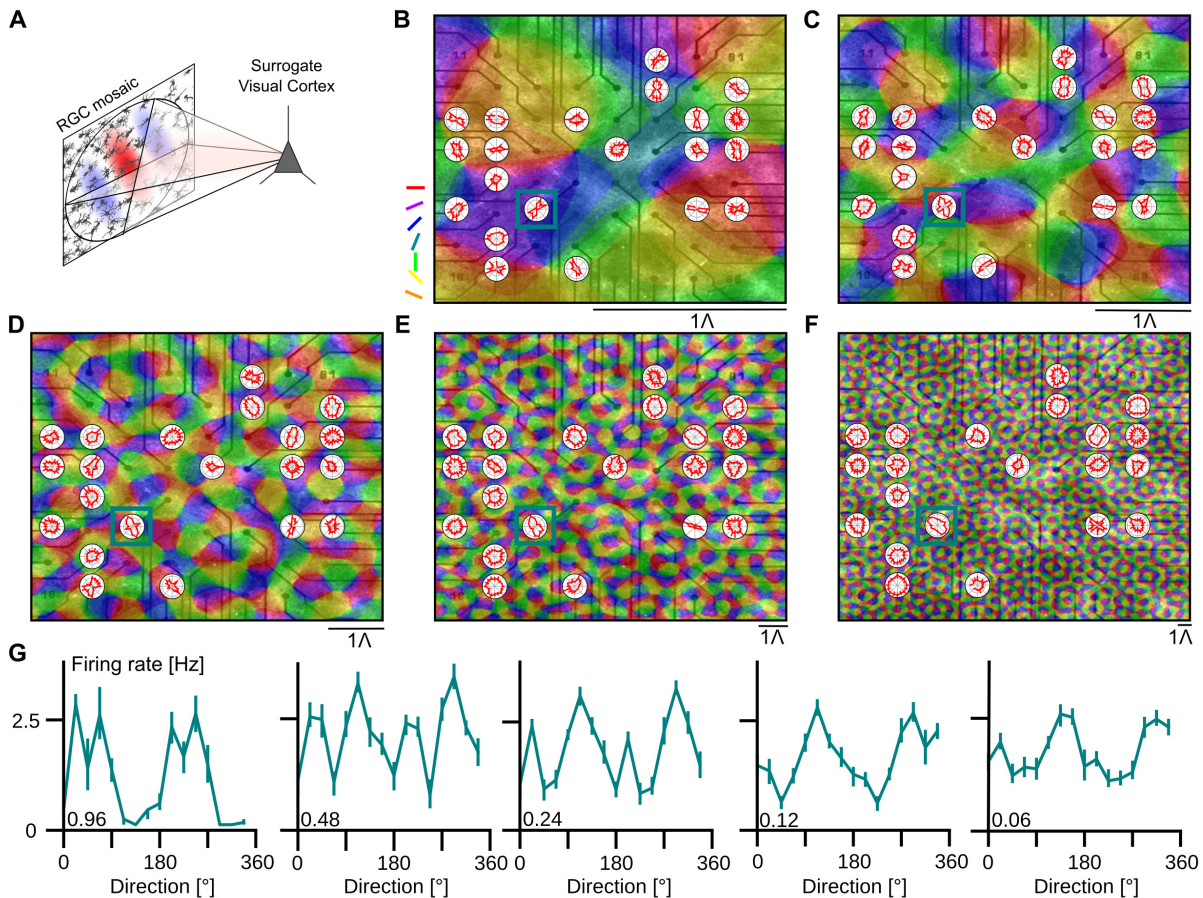


Figure 5.4: **Orientation selective inputs generate tuned responses.** **A** We first provide neurons with orientation tuned input, duplicating the specificity of the thalamocortical connectome. **B-F** Providing the cells with a layout of orientation domains, we find orientation selective responses on a number of electrodes. Remarkably, with smaller domains, there is still a surprising degree of orientation bias. **G** Example tuning curves taken from the unit in the blue box. Note the substantial tuning in the limit of almost fully randomized inputs (far right). This cell is spontaneously tuned and in parts of the experiment driven against its innate tuning. Errors are 95% bootstrapped confidence intervals across randomized blocks of 16 directions each.

the superposition of many different Gabor filter orientations in the area A averages out the orientation selective component. We refer to this limit as the randomized connectome. Thus, in the linear feed-forward scheme, shrinking the visual system leads to a loss of orientation selectivity. Surprisingly, cells as shown in **Fig. 5.4G** retain orientation selectivity even in the effective absence of orientation tuned input.

Spontaneous tuning in synthetic circuits

To show that orientation biased responses are not caused by residual tuning of the input, we next used exclusively moving gratings as input. **Fig. 5.6** shows eight example tuning curves together with the raw data. For these experiments, we completely randomized the presentation sequence of the 16 grating directions while making sure that every grating was presented at least 15 times. **Fig. 5.6A** shows the typical response to a single grating presentation. There is some spontaneous activity and the cell becomes active with light onset. It remains active during

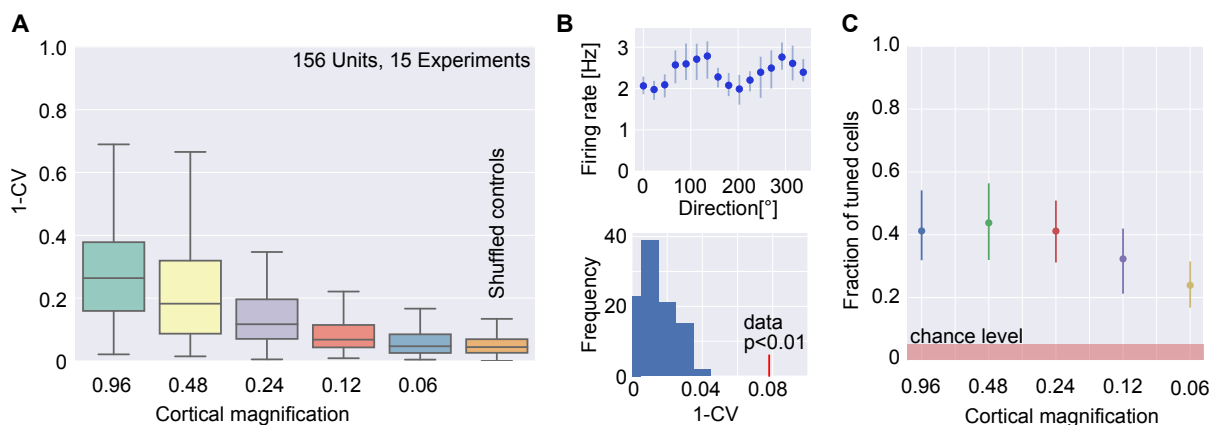


Figure 5.5: **Statistics of imposed tuning.** **A** The distribution of orientation selectivities, measured with circular variance, across all 15 experiments. Notably, for a cortical magnification of 0.06 mm/λ, there exists still a surprising fraction of tuned cells across experiments. **B** We assess the tuning by comparing every single observed tuning curve (example shown top) with the selectivities of the direction-randomized controls (example shown below) and obtain a p-value for every cell. This is a weakly but significantly tuned cell. **C** Following the procedure in B reveals a large fraction of significantly tuned cells across conditions.

the grating presentation, and then activity drops. This specific cells responds in phase with the stimulating moving grating. **Fig. 5.6B** shows the order of plotting of the raw spike trains in **Fig. 5.6C-K**. To assess the strength of orientation tuning, and to quantify the responses of every single cell, we extract several metrics for every cell. We first calculate the mean firing rate for every condition, and the 95% bootstrapped confidence intervals of the mean. This gives a tuning curve, shown in blue in **Fig. 5.6C-K**. We refer to this tuning curve as the F0 tuning curve. We next convolve the spike train with a rectangular function of width 100 ms to obtain a firing rate. We next apply a Fourier transformation and extract the component at the drift frequency, in our case 2 Hz. The mean of this F1 component together with its 95% bootstrapped confidence intervals is shown as orange curve in **Fig. 5.6C-K**. After the extraction of F0 and F1 tuning curves, we fit a sum of two Gaussians to the tuning curve, shown in **Fig. 5.6E-I** and from the Gaussians extract the orientation selectivity index (OSI), the direction selectivity index (DSI) and half width at half maximum (HWHM) as presented in³⁴⁹. We also calculate $1 - CV$ from the tuning curves, either directly (denoted as 1-CV F0 and 1-CV F1) or with the spontaneous firing rate subtracted (1-CV F0 corr.). We also extract a measure of linearity, F1/F0 at the preferred orientation. Across our experiments, we find cells that are orientation unselective and respond typically in phase with the stimulus. We refer to these cells as linear and orientation unselective, see **Fig. 5.6C**. We also find cells that are unselective, but not in phase with the stimulus. We refer to these cells as nonlinear and orientation unselective, see **Fig. 5.6D**. In our dataset, there is a surprising number of cells with linear and tuned properties, see **Fig. 5.6E-G** which resemble simple cells of the visual cortex. **Fig. 5.6H** shows a direction tuned, **Fig. 5.6I** a complex cell and **Fig. 5.6K** prefers cardinal orientations. How many of these different cell types are there? The summary across all 39 experiments with 1117 units in total is shown in **Fig. 5.7**. We first looked at the fraction of visually responsive neurons. **Fig. 5.7A** shows the firing rate without stimulation plotted against the evoked firing rate. Most of the cells ($\approx 80\%$) increase their firing rate by at least 15% upon stimulation and we consider these cells visually responsive. **Fig. 5.7B** shows 1-CV and the orientation selectivity index of all visually responsive units. **Fig. 5.7C** shows the orientation selectivity, assessed with circular variance

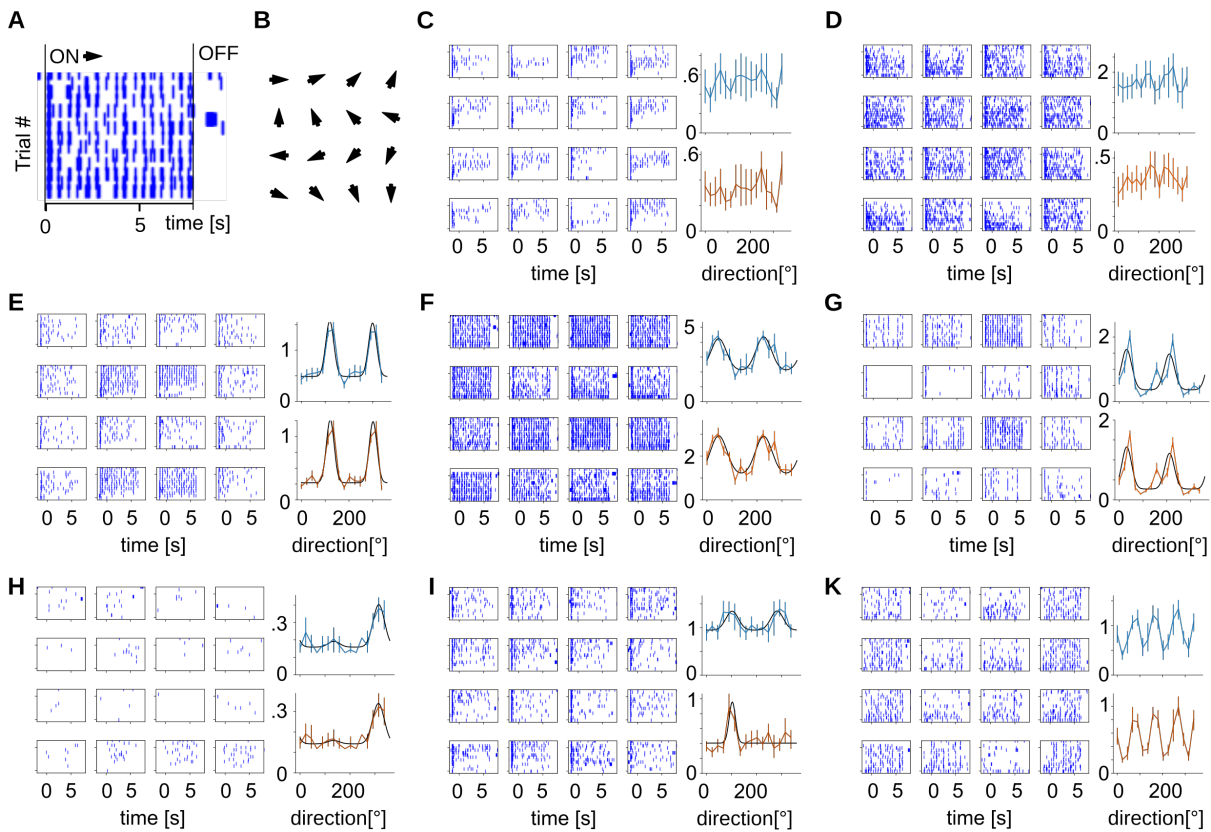


Figure 5.6: **Examples of spontaneous tuning with randomized inputs.** **A** Stacked are independent trials of 8 s stimulation windows. This visually responsive unit typically responds with a train of action potentials during presentation. Note the typical distance between spikes of ≈ 500 ms, which is the temporal frequency of the stimulating moving grating. The frequency of the response corresponding to the stimulating grating is called F1 (orange, see text). The total firing rate is F0 (blue). **B** The plotting order of the raw data for C-K. **C** An orientation unselective, linear unit. It is linear, because the spiketrain is dominated by the F1 component (orange). **D** An orientation unselective and nonlinear unit: the F1 component of the tuning curve is small. **E-G** Three examples for simple cells with strongly tuned F0 and F1 tuning curves. **H** A direction tuned cell. **I** A complex cell where the F0 component is tuned, but the F1 component is not. **K** A cell which prefers cardinal orientations.

as function of the firing rate. Most of the orientation biased cells have firing rates of around 1 Hz. **Fig. 5.7D** shows the correlation coefficients of all extracted metrics. **Fig. 5.7E** shows that the F1 tuning is typically stronger than the F0 tuning, indicative of simple cells, while the preferred orientations of F0 and F1 tuning curve are highly correlated, **Fig. 5.7F**. **Fig. 5.7G** shows a histogram of F1/F0, and **Fig. 5.7H** shows F1/F0 as function of the tuning strength of the F0 component. We next sort the cells into 5 categories, using $F1/F0 = 1$ and $1 - CV = 0.1$ as thresholds for linearity and orientation tuning. Note that this choice is somewhat arbitrary as long as the metrics considered are not bimodal. The categories thus only serve as a point of reference for a comparison with other studies^{349,405}. A pie chart summarizing our dataset is shown in **Fig. 5.8A**. We observed a fraction of $\approx 5\%$ of cells with firing rates > 10 Hz. Considering the duration of our experiment, it is unlikely that these are pyramidal cells with such high sustained firing rates. Even though we could not find any difference in the shape of the waveform (see **Fig. 5.14**), we consider them as tentative fast-spiking inhibitory cells. Among

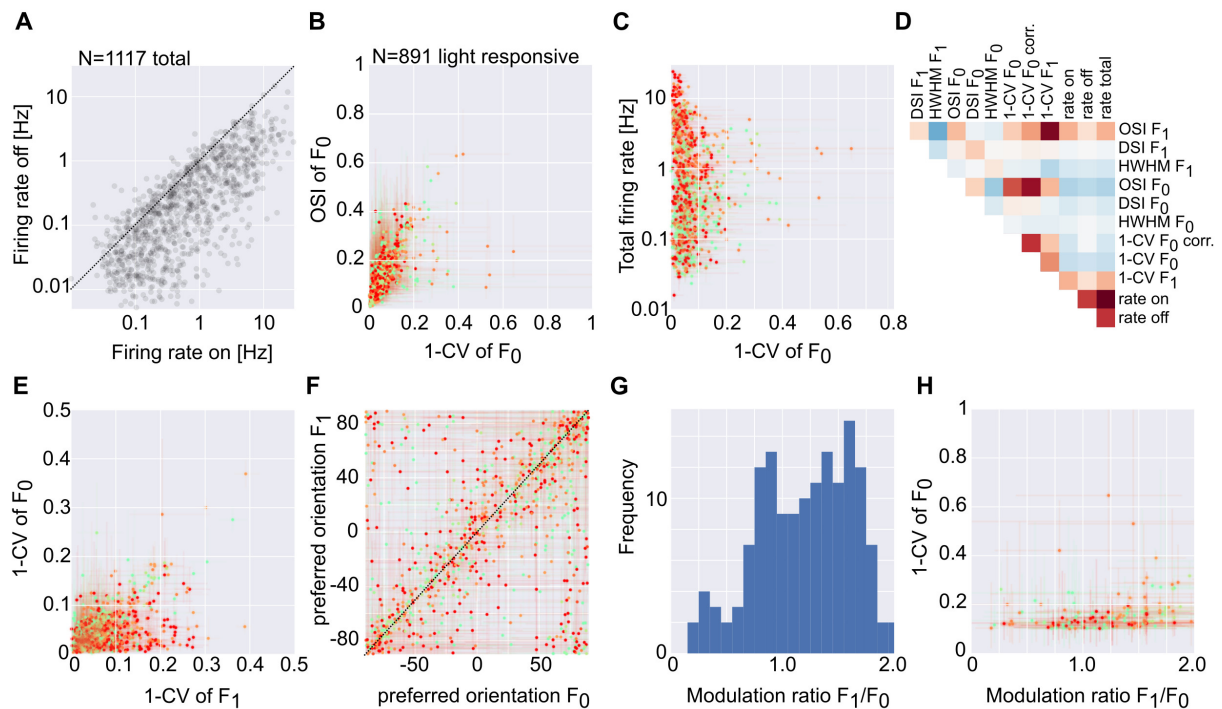


Figure 5.7: **Statistics of spontaneously tuned cells.** **A** Firing rate during stimulation vs spontaneous rate reveals that most cells are light responsive. **B** Across all experiments, OSI as well as circular variance reveal tuned responses and are strongly correlated. **C** Tuning is weakly anti-correlated with the firing rate. Tuned cells have firing rates of ≈ 1 Hz. **D** Correlation coefficient of various metrics (see text). **E** Tuning of the F0 vs the F1 component reveals hint at mostly simple cells. **F** The preferred orientation of F0 and F1 are highly correlated. **G** The modulation ratio for the majority of units is above 1, indicating mostly simple cells. **H** Modulation ratio vs. orientation selectivity shows that the well tuned cells are simple cells.

these cells, most are nonlinear and untuned, see **Fig. 5.8B**, which is consistent with their firing rate being factor 5 larger than the drift frequency of the grating.

Oriented receptive field and the origins of tuning

To study the emergent tuning further, we next stimulated the cell culture with checkerboards and assessed receptive fields using reverse correlation. For a typical culture, imaged and stimulated through a 5x objective, **Fig. 5.9A**, we find spatial receptive fields as in the examples above, in close vicinity to the recording electrode. **Fig. 5.9A** shows the uniform expression of YFP labeled ChR2(H134R) across the electrode array. **Fig. 5.9B** shows the reverse correlation receptive field 100 ms before the spike time. **Fig. 5.9C** shows the temporal dimension of the reverse correlation dataset for a few example cells. Temporally, we find that most cells respond strongest to sustained darkness, followed by a short flash of light, similar to other studies³⁴⁷. To study receptive fields with higher spatial resolution, we repeated this experiment with a different culture through a 10x objective. The culture is shown in **Fig. 5.9D-F**. As before, the excitatory subregion of the receptive fields closely trace the electrode field, with a few exceptions. One receptive field (electrode 75) shows a functional connection across the entire grid, 1 mm long (see also **Fig. 10.1B**). Another signal (electrode 17) reveals only an inhibitory region, and in the temporal domain reacts inversely compared to the other cells. This cell arguably receives input from an inhibitory cell that in turn reacts well to light.

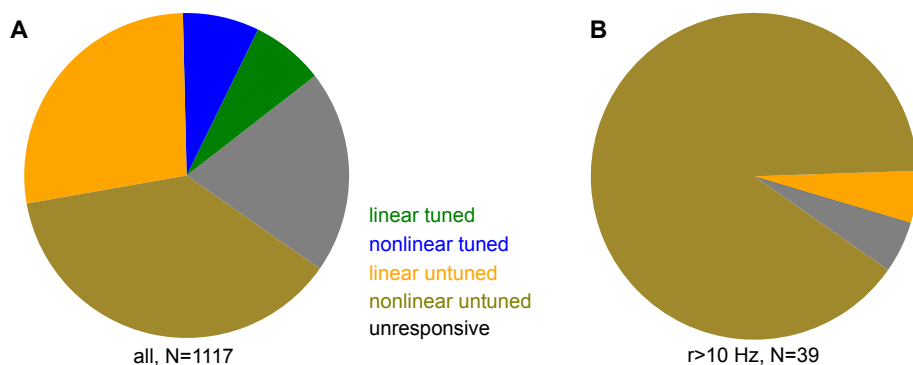


Figure 5.8: **Pie charts showing the functional composition of the surrogate cortex.**

A We group cells into linear tuned ($F1 > F0$ and $1 - CV \geq 0.1$), nonlinear tuned ($F1 \leq F0$ and $1 - CV \geq 0.1$), linear untuned ($F1 > F0$ and $1 - CV < 0.1$), nonlinear untuned ($F1 \leq F0$ and $1 - CV < 0.1$) and not visually responsive (rate on $<$ rate off $\times 1.15$). **B** Same as A, but for tentative inhibitory and fastspiking cells. Not surprisingly, most of the cells are nonlinear and untuned.

We found in the theory section of this chapter, that a generic scale of stimulation for the visual system is $\approx \lambda = 0.8$ mm. Is this consistent with our observations in the culture? We saw in **Fig. 5.9** receptive fields with a scale of 0.5 mm to 1 mm and we next averaged all biased receptive fields, see **Fig. 5.10A**. The averaged receptive field is shown in **Fig. 5.10B**. Here, we only colored regions with significant entries, compared to the 95% bootstrapped confidence intervals. Note the central excitation, surrounded by an inhibitory region. Calculating the angular average of **Fig. 5.10B** is shown in **Fig. 5.10C** with 95% bootstrapped confidence intervals. It reveals an inhibitory region, extending to ≈ 500 μm . This typical scale is also apparent in Fourier space. To this end, we calculated the spectra of the data in **Fig. 5.10A**, and averaged the power spectra. The averaged power spectrum is shown in **Fig. 5.10D** and its marginal is shown in **Fig. 5.10E**. We again find a typical spatial frequency of ≈ 1 mm. If these receptive fields are responsible for the tuning, increasing the spatial frequency of the stimulus should lower the fraction of tuned cells. **Fig. 5.10F** shows the fraction of orientation selective cells pooled across moving gratings with $\lambda \geq 400$ μm and for a high spatial frequency with a grating wavelength of $\lambda = 200$ μm . Shown are box plots for the fraction of tuned cells across experiments, together with the mean and the bootstrapped 95% confidence intervals of the mean. While the fraction of tuned cells decreases significantly for the rate, the tuning for latency is always very small. We identified most of the tuned cells as simple cells, and we showed that reverse correlation from checkerboards yields receptive fields which resemble cortical simple cell receptive fields. For a linear system, the receptive fields should provide a good proxy for the tuning curve. In **Fig. 5.11A**, we show a measured tuning curve, together with its receptive field, measured consecutively twice. This is the same cell as shown in **Fig. 5.6F**. From the receptive field, one can estimate a tuning curve either directly, i.e. by calculating the powerspectrum and from the spectrum extract the expected response to a wave with specific spatial frequency. One can also fit a model function, here a Gabor patch, to the data, and extract the predicted curve from the Gabor fit. Both methods are shown in **Fig. 5.11B**. The tuning curve of this cell can be well approximated from the receptive field, further highlighting their simple cell character. Note that the receptive fields point not only to a typical spatial scale, but also a temporal scale. We have observed only few direction tuned cells, but this low number might be related to our specific choice of grating drift frequency. Considering that the receptive fields exist on temporal scales of 100 ms, it might be more appropriate to screen for direction tuning with at least 10 Hz drift

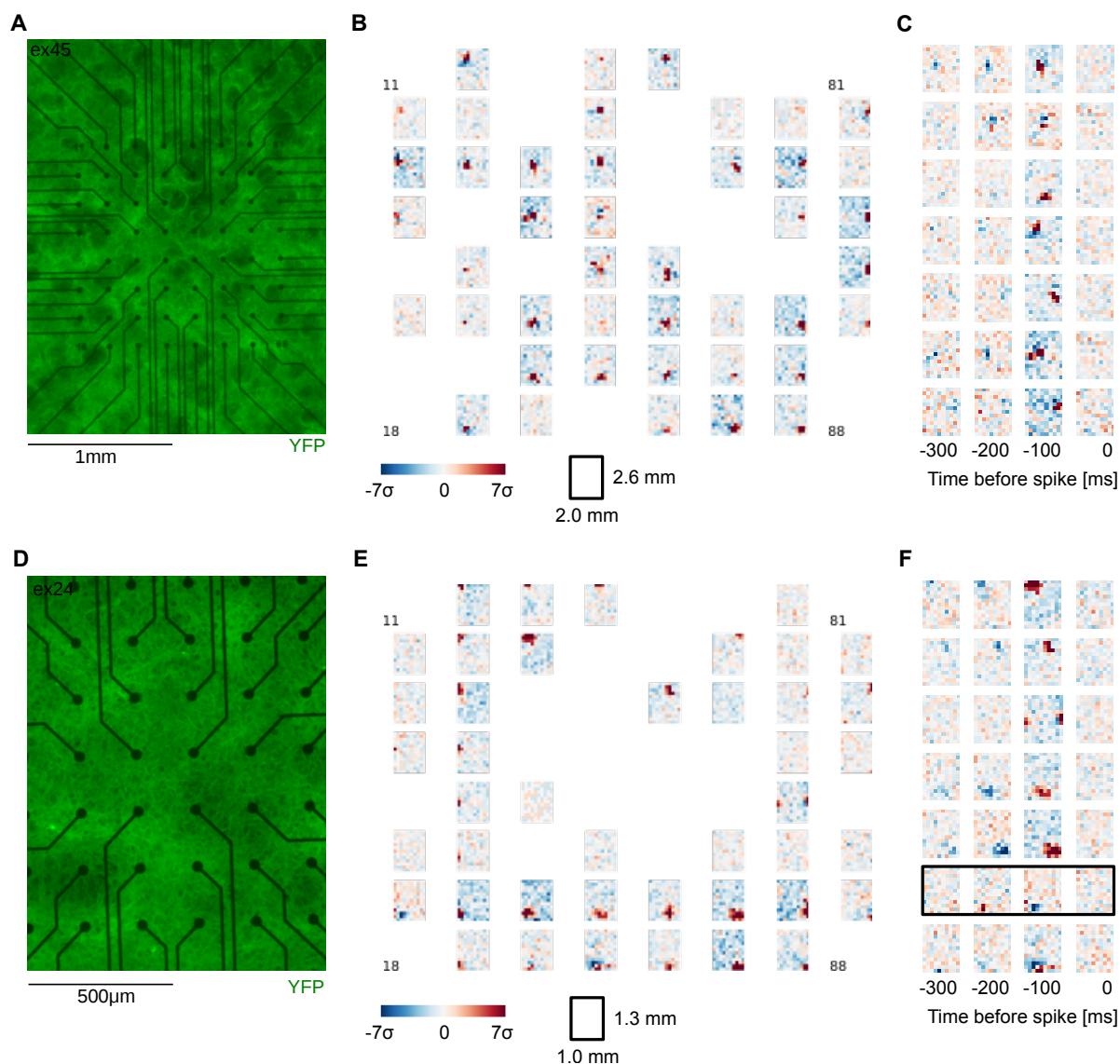


Figure 5.9: **Spatiotemporal receptive fields.** **A** Fluorescence image of the MEA. Fluorescence is generated by the YFP label of Chr2(H134R). **B** Receptive fields of all active electrodes, in a time window 100 ms before the spike. Note that the excitatory region closely tracks the recording electrode position. **C** The temporal component of several examples cells in B. Most neurons respond strongest to darkness, followed by a flash of light, consistent with earlier studies³⁴⁷. However, some cells have excitatory and inhibitory subregions. **D** Same as in A, but for a different culture with higher spatial resolution. **E** same as B for the culture shown in D. **F** Same as C. Note the cell with only an inhibitory subregion (boxed). Such RFs can only form in a network of cells.

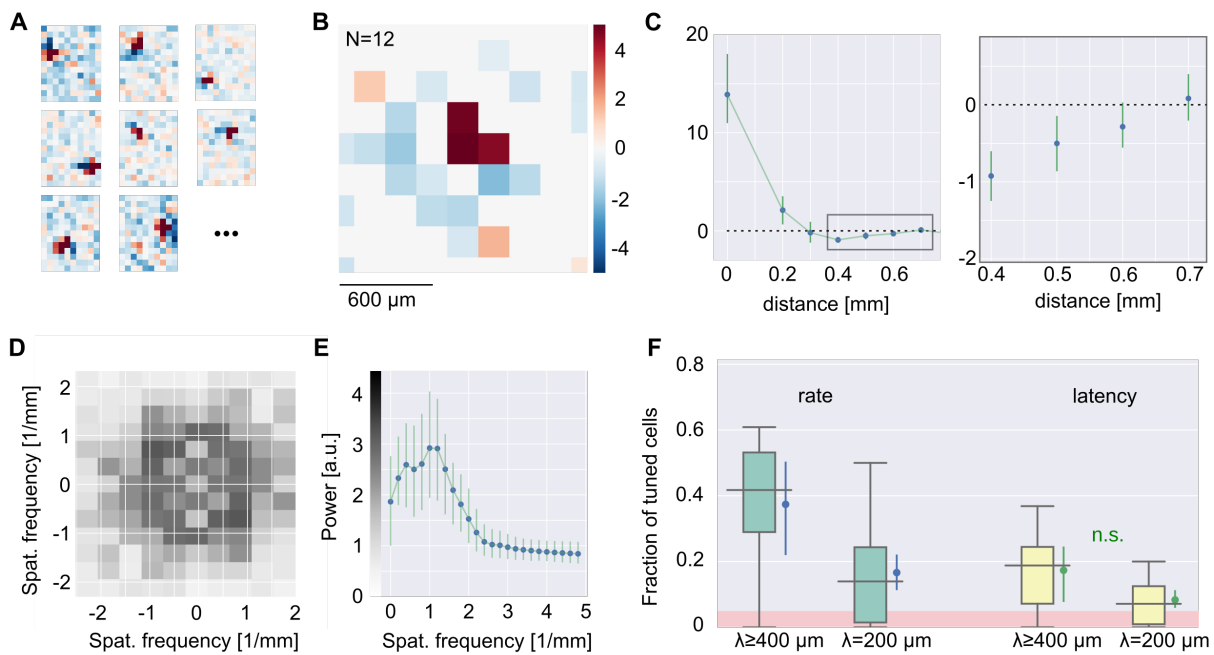


Figure 5.10: **The typical receptive field is consistent with the theoretical estimate of $\lambda \approx 0.8 \text{ mm}$.** **A** Examples for simple-cell like receptive fields. **B** Averaging tuned receptive fields reveals a weak mexican hat. All non-significant bins (bootstrapped 95% CIs) have been set to zeros. **C** The radially averaged mean receptive field from B reveals a mexican hat. Errorbars are 95% bootstrapped CIs across cells. **D** The averaged power spectrum of individual receptive fields. Note the ring shape. **E** Marginal powerspectrum of D with bootstrapped 95% confidence intervals across cells. **F** Increasing the spatial frequency removes tuning. Shown are the fraction of tuned cells with tuning curves either extracted from firing rate or spike latency for two different scales of stimuli. Shaded in red is the chance level. Note that the fraction of tuning among spike latencies does not change significantly, and is barely significant.

frequency.

How are the orientation biased cells and mostly simple cells arranged in space? **Fig. 5.12A** shows a recording with evident orientation biased responses on several electrodes. Notably, neighboring cells can have very different preferred orientations. To further study their spatial arrangement, we use the spectral separation of the calcium indicator and the light-sensitive ion channel, **Fig. 5.12B**, to optically screen for orientation selective cells. **Fig. 5.12C** shows a few examples of orientation biased cells. As expected from the electrode recordings, these cells are relatively rare, and can be close to one another with different preferred orientation. The layout of orientation selectivities thus resembles a very sparse salt and pepper pattern.

Receptive fields with excitatory and inhibitory subregions (cf. **Fig. 5.10A**) indicate that the underlying mechanism of orientation bias are networks of excitatory and inhibitory cells, strongly coupled together. Driving the inhibitory cells within these groups with spatially patterned illumination would result in a net suppression of activity. Using calcium imaging, we can study functional connectivity in large numbers of cells, and we asked whether there exist in our surrogate cortex assemblies that could serve as candidates for such a mechanism. **Fig. 5.12C** shows the spike triggered calcium activity of two electrode channels. Remarkably, we find small networks with cells that have very similar calcium activity. The dF/F traces of the two groups of cells are shown in **Fig. 5.12E**. Note that the typical size and small number of neurons within

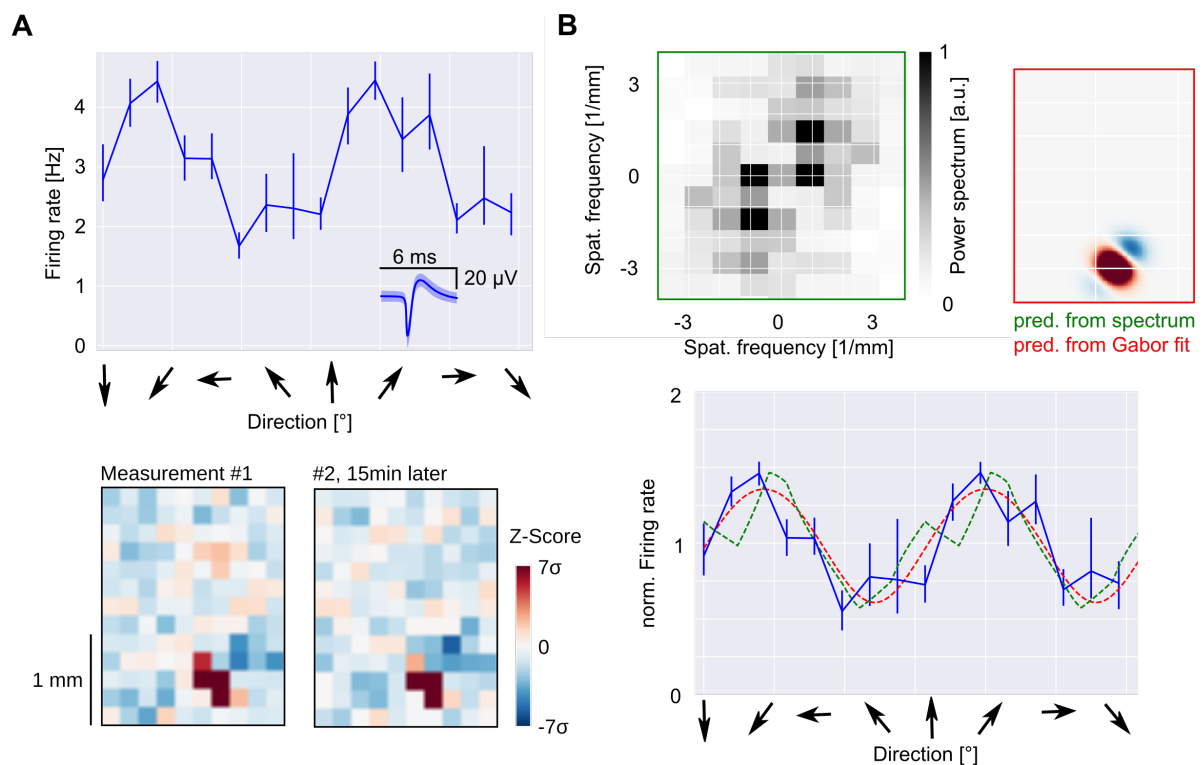


Figure 5.11: **Tuning prediction from RF.** **A** Example of a tuned unit with a tuning curve shown on top, and its receptive field from reverse correlation shown bottom. The raw data for this cell is shown in **Fig. 5.6F**. **B** From the receptive field, tuning can be estimated using the Power spectrum (green) or a fit with model function (red). Both methods compared with the data are shown on the bottom.

these groups is consistent with the spatial extent of the receptive fields. These groups are therefore prime candidates to account for the observed tuning in the surrogate cortex. A key aspect of orientation selectivity in the primary visual cortex is its invariance with respect to contrast³⁸⁸. This phenomenon has long been considered a prime example of cortical processing because most feed-forward models predict an increase of tuning width, i.e. a decrease of selectivity, with increasing contrast. This invariance might be present in our surrogate cortex. To test for contrast invariance, we stimulated a network, **Fig. 5.13A**, with various light intensities. **Fig. 5.13B** shows the tuning curves for three different light levels. We find that above a certain limit required to elicit a sufficient response in the ion channel, the overall orientation selectivity is invariant. While this would be consistent with contrast invariance, these experiments should be treated with caution because the light intensities and the dynamic range of Channelrhodopsin naturally limit the scope of such experiments.

5.4 Discussion

First, we confirmed that the Hubel&Wiesel connectome is a viable circuit to generate orientation specificity in the afferent connectome. We then miniaturize the early visual afferent pathway, shrinking eye size, cranium and the cortical target area, but preserving the total number of hypercolumns and therefore arguably the number of processing units to process natural scenes in the framework of the cortical miniaturization scenario. In the limit of a small brain, the synthetic visual system resembles a mouse visual pathway, or the layout of late cretaceous eutherians, like

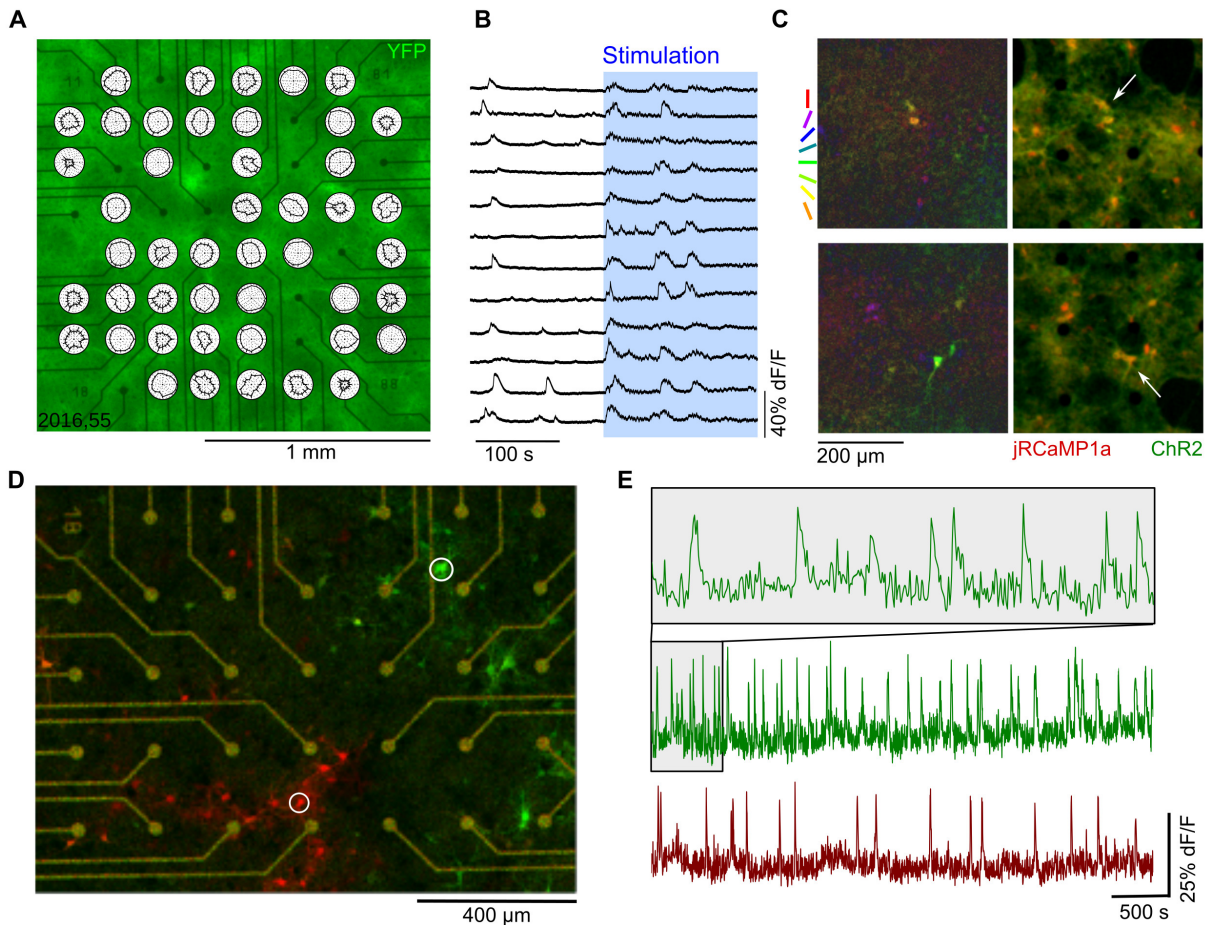


Figure 5.12: **The spatial organization of tuning is sparse.** **A** Electrode recordings reveal no similarity in tuning between neighboring electrodes. **B** Spectral separation between stimulation and calcium light (see methods) allows simultaneous recording and stimulation. **C** Calcium imaging also reveals a small subset of spatially unorganized and orientation tuned cells; shown are two examples of tuned cells. Left is a polar map of tuned pixels. Shown right is a fluorescence image. **D** Calcium imaging also reveals groups of neurons with highly correlated calcium activity, shown in red and green. **E** The calcium fluorescence signals from the two groups of neurons in D. The calcium data was processed by Julian Vogel.

Asioryctes, closely related to the eutherian common ancestor. We found that shrinking the visual system leads to a massive loss of visual acuity, to a loss of the orientation specificity of the afferent connectome and to a larger point spread function. Surprisingly, we also found that a number of neurons exhibited orientation biased responses in the limit of homogeneous and unselective input, that are generated by the recurrent network alone. We find that these cells are mostly simple cells. In addition, we also find a small number of complex and direction tuned cells. This diversity of responses suggests that even in this most generic case, a recurrent circuit is sufficient to spontaneously generate a basic level of orientation selectivity. This phenomenon, already present in recurrent networks as disorganized as a primary culture, might provide a robust and generic scaffold for input classification and is potentially the first workpiece refined by the selective forces of natural selection to generates the functional organization of neuronal circuits across many species of mammals.

Orientation selectivity in this system might seem surprising, but is in fact consistent with

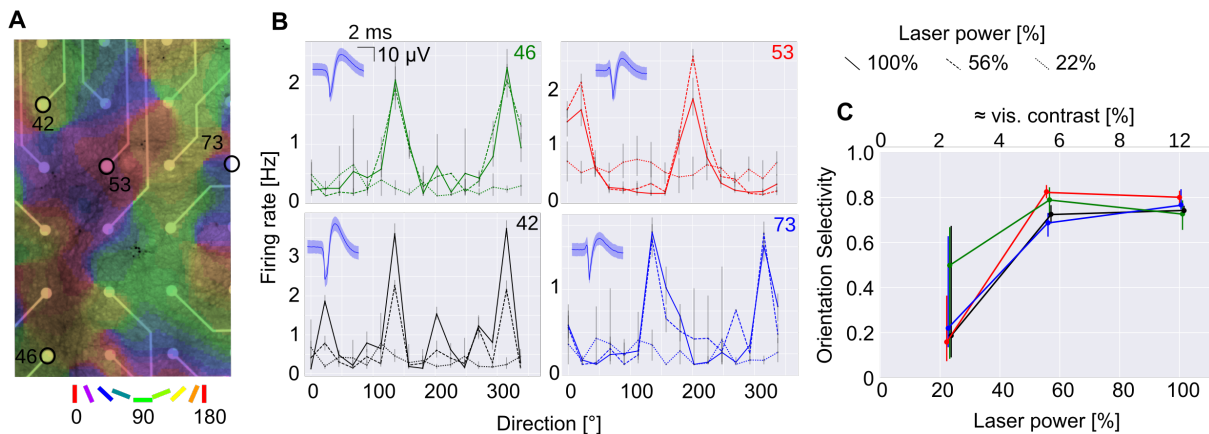


Figure 5.13: **Contrast invariant tuning.** **A** Stimulating a patch of the surrogate cortex with tuned inputs. **B** Four tuning curves recorded from the culture in **A** with three different contrasts (see text). **C** Orientation selectivity index for the three contrast levels. Confidence intervals are 95% statistical CIs for the fits.

several models that build on very different ideas. While many models are hard to test experimentally due to the precision connectome required^{68,323,445} or the interplay of intracortical dynamics and plasticity of the projections^{305,456}, other models that use generic mechanisms should work in living recurrent networks, too. These models for orientation selectivity cannot be tested in a living animal, but *in vitro* they can. It was shown that sharp orientation tuning can emerge from only weakly tuned inputs in a random network in the balanced state. In this state, the untuned fractions of excitation and inhibition roughly cancel and allow the tuned components to render neurons strongly orientation selective. The result is a spatial structure of orientation preference similar to the interspersed layout which is observed in rodents^{173,377}. Furthermore, a network with stochastic mexican hat interconnectivity can create layouts of orientation domains, similar to the layout in carnivores and primates¹³¹, basically realizing a ring network in two dimensions, that form bumps by spontaneous symmetry breaking. Attractor models are used for a variety of purposes^{22,23,521}. Several experiments might yield deeper insights into the underlying mechanisms of orientation selectivity in the cell culture. The application of a threshold to a contrast dependent tuning curve appears to broaden orientation tuning. This broadened orientation tuning with contrast is called iceberging or the Iceberg-effect^{411,529}. Contrast invariance can be generated intracortically, or by mechanisms of synaptic depression between thalamus and cortex³⁸⁸. For a long time, it has been considered a smoking gun of cortical processing. The discovery of the alternative explanation shifted the interested away from the field. However, for our system it is still an important property, as our holographic system, by construction, does not have depressing synapses and contrast invariance is a feature in a variety of models^{30,377,380}. Also, considering that simple and complex cells might be generated with a similar circuit with various contributions of recurrent connections⁷², our synthetic hybrid system might contain neuronal circuits with functions, surprisingly similar to circuits in the living brain.

The scales of projections into the primary visual cortex seemed to imply a common organizing scheme. Is there more evidence to it? Let us first look at cortical coverage in cat and mouse. Coverage here is defined as the number of geniculate centers covering every point in the visual world. Area 17 in cats is typically around 400 to 500 mm², and grows with age^{247,392}. A cat has a field of view of around 200 deg, and 140 deg of binocular overlap (very similar to humans with 180 deg field of view with also 140 deg binocular overlap)³⁰⁰. In the cat, there are 90.000 β -cells

in the retina^{203,209}, from a total of about 200,000 RGCs and a similar number of fibers in the optic nerve²⁰³, so that across the entire cortex, ≈ 200 RGCs provide input into one hypercolumn. Note that the scaling of receptive field sizes with eccentricities¹⁴⁵ might keep the number of inputs in units of fibers into each column roughly constant. In cat, layer IV spiny stellate cells are roughly isotropic with a radius of $\approx 200 \mu\text{m}$ ⁹³. In the mouse, V1 is typically 4 mm²¹⁵³, its binocular view of view is about 45 degrees. the total field of view exceeds 240 deg¹¹⁶. The mouse retina contains 48000 to 70000 RGCs, has a radius of about 2 mm with a typical density between 8000 – 2000 mm⁻²^{116,117,223}, which scales with distance from the optic disc. The optic nerve of the mouse contains around 55000 axons (C57/B6), of which only a fraction targets the dLGN⁵⁰⁹. In a mouse, the brain receives input from factor two to four less retinal fibers than a cat, but projecting to a factor 225-fold smaller cortex⁴⁴³. Geniculocortical arbors in mice are small, typically around 0.5 mm in diameter and not as finely branched as in cat¹⁴. In rats and mice, the radius of a spiny stellate layer IV cell is about 100 – 150 μm ^{31,124,169}. There are also genuine differences in the excitatory/inhibitory loop between mice and cat^{49,313} and potentially even in cellular organization between cat, rat and mouse on one side and primates on the other⁴⁵². One should note at this point that the neurons in our surrogate cortex certainly do not have apical and basal dendrites and thus the surrogate cortex forms a generic proxy for the input layer of sensory cortex. At this scale of approximation, the neocortices of mammals are remarkably similar regarding the typical size of cells and the cellular densities, and consistent with measurements in our surrogate cortex. Despite a difference of $\mathcal{O}(100)$ in size, we find that the scale of projections and cell densities are similar to $\mathcal{O}(1)$, and consistent within the experimental error margins. This highlights the possibility of a common organizing scheme.

The contributions from recurrent inputs change orientation selective responses and the existence of inhibitory OFF regions in the receptive fields highlights that the tuning is a network effect. If anisotropic dendrites or fiber tracts mattered, the receptive fields would rather resemble single elongated ON regions, reflecting the expression of ChR2 across the dendrite or across the fibers. An explicit test could be done using ChR2 expressed only in the axon initial segment¹⁶⁷, but the light intensities required would make long experiments and the collection of large statistics challenging. We can not study the complete connectome of neurons in the culture, but there is a set of rules for the thalamocortical connectome, referred to as Peter’s rule, that might at least serve as a proxy. It states that the expected number of synapses between neurons is proportional to the occurrence of possible synaptic targets, i.e. to the product of their dendritic and axonal tree densities³⁵. It would not be surprising to find such simple rules governing neuronal circuits in a dish, too, and as this overlap has a stochastic component, so should the network. An additional source of feed-forward randomness are speckles in the holographic patterns. Taking the hypothesis seriously that stochasticity in the network contributes critically to orientation bias, can we test this hypothesis? (1) We can pharmacologically potentiate synapses using Phorbol esters^{189,338} and thus increase stochasticity in the network by increasing synaptic strength. (2) Alternatively, cultures grown under Tetrodotoxin (TTX) blockade show no activity during development, but connections between neurons form^{78,143}. After washout of the TTX, these cultures burst⁷⁸ with larger synaptic currents, compared to untreated controls¹⁴³. (3) The strength of synapses also depends very much on the density of a culture²¹⁵, the denser a culture, the smaller the typical epsc and ipsc amplitude, and the more inputs. To test this hypothesis, we would need to study various cell densities. (4) Finally, we could test how removal of the contributions of single neurons pharmacologically impairs tuning, similar to the methods in⁴⁴⁸.

Despite the relatively controlled system, there is still substantial variability across individual

cultures. The most crucial step should therefore be reducing the variability of the living cell component. One method would be to further abstract the network, for instance by designing virtual networks using a single neuron as computing element¹⁶². The inter-sample variability might be related to variations in cellular content and differences in the tissue extraction. These points might be addressed using more homogeneous samples, for instance by FACS sorting of neurons. Alternatively, with the advent of iPSC-technologies³²⁶, we might circumvent the problem by not using rodent tissue in the first place, but both methods do not come for free. FACS sorting reduces the number of neurons massively, and neurons differentiated from stem cells often come with peculiar gene expression patterns and protein composition.

We showed that recurrent networks as disorganized as in the surrogate cortex can generate feature selectivity. Theoretically, neural networks with connections organized by probabilistic rules are conceptually powerful model systems. Random neural networks have been shown to generically exhibit computationally favorable properties for stimulus representation and information processing, for instance by reservoir computing²⁹³, liquid state machines, a particular type of a reservoir computer which consists of randomly connected spiking neurons²⁹⁸ and more recently FORCE learning in random rate network⁴⁶¹. Our experimental data highlights that feature selectivity generated by the disorganized connections in living recurrent networks might be a generic scaffold for input classification, and the first workpiece refined by the selective forces of natural selection.

5.5 Supplemental

Several experimental studies label electrically active cells as either excitatory or inhibitory depending on their waveform³⁴⁹. This is probably not a viable option in cell culture⁵¹⁰, but the broad distribution of firing rates made us wonder whether one can in principle define a subpopulation of fast spiking inhibitory cells. Sustained firing rates above 10 Hz seem unlikely for pyramidal cells. To this end, we analyzed waveforms as function of the firing rate in **Fig 5.14** in the hope that small and fast spiking cells might have shorter waveforms. We could not detect any robust clusters depending on the waveform, and we therefore assign tentative inhibitory cells only according to their firing rate.

5.6 Materials and Methods

Cell culture

We used commercially available multielectrode arrays (60MEA200/30iR-Ti; Multi Channel Systems, Reutlingen, Germany) after coating the surface with Poly-D-Lysine. To this end, we add 1 ml of a 50 $\mu\text{g}/\text{ml}$ solution into the well of a MEA. The PDL solution was left on the MEAs and coverslips for at least 24 h. Typically, we prepared MEAs and coverslips a few days in advance, and stored them with PDL solution in an incubator in the dark at 37°C and 5% CO₂. Cell cultures were prepared according to Brewer⁵⁹. Briefly, cortical neurons were obtained from Wisteria WU rat embryos at 18 days of gestation (E18). The pregnant rat was anesthetized with CO₂. The embryos were removed by a cesarean section, decapitated and transferred to cooled petri dishes. The skull cavity was opened and the brain removed. Cortices were surgically extracted, the hippocampus removed with iris scissors, and transferred to a HEPES (Invitrogen, Germany) buffer. The supernatant was removed and the extracted cortices were trypsinized in a Trypsin/EDTA (trypsin: 0.05%; EDTA: 0.02%; Sigma Aldrich, Taufkirchen, Germany) buffer for 15 minutes at 37°C. Trypsinized cells were then transferred to a 10% Fetal calf serum (FCS)

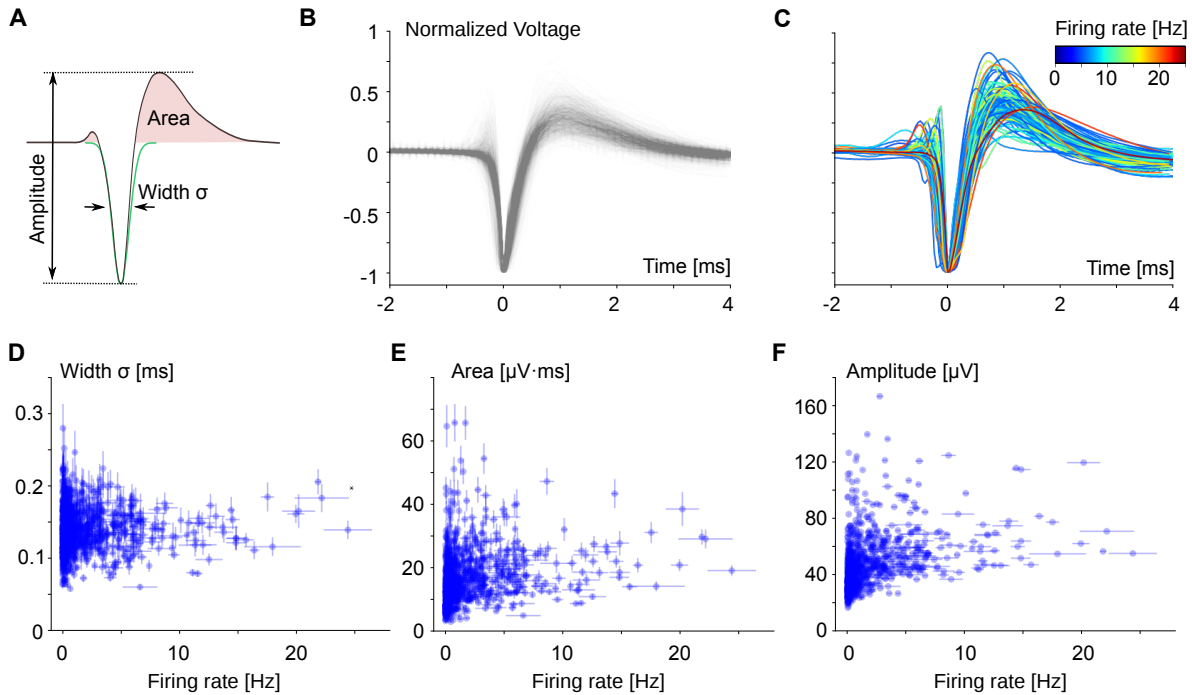


Figure 5.14: **There are no obvious clusters with discernibly different waveforms.** **A** A typical waveform and the extracted metrics: Total amplitude, width of the initial dip, and scale of the positive fraction of the waveform. **B** All waveforms aligned to the negative peak and with normalized voltage. **C** Same as B, but with color-coded firing rate. Fast spiking cells do not have specific waveforms. **D** Width of the waveform vs. firing rate. Errors of the width are $\pm 1\sigma$ estimated from the fit covariance. Errors of the rate are errors of the mean, estimated from binning the spiketrain in 10 sets of equal duration. **E** Same as D but for the scale of the positive fraction of the waveform. **F** Same as D but for the voltage amplitude.

solution. Thorough trituration using a syringe and a needle with a diameter of 1 mm followed. The cell suspension was then centrifuged at 1200 rpm for 2 minutes. The pellet was re-suspended in serum-free B27/Neurobasal (Gibco) medium supplemented with Glutamax and Basic Fibroblast Growth Factor (bFGF). Cells were counted with a Neubauer improved counting chamber. A droplet of $\approx 100 \mu\text{l}$ cell suspension containing 1.000.000 cells was added on top of the electrode field of the MEAs. The MEAs were then kept in an incubator providing a humidified atmosphere containing 5% CO_2 at 37°C for 4 hours to allow the cells to settle. 1 ml of the B27/Neurobasal medium was then added to the cell chamber. After two days, we added 1 μl of a solution, containing 3.4×10^{10} genome copies (GC) of AAV9-hSyn-hChR2(H134R)-eYFP-WPRE-hGH (UPenn Vectorcore) and 1 μl of AAV1.Syn.NES.jRCaMP1a.WPRE.SV40, containing 3.36×10^{10} GC of this construct. Half of the medium was changed every seven days. All animals were kept and bred in the animal house of the Max Planck Institute of Experimental Medicine according to European and German guidelines for experimental animals.

Stimulation and stimuli

The holographic projection system is constructed from a 473 nm diode laser (DL-473, Rapp OptoElectronic) and a liquid crystal on silicon spatial light modulator (OEM SLM X11840, Hamamatsu). This SLM has a resolution of $600 \text{ px} \times 800 \text{ px}$, a $12.5 \mu\text{m}$ pixel pitch and a fill factor of 95%. To remove the maximum of zeroth order, we employ an axial displacement of the hologram by a superimposed Fresnel lens of $\approx 2 \text{ mm}$. Thus, the hologram is spatially separated

from the focal point of the maximum of zeroth order. At the focal point of the maximum of zeroth order, it is blocked with a mask, a $d=500$ μm aluminum dot on a glass plate. The axial displacement leaves the hologram intact, except a small loss of contrast and slight distortions. The holograms are then projected in the conjugated plane of a Zeiss Axio Observer.Z1 inverted microscope.

The SLM is operated by a controller which allows us to control the phase shift on each pixel via a standard DVI interface. We calculate phase fields with the Gerchberg-Saxon method; $N=20$ iterations¹⁵⁶, implemented in Matlab. The holographic frame transitions were recorded from a screen receiving the same signal as the SLM after a DVI splitter. We measured the screen signal with a OPT101 photodiode and transimpedance amplifier (Texas Instruments) and recorded it with the electrophysiology setup. The reliability of this system in counting frames is higher than 1 missed frame in 10.000.

Recordings were made on a 60 channel MEA amplifier (MEA-1060 Inv, Multichannel Systems, Reutlingen, Germany). Data from MEAs were registered at 25 kHz using a 64-channel A/D converter and MC_Rack software (Multichannel Systems, Reutlingen, Germany). After high pass filtering (Butterworth second order, 100 Hz) events were detected in a cutout recorded 2 ms before and 4 ms after crossing a threshold of -5σ of the filtered electrode signal²⁷⁷. The threshold was evaluated for every channel individually. The identified events were then sorted to remove false positives (see chapter 6)

For recordings of calcium dynamics, we use a red-shifted calcium indicator, jRCaMP1a, to combine the optical excitation with calcium imaging¹⁰³ and use an all-optical interface^{129,369}. The excitation filter for the jRCaMP1a fluorescence is a 572/28 bandpass (FF01-572/28-25, Semrock), operated after a Zeiss HXP-120C metal halide light source. For calcium imaging, cells were illuminated with 0.10 ± 0.01 mW/mm^2 ($\lambda = 572 \pm 14$ nm) and holographically up to 2 mW/mm^2 ($\lambda = 473$ nm), close to³⁷¹. The bandpass-filtered excitation light is combined with the holographic light through a 495 nm dichroic longpass (FF495-Di03-25x36, Semrock). The beam then enters the microscope through the epifluorescence port. To record fluorescence, we project the beam with a 593 nm dichroic longpass (FF593-Di03-25x36, Semrock) through the objective (a Zeiss Plan-Apochromat 10x/0.45 M27 or a Zeiss EC Plan-Neofluar 5x/0.16 M27), and collect fluorescence after filtering with a 641/75 emission filter (# 67036, Edmund Optics) with a commercial camera (ProgRes MF 1.4 Megapixel CCD monochrom, 2/3", firewire, Jenoptik, Germany). The camera's trigger pulses are used to open and close the shutter of the metal halide lamp, to avoid excessive photo bleaching. The camera trigger is recorded together with the holography trigger with the MEA amplifier.

To study the response properties of the cultured neurons, we use the same set of stimuli as presented in the literature^{47,212,422,439,464}: we simulate the presentation of moving gratings in pseudorandom order and to study circuits that formed in the culture dish, we use spike triggered reverse correlation of white noise inputs^{107,487}.

Numerical procedures for PIPP RGC mosaics

We generated RGC mosaics with a pairwise interacting point process using the code published by Schottdorf et al.⁴²⁷ derived from the method developed in^{125,404}. In short, we initially positioned n_{OFF} OFF cells and n_{ON} ON cells independently according to a two-dimensional Poisson point process with fixed cell density. We then updated these positions according to the following loop: For each ON center cell a new candidate position was generated at random. Considering the i -th ON center cell, this new position was accepted with probability p_i that depends on the distance to the other cells. After updating all ON center cells' positions, the procedure was repeated for the OFF center cells. Both loops were repeated between 20 and 50 times at which point the cell positions had converged to a stable pattern.

Developmental manipulation of the surrogate cortex

“A good theoretical model of a complex system should be like a good caricature: it should emphasize those features which are most important and should downplay the inessential details. Now the only snag with this advice is that one does not really know which are the inessential details until one has understood the phenomena under study. Consequently, one should investigate a wide range of models and not stake one’s life (or one’s theoretical insight) on one particular model only.”

Yakov Frenkel, cited in¹⁸³.

6.1 Content

The surrogate cortex is based on neuronal circuits generated in the absence of any input. The processes by which the neurons wire up to form these circuits are most likely partially activity dependent. One way to manipulate the circuit’s connectome is thus by controlling the prevalent activity patterns during the course of circuit formation. In this chapter, we therefore ask whether the local circuits can be configured differently by supplying external inputs during development. We first construct a device, a *light disco*, to provide a developing culture with spatiotemporally complex input patterns inside the incubator for several weeks. Using this device, we find strong evidence that self-organization in the presence of external, correlated inputs changes the collective dynamics of the surrogate cortex. Finally, we discuss whether these results have relevant consequences for our current understanding of the role of spontaneous and driven activity in the developing brain.

6.2 Introduction

Spontaneous neural activity together with genetic programs in the developing brain are key contributors governing functional and structural aspects of neuronal circuits, for instance in the retina, the cochlea, the spinal cord, the cerebellum, the thalamus, the neocortex, and the hippocampus^{1,38,201,249,450}. In the mammalian visual system specifically, the functional architecture and the development of neurons and their connections is laid out by spatiotemporal patterns of neural activity^{82,89,171,332,513}. Even in the earliest stages of the sensory periphery, so-called *retinal waves* shape the topographic organization of projections from the retina to the brain. Patterned activity is a fundamental prerequisite for the refinement of visual circuits, but not always in the form of spontaneous activity. Retinal waves do not occur in all tetrapode vertebrates during early development. Amphibians lack such waves but are visually responsive very early on. This lead to the speculation that amphibians and amniotes, see **Fig. 6.1A**, evolved different strategies to generate appropriately patterned retinal ganglion cell (RGC) activity; where the spontaneous activity in mammals, chicks and turtles periodically spread across the retina with highly correlated activity between neighboring RGCs without visual stimuli, young amphibians as the *Xenopus* tadpole seem to rely on visual inputs for the development of organized topographic maps^{1,111}. These findings highlight that for all tetrapods, patterned activity is a necessity and the developing brain goes to great length to provide such patterns. In this chapter, we will develop a system that allows us to experimentally dissect the contributions of patterned activity on functional aspects of neural circuits.

Mammals have a very specific layout of their early visual pathway, see **Fig. 6.1B**, with precise wiring from the retina through the thalamus to the visual cortex. What are the effects of disrupting spontaneous activity for mammalian neural circuits? In mice, disruption of the Munc13 proteins completely abolishes synaptic transmission, and with it the spatial structure of spontaneous activity, but leaves the large scale organization and the synapse density of neural tissue largely intact⁴⁹⁰. In contrast to this large scale organization, other aspects critically depend on spontaneous activity. Interrupting retinal waves either genetically or pharmacologically disrupts the orderly arrangement of thalamocortical projections⁶⁵. In cats, pharmacological blockade of activity in the lateral geniculate nucleus during early development leaves a majority of LGN projections terminating not in the visual cortex. The small fraction reaching their original destination are topographically disorganized⁷⁰. In young ferrets^{82,513}, spontaneous activity in the LGN and the visual cortex is complex in space and time. In the cortex^{82,175,177}, it is composed of bursts and correlated on mm scales, see **Fig. 6.1C**. These bursts persist during the blockade of external drive, but they become more synchronous, see **Fig. 6.1D**. The correlation structure of the spontaneous activity has also been shown to form a scaffold for the functional architecture of the adult ferret visual cortex^{175,177}. These studies show that specific neural activity is required for functional neural circuits, and that spontaneous activity in cortical circuits has an endogenous and an exogenous component. The relative contributions of both remain unclear and are hard to assess *in vivo*.

Here, we separate these activity patterns *in vitro*. Recent advances in Lab-on-a-Chip technologies, optogenetics and cell culture allow, for the first time, to study the effects of prolonged optogenetic stimulation on developing circuits *in vitro*, and we build on these technologies. In principle, activity can be evoked electrically^{44,224,308,367,488,498,499} and pharmacologically²⁴⁴. Electrical stimulation has been shown to affect the behavior of cultured neuronal networks on the scale of several hours⁴⁸⁸, up to several days⁴⁴. More recently, optical tools and optogenetics started to emerge^{371,400}, which at least in principle can overcome fundamental limitations of electrical interfaces, as the substantial subsampling, the effects of photochemistry, and the pho-

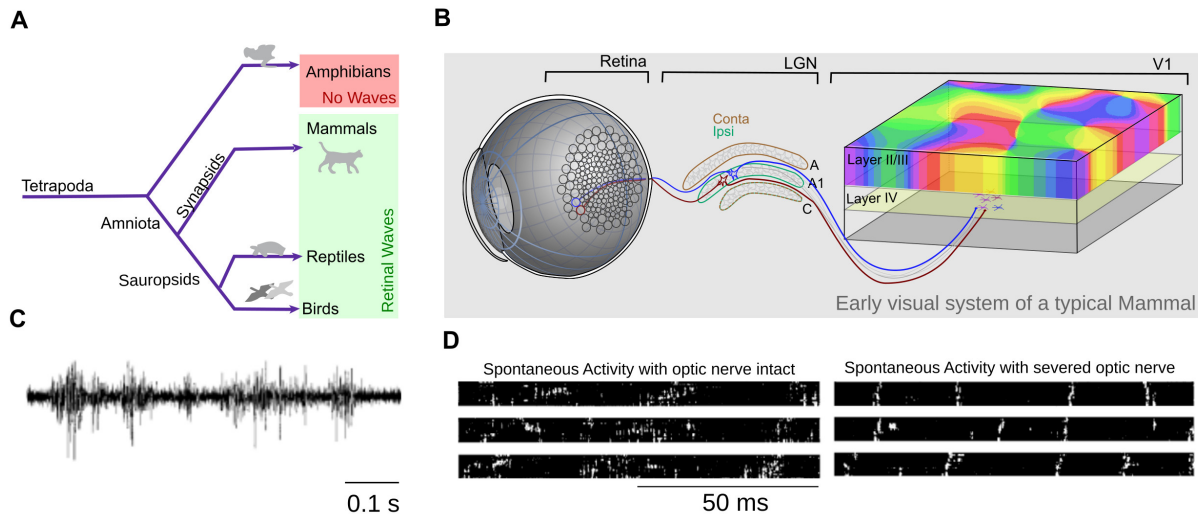


Figure 6.1: **Spontaneous activity in the visual system.** **A** Macroevolution of the tetrapods; amphibians might have evolved a different strategy for neural circuit development. **B** The typical layout of the mammalian visual system, here the cat. Notably, spontaneous activity early in development exists in the retina, the thalamus and the visual cortex^{82,280,513}. **C** Electrical recording from an awake ferret in the visual cortex at postnatal day 27, three to four days before eye opening (adapted from⁸²): Spontaneous activity is bursty with several temporal components. Shown here is a macroburst (see text). **D** Optic nerve transection changes the spontaneous activity patterns into a more synchronous bursty regime (adapted from⁸²).

toelectric effect at high light intensities^{403,437}. *In vitro* systems recently developed include an integrated platform of optrode arrays⁵¹⁴ and multi well multielectrode arrays (MEAs) with few LEDs⁸⁶ or a single channel optogenetic feedback control³⁴⁸. Such technologies allow long-term stimulation with a single LED for few days²⁸¹ and the design of LED array approaches⁶¹ in cultures that can be kept alive for more than a year³⁸⁵.

We explored neuronal circuits formed spontaneously from dissociated rat E18 cortical neurons grown in culture. We analyzed how these circuits change during week-long stimulation throughout development with spatiotemporally complex patterns of activity. In cortical cultures, periodic bursts of action potentials emerge after typically 10 days *in vitro* in 2D^{497,498} and also 3D cultures^{102,146,307}, notably resembling to some extent the spontaneous activity in immature cortex after deafferentation⁸². With development, the patterns increase in complexity³⁰⁸, but the activity remains highly synchronous. We show that the spontaneous behavior of cultures subjected to external drive is fundamentally different to unstimulated control cultures. The spontaneous electrical activity, recorded with multielectrode arrays (MEAs) in the controls is bursty, i.e. highly irregular with large deviations in the interspike intervals. The spikes on different channels, however, are highly correlated and show that these bursts are a genuine network phenomenon. The cultures subjected to external inputs show similar firing rates, and optical appearance. However, the electrical activity on single channels is much less bursty. The coefficients of variation (the ratio of standard deviation to mean) of the interspike interval distribution is close to 1, resembling a Poisson process. Also, the correlation between individual channels is much smaller, implying an asynchronous and irregular regime. This study shows that the functional aspects of a neural network massively depend on structured activity patterns in development, and that an *in vitro* system can be a viable tool to disentangle the relative contributions of recurrent and external influences.

6.3 Results

To first evaluate the composition of the primary culture, we use immuno stainings and confocal microscopy, as is shown in **Fig. 6.2A**. The cultures contain neurons of various types and glial cells (here GFAP positive). The cultures are very thin, typically around 10 μm and composed of about two cell layers. At 2 days *in vitro* (DIV) we transfect the cells with an Adeno-associated virus (AAV) that expresses the Channelrhodopsin 2 variant ChR2(H134R), labeled with eYFP, after a neuron specific Synapsin promoter. With our protocol, about 40% of neurons express ChR2 (see methods). A fluorescence image of such a culture grown on a multielectrode array (MEA) is shown in **Fig. 6.2B**. It illustrates a dense and uniform expression of the construct across the surface of the electrode array. The expression of this light sensitive ion channel allows us to generate spatially and temporally complex activity patterns in the layer of cells. Our target is a continuous stimulation during development. Therefore we developed a small and integrated device that fits into an incubator, **Fig. 6.2C**, and that can supply the culture for weeks with inputs. It consists of an LED array of 16×16 blue LEDs that is projected through a single objective on the transparent multielectrode array. The LED array is controlled with an Arduino 2560 and both are integrated into a moisture insulated box. The Arduino receives commands from a laptop outside of the incubator. The LEDs are InGaN LEDs that emit light of $\lambda = 470 \pm 18$ nm, close to the excitation maximum of ChR2(H134R), **Fig. 6.2D**. To assess the light patterns, we glued a CMOS Chip from a commercial web cam on a piece of glass with the same spatial dimensions as the MEA. **Fig. 6.2E** shows that distribution of light intensities. We projected the LEDs slightly out of focus, to generate approximately continuous illumination. The anisotropies in the image of each SMD-LED are due to spherical aberration of the objective lens. **Fig. 6.2F** shows a snapshot of a moving grating, the stimulus employed throughout this study, modeling the spontaneous activity in the young ferret visual system.

Electrode recordings *in vivo* revealed a complex structure of this spontaneous activity. In the cortex of young ferrets, one can observe spontaneous activity patterns covering at least three orders of magnitude in time. On the largest timescales, there are typically two to three macrobursts per minute. A macroburst consists of microbursts that vary in duration up to several 100 ms. Within them, spike discharges can reach firing rates of 50 Hz or more, see **Fig. 6.1C**⁸². The temporal scales of these bursts resemble spontaneous activity in the LGN⁵¹³ and the retina²⁸⁰. In the retina, the spontaneous firing rate of ganglion cells depends on the ganglion cell type. For β -cells, the average spontaneous firing rate is close to 3 Hz²⁸⁰. For our experiment, to reduce the number of parameters as much as possible, we modeled only the most basal contribution of spontaneous activity: We chose moving gratings because they are defined by only two parameters, a wavelength and a periodicity. We choose a repetition rate of 3 Hz, consistent with the data in^{82,280,513}. In the developing ferret visual cortex, there are large scale spatial correlations within the activity patterns, up to 1 mm⁸², so that we choose moving gratings with a periodicity of $\lambda \approx 0.5$ mm.

Right after the viral transduction on DIV 2, we placed the electrode array with the neurons on top of the projection device. Note that this is earlier than the first expression of the ChR2 ion channel, such that the neurons receive increasing input, the more ChR2 they express. The light intensities here are high enough to activate the ChR2(H134R) variant, but not high enough to elicit damage. We chose this channel because it is slightly more light responsive with larger photocurrents than ChR2. It has a EC_{50} of 1.0 ± 0.1 mW/mm² and a closing time of around 4 ms at 37°C. With the light intensities of our system, we can reach 30% of the maximum response of the channel^{282,283}.

Next, we measured the spontaneous activity of cultured neurons subjected to external inputs vs. controls. To this end, we removed the cultures from the incubator, and recorded electrical activity with a commercially available system, making sure that the cells are kept at 37°C. **Fig. 6.3A**

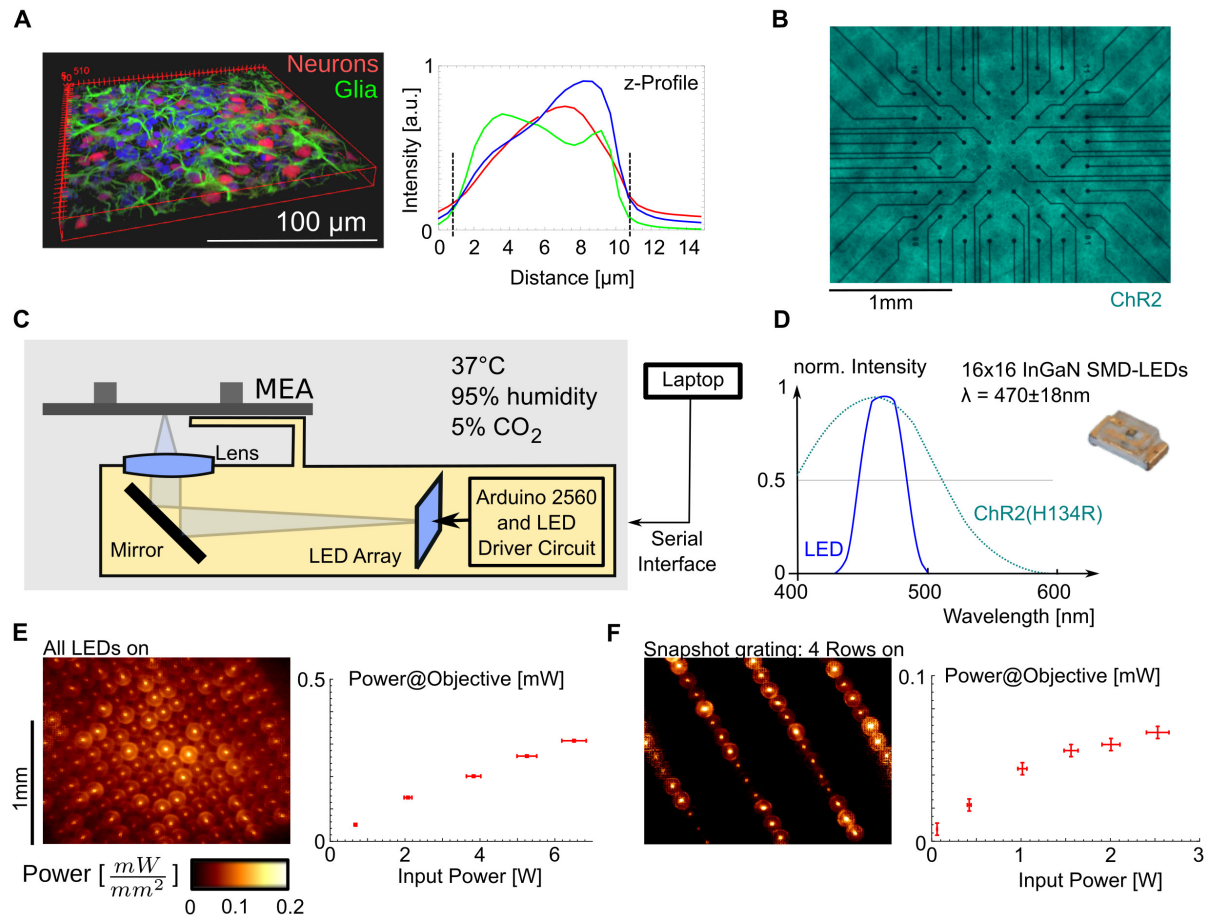


Figure 6.2: The light disco: Separating activity patterns from the genetic program. A The primary culture of rodent cortical tissue contains neurons (NeuN positive) and glia (GFAP positive). The typical neuron density is 60.000 mm^{-3} . **B** We use neurons expressing the light sensitive ionchannel ChR2 after viral transduction (see methods). Shown here is the fluorescence of the YFP label of the channel, on a transparent multielectrode array (MEA). **C** The system used to provide the developing circuits with spatiotemporal complex light patterns is similar to an inverted microscope. The light source is a 16×16 custom built LED grid, projected through an objective lens. **D** The LED light emission is centered around the excitation maximum of the ChR2(H134R) channel²⁸³. **E** With this system, we can produce arbitrary light densities of up to 0.2 mW/mm^2 . The entire patterns is projected to an area of $\approx 9 \text{ mm}^2$. **F** The excitation pattern used throughout this study: a moving grating of one row on, and three rows off, with a temporal frequency of 3 Hz.

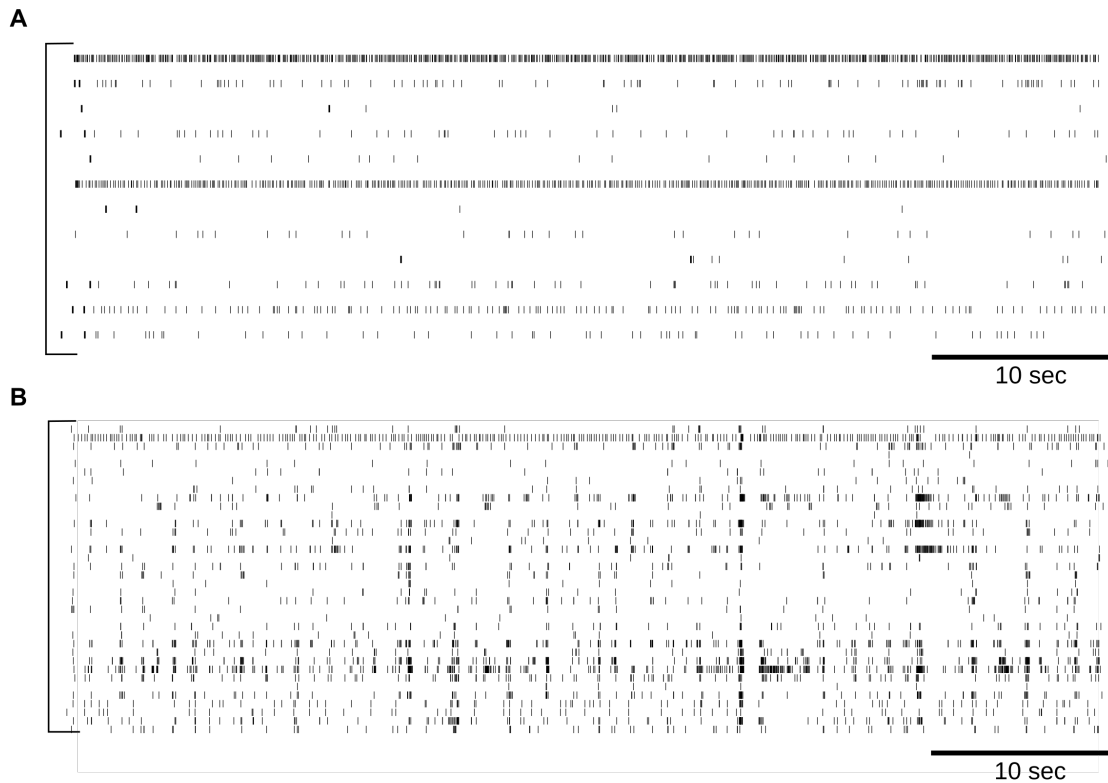


Figure 6.3: **Correlated activity during development qualitatively changes spontaneous activity.** **A** Spontaneous activity of a culture, subjected to continuous stimulation for three weeks (23DIV). **B** Spontaneous activity of a control culture, also expressing ChR2, but developing without perturbation in a dark incubator. This culture shows very typical bursts of electrical activity.

and **Fig. 6.3B** show rasterplots of two 23 day old cultures, 21 days after viral transfection. We identified events on the electrodes after threshold-crossings of -5σ of the noise on each electrode, and a PCA-based scheme to remove a small fraction of false positives in the data. Notably, we did not perform spike sorting, so the events could be generated by several neurons. The culture subjected to external inputs shows a substantial variability in firing rates across channels. The control shows a large number of bursts, i.e. synchronized events across different channels, that occur irregularly. This behavior is well documented in a large number of other studies. To quantitatively assess the differences in synchrony and regularity, we next calculated correlograms of the active channels. The correlograms measure the occurrence of a spike in channel (1), given a spike in channel (2) occurred. If (1)=(2), then it calculates the autocorrelation, see **Fig. 6.4A**. Such an analysis of the recordings in **Fig. 6.3** is shown in **Fig. 6.4B,C**. It shows the absence of high correlations among events in the cultures subjected to external stimuli, whereas there are high correlations among the channels in the controls. In addition to the cross correlation analysis, we also looked at the interspike interval distributions. For the two recordings, the data is shown in **Fig. 6.4D** and **Fig. 6.4E**. The heavy tails in the control, **Fig. 6.4E**, highlight the irregularity of the bursting process. We used the ISI distribution to calculate the coefficient of variation, to measure the regularity of the spike train. The coefficient of variation (CV), i.e. the standard deviation relative to the mean, of cultures subjected to external input, 'Disco', and controls are shown in **Fig. 6.5A**. In the controls, the CV increases continuously, indicating more and more bursting of the cells. In the cultures subjected to external stimuli, the CVs remain

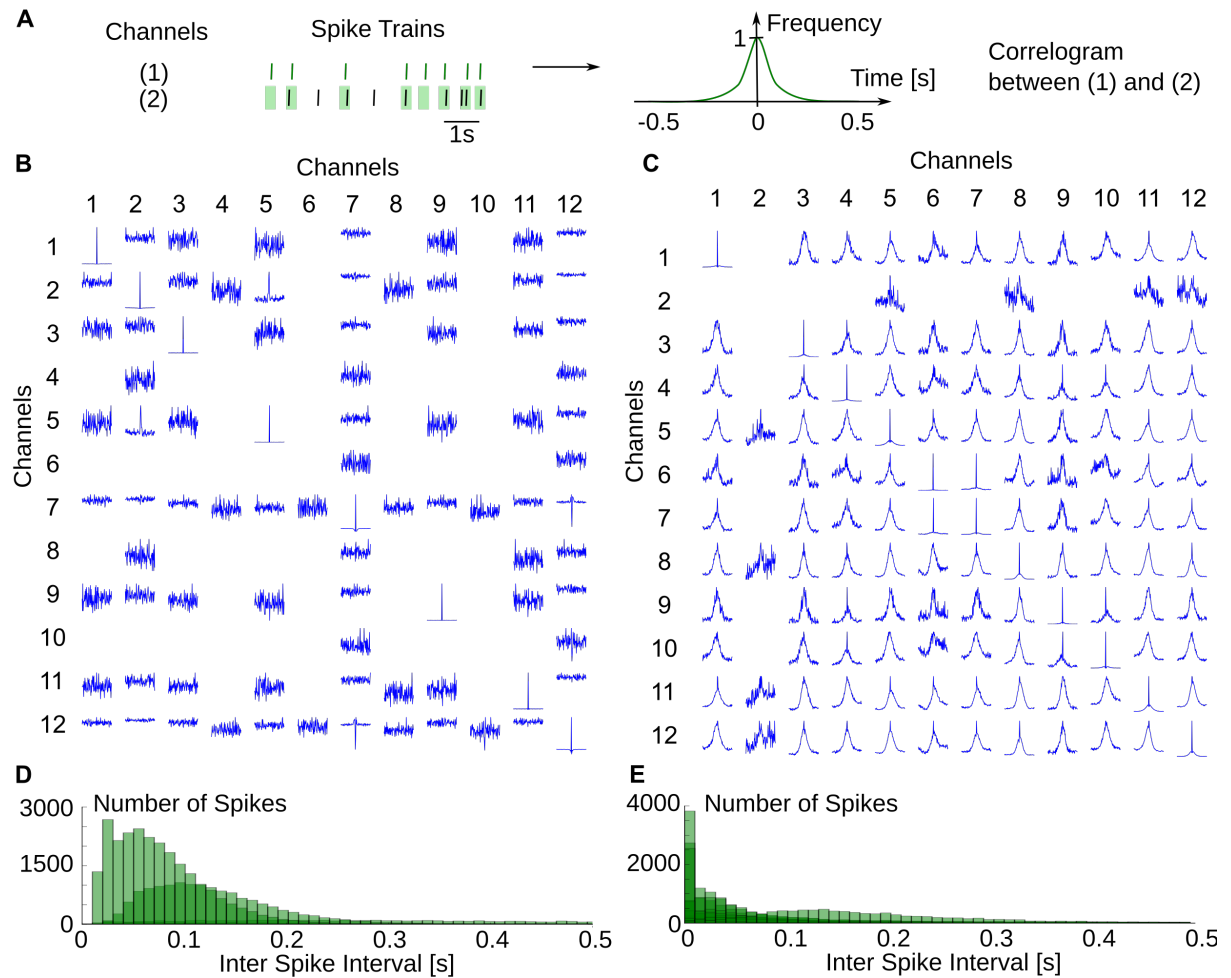


Figure 6.4: **Generating complex activity throughout development disrupts synchrony across neurons.** **A** To evaluate the cross-channel correlation, we calculate the cross correlogram of the spike trains. This means: Triggering on channel 1, count when spikes occurred in channel 2. **B** For the data shown in **Fig. 6.3A**, this shows a very small cross-channel correlation (notably except channel 7/12 and 5/3). **C** The control culture shows correlations across almost all channels. **D** The interspike interval (ISI) distributions from **Fig. 6.3A** reveal irregular spiking. Data of several electrodes (green) is superimposed. **E** The ISI distributions from **Fig. 6.3B** reveal heavy tails, indicating highly irregular spiking.

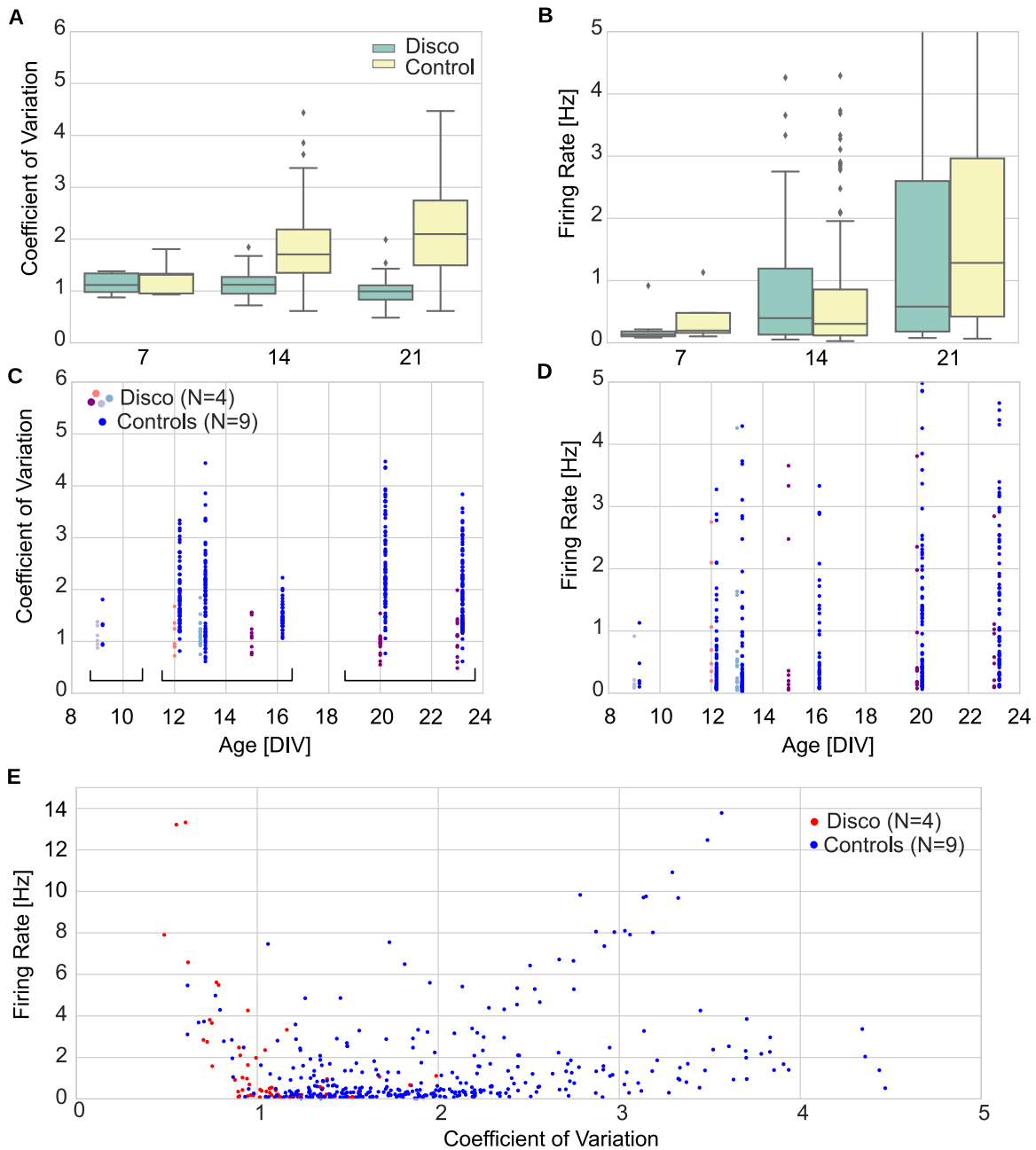


Figure 6.5: **The individual units lose their burstiness.** **A** The coefficient of variation (CV) of the spike trains of the cultures with external input is substantially lower than the controls. Note that this translates to a less bursty firing patterns. **B** The firing rates increase with time, but are comparable between conditions. **C** Raw data to A. Every dot corresponds to a spiketrain of 30 min to 90 min duration, recorded with an electrode array. **D** Raw data to B. **E** A scatterplot of CVs versus firing rates reveals that the low CV end is almost exclusively populated by the cultures subjected to external input during development (red).

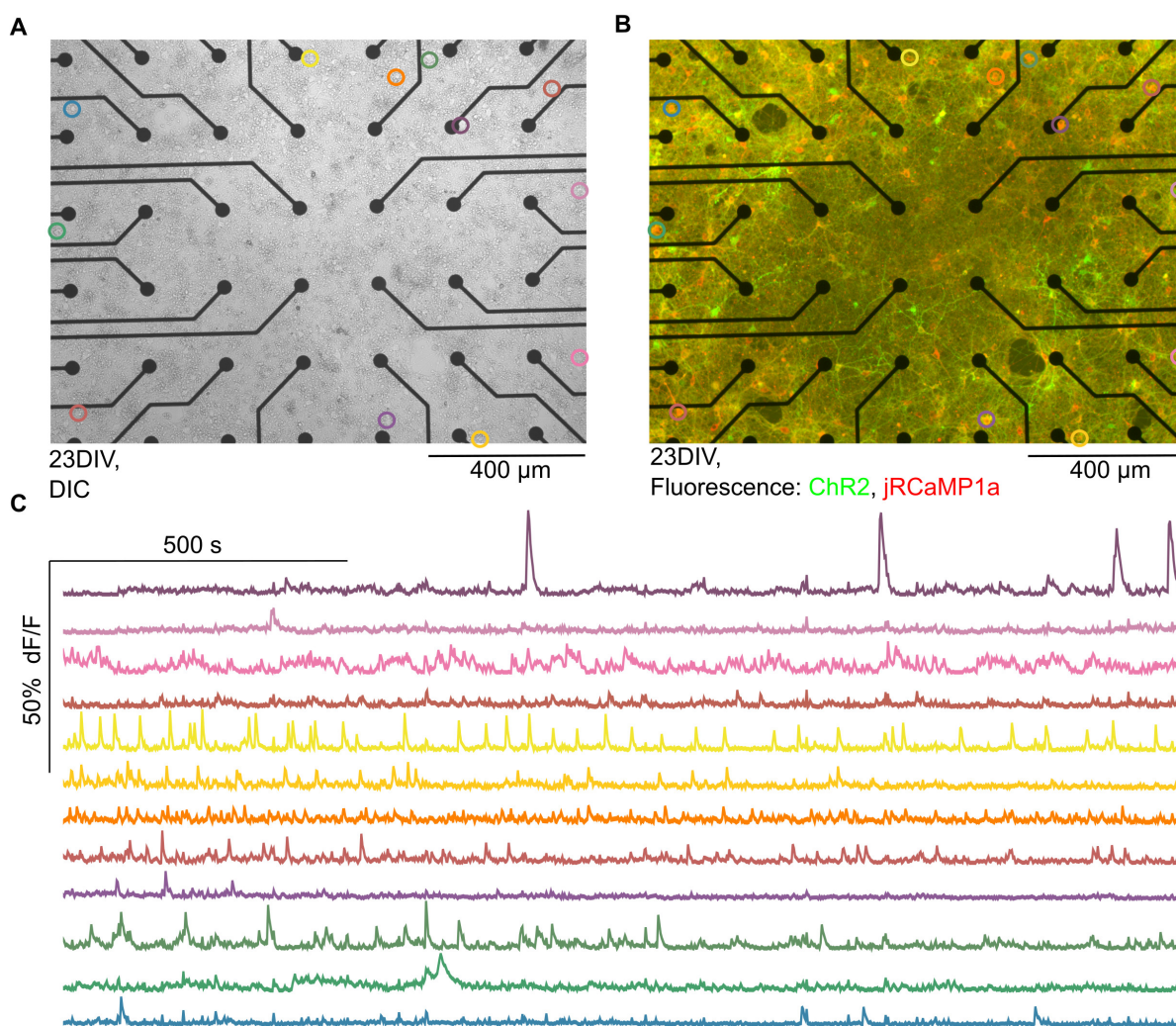


Figure 6.6: **Asynchronous and irregular calcium fluorescence of individual cells.** **A** A DIC Image of a section of a culture after three weeks of external inputs reveals a dense layer of cells. Indicated are cell positions for calcium fluorescence. **B** The neurons also express fluorescent labels, indicating that their protein production machinery is intact. The expression of jRCaMP1a specifically allows to measure neuronal activity via calcium fluorescence. **C** The calcium fluorescence of $N=12$ individuals cells with cell position indicated in A and B; data analysis by Julian Vogel.

close to 1, resembling a Poisson process. While the CVs are genuinely different for both types of conditions, the firing rates are similar and reproduce the measurements in other labs^{79,214}, see **Fig. 6.5B**. To generate the two figures, we pooled all available spiketrains, see **Fig. 6.5C,D**. Plotting the firing rate versus the CV shows that small CVs are almost exclusively found in cultures subjected to external inputs. In **Fig. 6.6A** and **Fig. 6.6B** we show a DIC and a fluorescence image of a 23 days old culture that received light input. The DIC image reveals a dense layer of cells, and the fluorescence image shows that the protein biosynthesis of the cells is intact. Together with the comparable firing rates, **Fig. 6.5B,D**, this indicates that there are no obvious pathologies that stem from the continuous illumination with blue light, but see below for a more detailed analysis. In **Fig. 6.6C** we show the integrated fluorescence of $N=12$ individual cells as function of time over a course of 30 minutes. The irregular and asynchronous activity is clearly visible in the jRCaMP1a signal and considering that this is calcium activity of single

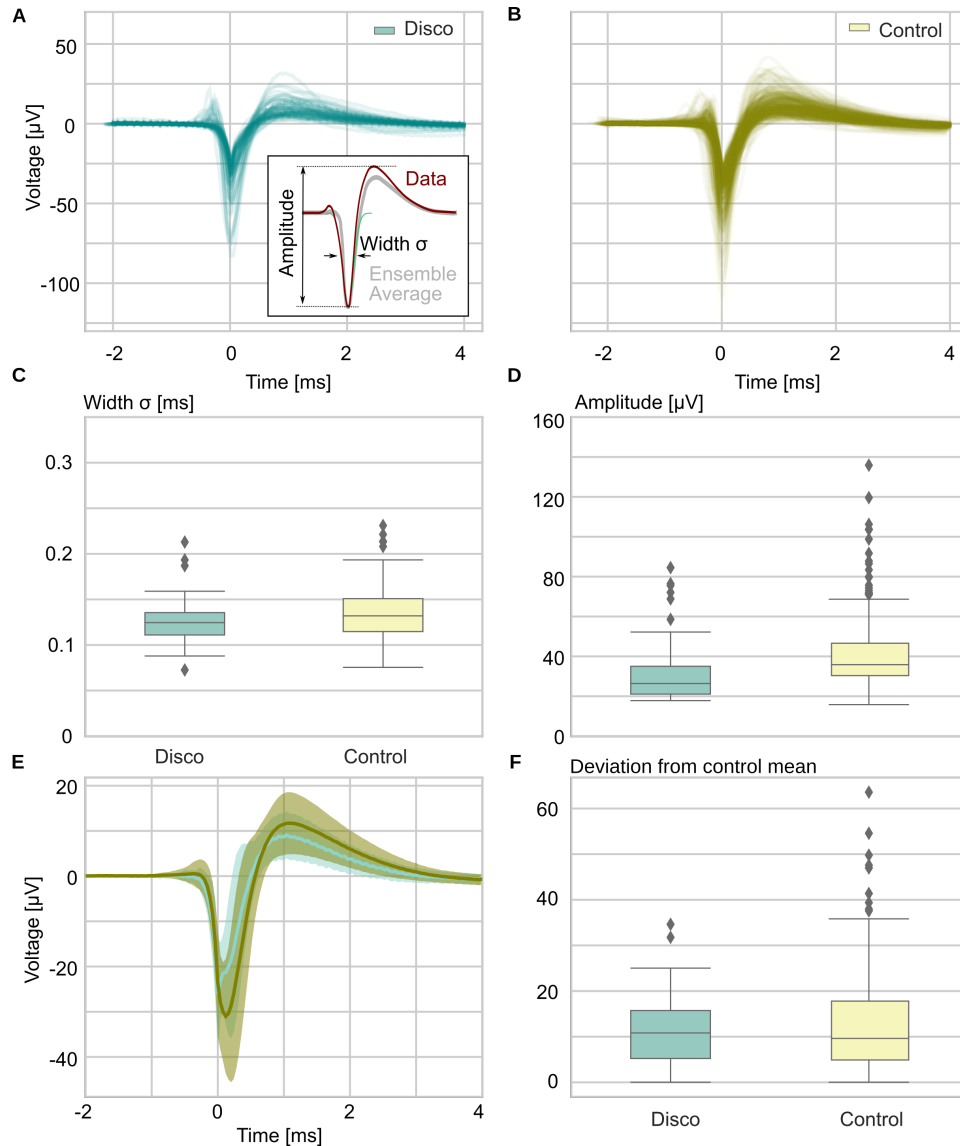


Figure 6.7: **Comparison of spike waveforms.** **A** Spike waveforms from all active channels of cultures subject to sustained stimulation. Inset shows two metrics extracted from each waveform: width and amplitude. **B** Spike waveforms of the controls. **C** The spike width and the spike amplitude **D** are very similar. **E** Averaged waveforms and ± 1 std. dev. of all waveforms. **F** Shown is the deviation from the average waveform of all controls for both conditions. There is no measurable difference as far as the waveforms are concerned.

cell regions of interests, we can make this statement now on the single-cell level. Finally, one might speculate that the observed qualitative differences in activity are caused by pathological changes on the single cell level, such as photo damage induced by the sustained illumination. As noted above, the stable expression of proteins (cf. **Fig. 6.6B**) and the comparable firing rates (cf. **Fig. 6.5B**) make this unlikely, but to be certain, we analyzed extracellular spike waveforms to see whether the waveforms as a proxy for the action potential waveform reveal any differences between cultures grown in the dark, and those stimulated. While there was no obvious difference comparing the waveforms, see **Fig. 6.7A** and **Fig. 6.7B**, we quantified every single trace by fitting a Gaussian function with width σ to the initial negative dip. We find that for all cultures, a typical width is around 0.1 ms. The results are summarized in **Fig. 6.7C**. We also measured

the absolute amplitude of the signals. Their distributions are shown in **Fig. 6.7D**. Notably, both distributions are indistinguishable with typical amplitudes between 20 μV and 40 μV . Next, we calculated the average of all control waveforms $w_i^c(t)$, i.e. $a^c(t) = \langle w_i^c(t) \rangle_i$. Assuming that this function, shown in yellow in **Fig. 6.7E**, is a typical waveform, we next measured the distance to every recorded waveform

$$d_i = \sqrt{\int dt (a^c(t) - w_i(t))^2}. \quad (6.1)$$

The distribution of these deviations is shown in **Fig. 6.7F** and shows that there is no noticeable difference between discos and controls. Remarkably the spread of values is higher for the controls than it is for the disco dataset.

6.4 Discussion

Synchronous electrical activity is a fundamental phenomenon of circuits in the brain and shapes its connectivity³³². Driving neural networks throughout development *in vitro* can help to better understand the specific mechanisms that connect activity with circuit elements. In principle, this allows us to study the effects of specific observed activity patterns once their phenomenology is established. A number of articles from the Lab of William Moody studies synchronized electrical activity in neonatal mouse cortex in slices. These *in vitro* studies revealed the wiring pathways and the phenomenology of such waves: Waves of activity within a coronal slice of the mouse brain can start in the hippocampal formation and propagate through this part of the brain and further through the neocortex. They can also originate in the neocortex, or remain confined to the neocortex²⁴. The spontaneous and synchronized activity has two components, driven by AMPA and NMDA receptors. GABA mediated inhibition helps terminate activity waves, and increases the likelihood of wave propagation to the neocortex³²¹. These spontaneous waves have specific and complex spatiotemporal order⁹¹ and are found in the intact brain, too²⁷³. Electrode recordings in the ferret *in vivo* revealed a complex structure of spontaneous activity. In the cortex of young ferrets, one can observe spontaneous activity patterns covering at least three orders of magnitude in time. On the largest timescales, there are typically two to three macrobursts per minute. A macroburst consists of microbursts that vary in duration up to several 100 ms. Within them, spike discharges can reach firing rates of 50 Hz or more, see **Fig. 6.1C**⁸². The temporal scales of these bursts resemble spontaneous activity in the LGN⁵¹³ and the retina²⁸⁰. More recently, these findings have been corroborated with chronic calcium imaging, further revealing how spontaneous activity forms a scaffold for the functional organization of the adult brain^{175,177}. In the retina, the spontaneous firing rate of ganglion cells depends on the ganglion cell type and for β -cells, the *average* spontaneous firing rate is close to 3 Hz²⁸⁰. For our experiment, to reduce the number of parameters as much as possible, we modeled only the most basal contribution of spontaneous activity: We chose moving gratings because they are defined by only two parameters, a wavelength and a periodicity. We choose a repetition rate of 3 Hz, consistent with the data in^{82,280,513}. In the developing ferret visual cortex, there are large scale spatial correlations within the activity patterns, up to 1 mm⁸², so that we choose moving gratings with a periodicity of $\lambda \approx 0.5$ mm. An interesting next stage of our experiments will involve variations of this stimulation paradigm. For instance: What are the effects of uncorrelated stimulation, i.e. with a pattern without spatial and temporal scales, for instance random checkerboards? This experiment can shed light on the relevance of specific spatiotemporal components and the responsible underlying mechanisms.

The absence of bursts in stimulated cultures shows that bursts might be a pathology associated with deafferentation, or sensory deprivation³⁸⁴. In primary cortical cultures, periodic bursts of action potentials emerge after typically 10 days *in vitro* in 2D^{79,497,498} and also 3D cultures¹⁴⁶, notably resembling to some extent the spontaneous activity in brain slices, or the deafferented cortex⁸². They are a robust feature of mature spontaneous activity in cultures^{224,232,244,448}. With development, the patterns increase in complexity^{308,498}, but the activity remains highly synchronous. Cell cultures form complex networks^{383,455} with high synapse density, high synapse turnover^{214,331,357} and a conceptual similarity to percolation^{56,133,448}, highlighting the involvement of synaptic transmission. Synchronized electrical activity is an extremely robust phenomenon, for instance lowering the environmental temperature does not stop bursting. Cooling decreases the overall activity, while cultures still remain bursty. Even at conditions of extreme hypothermia at 12°C, at which cultured cortical networks can survive for hours, they continue to generate extremely sporadic bursts^{414,415}. This is not too surprising, considering (1) activation of a single neuron in a microculture can elicit a burst, (2) bursts terminate by exhaustion of vesicle pools⁸⁷ and (3) synaptic processes as the refilling rate of the readily releasable pool are heavily temperature dependent³⁹⁰. One established method to control bursts employs closed-loop electrophysiology⁵⁰⁰, providing external input tuned to counteract global network activity, but this *ad hoc* method does not address the responsible mechanisms. Alternatively, pharmacological interference with neuro modulators, antagonists to NMDA and non-NMDA receptors, Tetrodotoxin, increasing extracellular Mg²⁺ and GABA agonists, can break the pattern of bursting. Interfering with synaptic transmission¹⁶⁵ by lowering extracellular calcium, revealed a different dynamical regime, in which single neurons behave oscillatory³⁷⁹. Neurobasal 1x Medium, the standard neuronal culturing medium used in this chapter, has a Ca²⁺ concentration of 1.8 mM, as many classical media. This value is similar to calcium concentrations in the range of 1.5-2.0 mM in the brain. These numbers are slightly higher than the ionized calcium concentration in blood of 1.0-1.3 mM, and much higher than intracellular levels from 50 to 100 nM¹²³. Bursting in cell primary cultures requires at least ≥ 0.5 mM³⁷⁹. In addition to these methods, lowering the cell density can stop spontaneous activity all together, but there is no cell density at which spontaneous activity would be asynchronous and irregular⁴⁹⁸. To sustain spontaneous activity, one needs a plating density of at least 250 neurons/mm², correspondingly a living cell density of at least 50 neurons/mm²²¹³. This indicates that the robust emergence of asynchronous and irregular activity is related to pushing the system to a different dynamical regime. If this is the case, stimulation during development might be the key ingredient for setting up specific and designed circuits and is a new tool in the toolbox of synthetic neurobiology.

Providing a developing culture with external input is a developmental circuit manipulation tool, resembling the mechanisms at work in the living brain³³². In contrast to other techniques as micro contact printing (the technique used in **chapter 4**), external input seems a natural choice to manipulate neuronal circuits. Other well established techniques to manipulate the connectome *in vitro* involve patterned surfaces to constrain the topology, either by topography or by chemical means. (1) Chemical patterning methods were introduced in 1965 by adhering fibroblasts to palladium islands evaporated onto a poly-acetate surface⁶⁹. Adhesion promoting molecules can then be transferred to the pattern²⁵¹. Another method is the patterned deposition of adhesion promoting proteins through silane- or alkanethiol based surface chemistry^{345,425,515}. Here, the properties of alkanethiolate monolayers on a substrate are altered through UV-Light exposure, which causes the oxidization to alkanesulfonate, thus altering its solubility. In a second step the exposed area can be linked to a second molecular layer by immersion, creating another monolayer on top of the first¹²⁰. These self-assembled monolayers (SAM) have been used to grow dissociated rat hippocampal neurons on circuit-like patterns⁴⁵³. SAMs of silanethioles have been used likewise to direct cell growth²⁹⁷. Uniformly coated MEA culture

chambers with Poly(L-lysine)-grafted-poly(ethylene glycol) (PLL-g-PEG), a polymer that has cell repelling properties, were locally freed from the polymer by electrical programmable desorption and in a multi process step subsequently coated with Poly-L-Lysine to establish a pattern of cell adhesive molecules. This method was developed for printing patterns of alkanethiolates on a gold substrate²⁵⁹, and has been used afterwards to topographically confine cell growth of neurons on a glass substrate^{73,220,230,231,265}. Using the cell repelling properties of Polyethylenglycol (PEG) through a photo-lithographic process was also shown to effectively direct cell growth²⁵⁹. More recently, seminal work on patterning using carbon nanotubes has been performed by the group of Yael Hanein⁴³⁶ where islands of carbon nanotubes lead to the preferential growth of clusters of neurons over the electrodes. These techniques have been used for confining cells to uniform patterns of rectangular, striped or triangular shape^{55,178,221,231,285,297,470,493,494}. (2) Lithographic methods with a precision down to tens of nm^{186,426} also allowed to grow neuronal cells on the bottom of deep pits on a silicon substrate and recorded through metal microelectrodes³⁰¹. Three-dimensional (3D) microfluidic arrays of poly-dimethylsiloxane (PDMS) were also used to confine cell topology to a certain pattern^{372,400} and were directly structured on silicon wafers using a negative photo resist¹⁰⁹. Building on the results of these experiments, defined networks of cultured neurons from the pond snail *Lymnaea stagnalis* have been grown in micro-structured polyester photo resist on a silicon substrate to study interconnected nerve cell pairs using electrophysiological methods²²². The method developed here complements these patterning techniques and might be the key ingredient to precisely manipulate the connectome of neuronal circuits *in vitro*.

What can we learn from circuits in a dish? One-dimensional neuronal cultures provide a platform to study the propagation speed of neuronal signals²¹⁶ and glial islands on which monolayers of neurons or single neurons are grown are widely used in electrophysiological studies^{60,264}. One has to be cautious about the implications of such research, considering that the circuits formed in a dish are substantially more disorganized than the precision wiring of the intact brain. Yet, cultures of neurons resemble to some extent *in vivo* neural tissue in structural features²⁰², activity^{88,366} and development²⁷⁵. Further, it has been shown that networks of dissociated cortical networks can store information²²⁹ and perform computational tasks as blind source separation²¹¹. They offer a simple, robust and very controllable model system for developing circuits. Our results specifically show the substantial influence of patterned activity during development for functional aspects of neuronal circuits. The asynchronous and irregular activity, that we observed, has long been considered a specific aspect of the precise cortical architecture in a healthy animal. Studies *in vivo* or *ex vivo* were restricted to the analysis of pathologies of activity patterns. We can, for the first time, design particular activity patterns, and study their influence on the development of circuits, an experiment that is impossible in the intact brain.

6.5 Materials and Methods

MEAs and Cell Culture

We used commercially available multielectrode arrays (60MEA200/30iR-Ti; Multi Channel Systems, Reutlingen, Germany) after coating the surface with Poly-D-Lysine. To this end, we add 1 ml of a 50 µg/ml solution into the well of a MEA. The PDL solution was left on the MEAs and coverslips for at least 24 h. Typically, we prepared MEAs and coverslips a few days in advance, and stored them with PDL solution in an incubator in the dark at 37°C and 5% CO₂.

Cell cultures were prepared according to Brewer⁵⁹. Briefly, cortical neurons were obtained from Wisteria WU rat embryos at 18 days of gestation (E18). The pregnant rat was anes-

thetized with CO₂. The embryos were removed by a cesarean section, decapitated and transferred to cooled petri dishes. The skull cavity was opened and the brain removed. Cortices were surgically extracted with iris scissors, and transferred to ice cold HEPES (Invitrogen, Germany) buffered Neurobasal (Gibco) medium. The supernatant was removed and the extracted cortices were trypsinized in a Trypsin/EDTA (trypsin: 0.05%; EDTA: 0.02%; Sigma Aldrich, Taufkirchen, Germany) buffer for 15 minutes at 37°C. Trypsinized cells were then transferred to a 10% fetal calf serum (FCS) in Neurobasal (Gibco) solution. Thorough trituration using a syringe and a needle with a diameter of 1 mm followed. The cell suspension was then centrifuged at 1200 rpm for 2 minutes. The pellet was re-suspended in serum-free B27/Neurobasal (Gibco) medium supplemented with Glutamax and Basic Fibroblast Growth Factor (bFGF). Cells were counted with a Neubauer improved counting chamber. A droplet of ≈ 100 μ l cell suspension containing 1.000.000 cells was added on top of the electrode field of the MEAs. The MEAs were then kept in an incubator providing a humidified atmosphere with 5% CO₂ at 37°C for 4 hours to allow the cells to settle. 1 ml of the B27/Neurobasal medium was then added to the cell chamber. After two days, we added 1 μ l of a solution, containing 3.4×10^{10} genome copies (GC) each of AAV9-hSyn-hChR2(H134R)-eYFP-WPRE-hGH AAV1.Syn.NES.jRCaMP1a.WPRE.SV40 (UPenn Vectorcore). Cultures were then directly placed on the light disco. Controls were kept in darkness¹. Half of the medium was changed every seven days. All animals were kept and bred in the animal house of the Max Planck Institute of Experimental Medicine according to European and German guidelines for experimental animals. We kept cultures until three weeks of age, when most developmental measures saturate. We used cortical cultures as the cell yield is higher than hippocampal cultures⁷⁹.

The light disco

We designed the light projection apparatus, the light disco, from components easily available in any laboratory. It consists of a LED array comprising 256 high luminance LEDs (Typ 19-213/B7C-AQ2S1B2/3T, Everlight Electronics, Karlsruhe, Germany), that are controlled by an Atmega 2560 (ATMega 2560-16AU AVR-RISC-Controller, Reichelt Elektronik, Sande, Germany). This chip provides 54 digital input/output pins and is tacked with a 16 MHz crystal oscillator. We use 32 of the digital output pins to control the 16×16 LEDs multiplexed at 10 kHz, well above the time constant of ChR2. The LED-drivers are two 8-channel ULN2803 sink drivers (ULN2803-D 8 channel Darlington sink driver, Reichelt Elektronik, Sande, Germany) and two 8-channel UDN2981 source drivers (A 2982 SLW-T Treiber IC, SO-20W, Reichelt Elektronik, Sande, Germany). The Atmega is programmed with a FT232 USB-serial converter (FT232RL USB UART IC, SSOP 28, Reichelt Elektronik, Sande, Germany). The entire system fits in an incubator, see **Fig. 6.8**. The LED array is positioned 20 cm away from a 45 deg mirror ($40 \times 30 \times 1.3$ mm coated Aluminium on glass, Astromedia, Germany), 3 cm above which a lens assembly with focal length $f=16$ mm and 21.4 mm aperture (16/21.4 mounted condenser combination, Spindler and Hoyer, Göttingen, Germany) projects the image in 1.7 cm distance on a MEA. The lens assembly, the mirror and the electronics are housed in a 3D printed gas-tight box.

We measured absolute light intensities with a calibrated photodiode (Type S2386-8K, Hamamatsu, Japan) that produces 274 mA/W at 470 nm illumination. We measure currents with a Keithley 2100 shortcircuiting the diode. We use this method, rather than a transimpedance amplifier and clamping the diode to 0 V, because this is how the diode was calibrated by Hamamatsu. We analyze the spatial organization of the holograms with the light sensitive chip of a commercial webcam, a Logitech C210, glued on a piece of glass with the size of a MEA. The

¹Pun intended.

sensor of this camera is a SIV100B, a 1/7" VGA/ISP CMOS chip with an integrated RGB color filter, 8 bit output, a pixel size of $3.2 \mu\text{m} \times 3.2 \mu\text{m}$ and a resolution of 640×480 pixels. Notably, every pixel has only one type of color filter on it, and color information is interpolated from that. Throughout the measurement, we fixed the exposure time and the gain of the CMOS with video for linux 2 (v4l2) to the smallest possible value.

6. DEVELOPMENTAL MANIPULATION OF THE SURROGATE CORTEX

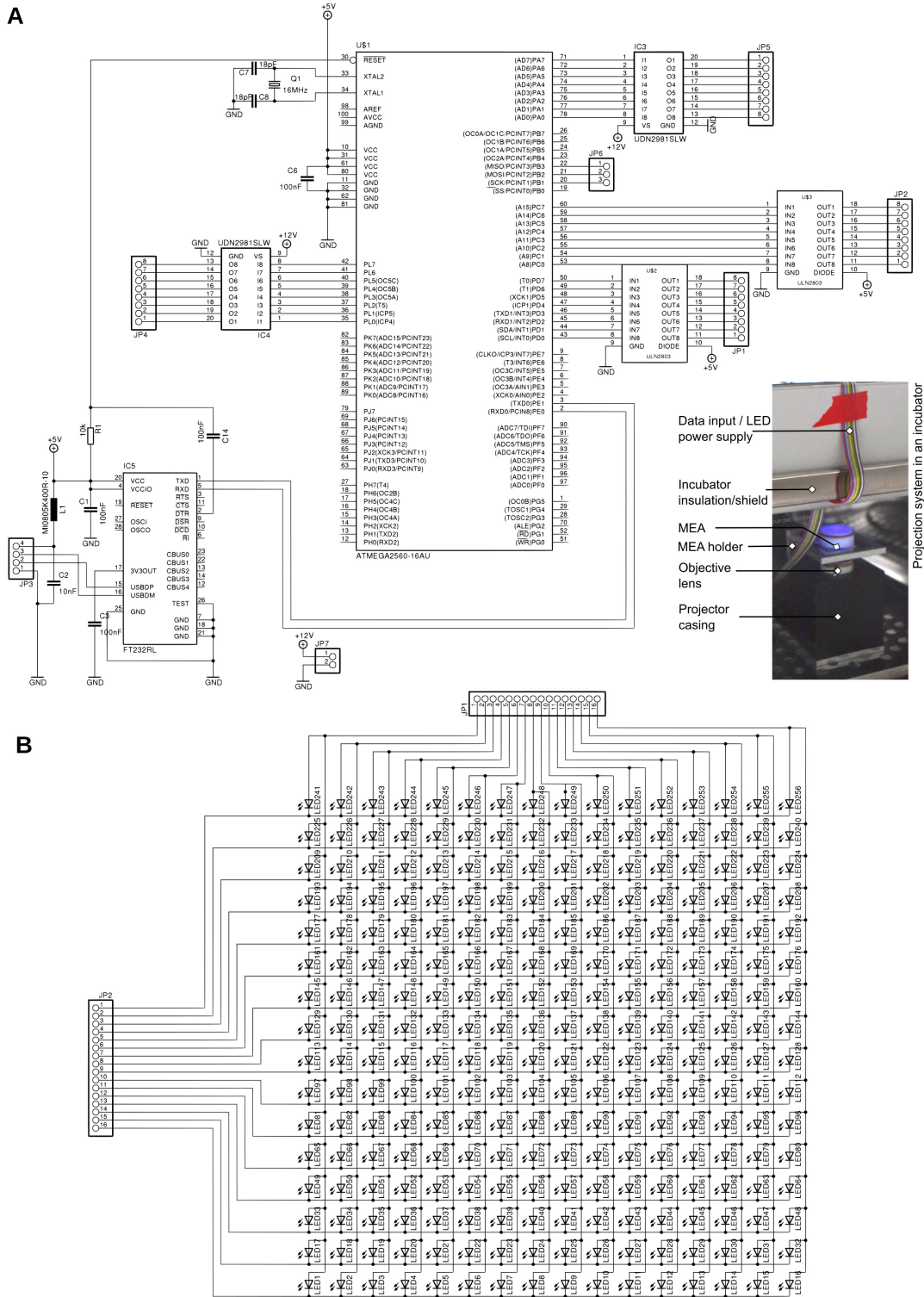


Figure 6.8: **The circuit of the light disco.** **A** An Atmega 2560 drives a series of ULN2803 and UDN2981 source drivers, that can generate the required current to operate the LED array. The ULN2803 is a low side driver to provide a current sink to ground. UDN2981 a high side driver to provide a current source. The FT232 is a USB to serial converter, connected serially to the Atmega and via USB to a Laptop (not shown). The inset shows the system in operation. Power/data is supplied by a rainbow colored ribbon cable that fits between the rubber seal and the door of the incubator. **B** The LED array.

Challenges to the common design

“The eye of man, with its pretty good accommodation, its fovea, its miscellaneous yellow filters, and its capacity for color vision, possesses in substantial degree the physiological capabilities of the standard sauropsidan eye as we see it in the lizard or the bird. But it has gained these powers through a lengthy process of re-differentiation, which was carried out largely within the confines of the primate order itself.”

Gordon Walls⁵⁰¹: “The vertebrate eye and its adaptive radiation”.

7.1 Content

In this chapter, we use an additional approach to study the organization principles of visual cortical circuits.

In the first section, we take the random wiring hypothesis for granted and construct ganglion cell mosaics that could within this framework seed iso-orientation domains in the visual cortex. We then compare the predictions of this model with data from cat and primate ganglion cell mosaics which imposes a strong quantitative constraint on the random wiring hypothesis. These studies further highlight that the assumptions of the previous chapters were justified and that the universality of self-organization is a simple and compelling explanation for the ubiquity of the common design. In the second section, we use the reinvention of color vision among primates as a natural laboratory experiments to study the selective forces that favor the common design. Trichromatic vision might have been one of the most fundamental and most recent changes in visual cortical circuitry potentially challenging the common design.

7.2 The random wiring hypothesis revisited

Here we study whether it is in principle possible for retinal ganglion cell mosaics to seed iso-orientation domains in the visual cortex. As presented in **chapter 3**, several studies explained the emergence of roughly periodic orientation preference maps (OPMs) in the primary visual cortex (V1) of carnivores and primates by a random wiring mechanism in which input to V1 neurons is dominated by a small set of feed-forward projections from retinal ganglion cells (RGC). In this model, the typical column spacing of cortical OPMs arises via Moiré-Interference between hexagonal ON/OFF RGC mosaics and critically depends on long-range hexagonal order within these mosaics. Here, we introduce a novel method to infer RGCs mosaics that within the statistical wiring framework yield realistic OPMs. Inferred mosaics lack long-range positional order yet lead to aperiodic OPMs. They are characterized by specific angular correlations between ON/OFF ganglion cell pairs. Comparing the model prediction with ganglion cell mosaics of cats and primates allows us to calculate a strong quantitative constraint on the retinal influence on visual cortical OPMs.

7.3 Citation and original contribution

Manuel Schottdorf, Stephen J. Eglén, Fred Wolf, and Wolfgang Keil: “*Can Retinal Ganglion Cell Dipoles Seed Iso–Orientation Domains in the Visual Cortex?*”, PLoS ONE 9(1): e86139 (2014)⁴²⁷

I analyzed all data and performed the numerical simulations. I generated all figures and all tables, except Figure 6. I wrote the manuscript together with all authors.

Can Retinal Ganglion Cell Dipoles Seed Iso-Orientation Domains in the Visual Cortex?

Manuel Schottdorf^{1,2,3,4,5}, Stephen J. Eglen⁶, Fred Wolf^{1,2,3,4}, Wolfgang Keil^{1,2,3,4,7*}

1 Max Planck Institute for Dynamics and Self-Organization, Göttingen, Germany, **2** Institute for Nonlinear Dynamics, University of Göttingen, Göttingen, Germany, **3** Bernstein Center for Computational Neuroscience, Göttingen, Germany, **4** Bernstein Focus for Neurotechnology, Göttingen, Germany, **5** Institute for Theoretical Physics, University of Würzburg, Würzburg, Germany, **6** Department of Applied Mathematics and Theoretical Physics, Cambridge Computational Biology Institute, University of Cambridge, Cambridge, United Kingdom, **7** Center for Studies in Physics and Biology, The Rockefeller University, New York, New York, United States of America

Abstract

It has been argued that the emergence of roughly periodic orientation preference maps (OPMs) in the primary visual cortex (V1) of carnivores and primates can be explained by a so-called statistical connectivity model. This model assumes that input to V1 neurons is dominated by feed-forward projections originating from a small set of retinal ganglion cells (RGCs). The typical spacing between adjacent cortical orientation columns preferring the same orientation then arises via Moiré-Interference between hexagonal ON/OFF RGC mosaics. While this Moiré-Interference critically depends on long-range hexagonal order within the RGC mosaics, a recent statistical analysis of RGC receptive field positions found no evidence for such long-range positional order. Hexagonal order may be only one of several ways to obtain spatially repetitive OPMs in the statistical connectivity model. Here, we investigate a more general requirement on the spatial structure of RGC mosaics that can seed the emergence of spatially repetitive cortical OPMs, namely that angular correlations between so-called RGC dipoles exhibit a spatial structure similar to that of OPM autocorrelation functions. Both in cat beta cell mosaics as well as primate parasol receptive field mosaics we find that RGC dipole angles are spatially uncorrelated. To help assess the level of these correlations, we introduce a novel point process that generates mosaics with realistic nearest neighbor statistics and a tunable degree of spatial correlations of dipole angles. Using this process, we show that given the size of available data sets, the presence of even weak angular correlations in the data is very unlikely. We conclude that the layout of ON/OFF ganglion cell mosaics lacks the spatial structure necessary to seed iso-orientation domains in the primary visual cortex.

Citation: Schottdorf M, Eglen SJ, Wolf F, Keil W (2014) Can Retinal Ganglion Cell Dipoles Seed Iso-Orientation Domains in the Visual Cortex? PLoS ONE 9(1): e86139. doi:10.1371/journal.pone.0086139

Editor: Jacob Engelmann, Universität Bielefeld, Germany

Received: May 2, 2013; **Accepted:** December 6, 2013; **Published:** January 24, 2014

Copyright: © 2014 Schottdorf et al. This is an open-access article distributed under the terms of the Creative Commons Attribution License, which permits unrestricted use, distribution, and reproduction in any medium, provided the original author and source are credited.

Funding: This work was supported by the HFSP (<http://www.hfsp.org>), BMBF (<http://www.bmbf.de>), DFG (<http://www.dfg.de>), and the MPG (<http://www.mpg.de>); Grant numbers SFB 889, BFL 01GQ0921, 01GQ0922, BCCN 01GQ0430, 01GQ1005B, 01GQ07113 and BFNT 01GQ0811. This work was supported in part by the National Science Foundation (<http://www.nsf.gov>), grant number PHY05-51164. SJE was supported by a Wellcome Trust program grant (083205/B/07/Z). The funders had no role in study design, data collection and analysis, decision to publish, or preparation of the manuscript.

Competing Interests: The authors have declared that no competing interests exist.

* E-mail: wkeil@mail.rockefeller.edu

Introduction

Many neurons in the primary visual cortex (V1) respond preferentially to edge-like stimuli of a particular orientation [1]. In carnivores and primates, orientation preference exhibits a columnar arrangement such that neurons positioned on top of each other from the white matter to the pia typically prefer similar orientations. Tangential to the visual cortical layers, orientation preference changes smoothly and progressively [1] except at the centers of so-called pinwheels where neurons exhibiting the whole range of orientation preferences are located in close vicinity [1,2]. The progression of orientation preferences across the visual cortical surface (Orientation preference map, OPM) appears as organized by a semiregularly spaced system of pinwheels and adjacent columns preferring the same orientation over roughly a millimeter distance [3–11].

Most models for the emergence of OPMs during postnatal development assume that their layout is determined by intracortical mechanisms (e.g. [12–17]). However, several recent studies advance the notion that the structure of OPMs may result from a statistical wiring of feed-forward inputs from the mosaic of ON/

OFF retinal ganglion cells (RGCs) to V1 [18–21] (Fig. 1A), an idea pioneered by Soodak [22,23]. ON/OFF ganglion cells are arranged in semiregular mosaics across the retina and project to the lateral geniculate nucleus (LGN) of the thalamus. Thalamic receptive fields resemble RGC receptive fields in shape, size, and spatial distribution [24,25]. The retinotopic map [26–29] allows neighboring retinal/thalamic ON and OFF center cells to project to neighboring neurons in the primary visual cortex. Most nearest neighbor RGCs are ON/OFF pairs [30]. According to the statistical connectivity model, a V1 neuron predominantly samples feed-forward inputs from geniculate projections in its immediate vicinity [31]. If so, it is likely to receive input from a single pair of ON/OFF RGCs, a so-called *dipole* [20] (Fig. 1A, left). The neuron's receptive field would then be dominated by one ON and one OFF subregion (Fig. 1A, middle left) and its response orientation-tuned [18–20]. In this picture, the preferred orientation is determined by the orientation of the RGC dipole (Fig. 1A, middle right, right). Consequently, a key prediction of the statistical connectivity model is that orientation preference across the surface of the primary visual cortex should mirror the spatial

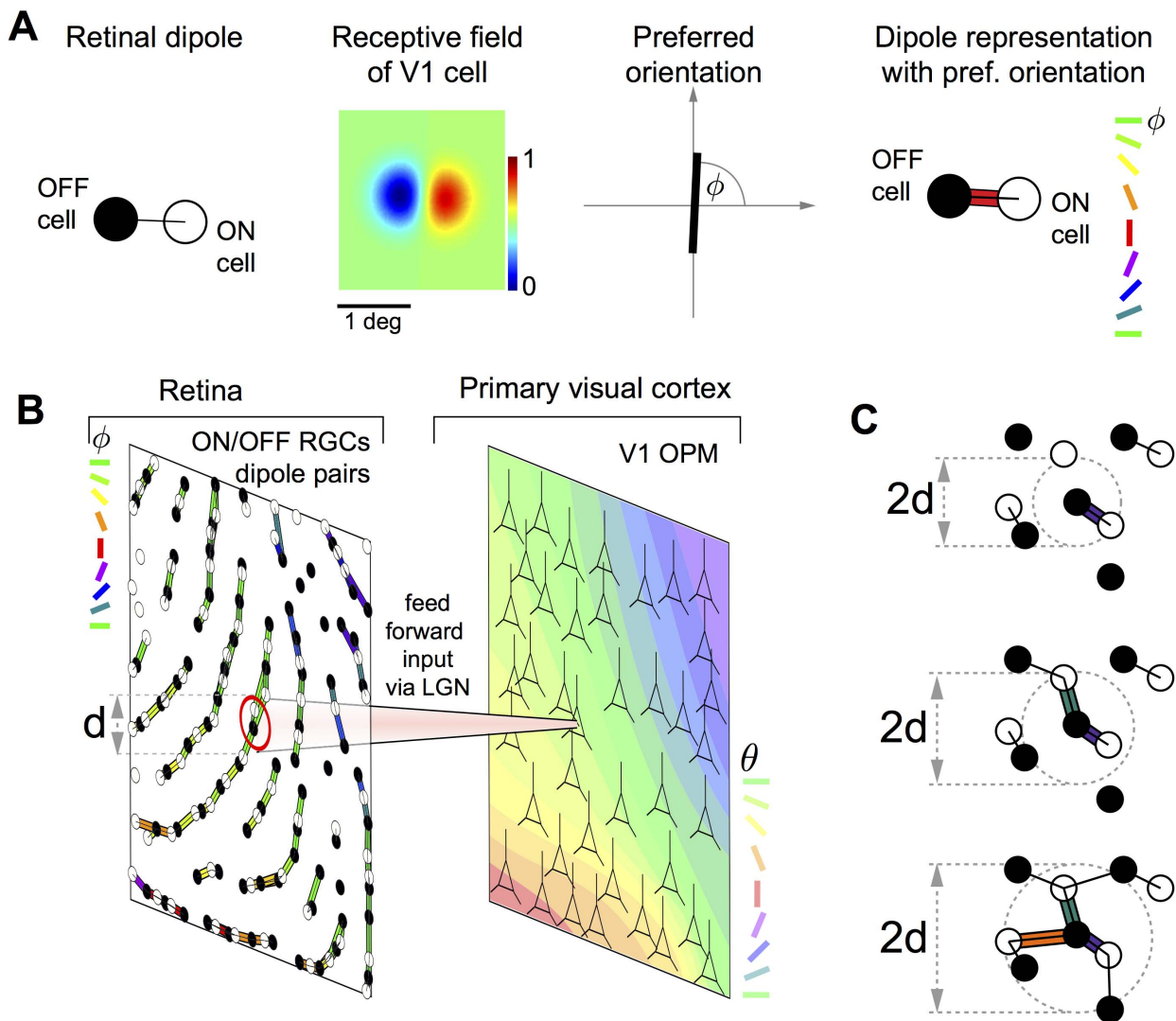


Figure 1. RGC dipoles and the statistical wiring model according to [20]. **A** Most left: A dipole of an ON center (empty circle) and OFF center (filled circle) retinal ganglion cell (RGC). The black line connecting the two cells indicates that the two cells form a dipole. A V1 cell with input dominated by this dipole has a receptive field with side-by-side subregions of opposite sign (middle left) and is consequently tuned to a specific orientation ϕ (middle right). We represent the preferred orientation of the V1 cell by the *color* of the bar connecting the two RGCs (most right). Note that the preferred orientation of the V1 is orthogonal to the bar connecting the two RGCs. **B** The statistical connectivity model for orientation preference maps. The receptive field midpoints of ON/OFF center RGCs are arranged in semiregular mosaics. The input to a cortical cell is dominated by a single pair of ON/OFF dipole and the cortical units have oriented receptive fields. If RGC dipole orientations are locally correlated, orientation preference θ within layer 4 of V1 is predicted to vary smoothly resulting in a smooth and continuous map of orientation preferences. **C** Parametrized definition of RGC dipoles. ON/OFF pairs with distance smaller than a parameter d are considered dipoles (black lines). For the centered OFF cell, preferred orientations of dipoles are indicated. With increasing d , the number of dipoles increases and one RGC can form multiple dipoles. doi:10.1371/journal.pone.0086139.g001

distribution of the ON/OFF dipole angles in the RGC mosaics [18,20,22,23] (Fig. 1B).

Paik and Ringach [20,21] showed how this model can explain the experimentally observed roughly periodic structure of visual cortical OPMs. In their model, ON and OFF cell mosaics are assumed to form two independent noisy hexagonal lattices. Superposing these two lattices leads to a hexagonal pattern of dipole orientations via Moiré interference [32]. The statistical connectivity hypothesis then implies that this hexagonal pattern is mapped onto the cortex creating a roughly hexagonal OPM [20].

Hore et al. recently cast substantial doubts on the presence of hexagonal order in experimentally measured RGC receptive field

mosaics [33]. They found that the positions of receptive fields of ON/OFF RGCs in monkey retina are inconsistent with long-range hexagonal order and are much better described by a so-called pairwise interacting point processes (PIPP) in a parameter regime where long-range positional correlations are absent [33–35]. Such PIPP mosaics lack the long-range order necessary to create a Moiré-Interference pattern and hence OPMs predicted by the statistical connectivity model with PIPP mosaics do not exhibit the experimentally observed spatially repetitive arrangement of orientation columns [18,19,33].

Moiré-Interference of hexagonal RGC lattices constitutes one particular way of creating an ordered arrangement of regularly

spaced orientation columns in the statistical connectivity model. Other spatial arrangements of RGCs are conceivable that might lead to spatially repetitive cortical orientation maps resembling the ones experimentally measured. Therefore, the lack of hexagonal structure in RGC mosaics found by Hore et al. does not *per se* dismiss the statistical connectivity hypothesis.

Here, we investigate a fundamental requirement on the spatial structure of RGC mosaics to seed the emergence of spatially repetitive cortical OPMs: a spatial correlation of RGC dipole angles across the retina. RGC dipole angle correlations are predicted to exhibit a spatial structure similar to that of OPM autocorrelation functions. This means that RGC dipole angles have to be locally positively correlated and anti-correlated on intermediate scales. The precise values for both of these scales depend on the column spacing of the OPM as well as the cortical magnification factor. We first systematically analyze two previously published mosaics of cat beta cell somata positions [30,35] as well as one primate parasol mosaic of RGC receptive field centers [36] with respect to their dipole angle correlation functions. In both species, we are unable to detect any statistically significant positive or negative correlation. Since all three mosaics analyzed each contain only around 100 cell positions (or RFs center positions), the absence of detectable correlations might be a consequence of the small size of the data sets. To address this question, we introduce a novel point process that generates mosaics with a tunable degree of spatial correlations of dipole angles. The spatial structure of these angular correlations is designed such as to match the autocorrelation functions of experimentally measured OPMs. At the same time, the local spatial statistical properties of the resulting model RGC mosaics agree well with the experiment. On the one hand, the mosaics generated by this process demonstrate that hexagonally organized RGCs are indeed not necessary to obtain realistic OPMs within the statistical connectivity model. On the other hand, the mosaics generated by the point process can be used as reference mosaics to access the amount of data needed to detect the presence or absence of correlations. Finally, by statistical comparison of mPIPP model mosaics and data, we show that, given the size of our data sets, the presence of even weak angular correlations in the data can be ruled out. We conclude, that the layout of ON/OFF ganglion cell mosaics apparently lack a fundamental feature necessary to explain the emergence of spatially repetitive orientation preference maps in V1 within the dipole approximation of the statistical connectivity model. Our results suggest that the ordered arrangement of orientation columns is unlikely to originate from the spatial layout of RGCs and, hence, likely set by intracortical mechanisms.

Results

Dipole Orientation Correlation Function in Cat and Primate RGC Mosaics

We first determined the correlation function of dipole orientations in the two published cat beta cell mosaics. These mosaic fields will be referred to by their keys: w81s1 and m623. Field w81s1 was created by digitizing the map shown in Figure 6 of [30]. Field m623 was taken from [35]. To limit the restriction of considering only nearest neighbor ON/OFF cells pairs, we followed the flexible dipole definition introduced in [37] (Fig. 1C). In this definition, a parameter d is introduced, describing a distance below which neighboring pairs of ON/OFF cells are considered as dipoles (see Eq. (4)). The larger d , the more dipoles are formed by each RGC cell (cf. Fig. 1C). The nearest neighbor distance distribution of the mosaic defines a

range of sensible d -values for each mosaic. For instance, the nearest neighbor distribution of cat beta cell mosaics peaks around $60\mu\text{m}$ [30] and, therefore, d -values smaller than $60\mu\text{m}$ lead to the extraction of only very few dipoles. On the other hand, values larger than $100\mu\text{m}$ lead to many dipoles between non-nearest neighbors.

Figures 2A–C show the m623 mosaic along with all the dipole pairs, color-coded according to their orientation extracted for $d=60\mu\text{m}$ (A), $d=80\mu\text{m}$ (B), and $d=100\mu\text{m}$ (C) (see Materials and Methods). Figures 2D–F display the dipoles found for the mosaic w81s1. For $d=80\mu\text{m}$ and $100\mu\text{m}$, dipoles in both mosaics appear as organized into linear chains which, at first sight, one might take as an indication of spatial correlation in the dipole orientations [37]. However, a quantitative analysis reveals that such correlations are absent for all d -values (Figs. 2G–J). The only statistically significant correlation present in both mosaics is a weak anti-correlation on very short scales ($<100\mu\text{m}$) for $d=100\mu\text{m}$. This finding will be explained in more detail below.

The two mosaics analyzed so far are based on the position of cell bodies and not those of the actual RGC receptive fields. Since these two do not match necessarily, it is important to test whether RGC receptive field mosaics substantially differ from cell position mosaics with respect to their dipole correlation structure. Therefore, we next repeated the above analysis for a previously published primate parasol cell receptive field mosaic (referred to by its key G09 [36] in the following). Figures 3A–C show the G09 mosaic along with all the dipole pairs, color-coded according to their orientation extracted for $d=60\mu\text{m}$ (A), $d=80\mu\text{m}$ (B), and $d=100\mu\text{m}$ (C). Again, a quantitative analysis reveals that dipole angular correlations are absent for all d -values (Figs. 3D–F).

To analyze local correlations more systematically, we varied the parameter d for all three mosaics in the data set over the entire range of sensible values and determined angular correlations in each of the mosaics in the first distance bin (see Materials & Methods). Figures 4A and B depict the results of this analysis. Interestingly, for small d -values, all mosaics exhibit a weakly positive local correlation, whereas for larger d -values dipoles appear anti-correlated in all three mosaics (see Fig. 2J for an example). Intuitively, this dependency of correlation values can be understood as a consequence of our flexible dipole definition together with a typical distance between nearest neighbor RGC (Fig. 4A). For small and intermediate d -values, an ON-cell positioned between several OFF-cells forms dipoles with mostly one or two of them. If dipoles are formed with two OFF cells, due to the regular spacing of OFF cells, the angles formed by these two dipoles are likely positively correlated (Fig. 4A, left inset). For larger d -values, more than two dipoles are typically formed. In this case, the regular spacing leads to an effective anti-correlation between their angles (Fig. 4A, right inset). To investigate whether such correlations suffice to seed the development of spatially repetitive and smooth OPMs in V1, we compared the correlation traces found in the experimentally measured mosaics to model mosaics obtained by a pairwise interacting point process (PIPP) [33,34]. The PIPP is a method for the generation of a spatial distribution of points specifying only pairwise interaction between individual points. It has been previously shown to accurately reproduce the spatial statistics of experimentally measured RGC mosaics [33,34]. With parameters fitted to experimental data, the PIPP generates regularly spaced RGC mosaics with radially isotropic autocorrelograms and lack of long-range positional order [33]. For such mosaics, the statistical connectivity framework predicts OPMs that lack a typical column spacing and are qualitatively different from experiment [18,33]. Figures 4D,E show that the local correlation of dipole angles in the model

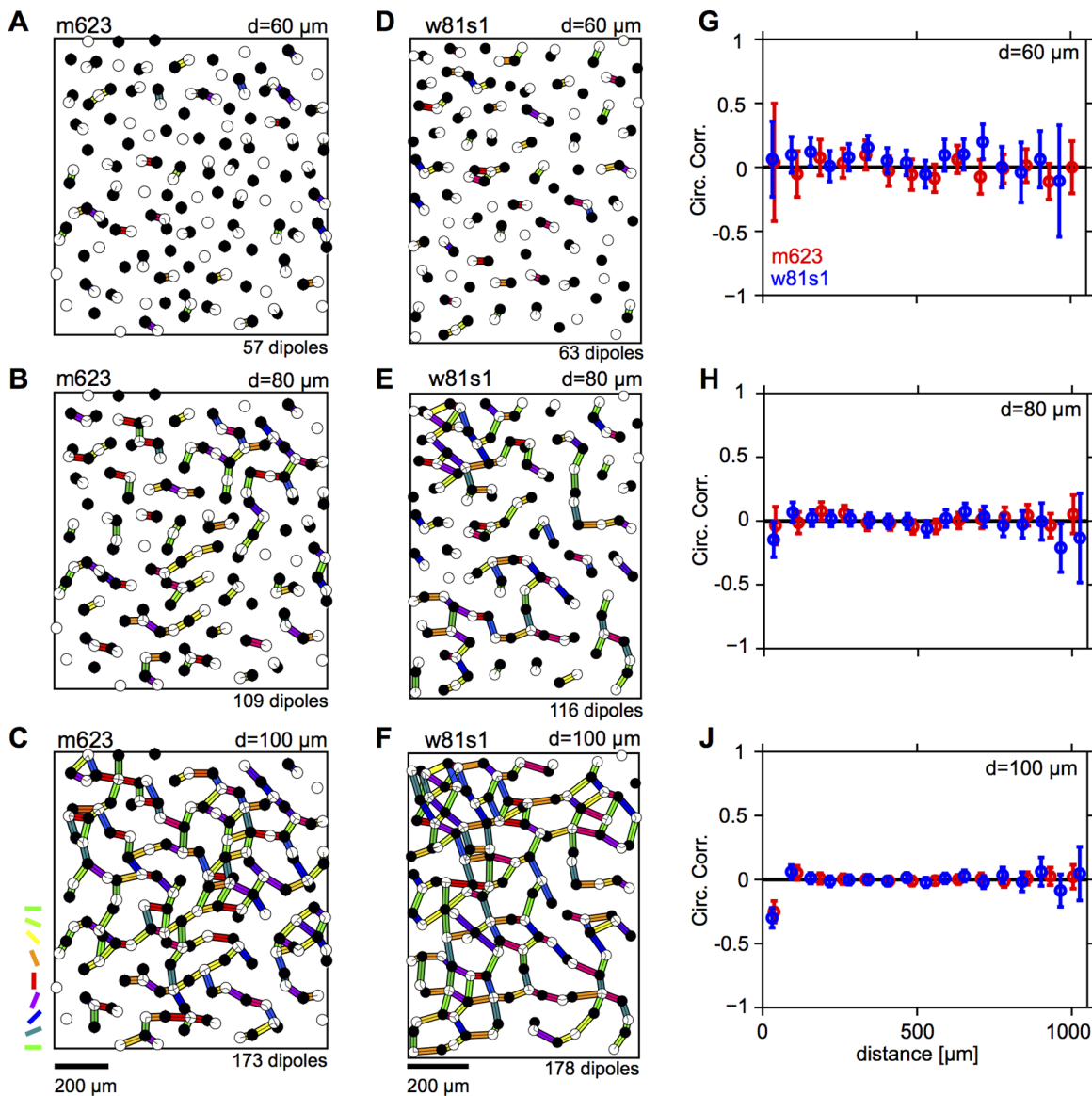


Figure 2. Spatial correlations of dipole orientations are absent in cat beta cell mosaics. **A** ON/OFF cells (empty/filled circles) for the cat beta cell mosaic m623 [35]. Preferred orientation of dipoles extracted for $d=60 \mu\text{m}$ are shown as colored bars. Colorcode as in Fig. 1C. **B** as A but for $d=80 \mu\text{m}$. **C** as A but for $d=100 \mu\text{m}$. **D–F** as A–C but for cat beta cell mosaic w81s1 [35]. **G** Correlation of dipole orientations for m623 (red) and w81s1 (blue), calculated from dipoles extracted for $d=60 \mu\text{m}$. Error bars indicate 95% confidence intervals of bootstrap distributions. **H** as G but for $d=80 \mu\text{m}$. **J** as G but for $d=100 \mu\text{m}$.
doi:10.1371/journal.pone.0086139.g002

mosaics exhibit the same d -dependence as the data. For small d -values mosaics exhibit a weakly positive local correlation, whereas for larger d -values dipoles are weakly anti-correlated. We conclude that the weak local correlations found in experimental mosaics are a consequence of our flexible definition of RGC dipoles together with a typical spacing between neighboring cells. The quantitative match between PIPP mosaics and experimental data together with the fact that PIPP mosaics seed unrealistic cortical OPMs in the statistical connectivity model indicate that these correlations are not sufficient to explain the layout of realistic cortical OPMs.

An OPM-modulated Pairwise Interacting Point Process

One might wonder whether the absence of detectable positive or negative correlations in dipole angles is merely a consequence of the small sizes of each of these data sets. In fact, all three mosaics analyzed each contain only about 100 cell positions (or RF center positions) and a similar number of dipoles. To clarify whether such small data sets are sufficient to detect both relevant dipole correlations, it is necessary to design model mosaics, e.g. defined by a some point process, with realistic spatial statistics and with a known degree of dipole angle correlations. Using such a point process, one can then ask whether the size of the available data sets in principle permits detection of such correlations. However, up to this point, a suitable point process with a known degree of dipole

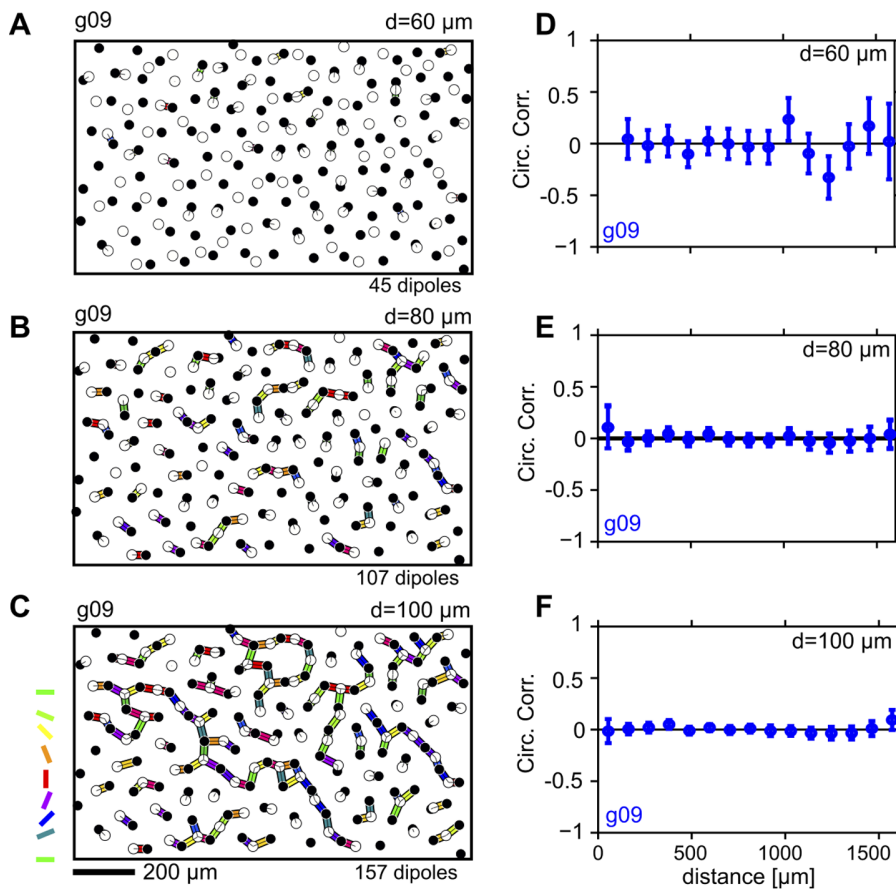


Figure 3. Spatial correlations of dipole orientations are absent in a primate parasol receptive field mosaic. **A** ON/OFF cells (empty/filled circles) for primate parasol cell receptive field mosaic G09 [36]. Preferred orientation of dipoles extracted for $d=60\ \mu\text{m}$ are shown as colored bars. Colorcode as in Fig. 1C. **B** as A but for $d=80\ \mu\text{m}$. **C** as A but for $d=100\ \mu\text{m}$. **D** Correlation of dipole orientations for mosaic G09, calculated from dipoles extracted for $d=60\ \mu\text{m}$. Error bars indicate 95% confidence intervals of bootstrap distributions. **E** as D but for $d=80\ \mu\text{m}$. **F** as D but for $d=100\ \mu\text{m}$. doi:10.1371/journal.pone.0086139.g003

angle correlations has not been proposed. We now introduce a pairwise interacting point process (PIPP) with such characteristics, and start by briefly outlining the definition of the conventional PIPP for RGC mosaics as introduced in [34].

The PIPP is a method for the generation of a spatial distribution of points specifying only pairwise interaction between individual points. Interactions between points are usually specified in pairwise interaction functions. The product of these pairwise interaction functions for a specific location for all possible pairs of points gives the probability of finding a point at a particular position. For bivariate data such as the positions \mathbf{x}_{ON}^i and $\mathbf{x}_{\text{OFF}}^j$ of a mosaic of ON-cells and a mosaic of OFF-cells, the PIPP is characterized by two intra-mosaic interaction functions $h_{\text{ON,ON}}(|\mathbf{x}_{\text{ON}}^i - \mathbf{x}_{\text{ON}}^j|)$, $h_{\text{OFF,OFF}}(|\mathbf{x}_{\text{OFF}}^i - \mathbf{x}_{\text{OFF}}^j|)$ and one inter-mosaic interaction $h_{\text{ON,OFF}}(|\mathbf{x}_{\text{ON}}^i - \mathbf{x}_{\text{OFF}}^j|)$. To describe the positioning of beta cells in the cat retina, Eglon et al. [34] used a parametric form of repulsion

$$h(r) = \begin{cases} 0 & \text{if } r \leq \delta \\ 1 - \exp\left(-\left|\frac{r-\delta}{\varphi}\right|^z\right) & \text{if } r > \delta \end{cases}$$

for all three interaction functions, with $r = |\mathbf{x}_{\text{ON}}^i - \mathbf{x}_{\text{ON}}^j|$, $r = |\mathbf{x}_{\text{OFF}}^i - \mathbf{x}_{\text{OFF}}^j|$ or $r = |\mathbf{x}_{\text{ON}}^i - \mathbf{x}_{\text{OFF}}^j|$ for $h_{\text{ON,ON}}$, $h_{\text{OFF,OFF}}$ or $h_{\text{ON,OFF}}$, respectively. By fitting the parameters α and φ to experimental data, they showed that inter-mosaic interactions are sufficiently described by solely ensuring that two cells are not less than the soma distance apart, i.e.

$$h_{\text{ON,OFF}}(r) = \begin{cases} 0 & \text{if } r \leq \delta \\ 1 & \text{if } r > \delta, \end{cases} \quad (1)$$

with δ being the soma diameter. Intra-mosaic interactions were best fit by values for α and φ which ensure a semiregular placement of RGC cells without long-range positional order [34]. Such mosaics lack non-local spatial order in their dipole angles and, hence, the statistical connectivity framework predicts orientation maps that lack a typical column spacing [18,33].

To introduce correlations of dipole angles into the PIPP, we start by formalizing the illustration in Fig. 1A. The dipole vector $\mathbf{x}_{\text{ON}}^i - \mathbf{x}_{\text{OFF}}^j$ between an ON/OFF pair of RGCs points in the direction $\arg(\mathbf{x}_{\text{ON}}^i - \mathbf{x}_{\text{OFF}}^j)$ in the interval $[-\pi, \pi)$. The preferred orientation of the dipole (Fig. 1A, most right) can then be mathematically expressed as

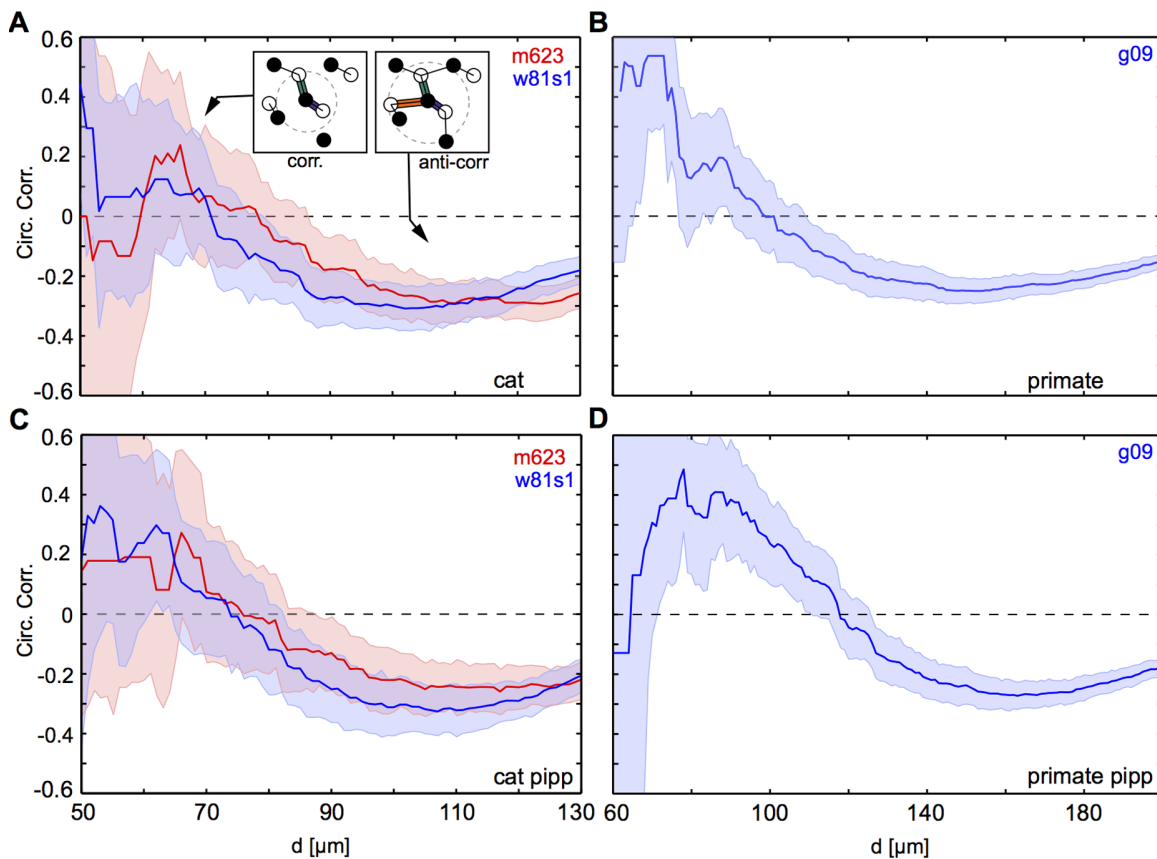


Figure 4. Measured local correlation values depend on choice of dipole distance parameter d . **A** Local correlations in cat beta cell mosaics (red: m623, blue: w81s1) as a function of the dipole extraction parameter d (see Fig. 1C). **B** As A but for primate parasol cell receptive field mosaic G09. **C** Weak local positive or negative correlations emerge in the same RGC configuration, depending on dipole extraction parameter d . **D** As A but for simulated PIPP mosaics with parameters fitted to cat beta cell mosaics m623 (red) and w81s1 (blue). **E** As B but for simulated PIPP mosaics with parameters fitted to primate parasol receptive field mosaics G09. All error bars indicate 95% confidence intervals of bootstrap distributions. doi:10.1371/journal.pone.0086139.g004

$$\phi(\mathbf{x}_{\text{ON}}^i, \mathbf{x}_{\text{OFF}}^j) = \text{mod}(\arg(\mathbf{x}_{\text{ON}}^i - \mathbf{x}_{\text{OFF}}^j) + \pi/2, \pi), \quad (2)$$

$$H_{\text{ON,OFF}}(\mathbf{x}_{\text{ON}}^i, \mathbf{x}_{\text{OFF}}^j) = h_{\text{ON,OFF}}(r) \cdot h_\gamma(\mathbf{x}_{\text{ON}}^i, \mathbf{x}_{\text{OFF}}^j). \quad (3)$$

varying in the interval $[0, \pi)$. The main idea is now to modify the inter-mosaic interaction function (Eq. (1)) to add a dipole correlational structure that matches the spatial correlations of orientation preferences in visual cortical OPMs. A visual cortical OPM can be represented as $\theta(\mathbf{x})$ with $\theta \in [0, \pi)$. Note that \mathbf{x} here describes positions on the retina. An OPM measured with optical imaging of intrinsic signals [3,38] is naturally given as $\theta'(\mathbf{X})$, where \mathbf{X} specifies cortical position. The retinotopic map $\mathbf{x} = \mathbf{R}(\mathbf{X})$ associates a cortical position \mathbf{X} with a position \mathbf{x} on the retina. Via the inverse transformation, the representation of the OPM in retinal coordinates is obtained, i.e. $\theta(\mathbf{x}) \equiv \theta'(\mathbf{R}^{-1}(\mathbf{x}))$. In the following, only small subregions of OPMs were considered and the retinotopic map was assumed to be linear.

Using the OPM representation $\theta(\mathbf{x})$, we modify the inter-mosaic interaction function Eq. (1) by multiplying it with a function $h_\gamma(\mathbf{x}_{\text{ON}}^i, \mathbf{x}_{\text{OFF}}^j)$ that depends on the difference between the preferred dipole angle $\phi(\mathbf{x}_{\text{ON}}^i, \mathbf{x}_{\text{OFF}}^j)$ and the preferred orientation specified in the OPM at position $(\mathbf{x}_{\text{ON}}^i + \mathbf{x}_{\text{OFF}}^j)/2$ (half way between the two RGCs):

We choose

$$h_\gamma(\mathbf{x}_{\text{ON}}^i, \mathbf{x}_{\text{OFF}}^j) = \begin{cases} \exp\{\gamma [\cos(\phi(\mathbf{x}_{\text{ON}}^i, \mathbf{x}_{\text{OFF}}^j) - \theta((\mathbf{x}_{\text{ON}}^i + \mathbf{x}_{\text{OFF}}^j)/2)) - 1]\} & \text{if } r \leq d \\ 1 & \text{if } r > d. \end{cases} \quad (4)$$

In addition to ensuring that two cells are not less than the soma distance apart, this new inter-mosaic interaction function enforces that the positioning of an ON cell at position \mathbf{x}_{ON}^i and an OFF cell at position $\mathbf{x}_{\text{OFF}}^j$ is such that the preferred orientation $\phi(\mathbf{x}_{\text{ON}}^i, \mathbf{x}_{\text{OFF}}^j)$ of the ON/OFF pair is similar to preferred orientation specified in the OPM at the corresponding point. In this way, the OPM $\theta(\mathbf{x})$ is expected to modulate the positioning of ON/OFF cells when numerically simulating the positioning of the RGC mosaics with a Monte-Carlo procedure [34] (Fig. 1D) such that preferred orientations of dipoles align with preferred orientations given in the OPM. Note that the preferred orientation

of a dipole is orthogonal to the dipole vector $\mathbf{x}_{\text{ON}}^i - \mathbf{x}_{\text{OFF}}^j$ (see Fig. 1A). With respect to the PIPP, this model has two additional parameters. The strength of modulation through the OPM is specified by a modulation parameter γ . If γ is zero, the positioning of ON/OFF pairs is not influenced by the OPM region and the model is equivalent to the PIPP model. The larger the value of γ , the stronger the penalty for OPM and dipole angle differing. We refer to the process specified by this inter-mosaic interaction function as *modulated PIPP* (mPIPP). The second parameter is the distance d below which neighboring pairs of ON/OFF cells are considered as dipoles (see Eq. (4)). This parameter is taken to be the same as the parameter for defining dipoles (cf. Fig. 1C). Again, the larger d , the more dipoles each RGC cell is assumed to form with surrounding cells (cf. Fig. 1C). The nearest neighbor distance distributions of the different mosaics imply sensible values for the choice of d .

We would like to emphasize that by defining the mPIPP as above, we by no means imply any influence of cortical orientation preference upon the positions of ON/OFF RGCs during postnatal development. The mPIPP merely is a phenomenological algorithm to attempt to “reverse engineer” one plausible realization of an RGC mosaic with the necessary spatial structure to yield an OPM with realistic spatial properties within the statistical connectivity model as considered in [20].

Statistical Characterization of mPIPP Mosaics

To characterize the mPIPP defined above, we first investigated how the positioning of ON/OFF RGC dipoles is altered by the modulation through realistic OPMs. To this end, we extracted small regions of previously published OPMs from cat area 17 (data courtesy of Z. Kisvarday, see Materials and Methods) and used them to modulate the PIPP according to the above description. Rectangular OPM regions must be chosen such that the size of the retinal region corresponding to the OPM fits the two cat beta cell somata position mosaics w81s1 and m623 [30,35]. Thus, the size of the extracted cortical region depends on the cortical magnification factor mm_c/mm_r at the position the mosaic has been recorded from. The larger the magnification factor, the larger the extracted cortical region has to be.

The center of mosaic w81s1 was located 19° below the mid line of the visual streak, 4mm from the area centralis [35]. The mosaic m623 has been obtained from 5 mm eccentricity and 5.5° below the mid line of the visual streak. Both fields are situated at positions in the visual field with similar cortical magnification factor (see Materials and Methods), estimated to be $\xi = 1.7\text{mm}_c/\text{mm}_r$, where mm_c is mm on the cortex and mm_r is millimeter on the retina. Both RGC fields are of similar linear extent ($\approx 1\text{ mm}$). Hence, extracted visual cortical regions were of $\approx 1.7\text{ mm}$ linear extent corresponding to an area of approximately 3 hypercolumns [9,39].

Figure 5A show mosaics obtained by simulating an mPIPP with a Monte-Carlo procedure for a cortical magnification of $\xi = 1.7\text{mm}_c/\text{mm}_r$, modulated by a cat OPM region for $\gamma = 0$ (left), $\gamma = 2.5$ (middle) and $\gamma = 30$ (right). ON/OFF pairs less than $d = 80\mu\text{m}$ apart were considered to form dipoles. All other parameters were chosen as in [34] for m623 (see also Table S1). In the case $\gamma = 0$ (original PIPP), the dipole orientations are not correlated with the preferred orientations specified in the OPM. For $\gamma = 2.5$, some dipoles tend to locally align their orientation to match the orientation preference given in the OPM but most dipoles have random orientations. For $\gamma = 30$, the dipole orientations are strongly correlated with preferred angles specified in the OPM. mPIPP realizations generally display fewer dipoles than the experimental mosaic m623 for the same d -values (cf. Fig. 2B). This is true even for the conventional PIPP process (m623: 109 dipoles;

mPIPP $\gamma = 0$: 98.6 dipoles on average; $\gamma = 2.5$: 77.8 dipoles on average; $\gamma = 30$: 55.4 dipoles on average). This can be attributed to a slightly increased inhomogeneity of both the PIPP and mPIPP compared to the experimental data (see also Fig. 2 in [34]). Figure 5B shows the spatial correlation of dipole angles for all three γ -values (see Materials and Methods). With increasing γ , dipole orientations become locally correlated for distance smaller than $200\mu\text{m}$. Correlation drops to zero around $200\mu\text{m}$ distance and negative values are obtained between 200 and $500\mu\text{m}$. Moreover, the correlation function of dipole orientations approaches the correlation function of the OPM for increasing γ (solid dark red lines in Fig. 5B). Similarly, the cross-correlation between the preferred orientation given by the OPM and the orientation of the dipole rapidly increases with γ (Fig. 5C). Finally, we considered mPIPP mosaics modulated by larger OPM regions (size 3×3 column spacings Λ , Fig. 5D). Again, spatial correlations of preferred dipole orientations approach the correlation of preferred orientations in the OPM for increasing γ (Fig. 5E).

The dipole angle correlation function periodically modulates around zero because in mPIPP mosaics dipole angles roughly repeat within a typical distance. This shows that the mPIPP can generate RGC mosaics that within the statistical connectivity framework predict orientation maps with a typical distance between adjacent column preferring the same orientation. The typical distance upon which dipole angles roughly repeat depends on the column spacing of the OPM used to modulate the PIPP as well as the assumed cortical magnification factor. Smaller column spacing or larger magnification factors will lead to a smaller scale of periodicity in the dipoles and vice versa. Importantly, however, dipole angle correlations decay to zero for distances larger than $2-3\Lambda$, even for large γ (Fig. 5E). Hence, long-range spatial order in the dipole angles are absent in the mPIPP mosaics. This clearly distinguishes the mPIPP dipoles from a pattern of dipoles obtained by Moiré interference of two noisy hexagonal lattices where long-range order is expected [33].

We next wondered whether the short-range spatial statistics of ON/OFF cell positions was affected by placing dipoles such that their preferred orientation tends to align with realistic OPMs. To answer this question, we compared the nearest neighbor distance distributions, autocorrelograms of cell positions as well as spatial regularity of mPIPP mosaics with the data using statistical measures defined in [33,34] (see Materials and Methods). Figure 6 depicts the results of this analysis for $\gamma = 0; 2.5; 30$ for the m623 OFF cell mosaic. Voronoi polygons and autocorrelograms of all simulated mPIPP mosaics bear close resemblance to the data (Figs. 6A and B). The nearest neighbor statistics of all three mPIPP mosaics are statistically indistinguishable from each other and all three are statistically indistinguishable from the m623 field (Figs. 6C and D). Figure 6E plots a topological disorder parameter [33,40], μ_2 , measuring the spread of the distribution of the number of sides in each Voronoi polygon (Fig. 6A, see Materials and Methods). μ_2 is plotted for 99 simulated mosaics as dots along with the value obtained from the data as a blue horizontal line. For each value of γ this line falls within the distribution of simulated values, indicating a good fit between mPIPP model mosaics and the data. Similar results were obtained when considering the w81s1 mosaic (data not shown). We conclude that the local statistics of cell positions is independent of the modulation parameter γ and matches the statistics of experimentally observed mosaics.

In summary, the proposed modulated PIPP generates semi-regular mosaics of ON and OFF center cells with realistic spatial statistics that within the statistical connectivity model predict experimentally observed OPMs. For increasing γ the local spatial

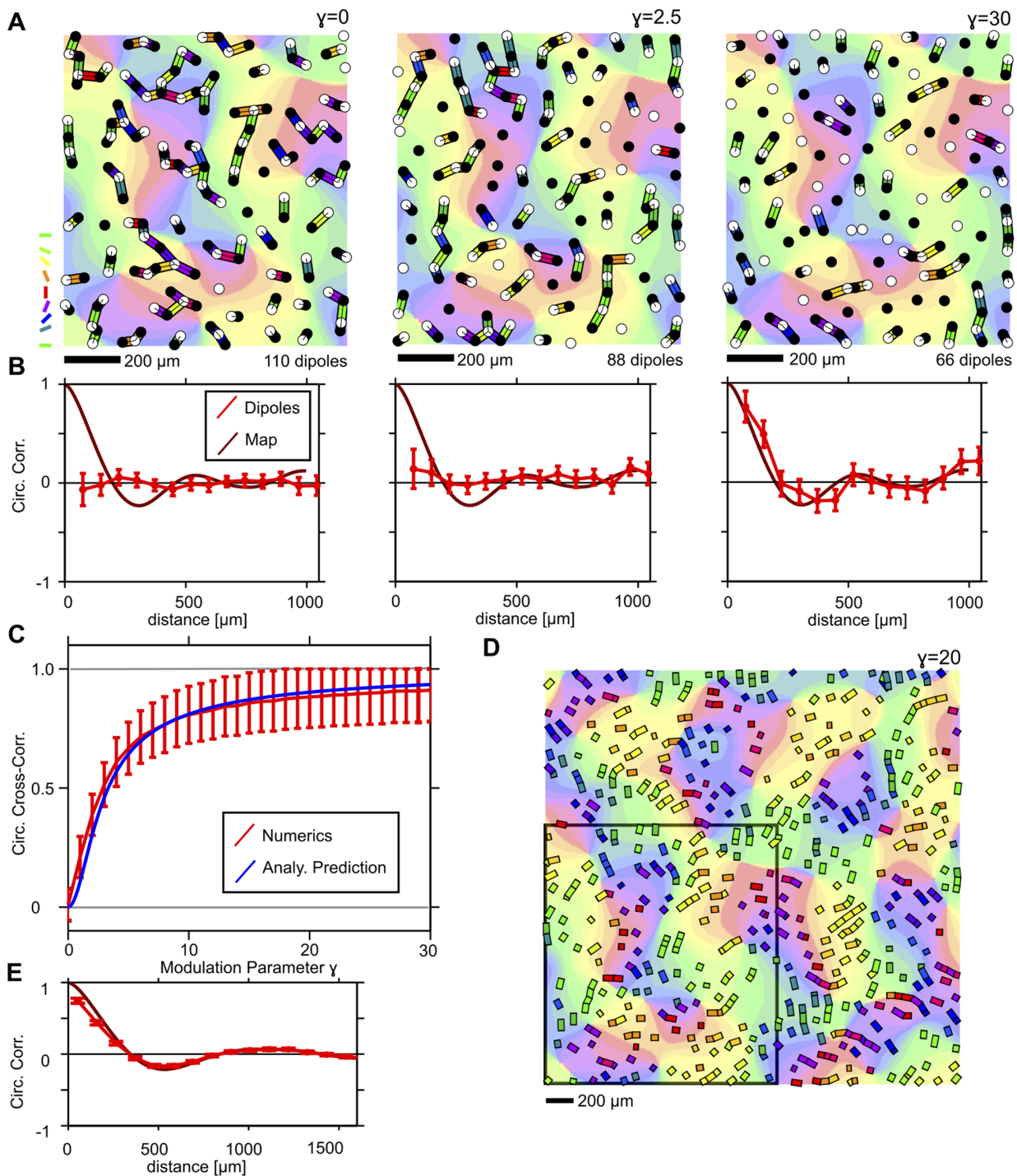


Figure 5. Statistical properties of mPIPP mosaics. **A** mPIPP RGC mosaics obtained with modulation parameter $\gamma=0$ (left), $\gamma=2.5$ (middle) and $\gamma=30$ (right). ON (OFF) cells are displayed as empty (filled) circles. Dipoles are indicated as colored bars with colors indicating their preferred orientation. OPM in the background is the region used to modulate the PIPP. Colorcodes as in Fig. 1C. Parameters for the PIPP were chosen as in [34] for cat beta cell mosaic m623 [35]. The cortical magnification is $\zeta = 1.7\text{mm}_v/\text{mm}_r$. Dipoles were extracted with $d = 80\mu\text{m}$ (see Materials and Methods). **B** Correlation of dipole angles for the mosaics shown in A (red circles: $\gamma=0$ (left), 2.5 (middle), 30 (right)). Dark red line indicates correlation function of the modulating OPM region in A. **C** Cross-correlation between dipole orientations and modulating OPM region for different values of the modulation parameter γ . Red line: numerical simulations. Blue line: analytical prediction (see Materials and Methods). **D** RGC dipole pattern obtained for an mPIPP with $\gamma=20$ from a $3\Lambda \times 3\Lambda$ -OPM. All other parameters as in A. For clarity, only the dipoles formed by the mosaics are shown as colored rectangles. The modulating OPM region is shown in the background. Black square indicates the OPM region used to simulated the mPIPP in A. **E** As B for the mosaic in D ($\gamma=20$). Note, that the dipole correlation function closely follows the correlation function of the modulating OPM. All error bars indicate 95% confidence intervals of bootstrap distributions. doi:10.1371/journal.pone.0086139.g005

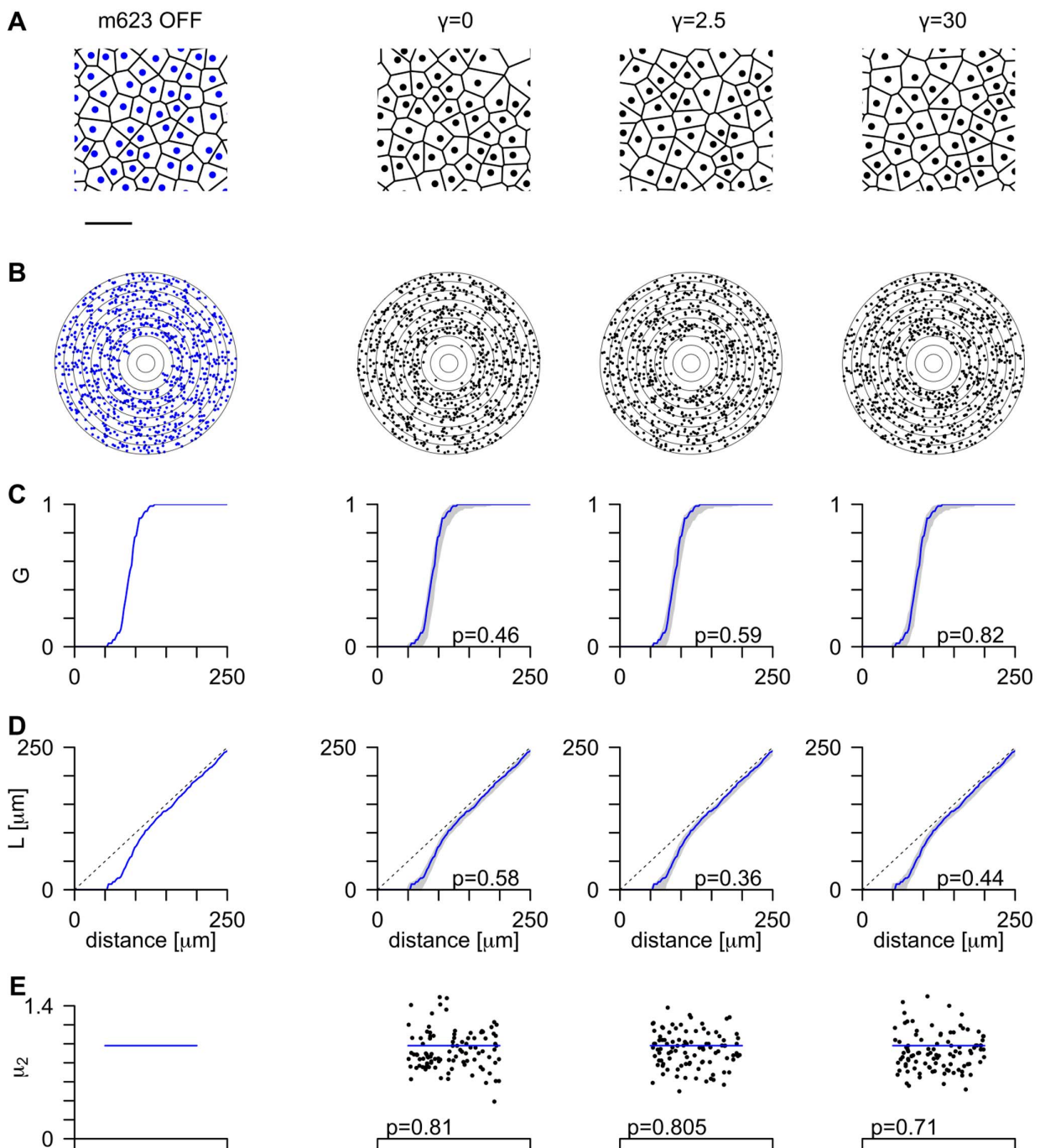


Figure 6. Spatial properties of cell positions in mPIPP mosaics are independent of γ and in agreement with experimental data. Spatial statistics of the experimental OFF cells in mosaic m623 (column 1) and mosaics obtained by simulating an mPIPP model for three different γ values (columns 2–4) and fixed $\xi = 1.7\text{mm}_e/\text{mm}_r$ and $d = 80\mu\text{m}$. **A** Central region of the mosaics. Each point denotes one receptive field midpoint and is surrounded by its Voronoi polygon. Scale bar: $250\mu\text{m}$. **B** Autocorrelogram of the points in **A**, with annuli drawn $25\mu\text{m}$ apart. **C** Cumulative distribution of nearest neighbor distances (G -function, see Materials and Methods). The gray region shows the 95% confidence interval of distributions from mPIPP simulations, and the solid line reflects the data (reprinted from column 1). **D** L -functions for data and models, drawn in the same format as for panel **C**. The dashed line indicates the expectation for Poisson point process (complete spatial randomness), $L(t) \sim t$. **E** Topological disorder parameter μ_2 for 99 realizations of the mPIPP (black dots) and for the data (horizontal blue line). doi:10.1371/journal.pone.0086139.g006

correlation between dipole orientations increases yet long-range positional order remains absent in the generated mosaics (Fig. 5). By varying a modulation parameter γ , we are able to tune cross-

correlations between dipole orientations in the RGC mosaics and the preferred orientations given in the modulating regions of OPMs. The spatial statistics of ON/OFF cells positions, however,

is unaffected by this modulation and all γ -values yield mosaics with spatial statistics consistent with the data.

Using mPIPP Mosaics to Assess the Statistical Power of Correlation Analysis

Having characterized its statistical properties, we used the mPIPP to estimate the size of a data set necessary to detect correlations between dipole angles that could seed the emergence of locally smooth and repetitive OPMs. More specifically, we wanted to estimate the so-called false negative rate of a test for dipole angle correlations, i.e. the rate of rejecting the presence of correlations when correlations of a certain degree are present in the ensemble the data is drawn from. In principle, testing the presence of positive local dipole angle correlations will require fewer and smaller mosaics than the detection of presumably smaller negative correlations on larger spatial scales. To estimate the necessary size of a data set, we generated a number of N mPIPP mosaics with known degree of spatial correlation (cf. above) and varied their spatial extent. We then statistically compared these ensembles to N conventional PIPP mosaics of the same spatial extents [34] (see Materials & Methods for details). Since PIPP mosaics lack the spatial dipole structure necessary for seeding cortical OPMs, this comparison can be employed to estimate a lower bound for detectable relevant dipole angle correlations, given a data set with N mosaics of fixed size, all measured at similar eccentricity. The latter implies that correlation functions of the mosaics can be averaged to improve the statistical power of the test. The two cat beta cell mosaics come from different eccentricities. Therefore, their correlation functions cannot be averaged.

Figure 7 depicts the estimates of the false negative error rate β of the statistical test for the presence of dipole angle correlations. Figure 7A shows the false negative rate for the detection of positive local correlation in mPIPP mosaics simulated with different modulation parameters γ as a function of the number of mosaics and their area. Even for small γ , already one mPIPP mosaic of an area of 1 mm^2 (the size of the cat beta cell data sets) yields $\beta=0.07$. This means that 93% of the realizations of such mosaics are statistically distinguishable in terms of local dipole angle correlations from an ensemble of PIPPs. Similarly, 5 mosaics with an area of around 0.4 mm^2 would be sufficient to reliably detect even weak local correlations ($\gamma=3$). Figure 7B displays the probability of failing to detect negative correlation of dipole angles around a distance of $300 \mu\text{m}$ in the mPIPP mosaics. As expected, averaging over more mosaics or, alternatively one larger mosaic is needed to detect such anti-correlations. From the above analysis, we conclude that both cat beta cell mosaics analyzed here are sufficiently large to detect even weak local positive correlations of dipole angles that could seed iso-orientation domains in V1, if present. However, a larger data set (e.g. $N>9$ mosaics of 1 mm^2 measured at the same eccentricity) is needed to reliably test for the negative correlations that would be indicative of seeding spatially repetitive OPMs. Note that, since the mPIPP mosaics generally contain slightly fewer dipoles than experimental RGC mosaics (cf. Fig. 5A), all of the above estimates of statistical power are conservative and most likely even fewer or smaller samples of real mosaics would suffice to detect the presence of the respective correlations.

Comparison between mPIPP Mosaics and Cat Beta-cell Mosaics

The absence of spatial correlations in dipole orientations in both published cat RGC mosaics can be employed to determine an

upper bound for the modulation parameter γ of the mPIPP. To do so, we synthesized mPIPP mosaics for a wide range of cortical magnification factors ξ between $0.2 \frac{\text{mm}_c}{\text{mm}_r}$ and $2.5 \frac{\text{mm}_c}{\text{mm}_r}$ (estimated value for both mosaics is $\xi=1.7$) and for a wide range of modulation parameters γ between 0 and 30. The maximum dipole distance was fixed at $d=80 \mu\text{m}$. However, similar results were obtained with $d=60 \mu\text{m}$ and $d=100 \mu\text{m}$. Each mPIPP mosaic realization was modulated by a randomly chosen rectangular OPM region from cat area 17. The size of the OPM region was determined by the respective magnification factor ξ (see Materials and Methods). For each pair of values (ξ, γ) , we generated 100 mPIPP realizations and calculated their dipole orientation correlation functions. Figures 8A and B depict these correlation functions for $\xi=1.7 \text{ mm}_c/\text{mm}_r$ and $\gamma=30$ (A) and $\gamma=0$ (B). For $\gamma=0$, dipole orientation correlations of mPIPP mosaics and the experimentally measured mosaic perfectly overlap. For $\gamma=30$, correlation values of experimental data lie far outside the min/max range of correlation values obtained with the mPIPP mosaics. To determine the range of γ for which mPIPP mosaics are consistent with the data, we then asked for each pair of values (ξ, γ) , how likely the correlation values in the data for distances smaller than $200 \mu\text{m}$ are generated by the corresponding mPIPPs. For each pair (ξ, γ) this resulted in a Monte-Carlo p-value, indicating the likelihood of finding the correlation value of the experimental mosaic in the ensemble of mPIPPs. The p-values for different (ξ, γ) are depicted in Figures 8C (m623) and D (w81s1). For both mosaics, $p<0.05$ if $\gamma>3$, indicating that the experimental data is only consistent with very small values of γ . For these values, positioning of RGC cells in the mPIPP is only very weakly modulated by the OPM region (see Figs. 5A and B). In fact, the data from both RGC mosaics w81s1 and m623 are most consistent with $\gamma=0$, i.e. the previously described PIPP [34] with complete absence of modulation from the OPM region. As emphasized before, in this regime the V1 OPM predicted by the statistical connectivity model does not exhibit a typical column spacing and therefore the model cannot account for the experimentally observed semiregular structure of visual cortical orientation maps.

Discussion

In this paper we tested a fundamental prediction of the statistical connectivity model [18–23]. When considered in the so-called dipole approximation, i.e. when each V1 neurons receives input from only a few number of RGCs, the statistical connectivity model predicts that RGC dipole angles exhibit spatial correlations similar to the spatial correlations of orientation preferences in V1 OPMs. This means that dipole angles should be locally positively correlated and anti-correlated on larger scales. We analyzed two cat beta cell mosaics as well as one primate parasol receptive field mosaic searching for the presence of such correlations. All three mosaics lack spatial correlations on the relevant spatial scales (Figs. 2, 3). Weak local correlations can be attributed to receptive fields being semi regularly spaced and are not sufficient to seed realistic cortical OPMs (Fig. 4).

To investigate whether the absence of detectable correlations was merely a consequence of the small size of the available mosaic data sets, we used a novel point process (mPIPP) which generates realizations of an ON/OFF ganglion cell mosaic that could seed realistic OPMs [18–20]. By modulating the positioning of ON/OFF cells with experimentally obtained OPMs, the mPIPP generates semi-regular ganglion cell mosaics which within the statistical connectivity model will generate realistic spatially repetitive OPMs. Notably, no Moiré-Interference mechanism

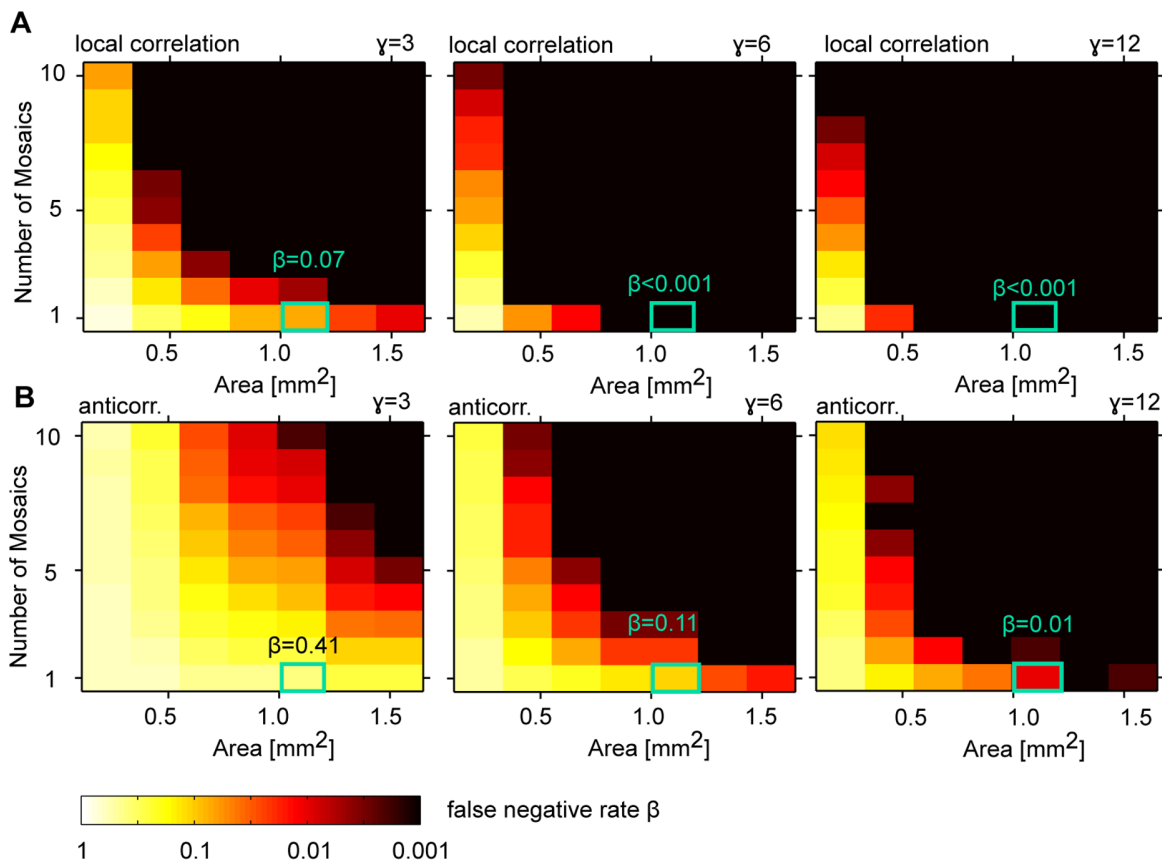


Figure 7. Estimating the statistical power of the test for the presence of spatial correlations in RGC dipole angles. A False negative rate (probability of failing to detect the positive local correlation) for mPIPP mosaics simulated with different modulation parameters γ as a function of the number of mosaics N and their area size (see Materials & Methods for details). Green box indicates size of cat RGC mosaic data sets analyzed in the present study ($N = 1$, area size $\approx 1 \text{ mm}^2$). Note that even for $\gamma = 3$, the false negative rate with this data set size is very small. **B** False negative rate for detecting negative correlation of dipole angles mPIPP mosaics around a distance of $300 \mu\text{m}$ (see Fig. 5, see Materials & Methods for details). In all panels, a cortical magnification of $\zeta = 1.7 \text{ mm}_c/\text{mm}_r$ was assumed and PIPP parameters were taken from the fit to the m623 mosaic [34]. doi:10.1371/journal.pone.0086139.g007

needs to be invoked to generate periodicity of the OPMs. The process extends previous work on PIPPs [33,34] to generate ON/OFF cell mosaics with realistic spatial properties. By varying a modulation parameter γ , the influence of the OPM region on the ON/OFF cells' position could be arbitrarily and predictably tuned (Fig. 5). The local spatial statistics of the model mosaics agree well with experiment (Fig. 6). They are essentially insensitive to the modulation through the OPM. However, the inferred mosaics are characterized by a salient local correlation between neighboring dipole orientations, anti-correlation at intermediate distances and correlation at greater distances (Fig. 5), an effect of the typical distance between adjacent columns preferring the same orientation in the OPM.

The mPIPP mosaics were then used as reference mosaics with a predictable degree of dipole correlations to determine the statistical power of inferring the presence/absence of correlations from finite samples of RGC mosaics. We find that both cat beta cell mosaics are sufficiently large to reliably detect even weak local positive correlations of dipole angles that could seed iso-orientation domains of the size observed in experimental OPMs (Fig. 7). However, a larger data set of mosaics measured at the same eccentricity would be needed to reliably detect the anti-correlations on larger spatial scales that would be indicative of seeding spatially repetitive OPMs. These findings then prompted us

determine an upper bound for the local dipole angle correlations in the data (Fig. 8). Our results show that even weak correlations are ruled out by the data. Thus, experimentally measured RGC mosaics lack the local dipole structure to seed iso-orientation domains of the size observed in experimental OPMs.

As explained above the data sets analyzed in the present study are not sufficiently large to rule out a weak periodicity of dipole angles in experimentally measured RGC mosaics. However, we would like to emphasize that the presence of local correlations in ON/OFF dipole angles appears as a necessary prerequisite for the statistical connectivity model to yield spatially repetitive OPMs. When hexagonal RGC mosaics are considered, dipole angle correlations emerge via Moiré Interference of hexagonal mosaics, that are *positionally* ordered over long distance ($> 1 \text{ mm}$) [20,21]. Our algorithm to “reverse engineer” plausible realizations of RGCs from measured OPMs shows that the statistical connectivity model does not necessarily rely on such long-range *positional* order. In the PIPP model, correlations of neighboring ON/OFF dipole angles could instead be build into the mosaics by a simple modification of the intra-mosaic interaction function studied in [34]. The absence of angular correlations in the data not only constrains the modulation parameter γ of the mPIPP to very small values. It also provides further evidence against the seeding of

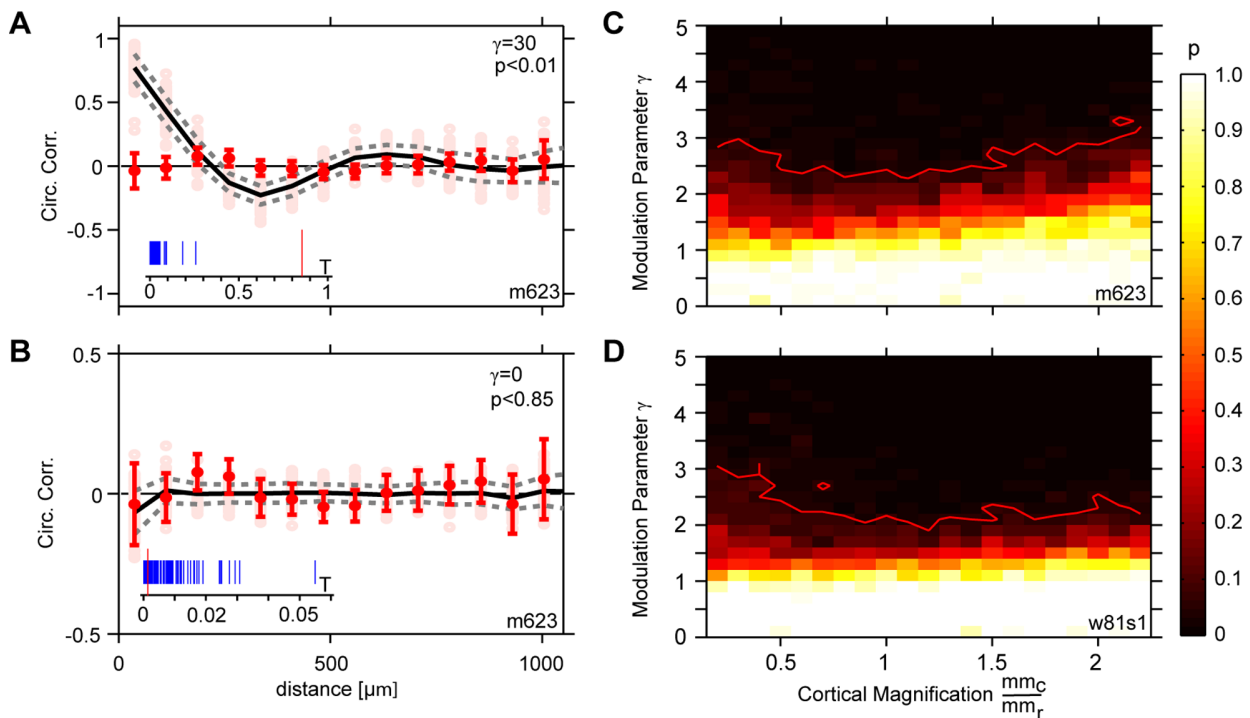


Figure 8. Constraining the modulation parameter γ with experimental data. **A** Correlation functions of dipole preferred orientations for 100 mPIPP realizations (pale pink dots, $\gamma = 30$, cortical magnification $\xi = 1.7 \text{ mm}_c / \text{mm}_r$, $d = 80 \mu\text{m}$). Black drawn line indicates average correlation function, dashed lines show $\pm 1\sigma$ deviation from the mean. Red dots indicate correlation function of dipole orientations for the mosaic m623 (redrawn from Fig. 2H). Insets show the T-distribution for Monte-Carlo data (blue) to estimate the p-value for the observed value (red) (see Materials and Methods). Note the correlation-anti-correlation-correlation structure of the correlation function. **B** As A but for $\gamma = 0$. **C** Monte-Carlo p-values (see Materials and Methods) for different values of γ and the cortical magnification factor ξ for m623. Red line indicates $p = 0.05$ significance value. **D** as C but for mosaic w81s1.

doi:10.1371/journal.pone.0086139.g008

cortical OPMs via feed-forward projection of a Moiré interference pattern from the retina.

One main simplification of the statistical connectivity approach is that the transformation of visual inputs by the LGN is usually ignored. RGC afferent terminal axons diverge in the A-lamina, providing a one-to-many mapping between one X-RGC axon and several X-type geniculate relay cells in cat LGN. Moreover, geniculate neurons often receive input from several retinal afferents [41]. However, these multiple retinal inputs have mostly overlapping receptive-field centers [41]. This has important implications for how the pattern of retinal dipoles might be transformed into a pattern of LGN dipoles. The increased density of LGN dipoles might not interpolate the sparsely sampled dipole pattern of the retina. Therefore, the size of the iso-orientation domains set by the LGN dipoles does not increase with respect to the iso-orientation domains set by the RGCs. Instead domains of dipoles of equal orientation sharply confined around RGC dipoles (similar to a Voronoi tessellation of the dipole center positions) might be the most likely outcome of the thalamic transformation. If so, the thalamic transformation would not be able to transform the uncorrelated dipole pattern in the retina into a pattern with angular correlations on the relevant scales.

The statistical connectivity model has been advanced as a theory explaining the establishment of a blueprint for the V1 orientation preference map during early visual development based on retinal inputs from the contralateral eye [20]. In fact, the spatial layout of initially established contralateral eye dominated OPM is similar to the binocular OPM of the mature animal [42]. Hence,

retinal inputs from the contralateral eye alone should be sufficiently structured to generate a spatially repetitive OPM with typical column spacing in the millimeter range. These findings usually justify the analysis of properties of mosaics from one eye only while, of course, in the adult most visual cortical neurons are binocular [1]. If, as our analysis suggests, mosaics in the individual eyes lack the spatial structure necessary to seed realistic OPMs, it appears unlikely to us that by combining inputs from ipsilateral and contralateral eye, a correctly spatially structured seed could be established. To establish the necessary spatial structure from two spatially unstructured inputs, a considerable fraction of V1 neurons would have to receive their OFF subfield input from one eye and their ON subfield input from the other. If this were the case, the OPMs measured by stimulating the ipsilateral or contralateral eye only in the adult animal should be considerably different. This is, however, not what Crair et al. have shown [42]. We conclude that competing eye inputs are unlikely to offer an alternative non-cortical mechanism for generating the structure of experimentally measured OPMs.

The hypothesis (in this study called statistical connectivity model) that cortical OPMs could emerge from a spatially structured retinal organization has been previously considered with three different RGC mosaic classes and in two different regimes in terms of the number of feed-forward retinal inputs N that a V1 neuron samples from. Both, Soodak and Ringach considered noisy hexagonal RGC mosaics and a large number of inputs to each cortical V1 cell ($N \approx 20$) [18,23]. In this setup, the statistical wiring model results in OPMs without a typical column

spacing and, hence, cannot account for the spatial structure observed in experimentally measured OPMs. Paik & Ringach considered the model with noisy hexagonal RGC mosaics in the so-called dipole approximation, where input to a V1 cell is dominated by on average a close-by pair of one ON and one OFF cell [20,21]. In this regime, OPMs predicted by the model exhibit a typical spacing between adjacent columns. However, as outlined in the introduction, the positional statistics of RGC mosaics is not well described by noisy hexagonal lattices [33] and the PIPP mosaics provide a much better fit to the data. The statistical connectivity model considered with these more realistic mosaics fails to generate maps with a typical column spacing [19,33]. Our study introduces a third class of RGC mosaics (mPIPP mosaics) with realistic positional statistics *and* a repetitive structure of cortical OPMs. The improved match between data and model, however, comes at the natural expense of spatial correlations in dipole angles in the mPIPP mosaics which are not found in experimentally measured mosaics.

The statistical connectivity model's mismatch with empirical evidence in each of the above mentioned parameter regimes suggests that the spatial layout of OPMs is not determined by the structure of RGC mosaics and may instead result from intracortical mechanisms. One of the most striking demonstrations of how such intracortical mechanisms can shape visual cortex architecture comes from cat primary visual cortex. Using pharmacological treatments, Hensch and Stryker [43] locally altered the balance between intracortical inhibition and excitation during OPM formation. Enhancement of inhibitory circuits locally widened column spacing in V1 while local reduction of inhibition broadened the spacing of columns. While those findings are difficult to reconcile with the statistical connectivity hypothesis, theories in which cortical columns arise from an intracortical interplay between inhibition and excitation, e.g. [15,16,44,45], could provide simple and plausible explanations for such an effect. Similarly, the progressive interareal and interhemispheric matching of features of columnar architecture such as the local column spacing in cat V1 suggests a strong influence of activity-dependent intracortical and even interareal interactions during postnatal column formation and critical period refinement and reorganization [9] (see also [46]).

The fact that RGC mosaics lack the spatial structure to seed realistic cortical OPMs does a priori not rule out the possibility that retinal/thalamic receptive field mosaics might exert an influence on the layout of OPMs during postnatal development or even provide a rough blueprint of visual cortical maps. In fact, the representations of retinal blood vessel angioscotomas in the visual cortex in some squirrel monkeys are a striking demonstration of the influence of retinal features on cortical selectivity layouts [47] (see [48] for a theoretical treatment in terms of activity-dependent mechanisms). If this is the case, preferred orientations of RGC dipoles on the retina might still be a fairly good predictor of cortical orientation preference for a substantial fraction of neurons, and intracortical network interactions might serve to organize a retinal seed of orientation preference into a pattern with a typical spacing and a semi regular arrangement of pinwheel centers. Furthermore, it remains possible that a higher order statistical structure of RGC mosaics beyond simple dipoles (or their thalamic transformation) is capable of driving the formation of realistic OPMs. Including retinal biases or constraints into existing models for the activity-dependent self-organization of visual cortical orientation preference is needed to elucidate the interplay between subcortical feed-forward constraints and intracortical network self-organization.

Finally, our conclusions are necessary limited by the fact that we do not have retinal fields and corresponding orientation maps from the same animal. This is clearly a large task, and one outside the scope of our current paper. Since anatomical RGC mosaics were first presented in 1981, there have been only a few mosaics published [30,35]. In particular, we have analyzed all retinal mosaic data available to us from the two recent publications [20,33]. Our results from the theoretical modeling presented here should thus also be viewed as predictions that we would like to revisit once more suitable data are available.

Materials and Methods

Optical Imaging Data & Preprocessing

Optical imaging data from twelve adult cat area 17 hemispheres were used in this study. No experiments were carried out for the sole purpose of the present study. We reanalyzed partially published data, collected by the laboratory of Z. Kisvárdy at Ruhr University Bochum. The original animal license for these experiments was issued to Prof. Ulf Eysel (Dept. Neurophysiology) and the research program was supported by SFB509. All experiments were conducted according to ethical regulations issued by the Ruhr University Bochum and conformed to the guidelines of the European Communities Council Directives, 1986 (86/609/EEC) as well as the German Animal Welfare Act. All animals derived from in house animal farm or from registered breeders for experimental animals.

Surgery and preparation protocols have been described in detail elsewhere [49,50]. Briefly, optical imaging of intrinsic signals were conducted on anesthetized (initial anesthesia: a mixture of ketamine, 7 mg/kg Ketanest (Parke-Davis, Berlin, Germany), and Xylazine, 1 mg/kg Rompun, Bayer Belgium, Sint-Truiden, Belgium), i.m.; prolonged anesthesia: 0.4–0.6% halothane in a 1:2 mixture of O₂ and N₂O using artificial ventilation) and paralyzed (alcuronium chloride (0.15 mg/kg/h, Alloferin, Hoffman-La Roche, Grenzach-Whylen, Germany, i.a.) animals using the imaging system Imager 2001 (Optical Imaging, Germantown, NY) and the data acquisition software VDAQ (Version No. VDAQ218k, Optical Imaging). A craniotomy was performed on one hemisphere between stereotaxic coordinates (Horsley–Clarke) P7–A12 and L0.5–L6.5 to expose the cortical region corresponding to the representation of the central and lower parts of the visual field in both area 17 and area 18 [27]. Animals were monitored continuously throughout all procedures to ensure that adequate anesthesia was maintained. Area 17 identification was made on the basis of stereotaxic coordinates. Before acquiring data, the camera was focused at 650–750 μm below the cortical surface that was illuminated with 609 ± 5 nm light. Visual stimuli were presented to one eye. Full-field visual stimuli were presented on a video screen (SONY, Pencoed, UK) in 120 Hz noninterlaced mode. High contrast, square-wave gratings were generated at optimal spatial (0.1–0.2 cycle/deg) and temporal frequencies (1–2 Hz), using the stimulus generator systems VSG Series Three (Cambridge Research Systems, Rochester, UK). After the recording session, the animals were euthanized with an overdose of anesthetics (Nembuthal). High vs. low spatial frequency stimuli characteristic, respectively, for area 17 and area 18 were used to visualize the area border.

Difference maps were obtained from single-condition maps as described previously [49,50]. For each hemisphere a region of interest (ROI) was defined containing the imaged part of area 17. ROIs typically contained around 10–20Λ² where Λ is the typical column spacing of the OPM. Each raw difference map was Fermi-bandpass filtered as in [10,11]. Low-pass cut-off was chosen as

1.5mm, high-pass cut-off was chosen as 0.4mm. This preprocessing ensured efficient removal of high-frequency noise from the CCD-camera and low frequency variations in signal strength while only weakly attenuating structures on the relevant scales.

Experimental Mosaics

All RGC mosaics used in the present study are available for download from the website of Dr. Stephen J. Eglén (<http://www.damp.cam.ac.uk/user/sje30/data/mosaics/>).

Numerical Procedures for mPIPP Mosaics

Numerical procedures to obtain mPIPP ON/OFF mosaics were chosen as previously described [19,34]. In short, we initially positioned n_{OFF} OFF-cells and n_{ON} ON-cells independently according to a two-dimensional Poisson point process with cell density matched to the density of cells in m623 and w81s1 respectively. We then updated these positions according to the following loop (see Fig. 9A): For each ON-center cell a new candidate position was generated at random. Considering the i -th ON-center cell, this new position was accepted with probability

$$p_i = \frac{\prod_{j=1, i \neq j}^{n_{ON}} h_{ON,ON}(|\mathbf{x}_{ON}^i - \mathbf{x}_{ON}^j|)}{\prod_{j=1}^{n_{OFF}} H_{ON,OFF}(\mathbf{x}_{ON}^i, \mathbf{x}_{OFF}^j)}, \quad (5)$$

where $H_{ON,OFF}$ is defined as in Eq. (3). After updating all ON center cells' positions, the procedure was repeated for the OFF center cells, here for the cell number i

$$p_i = \frac{\prod_{j=1, i \neq j}^{n_{OFF}} h_{OFF,OFF}(|\mathbf{x}_{OFF}^i - \mathbf{x}_{OFF}^j|)}{\prod_{j=1}^{n_{ON}} H_{ON,OFF}(\mathbf{x}_{ON}^j, \mathbf{x}_{OFF}^i)} \quad (6)$$

with different parameters for $h_{OFF,OFF}$ and $h_{ON,ON}$. Both loops were repeated between 20 and 50 times. Note that from one complete iteration of the algorithm to the next, the absolute positions of all cells show no correlation (cf. Fig. 9). However, the spatial statistics of the pattern including dipole angle correlations are stable characteristics of the mosaics after only a few iterations.

Model parameters besides γ and d were chosen as to match the local spatial statistics of m623, w81s1 [34] and g09 [33], respectively, and are summarized in Table S1. RGCs close to the boundary of the simulated domain can only form dipoles in a subset of all possible directions, potentially leading to boundary effects in the mPIPP simulations. Since the dipole orientation is enforced by a given OPM, we usually observe a slight decrease in the dipole density towards the very edge of the retinal patches. However, for the rather small beta-values that are consistent with the experimental data (cf. Fig. 8), such boundary effects were observed to play a negligible role. Source code for generating mPIPP mosaics along with Matlab code for visualization is provided as supplementary material to the manuscript.

Dipole Extraction and Correlation Function

Following [37], we assumed a pair of ON/OFF ganglion cells at position \mathbf{x} and \mathbf{y} respectively to form a dipole if their distance was smaller than a parameter d , i.e. $\|\mathbf{x} - \mathbf{y}\|_2 < d$. A dipole's preferred orientation was defined as in Eq. (2). Note that this orientation is orthogonal to the orientation of the dipole vector connecting the ON/OFF pair (see Fig. 1A). A dipole's position was defined as $(\mathbf{x} + \mathbf{y})/2$, i.e. half way between the ON and the OFF cell. Note that one RGC can form multiple dipoles depending on the choice

of d . Spatial correlations $C(R)$ between dipole angles $\phi(\mathbf{x})$ and $\phi(\mathbf{y})$ were calculated as [51,52]

$$C(R) = \langle \cos(\phi(\mathbf{x}) - \phi(\mathbf{y})) \rangle_{(R-b/2) \leq \|\mathbf{x} - \mathbf{y}\|_2 < (R+b/2)},$$

where b is a fixed bin size. To obtain Fig. 5B, Figs. 2G–J and Fig. 8, for a given mosaic, the bin size was chosen such that the diagonal of the rectangular retinal section considered contained 20 equidistant bins. Cross-correlation between the modulating OPM $\theta(\mathbf{x})$ and the dipole orientations $\phi(\mathbf{x})$ (Fig. 1D, lower panel) were determined with

$$C_{cross} = \langle \cos(\phi(\mathbf{x}) - \theta(\mathbf{x})) \rangle_{dipoles}$$

where the average is taken over all dipoles in the retinal region considered. The expected value of C_{cross} for an mPIPP with a given γ can be estimated using the probability p of positioning an ON/OFF cell

$$p(\Delta\theta) = \frac{1}{N} \exp(\gamma(\cos(\Delta\theta) - 1)),$$

where $\Delta\theta$ is the difference between the dipole orientation ϕ and the preferred orientation specified in the orientation map $\theta(\mathbf{x})$ and N is a normalizing factor, i.e. $N = \int d(\Delta\theta) \exp(\gamma(\cos(\Delta\theta) - 1))$. For large enough retinal regions, we have

$$\langle \cos(\Delta\theta) \rangle_{dipoles} = \int_{-\pi}^{\pi} d(\Delta\theta) p(\Delta\theta) \cos(\Delta\theta) = \frac{I_2(\gamma)}{I_0(\gamma)},$$

where $I_j(\gamma)$ is the j -th modified Bessel function of the first kind. This function is depicted in Fig. 5C (blue line) along with the numerically obtained cross-correlation values (red line).

Cortical Magnification Factor at the Position of the Measured Mosaics

To determine the V1 OPM region sizes to which the two published cat beta cell mosaics correspond, we estimated the cortical magnification factor at the respective retinal positions. The center of mosaic w81s1 was located 19° below the mid line of the visual streak, $4mm_r$ from the area centralis [35]. With respect to a cartesian coordinate system with origin at the area centralis and x -axis along the visual streak this position is

$$\begin{pmatrix} 4mm_r \cos(19^\circ) \\ 4mm_r \sin(19^\circ) \end{pmatrix} = \begin{pmatrix} 1.3mm_r \\ 3.8mm_r \end{pmatrix}$$

In the cat retina, $1mm_r$ roughly corresponds to 4.4 deg visual angle [53,54]. Thus

$$\begin{pmatrix} 1.3mm_r \\ 3.8mm_r \end{pmatrix} \rightarrow \begin{pmatrix} 5.9^\circ \\ 17.2^\circ \end{pmatrix}.$$

From [27], we determined the cortical magnification for elevation 5.9° and azimuth 17.2° to be about $0.15mm_c^2/\text{deg}^2$. Thus, via

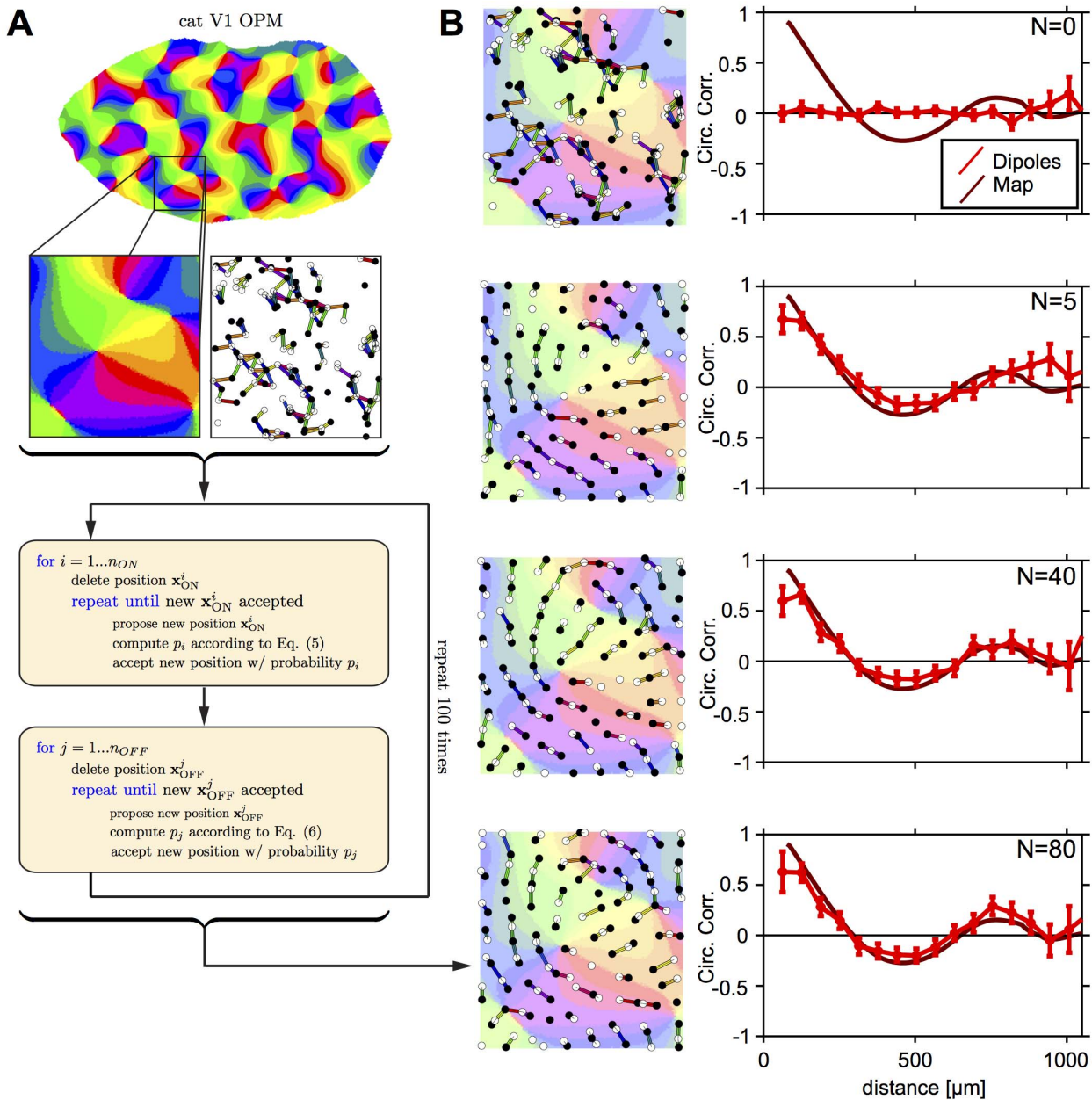


Figure 9. Constructing RGC mosaics from measured OPMs with an mPIPP. Upper panel: OPM measured in cat V1. Below, left: Inset of OPM used for modulating the mPIPP; right: Initial condition of the Monte-Carlo optimization procedure. ON/OFF RGC mosaic are specified by a homogeneous Poisson process. Positioning of RGCs is irregular. The preferred orientations of dipoles (colored bars) do not match the orientation preferences of the OPM region. Lower most panel: ON/OFF RGC mosaic after 20 iterations of the Monte-Carlo procedure with $\gamma=30$ and $\zeta=0.6\text{mm}_c/\text{mm}_r$ for mosaic m623 (see Materials and Methods). Positioning of RGCs is semiregular and preferred orientation of dipoles are almost perfectly aligned with orientation preferences of the OPM region (background). Colorcode as in Fig. 1C. **B** Orientation map region, superimposed mPIPP mosaics (left) and corresponding dipole correlation function (right) for 0,5,40, and 80 iterations (upper most to lower most panels). Note that the dipole angle correlations settle around their final values within only a few iterations of the process, whereas the precise positions of the ON/OFF cells continues to change.
 doi:10.1371/journal.pone.0086139.g009

$$\xi = \sqrt{0.15 \frac{\text{mm}_c^2}{\text{deg}^2} \cdot 4.4 \frac{\text{deg}}{\text{mm}_r}} = 1.7 \frac{\text{mm}_c}{\text{mm}_r},$$

we estimate that, at the location of w81s1, 0.6mm on the retina correspond to 1mm visual cortex. The typical column spacing of

cat OPMs is $\Lambda_c \approx 1\text{mm}_c$ [39,55]. Hence, we would expect a periodicity of about $\Lambda_r = 0.6\text{mm}_r$ on the retina.

The mosaic m623 has been obtained from 5mm eccentricity and 5.5deg below the mid line of the visual streak. This corresponds to the point $(2.1^\circ, 22.6^\circ)$ in the visual field, which again has $0.15\text{mm}_c^2/\text{deg}^2$ cortical magnification. Thus $0.6\text{mm}_r \approx 1\text{mm}_c$ for m623.

The mosaic g09 was measured at 9 mm eccentricity (temporal retina) at 41° visual angle in *Macaca mulatta*, *Macaca fascicularis*. At this point 1.4mm, $\approx 1\text{mm}_c$ ([20], Suppl. Inf.).

Spatial Statistics of mPIPP Mosaics

We have analyzed the spatial statistics of mPIPP mosaics using previous methods [33,34]. In short, to obtain the G -function, for each point in a mosaic the distance to its nearest neighbor was calculated and the cumulative distribution of these distances was computed. The L -function is the scaled expectation of the number of points observed within a given distance of any point. In Figures 6C and D, we have drawn the 95% confidence levels from 99 mPIPP simulations (gray shading). Informally, if the measure from the observed mosaics (solid lines in Fig. 6) falls within the confidence intervals, then the model is a good fit to the observed mosaic. Topological disorder, μ_2 was quantified using [40]

$$\mu_2 = \sum_n (n-6)^2 P_n,$$

where P_n is the probability of a Voronoi polygon having n edges.

Calculation of p-values for Local Spatial Statistics

All p-values used in the present study are Monte Carlo P values [34,56]. Each model is run, using the same parameters but with different initial conditions, 99 times. Each mosaic (both observed and simulated) is then compared against the other 99 mosaics, and a certain measure T is calculated. The 99 T values are sorted, and the rank of the T measure corresponding to the observed field is divided by 99 to calculate a p-value. p-values of 0.05 and smaller indicate that the model does not fit the observed data at the 5% significance level. The smallest p-value calculated is thus 0.01 with 99 simulations.

Calculation of p-values for Spatial Correlation of Dipole Angles

From $N=100$ independent realizations of the mPIPP, we obtained circular correlation functions $C^i(R)$ with $i \in [1,100]$ and R being the binned distance (see above). We introduced a measure

$$T_i = \sum_{R=0\mu\text{m}}^{200\mu\text{m}} (C^i(R) - \langle C(R) \rangle)^2 \quad (7)$$

where $\langle C(R) \rangle = \frac{1}{N} \sum_i C^i(R)$ is the average correlation of the mPIPP simulations. Note that only bins with $R \leq 200\mu\text{m}$ were used (the region of strong positive correlation). The distribution of values T quantifies how much the test ensemble of C_i deviates from the average. Next, we repeated this evaluation with the correlation function $M(R)$ obtained from the cat mosaics:

$$S = \sum_{R=0\mu\text{m}}^{200\mu\text{m}} (M(R) - \langle C(R) \rangle)^2 \quad (8)$$

From the distribution of the T_i 's and value of S , the Monte-Carlo p-value was estimated as described above.

Estimation of the Statistical Power of Hypothesis Test

The null hypothesis of the statistical test is that RGC dipole angles are correlated in space. To estimate the statistical power of our hypothesis test for the presence of correlations, it is

necessary to estimate the probability that the test will reject the presence of correlations when the alternative hypothesis is true, i.e. the RGC mosaics stems from an ensemble of correlations. To do so, we simulated an ensemble of mPIPP mosaics with known correlational statistics. Different realizations of the mPIPP were then compared to a PIPP control ensemble with respect to their dipole angle correlations. In some mPIPP realizations, the angular correlation of the mPIPP will be within the range of correlations of the PIPP ensemble. Comparing these correlations values and concluding that the mPIPP realization stems from a PIPP ensemble without angular correlations would constitute a type II statistical error (false negative). The probability of such an error, i.e. false negative rate, is a measure of the statistical power of the test. This probability was estimated by repeatedly comparing mPIPP realizations to PIPP ensembles.

More precisely, we first chose a value γ , an area size A and a number of mosaics N . Within the area A of the retinal patch, the RGC density was fixed to the values of mosaic m623, $\rho_{\text{ON}} = 67\text{mm}^{-2}$ and $\rho_{\text{OFF}} = 74\text{mm}^{-2}$. Then, we calculated 500 realizations of mosaics for this area and $\gamma=0$ to obtain the PIPP ensemble. From this ensemble, we randomly drew 100 mosaics with replacement and calculated their correlation functions. From the 100 correlation functions, N were drawn and averaged, in total a 100 times. From this set of averaged correlation functions we calculate the distribution of T_i according to Eq. (7). Next, we compare these T_i with an S (Eq. (8)) obtain from averaging correlations functions of N random mPIPP realizations of the chosen γ and with the same A . This resulted in a single p-value for this particular set of realizations. To estimate the probability of falsely rejecting the presence of angular dipole correlation, we calculated a distribution of such p-values by repeating the above stated steps a 1000 times. p-values larger than 0.05 (our significance level) in this distribution indicate the occurrence of type II statistical error. Fig. 7A shows the percentage of p-values larger than 0.05 (i.e. the false negative rate, β) as function of A and N for different values of γ . Fig. 7A shows the same analysis for periodicity. It is done analogously with correlations evaluated between $200\mu\text{m}$ and $400\mu\text{m}$.

Supporting Information

Figure S1 Spatial properties of ON cell positions in mPIPP mosaics are independent of γ and in agreement with experimental data. Same as Fig. 6, but for ON cells in RGC mosaic m623.

(TIF)

Table S1 Model parameters for PIPP and mPIPP simulations used in the current study. Parameters are chosen such that PIPP mosaics match the local spatial statistics of m623, w81s1 (see [34]) and G09 (see [33]).

(PDF)

Source Code S1 Source code for simulating mPIPP mosaics

(C)

Source Code S2 Source code for simulating mPIPP mosaics

(DAT)

Source Code S3 Source code for simulating mPIPP mosaics

(M)

Acknowledgments

We are grateful to Z. Kisvarday (University of Debrecen, Debrecen, Hungary) for sharing optical imaging data. We thank Ana Hočevnar Brezavšček (Center for Studies in Physics and Biology, The Rockefeller University, New York, NY, USA) for fruitful discussions and detailed comments on an earlier version of this manuscript.

References

- Hubel DH, Wiesel TN (1962) Receptive fields, binocular interaction and functional architecture in the cat's visual cortex. *The Journal of Physiology* 160: 106–154.
- Ohki K, Chung S, Kara P, Hübener M, Bonhoeffer T, et al. (2006) Highly ordered arrangement of single neurons in orientation pinwheels. *Nature* 442: 925–928.
- Blasdel GG (1992) Orientation selectivity, preference, and continuity in monkey striate cortex. *The Journal of Neuroscience* 12: 3139–3161.
- Chapman B, Stryker MP, Bonhoeffer T (1996) Development of orientation preference maps in ferret primary visual cortex. *The Journal of Neuroscience* 16: 6443–6453.
- Crair MC, Ruthazer ES, Gillespie DC, Stryker MP (1997) Ocular dominance peaks at pinwheel center singularities of the orientation map in cat visual cortex. *The Journal of Neurophysiology* 77: 3381–3385.
- Obermayer K, Blasdel GG (1997) Singularities in primate orientation maps. *Neural Computation* 9: 555–575.
- Bosking WH, Zhang Y, Schofield B, Fitzpatrick D (1997) Orientation selectivity and the arrangement of horizontal connections in tree shrew striate cortex. *The Journal of Neuroscience* 17: 2112–2127.
- Shmuel A, Grinvald A (2000) Coexistence of linear zones and pinwheels within orientation maps in cat visual cortex. *Proceedings of the National Academy of Sciences, USA* 97: 5568–5573.
- Kaschube M, Schnabel M, Wolf F, Löwel S (2009) Interareal coordination of columnar architectures during visual cortical development. *Proceedings of the National Academy of Sciences, USA* 106: 17205–17210.
- Kaschube M, Schnabel M, Löwel S, Coppola DM, White LE, et al. (2010) Universality in the evolution of orientation columns in the visual cortex. *Science* 330: 1113–1116.
- Keil W, Kaschube M, Schnabel M, Kisvarday ZF, Löwel S, et al. (2012) Response to Comment on “Universality in the Evolution of Orientation Columns in the Visual Cortex”. *Science* 336: 413–413.
- Durbin R, Mitchison G (1990) A dimension reduction framework for understanding cortical maps. *Nature* 343: 644–647.
- Obermayer K, Blasdel GG, Schulten K (1992) Statistical-mechanical analysis of self-organization and pattern formation during the development of visual maps. *Physical Review A* 45: 7568–7589.
- Swindale NV (1996) The development of topography in the visual cortex: a review of models. *Network* 7: 161–247.
- Wolf F, Geisel T (1998) Spontaneous pinwheel annihilation during visual development. *Nature* 395: 73–78.
- Wolf F (2005) Symmetry, Multistability, and Long-Range Interactions in Brain Development. *Physical Review Letters* 95: 208701.
- Keil W, Wolf F (2011) Coverage, continuity, and visual cortical architecture. *Neural Systems & Circuits* 1: 1–17.
- Ringach DL (2004) Haphazard wiring of simple receptive fields and orientation columns in visual cortex. *The Journal of Neurophysiology* 92: 468–476.
- Ringach DL (2007) On the origin of the functional architecture of the cortex. *PLoS One* 2: e251.
- Paik SB, Ringach DL (2011) Retinal origin of orientation maps in visual cortex. *Nature Neuroscience* 14: 919–925.
- Paik SB, Ringach DL (2012) Link between orientation and retinotopic maps in primary visual cortex. *Proceedings of the National Academy of Sciences, USA* 109: 7091–7096.
- Soodak RE (1986) Two-dimensional modeling of visual receptive fields using Gaussian subunits. *Proceedings of the National Academy of Sciences, USA* 83: 9259–9263.
- Soodak RE (1987) The retinal ganglion cell mosaic defines orientation columns in striate cortex. *Proceedings of the National Academy of Sciences, USA* 84: 3936–3940.
- Cleland BG, Dubin MW, Levick WR (1971) Simultaneous recording of input and output of lateral geniculate neurones. *Nature New Biology* 231: 191–192.
- Cleland BG, Lee BB (1985) A comparison of visual responses of cat lateral geniculate nucleus neurones with those of ganglion cells afferent to them. *The Journal of Physiology* 369: 249–268.
- Daniel PM, Whitteridge D (1961) The representation of the visual field on the cerebral cortex in monkeys. *The Journal of Physiology* 159: 203–221.
- Tusa RJ, Palmer LA, Rosenquist AC (1978) The retinotopic organization of area 17 (striate cortex) in the cat. *The Journal of Comparative Neurology* 177: 213–235.
- Tootell RB, Silverman MS, Switkes E, Valois RL (1982) Deoxyglucose analysis of retinotopic organization in primate striate cortex. *Science* 218: 902–904.

Author Contributions

Analyzed the data: MS. Wrote the paper: MS SJE FW WK. Performed numerical simulations: MS. Conceived and designed the study: FW WK. Provided statistical analysis in Figure 6: SJE.

- Djavanian RL, Harutiunian-Kozak BA (1983) Retinotopic organization of the lateral suprasylvian area of the cat. *Acta Neurobiologica Experimentalis* 43: 251–262.
- Wässle H, Boycott BB, Illing RB (1981) Morphology and mosaic of on- and off-beta cells in the cat retina and some functional considerations. *Proceedings of the Royal Society of London Series B* 212: 177–195.
- Alonso JM, Usrey WM, Reid RC (2001) Rules of connectivity between geniculate cells and simple cells in cat primary visual cortex. *The Journal of Neuroscience* 21: 4002–4015.
- Amidror I (2009) *The Theory of the Moiré Phenomenon, Volume I*. Springer Verlag.
- Hore VRA, Troy JB, Eglén SJ (2012) Parasol cell mosaics are unlikely to drive the formation of structured orientation maps in primary visual cortex. *Visual Neuroscience* 29: 283–299.
- Eglén SJ, Diggle PJ, Troy JB (2005) Homotypic constraints dominate positioning of on- and off-center beta retinal ganglion cells. *Visual Neuroscience* 22: 859–871.
- Zhan XJ, Troy JB (2000) Modeling cat retinal beta-cell arrays. *Visual Neuroscience* 17: 23–39.
- Gauthier JL, Field GD, Sher A, Greschner M, Shlens J, et al. (2009) Receptive fields in primate retina are coordinated to sample visual space more uniformly. *PLoS Biology* 7: e1000063.
- Paik SB, Li PH, Chichilnisky EJ, Ringach DL (2012) Analysis of ON/OFF-dipole spatial statistics in retinal ganglion cell mosaics. In: *Society for Neuroscience Annual Meeting*.
- Bonhoeffer T, Grinvald A (1991) Iso-orientation domains in cat visual cortex are arranged in pinwheel-like patterns. *Nature* 353: 429–431.
- Kaschube M, Wolf F, Geisel T, Löwel S (2002) Genetic influence on quantitative features of neocortical architecture. *The Journal of Neuroscience* 22: 7206–7217.
- Kram YA, Mantey S, Corbo JC (2010) Avian cone photoreceptors tile the retina as five independent, self-organizing mosaics. *PLoS One* 5: e8992.
- Usrey WM, Reppas JB, Reid RC (1999) Specificity and strength of retinogeniculate connections. *The Journal of Neurophysiology* 82: 3527–3540.
- Crair MC, Gillespie DC, Stryker MP (1998) The Role of Visual Experience in the Development of Columns in Cat Visual Cortex. *Science* 279: 566–570.
- Hensch TK, Stryker MP (2004) Columnar architecture sculpted by GABA circuits in developing cat visual cortex. *Science* 303: 1678–1681.
- von der Malsburg C (1973) Self-organization of orientation sensitive cells in the striate cortex. *Kybernetik* 14: 85–100.
- Swindale NV (1982) A model for the formation of orientation columns. *Proceedings of the Royal Society of London Series B* 215: 211–230.
- Keil W, Schmidt KF, Löwel S, Kaschube M (2010) Reorganization of columnar architecture in the growing visual cortex. *Proceedings of the National Academy of Sciences, USA* 107: 12293–12298.
- Adams DL, Horton JC (2002) Shadows cast by retinal blood vessels mapped in primary visual cortex. *Science* 298: 572–576.
- Giacomantonio CE, Goodhill GJ (2007) The effect of angioscotomas on map structure in primary visual cortex. *J Neurosci* 27: 4935–4946.
- Buzás P, Eysel UT, Kisvarday ZF (1998) Functional topography of single cortical cells: An intracellular approach combined with optical imaging. *Brain Research Protocols* 3: 199–208.
- Yousef T, Bonhoeffer T, Kim DS, Eysel UT, Tóth E, et al. (1999) Orientation topography of layer 4 lateral networks revealed by optical imaging in cat visual cortex (area 18). *European Journal of Neuroscience* 11: 4291–4308.
- Wolf F, Geisel T (2003) Universality in visual cortical pattern formation. *The Journal of Physiology* 97: 253–264.
- Schnabel M, Kaschube M, Löwel S, Wolf F (2007) Random waves in the brain: Symmetries and defect generation in the visual cortex. *The European Physical Journal Special Topics* 145: 137–157.
- Barlow HB, Fitzhugh R, Kuffler SW (1957) Change of organization in the receptive fields of the cat's retina during dark adaptation. *The Journal of Physiology* 137: 338–354.
- Bishop PO, Kozak W, Vakkur GJ (1962) Some quantitative aspects of the cat's eye: axis and plane of reference, visual field co-ordinates and optics. *The Journal of Physiology* 163: 466–502.
- Rathjen S, Schmidt KE, Löwel S (2003) Postnatal growth and column spacing in cat primary visual cortex. *Experimental Brain Research* 149: 151–158.
- Diggle PJ (1986) Displaced amacrine cells in the retina of a rabbit: analysis of a bivariate spatial point pattern. *Journal of Neuroscience Methods* 18: 115–125.

7.4 The evolution of color vision and the functional architecture of the visual cortex

Content

Color vision was lost in mammals during the *nocturnal bottleneck* when our ancestors were small, dark-dwelling animals between 205 to 65 Million years ago (Ma). Among modern mammals old world monkeys and great apes (re-)invented trichromacy 30–40 Ma. The newly developed color vision inserted new pathways into cortical functional architecture, potentially perturbing the layout of orientation domains in the primary visual cortex (V1) through non-orientation selective cytochrome oxidase (CO) blobs. How much impact color vision had on the overall functional architecture of V1 remains unclear. We investigate this question focusing on orientation domains, a key characteristic of V1 functional architecture. Orientation domains are arranged around pinwheel singularities, whose spatial distribution in ferrets, shrews, galagos and cats is quantitatively indistinguishable. At least for dichromats, there exists a *common design*.

Here, we show that trichromacy might leave a detectable fingerprint in the metrics of the common design by analysing a coupled optimization model between orientation and color selective cells. We therefore compared trichromatic macaque (N=6) and monochromatic owl monkeys (N=8) orientation domains against a background of normal (N=82) and dark-reared (N=21) ferret, shrew (N=25), galago (N=9), and cat (N=13) and found that their layout adheres to the common design. The common design is a specific and arguably small set of quantitative layout rules and we next asked whether other metrics can reveal a difference between orientation domains of trichromatic vs. color-blind species. To this end, we next develop a phenomenological model to incorporate orientation unselective and color selective cells into a layout of orientation domains using geometric distortions. Models of this type leave the measures of the common design invariant and make the prediction that randomization of the Fourier components decreases the pinwheel density. In our data, however, we find a statistically identical and highly significant increase of the pinwheel density across all Euarchontans and primates, showing that the evolutionary invention of the color vision machinery in primates induced only a minor perturbation to the modular organization of V1. The selective forces that favor the common design might thus be so powerful as to preserve it under major transformations of the retinocortical pathway.

Citation and original contribution

Manuel Schottdorf, Wolfgang Keil, Juan Daniel Flórez Weidinger, David M. Coppola, Amiram Grinvald, Koji Ikezoe, Zoltán F. Kisvárdy, Tsuyoshi Okamoto, David B. Omer, Leonard White, and Fred Wolf: “*How did the evolution of color vision impact V1 functional architecture?*” Presented as:

Contributing Talk at the 1st ICMNS, Antibes, France, June 8-10 2015 and

Poster at Cosyne 2015, Salt Lake City, Utah, March 5-8 2015.

I conceived and designed the study together with F. Wolf. I analyzed all data, developed the model and wrote the manuscript. Joscha Liedtke contributed the mathematical analysis of the joined optimization model for cytochrome oxidase and orientation preference. All other authors contributed and curated experimental data.

Introduction

Neuronal circuits in the mammalian primary visual cortex have been shaped during the last 200 million years to effectively extract visual information from natural scenes. One approach to further our understanding of these circuits is by comparative studies of phylogenetically distant species. Two large groups of mammals, Carnivora and Euarchonta, have evolved large brains independently and are widely separated in terms of evolutionary descent, belonging to distinct supra-ordinal clades that split already during basal radiation of placentals^{34,257,325,342,353,354,451}, **Fig. 7.1A**. In all studied species within these two groups of animals, neurons in the primary visual cortex respond selectively to edge-like stimuli of a particular orientation. Its spatial layout reveals a patterns of iso-orientation domains, **Fig. 7.1B**, that exhibit a continuous, roughly repetitive arrangement. A distance in the millimeter range, called the column spacing, separates neighboring domains preferring the same orientation. The continuous progression of preferred orientations is interrupted by a system of topological defects, called pinwheel centers. At a pinwheel, neurons selective to the whole complement of stimulus orientations are located in close vicinity^{41,46,50,76,166}, see **Fig. 7.1B**. These topological defects exhibit two distinct topological charges, indicating that preferred orientations change clockwise or counterclockwise around the defect center^{46,166,242,462,527}. Kaschube et al. demonstrated that in Carnivorans and Euarchontans, the statistics of the pinwheel configuration is quantitatively invariant, with potential deviations in geometrical layout parameters of at most a few percent²⁴². Specifically, the overall pinwheel density, defined as the average number of defects within the area of one square column spacing was found to be virtually identical. Subsequently, orientation domain layouts from cat V1 were shown to exhibit pinwheel densities very close to those of the three species previously studied²⁴⁵. During mammalian evolution, this common design most likely arose independently in Carnivorans and Euarchontans and potentially even in Scandentia^{242,245}, **Fig. 7.1A**, despite the differently organized visual systems, **Fig. 7.1C**. This highlights the potential advantages of this type of architectural layout in large brains^{239,242,245}, but the strength of the selective forces that favor the common design over other layouts of orientation selectivity is not known. Here, we use the reinvention of color vision in primates as a natural laboratory experiment because it required both the wiring of a new afferent pathway into the visual cortex and the rearrangement of the visual cortical processing machinery. Considering this scale of modification, the reinvention of color vision, possibly multiple times²¹⁹, might have been one of the most fundamental and most recent changes in visual cortical circuitry.

Many animals among fish, birds and insects are tetrachromats. Mammals lost most of their color seeing ability in the nocturnal bottleneck, a period in time during which our common ancestor was a small and dark-dwelling creature (a process that might have occurred again when some mammals returned to the ocean, losing their S-cone, further deteriorating their color-seeing abilities¹⁶⁴). As a rule of thumb, most current day mammals are dichromats and arguably the most relevant exception to this rule exist among the primates. For a phylogeny of primates see³⁷⁵ and **Fig. 7.1A**. All primates share the same S (short wavelength, blue) opsin that they express in retinal cone detectors. Catarrhines have two additional adjacent opsin genes on the X chromosome that express the L (long wavelength, yellow-green) and the M (medium wavelength, green) opsin. Therefore, old world monkeys are routinely trichromats and both males and females express three opsins (cf. **Fig. 7.2A,B**). Most Platyrrhini (new world monkeys) as for instance the marmoset have a single polymorphic M/L opsin; males are dichromatic and heterozygous females are trichromats⁵³⁴. Known exceptions to these rules are the Howler monkey, which is routinely trichromatic, and the Owl monkey and the galago with only one middle-wavelength opsin. M and L photopigments probably emerged as duplication of the original X-chromosome opsin gene, believed to have occurred at the base of the catarrhine radiation, some 30 to 40

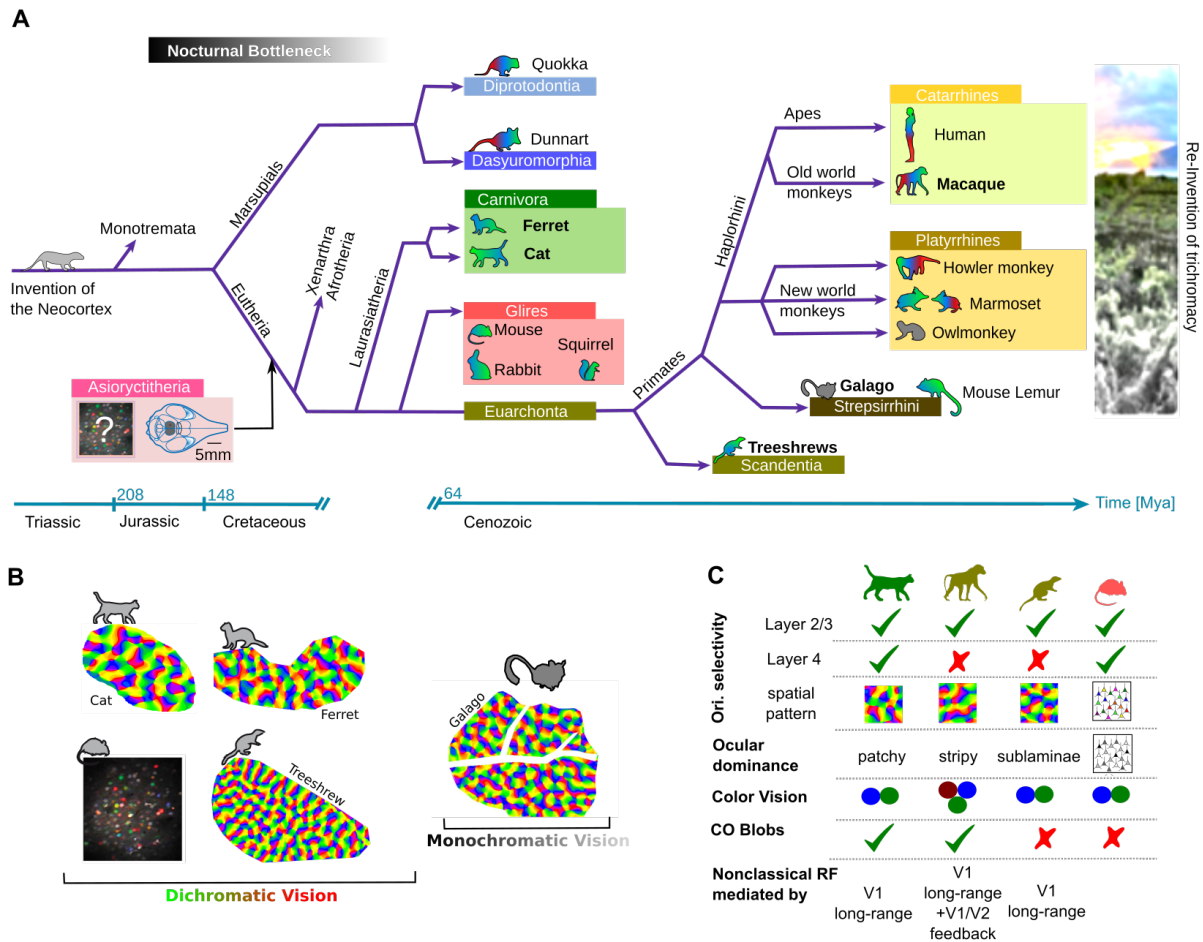


Figure 7.1: **Phylogenetic relationships and macroevolution of mammals.** **A** The evolutionary lineage of mammals diverged in the Triassic. Our early ancestors were small with poor sight and small brains. Color vision was lost during this time, the *Nocturnal bottleneck*, and only reinvented among few species. Colors indicate color vision abilities, type gray: monochromats, blue/green: dichromats, blue/green/red: trichromats. The phylogenetic relationship between separated species enables to critically test the convergent evolution hypothesis of orientation domains and the impact of the reinvention of trichromatic vision in primates. **B** The layout of orientation preference in five different species. Layouts of orientation domains exist in dichromats, and monochromats, with the exception of rodents. **C** Qualitative differences of the early visual pathway in cat, macaque, treeshrew and mouse, see⁴²⁸. The only trichromatic animal is the macaque monkey.

million years ago²¹⁹. The selective advantages of trichromacy are not clear and neither are the circuit modifications that correlate with complex color vision^{334,495}. Color selective cells in the higher primates exist in the retina, the thalamus¹¹³ and the cortex²⁸⁷. For primates, luminance and color might go through different pathways, see **Fig. 7.2A,B**. Retinal parasol cells respond well to luminance changes, and midget cells respond to changes in red-green color. The S-cone pathway is distinct and part of the konio pathway. In the primate visual cortex, there exist cells with color selective receptive fields, **Fig. 7.2C**. This example cell is a red-ON green-OFF double-opponent cell, located in a region of the visual cortex, called a Cytochrome Oxidase (CO) blob²⁸⁷. These blobs are regions with high metabolic activity that stand out in a cytochrome oxidase stain. The clustering of color selective neurons in CO blobs together with the two distinct pathways that terminate in different cortical layers²⁸⁷ could indicate the existence of a distinct color pathway in primates²⁷⁰, that is relying on the CO blob system present in many other mammals^{340,352,474}. Other evidence supports this idea of a distinct and parallel color pathway. Gerald Jacobs and colleagues engineered knock-in mice that can express a third L-cone photopigment, and gained improved chromatic discrimination. The authors speculate that their experiment indicates inherent plasticity of visual circuits, that can incorporate a new sensory modality without further evolutionary adaptation^{217,218,303}. A more recent study with Squirrel monkeys, a new world monkey with a polymorphic M/L opsin, described how the viral expression of a third cone pigment in color-blind animals, made them color-sensitive³⁰⁶. If these results hold, this would be consistent with a cortical machinery adaptable enough to process information from an additional chromatic channel.

What are the signatures of the color vision machinery? Remarkably, when Margaret Livingston and David Hubel studied orientation selectivity of neurons within CO blobs, they found that orientation tuning in these regions is weaker, **Fig. 7.2C**, and that the smooth progression of orientation domains is interrupted by CO blobs, **Fig. 7.2D**. More recent experimental studies show that the fraction of V1 neurons that clearly prefer a chromatic stimulus are usually insensitive to orientation and have homogeneous receptive fields^{226,433,444}. Also, color-selective neurons were found to be clustered and correlated with CO blobs^{92,262,263}, a finding supported by preliminary two-photon microscopy and histology⁸⁰ which also indicated that color-selective cells might exist in a specific spot within the cortical column. Theoretically, the presence of CO blobs certainly breaks homogeneity and isotropy most notably changing the dynamics of the system if coupled⁵⁷. In addition, a number of theoretical models for the joined organization of feature preferences^{245,395,396,397,427}, most notably dimension-reduction models²⁵³, generically predict that the presence of color vision directly affects the layout of orientation preference. Several studies have shown that the common design is a very specific set of layout rules and most models fall short in a direct quantitative comparison with data^{245,428}. The common design might therefore be the ideal tool to assess the impact of color vision on the layout of orientation domains.

Here, we first develop a model for the joined organization of feature preferences. This model predicts a detectable signature by groups of color-selective cells in the layout of orientation domains reflected by the metrics of the common design. We therefore compare (N=6) orientation domains from trichromatic macaques and monochromatic owl monkeys (N=8) against a background of normal (N=82) and dark-reared (N=21) ferret, treeshrew (N=25), galago (N=9), and cat (N=13). We first find that the evolutionary invention of the color vision machinery induced only a minor perturbation of the system of orientation domains as far as the measures of the common design are concerned. The common design is a specific and arguably small set of quantitative layout rules and we next asked whether other metrics can reveal a difference between orientation domains of trichromatic vs. color-blind species. To this end we develop a phenomenological model class for the geometric insertion of cytochrome oxidase blobs into

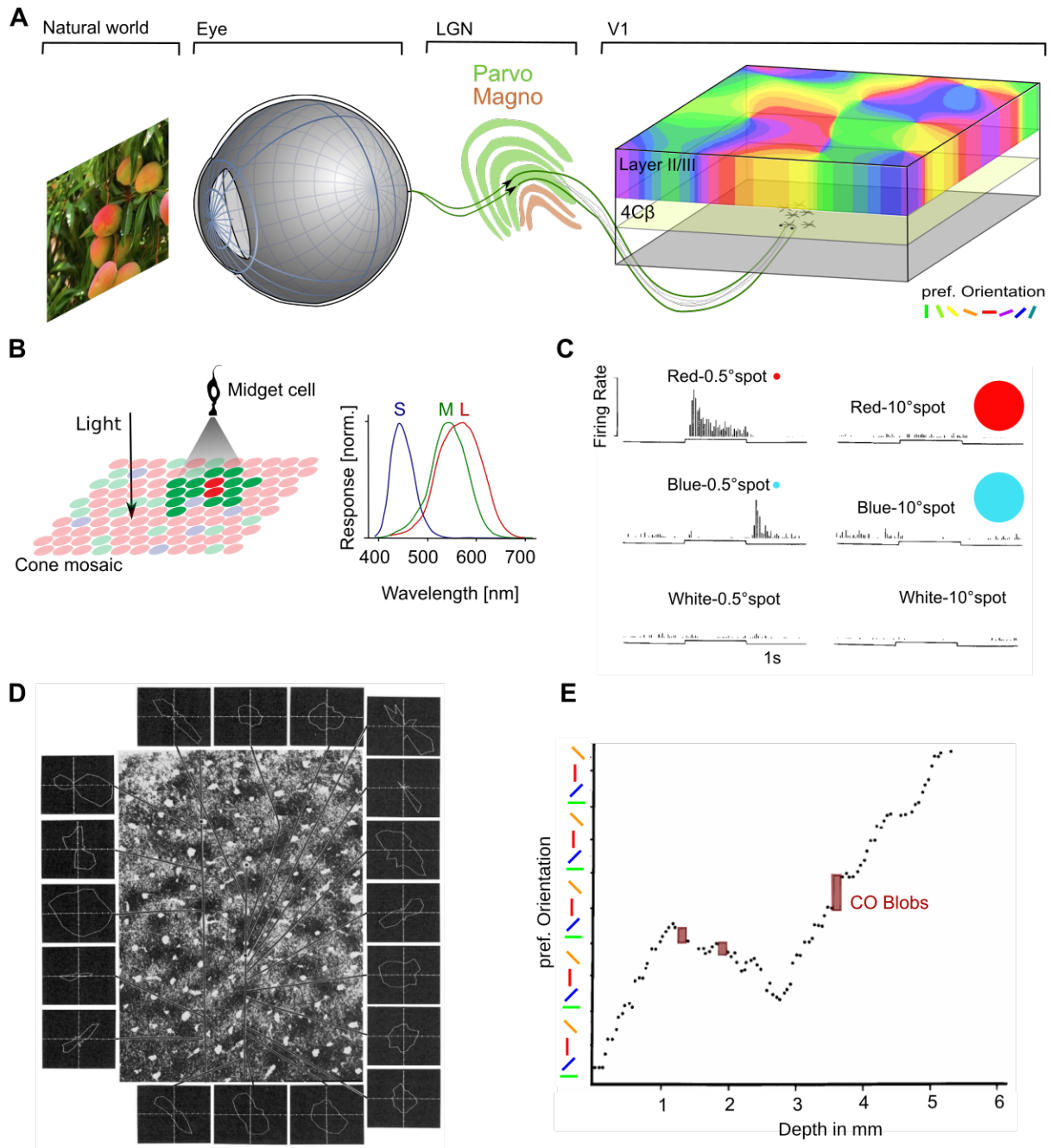


Figure 7.2: **Color vision in higher primates.** **A** Color pathways in primates. The P-Pathway connecting retinal midget cells to neurons in layer 4 of the primary visual cortex is responsible for color vision²⁷⁰. **B** The input from distinct cone types generates color selective responses^{92,444}. **C** An example for a color selective receptive field of a cell in an upper layer blob in macaque striate cortex. This is a red-ON green-OFF double-opponent cell. **D** Neurons within cytochrome oxidate blobs have impaired orientation selectivity. This figure shows example tuning curves with the associated region on the surface of the visual cortex. **E** An electrode penetration, indicating the preferred orientation and the occurrence of CO blobs as vertical bars. Panels C, D and E are adapted from²⁸⁷.

a layout of orientation domains that leaves the measure of the common design invariant. We find that layouts generated by such models are particularly sensitive to phase randomization which generically decreases their pinwheel density while in the data, phase randomization significantly increases the pinwheel density. This increase of the pinwheel density is comparable in all Euarchontan species studied here. Our results therefore show that the selective forces that favor the common design are so powerful as to preserve it under a major transformations of the retinocortical pathway.

Results

Symmetry based optimization model for CO blobs and orientation domains

To assess the conceivable signatures of the presence of orientation unselective and color selective CO blobs in a layout of orientation domains, we first model the joined dynamics of an orientation field $z(\mathbf{x}, t)$ and a cytochrome oxydase field $c(\mathbf{x}, t)$ as an optimization process of an unknown energy functional $\mathcal{F}[z, c]$ by

$$\partial_t z(\mathbf{x}, t) = \hat{F}_z[z, c] = -\frac{\delta \mathcal{F}[z, c]}{\delta \bar{z}(\mathbf{x}, t)} \quad (7.1)$$

$$\partial_t c(\mathbf{x}, t) = \hat{F}_c[z, c] = -\frac{\delta \mathcal{F}[z, c]}{\delta c(\mathbf{x}, t)}. \quad (7.2)$$

In order to ensure equity of orientation preference, orientation field solutions $z(\mathbf{x})$ shifted globally by a phase ϕ , that is $e^{i\phi}z(\mathbf{x})$, are required to be an additional solution of the dynamics. This requirement can be realized by equivariance of the nonlinear operators to a global phase shift $\hat{F}_z[e^{i\phi}z, c] = e^{i\phi}\hat{F}_z[z, c]$ and $\hat{F}_c[e^{i\phi}z, c] = e^{i\phi}\hat{F}_c[z, c]$. Thus, only odd operators in z remain and the vanishing orientation field $z(\mathbf{x}) = 0$ becomes a solution of the dynamics. Cytochrome oxydase is observed to evolve around an homogeneous equilibrium point c_0 . Orientation preference and cytochrome oxydase is observed to be arranged into continuous and roughly repetitive domains. The emergence of these patterns can be mimicked by a linear operator of Swift-Hohenberg type $\hat{L}_{z/c} = r_{z/c} - (k_c^2 + \Delta)^2$. Expanding the unknown energy functional^{242,396,397,525} around the equilibria up to third order yields the simplest optimization model for the emergence of an orientation preference and cytochrome oxydase pattern

$$\mathcal{F}[z, c] = -\int d^2\mathbf{x} \left(\bar{z}(\mathbf{x}, t) \hat{L}_z z(\mathbf{x}, t) - \frac{1}{2} |z(\mathbf{x}, t)|^4 \right) \quad (7.3)$$

$$-\int d^2\mathbf{x} \left(\frac{1}{2} c(\mathbf{x}, t) \hat{L}_c c(\mathbf{x}, t) + \frac{1}{3} \tilde{\gamma} c(\mathbf{x}, t)^3 - \frac{1}{4} c(\mathbf{x}, t)^4 \right) \quad (7.4)$$

$$-\int d^2\mathbf{x} U[z(\mathbf{x}), o(\mathbf{x})]. \quad (7.5)$$

where $U[z(\mathbf{x}), o(\mathbf{x})] = -\tilde{\kappa} c(\mathbf{x}, t) |z(\mathbf{x}, t)|^2$ is a coupling energy. The coupling energy of $U[z(\mathbf{x}), o(\mathbf{x})] = -\tilde{\kappa} c(\mathbf{x}, t) |z(\mathbf{x}, t)|^2$ is minimal if the roots of $|z|$, pinwheels, co-localizes with maxima of o and roots of o co-localize with maxima of $|z|$ and captures the phenomenology of grouping orientation unselective cells in CO blobs and vice versa. The variational dynamics of orientation preference and cytochrome oxydase are given by

$$\partial_t z(\mathbf{x}, t) = \hat{L}_z z(\mathbf{x}, t) - z(\mathbf{x}, t) |z(\mathbf{x}, t)|^2 - \tilde{\kappa} c(\mathbf{x}, t) z(\mathbf{x}, t) \quad (7.6)$$

$$\partial_t c(\mathbf{x}, t) = \hat{L}_c c(\mathbf{x}, t) + \tilde{\gamma} c(\mathbf{x}, t)^2 - c(\mathbf{x}, t)^3 - \tilde{\kappa} |z(\mathbf{x}, t)|^2. \quad (7.7)$$

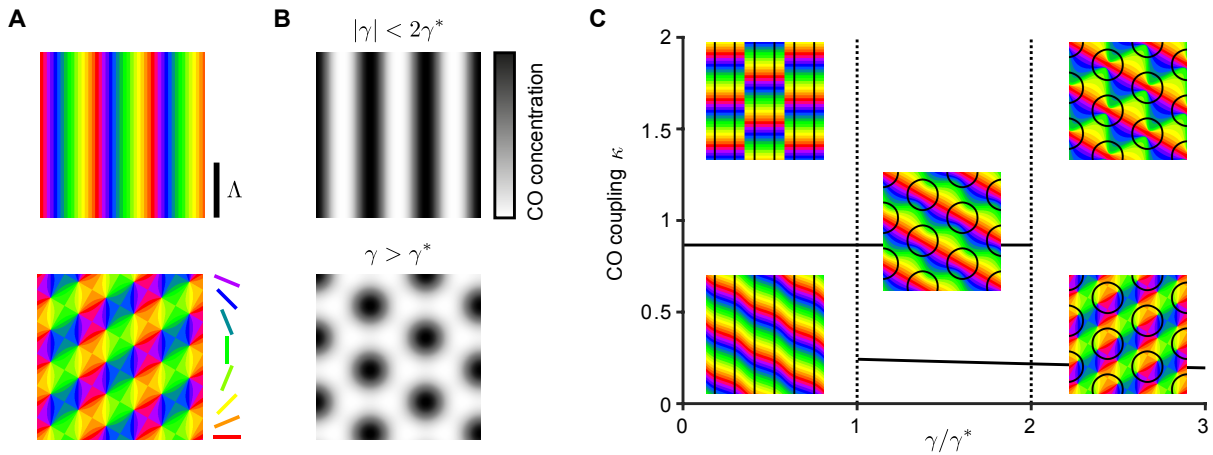


Figure 7.3: **A joined optimization model for cytochrome oxidase and orientation preference.** **A** Stable closed-form solutions of orientation preference layouts in the absence of CO coupling. **B** Stable closed-form solutions of CO. Above γ^* , hexagons are stable solutions. **C** Phase diagram of orientation preference layout. At γ^* CO hexagons become stable solutions, and at γ_2^* , stripes lose their stability. In the region with hexagonal CO layouts, orientation domains are dominated by various rhombic and stripe solutions.

Close to symmetry breaking $0 < r_{z/c} \ll 1$, the equations can be analyzed by weakly nonlinear analysis and solutions are superpositions of plane waves

$$z(\mathbf{x}, t) = \sum_{j=1}^n (A_j(t)e^{i\mathbf{k}_j \mathbf{x}} + A_{j-}(t)e^{-i\mathbf{k}_j \mathbf{x}}) \quad (7.8)$$

$$c(\mathbf{x}, t) = \sum_{j=1}^n (B_j(t)e^{i\mathbf{k}_j \mathbf{x}} + \bar{B}_j(t)e^{-i\mathbf{k}_j \mathbf{x}}). \quad (7.9)$$

The stability of the solutions can be calculated by adding small perturbations to the solutions (see methods). For decoupled fields $U = 0$, the orientation preference field $z(\mathbf{x})$ is a classical Swift-Hohenberg equation. In the expression for the CO-field, inversion symmetry $o \rightarrow -o$ is broken by the constant γ . With increasing γ , CO-layouts formed by blobs on a hexagonal layout become stable solutions, see **Fig. 7.3A**. This transition occurs at a critical value of γ^* . Beyond γ_2^* waves become unstable. **Fig. 7.3B** shows the model's phase space mapped by solving coupled amplitude equations. The solution space for CO blobs is in large parts dominated by hexagonal crystals, see **Fig. 7.3B**, and the orientation domains by stripy and rhombic solutions. Both crystals leave strong signatures in the metrics of the common design and should be detectable in the data²⁴².

Signatures of distortions in experimental layouts of orientation domains

We first analyzed the layout of orientation domains, measured with intrinsic signal imaging from $N=8$ owl monkeys and either with intrinsic signal imaging ($N=4$) or voltage sensitive dyes ($N=2$) from a total of six trichromatic macaque monkeys using the fully automated method described in²⁴². Pinwheel densities of macaque were statistically indistinguishable from each other and statistically indistinguishable from π the value predicted for the average pinwheel density by the long-range interaction model²⁴², see **Fig. 7.4A**. As a measure of pinwheel position variability, spanning all scales from single hypercolumn to the entire imaged region, we calculated the standard deviation, SD, of pinwheel density estimates in circular subregions of area A . For all species, the function $\text{SD}(A)$ was well described by

$$\text{SD}(A) = c \left(\frac{\rho}{A} \right)^\gamma \quad (7.10)$$

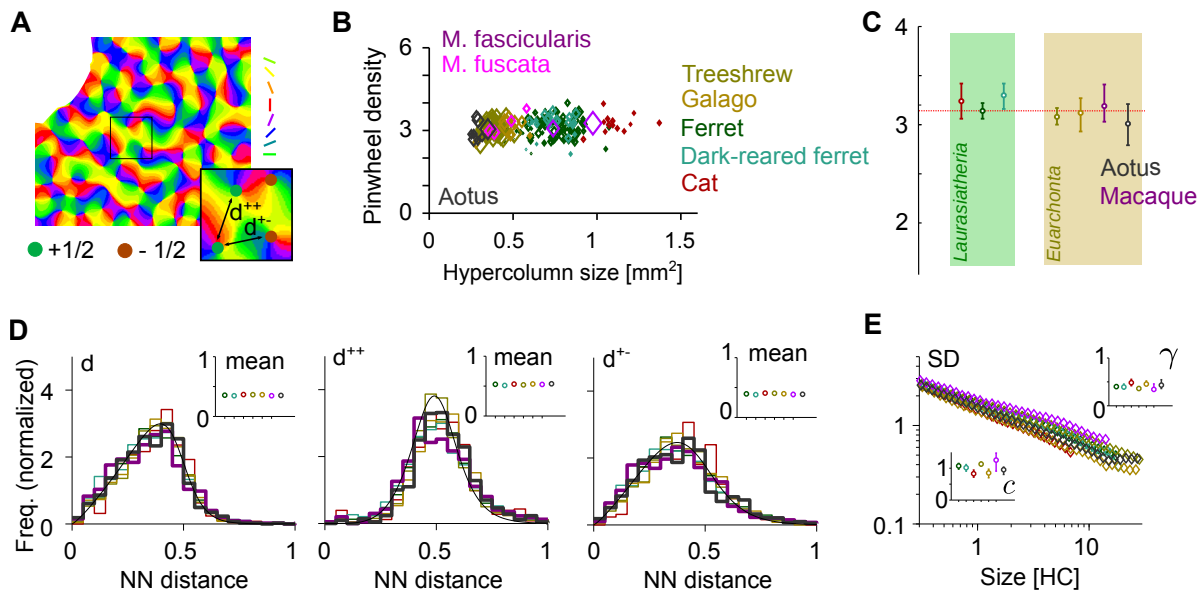


Figure 7.4: **Pinwheel statistics of macaque monkey V1.** **A** An example layout of orientation domains from *M. fuscata*. **B** Shown are pinwheel densities of individual animals from six species as function of the respective animal’s column spacing. The pinwheel density of individual macaque monkeys is comparable to other mammals. **C** Averaging across all individuals reveals that within statistical errors, the layouts of orientation domains are indistinguishable. **D** Shown are the nearest neighbor distributions between pinwheels independent of their topological charge d , between pinwheels of equal charge d^{++} , and pinwheels of opposite charge, d^{+-} . The drawn lines are fit functions from²⁴². **E** Shown is the scatter of pinwheel densities in subregions of varying size. The standard deviation follows an approximate power law. Note that layouts of macaque monkeys are slightly more irregular, although not significantly so: the prefactor c and the exponent γ are within errorbars consistent with other Euarchontans.

(**Fig. 7.4B**) with ρ denoting the average pinwheel density. The variability exponents γ and variability coefficients c were similar in all five species (**Fig. 7.4D**). As a measure of relative pinwheel positioning on the hypercolumn scale, we computed the nearest neighbor (NN) distance statistics for pinwheels of same or opposite topological charge as well as independent of their topological charge. All three distance distributions were unimodal and very similar. Importantly, the distributions obtained from macaque and aotus V1 were indistinguishable from the other three species (**Fig. 7.4C**, insets) and are summarized in **Tab. 7.1**. These findings confirm the

Measure	Macaque	Owl monkey
Mean pinwheel density	3.19 [3.03, 3.42]	3.01 [2.79, 3.21]
Mean NN distance, independent of sign	0.347 [0.320, 0.367]	0.351 [0.341, 0.363]
Mean NN distance, equal sign	0.527 [0.502, 0.542]	0.539 [0.522, 0.561]
Mean NN distance, opposite sign	0.384 [0.350, 0.412]	0.387 [0.373, 0.403]
Mean gamma	0.34 [0.30, 0.46]	0.43 [0.36, 0.55]
Mean c	1.26 [0.90, 1.51]	0.95 [0.80, 1.04]

Table 7.1: The metrics of the common design measured for $N=6$ macaque and $N=8$ owl monkeys. Shown are mean and 95% bootstrapped confidence intervals.

results of^{242,245,428} and show that macaque primary visual cortex follows the same quantitative layout laws as cat, tree shrew, galago, ferret and aotus.

We find that the evolutionary invention of the color vision machinery induced only a minor perturbation of the system of orientation domains as far as the measures of the common design are concerned. Considering that earlier studies, most recently by Schottdorf et al.⁴²⁸ and Keil et al.²⁴⁵ revealed that the common design is a set of very specific layout rules that imposes serious constraints on models, does the consistency of the macaque data with the common design rule out any effect of the color vision machinery on the layout of orientation domains? To answer this question we next construct a phenomenological model with several degrees of freedom which leaves the measures of the common design invariant.

Distortions of orientation domains

While large scale distortions in layouts of cortical columns would be detectable by finite sized wavelets²³⁷, local distortions with the same scale as orientation domains might have been overlooked because our finite sized wavelet-based tools average across finite regions to take anisotropies of the column spacing across several hypercolumns into account²⁴². It is thus conceivable that in order to incorporate orientation unselective CO blobs into a layout of orientation domains, local geometric distortions can free space for color-selective and orientation-unselective cells, while being undetectable with the common design.

To assess the merit of this idea, we model layouts of CO blobs as a smooth, real valued field $c(\mathbf{x})$, where the absolute value corresponds to intensity of the CO staining and \mathbf{x} is the position on the surface of the visual cortex. We represent a layout of orientation domains as complex field $z(\mathbf{x})$ where the half the phase is the preferred orientation, and the absolute value is the orientation selectivity⁴⁶². The simplest framework to conceptualize distorted domains is

$$z(\mathbf{x}) = z_0 \left(\mathbf{x} + \epsilon \frac{\partial}{\partial \mathbf{x}} c(\mathbf{x}) \right) \quad (7.11)$$

where z_0 is the undistorted, *free*, layout of orientation domains. We choose the distortion field to be the gradient of the scalar field $c(\mathbf{x})$. The amplitude ϵ has to be small enough for the map into distorted coordinates

$$\mathbf{y} = \mathbf{x} + \epsilon \frac{\partial}{\partial \mathbf{x}} c(\mathbf{x}) \quad (7.12)$$

to remain bijective (generating a one-to-one correspondence). We write $\frac{\partial}{\partial \mathbf{x}}$ and $\frac{\partial}{\partial \mathbf{y}}$ instead of ∇ to clearly differentiate between derivatives in respect to \mathbf{x} and \mathbf{y} . The distortions of the layout are given by the Jacobian of the map,

$$\left| \frac{\partial \mathbf{y}}{\partial \mathbf{x}} \right| = 1 + \epsilon \Delta c(\mathbf{x}). \quad (7.13)$$

With a Taylor-expansion of $c(\mathbf{y})$,

$$c(\mathbf{y}) = c \left(\mathbf{x} + \epsilon \frac{\partial}{\partial \mathbf{x}} c(\mathbf{x}) \right) = c(\mathbf{x}) + \epsilon \left| \frac{\partial}{\partial \mathbf{x}} c(\mathbf{x}) \right|^2 + \mathcal{O}(\epsilon^2), \quad (7.14)$$

we can write the inversion of the map to leading order in ϵ as

$$\mathbf{x} = \mathbf{y} - \epsilon \frac{\partial}{\partial \mathbf{x}} c(\mathbf{x}) = \mathbf{y} - \epsilon \frac{\partial}{\partial \mathbf{y}} c(\mathbf{y}) + \mathcal{O}(\epsilon^2). \quad (7.15)$$

Then, the power spectrum of the distorted map is

$$\tilde{z}(\mathbf{k}) = \int d^2 \mathbf{x} e^{i\mathbf{k}\mathbf{x}} z(\mathbf{x}) \quad (7.16)$$

$$= \tilde{z}_0(\mathbf{k}) - \epsilon \int d^2 \mathbf{y} e^{i\mathbf{k}\mathbf{y}} z_0(\mathbf{y}) \left(\Delta c(\mathbf{y}) + i\mathbf{k} \frac{\partial}{\partial \mathbf{y}} c(\mathbf{y}) \right) + \mathcal{O}(\epsilon^2) \quad (7.17)$$

The same result can be obtained by expanding

$$z_0\left(\mathbf{x} + \epsilon \frac{\partial}{\partial \mathbf{x}} c(\mathbf{x})\right) = z_0(\mathbf{x}) + \epsilon \frac{\partial}{\partial \mathbf{x}} c(\mathbf{x}) \frac{\partial}{\partial \mathbf{x}} z_0(\mathbf{x}) + \mathcal{O}(\epsilon^2) \quad (7.18)$$

and then moving the term $\partial_{\mathbf{x}} z_0(\mathbf{x})$ by integration by parts, assuming a vanishing surface term. We see that the first correction of the distorted layout is a mixture of the distortion field and the unperturbed layout.

To illustrate this, we distort the simplest layout of an orientation domains field $z_0(\mathbf{x}) = \exp(i\mathbf{k}\mathbf{x})$ with CO blobs modeled as Gaussians of finite width σ on a hexagonal lattice, see **Fig. 7.5A**. The distorted layout is shown to the right. Layouts of orientation domains that fit the experimental data best are so-called essentially complex planforms (ECPs). These planforms are solutions of a symmetry defined class of models for the self-organization of iso-orientation domains^{240,242,525}. ECPs are monochromatic superpositions of plane waves and reproduce the measures of the common design with remarkable precision. They are defined by

$$z(\mathbf{x}) = \sum_{j=1}^n e^{i(l_j \mathbf{k}_j \mathbf{x} + \phi_j)} \quad (7.19)$$

where

$$\mathbf{k}_j = \frac{2\pi}{\Lambda} \begin{pmatrix} \cos\left(\frac{\pi j}{n}\right) \\ \sin\left(\frac{\pi j}{n}\right) \end{pmatrix} \quad (7.20)$$

and $l_j = \pm 1$ and the phase are chosen randomly. Planforms are essentially complex because they can not be real valued. With a more complex free field, here a superposition of $n = 9$ ECP, the distortions are more subtle, **Fig. 7.5B**. The spectrum of the distorted map reveals the contributions of the nine modes of the layout of domains and the hexagonal distortion field, **Fig. 7.5C**.

Distorted orientation domains and the measures of the common design

The algorithm to analyze experimental data specifically takes into account that experimentally measured domain layouts often exhibit local variations in column spacing^{237,242}. Accordingly, the metric of the common design might be robust against distortions of the layout of orientation domains which are generated by the method above. To assess whether this is the case, we designed a set of model layouts, calculated from ECPs with $\Lambda = 0.6$ mm, the reported column spacing of orientation columns in macaque. In our data we measured the column spacing as $\Lambda = 0.66$ (0.61, 0.73) mm for *M. fuscata* and $\Lambda = 0.94$ (0.85, 0.99) mm for *M. fascicularis*. This difference between *M. fuscata*³⁶² and *M. fascicularis*^{263,365} has been reported in the literature, but note that the numerical value is not a critical parameter, because all results are normalized with respect to Λ . We modeled the CO layout as a hexagonal lattice with the same spacing as orientation domains³⁴¹ and modeled each CO blob as a Gaussian with width $\sigma = \Lambda/3 = 0.2$ mm, so that the layout consists of individual peaks^{57,341}, see **Fig. 7.6A**. To analyze these model maps, we used the fully automated procedure in²⁴² in a circular region of interest to emulate the geometry of experimental data. The resolution of our simulation is 50 pixels per mm and close to experimental values. We study ensembles of 30 randomly chosen planforms with $n = 8$ and $n = 20$ modes (as in the supplemental material of²⁴²), see **Fig. 7.6B**. **Fig. 7.6C** shows a $n = 20$ ECP, distorted with the layout of CO blobs in **Fig. 7.6A**. For both, ECPs with $n = 8$, see **Fig. 7.6D** and $n = 20$, see **Fig. 7.6E** we found no deviation from the measures of the common design as a function of the average distortion strength (in units of hypercolumns),

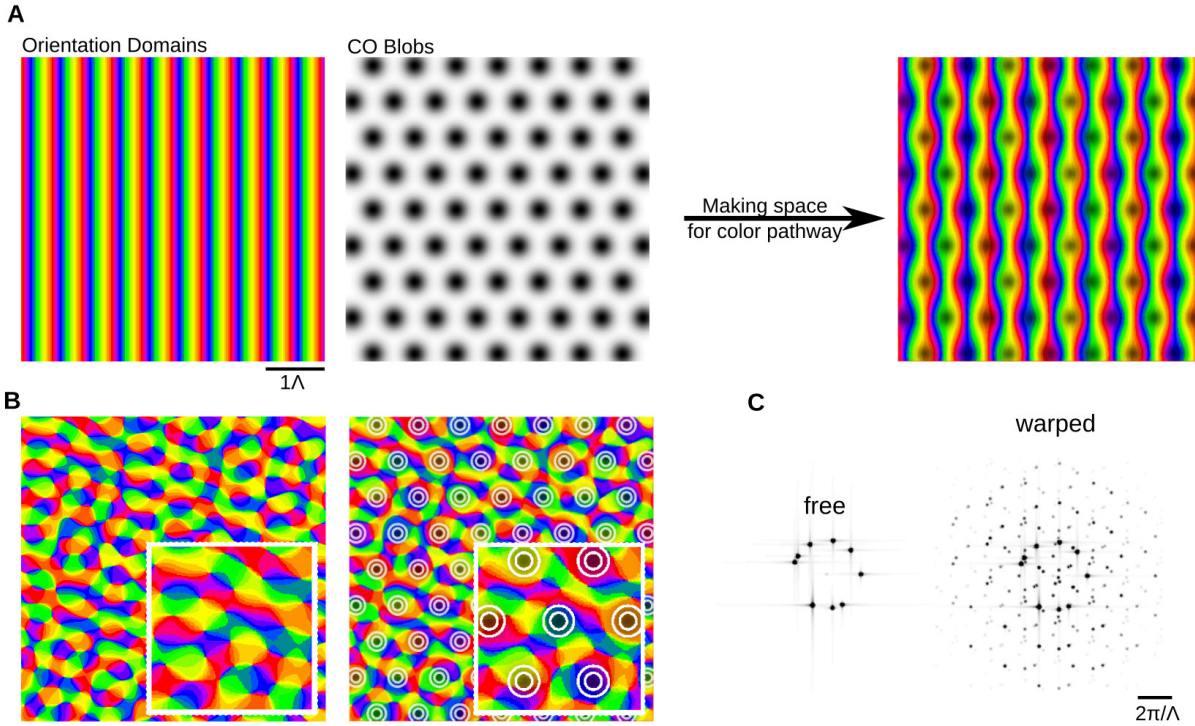


Figure 7.5: **The distortion model.** **A** The simplest layout of orientation domains, $z_0 = \exp(i\mathbf{k}\mathbf{x})$, (left) is distorted by a hexagonal grid of CO blobs (center), yielding a distorted layout (right). **B** The same as A but for a pinwheel rich layout of orientation domains. The insets show magnified regions of the layouts, and white lines indicate contour lines of the CO field. **C** The powerspectra of the layouts in B, before and after warping. Note the N=8 modes of the ECP.

despite obvious distortions in the layout of domains (cf. **Fig. 7.6B** vs. see **Fig. 7.6C**). This results shows that even though the layout properties of orientation domains in most models can easily be distinguished by the measures of the common design, there exist other models where this is not the case. Given the multitude of options to extend the common design, we next developed a generic method to assess structure in the experimental data. One viable approach is based on phase randomization³⁸⁷ where the ad-hoc method is via a rotation of the phase at each frequency²⁴²:

$$z_{\text{rnd}}(\mathbf{x}) = \frac{1}{(2\pi)^2} \int d^2\mathbf{k} e^{-i\mathbf{k}\mathbf{x}} \times e^{i\phi(\mathbf{k})} \int d^2\mathbf{y} z(\mathbf{y}) e^{i\mathbf{k}\mathbf{y}} \quad (7.21)$$

where $\phi(\mathbf{k}) \in [0, 2\pi[$ is a uniformly distributed random number. By construction, layouts generated with Eq. (7.21) have the same powerspectrum and the same autocorrelation function as the original dataset, however, the linear correlation between real and imaginary part of the complex field is not conserved. This correlation might be critical, and we therefore follow a different route: One can show that the linear correlation between multivariate data only depends on relative phase differences³⁸⁷. Therefore we calculate a set of uniform random phases in the interval $\phi_s(\mathbf{k}) \in [0, 2\pi[$ which fulfill

$$\phi_s(-\mathbf{k}) = -\phi_s(\mathbf{k}) \quad (7.22)$$

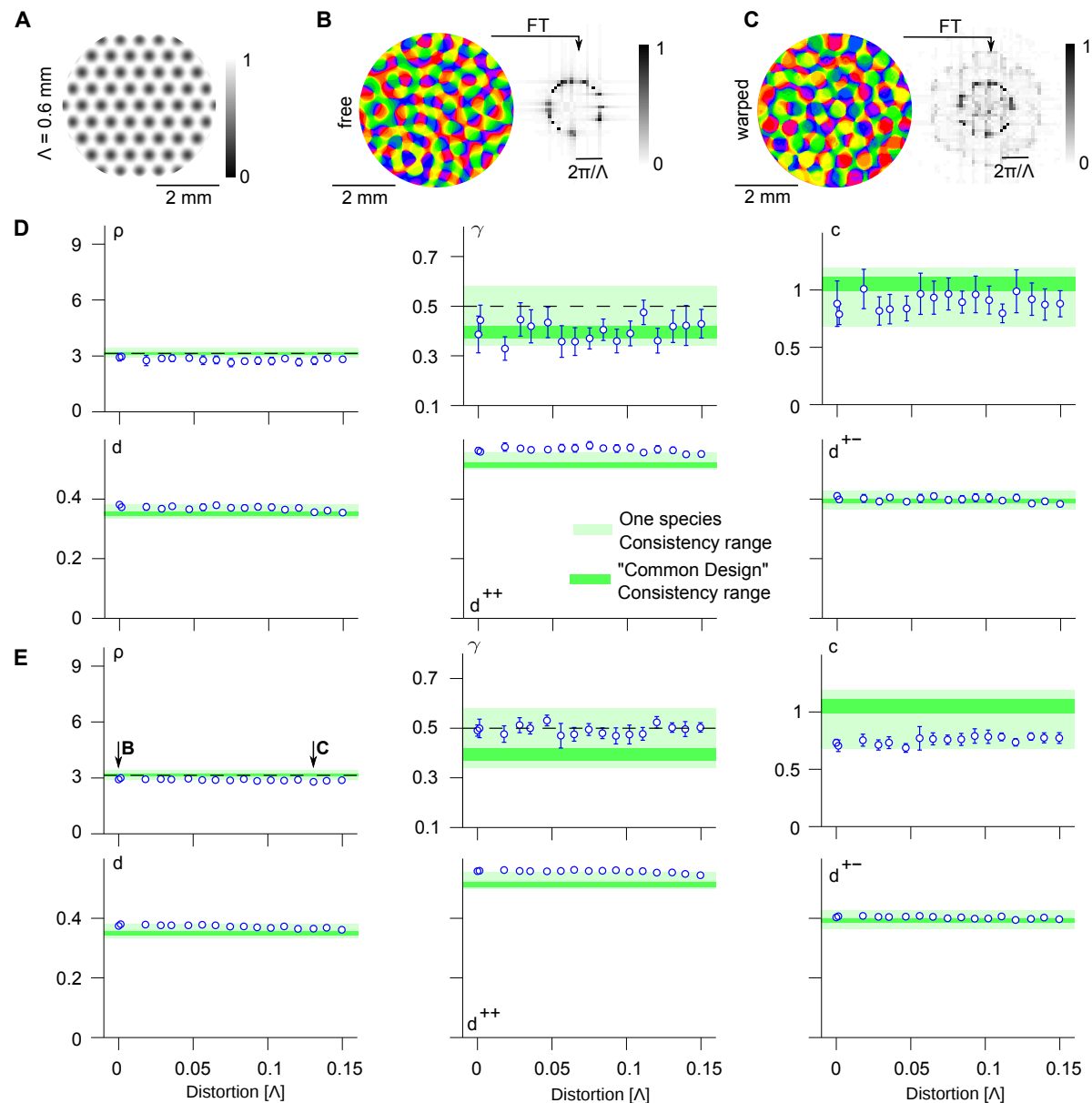


Figure 7.6: **The common design measures are invariant against distortions.** **A** A hexagonal layout of blobs with a spacing of 0.6 mm. The width of the Gaussian blobs is $\sigma = 0.2$ mm. **B** A 20-mode planform with a periodicity of $\Lambda = 0.6$ mm and its normalized amplitude spectrum. **C** A 20-mode planform after distortion with the hexagonal blob system in A; the strength of the distortion is 0.13Λ . Shown is also the normalized amplitude spectrum. **D** The common design measures as function of the distortion strength for 8-mode planforms. The confidence intervals are bootstrapped across 30 random patterns. We used the fully automated procedure in²⁴² in a circular region of interest to emulate the geometry of experimental data. **E** The same as D, but for 20-mode planforms. Note the substantially smaller errorbars than in D, indicating a more homogeneous ensemble. The two examples in B and C are indicated by arrows.

and apply this set of phases to both real and imaginary part of $z(\mathbf{x})$ separately,

$$\Re z_{\text{rnd}}(\mathbf{x}) = \frac{1}{(2\pi)^2} \int d^2\mathbf{k} e^{-i\mathbf{k}\mathbf{x}} \times e^{i\phi_s(\mathbf{k})} \int d^2\mathbf{y} \Re(z(\mathbf{y})) e^{i\mathbf{k}\mathbf{y}} \quad (7.23)$$

$$\Im z_{\text{rnd}}(\mathbf{x}) = \frac{1}{(2\pi)^2} \int d^2\mathbf{k} e^{-i\mathbf{k}\mathbf{x}} \times e^{i\phi_s(\mathbf{k})} \int d^2\mathbf{y} \Im(z(\mathbf{y})) e^{i\mathbf{k}\mathbf{y}}. \quad (7.24)$$

Note that the symmetry of $\phi_s(\mathbf{k})$ constrains both $\Re(z_{\text{rnd}}(\mathbf{x}))$ and $\Im(z_{\text{rnd}}(\mathbf{x}))$ to be real-valued. The randomized layout obtained has exactly the same two-point correlation functions as the original data. For the subsequent measurement of the pinwheel density, we restrict the new map to a geometry identical to the measured maps.

$$z_{\text{rnd}}(\mathbf{x}) = [\Re z_{\text{rnd}}(\mathbf{x}) + i \Im z_{\text{rnd}}(\mathbf{x})] \cdot \text{roi}(\mathbf{x}) \quad (7.25)$$

Note that the last step influences both phase and amplitude, but is necessary to construct a fair control ensemble. Using this technique, we can generate an arbitrary number of surrogate maps. In **Fig. 7.7A**, we show one example. The layout to the left is distorted and its Fourier spectrum shows complex structure. Phase-shuffling destroys parts of this structure, and the layout of domains appears more disorganized, see **Fig. 7.7B**. Notably after low pass filtering (one of the critical steps of the analysis of experimental data) large regions can become devoid of pinwheels. A more formal argument shows why randomization of the phases should decrease the pinwheel density. We first assume that after shuffling the layout of orientation domains is composed of two contributions

$$z(\mathbf{x}) = z_0(\mathbf{x}) + z_l(\mathbf{x}) \quad (7.26)$$

where $z_0(\mathbf{x})$ is the field from contributions around the critical circle and $z_l(\mathbf{x})$ are the components with small spatial frequencies (cf. **Fig. 7.7C** and **Fig. 7.5A**). These fields are defined through their correlation functions,

$$C_{0/l}(\mathbf{x}) = \langle z_{0/l}(0) \bar{z}_{0/l}(\mathbf{x}) \rangle. \quad (7.27)$$

For isotropic and shift-symmetric Gaussian random fields, the pinwheel density is given⁵²⁷ by

$$\rho = -\frac{1}{4\pi} \frac{\Delta C(0)}{C(0)}. \quad (7.28)$$

For long spatial correlations of the low-frequency contributions, $\Delta C_l(0) \ll \Delta C_0(0)$ and for moderate strength $C_l(0) \leq C_0(0)$. The pinwheel density can then be approximated by

$$\rho = -\frac{1}{4\pi} \frac{\Delta C_0(0) + \Delta C_l(0)}{C_0(0) + C_l(0)} \approx \rho_0 \left(1 - \frac{C_l(0)}{C_0(0)} \right) \quad \text{with } \rho_0 = \frac{-\Delta C_0(0)}{4\pi C_0(0)}. \quad (7.29)$$

The pinwheel density of an isotropic and monochromatic Gaussian randomfields is $\rho_0 = \pi$; any uncorrelated additive low-frequency noise will decrease the pinwheel density. The same technique can also be applied to data. **Fig. 7.7C** shows the layout of orientation domains of a macaque together with the Fourier spectrum. The phase shuffled layout is shown below. Qualitatively, both layouts appear similar. **Fig. 7.7D** shows the same for a galago. Note the small artifacts from blood vessels in the raw data. **Fig. 7.7E** summarizes the results for model and data. Across all species, pinwheel density increased significantly in the data, **Fig. 7.7F**. In **Fig. 7.7F**, we show both, the shuffled pinwheel densities obtained with Eq. (7.24) and Eq. (7.21). Note that the pinwheel densities increase slightly, but not significantly so. Across all Euarchontans, i.e. tree shrews and primates in our dataset, the pinwheel density is highly sensitive to phase perturbation and increases significantly and comparably. In our model, phase randomization has the opposite effect, and necessarily so. This more general test shows that the model is incompatible with the data.

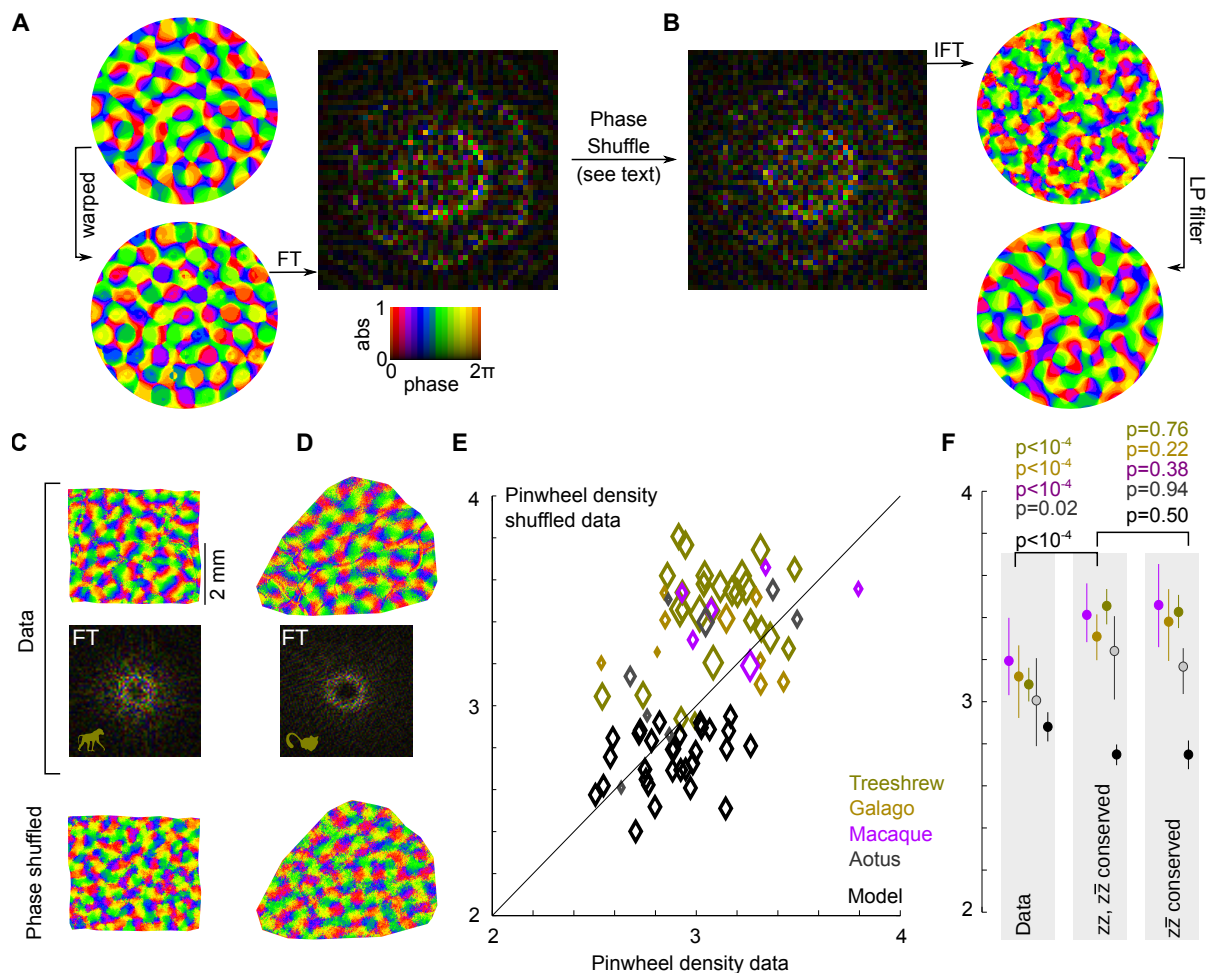


Figure 7.7: **Phase shuffling distinguishes model and data.** **A** Shown is a layout of orientation domains distorted as in Fig. 7.5A for a $n = 20$ ECP and its Fourier spectrum as polar plot (colorcoded phase and saturation coded amplitude). **B** The same amplitudes but randomized phases (see text) generate a different layout. Notably after low-pass filtering large regions become devoid of pinwheels. **C** Phase shuffling of a macaque dataset yields qualitatively similar layouts of orientation domains. **D** same as C for a galago. **E** Plotting the pinwheel density of all treeshrews, galagos, owl monkeys, macaques and the model in the dataset reveals that phase shuffling increases the pinwheel density. Phase shuffling the model layouts decreases the pinwheel density. **F** Same as E as ensemble average.

Discussion

In this study, we analyzed the layout of orientation domains in macaque monkeys and found it to be consistent with the common design. The common design is a specific and arguably small set of quantitative layout rules and we next developed a phenomenological model class for the geometric insertion of cytochrome oxidase blobs into a layout of orientation domains that leaves the measure of the common design invariant. We found that layouts generated by such models are particularly sensitive to phase randomization which generically decreases their pinwheel density. In the data, we found phase randomization to significantly increase the pinwheel density and this increase is comparable across all Euarchontan species studied here.

The universality of self-organization is a plausible mechanism to account for the common design in trichromatic mammals. In addition, **Tab. 7.1** verified the prediction of a universal solution set of a large symmetry defined class of self-organization models and highlights that self-organization is a simple and attractive answer to account for the remarkable similarity and robustness of orientation domains across diverse species with differently organized visual systems (cf. **Fig. 7.1C**). The comparison with the phase shuffled ensembles further shows that the experimentally observed layouts are also distinct from Gaussian random fields^{242,423}. Most theoretical models generate layouts and crystals with vastly different pinwheel statistics^{57,131,163,254,271,305,319,320,395,396,397,525} and therefore there exist currently no plausible alternatives⁴²⁸.

In this study, we used a precision measurement of the layout of pinwheels to constrain the relative influence of the color vision machinery on the layout of orientation domains. Another example is a study by Matthias Kaschube and colleagues²³⁶, in which they used a wavelet tool to measure column spacing, and stripiness of orientation domains in young cats. They found a highly significant correlation between litter mates. A precision measurement also presented evidence for distorted layouts of orientation domains, most notably associated with the anisotropic coverage of visual space²³⁷. This study found three contributions to the anisotropy: a mean column spacing, a systematic topographic variation (that correlations with the visuotopic map) and an additional individual topographic variation, notably the largest contribution. The precision measurement of a pinwheel density close to π , that emerges naturally from monochromatic waves^{240,423,525}, was difficult to reconcile with the finite power spectrum of experimentally observed layouts³³⁰ and the model developed here can serve as a key building block to incorporate wavelength anisotropy into existing models, while being consistent with the common design within the confidence intervals.

In fact, a key finding of this study are phase correlations in the waves constituting the layout of orientation domains. These correlations are required to generate orientation domains consistent with the common design and distinguish them from Gaussian random fields⁴²³. A potential mechanism to generate a finite power spectral width with organized phases are self-organizing systems with boundaries, spatial anisotropies or other forms of disorder^{427,428}. The specific phase and amplitude structure of the Fourier components that give rise to layouts consistent with the common design are currently unknown and hard to assess given the finite quality of the data. In principle there are two ways to shed more light on these structures: (1) Novel theoretical model types like the distortion model developed here might be a first step towards a revised common design, that is even more sensitive to small deviations in the layout of orientation domains. The distortion model moves pinwheels relative to one another, so that it is not surprising that density and mean distance between pinwheels do not change massively. Higher moments, for instance the variance of the pinwheel distance distributions, might be much more

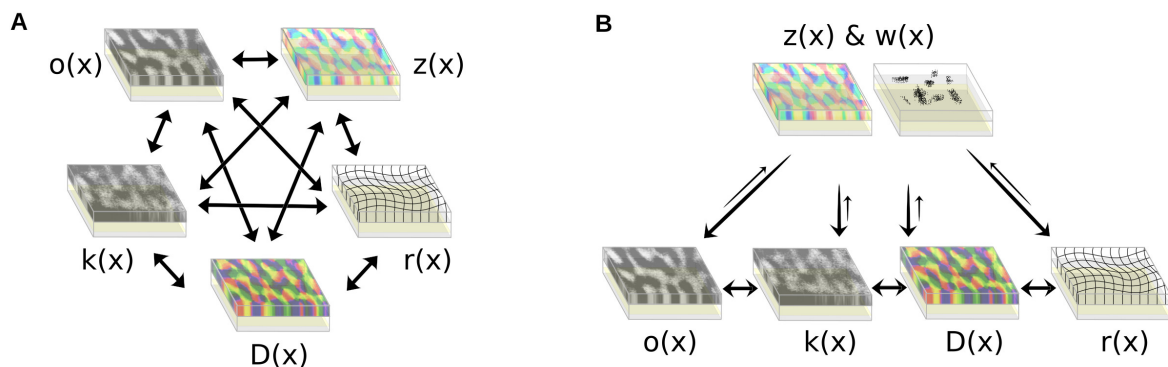


Figure 7.8: **Two conceptually different views on the organization of functional architecture** **A** The layout of ocular dominance, $o(\mathbf{x})$, orientation domains $z(\mathbf{x})$, spatial frequency domains $k(\mathbf{x})$, the retinotopic map $r(\mathbf{x})$ and direction selectivity $D(\mathbf{x})$ all interact with each other. **B** In this picture, the orientation domains $z(\mathbf{x})$ and the connectome $w(\mathbf{x})$ govern the spatial layout of the other layouts.

susceptible to small differences. Such models might also help to systematically understand the relation between phase-correlation of the Fourier representation and the measures of the common design. (2) Experimental data with substantially improved signal-to-noise, most notably calcium imaging, will make pinwheel analysis simpler and more robust. Our current pinwheel analysis routine scans through spatial filter settings to find an optimal filtering condition. If pinwheels were extractable from the data without this trouble, we can expect novel insights into pinwheel layouts and the structure of its Fourier representation. Until now, both are obfuscated by finite experimental precision.

The common design hints towards a hierarchy of cortical maps with orientation preference as one of the key players. There are substantial and qualitative differences in the visual systems of animals that give rise to statistically indistinguishable layouts of orientation domains (cf. **Fig. 7.1C**) even though there is an apparent tendency of iso-orientation lines to intersect OD borders perpendicularly and the preferential positioning of pinwheels at ocular dominance maxima^{27,40,200,355}. The quantitative resemblance of orientation domains in ferret²⁴², three-shrew²⁴², galago²⁴², cat^{245,428} and macaque together with the similarity of the superficial patch system³³⁷ and the synchronous emergence of ordered layouts and the formation and development of horizontal connections^{50,63,121,516,517}, originating from a diffused pattern^{63,292}, implies that there is a subset of models, in which the selective responses to various features, mapped on the two dimensional surface, interact in an all to all fashion, see **Fig. 7.8A**. The most relevant examples in the literature include Kohonen’s self-organized maps²⁵³, the elastic net^{122,246}, dimension reduction^{463,536} and symmetry coupled map formation⁴⁷¹. Qualitatively different are hierarchical models in which the layout of orientation domains provides the scaffold for the other layouts, see **Fig. 7.8B**. This class of models includes the work of Lars Reichl^{395,396,397} building on the joint optimization framework where the dynamic connectome $w(\mathbf{x}, \mathbf{y}, t)$ and the layout of orientation domains $z(\mathbf{x}, t)$ provide a scaffold⁵²⁵ for other functional aspects of cortical feature selectivity. The absence of any significant deviation from the common design in trichromatic macaque, dichromatic treeshrews and monochromatic galagos indicates that the latter class of models might be more relevant and also explains the apparent absence of an obvious relation between CO blobs and the layout of orientation domains in various species^{27,531}.

To further test how strong the selective forces are that favor the common design, one can in

the future look into more exotic animals, more specifically along the marsupial branch of the mammals, see **Fig. 7.1A**, that diverged from the placental mammals 150 million years ago⁵⁰⁴. In fact, the only other known cases for trichromacy in mammals exists in marsupials¹⁷. Deviations from the common design in this branch of mammals might yield key insights into cortical evolution and evolutionary principles of brain organization. If any deviations exist, this will be a key insight for the selective pressures and evolutionary constraints that shape visual cortical architecture. The two examples show in **Fig. 7.1A** are specifically interesting because the fat-tailed dunnart (*Sminthopsis crassicaudata*) is a highly visual animal with trichromatic vision^{16,17}, a carnivorous diet and a small brain. The quokka wallaby (*Setonix brachyurus*) is a nocturnal herbivore with a very high visual acuity⁴⁹¹ and trichromacy¹⁷. It has a large brain and patchy long-range horizontal connections in the visual cortex⁴⁸⁶. At some point the selective forces favoring the common design are known to break down. In the primary visual cortex of rodents, electrode penetration experiments since the 1970s suggested a lack of orderly layouts of orientation domains. These experiments were conducted in the visual cortices of rat^{159,359,374}, gray squirrel⁴⁸⁹, mouse^{327,349} and rabbits³³⁹. More advanced imaging techniques^{112,458} revealed a true dichotomy in the layouts of visual cortical architecture, **Fig. 7.1B**, between orientation domains and a salt and pepper pattern. Filling “*the evolutionary tree of orientation maps*”³³⁰ can help to answer some of the open theoretical questions.

Conclusion

Despite the massive variations of visual cortical circuits in all these animals, salt and pepper, and orientation domains are the only known layouts of orientation preference. Adding the macaque to animals that adhere to the common design highlights the need for a new generation of measurements and theoretical tools, ultimately challenging the selective forces that govern the common design. Alternative layouts might ultimately lead to a genuine insight into the computations performed by neuronal circuits in the primary visual cortex.

Materials and Methods

Solving the symmetry based optimization model for CO blobs and orientation domains

To find solutions to Eq. (7.9), we use a multi-scale expansion of

$$z(\mathbf{x}, t) \rightarrow \sqrt{\epsilon}z(\mathbf{x}, t), c(\mathbf{x}, t) \rightarrow \sqrt{\epsilon}c(\mathbf{x}, t), r_{z/c} \rightarrow \epsilon r_{z/c}, t \rightarrow t/\epsilon, \tilde{k} \rightarrow \sqrt{\epsilon}\tilde{k}, \tilde{\gamma} \rightarrow \sqrt{\epsilon}\tilde{\gamma} \quad (7.30)$$

with a parameter ϵ such that $\epsilon r_{z/c}$ is small. This leads to dynamics on the critical circle $\|\mathbf{k}\| = k_c$. The field dynamics are hence described by modes on the critical circle

$$z(\mathbf{x}, t) = \sum_{j=1}^n (A_j(t)e^{i\mathbf{k}_j\mathbf{x}} + A_{j^-}(t)e^{-i\mathbf{k}_j\mathbf{x}}) \quad (7.31)$$

$$c(\mathbf{x}, t) = \sum_{j=1}^n (B_j(t)e^{i\mathbf{k}_j\mathbf{x}} + \bar{B}_j(t)e^{-i\mathbf{k}_j\mathbf{x}}) \quad (7.32)$$

with $\mathbf{k}_j = k_c(\cos(j\pi/n), \sin(j\pi/n))^T$ and $j^- = j + n$ the mode on the opposite site of the critical circle. Note that the coefficients of $c(\mathbf{x}, t)$ are identical so that $c(\mathbf{x}, t)$ is real valued and $z(\mathbf{x}, t)$ is complex. The rescaled amplitude dynamics of $A_j \rightarrow \sqrt{r_z}A_j$ and $B_j \rightarrow \sqrt{r_c}B_j$ in units of the

rescaled time $t \rightarrow t/r_z$ are given by

$$\begin{aligned}\partial_t A_j &= A_j - A_j \sum_{j=1}^{2n} g_{jk} |A_k|^2 - \bar{A}_{j-} \sum_{j=1}^{2n} f_{jk} A_k A_{k-} - \\ &\quad - \kappa (A_{j-\nu} B_{j+\nu} + A_{j+\nu} B_{j-\nu}) \\ \tau \partial_t B_j &= B_j - B_j \sum_{j=1}^n h_{jk} |B_k|^2 - \kappa_2 (A_{j-\nu} \bar{A}_{j-2\nu} + A_{j+\nu} \bar{A}_{j+2\nu}) + \gamma B_{j-\nu} B_{j+\nu}\end{aligned}$$

with $\nu = n/3$, $\tau = r_z/r_c$, $g_{jk} = 2(1 - \delta_{jk}/2)$, $f_{jk} = (1 - \delta_{jk} - \delta_{jk-})$, $h_{jk} = 6(1 - \delta_{jk}/2)$, $\kappa = \tilde{\kappa} \sqrt{r_c}/r_z$, $\kappa_2 = \tilde{\kappa}/r_z$ and $\gamma = 2\tilde{\gamma}/\sqrt{r_c}$. Notice that quadratic coupling is only present if the total number of modes are multiples of 6, that is $n = 3\mathbb{Z}$. If $\kappa_2 \ll 1$, the coupling becomes unidirectional from cytochrome oxydase to orientation selectivity

$$\begin{aligned}\partial_t A_j &= A_j - A_j \sum_{j=1}^{2n} g_{jk} |A_k|^2 - \bar{A}_{j-} \sum_{j=1}^{2n} f_{jk} A_k A_{k-} - \\ &\quad - \kappa (A_{j-\nu} B_{j+\nu} + A_{j+\nu} B_{j-\nu}) \\ \tau \partial_t B_j &= B_j - B_j \sum_{j=1}^n h_{jk} |B_k|^2 + \gamma B_{j-\nu} B_{j+\nu}.\end{aligned}$$

Stable closed-form solutions in the absence of coupling

In order to analysis closed-form solutions and their stability, it is convenient to decompose the amplitude equations of cytochrome oxydase and orientation preference into amplitudes and phases $A_j \rightarrow \mathcal{A}_j e^{i\phi_j}$ and $B_j \rightarrow \mathcal{B}_j e^{i\varphi_j}$, respectively. In the absence of mutual coupling, cytochrome oxydase dynamics are given by

$$\tau \partial_t \mathcal{B}_j = \mathcal{B}_j - \mathcal{B}_j \sum_{j=1}^n h_{jk} \mathcal{B}_k^2 + \gamma \mathcal{B}_{j-\nu} \mathcal{B}_{j+\nu} \cos(\varphi_{j-\nu} + \varphi_{j+\nu} - \varphi_j) \quad (7.33)$$

$$\tau \mathcal{B}_j \partial_t \varphi_j = \gamma \mathcal{B}_{j-\nu} \mathcal{B}_{j+\nu} \sin(\varphi_{j-\nu} + \varphi_{j+\nu} - \varphi_j) \quad (7.34)$$

and orientation preference dynamics by

$$\begin{aligned}\partial_t \mathcal{A}_j &= \mathcal{A}_j - \mathcal{A}_j \sum_{j=1}^{2n} g_{jk} \mathcal{A}_k^2 - \\ &\quad - \mathcal{A}_{j-} \sum_{j=1}^{2n} f_{jk} \mathcal{A}_k \mathcal{A}_{k-} \cos(\phi_k + \phi_{k-} - \phi_j - \phi_{j-}) \\ \mathcal{A}_j \partial_t \phi_j &= -\mathcal{A}_{j-} \sum_{j=1}^{2n} f_{jk} \mathcal{A}_k \mathcal{A}_{k-} \sin(\phi_k + \phi_{k-} - \phi_j - \phi_{j-}).\end{aligned}$$

Notice that uncoupled amplitude equations with local interactions are typically converging to solutions with only a few modes and quadratic interactions are only present for $n = 3\mathbb{Z}$. Hence, we restrict the analysis to $n = 3$ in the following.

Cytochrome oxidase stripes Cytochrome oxydase stripes are closed-form solutions with a single non-vanishing mode of amplitude $\mathcal{B}_{\text{st}} = 1/\sqrt{3}$, see **Fig. 7.9B**. The stability of cytochrome oxydase stripes is determined by the amplitude dynamics, because perturbations in the phase dynamics are of quadratic order. The dynamics of a small perturbation in amplitudes

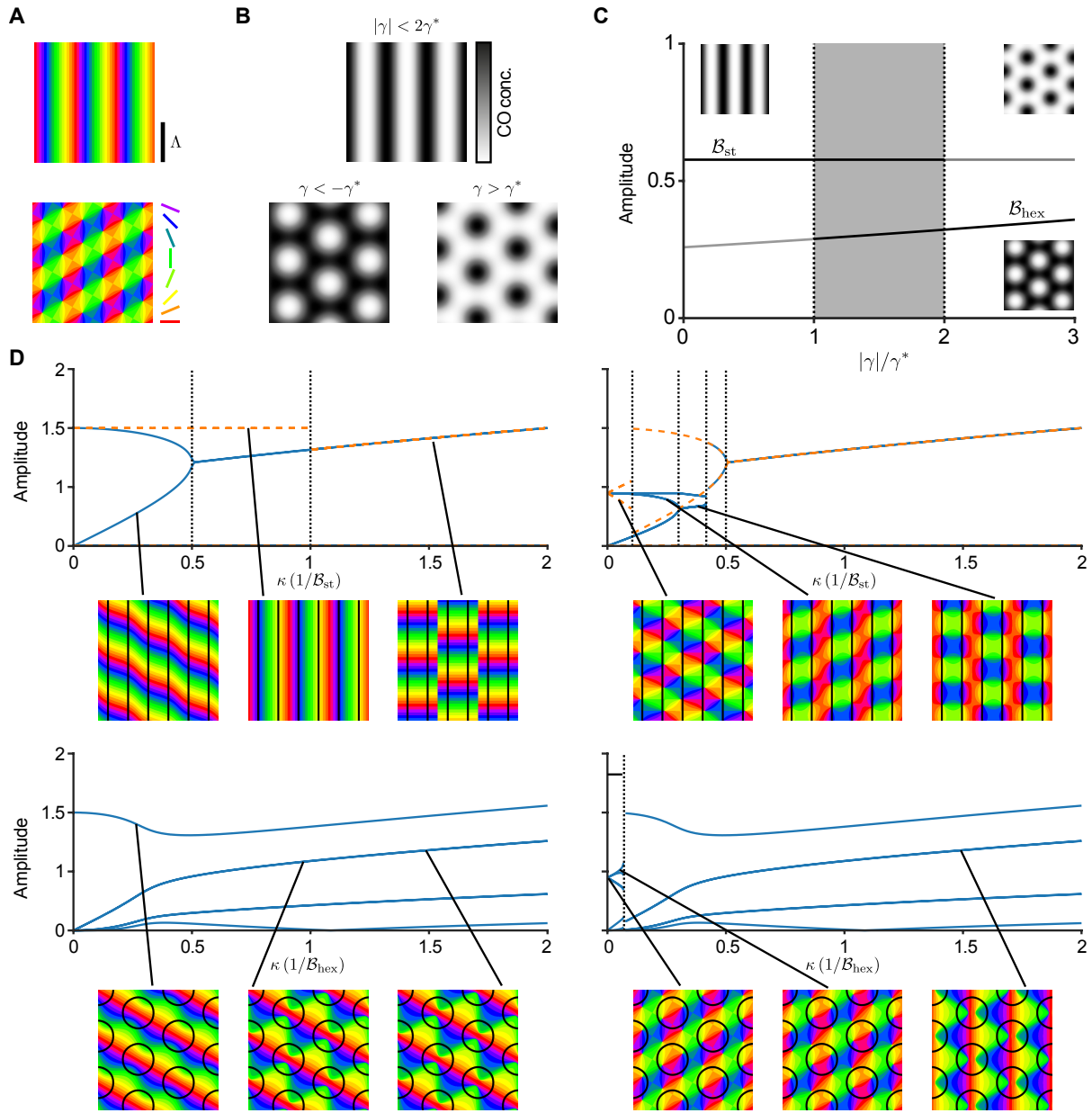


Figure 7.9: **Bifurcation diagrams and solutions of the joined optimization model for cytochrome oxidase and orientation preference.** **A** Stable closed-form solutions of orientation preference layouts in the absence of CO coupling. **B** Stable closed-form solutions of CO. **C** Amplitude and stability region of closed-form CO solutions. Grey area: Co-existence of CO stripes and CO hexagons, see Eq. (7.36). **D** Bifurcation diagrams of orientation preference layouts with varying CO coupling strength κ and distinct initial closed-form solutions. Top row for stripy CO layouts, bottom row for hexagonal CO blobs. Shown as lines are the amplitudes of the constituting plane waves that solve the orientation amplitude equations. Note that some of the amplitudes can be degenerated. Blue lines in the upper row are calculated for an intersection angle of the initial condition of CO and orientation stripes of 90° and orange for an intersection angle of 0° .

$(\mathcal{B}_{\text{st}}, 0, 0)^T \rightarrow (\mathcal{B}_{\text{st}}, 0, 0)^T + \mathbf{b}$ and phases $(\varphi_1, \varphi_2, \varphi_3)^T \rightarrow (\varphi_1, \varphi_2, \varphi_3)^T + \boldsymbol{\psi}$ is in linear order given by

$$\tau \partial_t \mathbf{b} = \begin{pmatrix} -2 & 0 & 0 \\ 0 & -1 & \gamma/\sqrt{3} \\ 0 & \gamma/\sqrt{3} & -1 \end{pmatrix} \mathbf{b}. \quad (7.35)$$

The eigenvalues of the stability matrix are given by $\lambda_1 = -2$, $\lambda_2 = \gamma/\sqrt{3} - 1$ and $\lambda_3 = -\gamma/\sqrt{3} - 1$. Cytochrome oxydase stripes are hence stable in the regime $\gamma \in (-2\gamma^*, 2\gamma^*)$ with $\gamma^* = \sqrt{3}/2$ as illustrated in **Fig. 7.9C**.

Cytochrome oxydase hexagons Cytochrome oxydase hexagons are closed-form solutions with three non-vanishing modes of equal amplitude

$$\mathcal{B}_{\text{hex}} = |\gamma|/30 + \sqrt{(\gamma/30)^2 + 1/15}. \quad (7.36)$$

The phase of the amplitudes fulfill the condition $\varphi_{j-\nu} + \varphi_{j+\nu} - \varphi_j = 2\mathbb{Z}\pi$ for $\gamma < 0$ and $\varphi_{j-\nu} + \varphi_{j+\nu} - \varphi_j = 2\mathbb{Z}\pi + \pi$ for $\gamma > 0$, see **Fig. 7.9B**. Phase dynamics of a small perturbation in amplitudes $(\mathcal{B}_{\text{hex}}, \mathcal{B}_{\text{hex}}, \mathcal{B}_{\text{hex}})^T \rightarrow (\mathcal{B}_{\text{hex}}, \mathcal{B}_{\text{hex}}, \mathcal{B}_{\text{hex}})^T + \mathbf{b}$ and phases $(\varphi_1, \varphi_2, \varphi_3)^T \rightarrow (\varphi_1, \varphi_2, \varphi_3)^T + \boldsymbol{\psi}$ is in linear order given by

$$\tau \partial_t \boldsymbol{\psi} = |\gamma| \mathcal{B}_{\text{hex}} \begin{pmatrix} -1 & 1 & -1 \\ -1 & -1 & 1 \\ 1 & -1 & -1 \end{pmatrix} \boldsymbol{\psi}. \quad (7.37)$$

The eigenvalues are given by $\lambda_1 = -1$, $\lambda_2 = -1 + i\sqrt{3}$ and $\lambda_3 = -1 - i\sqrt{3}$. Perturbed amplitude dynamics are given by

$$\tau \partial_t \mathbf{b} = \begin{pmatrix} 1 - 21\mathcal{B}^2 & -12\mathcal{B}^2 + |\gamma|\mathcal{B} & -12\mathcal{B}^2 + |\gamma|\mathcal{B} \\ -12\mathcal{B}^2 + |\gamma|\mathcal{B} & 1 - 21\mathcal{B}^2 & -12\mathcal{B}^2 + |\gamma|\mathcal{B} \\ -12\mathcal{B}^2 + |\gamma|\mathcal{B} & -12\mathcal{B}^2 + |\gamma|\mathcal{B} & 1 - 21\mathcal{B}^2 \end{pmatrix} \mathbf{b} \quad (7.38)$$

with the eigenvalues $\lambda_{1/2} = 6\mathcal{B}^2 - 2|\gamma|\mathcal{B}$ and $\lambda_3 = -30\mathcal{B}^2 + |\gamma|\mathcal{B}$. Cytochrome oxydase hexagons are hence stable in the regime $|\gamma| \in (\gamma^*, \infty)$ with $\gamma^* = \sqrt{3}/2$ as illustrated in **Fig. 7.9C**.

Orientation preference stripes Orientation preference stripes are closed-form solutions with a single non-vanishing mode $\mathcal{A}_{\text{st}} = 1$, see **Fig. 7.9A**. A perturbation around orientation preference stripes in the amplitudes $(\mathcal{A}_{\text{st}}, 0, 0, 0, 0)^T \rightarrow (\mathcal{A}_{\text{st}}, 0, 0, 0, 0)^T + \mathbf{a}$ and phases $(\phi_1, \phi_2, \phi_3, \phi_4, \phi_5, \phi_6)^T \rightarrow (\phi_1, \phi_2, \phi_3, \phi_4, \phi_5, \phi_6)^T + \boldsymbol{\psi}$ leads in linear order to

$$\partial_t \mathbf{a} = M \mathbf{a} \quad (7.39)$$

$$\partial_t \boldsymbol{\psi} = 0 \quad (7.40)$$

with $(M)_{kl} = -\delta_{kl}(1 + \delta_{k1})$. Thus, orientation preference stripes are stable closed-form solutions.

Orientation preference rhombs Orientation preference rhombs are closed-form solutions with four non-vanishing modes of equal amplitude $\mathcal{A}_2 = \mathcal{A}_{2-} = \mathcal{A}_3 = \mathcal{A}_{3-} = \mathcal{A}_{\text{rh}} = 1/\sqrt{5}$ and phases $\phi_{3-} = \phi_2 + \phi_{2-} - \phi_3 + \pi$, see **Fig. 7.9A**. A perturbation around orientation preference stripes in the amplitudes $(0, \mathcal{A}_{\text{rh}}, \mathcal{A}_{\text{rh}}, 0, \mathcal{A}_{\text{rh}}, \mathcal{A}_{\text{rh}})^T \rightarrow (0, \mathcal{A}_{\text{rh}}, \mathcal{A}_{\text{rh}}, 0, \mathcal{A}_{\text{rh}}, \mathcal{A}_{\text{rh}})^T + \mathbf{a}$ and phases

$(\phi_1, \phi_2, \phi_3, \phi_{1-}, \phi_{2-}, \phi_2 + \phi_{2-} - \phi_3 + \pi)^T \rightarrow (\phi_1, \phi_2, \phi_3, \phi_{1-}, \phi_{2-}, \phi_2 + \phi_{2-} - \phi_3 + \pi)^T + \boldsymbol{\psi}$ leads in linear order to

$$\partial_t \mathbf{a} = \frac{1}{5} \begin{pmatrix} -3 & 0 & 0 & 0 & 0 & 0 \\ 0 & -4 & -2 & 0 & -2 & -2 \\ 0 & -2 & -4 & 0 & -2 & -2 \\ 0 & 0 & 0 & -3 & 0 & 0 \\ 0 & -2 & -2 & 0 & -4 & -2 \\ 0 & -2 & -2 & 0 & -2 & -4 \end{pmatrix} \mathbf{a} \quad (7.41)$$

$$\partial_t \boldsymbol{\psi} = \frac{1}{5} \begin{pmatrix} 0 & 0 & 0 & 0 & 0 & 0 \\ 0 & -2 & 2 & 0 & -2 & 2 \\ 0 & 2 & -2 & 0 & 2 & -2 \\ 0 & 0 & 0 & 0 & 0 & 0 \\ 0 & -2 & 2 & 0 & -2 & 2 \\ 0 & 2 & -2 & 0 & 2 & -2 \end{pmatrix} \boldsymbol{\psi} \quad (7.42)$$

with eigenvalues of the amplitude stability matrix $\lambda_1 = -2$, $\lambda_{2/3} = -3/5$ and $\lambda_{4/5/6} = -3/5$ and of the phase stability matrix $\lambda_1 = -8/\sqrt{5}^3$ and $\lambda_{2-6} = 0$. Thus, orientation preference rhombs are stable closed-form solutions.

Impact of cytochrome oxydase on orientation preference layout

A realistic account for hexagonal cytochrome oxydase patterns is the regime $\gamma > 0$. The impact of cytochrome oxydase on the layout of orientation preference is examined by simulating the amplitude equations of orientation preference, while fixing cytochrome oxydase to the closed-form solutions. The gradual increase of cytochrome oxydase coupling κ with initial conditions of orientation preference taken from weaker coupling with small additional noise results in the bifurcation diagram shown in **Fig. 7.9C**.

Data

We analyzed four data sets obtained with intrinsic signal imaging from *Macaca fuscata* originally published in³⁶² and processed with the generalized indicator function method⁵³⁵. The other two data sets were recorded from their southern cousins, *Macaca fascicularis*, with voltage sensitive dyes³⁶⁵. The Aotus dataset was originally published in⁵³¹. The other datasets are publicly available with⁴²⁸.

Analysis of model and experimentally obtained orientation domain layouts

Column spacing of both data and simulation were analyzed using the wavelet method introduced in^{236,238,241}. This method specifically takes into account that experimentally measured domain layouts often exhibit local variations in column spacing. This method is also the foundation for an unbiased comparison of the pinwheel layouts in experimental data²⁴². To estimate the pinwheel density and other pinwheel layout parameters, we used a fully automated procedure in²⁴². We refer to its Supplemental Material for further details.

Gender bias in peer review

$$Y = \lambda f.(\lambda x.f(x x))(\lambda x.f(x x))$$

Haskell Curry.

8.1 Content

Peer review is the *“life-blood of research in academia [...] the social structure that subjects research to the critical assessment of other researchers”*⁵³. In a merit-based scientific world, scientific results should be validated without regard to a scientist’s personal characteristics. This chapter is a metascientific study whether this is actually the case.

Based on a large data set of more than 40.000 articles published in the last 10 years we found that during the peer review process especially male editors select male reviewers to assess an article’s merit. Hence, female scientists are participating even less in the scientific publishing process than expected by their numerical underrepresentation alone. We also found that the mechanisms of homophily differ between male and female editors. While this same-gender preference is restricted to a small number of female editors, it is wide-spread among male editors. The large majority of female editors, thus, already selects reviewers without gender-bias. We show that homophily will persist even if numerical parity between genders is reached, highlighting the need for increased efforts to combat distortion effects in general and gender bias in particular in scholarly publishing.

8.2 Citation and original contribution

Markus Helmer, Manuel Schottdorf, Andreas Neef, and Demian Battaglia: *“Gender bias in scholarly peer review”*, eLife 6: e21718 (2017)¹⁷⁹

I conceived and designed the study together with all authors. I contributed to the formal analysis, the validation, the methodology and the analysis tools. I wrote the manuscript together with all authors.



RESEARCH

Gender bias in scholarly peer review

Abstract Peer review is the cornerstone of scholarly publishing and it is essential that peer reviewers are appointed on the basis of their expertise alone. However, it is difficult to check for any bias in the peer-review process because the identity of peer reviewers generally remains confidential. Here, using public information about the identities of 9000 editors and 43000 reviewers from the Frontiers series of journals, we show that women are underrepresented in the peer-review process, that editors of both genders operate with substantial same-gender preference (homophily), and that the mechanisms of this homophily are gender-dependent. We also show that homophily will persist even if numerical parity between genders is reached, highlighting the need for increased efforts to combat subtler forms of gender bias in scholarly publishing.

DOI: [10.7554/eLife.21718.001](https://doi.org/10.7554/eLife.21718.001)

MARKUS HELMER*, MANUEL SCHOTTDORF, ANDREAS NEEF AND DEMIAN BATTAGLIA*

Introduction

Peer review has an important role in improving the quality of research papers. It is the “life-blood of research in academia [...] the social structure that subjects research to the critical assessment of other researchers” (Bourdieu, 1975). This structure relies on self-regulated interactions within the scientific community, in which a journal editor appoints peer reviewers with expertise in the subject of a particular manuscript to report on the quality of that manuscript and to provide recommendations for its improvement. Other attributes of the peer reviewer, such as their gender, should be irrelevant (Moss-Racusin et al., 2012; Nature, 2013). However the identities of peer reviewers and editors are usually confidential, so previous work on gender balance in the peer-review process has relied on small, monodisciplinary data sets and these studies have given partly contradictory reports (Lloyd, 1990; Gilbert et al., 1994; Budden et al., 2008; Borsuk et al., 2009; Knobloch-Westerwick et al., 2013; Larivière et al., 2013; Buckley et al., 2014; Demarest et al., 2014; Handley et al., 2015b; Fox et al., 2016).

Frontiers journals (www.frontiersin.org) differ from most journals in that they generally disclose

the identities of peer reviewers and associate editors alongside each published article in an attempt to increase the transparency and quality of the publication process (Poynder, 2016). This allowed us to extract the names of associate editors, peer reviewers and authors for articles published in Frontiers journals between 2007 (when the first Frontiers journal was published) and the end of 2015. This data set included the names of more than 9000 editors, 43,000 reviewers, and 126,000 authors for about 41,000 articles published in 142 journals in Science, Health, Engineering and the Humanities and Social Sciences (see Materials and methods). This data set is one of the largest available to date, and contains at least an order of magnitude more information than most data sets used in previous studies of peer review (see **Supplementary file 2** for comparison).

Analysis of this data set reveals that women are underrepresented in the peer-review process, and that editors of both genders operate with substantial same-gender preference (homophily) when appointing reviewers. Moreover, our analysis suggests that this homophilic tendency will persist even when men and women are fairly represented in the peer-review process. Our results confirm the need for increased efforts to

Reviewing editor: Peter Rodgers, eLife, United Kingdom

© This is an open-access article, free of all copyright, and may be freely reproduced, distributed, transmitted, modified, built upon, or otherwise used by anyone for any lawful purpose. The work is made available under the [Creative Commons CC0 public domain dedication](https://creativecommons.org/licenses/by/4.0/).

fight against subtler forms of gender bias in scholarly publishing and not just focus on numerical under-representation alone.

Results

To assess whether our data set was representative of an active and mature research community, we created directed networks (**Figure 1a₁**), in which individual scientists appeared as vertices, while arrows denoted interactions between them (“*is appointing*” in the editor-to-reviewer network, and “*is editing (reviewing) a manuscript of*” in the editor (reviewer)-to-author network). As a whole, the networks had an exponentially fast growth in time, with a large fraction of people participating in a connected component of the graph reaching 90% of the total network size. Furthermore, graph theoretical metrics such as shortest path length, small-world index as well as several other network properties have changed little in the 3-5 last considered years (**Figure 1—figure supplement 1**). Thus, peer-reviewing interactions in the Frontiers journal series gave rise to a mature, topologically stable and integrated community, even though its contributors constitute only a small subset of researchers worldwide.

We then looked for signatures of gender bias and of its evolution across time in the structure of these large networks. We study first the fractions of assignments for reviewing or editing given to female or male scientists and, for comparison, we also show the fractions of author contributions. **Figure 1b** reveals that the fractions of authoring, reviewing and editing contributions by women — amounting to 37%, 28% and 26%, respectively, in the complete accumulated data until 2015 — are always significantly smaller than the corresponding fractions for men. The unbalance between male and female contributions thus worsens when gradually ascending through the peer-review hierarchy. Apart from a few outlier countries, this pattern was dominant worldwide (**Figure 1—figure supplement 2**). It was also largely present in all the considered journals when looking at them individually (**Figure 1c**). Overall, the number of contributions by female authors varies between about 15% (Frontiers in Neurorobotics) and 50% (Public Health), by female reviewers between about 15% (Surgery) and 50% (Public Health), and by female editors from ca. 5% (Robotics AI) to 35% (Aging Neuroscience). Globally, we observed a trend towards gender parity across time. The rates of change were, however, very

slow. Linear extrapolation based on the fractions observed from 2012 to 2015 would predict that exact parity could be achieved as late as 2027 for authoring, 2034 for reviewing and 2042 for editing.

We wondered whether these lower fractions of contributions to the different roles were just due to the fact that overall there are numerically less female than male authors, reviewers and editors (39%, 30% and 28% out of all available authors, reviewers and editors, respectively, were women, closely mirroring the observed fractions of assignments). To test this hypothesis, we took the exact same network of peer-review interactions in the Frontiers journals for given, and randomly permuted gender labels among scientists of a given role (**Figure 1a₂**). This procedure maintained the ratio of female and male scientists acting in the different roles, but destroyed all direct correlations between gender and numbers of contributions. Repeatedly drawing random genders for the scientists in the network generated a surrogate ensemble that we used to estimate the expected number of contributions in a gender-blind control network. Author and reviewing contributions by women lay significantly below the confidence intervals obtained through this permutation testing procedure since 2009 and 2011, respectively. For female editing contributions we found the same, though non-significant, trend. Thus, the mere overall smaller number of female actors cannot explain the observed unbalanced fractions of female contributions to the peer-review chain.

We then looked for possible differences over the entire distributions of the number of peer-review tasks and authoring contributions for men and women. These distributions are fat-tailed (**Figure 2a-c**), indicating that some individuals provided a large number of contributions to the publication chain, while a majority of scientists authored, reviewed or edited only a small number of manuscripts. Moreover, comparing the observed degree distributions to the expectations derived from the same null hypothesis used above, women had a significantly smaller than chance probability to review (and author) more than one article, while their probability to act as single-time reviewer or author exceeded the expected chance level (**Figure 2e-f**). In the editing role, women underrepresentation was significant only for a high number of contributions. Furthermore, we found significant deviations from chance-level expectations across the

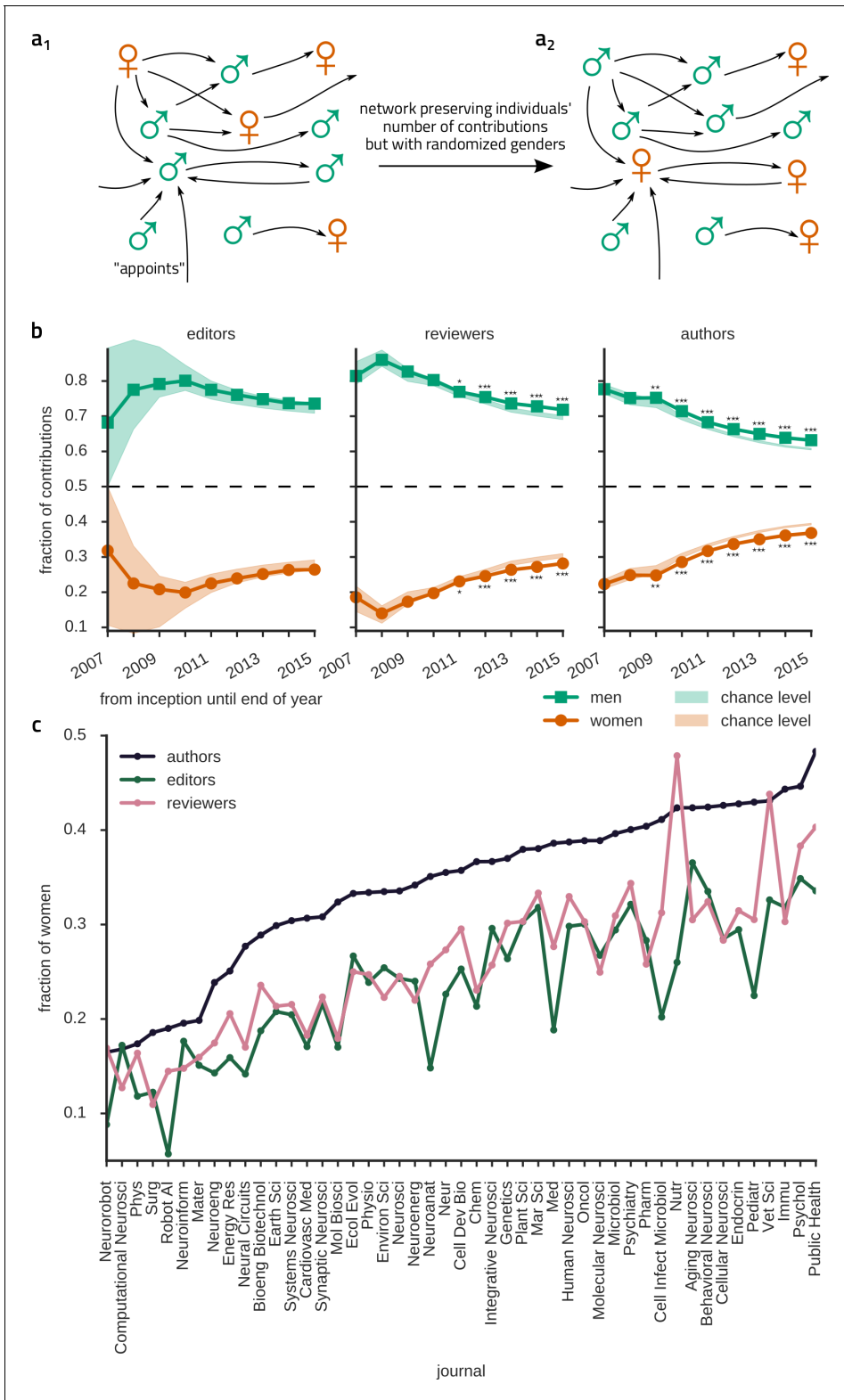


Figure 1. Women review and author even less articles than expected from their numeric underrepresentation. (a₁) We represent peer-reviewing interactions as directed graphs, in which vertices denote scientists. In the editor-to-reviewer network every edge represents the act of an editor (source vertex) appointing a reviewer (target vertex) to review a manuscript (and the reviewer has accepted the invitation). Analogously, in the reviewer-to-author network edges represent a reviewer reviewing a manuscript of an author. (b) The development of the fraction of contributions for each gender *Figure 1 continued on next page*

Figure 1 continued

are shown for editors, reviewers and authors. Since the start of the Frontiers journals in 2007 until 2015, women (circles) edit, review and author much less than 50% of manuscripts, as expected from their numeric underrepresentation. However, the actual numbers of reviewing and authoring contributions by women are even smaller than expected by chance, taking into account their numeric underrepresentation. This is revealed by comparison with a null hypothesis in which gender and number of contributions are assumed to be independent. To this end, we generated surrogate ensembles by shuffling the genders of scientists appearing in a given role in the network (a_2). From the surrogate ensembles, we obtained 95% confidence intervals (CIs; shaded areas in b). *, **, *** over (under) the data symbols denote the data lying over (under) the 95%, 99%, 99.9% CIs. Note that for all three subnetworks, there is a noticeable, but extremely slow trend towards equity (dashed line) for the fraction of contributions. (c) The fraction of female contributors, ranked in increasing order of authoring contributions, for the 47 frontier journals, whose published articles were handled by at least 25 distinct editors. Women were underrepresented consistently across all fields and particularly severely in math-intensive disciplines.

DOI: [10.7554/eLife.21718.002](https://doi.org/10.7554/eLife.21718.002)

The following figure supplements are available for figure 1:

Figure supplement 1. Analysis of network topology.

DOI: [10.7554/eLife.21718.003](https://doi.org/10.7554/eLife.21718.003)

Figure supplement 2. Gender disparities vary between countries.

DOI: [10.7554/eLife.21718.004](https://doi.org/10.7554/eLife.21718.004)

entire studied time-span (**Figure 2—figure supplement 1**).

The differences in assignment numbers may reflect behavioral or psychological differences between the groups of male and female scientists — either intrinsic or due to sociocultural context (*Moss-Racusin et al., 2012; Nature Neuroscience, 2006; Ceci et al., 2009; Ceci and Williams, 2010; Goulden et al., 2011; Ceci and Williams, 2011; Bloch, 2012; Raymond, 2013; Shen, 2013; Handley et al., 2015a*). Nevertheless, assignment numbers are also ultimately influenced by the editors' active choices. To reveal whether any bias exists in the reviewer assignment relation, we first analyzed gender correlations between directly connected pairs of nodes in the editor-to-reviewer appointment network (**Figure 3a**) and found a marked gender homophily bias for both male and female editor nodes. Specifically, 73% of reviewers appointed by men were also men, 33% of reviewers appointed by women were women, but, importantly, both these numbers laid above the expectations drawn from the assumption that genders were randomly distributed in the given editor-to-reviewer network topology. Similarly, in the reviewer-to-author network (**Figure 3b**), male (female) reviewers assessed articles authored by male (female) authors significantly more often than expected.

While these findings seem to point at homophily created by choices, they might also stem from "baseline" homophily (*McPherson et al., 2001*), i.e. subtle but unavoidable bias caused by disproportions in the number of reachable male and female nodes due to heterogeneous network structure. We first checked for the influence of local subnetwork structure on apparent gender bias by looking at different scientific

fields, including those with relatively mild underrepresentation of women, and found homophily widespread across disciplines (**Figure 3c**). Second, a more detailed analysis of inter-node gender correlations in the editor-to-reviewer appointment network detected a clear tendency to gender homophily already at the level of the narrow neighborhood of individual nodes (**Figure 3d**). Specifically, to control for baseline homophily at the level of a narrow local neighborhood, we measured, for each editor node, the actual number of reviewer assignments given to women. We then subtracted from this number its chance expectation, derived individually for every node from the frequency of *locally reachable* female reviewers, i.e. reviewers situated at most five links away (which is a short distance relative to the average shortest path length of 12 steps for the editor-to-reviewer network, cf **Figure 1—figure supplement 1e**). Even at this local neighborhood level, we continued to find that male (female) editors generally appointed female reviewers at a lower (higher) rate than expected. Both independent analyses – by topic or localized – validate the existence of a so-called "inbreeding" homophily, i.e. an active preference to connect with same-gender network nodes, on top of "baseline" homophily (*McPherson et al., 2001*).

Finally, we wondered whether the observed inbreeding homophily in the network was due to the presence of a few strongly homophilic editors or whether, alternatively, homophilic attachment was a feature shared by most editors. To that end, we defined an index of inbreeding homophily at the local level of each editor node. For each considered editor node, we first evaluated the number k of connected same-gender reviewers. We then evaluated the

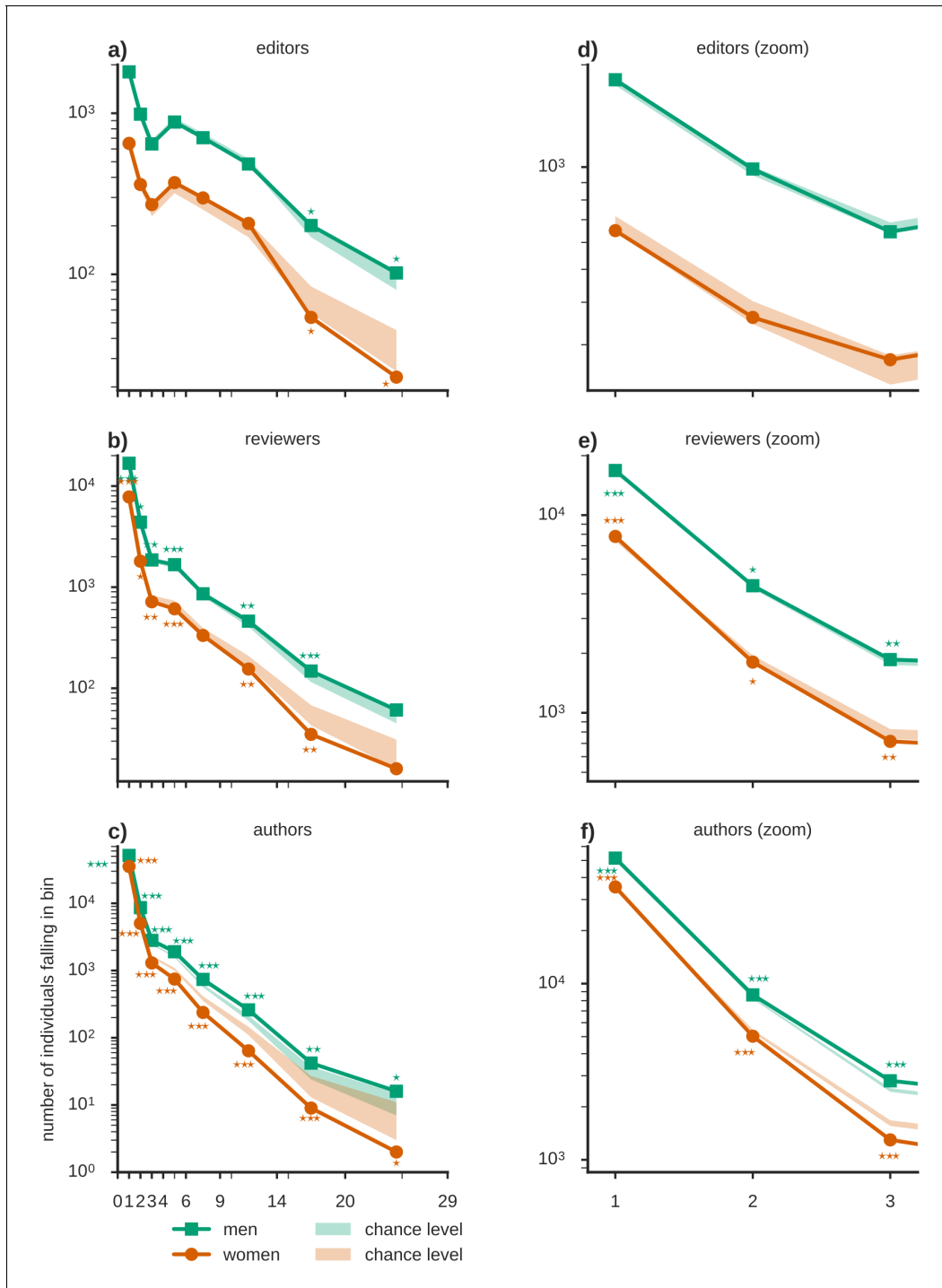


Figure 2. Women are underrepresented in the fat tail of contributions. A break-down of the number of individuals contributing a given number of times as editors, reviewers and authors (binned, x-axis is marking the bin edges) shows that the majority of scientists (a) edited, (b) reviewed or (c) authored (corresponding zooms for small contribution numbers are shown in e-f) only a small number of manuscripts. Chance levels (shaded) were derived from an ensemble of reference networks constructed as shown in Figure 1a. The underrepresentation of women in relation to these chance levels tends to increase towards the fat tail of the distribution, associated to the relatively few individuals that made many contributions. In the group of one-time authors or reviewers however, women are overrepresented. Time resolved distributions are shown in Figure 2—figure supplement 1.

DOI: 10.7554/eLife.21718.005

The following figure supplement is available for figure 2:

Figure 2 continued on next page

Figure 2 continued

Figure supplement 1. Time- and gender-resolved histograms of the number of contributions.
DOI: 10.7554/eLife.21718.006

probability $0 \leq \Phi_{\text{hom}} \leq 1$ that k (or more) homophilic connections could arise by baseline homophily only, taking into account the editor-specific basin of locally reachable male and female reviewers (defined as for **Figure 3d**). Such Φ_{hom} can serve as an index tracking the strength of inbreeding homophily in shaping the actual reviewer appointments by an editor. Large values of Φ_{hom} approaching 1 indicate that the observed gender homophilic choices of a given editor are plausibly just due to “passive” baseline homophily. In contrast, small values of Φ_{hom} approaching 0 hint at a stronger tendency to “active” – consciously or unconsciously, see Discussion – inbreeding homophily. **Figure 3e** shows the histograms of the index Φ_{hom} for male and female editors, compared with expectations from gender-shuffled networks. For male editors, most histogram bins for $\Phi_{\text{hom}} < 0.6$ displayed node counts significantly larger than gender-shuffled estimations. The histogram of Φ_{hom} for female editors showed much fewer significant overrepresentation and most of them at very low values of Φ_{hom} , however it remained compatible with gender-shuffled estimations for most of the Φ_{hom} range.

These different distributions of inbreeding homophilic tendencies resulted in a gender-dependent impact of the reviewer-appointment choices of male and female editors in determining the overall number of female reviewer appointments. To determine this impact we pruned links originating from editors with inbreeding homophily index Φ_{hom} below a growing threshold Φ_{thr} (retaining only editors whose Φ_{hom} satisfies $0 \leq \Phi_{\text{thr}} \leq \Phi_{\text{hom}} \leq 1$) and we did so separately for male and female editors (**Figure 3f**). After pruning the most homophilic male or female editors, we evaluated the new resulting probabilities of appointing a female reviewer. On the one hand, we found that it was enough to remove the few most homophilic female editors with the lowest values of Φ_{hom} from the network, to bring the probability for a female editor to appoint a female reviewer back to chance-level. On the other hand, the probability for a male editor to appoint a female reviewer increased only very slowly by pruning more and more male editors. In particular, it remained significantly below chance expectations for all the considered thresholds for inclusion, $0 \leq \Phi_{\text{thr}} \leq$

0.5. This means that the overall smaller-than-chance probability of appointing female reviewers for male editors is due to inbreeding homophilic tendencies that are *widespread among male editors*, although at varying degrees of strength. In contrast, the overall larger-than-chance probability to appoint female reviewers for female editors is driven by the action of just a *small number of strongly homophilic female editors*, with most other female editors showing only “passive” baseline homophily.

Discussion

In this study, we found that apart from a few outliers depending on country and discipline, women are underrepresented in the scientific community with a very slow trend towards balance, which is consistent with earlier studies (*Larivière et al., 2013; Fox et al., 2016; Topaz and Sen, 2016; Lerback and Hanson, 2017; Nature Neuroscience, 2006; Shen, 2013; Nature, 2012*). In addition, we found that women contribute to the system-relevant peer-reviewing chain even less than expected by their numerical underrepresentation, revealing novel and subtler forms of bias than numeric disproportion alone. We reported clear evidence for homophily beyond the expected baseline levels in both genders (**Figure 3**) using a very large trans-disciplinary data set that allowed us to clarify a previously ambiguous picture (*Lloyd, 1990; Gilbert et al., 1994; Borsuk et al., 2009; Buckley et al., 2014; Fox et al., 2016*). This network-level inbreeding homophily is driven by a large fraction of male editors, together with only a few highly homophilic female editors.

Evolution of participation rates by gender and causes for remaining inequity

To start our discussion on a positive note, we found that the participation of women in science, at least in terms of their numerical representation, has increased during the last years, which is consistent with other studies. The number of female doctoral recipients at US institutions increased by, on average, 0.1% - 0.6% per year between 2005 and 2015, depending on broad field of study (*National Science Foundation, 2016*). *Ley and Hamilton (2008)* reported that the number of fraction of women in medical schools

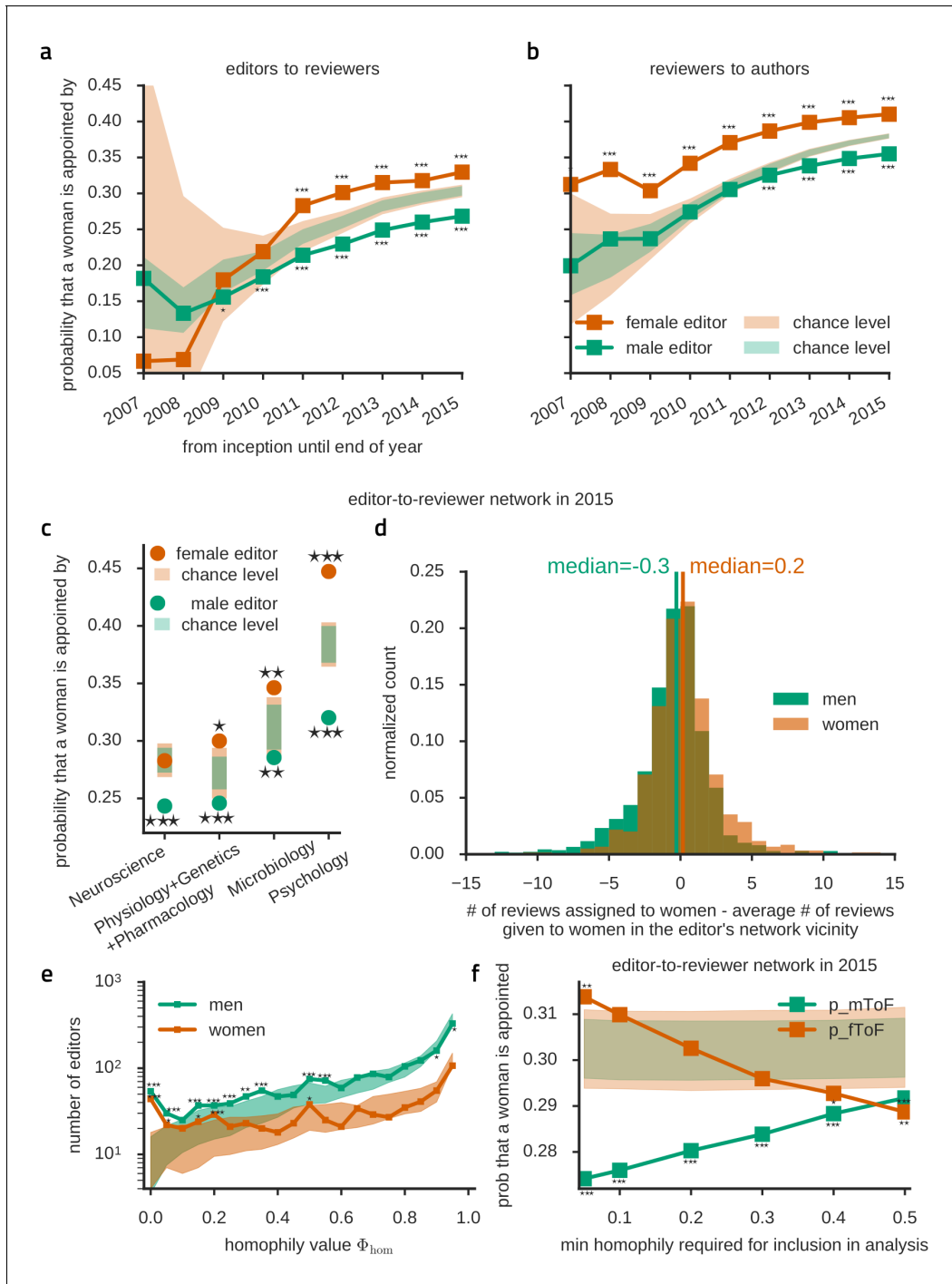


Figure 3. Editors have a same-gender preference for appointing reviewers. (a) Female editors (orange) appoint significantly more female reviewers than expected under the gender-blind assumption (shaded area). At the same time, male editors (green) appoint less women than expected. The development of this trend over time is shown, including articles cumulatively until the indicated year. (b) Likewise, female/male reviewers review significantly more female/male-authored articles than expected. (c) Homophily is widespread across scientific fields, including those with relatively mild underrepresentation of women. We here report four example disciplinary groupings, with large numbers of contributions (from left to right, respectively, 13416, 4721, 4020, 5680) and the propensity of appointing a female reviewer depending on the editor’s gender for each of these groupings. Only assignments by female neuroscience editors were not homophilic, otherwise the occurrence of same-gender preferences was general, arguing against heterogeneity between subfields as a cause for homophily in assignments. (d) Plotted here are distributions of a measure of inbreeding homophily. To control for baseline homophily at the level of a narrow local neighborhood, we measure, for each editor node, the actual number of

Figure 3 continued on next page

Figure 3 continued

reviewer assignments given to women and subtract the expected number, which would be observed if the considered editor appointed women with the same frequency as in his/her local vicinity. For male editors (green) the distribution is skewed towards an underrepresentation of female assignments (left-leaning), while for female editors the distribution is skewed towards an overrepresentation of female assignments. This highlights that homophily bias is detectable even at the level of the reachable narrow surrounding of each editor. (e) Histogram of the probability that an editor assigns as least as many reviews to people of the same gender as he/she actually does reveals that there's an excess of strongly inbreeding-homophilic editors (small Φ_{hom} -values) among both men and women compared to expectation (shaded area). Note that below $\Phi_{\text{hom}} < 0.1$ there are only few strongly homophilic female editors. For male editors, significant homophily extends through many more editors until $\Phi_{\text{hom}} < 0.6$. (f) Using all data until 2015, the probability that a women is appointed is above expectation (shaded areas) only for female editors and only when all or all but the most extremely inbreeding-homophilic editors are included in the analysis.

DOI: [10.7554/eLife.21718.007](https://doi.org/10.7554/eLife.21718.007)

increased by, on average, 0.6% to 0.8% per year (depending on the scientists' rank) between 1996 and 2007. Percentages of women professors has increased at a rate of 0.5%-1% per year in the European Union (**ETAN Expert Working Group on Women and Science, ETAN Expert Working Group on Women and Science, 2000**). The fraction of publishing female scientists in Germany increased by, on average 0.7% from 2010 to 2014, it is now 30.9% (**Pan and Kalinaki, 2015**). **Fox et al. (2016)** found that the number of selected female reviewers in Functional Ecology increased by, on average, 0.8% per year between 2004 and 2014, while, notably, the number of female editors increased by, on average, 3.8% per year. **Caplar et al. (2016)** noted that the number of female first authors of astronomy articles increased by about 0.4% per year between 1960 and 2015. In the Frontiers series of journals, we found that the number of contributions by female authors, reviewers and editors increased by, on average, 1.1% / year, 1.2% / year and 0.9% / year between 2012 and 2015, respectively, similar to the numbers above.

What could be the reasons for the remaining inequity? It has been argued that underrepresentation of women in science may be due to conscious career choices by female researchers (**Ceci et al., 2009; Ceci and Williams, 2010, 2011**), even if it is not clear to which extent these choices are really free or rather constrained by society. Previous studies reported that, measured by their number of publications, women are generally less productive than men (**Cole and Zuckerman, 1984; Zuckerman, 1991; Long and Fox, 1995; Xie and Shauman, 1998; Pan and Kalinaki, 2015; Caplar et al., 2016**) and it has been suggested (**Xie and Shauman, 1998**) that this might be due to personal characteristics, structural positions, and marital status. Moreover, the fraction of female scientists decreases with rank or age (**ETAN Expert Working Group on Women and Science, 2000; Ley and Hamilton,**

2008; Goulden et al., 2011) and this shorter career length might contribute to the drop of female-to-male ratio for a high number of contributions. Nevertheless, women who persevere longer in their career despite obstacles are highly performing. While the productivity of young publishing female scientists in Germany was 10% lower than that of their male counterparts, the discrepancy reduced to just 3% for more senior scientists (**Pan and Kalinaki, 2015**). Also, it has been reported that women with children are not less productive than those without (**Hamovitch and Morgenstern, 1977; Cole, 1979; Cole and Zuckerman, 1987**), although young children might decrease productivity (**Kyvik, 1990; Kyvik and Teigen, 1996**). The low number of women among senior scientists might be particularly detrimental for a gender-neutral evaluation of scientific work, as the implicit association of "male" and "science" is strongest in the group of 40-65 year olds (**Nosek et al., 2007**). Moreover, declining an invitation to review is often due to a lack of time (**Tite and Schroter, 2007**) and it is possible that female scientists spend more time with duties beyond research (e.g. teaching, mentoring, service; **ETAN Expert Working Group on Women and Science, 2000; Knapp, 2005; Misra et al., 2011**). On the other hand, a compensating factor seems to be that female editors, in contrast to authors, have been reported to be more productive than male editors (**Gilbert et al., 1994**). Interestingly, men and women who are invited to review a manuscript have very similar propensities to accept the invitation (**Fox et al., 2016; Lerback and Hanson, 2017**), suggesting: (1) that simply increasing the number of invitations to female reviewers would have a direct and proportional effect; and, (2) that the low number of female reviews in our data is caused in part by a lower number of invitations.

The underrepresentation and discrimination of women in the scientific community is a problem

that will not solve by itself, given the pervasive, generally unconscious nature of gender bias. Women have been reported to be less likely to be hired (*Moss-Racusin et al., 2012*), to receive a grant (*Wennerås and Wold, 1997*), and to receive higher salaries (*Shen, 2013*). Still today, most people implicitly associate science with men, and liberal arts with women more than the other way round (*Nosek et al., 2007*), and this tendency, for both men and women, is apparent from a very young age (*del Río and Strasser, 2013; Bian et al., 2017*) and possibly reinforced by social dynamics in school education (*American Psychological association, 2007; Duru-Bellat, 2008*). Beyond that, men are more reluctant than women to believe that such a bias exists (*Handley et al., 2015a*), manifesting lack of interest for the problem (“negligence”) or, even, consciously assuming that gender discrimination cannot be avoided (“philosophical acceptance”) more often than females (*Parodi, 2011*).

How representative are the Frontiers journals?

The data analyzed here comprises a wide spectrum of scientific topics and the findings should generalize. However, Frontiers articles are unusual insofar as they undergo open peer review, whereas the identity of reviewers is not revealed in most other journals. Ambiguous reports exist whether open-peer review (as opposed to single- or double-blind peer-review) affects potential reviewers’ willingness to assess a paper (*Nature Neuroscience, 1999, van Rooyen et al., 1999; Ware, 2008; Baggs et al., 2008*). In particular, a primary concern in disclosing reviewer’s identity is the possibility that a rejected author may also become a prospective employer for the reviewer and hence a possible reluctance of peers in more vulnerable positions to accept an invitation to review. While it is conceivable that assignment rejection due to non-anonymity is more likely for early career scientists, we do not see any reason for a direct effect of gender and such an effect has not been reported to the best of our knowledge.

Then, how does the population of scientists contributing to the Frontiers series of journals compare to other scientometric populations? First, we compared our authorship data to that of *Larivière et al. (2013)* who analyzed gender bias in articles from a wide range of journals that were published between 2008 and 2012, comprising about 3 million authors. While no analysis of peer review is performed therein, this study

comprises an order of magnitude more authors than in our study. It can therefore serve as a benchmark for gender-composition among authors. They reported that 42% of authors in their analyzed scientific articles were women, whereas we found that number to be 39% in the Frontiers journals. Given uncertainties in determining a person’s gender these numbers are comparable. Broken down by country, we find overall similar fractions of female authors, although, for some countries, the relative deviations can rise up to 29% (*Supplementary file 1*). However, small sample sizes, together with, possibly, a varying popularity of the Frontiers journals in different countries, might contribute to such deviations.

Second, not much data was available concerning gender bias among reviewers and editors, until very recently. Many previous studies (cf. *Supplementary file 2*) were self-diagnoses performed by editorial boards of the corresponding journal and, as a consequence, tended to be based on mono-disciplinary data of relatively small sample size. Larger sample sizes, but limited to editors, were considered in an analysis of the composition of editorial boards of 435 mathematical journals (*Topaz and Sen, 2016*). Only 9% of editors were women. Other reported numbers for the fraction of women editors in journals of different disciplines range from 38% to 54% (cf. *Supplementary file 2*). These numbers lie at the lower and upper end of the female editor fractions across the Frontiers journals, ranging between 6% (Frontiers in Robotics and AI) and 37% (Frontiers in Aging Neuroscience), with an average of 28%. Concerning female reviewers or female reviewer appointments, fractions reported in the literature range between 16% and 48% (cf. *Supplementary file 2*), to be compared with the range between 11% and 48% for the Frontiers journals with an average of 30%. Concerning female authors, *Pan and Kalinaki (2014)* report fractions ranging from 15% in computer science to 57% in veterinary science. These numbers are once again comparable to female author fractions in Frontiers journals, ranging from 17% (Neurorobotics) to 48% (Public Health). Overall, our study provides thus a global account on the prevalence of women among editors and reviewers and ranks previous reports in a continuum of field-specific participation numbers. Importantly, our data is consistent with these diverse reports, highlighting that the Frontiers peer-review networks are well representative of widespread patterns.

Our work calls for a detailed comparison with another recently published report about peer reviewer assignments in 20 journals of the American Geophysical Union (AGU), based on a slightly smaller sample size compared to ours (Lerback and Hanson, 2017). This study reports information about aspects that our study could not have access to, breaking down women's underrepresentation by age and showing that the decline rate for invited reviews is only slightly smaller for women than men. Overall, relative fractions of female participation reported by this study are compatible with numbers we found for the journal *Frontiers in Earth Science*, with e.g. a matching female reviewer appointments fraction close to 20%, suggesting that women play a larger role in other fields compared to that report (cf. Figure 1c). For the AGU journals the authors conclude that editors, especially male ones, appoint too few female reviewers. Male editors' behavior in that study thus agrees with our findings for the entirety of *Frontiers* journals, while we find an opposite trend for female editors. We note here that Lerback and Hanson (2017) reached their conclusion of women's underrepresentation by comparing actual reviewer appointment numbers to the fraction of female first authors. This comparison, however, might be questionable, because reviewers in low age groups are rarely invited by editors (3% of times) whereas first authors tend to be young. To account for such differences, we determined expectation levels by gender shuffling among the reviewers and editors in the fixed network of actual reviewer-editor interactions and find that the fraction of female authors (the expectation value that Lerback and Hanson used) is much higher than the expected number of female reviewer contributions (our expectation value; cf. Figures 1b and 3a). For that reason, Lerback and Hanson may have quantitatively overestimated the female editors' bias against female reviewer appointments. Still, despite this overestimation, even Lerback and Hanson reported female editors' preference for female reviewers for certain age classes (although not commented upon).

Homophily in society and science

The phenomenon of gender homophily in peer-reviewing networks have already been described, but these previous reports have reached ambiguous conclusions. Lloyd (1990) found that female reviewers accepted female-

authored papers at a higher rate than those of male authors, whereas male reviewers did not show such a bias. In contrast, Borsuk et al. (2009) reported that male and female reviewers were equally likely to reject a female-authored paper. The probability that a female editor appoints a female reviewer was reported to be 31%-33%, whereas male editors appointed female reviewers in 22%-27% of cases (Gilbert et al., 1994; Buckley et al., 2014; Fox et al., 2016). Here, for the whole spectrum of *Frontiers* journals we found these numbers to be similar: 33% and 27%, respectively. However, our study concludes for the existence of significant inbreeding homophily in the reviewer appointing behavior for both male and female editors, and does so based on a pluri- rather than mono-disciplinary data set, substantially larger than all previous accounts of homophily in peer review.

Socrates, in Plato's *Phaedrus*, already asserted that: "similarity begets friendship". Homophily – or "attraction for the similar", not only limited to the gender attribute – is ubiquitous in social networks. Since the classic studies of Park and Burgess (1921) and Lazarsfeld and Merton (1954), gender homophily has been found in groups of playing children (Bott, 1928; Shrum et al., 1988) and adult friends (Verbrugge, 1977) and is also present in work environments (Brass, 1985; Bielby and Baron, 1986; Ibarra, 1992) and voluntary organizations (Popielarz, 1999). Since focused interactions between co-workers favor the formation of relations, operation in already homophilic environments will lead to an amplification of homophily (Feld, 1981; Feld, 1984). In particular, homophilic styles of professional interaction with peers may persist since the time in which they were (un-)consciously learned in homophilic school environments (Vinsonneau, 1999).

Importantly, even a slight homophily can influence and alter the way in which information spreads (Yava and Yucel, 2014) and opinions form through the social network of interactions, leading to the emergence of "dead-end" cultural niches (Mark, 2003). Homophilic groups indeed tend to vote together when asked to decide for something (Caldeira and Patterson, 1987) and have similar prospective evaluations, a same mindset (Galaskiewicz, 1985). While homophily can in principle be put to good use, as for instance in the education about good health practices (Centola, 2011), the uncontrolled effects of homophily may constitute a

threat to the universalism of the peer-review system, and thus to science.

Gender-specific mechanisms of homophily

We observed very different patterns of homophily for male and female editors, with a widespread homophily across men, while dominated by very few highly homophilic editors for women. After removal of their contribution, homophily became insignificant (cf. **Figure 3e,f**). This suggests that there is only baseline homophily for the majority of female editors and most assignments are gender-blind (for instance in the neuroscience community, cf. **Figure 3c**). Differences between men's and women's homophily patterns are classically known, finding their root in different styles of social network construction. For instance, in situations where a mutual friendship exists between A and B a friendship initiation with C tends to be reciprocated by boys, but not by girls (**Eder and Hallinan, 1978**). Such differences in attachment strategies tend to generate gender-segregated worlds for children to preadolescents in which girls evolve in small homogeneous groups and boys form larger but more heterogeneous cliques, with boundaries made looser only later by romantic ties (**Shrum et al., 1988**). Professional social networks of men are more homophilic than women's, especially in work environments in which men are dominant (**Brass, 1985; Ibarra, 1992**). Another source of asymmetry may be that both men and women tend to form connection routes passing through a male node when reaching toward distant domains (**Aldrich, 1989**).

One could speculate that other factors might contribute, like friendship or (perceived) status, competency and reputation. These factors might, in turn, be partly depending on gender, e.g. through implicit biases (**Nosek et al., 2007; Merton, 1968; Paludi and Bauer, 1983**). Multiple categories of relationships were analyzed, for instance, by **Ibarra (1992)** who reported that, in a company setting, men named mostly men as points of contact for five different business-relationship categories, whereas for women the preferred gender was category-dependent. A similar situation could be at work here: one could speculate that a set of other, hidden, variables influence reviewer appointment decisions, and that these variables have a different importance for male and female editors. Determining which factors are most important for male and female editors in the choice of the reviewer and how these factors are or are not, in principle,

related to gender, might thus aid in reducing homophily in the peer-review system.

Our finding of strongly homophilic "topology-organizer" female editors is reminiscent of the notion of "femocrat" introduced in political studies, referring to the role played by isolated feminists who, after having managed to integrate inside men-dominated decisional organisms, provide a bridge to the spheres of power for the requests of activists outside of them (**Yeatman, 1990**). Now, while the active engagement of these femocrats is very useful in pushing forward technocratic (i.e. top-down) solutions aiming at reducing gender discriminations, especially at an early stage, on the long-term, the effects of their action may be precarious. Indeed political experiences have shown that when an external event reduces the influence of these isolated driver women, the situation can quickly deteriorate again (**Outshoorn, 2005**), aggravated by the suspicious look toward femocrats held by formerly dominant men or, paradoxically, even women, finding them too prone to compromise or too aggressive (**Outshoorn and Kantola, 2007**). It is thus important to devise strategies 'healing' network topology in depth, and in a bottom-up fashion, via pervasive education campaigns targeted to the deciders (**Sainsbury, 1994**), in our case chiefly the editors. Such strategies are required to protect the acquisitions of top-down actions against gender discriminations: increasing the number of women will not be enough to overcome gender bias (**Isbell et al., 2012; Avin et al., 2015**).

Conclusions

Ideally, all scientific interactions are gender-blind. A scientist's status and the provision of resources to scientists should not be influenced by gender but solely depend on the value of the scientific contributions. Access to the publication systems is a critical determinant of a scientist's success. Accordingly, reviewers and editors, the gatekeepers of the scientific canon, should be particularly sensitive to base their judgment solely on the merit of scientific work. This merit, however, is difficult to determine and any assessment is necessarily influenced by the assessor's view of the field, including his or her personal position in the network of colleagues and the interactions with them (**Mulkay, 1979; Cole, 1992**).

Inbreeding homophily, an increased affinity between persons with similar attributes, appears to be a sociological, population-level trait of

human societies. It is only natural, thus, that we find gender homophily in interactions between editors, reviewers and authors. Nonetheless, this inbreeding homophily is damaging to female scientists, whose work ends up being overlooked, due to unconscious negative bias. The phenomenon of inbreeding homophily is also likely not restricted to the peer review of manuscripts, so it needs to be taken into account for grant evaluation, hiring, or when designing mentoring programs. Importantly, it is likely to persist even when numerical balance between genders is achieved (Isbell *et al.*, 2012). Altogether, inbreeding homophily negatively affects science as a whole because a stronger involvement of women would increase the quality of scientific output (Merton, 1973; Woolley *et al.*, 2010; Nature, 2013; Campbell *et al.*, 2013). Consequently, all scientists should wholeheartedly support the endeavor to remove gender bias from science - but how could that be achieved?

Initiatives to remove gender-based inequality can roughly be divided into two different categories. On the one hand, "gender mainstreaming" (Special Adviser on Gender Issues and Advancement of Women, 2002) promotes the consideration among actors at all levels of every action's and policy's implications on women and men and is geared towards creating long lasting "bottom-up" changes. On the other hand, fast progress could be attempted through "top-down" implementation of technocratic instruments such as quota. This politically issued 'state feminism' (Mazur and McBride Stetson, 1995), is suboptimal in that it might even "provide an alibi" for not modifying attitudes in depth (Squires, 2008). As inbreeding homophily is an expression of a state of mind it is likely little amenable to change by externally enforced measures. Raising awareness, in comparison, seems to be the most promising route. The goal should be to motivate all scientific actors to "integrate thinking about gender discrimination in every decisional process" (translated from Woodward, 2008). Educative actions should be conducted with tact, not based uniquely on inducing feeling of guilt and shame, in order not to be perceived as annoying (Woodward, 2003). At the same time, existing formal actions to reduce bias should be upheld.

In the field of peer review two more specific strategies are available to reduce bias: blind review and automated editorial management. However, both strategies are of limited acceptance and use. First of all, removing the authors' names is often not sufficiently blinding.

References to the authors' previous publications or to the approving ethics committee all but spell out the authors. Second, while removal of the authors' names does indeed blind the reviewers to all irrelevant attributes, it also blinds them to relevant meta-data, such as the scientific experience of the authors, which might be considered as relevant by many reviewers. In an attempt to assist editors of Frontiers journals, keyword-based reviewer suggestions are automatically provided to them but the editors remain free to make their own choices. While these gender-blind automated suggestions could already contribute to an assignment that is less influenced by homophily, an editorial management software is also the ideal platform to routinely direct the editor's attention to the issue of homophily. It could display statistics similar to our Figure 3 and encourage non-homophilic choices of reviewers. Such a strategy maintains full editorial freedom and could easily be evaluated, either internally or, in the case of open review as in the Frontiers journals, through analysis of the publicly available data.

Given how engrained homophily is in our nature, the path towards a gender-blind science will be arduous. Yet, with the joined effort of the scientific community to overcome partisanship and discrimination, a merit-based system with equal opportunities for all scientists might just be within reach. After all, which social enterprise would be more apt to follow ratio over instinct than science?

Materials and methods

Collection and parsing of data

All article data were exclusively obtained from the publicly available articles web pages from the Frontiers Journal Series (RRID:SCR_007214), which was listed (at the date of last data download in March 2016) on: http://www.frontiersin.org/SearchIndexFiles/Index_Articles.aspx, as well as the associated XML file if the HTML code of the article web page contained a corresponding reference. Subsequently, articles' metadata (article id, authors, reviewers, editors, publication date, etc.) were extracted from the XML files and the web pages. All gathered personal identity information was deleted after inference of individual genders (see later), resulting thus in a fully anonymized data set. In total, we analyzed 41'100 articles published before January 1st, 2016, covering 142 Frontiers journals from Science, Health, Engineering, and Humanities and

Social Sciences. Our parsing routine was able to find information about authors in 41'092 of these articles, about reviewers in 39'788 articles (note that some articles, like editorial articles, might not have been reviewed), and about editors in 40'405 articles. The anonymized network data is provided as **Supplementary file 3**.

To recognize and identify people re-occurring in more than one article, every person was assigned a unique identifier number (UID). When a contributor was found to be associated to an official profile identification number in the Frontiers database, then we relied on it, directly translating it into a UID (this happened for 71% of contributors). In the remaining cases, we decided whether a record matched another based on the names and affiliations of people. Specifically, for two names to be matched, we required that the surnames coincided and that each given name of the contributor with less given names needed to have a corresponding match in the other contributor's name (a match could also be an initial like "J" with a fully specified name like "John"). In case both contributors' given names consisted of only initials, we required, in addition, that their affiliations were sufficiently similar. **Newman (2001)** found that name-matching in the absence of UIDs, and even abbreviating all given names to initials, resulted in errors on the order of few percent in a data set comprising more than a million people. Correspondingly, as we expect the UIDs to be correctly associated with a contributor in the vast majority of cases, erroneously matching or not matching people is likely relatively uncommon.

Determination of gender

Each UID was assigned a gender based on their associated given names (note that after the steps described in the previous section, at least one first name was fully specified for 99.6% of the UIDs, while for the remaining 0.4% of UIDs all given names consisted of only initials so that no gender could be attributed). The extracted given names were compared with an extensive name list, assembled from public web-sources, such as:

- [http://japanese.about.com/library/blgirls-name_\[a-z\].htm](http://japanese.about.com/library/blgirls-name_[a-z].htm),
- [http://japanese.about.com/library/blboys-name_\[a-z\].htm](http://japanese.about.com/library/blboys-name_[a-z].htm) (retrieved December 9, 2015)
- <http://www.top-100-baby-names-search.com/chinese-girl-names.html>,

- <http://www.top-100-baby-names-search.com/chinese-boys-names.html>
- <http://www.babynames.org.uk> (retrieved December 11, 2015)
- US census data (<https://www.ssa.gov/oact/babynames/limits.html>; retrieved March 17, 2016).

Note that some given names (like Andrea) are in use for both men and women. Gender-ambiguous given names present in the US census database were categorized to the gender to which they were more frequently attributed. When a name appeared as both male and female in one of the other sources, or when different sources did not agree on the gender for a name, we decided not to associate that given name with a gender.

We validated the gender assignment procedure by performing a web search for 1053 randomly selected people from our data set, and determining their gender based on a picture or the use of gender-specific pronouns in a biographical text. We were able to find such information for 924 out of the 1053 people (88%). The gender automatically assigned by our algorithm to those identified was correct in 96 % of cases. For comparison, we note that the name-gender algorithm used in **Larivière et al. (2013)** misclassified male and female names in 8% of cases.

Our list thus comprised 66605 female and 43482 male names. In addition to the name list, we manually assigned the non-automatically-identified gender of 643 people with a high number of re-occurrences. In total, we were thereby able to assign gender to 131885, that is 87 % of UIDs. All further analyses were done ignoring the remaining 13% of scientists.

Network construction

We represented the available data in directed networks (**Figure 1a**), in which vertices were individual scientists and edges denoted peer-reviewing interactions: is appointing in the editor-to-reviewer network, and is editing (reviewing) a manuscript of in the editor (reviewer)-to-author network. Year-resolved graphs were constructed by deleting all links representing articles that were published later than the given year.

Graph analytics

All graph analyses (**Figure 1—figure supplement 1**) were performed with the freely-available Python igraph package.

In graph theory, a connected component is a subgraph in which any two vertices are connected to each other by at least one path, and which is connected to no additional vertices in the full graph. The largest of all the connected components of a graph is called its giant component. One can distinguish between the weak giant component (in which the direction of edges is ignored when building inter-node paths) and the strong giant component (in which the direction is taken into account). All the following graph analyses have been performed on the weak giant component of the networks observed at each time.

Transitivity undirected (clustering coefficient) is calculated as the ratio of triangles to connected triangles (triplets) in the graph, considering connections between nodes independent of their direction.

Average path length calculates the mean of the geodesic directed path lengths between all pairs of nodes in a connected component. The geodesic path length between a given pair of nodes is the minimum number of links needed to travel between the nodes along connected edges.

Small-worldness S is defined in *Humphries and Gurney (2008)*, as $S = \gamma / \lambda$. γ is the undirected transitivity of the graph divided by k/n , which is an approximation for the undirected transitivity of an Erdős-Rényi random graph with n nodes and average degree (in+out) of k . λ is the ratio of the average shortest path length of the graph to $\ln(n)/\ln(k)$, which is the average shortest path length of an Erdős-Rényi graph with n nodes and average degree k .

Statistical testing

Statistical significance was established by comparing a feature of the data to its confidence interval (CI). The graphic notations *, ** and *** denote that this feature lay outside the 95%, 99% and 99.9% CI, respectively. Confidence intervals were calculated by recalculating the given feature 10000 times, after permuting gender labels (with the exception of *Figure 3e* where, for computational reasons, only 100 recalculations were performed). Specifically, *Figures 1* and *2* are derived from a table with a column given the number of contributions (up to a specified time point) in a given role for each person, and another column of each person's gender, and the latter column was permuted keeping the former constant. On the other hand, confidence intervals in *Figure 3* were obtained by repeatedly permuting genders among all nodes in a given graph, independent

of their associated roles. The underlying graph used for *Figure 3a* and *Figure 3c-f* was a suitably pruned editor-to-reviewer graph, out of which: we first removed all self-loops (i.e. editor and reviewer are identical); second, we deleted all leaf nodes, i.e. scientist who never edited or reviewed anything and had therefore a null out-degree; third, for *Figure 3c*, we removed cross-disciplinary assignments from journals not belonging to the indicated category. Similarly, *Figure 3b* was derived from a deleafed reviewer-to-author graph.

Inbreeding homophily at a local level

Figure 3d shows two histograms, one over all male editor nodes, the other over all female editor nodes. For each editor i who appointed at least 2 distinct reviewers we calculated a measure H_i of inbreeding homophily. To compute it, we first measured the actual number of reviewer assignments given to women nodes by the considered editor i , W_i . The next step was to subtract the expected number of reviewer assignments given to women, which would be observed if the given editor node appointed women with the average frequency p_i ; they are appointed in its local vicinity. To evaluate p_i we took the set of all editors (both males and females) at a distance of at most 5 directed edges from the considered editor node i . We counted the overall number A_{all} of reviewer assignments made by these editors (i.e. the total number of edges originating from editor nodes in the neighborhood shell), and neglected those editors for which $A_{\text{all}} < 62$ (i.e. we required that, on average, at each of the 5 steps away from the considered editor at least 2 novel reviewers are encountered that could not have been reached in a shorter step count). We then determined the number $A_{\text{female}} \leq A_{\text{all}}$ of reviewer assignments made toward female nodes. We finally assumed $p_i = A_{\text{female}} / A_{\text{all}}$.

We could then compute the local inbreeding homophily measure $H_i = W_i - A_i p_i$, where A_i was the total number of assignment made by each considered editor i .


We used a similar technique to assess the impact of the most homophilic editors on the overall network-homophily in the female editor-to-reviewer and male editor-to-reviewer networks. Let q_i be the probability a person of the same gender is chosen by an editor i , where q_i is calculated exactly as p_i in the previous paragraph, i.e. by considering all people at most 5 directed edges away from editor i in the editor-to-reviewer network, counting the number of

assignments these people gave to people of the same gender and dividing by the total number of assignments these people made. Next, let k_i denote the number of assignments editor i gives to a person of the same gender and n_i the total number of assignments editor i makes. Assuming editor i chooses the gender of a reviewer at random, the probability that i assigns k_i out of the n_i reviewers to have the same gender follows a binomial distribution $\text{binom}(k_i; n_i, q_i)$ and $\Phi_{\text{hom}} = \sum_{v=k_i}^{n_i} \text{binom}(v; n_i, q_i)$ measures how likely it is that editor i assigns at least k_i reviews to a person of the same gender.

Markus Helmer is in the Max Planck Institute for Dynamics and Self-Organization, Göttingen, Germany, the Bernstein Center for Computational Neuroscience, Göttingen, Germany, and Yale University, New Haven, United States
markus.helmer@yale.edu


 <http://orcid.org/0000-0001-9680-0595>

Manuel Schottdorf is in the Max Planck Institute for Dynamics and Self-Organization, Göttingen, Germany, and the Bernstein Center for Computational Neuroscience, Göttingen, Germany

 <http://orcid.org/0000-0002-5468-4255>

Andreas Neef is in the Max Planck Institute for Dynamics and Self-Organization, Göttingen, Germany, and the Bernstein Center for Computational Neuroscience, Göttingen, Germany

Demian Battaglia is in the Bernstein Center for Computational Neuroscience, Göttingen, Germany, and the Institute for Systems Neuroscience, Aix-Marseille University, Marseille, France
demian.battaglia@univ-amu.fr

 <http://orcid.org/0000-0003-2021-7920>

Author contributions: MH, Conceptualization, Data curation, Software, Formal analysis, Validation, Investigation, Visualization, Methodology, Writing—original draft, Writing—review and editing; MS, AN, Conceptualization, Formal analysis, Validation, Investigation, Methodology, Writing—original draft, Writing—review and editing; DB, Conceptualization, Formal analysis, Validation, Investigation, Methodology, Writing—original draft, Project administration, Writing—review and editing

Competing interests: The authors declare that no competing interests exist.

Received 20 September 2016

Accepted 27 February 2017

Published 21 March 2017

Additional files

Supplementary files

- Supplementary file 1. Comparison of female author contributions by country between *Larivière et al. (2013)* and the Frontiers series of journals.

DOI: [10.7554/eLife.21718.008](https://doi.org/10.7554/eLife.21718.008)

- Supplementary file 2. Reported fractions of female authors, reviewers and editors in previous studies.

DOI: [10.7554/eLife.21718.009](https://doi.org/10.7554/eLife.21718.009)

- Supplementary file 3. Network data. Contains two files, one (graph_nodes.csv) giving a random ID per person in the network together with that person's gender, the other (graph_edges.csv) indicating which IDs interact together with the roles of each ID (a: author, r: reviewer, e: editor).

DOI: [10.7554/eLife.21718.010](https://doi.org/10.7554/eLife.21718.010)

Funding

Funder	Grant reference number	Author
Bundesministerium für Bildung und Forschung	01GQ1005B	Andreas Neef Demian Battaglia
Marie Curie Career Development Fellowship	FP7- IEF 330792 (DynViB)	Demian Battaglia
Boehringer Ingelheim Fonds		Manuel Schottdorf

The funders had no role in study design, data collection and interpretation, or the decision to submit the work for publication.

References

- Aldrich H.** 1989. Networking among women entrepreneurs. In: Hagan O, Rivchun C, Sexton D (ed). *Women-Owned Businesses*. New York: Praeger. p. 103–132.
- American Psychological Association.** 2007. *Report of the APA Task Force on the Sexualisation of Girls*. Washington: APA.
- Avin C, Keller B, Lotker Z, Mathieu C, Peleg D, Pignolet Y-A.** 2015. Homophily and the glass ceiling effect in social networks. *Proceedings of the 2015 Conference on Innovations in Theoretical Computer Science*. doi: [10.1145/2688073.2688097](https://doi.org/10.1145/2688073.2688097)
- Baggs JG, Broome ME, Dougherty MC, Freda MC, Kearney MH.** 2008. Blinding in peer review: the preferences of reviewers for nursing journals. *Journal of Advanced Nursing* **64**:131–138. doi: [10.1111/j.1365-2648.2008.04816.x](https://doi.org/10.1111/j.1365-2648.2008.04816.x), PMID: [18764847](https://pubmed.ncbi.nlm.nih.gov/18764847/)
- Bian L, Leslie S-J, Cimpian A.** 2017. Gender stereotypes about intellectual ability emerge early and influence children's interests. *Science* **355**:389–391. doi: [10.1126/science.aah6524](https://doi.org/10.1126/science.aah6524)
- Bielby WT, Baron JN.** 1986. Men and women at work: sex segregation and statistical discrimination.

- American Journal of Sociology* **91**:759–799. doi: [10.1086/228350](https://doi.org/10.1086/228350)
- Bloch C.** 2012. The Janus face of the peer-review. In: *Passion and Paranoia: Emotions and the Culture of Emotion in Academia*. Surrey, UK: Ashgate. p. 55–69.
- Borsuk RM, Aarssen LW, Budden AE, Koricheva J, Leimu R, Tregenza T, Lortie CJ.** 2009. To name or not to name: the effect of changing author gender on peer review. *BioScience* **59**:985–989. doi: [10.1525/bio.2009.59.11.10](https://doi.org/10.1525/bio.2009.59.11.10)
- Bott H.** 1928. Observation of play activities in a nursery school. *Genetic Psychology Monographs* **4**: 44–88.
- Bourdieu P.** 1975. The specificity of the scientific field and the social conditions of the progress of reason. *Social Science Information* **14**:19–47. doi: [10.1177/053901847501400602](https://doi.org/10.1177/053901847501400602)
- Brass DJ.** 1985. Men's and women's networks: A study of interaction patterns and influence in an organization. *Academy of Management Journal* **28**: 327–343. doi: [10.2307/256204](https://doi.org/10.2307/256204)
- Buckley HL, Sciligo AR, Adair KL, Case BS, Monks JM.** 2014. Is there gender bias in reviewer selection and publication success rates for the 'New Zealand Journal of Ecology'? *New Zealand Journal of Ecology* **38**:335–339.
- Budden A, Tregenza T, Aarssen L, Koricheva J, Leimu R, Lortie C.** 2008. Double-blind review favours increased representation of female authors. *Trends in Ecology & Evolution* **23**:4–6. doi: [10.1016/j.tree.2007.07.008](https://doi.org/10.1016/j.tree.2007.07.008)
- Caldeira GA, Patterson SC.** 1987. Political friendship in the legislature. *The Journal of Politics* **49**:953–975. doi: [10.2307/2130779](https://doi.org/10.2307/2130779)
- Campbell LG, Mehtani S, Dozier ME, Rinehart J.** 2013. Gender-heterogeneous working groups produce higher quality science. *PLoS One* **8**:e79147. doi: [10.1371/journal.pone.0079147](https://doi.org/10.1371/journal.pone.0079147)
- Caplar N, Tacchella S, Birrer S.** 2016. Quantitative evaluation of gender Bias in astronomical publications from citation counts. *arXiv*. [1610.08984](https://arxiv.org/abs/1610.08984).
- Ceci SJ, Williams WM, Barnett SM.** 2009. Women's underrepresentation in science: Sociocultural and biological considerations. *Psychological Bulletin* **135**: 218–261. doi: [10.1037/a0014412](https://doi.org/10.1037/a0014412)
- Ceci SJ, Williams WM.** 2010. Sex differences in math-Intensive fields. *Current Directions in Psychological Science* **19**:275–279. doi: [10.1177/0963721410383241](https://doi.org/10.1177/0963721410383241)
- Ceci SJ, Williams WM.** 2011. Understanding current causes of women's underrepresentation in science. *PNAS* **108**:3157–3162. doi: [10.1073/pnas.1014871108](https://doi.org/10.1073/pnas.1014871108)
- Centola D.** 2011. An experimental study of homophily in the adoption of health behavior. *Science* **334**: 1269–1272. doi: [10.1126/science.1207055](https://doi.org/10.1126/science.1207055)
- Cole JR, Zuckerman H.** 1984. The productivity puzzle: persistence and change in patterns of publication of men and women scientists. *Advances in Motivation and Achievement* **2**:1.
- Cole JR, Zuckerman H.** 1987. Marriage, motherhood and research performance in science. *Scientific American* **256**:119–125. doi: [10.1038/scientificamerican0287-119](https://doi.org/10.1038/scientificamerican0287-119)
- Cole JR.** 1979. 1st Edition. *Fair Science: Women in the Scientific Community*. New York: The Free Press.
- Cole S.** 1992. *Making Science*. Harvard University Press.
- del Río MF, Strasser K.** 2013. Preschool children's beliefs about gender differences in academic skills. *Sex Roles* **68**:231–238. doi: [10.1007/s11199-012-0195-6](https://doi.org/10.1007/s11199-012-0195-6)
- Demarest B, Freeman G, Sugimoto CR.** 2014. The reviewer in the mirror: examining gendered and ethnicized notions of reciprocity in peer review. *Scientometrics* **101**:717–735. doi: [10.1007/s11192-014-1354-z](https://doi.org/10.1007/s11192-014-1354-z)
- Duru-Bellat M.** 2008. La (re)production de rapports sociaux de sexe: quelle place pour l'institution scolaire? *Travail Genre Et Sociétés* **19**:131–149. doi: [10.3917/tgs.019.0131](https://doi.org/10.3917/tgs.019.0131)
- Eder D, Hallinan MT.** 1978. Sex differences in children's friendships. *American Sociological Review* **43**:237–250. doi: [10.2307/2094701](https://doi.org/10.2307/2094701)
- ETAN Expert Working Group on Women and Science.** 2000. *Science Policies in the European Union: Promoting Excellence Through Mainstreaming Gender Equality*. Luxembourg: European Commission.
- Federal Glass Ceiling Commission.** 1995. *Solid Investments: Making Full Use of the Nation's Human Capital*. Washington, DC: US Department of Labor.
- Feld SL.** 1981. The focused organization of social ties. *American Journal of Sociology* **86**:1015–1035. doi: [10.1086/227352](https://doi.org/10.1086/227352)
- Feld SL.** 1984. The structured use of personal associates. *Social Forces* **62**:640–652. doi: [10.2307/2578704](https://doi.org/10.2307/2578704)
- Fox CW, Burns CS, Meyer JA.** 2016. Editor and reviewer gender influence the peer review process but not peer review outcomes at an ecology journal. *Functional Ecology* **30**:140–153. doi: [10.1111/1365-2435.12529](https://doi.org/10.1111/1365-2435.12529)
- Galaskiewicz J.** 1985. Professional networks and the institutionalization of a single mind set. *American Sociological Review* **50**:639–658. doi: [10.2307/2095379](https://doi.org/10.2307/2095379)
- Gilbert JR, Williams ES, Lundberg GD.** 1994. Is there gender bias in JAMA's peer review process? *JAMA* **272**:139–142. doi: [10.1001/jama.1994.03520020065018](https://doi.org/10.1001/jama.1994.03520020065018)
- Goulden M, Mason MA, Frasch K.** 2011. Keeping women in the science pipeline. *The Annals of the American Academy of Political and Social Science* **638**:141–162. doi: [10.1177/0002716211416925](https://doi.org/10.1177/0002716211416925)
- Hamovitch W, Morgenstern RD.** 1977. Children and the productivity of academic women. *The Journal of Higher Education* **48**:633–645. doi: [10.2307/1979009](https://doi.org/10.2307/1979009)
- Handley G, Frantz CM, Kocovsky PM, DeVries DR, Cooke SJ, Claussen J.** 2015b. An examination of gender differences in the American Fisheries Society peer-review process. *Fisheries* **40**:442–451. doi: [10.1080/03632415.2015.1059824](https://doi.org/10.1080/03632415.2015.1059824)
- Handley IM, Brown ER, Moss-Racusin CA, Smith JL.** 2015a. Quality of evidence revealing subtle gender biases in science is in the eye of the beholder. *PNAS* **112**:13201–13206. doi: [10.1073/pnas.1510649112](https://doi.org/10.1073/pnas.1510649112)
- Holt A, Webb T.** 2007. Gender in ecology: where are the female professors. *Bull Br Ecol Soc* **38**:51–62.
- Humphries MD, Gurney K.** 2008. Network 'small-world-ness': A quantitative method for determining canonical network equivalence. *PLoS One* **3**: e0002051. doi: [10.1371/journal.pone.0002051](https://doi.org/10.1371/journal.pone.0002051)

- Ibarra H. 1992. Homophily and differential returns: sex differences in network structure and access in an advertising firm. *Administrative Science Quarterly* **37**:422–447. doi: [10.2307/2393451](https://doi.org/10.2307/2393451)
- Isbell LA, Young TP, Harcourt AH. 2012. Stag parties linger: Continued gender bias in a female-rich scientific discipline. *PLoS One* **7**:e49682. doi: [10.1371/journal.pone.0049682](https://doi.org/10.1371/journal.pone.0049682)
- Knapp S. 2005. A suitable job for a woman. *Trends in Ecology & Evolution* **20**:55–56. doi: [10.1016/j.tree.2004.11.016](https://doi.org/10.1016/j.tree.2004.11.016)
- Knobloch-Westerwick S, Glynn CJ, Huge M. 2013. The Matilda effect in science communication an experiment on gender bias in publication quality perceptions and collaboration interest. *Science Communication* **35**:603–625.
- Kyvik S, Teigen M. 1996. Child care, research collaboration, and gender differences in scientific productivity. *Science, Technology & Human Values* **21**:54–71. doi: [10.1177/016224399602100103](https://doi.org/10.1177/016224399602100103)
- Kyvik S. 1990. Motherhood and scientific productivity. *Social Studies of Science* **20**:149–160. doi: [10.1177/030631290020001005](https://doi.org/10.1177/030631290020001005)
- Larivière V, Ni C, Gingras Y, Cronin B, Sugimoto CR. 2013. Bibliometrics: Global gender disparities in science. *Nature* **504**:211–213. doi: [10.1038/504211a](https://doi.org/10.1038/504211a)
- Lazarsfeld PF, Merton RK. 1954. Friendship as a social process: a substantive and methodological analysis. In: Berger M (ed.). *Freedom and Control in Modern Society*. New York: Van Nostrand. p. 18–66.
- Lee CJ, Sugimoto CR, Zhang G, Cronin B. 2013. Bias in peer review. *Journal of the American Society for Information Science and Technology* **64**:2–17. doi: [10.1002/asi.22784](https://doi.org/10.1002/asi.22784)
- Lerback J, Hanson B. 2017. Journals invite too few women to referee. *Nature* **541**:455–457. doi: [10.1038/541455a](https://doi.org/10.1038/541455a)
- Ley TJ, Hamilton BH. 2008. The gender gap in NIH grant applications. *Science* **322**:1472–1474. doi: [10.1126/science.1165878](https://doi.org/10.1126/science.1165878)
- Lloyd ME. 1990. Gender factors in reviewer recommendations for manuscript publication. *Journal of Applied Behavior Analysis* **23**:539–543. doi: [10.1901/jaba.1990.23-539](https://doi.org/10.1901/jaba.1990.23-539)
- Long JS, Fox MF. 1995. Scientific careers: universalism and particularism. *Annual Review of Sociology* **21**:45–71. doi: [10.1146/annurev.so.21.080195.000401](https://doi.org/10.1146/annurev.so.21.080195.000401)
- Mark NP. 2003. Culture and competition: homophily and distancing explanations for cultural niches. *American Sociological Review* **68**:319–345. doi: [10.2307/1519727](https://doi.org/10.2307/1519727)
- Mazur A, McBride Stetson D. 1995. *Comparative State Feminism*. London: Sage.
- McPherson M, Smith-Lovin L, Cook JM. 2001. Birds of a feather: homophily in social networks. *Annual Review of Sociology* **27**:415–444. doi: [10.1146/annurev.soc.27.1.415](https://doi.org/10.1146/annurev.soc.27.1.415)
- Merton RK. 1968. The Matthew effect in science. *Science* **159**:56–63.
- Merton RK. 1973. The Normative Structure of Science. *The Sociology of Science: Theoretical and Empirical Investigations*. Chicago: University of Chicago Press. p. 267–280.
- Misra J, Lundquist JH, Holmes E, Agiomavrits S. 2011. The ivory ceiling of service work. *Academe* **97**:22–26.
- Moss-Racusin CA, Dovidio JF, Brescoll VL, Graham MJ, Handelsman J. 2012. Science faculty's subtle gender biases favor male students. *PNAS* **109**:16474–16479. doi: [10.1073/pnas.1211286109](https://doi.org/10.1073/pnas.1211286109)
- Mulkay MJ. 1979. *Science and the Sociology of Knowledge*. Allen & Unwin.
- National Science Foundation. 2016. National center for science and engineering statistics. *Doctorate Recipients From US*. www.nsf.gov/statistics/2017/nsf17306/
- Nature Neuroscience. 1999. Pros and cons of open peer review. *Nature Neuroscience* **2**:197–198. doi: [10.1038/6295](https://doi.org/10.1038/6295), PMID: 10195206
- Nature Neuroscience. 2006. Women in neuroscience: a numbers game. *Nature Neuroscience* **9**:853. doi: [10.1038/nn0706-853](https://doi.org/10.1038/nn0706-853), PMID: 16801912
- Nature. 2012. Nature's sexism. *Nature* **491**:495. doi: [10.1038/491495a](https://doi.org/10.1038/491495a), PMID: 23189321
- Nature. 2013. Science for all. *Nature* **495**:5. PMID: 23472264
- Newman MEJ. 2001. The structure of scientific collaboration networks. *PNAS* **98**:404–409. doi: [10.1073/pnas.98.2.404](https://doi.org/10.1073/pnas.98.2.404)
- Nosek BA, Smyth FL, Hansen JJ, Devos T, Lindner NM, Ranganath KA, Smith CT, Olson KR, Chugh D, Greenwald AG, Banaji MR. 2007. Pervasiveness and correlates of implicit attitudes and stereotypes. *European Review of Social Psychology* **18**:36–88. doi: [10.1080/10463280701489053](https://doi.org/10.1080/10463280701489053)
- Outshoorn J, Kantola J. 2007. *Changing State Feminism*. Palgrave MacMillan.
- Outshoorn J. 2005. New politics, new opportunities? The women's policy agency in the Netherlands in the last decade. *Paper for the ECPR Joint Sessions of Workshop*. Granada. p. 14–19.
- Paludi MA, Bauer WD. 1983. Goldberg revisited: what's in an author's name. *Sex Roles* **9**:387–390. doi: [10.1007/BF00289673](https://doi.org/10.1007/BF00289673)
- Pan L, Kalinaki E. 2015. *Mapping Gender in the German Research Arena*: Elsevier Analytical Services.
- Park RE, Burgess EW. 1921. *Introduction to the Science of Sociology*. Chicago: University Chicago Press.
- Parodi M. 2011. Les discriminations entre les hommes et les femmes au prisme de l'opinion. In: Milewski F, Perivier H (eds). *Les Discriminations Entre Les Femmes Et Les Hommes*. Sciences Po Les Presses.
- Popielarz PA. 1999. (In)voluntary association: a multilevel analysis of gender segregation in voluntary organizations. *Gender Soc* **13**:234–250. doi: [10.1177/089124399013002005](https://doi.org/10.1177/089124399013002005)
- Poynder R. 2016. *The OA Interviews: Kamila Markram, CEO and Co-Founder of Frontiers*. <http://poynder.blogspot.co.at/2016/02/the-oa-interviews-kamila-markram-ceo.html#more>
- Raymond J. 2013. Sexist attitudes: most of us are biased. *Nature* **495**:33–34. doi: [10.1038/495033a](https://doi.org/10.1038/495033a), PMID: 23467152
- Sainsbury D. 1994. *Gendering Welfare States*. London: Sage Publications.
- Shen H. 2013. Mind the gender gap. *Nature* **495**:22–24. doi: [10.1038/495022a](https://doi.org/10.1038/495022a)
- Shrum W, Cheek NH, Hunter SM. 1988. Friendship in school: gender and racial homophily. *Sociology of Education* **61**:227–239. doi: [10.2307/2112441](https://doi.org/10.2307/2112441)

- Special Adviser on Gender Issues and Advancement of Women.** 2002. *Gender Mainstreaming: An Overview*. New York: United Nations.
- Squires J.** 2008. Diversity mainstreaming: dépasser les approches technocratiques et d'addiction des inégalités. *Cahiers du Genre*. **44** :73–94.
- Szell M, Thurner S.** 2013. How women organize social networks different from men. *Scientific Reports* **3**: 1214. doi: [10.1038/srep01214](https://doi.org/10.1038/srep01214), PMID: [23393616](https://pubmed.ncbi.nlm.nih.gov/23393616/)
- Tite L, Schroter S.** 2007. Why do peer reviewers decline to review? A survey. *Journal of Epidemiology & Community Health* **61**:9–12. doi: [10.1136/jech.2006.049817](https://doi.org/10.1136/jech.2006.049817)
- Topaz CM, Sen S.** 2016. Gender representation on journal editorial boards in the mathematical sciences. *PLoS One* **11**:e0161357. doi: [10.1371/journal.pone.0161357](https://doi.org/10.1371/journal.pone.0161357)
- van Rooyen S, Godlee F, Evans S, Black N, Smith R.** 1999. Effect of open peer review on quality of reviews and on reviewers' recommendations: a randomised trial. *BMJ* **318**:23–27. doi: [10.1136/bmj.318.7175.23](https://doi.org/10.1136/bmj.318.7175.23)
- Verbrugge LM.** 1977. The structure of adult friendship choices. *Social Forces* **56**:576–597. doi: [10.2307/2577741](https://doi.org/10.2307/2577741)
- Vinsonneau G.** 1999. *Inégalités Sociales Et Procédés Identitaires*. Paris: Armand Colin.
- Ware M.** 2008. Peer review in scholarly journals: Perspective of the scholarly community. *Information Services and Use* **28**:109–112. doi: [10.3233/ISU-2008-0568](https://doi.org/10.3233/ISU-2008-0568)
- Wennerås C, Wold A.** 1997. Nepotism and sexism in peer-review. *Nature* **387**:341–343. doi: [10.1038/387341a0](https://doi.org/10.1038/387341a0)
- Woodward A.** 2003. European gender mainstreaming: innovative policy or disappearing act? *Review of Policy Research* **20**:65–88.
- Woodward A.** 2008. Est-il trop tard pour une approche de l'égalité? *Le Point Sur La Situation À Bruxelles*. *Cahiers Du Genre*. **44** 95–116.
- Woolley AW, Chabris CF, Pentland A, Hashmi N, Malone TW.** 2010. Evidence for a collective intelligence factor in the performance of human groups. *Science* **330**:686–688. doi: [10.1126/science.1193147](https://doi.org/10.1126/science.1193147)
- Xie Y, Shauman KA.** 1998. Sex differences in research productivity: new evidence about an old puzzle. *American Sociological Review* **63**:847–870. doi: [10.2307/2657505](https://doi.org/10.2307/2657505)
- Yava M, Yucel G.** 2014. Impact of homophily on diffusion dynamics over social networks. *Social Science Computer Review* **32**:354–372. doi: [10.1177/0894439313512464](https://doi.org/10.1177/0894439313512464)
- Yeatman A.** 1990. *Bureaucrats, technocrats, femocrats: essays on the contemporary Australian state*. Sydney: Allen & Unwin.
- Zuckerman H.** 1991. The careers of men and women scientists: A review of current research. *The Outer Circle: Women in the Scientific Community*. p. 27–56.

Summary and outlook

“No practical biologist interested in sexual reproduction would be led to work out the detailed consequences experienced by organisms having three or more sexes; yet what else should he do if he wishes to understand why the sexes are, in fact, always two.”

Ronald Fisher¹⁴⁴: “The genetic theory of natural selection”.

9.1 Summary

Synthetic biology is the engineering of biology⁶⁴. This emerging field was established barely 10 years ago and is already a growing focus of attention in the academic world with extraordinary scientific and technological output. I would like to mention three particular examples of such engineering which I believe highlight its value. One of the first synthetic genetic circuits was the Repressilator, a system of three coupled genes that inhibit each other generating oscillatory gene expression¹²⁸. Even though this is not how bacteria measure time, it was one of the first genetic circuits with bespoke functionality. More recently, the complete construction of a minimal organism from scratch²⁰⁶ made it explicit how many genes are actually necessary for life. Third, recent work on organoids²⁶⁰, organized heaps of tissue grown from stem cells, shows a growing interest in the self-organizing properties of tissue formation and even medical applications by engineering neurons from human donor cells³²⁶.

In this thesis, we developed a *synthetic neurobiology* and created, controlled and designed neuronal circuits while performing a first connectomic structure-function study. To design neuronal circuits, we used a hybrid system of *in silico* and *in vitro* components. The model system for this study was the mammalian early visual system, for which we first confirmed that the Hubel&Wiesel connectome is a viable circuit to generate orientation specificity. We then miniaturize the early visual afferent pathway, to some extent modeling an evolutionary transition within a few hours of a typical experiment. To this end, we virtually shrunk eye size, cranium and the cortical target area of the simulated pathway, but preserved the total number of hypercolumns and therefore arguably the number of processing units to process natural scenes. In the limit of a small brain, the synthetic hybrid visual system resembles a mouse visual pathway, or the layout of late cretaceous eutherians, like *Asioryctes*, closely related to the eutherian common ancestor. We found that shrinking the visual system leads to a massive loss of visual acuity, to a loss of the orientation specificity of the afferent connectome and to a larger point spread function. Surprisingly, we also found that a number of neurons exhibited orientation biased responses in the limit of homogeneous and unselective input, that are generated by the recurrent network alone. We find that these cells are mostly simple cells. In addition, we also find a small number of complex and direction tuned cells. This diversity of responses suggests that even in this most generic case, a recurrent circuit is sufficient to spontaneously generate a basic level of orientation selectivity. This phenomenon, already present in recurrent networks as disorganized as a primary culture, might provide a robust and generic scaffold for input classification, potentially the first workpiece refined by the selective forces of natural selection. The synthetic neurobiology nature of these experiments enabled us to systematically approach the contributions of feed-forward and recurrent connectomes to the generation of cortical feature selectivity, because (1) the in surrogate cortex realizes a dense medium scale recurrent circuit, composed of thousands of neurons, with spontaneously emerging collective processing functions. (2) We freely configured the wiring diagram of the feed-forward input connectome in the limits from highly specific to completely random to assess the degree of spontaneous orientation tuning. (3) We switched the system rapidly and reversible between different pathway connectomes, identifying various tuned responses and receptive fields. (4) We connected different pathway connectomes to the same target circuit of living neurons, which provided us with an control and made the different experimental conditions comparable. (5) We used the high quality optical access to the recurrent circuit for all-optical interfacing and optical monitoring of activity which revealed a spatial organization resembling a sparse salt and pepper pattern. We also used the all-optical interface to confirm that a surrogate cortex, provided with spatiotemporally complex input patterns during development, changes its spontaneous activity patterns. In the following paragraphs, I will summarize the content of each chapter and provide an outlook.

In **chapter 3** we first developed a framework for the afferent visual pathway. It has long been controversial whether and how the emergence of orientation preference maps (OPMs) can be explained by self-organized activity-dependent development of cortical circuits and to what degree their development is influenced or dominated by subcortical feed-forward constraints. Several recent studies foster this controversy. On the one hand, OPMs in species widely separated in evolutionary terms have been shown to exhibit invariant spatial statistics, which are in quantitative agreement with predictions from a class of self-organization models. On the other hand, two recent studies found evidence in experimental maps in favor of a hexagonal arrangement underlying OPM layouts. These hexagonal arrangements could be qualitatively accounted for by a purely linear feed-forward model in which OPMs arise as a constraint from the structure of retinal inputs. The idea that orientation preference across primary visual cortex should mirror the distribution of the ON/OFF center retinal ganglion cells (RGCs) dates back to pioneering work by Soodak⁴⁴⁶. Without spatially irregular arrangements of ON and OFF RGCs across the retina, the spatial layout of the resulting OPM lacks a typical distance between orientation columns^{188,404} - a salient feature of experimentally measured OPMs. When ON/OFF RGCs are placed on two independent hexagonal lattices, periodic OPMs arise with a typical column spacing set by a Moiré-Interference effect between the two lattices. We employed the theory of the Moiré-Interference phenomenon to analytically determine OPMs predicted by this interference effect, their representation in Fourier space, as well several spatial statistics. In particular, we show that the model's predicted pinwheel density for OPMs is $2\sqrt{3} \approx 3.46$ - a value far from matching experimental observations. When noise of increasing strength is added to the lattice positions of the RGCs, the Moiré-Fourier-Modes dissolve into an isotropic background, decaying as a Gaussian with increasing spatial frequency. Hence, for small amount of spatial noise, OPMs exhibit a typical column spacing and an excess hexagonal order compared to spatially isotropic maps. Above a critical noise strength, OPMs become spatially isotropic and lack a typical column spacing. These findings prompted us to perform a quantitative assessment of pinwheel statistics in a large data set of experimentally measured OPMs from tree shrew, galago and ferret and also cat. We show that the the statistics of pinwheels in OPMs are indistinguishable from one another and from quasi-periodic solutions of models for the activity-dependent development of OPMs. We conclude that the spatial structure of real OPMs provides no prima facie support for the retinal constraint hypothesis. Consequently, the contribution of subcortical constraints to the spatial layout of OPMs is likely to be small compared to activity-dependent processes during postnatal development.

In **chapter 4**, we connected the computational model of the early visual pathway to the surrogate cortex. We first assessed the viability of what we call *virtual networks*, realized by closed loop optogenetic connections^{162,348} between islands of individual neurons grown on multielectrode arrays. Virtual networks are artificial neural networks with biological neurons as nodes. This approach seemed promising because it allows in principle to construct arbitrary networks. To generate such islands, we developed a patterning technique to constrain the growth of cells to individual electrodes of a MEA. This required substrate preparation in order to constrain neuronal growth and adhesion. We developed a novel and reproducible approach utilizing micro-contact printing (μ -CP) combined with a custom-made device to fine-place patterns on MEAs with high precision. Neuronal islands grown on multielectrode arrays combined with optical neurostimulation can provide a unique tool, but we found that this is not the way to go: Considering the finite yield of populated islands together with only a fraction of active electrodes generates substantial variability and we would in turn need to adapt the circuit to the culture. A second path that we followed, was to design a neuronal circuit from dissociated neurons in which the local neuronal circuits are as realistic as possible. We designed cultures

with the same cell density and cellular content as the neocortical input layer IV and let them develop naturally. These cultures are easy to produce on a large scale and show rich spontaneous activity, resembling the spontaneous activity in the young neocortex. To interface this surrogate cortex with the virtual sensory pathway, we next constructed a digital phase-only holographic projection system. We use digital holography, because it is the most flexible technique to generate spatially structured light pattern at specific wavelengths, and surpasses micromirror arrays in terms of light-efficiency by orders of magnitude¹⁶¹.

In **chapter 5**, we constructed the *in silico* visual pathway and connected it to the living surrogate cortex. The neurons in this recurrent neural network are derived from the cortices of embryonic rats expressing the light-sensitive ionchannel ChR2(H134R) after viral transduction. We monitor neural responses both optically with a redshifted genetically encoded calcium indicator and extracellularly with a multielectrode array. We use a generic scaling law for the layout of the early visual system to transform the visual pathway of a cat into that of a mouse. These different pathway connectomes can be connected to the same target circuit of living neurons, providing for an internal control. We find that shrinking the visual system leads to a loss of orientation selectivity in the afferent input. Surprisingly, we discovered that a number of neurons exhibited orientation biased responses in the limit of homogeneous and unselective input and these orientation biased responses are generated by the recurrent network alone. These cells are simple cells with a small number of complex and direction tuned cells. We also find cells with receptive fields composed of excitatory and inhibitory subregions, and these receptive fields have a typical spatial scale of ≈ 1 mm, consistent with the generic scaling laws which we extracted from already available data. Consistent with simple cells, the tuning can be predicted from the receptive field. The spatial arrangement of spontaneously tuned cells resembles a sparse salt and pepper pattern. This diversity of responses suggests that even in this most generic case, a recurrent circuit is sufficient to spontaneously generate a basic level of feature selectivity. Theoretically, neural networks with connections organized by probabilistic rules are conceptually powerful model systems. Random neural networks have been shown to generically exhibit computationally favorable properties for stimulus representation and information processing, for instance by reservoir computing²⁹³, liquid state machines, a particular type of a reservoir computer which consists of randomly connected spiking neurons²⁹⁸ and more recently FORCE learning in random rate networks⁴⁶¹. Our experimental data highlights that feature selectivity generated by the disorganized connections in the surrogate cortex might be a generic scaffold for input classification, and the first workpiece refined by the selective forces of natural selection.

In **chapter 6** we developed the technology to manipulate the remaining degree of freedom: the structure of the recurrent connections in the surrogate cortex. We provided a developing culture with external input as a developmental circuit manipulation tool, resembling the mechanisms at work in the living brain³³². In contrast to other techniques as micro contact printing (the technique used in chapter 4), external input seems a natural choice to manipulate neuronal circuits. We construct a device, a *light disco*, to provide a developing culture with spatiotemporally complex input patterns inside the incubator for several weeks. Using this device, we find strong evidence that self-organization in the presence of external, correlated inputs changes the collective dynamics of the surrogate cortex. These results might have relevant consequences for our current understanding of the role of spontaneous and driven activity in the developing brain, highlighting the need for appropriate input to tune a neuronal circuit to its working point. We find that activity in cell cultures, resembling cortical waves, generates a state of irregular activity, while the overall neuronal firing rates do not change. This finding indicates that the asynchronous irregular activity in the healthy brain is mediated by recurrent circuits that are shaped during development by correlated activity patterns. This chapter is the last chapter

where we used synthetic hybrid circuits, composed of a *in silico* feed-forward connectome providing input to a living neural network *in vitro*.

In chapter 3 we showed that a Moiré mechanism is unlikely to yield layouts of orientation domains consistent with experimental data. This does, however, not rule out the principal mechanism, leaving open whether the statistical wiring framework can in principle explain the formation of aperiodic layouts of domains consistent with the common design. In **chapter 7**, we introduce a novel method to infer RGCs mosaics that within the statistical wiring framework yield realistic OPMs. Inferred mosaics lack long-range positional order yet lead to aperiodic OPMs. They are characterized by specific angular correlations between ON/OFF ganglion cell pairs. Comparing this model's prediction with X ganglion cell mosaics of a cat and parasol cell mosaics of a primate allows us to calculate a strong quantitative constraint on the retinal influence on visual cortical OPMs and in fact the observed ganglion cell mosaics are best explained by a total absence of angular correlation between ON/OFF cell pairs. From this study, together with chapter 3, we conclude that V1 layout invariants are specific quantitative signatures of visual cortical optimization, which cannot be explained by generic random feed-forward models. Considering the relation to cortical optimization, we next asked whether the specific layout rules of the common design can in principle break down. We use the reinvention of color vision in primates as a natural laboratory experiment because it required both the wiring of a new afferent pathway into the visual cortex and the rearrangement of the visual cortical processing machinery. Considering this scale of modification, the reinvention of color vision, possibly multiple times²¹⁹, might have been one of the most fundamental and most recent changes in visual cortical circuitry. Color vision was lost in mammals during the *nocturnal bottleneck* when our ancestors were small, dark-dwelling animals between 205 to 65 Million years ago (Ma). Among modern mammals old world monkeys and great apes (re-)invented trichromacy 30–40 Ma. The newly developed color vision inserted new pathways into cortical functional architecture, potentially perturbing the layout of orientation domains in the primary visual cortex (V1) through non-orientation selective cytochrome oxidase (CO) blobs. We first show that trichromacy might leave a detectable fingerprint in the metrics of the common design by analyzing a coupled optimization model between orientation and color selective cells. We therefore compared trichromatic macaque (N=6) and monochromatic owl monkeys (N=8) orientation domains against a background of normal (N=82) and dark-reared (N=21) ferret, shrew (N=25), galago (N=9), and cat (N=13) and found that their layout adheres to the common design. The common design is a specific and arguably small set of quantitative layout rules and we next asked whether other metrics can reveal a difference between orientation domains of trichromatic vs. color-blind species. To this end, we next develop a phenomenological model to incorporate orientation unselective into a layout of orientation domains using geometric distortions. Models of this type leave the measures of the common design invariant and make the prediction that randomization of the Fourier components decreases the pinwheel density. In our data, however, we find a statistically identical and highly significant increase of the pinwheel density across all Euarchontans and primates, showing that the evolutionary invention of the color vision machinery in primates induced only a minor perturbation to the modular organization of V1. The selective forces that favor the common design might thus be so powerful as to preserve it under major transformations of the retinocortical pathway.

Finally, in **chapter 8** we reveal distortions in the peer review process, specifically showing that a scientist's personal attributes matter. This chapter was originally motivated by personal observations, and made rigorous by web-crawling the publicly available article web pages from the Frontiers Journal Series to obtain one of the largest datasets available in to sociology of science including more than 175,000 individuals. While it is not related to synthetic neurobiology,

it is of critical importance that peer reviewers are appointed on the basis of their expertise alone. We show that specifically homophily is widespread and our analysis suggests that without focused effort, the homophilic tendency in the scientific community will persist. Revealing such distortions is imperative to improve the quality of published articles, and science as a whole.

9.2 Outlook

Over the past 10 years, several studies used living neuronal networks for information processing, some to control robots^{19,20,108,386} and others to compute, for example using only one neuron in a virtual network¹⁶² or by designing logic elements in particular topographies¹³⁴. More recent studies showed the ability of living neural network to classify inputs in space and time^{118,119,229}. These approaches appear to me fundamentally limited by the current lack of specific circuit elements available to a biological engineer. We overcame this obstacle and designed neuronal circuits with bespoke functionality which allowed us for the first time to perform a structure-function study with a neuronal circuit, and more specifically to experimentally study an evolutionary transformation between a small and a large brain. Synthetic neurobiology thus complements classical neurobiology and extends the realm of questions which can be experimentally addressed.

I see potential applications of this method *in vivo* in neuroprosthetics and neuroenhancement. Recent studies use single fibers for optogenetic stimulation, but such stimuli are simple and unspecific. Our approach for holographic stimulation could serve to provide 3D input into the visual cortex of a living organism^{317,369,401}. A potential application might lay in an optogenetically based intracortical visual prosthesis, circumventing a substantial part of the visual system and specifically targeting the input layer of sensory cortex. The artificial replacement and reconstitution of fundamental building blocks of the nervous system *in vivo* might lead to genuine insights into the logic of neuronal circuits, and neuronal codes. I am positive that such experiments are within reach using technologies developed here.

Future applications *in vitro* rest in novel diagnostics from optically interfaced networks of patient derived neuronal cultures using induced pluripotent stem cells^{260,326}. Optogenetic tools were also recently used to control intracellular signals and transcription within a cell¹²⁷. Similarly, gene expression signals can be controlled optically^{151,363} with the potential to extend the methodology developed here to intracellular processes and hybrid gene regulation.

Materials and Methods

“To the natural philosopher there is no natural object unimportant or trifling. From the least of nature’s works he may learn the greatest lessons.”

John Herschel¹⁸²: “The Study of Natural Philosophy”.

10.1 Experimental protocols

Primary culture of neurons

Primary cell cultures were prepared from embryonic rat cortices. We use Wistar WU rat embryos at 18 or 19 days of gestation. All animals were kept and bred in the animal house of the Max Planck Institute for Experimental Medicine according to the guidelines for experimental animals. We use a protocol derived from the procedure by Brewer et al.⁵⁹

- We sacrificed a pregnant rat with CO₂ at gestation day 18 or 19. Next, we performed a cervical dislocation. This was done by placing the animal belly down on the operation table, fixing the neck with a pair of tweezers, firmly pulling its tail and bending the body over the head. This step requires some force. Then, the animal is flipped belly up and the fur is sterilized by flushing with 70% ethanol.
- Next, we cut through the fur and the skin of the rat. This reveals muscular tissue covering the intestines. Cutting through the muscles opens the abdominal cavity and the embryos in the uterus are visible right away. They are removed by grasping an edge of the uterus with surgical tweezers and pulling the uterus out of the body. The distribution of the number of embryos for our animals is shown in **Fig. 10.1A**. The filaments connecting the uterus with the body are cut with a pair of scissors. After this procedure, the uterus is put in a petri dish on ice. The embryonic sacks are cut one by one and the embryos are extracted with a pair of surgical tweezers. The embryos are decapitated and the heads transferred to a petri dish on ice. There were typically 10 embryos per rat. All following steps were performed in a sterile environment.
- The heads were processed one after the other on a second petri dish on ice. First, under a microscope, the skull cavity was opened and the brain removed. Then, the cortex was separated from the brain using a sharp spoon and sharp tweezers. This was done by putting the brain in a small petri dish, cutting the brain along the central line with a sharp spoon and opening the brain along the central line. First, we removed the meninges and then cut the cortex, making sure not to include parts of the striatum or the hippocampus. The cortices were stored in ice cold buffered neurobasal medium (100 mM HEPES) until all hemispheres from all embryos were processed.
- After the surgical preparation of the cortices, the supernatant was removed and the prepared cortices were trypsinized in Trypsin/EDTA for 15 minutes at 37°C. Then, the Trypsin/EDTA was removed and replaced with a 10% FCS solution in Neurobasal medium. The cells were homogenized 10 times with a syringe and a needle of 1 mm diameter. The cell suspension was then centrifuged at 1200 rpm for 2 minutes. The pellet was re-suspended in serum free B27/Neurobasal medium supplemented with Glutamax and Basic Fibroblast Growth Factor (bFGF), see **Tab. 10.1**. Typically, 1 ml medium was used for two embryos / four hemispheres. This generates a cell density of roughly 10 million cells/ml.
- To measure the cell density, 50 μ l of the cell suspension was mixed with 50 μ l of a 0.4% Tryptane blue solution (Prepared in 0.81% sodium chloride and 0.06% potassium phosphate, dibasic.). A drop of this mixture was placed on a Neubauer counting chamber.
- We seed 1 million primary cells, after Tryptan blue stain identified as membrane-intact, in 100 μ l medium. The cells were placed on multielectrode arrays coated with poly-D-lysine. A droplet with 1 million cells (in typically around 100 μ l cell suspension) was added in

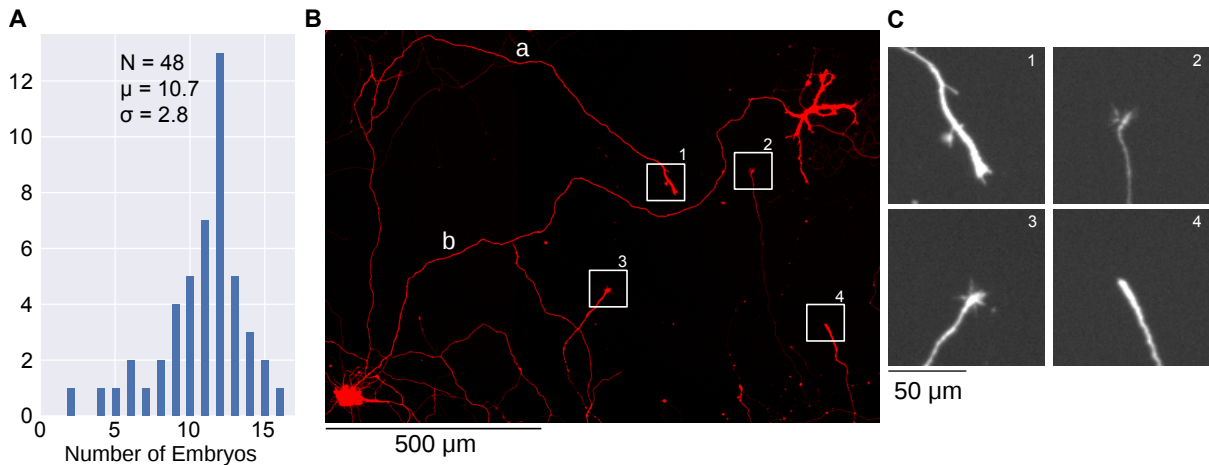


Figure 10.1: **Typical number of embryos and size of neurons grown in culture.** **A** The distribution of the number of embryos for the animals used here, outbred Wistar (WU) rats. The typical number scatters around 11. **B** Neurons grown for 20 days on a coverslip. Transduction with AAV9.hSyn.TurboRFP on DIV 2. The connection between both cells (b) and the filament with the growth cone (a) are equally long and measure 1.70 ± 0.05 mm. **C** Magnification of the insets in A, raw data, reveal growth cones²⁹¹.

the middle of the multielectrode array to cover the recording area and the MEAs were placed in an incubator for 2h to 5h. The droplet extends to about 1 cm^2 so that the final seeding cell density is typically $10.000 \text{ cells/mm}^2$. After several hours, the arrays were filled up with 1 ml of the aforementioned serum free B27/Neurobasal medium.

The cells were kept in an incubator at 37°C and a mixture of $8\% \text{ CO}_2 + 92\% \text{ ambient air}$. Half of the medium was changed once a week. The MEAs were capped³⁸⁵ with a Teflon membrane (ALA-science caps, ALA Scientific Instruments, USA). Cell cultures were typically prepared on Wednesdays, transduction and medium changes were done on Fridays. The cells can be transduced virally and neurons grow long filaments, **Fig. 10.1B**, including growth cones, **Fig. 10.1C**. In comparison to the literature, our preparation yields very high cell densities. Below we will measure neuron and glia density to around 2000 cells/mm^2 , i.e. 80% of cells are lost during the preparation. Most other studies only report the seeding density. Tetzlaff et al.⁴⁶⁹, studying self-organized criticality, use a density of 5000 mm^{-2} . Yaron Penn and colleagues seed $3000 - 4000 \text{ mm}^{-2}$ of which around 800 mm^{-2} survive³⁷⁹. The fraction of surviving cells is consistent with our measurements. Soriano et al.⁴⁴⁸ probe the effects of various densities by seeding between 1300 and 21000 mm^{-2} , however, typically obtained $< 1000 \text{ mm}^{-2}$ in the end. This is the same density as with the cortical cultures in²⁷⁵ or the study of²¹³ in which they varied the seeding density between 100 mm^{-2} and 2500 mm^{-2} . The highest reported measured cell densities are by⁴⁹⁸ with about 2500 mm^{-2} .

Cleaning and Coating of MEAs/Coverslips

MEAs were produced by MultiChannel Systems (MCS), 60MEA200/30iR-TiN, and Coverslips were Marienfeld Superior, $\varnothing 12 \text{ mm}$, # 1.5.

- We cleaned MEAs, and MEA-caps following the MCS recommendation, by immersing them in a 1% Tergazym solution in ddH_2O for a few hours. Typically, this was enough to remove any dirt, cellular debris and contamination, such as mold. If any residues remained

Agent	Stock Solution	Storage
B27	400 μ l	-20°C
Glutamax	50 μ l	$+4^{\circ}\text{C}$
bFGF	2 μ l of (10 μ g in 100 μ l 0.1% BSA in 10mM TRIS pH 7.6) stock	-20°C

Table 10.1: Constituents of the supplemented Neurobasal Medium. B27, Glutamax and Basic Fibroblast Growth Factor (bFGF) were added to 20 ml of NB Medium, yielding as final concentrations 1:50 B-27, 1:400 Glutamax (0.5 mM L-alanyl-L-glutamine dipeptide), 10 ng/ml bFGF.

in the well, we gently removed debris with a Q-Tip. We then flushed them thoroughly with ddH₂O and left them in a beaker with ddH₂O over night to remove all left traces of Tergazym. After drying the MEAs, they were autoclaved at 120°C for 25 min.

- We heat sterilized coverslip at 200°C for 4h and placed them in sterile 12-Well plates (Cell Star Cat. 665 180, Greiner).

Before usage, we coated the surface of both, MEAs and coverslips, with Poly-D-Lysine (PDL). For MEAs this is the recommended procedure by Multichannel Systems. To this end, we add 1 ml of a sterile filtered 50 μ g/ml Poly-D-Lysine Hydrobromide solution in ddH₂O into the well of a MEA. We also tried variations of this technique, for instance by first hydrophilizing the surface with FCS, or adding Laminin to the coating solution¹²⁶. Both did not substantially affect culture development and therefore we decided to use the simple protocol. The PDL solution was left on the MEAs and coverslips for at least 24h. Typically, we prepared MEAs and coverslips a few days in advance and stored them with PDL solution in an incubator at 37°C and 5% CO₂. Before plating the cells, we sucked off the PDL solution, flushed the coverslips/MEAs twice with sterile ddH₂O, and left them to dry under the UV light of the sterile bench.

Recordings

We recorded data from 30 μ m diameter TiN-MEAs with the commercial Multichannel systems setup (a 60 channel MEA amplifier, MEA-1060 Inv, Multichannel Systems, Reutlingen, Germany). Briefly, the electrode signals were preamplified and sampled with 25 kHz from each of the 60 electrodes. We further used two additional analog channels to synchronize stimulation, recording, and trigger pulses from the camera (Progres MF firewire, Jenoptik, Jena, Germany) for calcium imaging. We first filtered the electrode data with a Butterworth filter of 2nd order at 100 Hz. We identified events as points in time where the filtered potential exceeded a given threshold. Typically, we chose a threshold of -5σ , individually for every electrode²⁷⁷, corresponding to about -20 μ V. We removed the fraction of accidental threshold crossings with a simple sorting scheme, see **Fig. 4.16**. Around every threshold crossing, we cut a segment 2 ms before and 4 ms after the event with 150 voltage values. On the collection of all N datapoints of an electrode, i.e. a cloud of N points in a 150 dimensional voltage-space, we first perform a principal component analysis and subsequently identify clusters using the mean-shift algorithm at a quartile of 0.3⁹⁰. For the identified clusters, typically one or two, we calculate averaged waveforms. If the averaged waveform within a cluster has a standard deviation larger than 5 μ V and a maximum larger than +4 μ V, we accept this cluster as action potentials; if not, we label the cluster as noise cluster. Please note that we only sort related to the rough shape of the waveform. The unit activity might still be taken as multiunit activity.

The holographic frame transitions were recorded from a screen receiving the same signal as the SLM after a DVI splitter. We measured the screen signal with a OPT101 photodiode and

Toxin	Concentration	Final Concentration
Na ₂ -NBQX	4 mg/ml ddH ₂ O → 10 mM	10 μM
APV	10 mg/ml ddH ₂ O → 50 mM	100 μM
Picrotoxin	30.1 mg/ml DMSO → 50 mM	100 μM
Bicuculline	18.4 mg/ml DMSO → 50 mM	50 μM

Table 10.2: Neurotoxins for blockade experiments.

transimpedance amplifier (Texas Instruments) and recorded it with the electrophysiology setup. We verified that this signal is within 2 ms synchronous to the SLM.

Toxins and synaptic blockade

For synaptic blockade, we used a mixture of the artificial NMDA receptor antagonist 2-Amino-5-phosphonovaleric acid (APV) as free acid^{105,364}, the AMPA/kainate receptor antagonist (2,3-Dihydroxy-6-nitro-7-sulfamoyl-benzo[f]quinoxaline-2,3-dione) (NBQX) as disodium salt⁴³⁵ and the plant-toxin and GABA receptor antagonist Picrotoxin (PTX) or Bicuculline. The agents were either dissolved in ddH₂O or in Dimethyl sulfoxide (DMSO). We kept the toxins in stock concentrations aliquoted and frozen at -20°C. Just before an experiment, we added 2 μl of PTX and APV together with 1 μl of NBQX per ml of medium. Note that the DMSO concentration reaches about 0.2%.

Perfusion

Perfusion is needed after about 12h experiments^{281,331,432}, with a small flow rate of 1.5-3.5 μl/min. We used a Gibson Minipulse 3 Perfusion pump, operated at 0.01 RPM, the smallest setting. With a narrow silicone tube, this yielded a steady flow of 2.7 μl/min. The medium was supplemented Neurobasal medium, with an additional 100 U/ml, 100 μg/ml Pen/Strep (200 μl of the Pen/Strep Stock Solution to 20 ml medium). The medium was kept warm in an oil bath, and all components were autoclaved and assembled on a sterile bench before use.

Immunostainings

For the immunostainings, we follow a standard protocol⁴¹⁸. Buffers are listed in **Tab. 10.3**.

- We take the cells from the incubator and wash them once with PBS
- We add 4% Formaldehyde, buffered at pH 6.9, to the cells. Fixation for 7 min at 4°C
- Next, we wash 3 times with PBS for 5 min each. This is done at room temperature on a shaker
- For permeabilization, we incubate the fixated cells with Triton-X for 5 min at room temperature on a shaker.
- Wash two times with PBT for 5 min at room temperature on a shaker.
- Next, we block unspecific binding sites by incubating the cells for about 2h with a BSA solution at room temperature.
- Then we apply the primary antibodies, diluted to the specified concentration in BSA. We do this by placing a drop of the antibody containing solution on a piece of parafilm and flipping the coverslip on top. This is left over night at 4°C.

Buffer	Stock solution	Storage
Triton-X	100 mL PBS with 500 μ l Triton-X 100	+4°C
PBT	500 mL PBS with 500 μ l Tween-20	+4°C
BSA	0.75 g BSA powder in 25 mL PBT	made freshly
FA	Commercial Formaldehyde solution, 4 %	+4°C

Table 10.3: Buffers for immunostainings.

Name	Viral construct	GC/ml
jRCaMP1a	AAV1.Syn.NES.jRCaMP1a.WPRE.SV40	3.36×10^{13}
GCaMP6f	AAV1.Syn.GCaMP6f.WPRE.SV40	2.65×10^{13}
Syn.RFP	AAV5.hSyn.TurboRFP.WPRE.rBG	4.40×10^{13}
GFAP.GFP	AAV5.GFAP.eGFP.WPRE.hGH	1.06×10^{13}
CamKII.GFP	AAV9.CamKII0.4.eGFP.WPRE.rBG	3.49×10^{13}
Syn.RFP	AAV9.hSyn.TurboRFP.WPRE.rBG	6.64×10^{13}
ChR2(H134R)-YFP	AAV9.hSyn.hChR2(H134R)-eYFP.WPRE.hGH	3.39×10^{13}
Chronos-GFP	AAV9.Syn.Chronos-GFP.WPRE.bGH	3.51×10^{13}

Table 10.4: Viruses used in this thesis. GC refers to the number of genome copies per volume.

- The next day, we flush out the primary antibody by washing twice with PBT for 5 min at room temperature on a shaker.
- We then apply the secondary antibody, again in BSA solution, at room temperature for at least 120 min.
- Finally we wash the sample 3 times with PBT for 5min at room temperature.
- We mount the slides to an objective slide with ProLong Gold + DAPI. To this end, we place a drop of Prolong Gold + DAPI on the objective slide, flip the coverslip on top and let it dry over night at 4°C.
- The next day, we seal the coverslip with clear nail polish (Jade Express Finish, Typ 10 Brilliant Transparent, Tegut, Göttingen, Germany).

10.2 Agents

The water used is ASTM Type 1 ultrapure and was cleaned by activated carbon and deionization in a Satorius Arium pro filter. Typical conductivities are 0.055 μ S/cm with < 50 μ g/l organic carbon. The other agents used are listed in Tab. 10.5. All viruses were procured at UPenn Vectorcore and the number of genome copies was measured with quantitative PCR²⁸⁸. They are listed in Tab. 10.4. Before use, the viruses were thawed once, aliquoted into 5 μ l portions, and then stored frozen at -80°C .

	Manufacturer	Number
Chemicals		
B27 Suppl. 50x	Gibco	17504-044
Basic fibroblast growth factor (bFGF)	Gibco	13256-029
Bicuculline	Sigma-Aldrich	14340
Bovine serum albumin (BSA)	Sigma-Aldrich	A3059
D-AP5	Sigma-Aldrich	A5282
Dimethyl Sulfoxide (DMSO)	Sigma-Aldrich	D8418
Fetal Calf Serum (FCS)	Biochrom	Cat. 0115
Fluorescein	Sigma-Aldrich	F2456
Formaldehyde, phosphate buffered at pH 6.9	Merck	100496
Glutamax 100x	Gibco	35050-038
(3-glycidyloxypropyl)trimethoxysilane (3-GPS)	Sigma-Aldrich	440167
HEPES 1M	Gibco	15630-056
Laminin	Sigma-Aldrich	L2020
NBQX Disodium salt	Sigma-Aldrich	N183
Neurobasal Medium	Gibco	12348-017
PBS Tablets for 500 ml ddH ₂ O	Gibco	18912-014
Pen/Strep 10.000 U/ml, µg/ml	Gibco	15140-122
PDMS Sylgard 184	Dow Corning	Base/Curing Agent
Picrotoxin	Sigma-Aldrich	P1675
Poly-D-lysine, Hydrobromide (PDL)	Sigma-Aldrich	P7886
Poly-L-lysine, FITC labeled (PLL-FITC)	Sigma-Aldrich	P3069
Prolong Gold + DAPI	Molecular Probes	P36931
Sodium dodecyl sulfate	Sigma Aldrich	L4509
Tergazym Alconox	Sigma-Aldrich	242985
Toluene	Merck	107019
Triton X-100	Sigma-Aldrich	X100
Trypsin/EDTA 0.05%/0.02% in PBS	Biochrom	L2143
Tryptanblue 0.4%	Sigma-Aldrich	T8154
Tween-20	Sigma-Aldrich	P7949
Antibodies (diluted in 3% BSA/PBT)		
Goat-Anti-GFP	Rockland 101-215	1:200
Rabbit-Anti-RFP	Rockland 401-379	1:200
Mouse-Anti-NeuN	EMD Millipore MAB377	1:50
Rabbit-Anti-GFAP	Abcam, ab33922	1:50
Donkey-Anti-Goat 647	Invitrogen A-21447	10 µg/ml
Donkey-Anti-Rabbit 488	Abcam, ab150061	1:1000
Donkey-Anti-Mouse 546	Invitrogen A-10036	10 µg/ml
Donkey-Anti-Mouse 647	Abcam, ab180111	1:1000

Table 10.5: Chemicals and Antibodies used in this thesis.

Bibliography

- [1] JB Ackman and MC Crair. “Role of emergent neural activity in visual map development”. In: *Current Opinion in Neurobiology* **24** (2014), pp. 166–175.
- [2] A Adamantidis et al. “Q&A Optogenetics: 10 years after ChR2 in neurons - views from the community”. In: *Nature Neuroscience* **18** (2015), pp. 1202–1212.
- [3] A Agudelo-Toro and A Neef. “Computationally efficient simulation of electrical activity at cell membranes interacting with self-generated and externally imposed electric fields”. In: *J Neural Engineering* **10** (2013), pp. 1–19.
- [4] B Ahmed et al. “An intracellular study of the contrast-dependence of neuronal activity in cat visual cortex”. In: *Cerebral Cortex* **7** (1997), pp. 559–570.
- [5] B Ahmed et al. “Map of the synapses onto layer 4 basket cells of the primary visual cortex of the cat”. In: *J Comparative Neurology* **380** (1997), pp. 230–242.
- [6] J Akerboom et al. “Optimization of a GCaMP Calcium Indicator for Neural Activity Imaging”. In: *J Neuroscience* **32** (2012), pp. 13819–13840.
- [7] J Akerboom et al. “Genetically encoded calcium indicators for multi-color neural activity imaging and combination with optogenetics”. In: *Frontiers in Molecular Neuroscience* **6** (2013), pp. 1–29.
- [8] DG Albrecht, SB Farrar, and DB Hamilton. “Spatial contrast adaptation characteristics of neurones recorded in the cat’s visual cortex”. In: *J Physiology* **347** (1984), pp. 713–739.
- [9] K Albus. “A Quantitative Study of the Projection Area of the Central and the Paracentral Visual Field in Area 17 of the Cat”. In: *Exp Brain Res* **24** (1975), pp. 159–179.
- [10] HJ Alitto and WM Usrey. “Corticothalamic feedback and sensory processing”. In: *Current Opinion in Neurobiology* **13** (2003), pp. 440–445.
- [11] JM Alonso, WM Usrey, and RC Reid. “Rules of connectivity between geniculate cells and simple cells in cat primary visual cortex.” In: *J Neuroscience* **21** (2001), pp. 4002–4015.
- [12] TJ Andrews, SD Halpern, and D Purves. “Correlated size variations in human visual cortex, lateral geniculate nucleus, and optic tract.” In: *J Neuroscience* **17** (1997), pp. 2859–2868.
- [13] A Anishchenko et al. “Receptive field mosaics of retinal ganglion cells are established without visual experience.” In: *J Neurophysiology* **103** (2010), pp. 1856–1864.
- [14] A Antonini, M Fagiolini, and MP Stryker. “Anatomical Correlates of Functional Plasticity in Mouse Visual Cortex”. In: *J Neuroscience* **19** (1999), pp. 4388–4406.

- [15] A Arieli et al. “Dynamics of Ongoing Activity: Explanation of the Large Variability in Evoked Cortical Responses”. In: *Science* **273** (1996), pp. 1868–1871.
- [16] CA Arrese et al. “Retinal Structure and Visual Acuity in a Polyprotodont Marsupial , the Fat-Tailed Dunnart (*Sminthopsis crassicaudata*)”. In: *Brain Behav Evo* **53** (1999), pp. 111–126.
- [17] CA Arrese et al. “Trichromacy in Australian Marsupials”. In: *Current Biology* **12** (2002), pp. 657–660.
- [18] T Baden et al. “The functional diversity of retinal ganglion cells in the mouse”. In: *Nature* **529** (2016), pp. 345–350.
- [19] DJ Bakkum, ZC Chao, and SM Potter. “Spatio-temporal electrical stimuli shape behavior of an embodied cortical network in a goal-directed learning task”. In: *J Neural Engineering* **5** (2008), pp. 310–323.
- [20] DJ Bakkum et al. “MEART: The semi-living artist”. In: *Frontiers in Neurobotics* **1** (2007), pp. 1–10.
- [21] Y Banitt, KAC Martin, and I Segev. “A biologically realistic model of contrast-invariant orientation tuning by thalamocortical synaptic depression”. In: *J Neuroscience* **27** (2007), pp. 10230–10239.
- [22] O Barak and M Tsodyks. “Working models of working memory”. In: *Current Opinion in Neurobiology* **25** (2014), pp. 20–24.
- [23] O Barak et al. “Progress in Neurobiology From fixed points to chaos: Three models of delayed discrimination”. In: *Progress in Neurobiology* **103** (2013), pp. 214–222.
- [24] Z Barger et al. “Early Network Activity Propagates Bidirectionally between Hippocampus and Cortex”. In: *Developmental Neurobiology* **76** (2015), pp. 661–672.
- [25] HB Barlow, R Fitzhugh, and SW Kuffler. “Change of organization in the receptive fields of the cat’s retina during dark adaptation”. In: *J Physiology* **137** (1957), pp. 338–354.
- [26] J Barral and AD Reyes. “Synaptic scaling rule preserves excitatory-inhibitory balance and salient neuronal network dynamics”. In: *Nature Neuroscience* **19** (2016), pp. 1690–1696.
- [27] E Bartfeld and A Grinvald. “Relationships between orientation-preference pinwheels, cytochrome oxidase blobs, and ocular-dominance columns in primate striate cortex.” In: *PNAS* **89** (1992), pp. 11905–11909.
- [28] J Bates and Y Chu. “Surface topography and impedance of metal-electrolyte interfaces”. In: *Physical Review Letters* **60** (1988), pp. 627–630.
- [29] C Beaulieu and M Colonnier. “The number of neurons in the different laminae of the binocular and monocular regions of area 17 in the cat”. In: *J Comparative Neurology* **217** (1983), pp. 337–344.
- [30] R Ben-Yishai, RL Bar-Or, and H Sompolinsky. “Theory of orientation tuning in visual cortex”. In: *PNAS* **92** (1995), pp. 3844–3848.
- [31] G Benshalom and EL White. “Quantification of thalamocortical synapses with spiny stellate neurons in layer IV of mouse somatosensory cortex.” In: *J Comparative Neurology* **253** (1986), pp. 303–314.
- [32] W Bialek. *Biophysics: Searching for Principles*. Princeton, NJ: Princeton University Press, 2012.

-
- [33] W Bialek. “Perspectives on theory at the interface of physics and biology”. In: *arXiv.org* (2015), p. 1512.08954. arXiv: arXiv:1512.08954v1.
- [34] ORP Bininda-Emonds et al. “The delayed rise of present-day mammals”. In: *Nature* **446** (2007), pp. 507–513.
- [35] T Binzegger, RJ Douglas, and KAC Martin. “A Quantitative Map of the Circuit of Cat Primary Visual Cortex”. In: *J Neuroscience* **24** (2004), pp. 8441–8453.
- [36] PM Birch et al. “Real-time optical aberration correction with a ferroelectric liquid-crystal spatial light modulator”. In: *Applied Optics* **37** (1998), pp. 2164–2169.
- [37] PO Bishop, W Kozak, and GJ Vakkur. “Some quantitative aspects of the cat’s eye: axis and plane of reference, visual field co-ordinates and optics”. In: *J Physiology* **163** (1962), pp. 466–502.
- [38] AG Blankenship and MB Feller. “Mechanisms underlying spontaneous patterned activity in developing neural circuits”. In: *Nature Reviews Neuroscience* **11** (2009), pp. 18–29.
- [39] GG Blasdel. “Orientation selectivity, preference, and continuity in monkey striate cortex”. In: *J Neuroscience* **12** (1992), pp. 3139–3161.
- [40] GG Blasdel, K Obermayer, and L Kiorpes. “Organization of ocular dominance and orientation columns in the striate cortex of neonatal macaque monkeys.” In: *Visual Neuroscience* **12** (1995), pp. 589–603.
- [41] GG Blasdel and G Salama. “Voltage-sensitive dyes reveal a modular organization in monkey striate cortex”. In: *Nature* **321** (1986), pp. 579–585.
- [42] A Bleckert et al. “Report Visual Space Is Represented by Nonmatching Topographies of Distinct Mouse Retinal Ganglion Cell Types”. In: *Current Biology* **24** (2014), pp. 310–315.
- [43] RD Boer and A van Oosterom. “Electrical properties of platinum electrodes: impedance measurements and time-domain analysis”. In: *Med & Biol Eng & Comput* **16** (1978), pp. 1–10.
- [44] LL Bologna et al. “Low-frequency stimulation enhances burst activity in cortical cultures during development”. In: *Neuroscience* **165** (2010), pp. 692–704.
- [45] I Bomash, Y Roudi, and S Nirenberg. “A Virtual Retina for Studying Population Coding”. In: *PLoS ONE* **8** (2013), e53363.
- [46] T Bonhoeffer and A Grinvald. “Iso-orientation domains in cat visual cortex are arranged in pinwheel-like patterns”. In: *Nature* **353** (1991), pp. 429–431.
- [47] T Bonhoeffer and A Grinvald. “The layout of iso-orientation domains in area 18 of cat visual cortex: optical imaging reveals a pinwheel-like organization.” In: *J Neuroscience* **13** (1993), pp. 4157–4180.
- [48] V Bonin, V Mante, and M Carandini. “The Suppressive Field of Neurons in Lateral Geniculate Nucleus”. In: *J Neuroscience* **25** (2005), pp. 10844–10856.
- [49] R Bopp et al. “Pyramidal Cells Make Specific Connections onto Smooth (GABAergic) Neurons in Mouse Visual Cortex”. In: *PLoS Biology* **12** (2014), e1001932.
- [50] WH Bosking et al. “Orientation selectivity and the arrangement of horizontal connections in tree shrew striate cortex.” In: *J Neuroscience* **17** (1997), pp. 2112–2127.
- [51] WH Bosking, JC Crowley, and D Fitzpatrick. “Spatial coding of position and orientation in primary visual cortex”. In: *Nature Neuroscience* **5** (2002), pp. 28–31.

- [52] JI Boulland et al. “Vesicular Glutamate and GABA Transporters Sort to Distinct Sets of Vesicles in a Population of Presynaptic Terminals”. In: *Cerebral Cortex* **19** (2009), pp. 241–248.
- [53] P Bourdieu. “The specificity of the scientific field and the social conditions of the progress of reason”. In: *Social Science Information* **14** (1975), pp. 19–47.
- [54] ES Boyden et al. “Millisecond-timescale, genetically targeted optical control of neural activity”. In: *Nature Neuroscience* **8** (2005), pp. 1263–1268.
- [55] DW Branch et al. “Long-Term Maintenance of Patterns of Hippocampal Pyramidal Cells on Substrates of Polyethylene Glycol and Microstamped Polylysine”. In: *IEEE Transactions on Biomedical Engineering* **47** (2000), pp. 290–300.
- [56] I Breskin et al. “Percolation in Living Neural Networks”. In: *Physical Review Letters* **97** (2006), p. 188102.
- [57] PC Bressloff. “Bloch waves, periodic feature maps, and cortical pattern formation.” In: *Physical Review Letters* **89** (2002), p. 088101.
- [58] AA Brewer et al. “Visual areas in macaque cortex measured using functional magnetic resonance imaging”. In: *J Neuroscience* **22** (2002), pp. 10416–10426.
- [59] GJ Brewer et al. “Optimized Survival of Hippocampal Neurons in B27-Supplemented Neurobasal, a New Serum-free Medium Combination”. In: *J Neuroscience Res* **35** (1993), pp. 567–576.
- [60] A Burgalossi et al. “Analysis of neurotransmitter release mechanisms by photolysis of caged Ca^{2+} in an autaptic neuron culture system”. In: *Nature Protocols* **7** (2012), pp. 1351–1365.
- [61] L Cai et al. “A 1024-channel 6 mW/mm² Optical Stimulator for In-Vitro Neuroscience Experiments”. In: *IEEE Eng Med Biol Soc* (2014), pp. 6133–6138.
- [62] EM Callaway and LC Katz. “Effects of binocular deprivation on the development of clustered horizontal connections in cat striate cortex”. In: *PNAS* **88** (1991), pp. 745–749.
- [63] EM Callaway and LC Katz. “Emergence and Refinement of Clustered Horizontal Connections in Cat Striate Cortex”. In: *J Neuroscience* **10** (1990), pp. 1134–1153.
- [64] DE Cameron, CJ Bashor, and JJ Collins. “A brief history of synthetic biology”. In: *Nature Reviews Microbiology* **12** (2014), pp. 381–390.
- [65] J Cang et al. “Development of Precise Maps in Visual Cortex Requires Patterned Spontaneous Activity in the Retina”. In: *Neuron* **48** (2005), pp. 797–809.
- [66] M Carandini. “Melting the Iceberg: Contrast Invariance in Visual Cortex”. In: *Neuron* **54** (2007), pp. 11–13.
- [67] M Carandini and DJ Heeger. “Summation and Division by Neurons in Primate Visual Cortex”. In: *Science* **264** (1994), pp. 1333–1336.
- [68] M Carandini and DL Ringach. “Predictions of a Recurrent Model of Orientation Selectivity”. In: *Vision Res* **37** (1997), pp. 3061–3071.
- [69] SB Carter. “Principles of cell motility: The direction of cell movement and cancer invasion”. In: *Nature* **5016** (1965), pp. 1183–1187.
- [70] S Catalano and C Shatz. “Activity-Dependent Cortical Target Selection by Thalamic Axons”. In: *Science* **281** (1998), pp. 559–562.
- [71] WA Catterall. “Ion channel voltage sensors: Structure, function, and pathophysiology”. In: *Neuron* **67** (2010), pp. 915–928.

-
- [72] FS Chance, SB Nelson, and LF Abbott. “Complex cells as cortically amplified simple cells”. In: *Nature Neuroscience* **2** (1999), pp. 277–282.
- [73] JC Chang, GJ Brewer, and BC Wheeler. “Neuronal network structuring induces greater neuronal activity through enhanced astroglial development”. In: *J Neural Engineering* **3** (2006), pp. 217–226.
- [74] B Chapman, I Gödecke, and T Bonhoeffer. “Development of orientation preference in the mammalian visual cortex”. In: *J Neurobiology* **41** (1999), pp. 18–24.
- [75] B Chapman and MP Stryker. “Development of orientation selectivity in ferret visual cortex and effects of deprivation”. In: *J Neuroscience* **13** (1993), pp. 5251–5262.
- [76] B Chapman, MP Stryker, and T Bonhoeffer. “Development of orientation preference maps in ferret primary visual cortex.” In: *J Neuroscience* **16** (1996), pp. 6443–6453.
- [77] B Chapman, KR Zahs, and MP Stryker. “Relation of cortical cell orientation selectivity to alignment of receptive fields of the geniculocortical afferents that arborize within a single orientation column in ferret visual cortex.” In: *J Neuroscience* **11** (1991), pp. 1347–1358.
- [78] P Charlesworth et al. “Neuropharmacology Canalization of genetic and pharmacological perturbations in developing primary neuronal activity patterns”. In: *Neuropharmacology* **100** (2016), pp. 47–55.
- [79] P Charlesworth et al. “Quantitative differences in developmental profiles of spontaneous activity in cortical and hippocampal cultures”. In: *Neural Development* **10** (2015), pp. 1–10.
- [80] S Chatterjee, K Ohki, and RC Reid. “Functional microarchitecture of orientation and color selectivity in macaque primary visual cortex”. In: *J Vision* **9** (2009), pp. 20–21.
- [81] TW Chen et al. “Ultrasensitive fluorescent proteins for imaging neuronal activity”. In: *Nature* **499** (2013), pp. 295–300.
- [82] C Chiu and M Weliky. “Spontaneous Activity in Developing Ferret Visual Cortex In Vivo”. In: *J Neuroscience* **21** (2001), pp. 8906–8914.
- [83] PG Clarke and D Whitteridge. “The cortical visual areas of the sheep.” In: *J Physiology* **256** (1976), pp. 497–508.
- [84] BG Cleland, MW Dubin, and WR Levick. “Simultaneous recording of input and output of lateral geniculate neurones”. In: *Nature* **231** (1971), pp. 191–192.
- [85] BG Cleland and BB Lee. “A comparison of visual responses of cat lateral geniculate nucleus neurones with those of ganglion cells afferent to them.” In: *J Physiology* **369** (1985), pp. 249–268.
- [86] IP Clements et al. “Optogenetic stimulation of multiwell MEA plates for neural and cardiac applications”. In: *Proc. of SPIE* **9690** (2016), pp. 1–10.
- [87] D Cohen and M Segal. “Network bursts in hippocampal microcultures are terminated by exhaustion of vesicle pools”. In: *J Neurophysiology* **106** (2011), pp. 2314–2321.
- [88] E Cohen et al. “Determinants of spontaneous activity in networks of cultured hippocampus.” In: *Brain Res* **1235** (2008), pp. 21–30.
- [89] MT Colonnese and R Khazipov. “Slow activity transients in infant rat visual cortex: a spreading synchronous oscillation patterned by retinal waves”. In: *J Neuroscience* **30** (2010), pp. 4325–4337.
- [90] D Comaniciu and P Meer. “Mean Shift: A Robust Approach Toward Feature Space Analysis”. In: *IEEE Transactions on Pattern Analysis and Machine Intelligence* **24** (2002), pp. 603–619.

- [91] J Conhaim et al. “Bimodal Septal and Cortical Triggering and Complex Propagation Patterns of Spontaneous Waves of Activity in the Developing Mouse Cerebral Cortex”. In: *Developmental Neurobiology* **70** (2010), pp. 679–692.
- [92] BR Conway et al. “Advances in color science: from retina to behavior.” In: *J Neuroscience* **30** (2010), pp. 14955–14963.
- [93] NM da Costa and KAC Martin. “How Thalamus Connects to Spiny Stellate Cells in the Cat’s Visual Cortex”. In: *J Neuroscience* **31** (2011), pp. 2925–2937.
- [94] BG Cragg. “The Development of Synapses in the Visual System of the Cat”. In: *J Comparative Neurology* **160** (1975), pp. 147–166.
- [95] MC Crair, DC Gillespie, and MP Stryker. “The Role of Visual Experience in the Development of Columns in Cat Visual Cortex”. In: *Science* **279** (1998), pp. 566–570.
- [96] MC Crair et al. “Emergence of ocular dominance columns in cat visual cortex by 2 weeks of age.” In: *J Comparative Neurology* **430** (2001), pp. 235–249.
- [97] F Crick. “The impact of molecular biology on neuroscience”. In: *Philosophical Transactions of the Royal Society B* **354** (1999), pp. 2021–2025.
- [98] JE Curtis, BA Koss, and DG Grier. “Dynamic holographic optical tweezers”. In: *Optics Communications* **207** (2002), pp. 169–175.
- [99] DM Dacey. “Primate retina: cell types, circuits and color opponency.” In: *Progress in Retinal and Eye Res* **18** (1999), pp. 737–763.
- [100] DM Dacey. “The mosaic of midget ganglion cells in the human retina.” In: *J Neuroscience* **13** (1993), pp. 5334–5355.
- [101] DM Dacey and MR Petersen. “Dendritic field size and morphology of midget and parasol ganglion cells of the human retina.” In: *PNAS* **89** (1992), pp. 9666–9670.
- [102] H Dana et al. “Hybrid multiphoton volumetric functional imaging of large-scale bioengineered neuronal networks”. In: *Nature Communications* **5** (2014), pp. 1–7.
- [103] H Dana et al. “Sensitive red protein calcium indicators for imaging neural activity”. In: *eLife* **5** (2016), e12727.
- [104] PM Daniel and D Whitteridge. “The representation of the visual field on the cerebral cortex in monkeys”. In: *J Physiology* **159** (1961), pp. 203–221.
- [105] J Davies and JC Watkins. “Actions of D and L forms of 2-amino-5-phosphonovalerate and 2-amino-4-phosphonobutyrate in the cat spinal cord”. In: *Brain Res* **235** (1982), pp. 378–386.
- [106] P Dayan and LF Abbott. *Theoretical Neuroscience*. London, England; Cambridge, Massachusetts: The MIT Press, 2002. ISBN: 0262041995.
- [107] GC DeAngelis, I Ohzawa, and RD Freeman. “Receptive-field dynamics in the central visual pathways.” In: *TINS* **18** (1995), pp. 451–458.
- [108] TB DeMarse et al. “The Neurally Controlled Animat: Biological Brains Acting with Simulated Bodies”. In: *Autonomous Robots* **11** (2001), pp. 305–310.
- [109] P Degenaar et al. “A Method for Micrometer Resolution Patterning of Primary Culture”. In: *J Biochem* **376** (2001), pp. 367–376.
- [110] K Deisseroth. “Optogenetics”. In: *Nature Methods* **8** (2011), pp. 26–29.
- [111] JA Demas, H Payne, and HT Cline. “Vision Drives Correlated Activity without Patterned Spontaneous Activity in Developing *Xenopus* Retina”. In: *Developmental Neurobiology* **72** (2011), pp. 537–546.

- [112] W Denk, JH Strickler, and WW Webb. “Two-Photon Laser Scanning Fluorescence Microscopy”. In: *Science* **248** (1990), pp. 73–76.
- [113] AM Derrington and P Lennie. “Spatial and Temporal Contrast Sensitivities of Neurones in Lateral Geniculate Nucleus of Macaque”. In: *J Physiology* **357** (1984), pp. 219–240.
- [114] SH Devries and Da Baylor. “Mosaic arrangement of ganglion cell receptive fields in rabbit retina.” In: *J Neurophysiology* **78** (1997), pp. 2048–2060.
- [115] UC Dräger. “Receptive fields of single cells and topography in mouse visual cortex.” In: *J Comparative Neurology* **160** (1975), pp. 269–290.
- [116] UC Dräger and JF Olsen. “Origins of crossed and uncrossed retinal projections in pigmented and albino mice.” In: *J Comparative Neurology* **191** (1980), pp. 383–412.
- [117] UC Dräger and JF Olsen. “Ganglion cell distribution in the retina of the mouse”. In: *Investigative Ophthalmology & Visual Science* **20** (1981), pp. 285–293.
- [118] MR Dranias et al. “Short-Term Memory in Networks of Dissociated Cortical Neurons”. In: *J Neuroscience* **33** (2013), pp. 1940–1953.
- [119] MR Dranias et al. “Stimulus information stored in lasting active and hidden network states is destroyed by network bursts”. In: *Frontiers in Integrative Neuroscience* **9** (2015), pp. 1–17.
- [120] CS Dulcey et al. “Deep UV Photochemistry of Chemisorbed Monolayers: Patterned Coplanar Molecular Assemblies”. In: *Science* **252** (1991), pp. 551–554.
- [121] JC Durack and LC Katz. “Development of Horizontal Projections in Layer 2/3 of Ferret Visual Cortex”. In: *Cerebral Cortex* **6** (1996), pp. 178–183.
- [122] R Durbin and G Mitchison. “A dimension reduction framework for understanding cortical maps”. In: *Nature* **343** (1990), pp. 644–647.
- [123] DM Egelman and PR Montague. “Calcium Dynamics in the Extracellular Space of Mammalian Neural Tissue”. In: *Biophysical J* **76** (1999), pp. 1856–1867.
- [124] V Egger, T Nevian, and RM Bruno. “Subcolumnar dendritic and axonal organization of spiny stellate and star pyramid neurons within a barrel in rat somatosensory cortex”. In: *Cerebral Cortex* **18** (2008), pp. 876–889.
- [125] SJ Eglén, PJ Diggel, and JB Troy. “Homotropic constraints dominate positioning of on- and off-center beta retinal ganglion cells”. In: *Visual Neuroscience* **22** (2005), pp. 859–871.
- [126] A El Hady et al. “Optogenetic stimulation effectively enhances intrinsically generated network synchrony”. In: *Frontiers in Neural Circuits* **7** (2013), pp. 1–15.
- [127] C Eleftheriou et al. “Optogenetic Modulation of Intracellular Signalling and Transcription: Focus on Neuronal Plasticity”. In: *J Experimental Neuroscience* **11** (2017), pp. 1–16.
- [128] MB Elowitz and S Leibler. “A synthetic oscillatory network of transcriptional regulators”. In: *Nature* **403** (1999), pp. 335–338.
- [129] V Emiliani et al. “All-Optical Interrogation of Neural Circuits”. In: *J Neuroscience* **35** (2015), pp. 13917–13926.
- [130] C Enroth-Cugell and JG Robson. “The contrast sensitivity of retinal ganglion cells of the cat”. In: *J Physiology* **187** (1966), pp. 517–552.
- [131] UA Ernst et al. “Intracortical origin of visual maps.” In: *Nature Neuroscience* **4** (2001), pp. 431–436.

- [132] E Erwin, K Obermayer, and K Schulten. “Models of orientation and ocular dominance columns in the visual cortex: A critical comparison”. In: *Neural Computation* **7** (1995), pp. 425–468.
- [133] D Eytan and S Marom. “Dynamics and Effective Topology Underlying Synchronization in Networks of Cortical Neurons”. In: *J Neuroscience* **26** (2006), pp. 8465–8476.
- [134] O Feinerman, A Rotem, and E Moses. “Reliable neuronal logic devices from patterned hippocampal cultures”. In: *Nature Physics* **2** (2008), pp. 967–973.
- [135] L Fenno, O Yizhar, and K Deisseroth. “The Development and Application of Optogenetics”. In: *Annual Review of Neuroscience* **34** (2011), pp. 389–412.
- [136] D Ferster, S Chung, and H Wheat. “Orientation selectivity of thalamic input to simple cells of cat visual cortex”. In: *Nature* **380** (1996), pp. 249–252.
- [137] D Ferster and S LeVay. “The axonal arborizations of lateral geniculate neurons in the striate cortex of the cat.” In: *J Comparative Neurology* **182** (1978), pp. 923–944.
- [138] D Ferster. “Orientation Selectivity of Synaptic Potentials in Neurons of Cat Primary Visual Cortex”. In: *J Neuroscience* **6** (1986), pp. 1284–1301.
- [139] D Ferster. “Spatially Opponent Excitation and Inhibition in Simple Cells of the Cat Visual Cortex”. In: *J Neuroscience* **8** (1988), pp. 1172–1180.
- [140] D Ferster. “X- and Y-mediated synaptic potentials in neurons of areas 17 and 18 of cat visual cortex”. In: *Visual Neuroscience* **4** (1990), pp. 115–133.
- [141] R Feynman. *Noted on the blackboard at his time of death*. 1988.
- [142] GD Field and EJ Chichilnisky. “Information Processing in the Primate Retina: Circuitry and Coding”. In: *Annual Review of Neuroscience* **30** (2007), pp. 1–30.
- [143] I Fishbein and M Segal. “Active cortical innervation protects striatal neurons from slow degeneration in culture”. In: *J Neural Transmission* **118** (2011), pp. 445–451.
- [144] R Fisher. *The Genetical Theory of Natural Selection*. Oxford at the Clarendon Press: The Internet Archive, 1930.
- [145] J Freeman and EP Simoncelli. “Metamers of the ventral stream”. In: *Nature Neuroscience* **14** (2011), pp. 1195–1201.
- [146] M Frega et al. “Network dynamics of 3D engineered neuronal cultures: a new experimental model for in-vitro electrophysiology”. In: *Scientific Reports* **4** (2014), p. 05489.
- [147] TF Freund, KAC Martin, and D Whitteridge. “Innervation of cat visual areas 17 and 18 by physiologically identified X- and Y- type thalamic afferents. I. Arborization patterns and quantitative distribution of postsynaptic elements.” In: *J Comparative Neurology* **242** (1985), pp. 263–74.
- [148] TF Freund et al. “Innervation of Cat Visual Areas 17 and 18 by Physiologically Identified X- and Y- Type Thalamic Afferents. II. Identification of Postsynaptic Targets by GABA Immunocytochemistry and Golgi Impregnation”. In: *J Comparative Neurology* **242** (1985), pp. 275–297.
- [149] P Fromherz. “Three levels of neuroelectronic interfacing: Silicon chips with ion channels, nerve cells, and brain tissue”. In: *Annals of the New York Academy of Sciences* **1093** (2006), pp. 143–160.
- [150] PLA Gabbott and P Somogyi. “Quantitative distribution of GABA-immunoreactive neurons in the visual cortex (area 17) of the cat”. In: *Exp Brain Res* **61** (1986), pp. 323–331.

-
- [151] L Gardner and A Deiters. “Light-controlled synthetic gene circuits”. In: *Curr Opin Chem Biol* **16** (2012), pp. 292–299.
- [152] LJ Garey and TP Powell. “An experimental study of the termination of the lateral geniculo-cortical pathway in the cat and monkey.” In: *Philosophical Transactions of the Royal Society B* **179** (1971), pp. 41–63.
- [153] ME Garrett et al. “Topography and Areal Organization of Mouse Visual Cortex”. In: *J Neuroscience* **34** (2014), pp. 12587–12600.
- [154] R Gattass, CG Gross, and JH Sandell. “Visual topography of V2 in the macaque.” In: *J Comparative Neurology* **201** (1981), pp. 519–539.
- [155] JL Gauthier et al. “Receptive fields in primate retina are coordinated to sample visual space more uniformly.” In: *PLoS Biology* **7** (2009), e1000063.
- [156] BRW Gerchberg and WO Saxton. “A Practical Algorithm for the Determination of Phase from Image and Diffraction Plane Pictures”. In: *Optik* **35** (1972), pp. 237–246.
- [157] CD Gilbert and TN Wiesel. “Morphology and intracortical projections of functionally characterised neurones in the cat visual cortex”. In: *Nature* **280** (1979), pp. 120–125.
- [158] CC Girardin and KAC Martin. “Cooling in cat visual cortex: stability of orientation selectivity despite changes in responsiveness and spike width”. In: *Neuroscience* **164** (2009), pp. 777–787.
- [159] SV Girman, Y Sauvé, and RD Lund. “Receptive field properties of single neurons in rat primary visual cortex”. In: *J Neurophysiology* **82** (1999), pp. 301–311.
- [160] I Gödecke et al. “Development of orientation preference maps in area 18 of kitten visual cortex”. In: *J Neuroscience* **9** (1997), pp. 1754–1762.
- [161] L Golan et al. “Design and characteristics of holographic neural photo-stimulation systems”. In: *J Neural Engineering* **6** (2009), pp. 1–14.
- [162] A Goldental et al. “Mimicking Collective Firing Patterns of Hundreds of Connected Neurons using a Single-Neuron Experiment”. In: *Frontiers in Neuroscience* **9** (2016), pp. 1–9.
- [163] A Grabska-Barwinska and C von der Malsburg. “Establishment of a scaffold for orientation maps in primary visual cortex of higher mammals”. In: *J Neuroscience* **28** (2008), pp. 249–57.
- [164] U Griebel and L Peichl. “Colour vision in aquatic mammals - facts and open questions”. In: *Aquatic Mammals* **29** (2003), pp. 18–30.
- [165] C Grienberger and A Konnerth. “Imaging Calcium in Neurons”. In: *Neuron* **73** (2012), pp. 862–885.
- [166] A Grinvald et al. “Functional architecture of cortex revealed by optical imaging of intrinsic signals”. In: *Nature* **324** (1986), pp. 361–364.
- [167] MS Grubb and J Burrone. “Channelrhodopsin-2 Localised to the Axon Initial Segment”. In: *PLoS ONE* **5** (2010), e13761.
- [168] G Grynkiewicz, M Poenie, and RY Tsien. “A new generation of Ca²⁺ indicators with greatly improved fluorescence properties”. In: *J Biological Chemistry* **260** (1985), pp. 3440–3450.
- [169] A Guellmar, J Rudolph, and J Bolz. “Structural alterations of spiny stellate cells in the somatosensory cortex in ephrin-A5-deficient mice”. In: *J Comparative Neurology* **517** (2009), pp. 645–654.

- [170] P Hammond. “Cat retinal ganglion cells: size and shape of receptive field centres”. In: *J Physiology* **242** (1974), pp. 99–118.
- [171] IL Hanganu, Y Ben-Ari, and R Khazipov. “Retinal Waves Trigger Spindle Bursts in the Neonatal Rat Visual Cortex”. In: *J Neuroscience* **26** (2006), pp. 6728–6736.
- [172] DE Hannula, DJ Simons, and NJ Cohen. “Imaging implicit perception: promise and pitfalls.” In: *Nature Reviews Neuroscience* **6** (2005), pp. 247–255.
- [173] D Hansel and C van Vreeswijk. “The mechanism of orientation selectivity in primary visual cortex without a functional map.” In: *J Neuroscience* **32** (2012), pp. 4049–4064.
- [174] JW Hastings et al. “Response of aequorin bioluminescence to rapid changes in calcium concentration”. In: *Nature* **222** (1969), pp. 1047–1050.
- [175] B Hein et al. “Early cortical spontaneous activity reflects the structure of mature sensory representations”. In: *SfN Abstracts* (2015), Program No. 59.12.
- [176] B Hein et al. “Simultaneous measurement of torsional oscillation and ultrasound propagation in solid ^4He at low temperatures”. In: *J Low Temperature Physics* **171** (2013), pp. 322–328.
- [177] B Hein et al. “The role of spontaneous correlations in structuring co-tuned networks in cortical development”. In: *SfN Abstracts* (2016), Program No. 799.11.
- [178] DA Heller et al. “Patterned networks of mouse hippocampal neurons on peptide-coated gold surfaces”. In: *Biomaterials* **26** (2005), pp. 883–889.
- [179] M Helmer et al. “Gender bias in scholarly peer review”. In: *eLife* **6** (2017), pp. 1–18.
- [180] M Hemberger, L Pammer, and G Laurent. “Comparative approaches to cortical microcircuits”. In: *Current Opinion in Neurobiology* **41** (2016), pp. 24–30.
- [181] Z Henderson, L Finlay, and KC Wikler. “Development of Ganglion Cell Topography in Ferret Retina”. In: *J Neuroscience* **8** (1988), pp. 1194–1205.
- [182] J Herschel. *Preliminary discourse on the study of natural philosophy*. London: Longman, Brown, Green & Longmans, 1851.
- [183] AVM Herz et al. “Modeling Single-Neuron Dynamics Detail and Abstraction”. In: *Science* **314** (2006), pp. 80–85.
- [184] PA Hetherington and NV Swindale. “Receptive field and orientation scatter studied by tetrode recordings in cat area 17.” In: *Visual Neuroscience* **16** (1999), pp. 637–652.
- [185] JA Hirsch et al. “Synaptic Integration in Striate Cortical Simple Cells”. In: *J Neuroscience* **18** (1998), pp. 9517–9528.
- [186] B Hofmann et al. “Nanocavity electrode array for recording from electrogenic cells.” In: *Lab on a Chip* **11** (2011), pp. 1054–1058.
- [187] R Honjin, S Sakato, and T Yamashita. “Electron microscopy of the mouse optic nerve: a quantitative study of the total optic nerve fibers.” In: *Arch Histol Jpn* **40** (1977), pp. 321–332.
- [188] VR Hore, JB Troy, and SJ Eglen. “Parasol cell mosaics are unlikely to drive the formation of structured orientation maps in primary visual cortex”. In: *Visual Neuroscience* **29** (2012), pp. 283–299.
- [189] T Hori, Y Takai, and T Takahashi. “Presynaptic Mechanism for Phorbol Ester-Induced Synaptic Potentiation”. In: *J Neuroscience* **19** (1999), pp. 7262–7267.
- [190] JC Horton. “Ocular integration in the human visual cortex.” In: *Canadian Journal of Ophthalmology* **41** (2006), pp. 584–593.

- [191] JC Horton and H Sherk. “Receptive field properties in the cat’s lateral geniculate nucleus in the absence of ON-center retinal input”. In: *J Neuroscience* **4** (1984), pp. 374–380.
- [192] DB Howard et al. “Tropism and toxicity of adeno-associated viral vector serotypes 1, 2, 5, 6, 7, 8, 9 in rat neurons and glia in vitro”. In: *Virology* **372** (2008), pp. 24–34.
- [193] DH Hubel and TN Wiesel. “Integrative action in the cat’s lateral geniculate body”. In: *J Physiology* **155** (1961), pp. 385–398.
- [194] DH Hubel and TN Wiesel. “Receptive fields, binocular interaction and functional architecture in the cat’s visual cortex”. In: *J Physiology* **160** (1962), pp. 106–154.
- [195] DH Hubel and TN Wiesel. “Receptive fields of cells in striate cortex of very young, visually inexperienced kittens”. In: *J Physiology* **26** (1963), pp. 994–1002.
- [196] DH Hubel and TN Wiesel. “Receptive fields of single neurones in the cat’s striate cortex”. In: *J Physiology* **148** (1959), pp. 574–591.
- [197] DH Hubel and TN Wiesel. “Shape and arrangement of columns in cat’s striate cortex”. In: *J Physiology* **165** (1963), pp. 559–568.
- [198] DH Hubel. “David H. Hubel.” In: *The History of Neuroscience in Autobiography*. Ed. by LR Squire. Washington DC: Society for Neuroscience, 1996, pp. 296–317.
- [199] DH Hubel and TN Wiesel. “Ferrier lecture. Functional architecture of macaque monkey visual cortex.” In: *Philosophical Transactions of the Royal Society B* **198** (1977), pp. 1–59.
- [200] M Hübener et al. “Spatial relationships among three columnar systems in cat area 17.” In: *J Neuroscience* **17** (1997), pp. 9270–9284.
- [201] AD Huberman, MB Feller, and B Chapman. “Mechanisms Underlying Development of Visual Maps and Receptive Fields”. In: *Annual Review of Neuroscience* **31** (2008), pp. 479–509.
- [202] JE Huettner and RW Baughman. “Primary Culture of Identified Neurons from the Visual Cortex of Postnatal Rats”. In: *J Neuroscience* **6** (1986), pp. 3044–3060.
- [203] A Hughes and H Wässle. “The Cat Optic Nerve: Fibre Total Count and Diameter Spectrum”. In: *J Comparative Neurology* **169** (1976), pp. 171–184.
- [204] AL Humphrey et al. “Projection patterns of individual X- and Y-cell axons from the lateral geniculate nucleus to cortical area 17 in the cat.” In: *J Comparative Neurology* **233** (1985), pp. 159–189.
- [205] Z Hussain et al. “Estimation of cortical magnification from positional error in normally sighted and amblyopic subjects”. In: *J Vision* **15** (2015), pp. 25–25.
- [206] CA Hutchison et al. “Design and synthesis of a minimal bacterial genome”. In: *Science* **351** (2016), pp. 1414–1414.
- [207] K Ikezoe et al. “Relationship between the Local Structure of Orientation Map and the Strength of Orientation Tuning of Neurons in Monkey V1: A 2-Photon Calcium Imaging Study”. In: *J Neuroscience* **33** (2013), pp. 16818–16827.
- [208] BA Illarionov et al. “Sequence of the cDNA encoding the Ca-activated photoprotein obelin from the hydroid polyp *Obelia longissima*”. In: *Gene* **153** (1995), pp. 273–274.
- [209] RB Illing and H Wässle. “The retinal projection to the thalamus in the cat: a quantitative investigation and a comparison with the retinotectal pathway.” In: *J Comparative Neurology* **202** (1981), pp. 265–285.

- [210] VM Ingram. “Gene mutations in human haemoglobin: the chemical difference between normal and sickle cell haemoglobin”. In: *Nature* **180** (1957), pp. 326–328.
- [211] T Isomura, K Kotani, and Y Jimbo. “Source Separation According to the Free-Energy Principle”. In: *PLoS Computational Biology* **11** (2015), e1004643.
- [212] NP Issa, C Trepel, and MP Stryker. “Spatial frequency maps in cat visual cortex.” In: *J Neuroscience* **20** (2000), pp. 8504–8514.
- [213] D Ito et al. “Minimum neuron density for synchronized bursts in a rat cortical culture on multielectrode arrays”. In: *Neuroscience* **171** (2010), pp. 50–61.
- [214] D Ito, T Komatsu, and K Gohara. “Measurement of saturation processes in glutamatergic and GABAergic synapse densities during long-term development of cultured rat cortical networks”. In: *Brain Res* **1534** (2013), pp. 22–32.
- [215] M Ivenshitz and M Segal. “Neuronal density determines network connectivity and spontaneous activity in cultured hippocampus.” In: *J Neurophysiology* **104** (2010), pp. 1052–1060.
- [216] S Jacobi and E Moses. “Variability and Corresponding Amplitude - Velocity Relation of Activity Propagating in One-Dimensional Neural Cultures”. In: *J Neurophysiology* **97** (2007), pp. 3597–3606.
- [217] GH Jacobs and J Nathans. “Response to Comment on ‘Emergence of Novel Color Vision in Mice Engineered to Express a Human Cone Photopigment’”. In: *Science* **318** (2007), p. 196c.
- [218] GH Jacobs et al. “Emergence of Novel Color Vision in Mice Engineered to Express a Human Cone Photopigment”. In: *Science* **315** (2007), pp. 1723–1726.
- [219] GH Jacobs. “Evolution of colour vision in mammals.” In: *Philosophical Transactions of the Royal Society B* **364** (2009), pp. 2957–2967.
- [220] CD James et al. “Aligned Microcontact Printing of Micrometer-Scale Poly-L-Lysine Structures for Controlled Growth of Cultured Neurons on Planar Microelectrode Arrays”. In: *IEEE Transactions on Biomedical Engineering* **47** (2000), pp. 17–21.
- [221] CD James et al. “Extracellular Recordings From Patterned Neuronal Networks Using Planar Microelectrode Arrays”. In: *IEEE Transactions on Biomedical Engineering* **51** (2004), pp. 1640–1648.
- [222] M Jenkner, B Muller, and P Fromherz. “Interfacing a silicon chip to pairs of snail neurons connected by electrical synapses”. In: *Biological Cybernetics* **84** (2001), pp. 239–250.
- [223] CJ Jeon, E Strettoi, and RH Masland. “The major cell populations of the mouse retina.” In: *J Neuroscience* **18** (1998), pp. 8936–8946.
- [224] Y Jimbo et al. “The dynamics of a neuronal culture of dissociated cortical neurons of neonatal rats”. In: *Biological Cybernetics* **83** (2000), pp. 1–20.
- [225] J Jin et al. “Population receptive fields of ON and OFF thalamic inputs to an orientation column in visual cortex.” In: *Nature Neuroscience* **14** (2011), pp. 232–238.
- [226] EN Johnson, MJ Hawken, and R Shapley. “The spatial transformation of color in the primary visual cortex of the macaque monkey”. In: *Nature Neuroscience* **4** (2001), pp. 409–416.
- [227] JP Jones and LA Palmer. “An evaluation of the two-dimensional Gabor filter model of simple receptive fields in cat striate cortex.” In: *J Neurophysiology* **58** (1987), pp. 1233–1258.

- [228] N Joye, A Schmid, and Y Leblebici. “A cell-electrode interface noise model for high-density microelectrode arrays.” In: *Annual International Conference of the IEEE Engineering in Medicine and Biology Society* **2009** (2009), pp. 3247–3250.
- [229] XH Ju et al. “Spatiotemporal Memory Is an Intrinsic Property of Networks of Dissociated Cortical Neurons”. In: *J Neuroscience* **35** (2015), pp. 4040–4051.
- [230] SB Jun et al. “Low-density neuronal networks cultured using patterned poly-L-lysine on microelectrode arrays”. In: *J Neuroscience* **160** (2007), pp. 317–326.
- [231] M Jungblut et al. “Triangular neuronal networks on microelectrode arrays: an approach to improve the properties of low-density networks for extracellular recording”. In: *Biomed Microdevices* **11** (2009), pp. 1269–1278.
- [232] H Kamioka et al. “Spontaneous periodic synchronized bursting during formation of mature patterns of connections in cortical cultures”. In: *Neuroscience Letters* **206** (1996), pp. 109–112.
- [233] ER Kandel, JH Schwartz, and TM Jessell. *Principles of neural science*. 4th ed. New York: McGraw-Hill New York, 2000.
- [234] R Kant, R Kumar, and VK Yadav. “Theory of Anomalous Diffusion Impedance of Realistic Fractal Electrode”. In: *J Physical Chemistry C Letters* **112** (2008), pp. 4019–4023.
- [235] E Kaplan, S Marcus, and Y Tat So. “Effects of dark adaptation on spatial and temporal properties of receptive fields in cat lateral geniculate nucleus”. In: *J Physiology* **294** (1979), pp. 561–580.
- [236] M Kaschube et al. “Genetic influence on quantitative features of neocortical architecture.” In: *J Neuroscience* **22** (2002), pp. 7206–7217.
- [237] M Kaschube et al. “Interareal coordination of columnar architectures during visual cortical development”. In: *PNAS* **106** (2009), pp. 17205–17210.
- [238] M Kaschube et al. “The pattern of ocular dominance columns in cat primary visual cortex: intra- and interindividual variability of column spacing and its dependence on genetic background”. In: *European Journal of Neuroscience* **18** (2003), pp. 3251–3266.
- [239] M Kaschube. “Neural maps versus salt-and-pepper organization in visual cortex”. In: *Current Opinion in Neurobiology* **24** (2014), pp. 95–102.
- [240] M Kaschube, M Schnabel, and F Wolf. “Self-organization and the selection of pinwheel density in visual cortical development”. In: *New Journal of Physics* **10** (2008), pp. 1–20.
- [241] M Kaschube et al. “Quantifying the variability of patterns of orientation domains in the visual cortex of cats”. In: *Neurocomputing* **33** (2000), pp. 415–423.
- [242] M Kaschube et al. “Universality in the evolution of orientation columns in the visual cortex.” In: *Science* **330** (2010), pp. 1113–1116.
- [243] LC Katz and EM Callaway. “Development of local circuits in mammalian visual cortex”. In: *Annual Review of Neuroscience* **15** (1992), pp. 31–56.
- [244] M Kaufman, S Reinartz, and NE Ziv. “Adaptation to prolonged neuromodulation in cortical cultures: an invariable return to network synchrony”. In: *BMC Biology* **12** (2014), pp. 1–22.
- [245] W Keil et al. “Response to Comment on ‘Universality in the Evolution of Orientation Columns in the Visual Cortex’”. In: *Science* **336** (2012), pp. 413–413.
- [246] W Keil and F Wolf. “Coverage, continuity, and visual cortical architecture.” In: *Neural Systems & Circuits* **1** (2011), pp. 1–55.

- [247] W Keil et al. “Reorganization of columnar architecture in the growing visual cortex.” In: *PNAS* **107** (2010), pp. 12293–12298.
- [248] CK Kim, A Adhikari, and K Deisseroth. “Integration of optogenetics with complementary methodologies in systems neuroscience”. In: *Nature Reviews Neuroscience* **18** (2017), pp. 222–235.
- [249] LA Kirkby et al. “A Role for Correlated Spontaneous Activity in the Assembly of Neural Circuits”. In: *Neuron* **80** (2013), pp. 1129–1144.
- [250] NC Klapoetke et al. “Independent optical excitation of distinct neural populations”. In: *Nature Methods* **11** (2014), pp. 338–346.
- [251] D Kleinfeld, KH Kahler, and PE Hockberger. “Controlled Outgrowth of Dissociated Neurons on Patterned Substrates”. In: *J Neuroscience* **8** (1988), pp. 4098–4120.
- [252] K Koepsell et al. “Retinal oscillations carry visual information to cortex.” In: *Frontiers in Systems Neuroscience* **3** (2009), pp. 1–18.
- [253] T Kohonen. “Self-Organized Formation of Topologically Correct Feature Maps”. In: *Biological Cybernetics* **43** (1982), pp. 59–69.
- [254] AA Koulakov and DB Chklovskii. “Orientation preference patterns in mammalian visual cortex: a wire length minimization approach”. In: *Neuron* **29** (2001), pp. 519–527.
- [255] S Kredel et al. “mRuby, a bright monomeric red fluorescent protein for labeling of sub-cellular structures”. In: *PLoS ONE* **4** (2009), e4391.
- [256] J Kremkow et al. “Principles underlying sensory map topography in primary visual cortex”. In: *Nature* **533** (2016), pp. 52–57.
- [257] JO Kriegs et al. “Retroposed elements as archives for the evolutionary history of placental mammals.” In: *PLoS Biology* **4** (2006), e91.
- [258] S Kuffler. “Discharge patterns and functional organization of mammalian retina”. In: *J Neurophysiology* **16** (1953), pp. 37–68.
- [259] A Kumar and GM Whitesides. “Patterned Condensation Figures as Optical Diffraction Gratings”. In: *Science* **263** (1994), pp. 1–4.
- [260] MA Lancaster et al. “Cerebral organoids model human brain development and microcephaly”. In: *Nature* **501** (2013), pp. 373–379.
- [261] MF Land and DE Nilsson. *Animal Eyes*. Oxford: Oxford University Press, 2012.
- [262] CE Landisman and DY Ts’o. “Color Processing in Macaque Striate Cortex: Electrophysiological Properties”. In: *J Neurophysiology* **87** (2002), pp. 3138–3151.
- [263] CE Landisman and DY Ts’o. “Color Processing in Macaque Striate Cortex: Relationships to Ocular Dominance, Cytochrome Oxidase, and Orientation”. In: *J Neurophysiology* **87** (2002), pp. 3138–3151.
- [264] PM Lau and GQ Bi. “Synaptic mechanisms of persistent reverberatory activity in neuronal networks”. In: *PNAS* **102** (2005), pp. 10333–10338.
- [265] L Lauer et al. “Aligned Microcontact Printing of Biomolecules on Microelectronic Device Surfaces”. In: *IEEE Transactions on Biomedical Engineering* **48** (2001), pp. 838–842.
- [266] MI Law, KR Zahs, and MP Stryker. “Organization of primary visual cortex (area 17) in the ferret”. In: *J Comparative Neurology* **278** (1988), pp. 157–180.
- [267] S LeVay and MP Stryker. “The development of ocular dominance columns in the cat”. In: *Society for Neuroscience Symposia* **4** (1979), pp. 83–98.

- [268] S LeVay and CD Gilbert. “Laminar patterns of geniculocortical projections in the cat”. In: *Brain Res* **113** (1976), pp. 1–19.
- [269] J Leach et al. “3D manipulation of particles into crystal structures using holographic optical tweezers”. In: *Optics Express* **12** (2004), pp. 220–226.
- [270] BB Lee, H Sun, and A Valberg. “Segregation of chromatic and luminance signals using a novel grating stimulus”. In: *J Physiology* **589** (2011), pp. 59–73.
- [271] HY Lee, M Yahyanejad, and M Kardar. “Symmetry considerations and development of pinwheels in visual maps.” In: *PNAS* **100** (2003), pp. 16036–16040.
- [272] Ks Lee, X Huang, and D Fitzpatrick. “Topology of ON and OFF inputs in visual cortex enables an invariant columnar architecture”. In: *Nature* **533** (2016), pp. 90–94.
- [273] X Leinekugel, R Khazipov, and R Cannon. “Correlated Bursts of Activity in the Neonatal Hippocampus in Vivo”. In: *Science* **296** (2002), pp. 2049–2053.
- [274] S Lem. *Memoirs of a Space Traveler*. Evanston, Illinois: Northwestern University Press, 1981.
- [275] C Lesuisse and LJ Martin. “Long-Term Culture of Mouse Cortical Neurons as a Model for Neuronal Development, Aging, and Death”. In: *J Neurobiology* **51** (2002), pp. 9–23.
- [276] JB Levitt et al. “Visual Response Properties of Neurons in the LGN of Normally Reared and Visually Deprived Macaque Monkeys”. In: *J Neurophysiology* **85** (2001), pp. 2111–2129.
- [277] MS Lewicki. “A review of methods for spike sorting: the detection and classification of neural action potentials”. In: *Network: Comput. Neural Syst.* **9** (1998), R53–R78.
- [278] Y Li, D Fitzpatrick, and LE White. “The development of direction selectivity in ferret visual cortex requires early visual experience”. In: *Nature Neuroscience* **9** (2006), pp. 676–681.
- [279] AD Lien and M Scanziani. “Tuned thalamic excitation is amplified by visual cortical circuits”. In: *Nature Neuroscience* **16** (2013), pp. 1315–1323.
- [280] LC Liets et al. “Spontaneous Activity of Morphologically Identified Ganglion Cells in the Developing Ferret Retina”. In: *J Neuroscience* **23** (2003), pp. 7343–7350.
- [281] G Lignani et al. “Long-term optical stimulation of channelrhodopsin-expressing neurons to study network plasticity”. In: *Frontiers in Molecular Neuroscience* **6** (2013), pp. 1–9.
- [282] JY Lin. “A User’s Guide to Channelrhodopsin Variants: Features, Limitations and Future Developments”. In: *Exp Physiology* **96** (2011), pp. 19–25.
- [283] JY Lin et al. “Characterization of Engineered Channelrhodopsin Variants with Improved Properties and Kinetics”. In: *Biophysical J* **96** (2009), pp. 1803–1814.
- [284] RA Linsenmeier et al. “Receptive field properties of X and Y cells in the cat retina derived from contrast sensitivity measurements”. In: *Vision Res* **22** (1982), pp. 1173–1183.
- [285] QY Liu et al. “Synaptic connectivity in hippocampal neuronal networks cultured on micropatterned surfaces”. In: *Developmental Brain Res* **120** (2000), pp. 223–231.
- [286] SH Liu. “Fractal model for the ac response of a rough interface”. In: *Physical Review Letters* **55** (1985), pp. 1–4.
- [287] MS Livingstone and DH Hubel. “Anatomy and Physiology of a color system in the primate visual cortex”. In: *J Neuroscience* **4** (1984), pp. 309–356.

- [288] M Lock et al. “Absolute Determination of Single-Stranded and Self-Complementary Adeno-Associated Viral Vector Genome Titers by Droplet Digital PCR”. In: *Human Gene Therapy Methods* **25** (2014), pp. 115–125.
- [289] S Löwel. “Ocular Dominance Column Development: Strabismus Changes the Spacing of Adjacent Columns in Cat Visual Cortex”. In: *J Neuroscience* **14** (1994), pp. 7451–7468.
- [290] S Löwel and W Singer. “Selection of Intrinsic Horizontal Connections in the Visual Cortex by Correlated Neuronal Activity”. In: *Science* **255** (1991), pp. 209–212.
- [291] LA Lowery and DV Vactor. “The trip of the tip: understanding the growth cone machinery”. In: *Nature Reviews Molecular Cell Biology* **10** (2009), pp. 332–343.
- [292] J Lubke and K Albus. “Lack of Exuberance in Clustered Intrinsic Connections in the Striate Cortex of One-month-old Kitten”. In: *J Neuroscience* **4** (1992), pp. 4–7.
- [293] M Lukosevicius and H Jaeger. “Reservoir computing approaches to recurrent neural network training”. In: *Computer Science Review* **3** (2009), pp. 127–149.
- [294] JS Lund et al. “Anatomical organization of the primary visual cortex (area 17) of the cat. A comparison with area 17 of the macaque monkey.” In: *J Comparative Neurology* **184** (1979), pp. 599–618.
- [295] C Lutz et al. “Holographic photolysis of caged neurotransmitters”. In: *Nature Methods* **5** (2008), pp. 821–827.
- [296] B Lyot. “The Study of the Solar Corona and Prominences without Eclipses”. In: *Monthly Notices of the Royal Astronomical Society* **99** (1939), pp. 580–594.
- [297] W Ma et al. “Central neuronal synapse formation on micropatterned surfaces”. In: *Developmental Brain Res* **111** (1998), pp. 231–243.
- [298] W Maass, T Natschlager, and H Markram. “Real-Time Computing Without Stable States: A New Framework for Neural Computation Based on Perturbations”. In: *Neural Computation* **14** (2002), pp. 2531–2560.
- [299] R Maex and GA Orban. “Model Circuit of Spiking Neurons Generating Directional Selectivity in Simple Cells”. In: *J Neurophysiology* **75** (1996), pp. 1515–1545.
- [300] DJ Maggs, PE Miller, and R Ofri. *Slatter’s Fundamentals of Veterinary Ophthalmology*. 4th ed. Elsevier Ltd, 2008.
- [301] MP Maher et al. “Microstructures for studies of cultured neural networks”. In: *Med Biol Eng Comp* **37** (1999), pp. 110–118.
- [302] V Maienschein, M Marxen, and W Volkandt. “A Plethora of Presynaptic Proteins Associated With ATP-Storing Organelles in Cultured Astrocytes”. In: *Glia* **26** (1999), pp. 233–244.
- [303] W Makous. “Comment on ‘Emergence of Novel Color Vision in Mice Engineered to Express a Human Cone Photopigment’”. In: *Science* **318** (2007), 196b.
- [304] HA Mallot. “An Overall Description of Retinotropic Mapping in the Cat’s Visual Cortex Areas 17, 18 and 19”. In: *Biological Cybernetics* **52** (1985), pp. 45–51.
- [305] C von der Malsburg. “Self-organization of orientation sensitive cells in the striate cortex.” In: *Biological Cybernetics* **14** (1973), pp. 85–100.
- [306] K Mancuso et al. “Gene therapy for red - green colour blindness in adult primates”. In: *Nature* **461** (2009), pp. 784–787.
- [307] A Marom et al. “Spontaneous activity characteristics of 3D ”optonets””. In: *Frontiers in Neuroscience* **10** (2017), pp. 1–10.

-
- [308] S Marom and G Shahaf. “Development, learning and memory in large random networks of cortical neurons: lessons”. In: *Quarterly reviews of biophysics* **35** (2002), pp. 63–87.
- [309] D Marr. “Vision”. In: *Minds, Brains, and Computers: The Foundations of Cognitive Science*. Ed. by R Cummins and DD Cummins. Blackwell Publishers, 1982. Chap. 5, pp. 69–83.
- [310] D Marr and T Poggio. “From Understanding Computation to Understanding Neural Circuitry”. In: *MIT Artificial Intelligence Memo* **357** (1976), pp. 1–22.
- [311] JR Martin. “In Vivo brain Imaging: Fluorescence or Bioluminescence, Which to Choose?” In: *J Neurogenetics* **22** (2008), pp. 285–307.
- [312] JR Martin et al. “In vivo bioluminescence imaging of Ca^{2+} signalling in brain of *Drosophila*”. In: *PLoS ONE* **2** (2007), e275.
- [313] KAC Martin, S Roth, and ES Rusch. “Superficial layer pyramidal cells communicate heterogeneously between multiple functional domains of cat primary visual cortex”. In: *Nature Communications* **5** (2014), p. 5252.
- [314] KAC Martin and D Whitteridge. “Form, Function and Intracortical Projections of spiny neurones in the striate visual cortex of the cat”. In: *J Physiology* **353** (1984), pp. 463–504.
- [315] LM Martinez et al. “Receptive field structure varies with layer in the primary visual cortex.” In: *Nature Neuroscience* **8** (2005), pp. 372–379.
- [316] LM Martinez et al. “Statistical wiring of thalamic receptive fields optimizes spatial sampling of the retinal image”. In: *Neuron* **81** (2014), pp. 943–956.
- [317] M Maschio et al. “Linking Neurons to Network Function and Behavior by Two-Photon Holographic Optogenetics and Volumetric Imaging”. In: *Neuron* **94** (2017), pp. 774–789.
- [318] RH Masland. “The fundamental plan of the retina.” In: *Nature Neuroscience* **4** (2001), pp. 877–886.
- [319] N Mayer, M Herrmann, and T Geisel. “Curved feature metrics in models of visual cortex”. In: *Neurocomputing* **44-46** (2002), pp. 533–539.
- [320] N Mayer et al. “Pinwheel Stability in a Non-Euclidean Model of Pattern Formation in the Visual Cortex”. In: *J Korean Physical Society* **50** (2007), pp. 150–157.
- [321] AK McCabe et al. “Roles of Glutamate and GABA Receptors in Setting the Developmental Timing of Spontaneous Synchronized Activity in the Developing Mouse Cortex”. In: *Developmental Neurobiology* **67** (2007), pp. 1574–1588.
- [322] A McGuire et al. “Patterns of Synaptic Input to Layer 4 of Cat Striate Cortex”. In: *J Neuroscience* **4** (1984), pp. 3021–3033.
- [323] D McLaughlin et al. “A neuronal network model of macaque primary visual cortex (V1): Orientation selectivity and dynamics in the input layer $4\text{C}\alpha$ ”. In: *PNAS* **97** (2000), pp. 8087–8092.
- [324] ET Mcadarns et al. “The linear and non-linear electrical properties of the electrode-electrolyte interface”. In: *Biosensors and Bioelectronics* **10** (1995), pp. 67–74.
- [325] RW Meredith et al. “Impacts of the Cretaceous Terrestrial Revolution and KPg Extinction on Mammal Diversification”. In: *Science* **334** (2011), pp. 521–525.
- [326] J Mertens et al. “Differential responses to lithium in hyperexcitable neurons from patients with bipolar disorder”. In: *Nature* **527** (2015), pp. 95–99.
- [327] C Metin, P Godement, and M Imbert. “The primary visual cortex in the mouse: receptive field properties and functional organization”. In: *Exp Brain Res* **69** (1988), pp. 594–612.

- [328] S Mikula et al. *BrainMaps: An Interactive Multiresolution Brain Atlas*; <http://brainmaps.org>. 2012.
- [329] KD Miller. “Understanding layer 4 of the cortical circuit: a model based on cat V1”. In: *Cerebral Cortex* **13** (2003), pp. 73–82.
- [330] KD Miller. “ π = Visual Cortex”. In: *Science* **330** (2010), pp. 1059–1061.
- [331] A Minerbi et al. “Long-Term Relationships between Synaptic Tenacity, Synaptic Remodeling, and Network Activity”. In: *PLoS Biology* **7** (2009), e1000136.
- [332] E Mire et al. “Spontaneous activity regulates Robo1 transcription to mediate a switch in thalamocortical axon growth”. In: *Nature Neuroscience* **15** (2012), pp. 1134–1143.
- [333] A Miyawaki et al. “Dynamic and quantitative Ca^{2+} measurements using improved cameleons”. In: *PNAS* **96** (1999), pp. 2135–2140.
- [334] JD Mollon. “Tho’ she kneel’d in that place where they grew... - the uses and origins of primate color vision”. In: *J Exp Biology* **146** (1989), pp. 21–38.
- [335] BD Moore and RD Freeman. “Development of orientation tuning in simple cells of primary visual cortex”. In: *J Neurophysiology* **107** (2012), pp. 2506–2516.
- [336] JA Movshon, ID Thompson, and DJ Tolhurst. “Spatial and temporal contrast sensitivity of neurones in areas 17 and 18 of the cat’s visual cortex.” In: *J Physiology* **283** (1978), pp. 101–120.
- [337] DR Muir et al. “Embedding of Cortical Representations by the Superficial Patch System.” In: *Cerebral Cortex* **21** (2011), pp. 2244–2260.
- [338] D Muller et al. “Phorbol ester-induced synaptic facilitation is different than long-term potentiation”. In: *PNAS* **85** (1988), pp. 6997–7000.
- [339] EH Murphy and N Berman. “The rabbit and the cat: a comparison of some features of response properties of single cells in the primary visual cortex.” In: *J Comparative Neurology* **188** (1979), pp. 401–427.
- [340] K Murphy, DG Jones, and RC Van Sluyters. “Cytochrome-Oxidase Blobs in Cat Primary Visual Cortex”. In: *J Neuroscience* **15** (1995), pp. 4196–4208.
- [341] KM Murphy et al. “Spacing of cytochrome oxidase blobs in visual cortex of normal and strabismic monkeys”. In: *Cerebral Cortex* **8** (1998), pp. 237–244.
- [342] WJ Murphy, E Eizirik, and SJO Brien. “Resolution of the Early Placental Mammal Radiation Using Bayesian Phylogenetics”. In: *Science* **294** (2001), pp. 2348–2351.
- [343] G Nagel et al. “Channelrhodopsin-2, a directly light-gated cation-selective membrane channel”. In: *PNAS* **100** (2003), pp. 13940–13945.
- [344] J Nakai, M Ohkura, and K Imoto. “A high signal-to-noise Ca^{2+} probe composed of a single green fluorescent protein”. In: *Nature Biotechnology* **19** (2001), pp. 137–141.
- [345] Y Nam et al. “Patterning to enhance activity of cultured neuronal networks”. In: *IEEE Proc Nanobiotechnology* **151** (2004), pp. 109–115.
- [346] I Nauhaus et al. “Efficient Receptive Field Tiling in Primate V1 Article Efficient Receptive Field Tiling in Primate V1”. In: *Neuron* **91** (2016), pp. 893–904.
- [347] A Neef et al. “Continuous Dynamic Photostimulation - inducing in-vivo-like fluctuating conductances with Channelrhodopsins”. In: *arXiv.org* (2013), p. 1305.7125.
- [348] JP Newman et al. “Optogenetic feedback control of neural activity”. In: *eLife* **4** (2015), pp. 1–24.

- [349] CM Niell and MP Stryker. “Highly selective receptive fields in mouse visual cortex.” In: *J Neuroscience* **28** (2008), pp. 7520–7536.
- [350] V Nikolenko et al. “SLM microscopy: scanless two-photon imaging and photostimulation using spatial light modulators”. In: *Frontiers in Neural Circuits* **2** (2008), pp. 1–14.
- [351] DE Nilsson and S Pelger. “A pessimistic estimate of the time required for an eye to evolve”. In: *Philosophical Transactions of the Royal Society B* **256** (1994), pp. 53–58.
- [352] LP O’Keefe et al. “Functional Organization of Owl Monkey Lateral Geniculate Nucleus and Visual Cortex”. In: *J Neurophysiology* **80** (1998), pp. 594–609.
- [353] MA O’Leary et al. “Response to Comment on ‘The Placental Mammal Ancestor and the Post-K-Pg Radiation of Placentals’”. In: *Science* **341** (2013), pp. 1–3.
- [354] MA O’Leary et al. “The Placental Mammal Ancestor and the Post-K-Pg Radiation of Placentals”. In: *Science* **339** (2013), pp. 662–668.
- [355] K Obermayer and GG Blasdel. “Geometry of orientation and ocular dominance columns in monkey striate cortex”. In: *J Neuroscience* **13** (1993), pp. 4114–4129.
- [356] K Obermayer, GG Blasdel, and K Schulten. “Statistical-mechanical analysis of self-organization and pattern formation during the development of visual maps”. In: *Physical Review A* **45** (1992), pp. 7568–7589.
- [357] MEJ Obien et al. “Revealing neuronal function through microelectrode array recordings”. In: *Frontiers in Neuroscience* **8** (2015), pp. 1–30.
- [358] D Oesterhelt and W Stoeckenius. “Rhodopsin-like protein from the purple membrane of *Halobacterium halobium*”. In: *Nature: New biology* **233** (1971), pp. 149–152.
- [359] K Ohki et al. “Functional imaging with cellular resolution reveals precise micro-architecture in visual cortex.” In: *Nature* **433** (2005), pp. 597–603.
- [360] K Ohki et al. “Highly ordered arrangement of single neurons in orientation pinwheels.” In: *Nature* **442** (2006), pp. 925–928.
- [361] I Ohzawa, G Sclar, and RD Freeman. “Contrast gain control in the cat’s visual system.” In: *J Neurophysiology* **54** (1985), pp. 668–675.
- [362] T Okamoto et al. “Predicted contextual modulation varies with distance from pinwheel centers in the orientation preference map.” In: *Scientific Reports* **1** (2011), p. 114.
- [363] EJ Olson et al. “Characterizing bacterial gene circuit dynamics with optically programmed gene expression signals”. In: *Nature Methods* **11** (2014), pp. 449–455.
- [364] HJ Olverman, AW Jones, and JC Watkins. “L-Glutamate has higher affinity than other amino acids for 3D-D-AP5 binding sites in rat brain membranes”. In: *Nature* **302** (1984), pp. 460–462.
- [365] DB Omer, R Hildesheim, and A Grinvald. “Temporally-structured acquisition of multidimensional optical imaging data facilitates visualization of elusive cortical representations in the behaving monkey”. In: *NeuroImage* **82** (2013), pp. 237–251.
- [366] T Opitz, AD De Lima, and T Voigt. “Spontaneous development of synchronous oscillatory activity during maturation of cortical networks in vitro.” In: *J Neurophysiology* **88** (2002), pp. 2196–2206.
- [367] JG Orlandi et al. “Dominance of Metric Correlations in Two-Dimensional Neuronal Cultures described through a Random Field Ising Model”. In: *Physical Review Letters* **118** (2017), p. 208101.

- [368] M Pabst, G Wrobel, and S Ingebrandt. “Solution of the Poisson-Nernst-Planck equations in the cell-substrate interface”. In: *The European Physical Journal* **24** (2007), pp. 1–8.
- [369] AM Packer et al. “Simultaneous all-optical manipulation and recording of neural circuit activity with cellular resolution in vivo”. In: *Nature Methods* **12** (2015), pp. 140–146.
- [370] L Palmer and T Davis. “Receptive-Field Structure in Cat Striate Cortex”. In: *J Neurophysiology* **46** (1981), pp. 260–276.
- [371] S Paluch-Siegler et al. “All-optical bidirectional neural interfacing using hybrid multiphoton holographic optogenetic stimulation using hybrid multiphoton holographic”. In: *Neurophotonics* **2** (2015), p. 031208.
- [372] L Pan et al. “An in vitro method to manipulate the direction and functional strength between neural populations”. In: *Frontiers in Neural Circuits* **9** (2015), pp. 1–14.
- [373] RM Paredes et al. “Chemical calcium indicators”. In: *Methods* **46** (2008), pp. 143–151.
- [374] JG Parnavelas, RA Burne, and CS Lin. “Receptive field properties of neurons in the visual cortex of the rat.” In: *Neuroscience Letters* **27** (1981), pp. 291–296.
- [375] DJ Pattinson et al. “Phylogeny, Paleontology, and Primates: Do Incomplete Fossils Bias the Tree of Life?” In: *Syst Biol* **64** (2015), pp. 169–186.
- [376] B Payne and A Peters. “The concept of cat primary visual cortex”. In: *The Cat Primary Visual Cortex*. Ed. by BR Payne and A Peters. 1st ed. San Diego, CA: Academic Press, 2002. Chap. 1, pp. 1–108.
- [377] C Pehlevan and H Sompolinsky. “Selectivity and Sparseness in Randomly Connected Balanced Networks”. In: *PLoS ONE* **9** (2014), e89992.
- [378] L Peichl and H Wässle. “Size, Scatter and Coverage of Ganglion Cell Receptive Field Centres in the Cat Retina”. In: *J Physiology* **291** (1979), pp. 117–141.
- [379] Y Penn, M Segal, and E Moses. “Network synchronization in hippocampal neurons”. In: *PNAS* **113** (2016), pp. 3341–3346.
- [380] E Persi et al. “Power-law input-output transfer functions explain the contrast-response and tuning properties of neurons in visual cortex”. In: *PLoS Computational Biology* **7** (2011), e1001078.
- [381] M Perutz and H Lehmann. “Molecular pathology of human hemoglobin”. In: *Nature* **219** (1968), pp. 902–909.
- [382] A Peters and B Payne. “Numerical relationships between geniculocortical afferents and pyramidal cell modules in cat primary visual cortex.” In: *Cerebral Cortex* **3** (1993), pp. 69–78.
- [383] D Poli, VP Pastore, and P Massobrio. “Functional connectivity in in vitro neuronal assemblies”. In: *Frontiers in Neural Circuits* **9** (2015), pp. 1–14.
- [384] SM Potter. “How should we think about bursts?” In: *Proceedings of the 6th International Meeting on Substrate-Integrated Microelectrodes*. 2008, pp. 22–25. ISBN: 3938345055.
- [385] SM Potter and TB Demarse. “A new approach to neural cell culture for long-term studies”. In: *J Neuroscience Methods* **110** (2001), pp. 17–24.
- [386] SM Potter, DA Wagenaar, and TB Demarse. “Closing the Loop: Stimulation Feedback Systems for Embodied MEA Cultures”. In: *Advances in Network Electrophysiology*. Ed. by M Taketani and M Baudry. Springer, 2000. Chap. 9, pp. 215–242.

-
- [387] D Prichard and J Theiler. “Generating Surrogate Data for Time Series with Several Simultaneously Measured Variables”. In: *Physical Review Letters* **73** (1994), pp. 951–954.
- [388] NJ Priebe and D Ferster. “Mechanisms of Neuronal Computation in Mammalian Visual Cortex”. In: *Neuron* **75** (2012), pp. 194–208.
- [389] Publius Vergilius Maro. *Georgica*. in the Public Domain; copied from Wikisource.
- [390] SJ Pyott and C Rosenmund. “The effects of temperature on vesicular supply and release in autaptic cultures of rat and mouse hippocampal neurons”. In: *J Physiology* **539** (2002), pp. 523–535.
- [391] S Ramon y Cajal. *Comparative study of the sensory areas of the human cortex*. Nabu Press, 2010, 1899, p. 80. ISBN: 1148925902.
- [392] S Rathjen, KE Schmidt, and S Löwel. “Postnatal growth and column spacing in cat primary visual cortex.” In: *Exp Brain Res* **149** (2003), pp. 151–158.
- [393] CP Ratliff et al. “Retina is structured to process an excess of darkness in natural scenes”. In: *PNAS* **107** (2010), pp. 17368–17373.
- [394] WG Regehr et al. “Sealing cultured invertebrate neurons to embedded dish electrodes facilitates long-term stimulation and recording”. In: *J Neuroscience Methods* **30** (1989), pp. 91–106.
- [395] L Reichl, S Löwel, and F Wolf. “Pinwheel Stabilization by Ocular Dominance Segregation”. In: *Physical Review Letters* **102** (2009), p. 208101.
- [396] L Reichl et al. “Coordinated optimization of visual cortical maps (I) Symmetry-based analysis”. In: *PLoS Computational Biology* **8** (2012), e1002466.
- [397] L Reichl et al. “Coordinated optimization of visual cortical maps (II) Numerical studies”. In: *PLoS Computational Biology* **8** (2012), e1002756.
- [398] RC Reid and JM Alonso. “Specificity of monosynaptic connections from thalamus to visual cortex”. In: *Nature* **378** (1995), pp. 281–284.
- [399] K Reinhold, AD Lien, and M Scanziani. “Distinct recurrent versus afferent dynamics in cortical visual processing”. In: *Nature Neuroscience* **18** (2015), pp. 1789–1797.
- [400] R Renault et al. “Combining Microfluidics, Optogenetics and Calcium Imaging to Study Neuronal Communication In Vitro”. In: *PLoS ONE* **10** (2015), e0120680.
- [401] I Reutsky-Gefen et al. “Holographic optogenetic stimulation of patterned neuronal activity for vision restoration”. In: *Nature Communications* **4** (2013), pp. 1–9.
- [402] J Richter and S Ullman. “A Model for the Temporal Organization of X- and Y-Type Receptive Fields in the Primate Retina”. In: *Biological Cybernetics* **145** (1982), pp. 127–145.
- [403] J Riera et al. “Concurrent observations of astrocytic Ca^{2+} and multisite extracellular potentials from an intact cerebral cortex”. In: *J Biophotonics* **160** (2010), pp. 147–160.
- [404] DL Ringach. “On the origin of the functional architecture of the cortex.” In: *PLoS ONE* **2** (2007), e251.
- [405] DL Ringach, RM Shapley, and MJ Hawken. “Orientation selectivity in macaque V1: diversity and laminar dependence.” In: *J Neuroscience* **22** (2002), pp. 5639–5651.
- [406] DL Ringach. “Haphazard wiring of simple receptive fields and orientation columns in visual cortex.” In: *J Neurophysiology* **92** (2004), pp. 468–476.

- [407] DA Robinson. “The electrical properties of metal microelectrodes”. In: *Proceedings of the IEEE* **56** (1968), pp. 1065–1071.
- [408] PRF Rocha et al. “Electrochemical noise and impedance of Au electrode/electrolyte interfaces enabling extracellular detection of glioma cell populations”. In: *Scientific Reports* **6** (2016), p. 34843.
- [409] NL Rochefort et al. “Sparsification of neuronal activity in the visual cortex at eye-opening”. In: *PNAS* **106** (2009), pp. 1–6.
- [410] RW Rodieck. “Quantitative analysis of cat retinal ganglion cell response to visual stimuli”. In: *Vision Res* **5** (1965), pp. 583–601.
- [411] D Rose and C Blakemore. “Effects of bicuculline on functions of inhibition in visual cortex”. In: *Nature* **249** (1974), pp. 375–377.
- [412] J Rovamo and V Virsu. “An estimation and application of the human cortical magnification factor”. In: *Exp Brain Res* **37** (1979), pp. 495–510.
- [413] NC Royo et al. “Specific AAV Serotypes Stably Transduce Primary Hippocampal and Cortical Cultures with High Efficiency and Low Toxicity”. In: *Brain Res* **1** (2008), pp. 15–22.
- [414] L Rubinsky et al. “Spatio-temporal motifs ‘remembered’ in neuronal networks following profound hypothermia”. In: *Neural Networks* **21** (2008), pp. 1232–1237.
- [415] L Rubinsky et al. “Study of hypothermia on cultured neuronal networks using multi-electrode arrays”. In: *J Neuroscience* **160** (2007), pp. 288–293.
- [416] O Sadakane et al. “Contrast-dependent, contextual response modulation in primary visual cortex and lateral geniculate nucleus of the cat”. In: *J Neuroscience* **23** (2006), pp. 1633–1642.
- [417] BT Sagdullaev and MA Mccall. “Stimulus size and intensity alter fundamental receptive-field properties of mouse retinal ganglion cells in vivo”. In: *Visual Neuroscience* **22** (2005), pp. 649–659.
- [418] R Samhaber et al. “Growing neuronal islands on multi-electrode arrays using an accurate positioning- μ CP device”. In: *J Neuroscience Methods* **257** (2016), pp. 194–203.
- [419] KJ Sanderson. “Visual Field Projection Columns and Magnification Factors in the Lateral Geniculate Nucleus of the Cat”. In: *Exp Brain Res* **13** (1971), pp. 159–177.
- [420] JR Sanes and RH Masland. “The Types of Retinal Ganglion Cells: Current Status and Implications for Neuronal Classification”. In: *Annual Review of Neuroscience* **38** (2015), pp. 221–248.
- [421] JD Schall, VH Perry, and AG Leventhal. “Ganglion cell dendritic structure and retinal topography in the rat”. In: *J Comparative Neurology* **257** (1987), pp. 160–165.
- [422] KF Schmidt and S Löwel. “The layout of functional maps in area 18 of strabismic cats.” In: *Neuroscience* **141** (2006), pp. 1525–1531.
- [423] M Schnabel et al. “Random waves in the brain: Symmetries and defect generation in the visual cortex”. In: *European Physical Journal* **145** (2007), pp. 137–157.
- [424] F Schneider, C Grimm, and P Hegemann. “Biophysics of Channelrhodopsin”. In: *Annual Review of Biophysics* **44** (2015), pp. 167–186.
- [425] M Scholl et al. “Ordered networks of rat hippocampal neurons attached to silicon oxide surfaces”. In: *J Neuroscience* **104** (2000), pp. 65–75.

- [426] M Schottdorf et al. “Frequency-dependent signal transfer at the interface between electrogenic cells and nanocavity electrodes”. In: *Physical Review E* **85** (2012), pp. 1–7.
- [427] M Schottdorf et al. “Can Retinal Ganglion Cell Dipoles Seed Iso-Orientation Domains in the Visual Cortex?” In: *PLoS ONE* **9** (2014), e86139.
- [428] M Schottdorf et al. “Random Wiring, Ganglion Cell Mosaics, and the Functional Architecture of the Visual Cortex”. In: *PLoS Computational Biology* **11** (2015), e1004602.
- [429] S Schuett, T Bonhoeffer, and M Hu. “Mapping Retinotopic Structure in Mouse Visual Cortex with Optical Imaging”. In: *J Neuroscience* **22** (2002), pp. 6549–6559.
- [430] G Sclar, JHR Maunsell, and P Lennie. “Coding of image contrast in central visual pathways of the macaque monkey”. In: *Vision Res* **30** (1990), pp. 1–10.
- [431] F Sengpiel and PC Kind. “The Role of Activity in Development of the Visual System”. In: *Current Biology* **12** (2002), pp. 818–826.
- [432] G Shahaf et al. “Order-Based Representation in Random Networks of Cortical Neurons”. In: *PLoS Computational Biology* **4** (2008), e1000228.
- [433] R Shapley and MJ Hawken. “Color in the Cortex: single- and double-opponent cells”. In: *Vision Res* **51** (2011), pp. 701–717.
- [434] J Sharma, A Angelucci, and M Sur. “Induction of visual orientation modules in auditory cortex.” In: *Nature* **404** (2000), pp. 841–847.
- [435] MJ Sheardown et al. “2,3-Dihydrox-6-nitro-7-sulfamoyl-benzo(F)quinoxaline: A Neuroprotectant for Cerebral Ischemnia”. In: *Science* **247** (1990), pp. 571–573.
- [436] M Shein-Idelson, E Ben-Jacob, and Y Hanein. “Engineered neuronal circuits : a new platform for studying the role of modular topology”. In: *Frontiers in Neuroengineering* **4** (2011), pp. 1–8.
- [437] WL Shew, T Bellay, and D Plenz. “Simultaneous multi-electrode array recording and two-photon calcium imaging of neural activity”. In: *J Neuroscience Methods* **192** (2010), pp. 75–82.
- [438] O Shimomura, FH Johnson, and Y Saiga. “Extraction, Purification and Properties of Aequorin, a Bioluminescent Protein from the Luminous Hydromedusan, Aequorea”. In: *J Cellular and Comparative Physiology* **59** (1962), pp. 223–239.
- [439] A Shmuel and A Grinvald. “Coexistence of linear zones and pinwheels within orientation maps in cat visual cortex.” In: *PNAS* **97** (2000), pp. 5568–5573.
- [440] AM Sillito. “The contribution of inhibitory mechanisms to the receptive field properties of neurones in the striate cortex of the cat.” In: *J Physiology* **250** (1975), pp. 305–329.
- [441] AM Smith, D Pappalardo, and WJA Chen. “Neurotoxicology and Teratology Estimation of neuronal numbers in rat hippocampus following neonatal amphetamine exposure : A stereology study”. In: *Neurotoxicology and Teratology* **30** (2008), pp. 495–502.
- [442] GB Smith et al. “The development of cortical circuits for motion discrimination”. In: *Nature Neuroscience* **18** (2015), pp. 252–261.
- [443] SL Smith and M Häusser. “Parallel processing of visual space by neighboring neurons in mouse visual cortex.” In: *Nature Neuroscience* **13** (2010), pp. 1144–1149.
- [444] SG Solomon and P Lennie. “The machinery of colour vision”. In: *Nature Reviews Neuroscience* **8** (2007), pp. 276–286.

- [445] DC Somers, SB Nelson, and S Mriganka. “An Emergent Model of Orientation Simple Cells Selectivity in Cat Visual Cortical Feedforward Inhibitory Recurrent”. In: *J Neuroscience* **15** (1995), pp. 5448–5465.
- [446] RE Soodak. “The retinal ganglion cell mosaic defines orientation columns in striate cortex”. In: *PNAS* **84** (1987), pp. 3936–3940.
- [447] RE Soodak. “Two-dimensional modeling of visual receptive fields using Gaussian sub-units.” In: *PNAS* **83** (1986), pp. 9259–9263.
- [448] J Soriano et al. “Development of input connections in neural cultures”. In: *PNAS* **105** (2008), pp. 13758–13763.
- [449] ME Spira and A Hai. “Multi-electrode array technologies for neuroscience and cardiology”. In: *Nature Nanotechnology* **8** (2013), pp. 83–94.
- [450] NC Spitzer. “Electrical activity in early neuronal development”. In: *Nature* **444** (2006), pp. 707–712.
- [451] MS Springer et al. “Technical Comment on ‘The Placental Mammal Ancestor and the Post-K-Pg Radiation of Placentals’”. In: *Science* **341** (2013), pp. 4–6.
- [452] S Srinivasan, CN Carlo, and CF Stevens. “Predicting visual acuity from the structure of visual cortex”. In: *PNAS* **112** (2015), pp. 7815–7820.
- [453] DA Stenger et al. “Microlithographic determination of axonal/dendritic polarity in cultured hippocampal neurons”. In: *J Neuroscience Methods* **82** (1998), pp. 167–173.
- [454] P Sterling. “Microcircuitry of the cat retina”. In: *Annual Review of Neuroscience* **6** (1983), pp. 149–185.
- [455] O Stetter et al. “Model-Free Reconstruction of Excitatory Neuronal Connectivity from Calcium Imaging Signals”. In: *PLoS Computational Biology* **8** (2012), e1002653.
- [456] JLR Stevens et al. “Mechanisms for Stable, Robust, and Adaptive Development of Orientation Maps in the Primary Visual Cortex”. In: *J Neuroscience* **33** (2013), pp. 15747–15766.
- [457] C Stone and LH Pinto. “Response properties of ganglion cells in the isolated mouse retina”. In: *Visual Neuroscience* **10** (1993), pp. 31–39.
- [458] C Stosiek et al. “In vivo two-photon calcium imaging of neuronal networks”. In: *PNAS* **100** (2003), pp. 7319–7324.
- [459] KJ Stratford et al. “Excitatory synaptic inputs to spiny stellate cells in cat visual cortex”. In: *Nature* **382** (1996), pp. 258–261.
- [460] W Stühmer. “Structure-Function Studies of Voltage-Gated Ion Channels”. In: *Annual Review of Biophysics and Biophysical Chemistry* **20** (1991), pp. 65–78.
- [461] D Sussillo and LF Abbott. “Article Generating Coherent Patterns of Activity from Chaotic Neural Networks”. In: *Neuron* **63** (2009), pp. 544–557.
- [462] NV Swindale. “A model for the formation of orientation columns.” In: *Philosophical Transactions of the Royal Society B* **215** (1982), pp. 211–230.
- [463] NV Swindale. “How Many Maps are there in Visual Cortex?” In: *Cerebral Cortex* **10** (2000), pp. 633–643.
- [464] NV Swindale, A Grinvald, and A Shmuel. “The spatial pattern of response magnitude and selectivity for orientation and direction in cat visual cortex.” In: *Cerebral Cortex* **13** (2003), pp. 225–238.

- [465] M Takao. “Changes in Visual Response Properties of Cat Retinal Ganglion Cells within Two Weeks after Axotomy”. In: *Exp Neurology* **177** (2002), pp. 171–182.
- [466] K Tanaka. “Cross-correlation analysis of geniculostriate neuronal relationships in cats.” In: *J Neurophysiology* **49** (1983), pp. 1303–1318.
- [467] SF Tavazoie and RC Reid. “Diverse receptive fields in the lateral geniculate nucleus during thalamocortical development”. In: *Nature Neuroscience* **3** (2000), pp. 608–616.
- [468] “Ten-year digital brain study yields first results”. In: *The Japan Times* **Oct 9** (2015).
- [469] C Tetzlaff et al. “Self-Organized Criticality in Developing Neuronal Networks”. In: *PLoS Computational Biology* **6** (2010), e1001013.
- [470] P Thiebaud et al. “PDMS device for patterned application of microfluids to neuronal cells arranged by microcontact printing”. In: *Biosensors & Bioelectronics* **17** (2002), pp. 87–93.
- [471] PJ Thomas and JD Cowan. “Symmetry Induced Coupling of Cortical Feature Maps”. In: *Physical Review Letters* **92** (2004), p. 188101.
- [472] C Tischbirek et al. “Deep two-photon brain imaging with a red-shifted fluorometric Ca²⁺ indicator.” In: *PNAS* **112** (2015), pp. 11377–11382.
- [473] T Tömböl. “An electron microscopic study of the neurons of the visual cortex”. In: *J Neurocytology* **3** (1974), pp. 525–531.
- [474] RB Tootell, SL Hamilton, and MS Silverman. “Topography of Cytochrome Oxidase Activity in Owl Monkey Cortex”. In: *J Neuroscience* **5** (1985), pp. 2786–2800.
- [475] RB Tootell et al. “Deoxyglucose analysis of retinotopic organization in primate striate cortex”. In: *Science* **218** (1982), pp. 902–904.
- [476] RB Tootell et al. “Functional anatomy of macaque striate cortex. II. Retinotopic organization”. In: *J Neuroscience* **8** (1988), pp. 1531–1568.
- [477] JB Troy and C Enroth-Cugell. “Dependence of center radius on temporal frequency for the receptive fields of X retinal ganglion cells of cat.” In: *J General Physiology* **94** (1989), pp. 987–995.
- [478] JB Troy and T Shou. “The receptive fields of cat retinal ganglion cells in physiological and pathological states: where we are after half a century of research.” In: *Progress in Retinal and Eye Res* **21** (2002), pp. 263–302.
- [479] TW Troyer et al. “Contrast-Invariant Orientation Tuning in Cat Visual Cortex: Thalamocortical Input Tuning and Correlation-Based Intracortical Connectivity”. In: *J Neuroscience* **18** (1998), pp. 5908–5927.
- [480] TW Troyer et al. “LGN Input to Simple Cells and Contrast-Invariant Orientation Tuning: An Analysis”. In: *J Neurophysiology* **87** (2002), pp. 2741–2752.
- [481] RY Tsien. “New Calcium Indicators and Buffers with High Selectivity against Magnesium and Protons: Design, Synthesis, and Properties of Prototype Structures”. In: *Biochemistry* **19** (1980), pp. 2396–2404.
- [482] DY Ts’o et al. “Functional organization of primate visual cortex revealed by high resolution optical imaging.” In: *Science* **249** (1990), pp. 417–420.
- [483] M Tsodyks et al. “Linking Spontaneous Activity of Single Cortical Neurons and the Underlying Functional Architecture”. In: *Science* **286** (1999), pp. 1943–1946.
- [484] RJ Tusa, LA Palmer, and AC Rosenquist. “The retinotopic organization of area 17 (striate cortex) in the cat.” In: *J Comparative Neurology* **177** (1978), pp. 213–235.

- [485] KM Tye and K Deisseroth. “Optogenetic investigation of neural circuits underlying brain disease in animal models”. In: *Nature Reviews Neuroscience* **13** (2012), pp. 251–266.
- [486] CJ Tyler et al. “Anatomical Comparison of the Macaque and Marsupial Visual Cortex: Common Features That May Reflect Retention of Essential Cortical Elements”. In: *J Comparative Neurology* **400** (1998), pp. 449–468.
- [487] WM Usrey, JB Reppas, and RC Reid. “Specificity and strength of retinogeniculate connections.” In: *J Neurophysiology* **82** (1999), pp. 3527–3540.
- [488] I Vajda et al. “Low-Frequency Stimulation Induces Stable Transitions in Stereotypical Activity in Cortical Networks”. In: *Biophysical J* **94** (2008), pp. 5028–5039.
- [489] SD Van Hooser et al. “Orientation selectivity without orientation maps in visual cortex of a highly visual mammal.” In: *J Neuroscience* **25** (2005), pp. 19–28.
- [490] F Varoqueaux et al. “Total arrest of spontaneous and evoked synaptic transmission but normal synaptogenesis in the absence of Munc13-mediated vesicle priming”. In: *PNAS* **99** (2002), pp. 9037–9042.
- [491] CC Veilleux and EC Kirk. “Visual Acuity in Mammals: Effects of Eye Size and Ecology”. In: *Brain, Behavior and Evolution* **83** (2014), pp. 43–53.
- [492] V Virsu and R Hari. “Cortical Magnification, Scale Invariance and Visual Ecology”. In: *Vision Res* **36** (1996), pp. 2971–2977.
- [493] AK Vogt, GJ Brewer, and A Offenhäusser. “Connectivity Patterns in Neuronal Networks of Experimentally Defined Geometry”. In: *Tissue Engineering* **11** (2005), pp. 1757–1767.
- [494] AK Vogt et al. “Micropatterned Substrates for the Growth of Functional Neuronal Networks of Defined Geometry”. In: *Biotechnol Prog* **19** (2003), pp. 1562–1568.
- [495] M Vorobyev. “Ecology and evolution of primate colour vision”. In: *Clinical and Experimental Optometry* **87** (2004), pp. 230–238.
- [496] DA Wagenaar. “An Optically Stabilized Fast-Switching Light Emitting Diode as a Light Source for Functional Neuroimaging”. In: *PLoS ONE* **7** (2012), e29822.
- [497] DA Wagenaar, Z Nadasdy, and SM Potter. “Persistent dynamic attractors in activity patterns of cultured neuronal networks”. In: *Physical Review E* **73** (2006), pp. 1–8.
- [498] DA Wagenaar, J Pine, and SM Potter. “An extremely rich repertoire of bursting patterns during the development of cortical cultures”. In: *BMC Neuroscience* **18** (2006), pp. 1–18.
- [499] DA Wagenaar, J Pine, and SM Potter. “Effective parameters for stimulation of dissociated cultures using multi-electrode arrays”. In: *J Neuroscience Methods* **138** (2004), pp. 27–37.
- [500] DA Wagenaar et al. “Controlling Bursting in Cortical Cultures with Closed-Loop Multi-Electrode Stimulation”. In: *J Neuroscience* **25** (2005), pp. 680–688.
- [501] GL Walls. *The vertebrate eye and its adaptive radiation*. 1963rd ed. New York, London: Hufner Publishing Company, 1942.
- [502] H Wang et al. “High-speed mapping of synaptic connectivity using photostimulation in Channelrhodopsin-2 transgenic mice”. In: *PNAS* **104** (2007), pp. 8143–8148.
- [503] X Wang et al. “Thalamic interneurons and relay cells use complementary synaptic mechanisms for visual processing”. In: *Nature Neuroscience* **14** (2011), pp. 224–231.
- [504] WC Warren et al. “Genome analysis of the platypus reveals unique signatures of evolution”. In: *Nature* **453** (2008), pp. 175–184.

-
- [505] H Wässle. “Parallel processing in the mammalian retina.” In: *Nature Reviews Neuroscience* **5** (2004), pp. 747–757.
- [506] H Wässle, BB Boycott, and RB Illing. “Morphology and mosaic of on- and off-beta cells in the cat retina and some functional considerations.” In: *Philosophical Transactions of the Royal Society B* **212** (1981), pp. 177–195.
- [507] H Wässle, WR Levick, and BG Cleland. “The distribution of the alpha type of ganglion cells in the cat’s retina.” In: *J Comparative Neurology* **159** (1975), pp. 419–438.
- [508] H Wässle, L Peichl, and BB Boycott. “A spatial analysis of on-and off-ganglion cells in the cat retina”. In: *Vision Res* **23** (1983), pp. 1151–1160.
- [509] C Watson, G Paxinos, and L Puelles. *The Mouse Nervous System*. 1st ed. Academic Press, 2012.
- [510] K Weir et al. “Comparison of spike parameters from optically identified GABAergic and glutamatergic neurons in sparse cortical cultures”. In: *Frontiers in Cellular Neuroscience* **8** (2015), pp. 1–12.
- [511] R Weis. “Neuron adhesion on a silicon chip probed by an array of field-effect transistors”. In: *Physical Review Letters* **76** (1996), pp. 327–330.
- [512] R Weis and P Fromherz. “Frequency dependent signal transfer in neuron transistors”. In: *Physical Review E* **55** (1997), pp. 877–889.
- [513] M Weliky and LC Katz. “Correlational Structure of Spontaneous Neuronal Activity in the Developing Lateral Geniculate Nucleus in Vivo”. In: *Science* **285** (1999), pp. 599–604.
- [514] M Welkenhuysen et al. “An integrated multi-electrode/optrode array for in vitro optogenetics”. In: *Scientific Reports* **6** (2016), pp. 1–10.
- [515] BC Wheeler et al. “Microcontact Printing for Precise Control of Nerve Cell Growth in Culture”. In: *J Biomechanical Engineering* **121** (1999), pp. 73–78.
- [516] LE White, DM Coppola, and D Fitzpatrick. “The contribution of sensory experience to the maturation of orientation selectivity in ferret visual cortex.” In: *Nature* **411** (2001), pp. 1049–1052.
- [517] LE White and D Fitzpatrick. “Vision and cortical map development.” In: *Neuron* **56** (2007), pp. 327–338.
- [518] TN Wiesel. “Recording inhibition and excitation in the cat’s retinal ganglion cells with intracellular electrodes.” In: *Nature* **183** (1959), pp. 264–265.
- [519] DE Wilson et al. “Orientation selectivity and the functional clustering of synaptic inputs in primary visual cortex”. In: *Nature Neuroscience* **19** (2016), pp. 1003–1009.
- [520] JR Wilson and S Murray. “Receptive-Field Characteristics of Neurons in Cat Striate Cortex: Changes With Visual Field Eccentricity”. In: *J Neurophysiology* **39** (1976), pp. 512–533.
- [521] K Wimmer et al. “Bump attractor dynamics in prefrontal cortex explains behavioral precision in spatial working memory”. In: *Nature Neuroscience* **17** (2014), pp. 431–439.
- [522] DA Winfield. “The postnatal development of synapses in the visual cortex of the cat and the effects of eyelid closure”. In: *Brain Res* **206** (1981), pp. 166–171.
- [523] DA Winfield, KC Gatter, and TPS Powell. “An electron microscopic study of the types and proportions of neurons in the cortex of the motor and visual areas of the cat and rat”. In: *Brain* **103** (1980), pp. 245–258.

- [524] A Witt et al. “Controlling the oscillation phase through precisely timed closed-loop optogenetic stimulation: a computational study”. In: *Frontiers in Neural Circuits* **7** (2013), pp. 1–17.
- [525] F Wolf. “Symmetry, Multistability, and Long-Range Interactions in Brain Development”. In: *Physical Review Letters* **95** (2005), p. 208701.
- [526] F Wolf, HU Bauer, and T Geisel. “Formation of field discontinuities and islands in visual cortical maps”. In: *Biological Cybernetics* **70** (1994), pp. 525–531.
- [527] F Wolf and T Geisel. “Spontaneous pinwheel annihilation during visual development”. In: *Nature* **395** (1998), pp. 73–78.
- [528] F Wolf and T Geisel. “Universality in visual cortical pattern formation.” In: *J Physiology* **97** (2003), pp. 253–264.
- [529] F Wörgötter and C Koch. “A detailed model of the primary visual pathway in the cat: comparison of afferent excitatory and intracortical inhibitory connection schemes for orientation selectivity.” In: *J Neuroscience* **11** (1991), pp. 1959–1979.
- [530] KD Wulff et al. “Aberration correction in holographic optical tweezers”. In: *Optics Express* **14** (2006), pp. 4170–4175.
- [531] X Xu et al. “Functional Organization of Visual Cortex in the Prosimian Bush Baby Revealed by Optical Imaging of Intrinsic Signals”. In: *J Neurophysiology* **94** (2005), pp. 2748–2762.
- [532] S Yang et al. “Three-dimensional holographic photostimulation of the dendritic arbor”. In: *J Neural Engineering* **8** (2011), pp. 1–9.
- [533] CI Yeh et al. “Stimulus ensemble and cortical layer determine V1 spatial receptive fields”. In: *PNAS* **106** (2009), pp. 14652–14657.
- [534] T Yeh et al. “Visual Responses in the Lateral Geniculate Nucleus of Dichromatic and Trichromatic Marmosets (*Callithrix jacchus*)”. In: *J Neuroscience* **15** (1995), pp. 7892–7904.
- [535] T Yokoo, BW Knight, and L Sirovich. “An optimization approach to signal extraction from noisy multivariate data.” In: *NeuroImage* **14** (2001), pp. 1309–1326.
- [536] H Yu et al. “The Coordinated Mapping of Visual Space and Response Features in Visual Cortex”. In: *Neuron* **47** (2005), pp. 267–280.
- [537] M Zahid et al. “Holographic photolysis for multiple cell stimulation in mouse hippocampal slices”. In: *PLoS ONE* **5** (2010), e9431.
- [538] BV Zemelman et al. “Selective photostimulation of genetically chARGed neurons”. In: *Neuron* **33** (2002), pp. 15–22.
- [539] A Zepeda, C Arias, and F Sengpiel. “Optical imaging of intrinsic signals: recent developments in the methodology and its applications”. In: *J Neuroscience Methods* **136** (2004), pp. 1–21.
- [540] XJ Zhan and JB Troy. “Modeling cat retinal beta-cell arrays”. In: *Visual Neuroscience* **17** (2000), pp. 23–39.

Acknowledgements and CV

Acknowledgements

I am grateful for the support of many people. Without them, this work would not have been possible. First of all I am grateful to Fred Wolf and Walter Stühmer for their enthusiasm and support. Without their scientific and personal expertise, their ingenuity and resourcefulness, their patience and encouragement this work would have been impossible. I am truly in debt for your scientific and personal guidance over the years. I would also like to thank Jörg Enderlein, Shy Shoham and Andreas Neef for their encouragement and the many creative ideas and Boehringer Ingelheim Fonds who provided my PhD fellowship.

For chapter 3 I am grateful for the input of Wolfgang Keil, David Coppola and Len White. I specifically want to thank Wolfgang Keil for five wonderful and productive years. I am grateful to Zoltán F. Kisvárdy for sharing his optical imaging data and Matthias Kaschube for providing his original PV-WAVE analysis routines and numerous stimulating discussions. For chapter 4, I am grateful for the support of my coauthors, Robert Samhaber, Ahmed El Hady, Kai Bröking, Andreas Daus and Christiane Thielemann. I particularly want to thank Robert Samhaber, Ahmed El Hady, and Kai Bröking for their introduction to the world of μ Contact printing, Markus Krohn for the excellent technical support and Ricardo Merino for his help in the lab. For chapter 5, I would like to express my gratitude for the ingenuity of Hecke Schrobsdorff and Oliver Wendt and his colleagues at Rapp Optoelectronics in setting up the original prototype of the holographic projection system, Julian Vogel for his work on the all-optical system, Kai Bröking for sharing his vast knowledge, and in particular Shy Shoham who endured me in his lab for several weeks and the many valuable suggestions of how to improve our system. I am also grateful for the helpful comments from Ulrich Egert, Alex Reyes, David Hansel, Kevan Martin, Elisha Moses and John Nicholls. For chapter 6, I am indebted to Andreas Neef, without whom this project would not have been done. I would also like to acknowledge the skillful assembly of electronics by Karl Lautscham and his team from the electronics workshop. I am grateful for many valuable discussions on the role of spontaneous activity with Bettina Hein, the input from Tūreiti Keith on clustering and the false-positive sorting and the helpful discussions with Viola Priesemann, Johannes Zierenberg and Jens Wilting on spike statistics and possible mechanisms. For chapter 7, I am indebted to Amiram Grinvald, Koji Ikezoe, Tsuyoshi Okamoto, David Omer, Xiangmin Xu and the late Vivien Casagrande for sharing their primate data, Juan Daniel Flórez Weidinger and Jonas Franz for data curation, Joscha Liedtke for solving the coupled model and Alessandra Angelucci, Matthias Kaschube, Wolfgang Keil, and Len White for very helpful discussions and their willingness to share code and ideas. I particularly want to thank Barry B. Lee for boosting my enthusiasm for color vision further into the sensory periphery, the many

insightful discussions and comments on this chapter in particular and the early visual system in general and also Stephen J. Eglen for his open spirit and enthusiasm for the vast family of visual maps. Finally, for chapter 8, I would like to thank Demian Battaglia, Andreas Neef and especially Markus Helmer for their collaborative spirit. I relied heavily on the expertise of technical staff. For that I want to thank Michael Günther, Sabine Klöppner, Christian Westendorf and Yorck-Fabian Beensen, Denny Fliegner and Hecke Schrobsdorff for the great IT support. I am grateful to Ayse Bolik, Viktoriya Novak, Regina Wunderlich, Zrinka Gattin and the GGNB office for all their support in administrative issues.

I would also like to specifically acknowledge the Genetically-Encoded Neuronal Indicator and Effector (GENIE) Project and the Janelia Research Campus of the Howard Hughes Medical Institute which have generously allowed the jRCaMP1a material to be used. Specifically I would like to express my gratitude towards Vivek Jayaraman, Douglas S. Kim, Loren L. Looger, and Karel Svoboda. I would also like to thank Karl Deisseroth for allowing to use the ChR2(H134) construct.

I would like to thank Bettina Hein, Walter Stühmer, Fred Wolf and Juan Daniel Flórez Weidinger for proof reading and critically examining this thesis and especially Rafael Brune, Rainer Engelken, Michael Fauth, Bettina Hein, Markus Helmer, Joscha Liedtke, Dennis Nestvogel and Frank Stollmeier for insightful discussions on many diverse subjects and their critical minds. Markus, the world from *affe* to the puzzle of consciousness would have been dull without you. Joscha, our journeys from a Buddhist monastery on the shores of a Korean tropical island, across the Chinese wall to the highest mountains (of Great Britain) will always be memorable to me. Frank, so will the wonderful office atmosphere, the cycling trips and the garden. Bettina, somewhere either in Pando's shade, the Amazon rainforest, or on the shores of the Pacific we will figure out how this mad clockwork works. Last but not least, I would like to thank my family for their sustained trust, love and support during the last years. You made this possible.

Curriculum Vitæ

Personal Details

Date of birth March 29, 1989
Place of birth Bad Kissingen
Nationality German
Orcid-ID 0000-0002-5468-4255

Education

- 06/2013 - present **Ph.D. student** The Max Planck Institute of Experimental Medicine & the Max Planck Institute for Dynamics and Self-Organization; Advisors: Prof. Dr. Fred Wolf (Max Planck Institute for Dynamics and Self-Organization), Prof. Dr. Walter Stühmer (Max Planck Institute for Experimental Medicine)
- 10/2011 - 2/2013 **M. Sc. with honors** in Physics, University of Würzburg & Max Planck Institute for Dynamics and Self-Organization, Grade 1.0, in words: *excellent*. Thesis: “Geometry and Statistical Physics of Retinal Ganglion Cell Mosaics and Orientation Preference Maps.”
- 9/2010 - 10/2011 **M. Sc.** in Physics, Rutgers, the State University of New Jersey, USA, GPA 3.9/4.0. Thesis: “A nanochannel with an embedded transverse graphene tunneling electrode for molecular probing and as a future tool for DNA sequencing.”
- 10/2007 - 7/2010 **B. Sc.** in Physics, University of Würzburg & Jülich Research Center, Grade 1.2, in words: *excellent*. Thesis: “Nanofluidic microelectrodes as cell-chip interface.”
- 07/2007 “Abitur” at Frobenius-Gymnasium Hammelburg, Germany.

Additional Training

- 1/2016 Participant at ICTP/SAIFR School on Physics Applications in Biology, Sao Paulo, Brazil.
- 6/2014 Participant at OIST Computational Neuroscience Course, Okinawa, Japan.
- 9/2014 Qualifying course in laboratory animals, Göttingen, Germany (following FELASA-B recommendations; GV-SOLAS certified).

Research

Scientific Papers M. Helmer[†], **M. Schottdorf**, A. Neef & D. Battaglia[†]: “*Gender bias in peer-review*”, [eLife](#) 6: e21718 (2017)

R. Samhaber*, **M. Schottdorf**^{†*}, A. El Hady*, K. Bröking, A. Daus, C. Thielemann, W. Stühmer & F. Wolf[†]: “*Growing neuronal islands on multi-electrode arrays using an Accurate Positioning- μ CP device*”, [J. Neurosc. Methods](#) 257(1): 194-203 (2016)

M. Schottdorf*, W. Keil^{†*}, D. Coppola, L. White & F. Wolf: “*Random wiring, ganglion cell mosaics, and the functional architecture of the visual cortex*”, [PLoS Comp. Bio.](#) 11(11): e1004602 (2015)

M. Schottdorf, S. Eglén, F. Wolf & W. Keil[†]: “*Can Retinal Ganglion Cell Dipoles Seed Iso-Orientation Domains in the Visual Cortex?*”, [PLoS ONE](#) 9(1): e86139 (2014)

M. Schottdorf[†], B. Hofmann, E. Kätelhön, A. Offenhäusser & B. Wolfrum[†]: “*Frequency-dependent signal transfer at the interface between electrogenic cells and nanocavity electrodes*”, [Phys. Rev. E](#) 85: 031917 (2012)

B. Hofmann, E. Kätelhön, **M. Schottdorf**, A. Offenhäusser & B. Wolfrum[†]: “*Nanocavity electrode array for recording from electrogenic cells*”, [Lab on a Chip](#) 11: 1054-1058 (2011)

(* shared first authorship / [†] corresponding author)

Scholarship & Fellowships

12/2013 - 12/2015 Boehringer Ingelheim Fonds PhD Fellowship.

9/2010 - 10/2011 Scholarship of the German Academic Exchange Service.

7/2010 - 12/2012 Fellow of the Graduate Program “FOKUS Physik” of the University of Würzburg/The Elite Network of Bavaria.

10/2009 - 2/2013 Max Weber scholarship of the Elite Network of Bavaria and the German National Academic Foundation (top 0.5% of students).

Professional Activity

- 9/2016 Main organizer of the aCNS 2016, Göttingen, Germany
- 9/2015 Organizer of the PhD student organized 2-week advanced computational neuroscience summer school (aCNS) 2015 in Göttingen, Germany.
- 9/2014 Main organizer of the PhD student organized event at the Bernstein Conference 2014: *Can the problem of consciousness be solved?*
- 1/2014 - 1/2017 Student representative of the graduate program *Physics of theoretical and computational neuroscience (PTCN)*.

Conferences

- (selected)
Conference Contributions **M. Schottdorf**, J Vogel, H. Schrobsdorff, W. Stühmer & F. Wolf: “*Spontaneous emergence of structured responses in a random neural network in-vitro*”, SfN in San Diego, California, USA, Nov 12-16 2016
- B. B. Lee & M. Schottdorf**: “*Responses of macaque ganglion cells to natural scenes: spatial and temporal factors*”, ECVF in Barcelona, Spain, Aug 28 - Sept 1 2016
- J. Liedtke, **M. Schottdorf** & F. Wolf: “*Maximum entropy models for 3D layouts of orientation selectivity*”, CNS in Jeju, Korea, July 2-7 2016
- M. Schottdorf**, H. Schrobsdorff, W. Stühmer & F. Wolf: “*Computer generated holography for optogenetic modulation of neural network activity in-vitro*”, Maps 2015 in Strasbourg, France, Dec 7-9 2015
- M. Schottdorf**, W. Keil, J. D. Flórez-Weidinger et al. : “*How did the evolution of color vision impact V1 functional architecture?*”, Cosyne 2015 in Salt Lake City, Utah, USA, Mar 5-10 2013
- M. Schottdorf**, W. Stühmer & F. Wolf: “*Reconstituting the emergence of visual cortical feature selectivity in-vitro*”, Maps 2014 in Edinburgh, UK, July 28-29 2014
- M. Schottdorf**, S. J. Eglan, F. Wolf & W. Keil: “*Can retinal ganglion cell dipoles seed iso-orientation domains in the visual cortex?*”, Cosyne 2014 in Salt Lake City, Utah, USA, Feb 27 - Mar 4 2014
- L. Somers, **M. Schottdorf**, M. Wanunu & E. Y. Andrei: “*Tunneling Currents through DNA Bases Tightly Constrained in a Fluid Channel*”, APS March meeting 2014 in Denver, Colorado, USA, Mar 3-7 2014
- M. Schottdorf**, W. Keil, M. Schnabel, D. M. Coppola, S. Löwel, L. E. White, M. Kaschube & F. Wolf: “*Do orientation preference maps arise from hexagonal retinal ganglion cell mosaics?*”, Cosyne 2013 in Salt Lake City, Utah, USA, Feb 28 - Mar 5 2013

Talks

- (selected)
Talks
- Conference Talk at 3rd Ringberg Conference on Ion Channels, Ringberg, Germany, Oct 21 2016
 - Conference Talk at ICMNS, Antibes, France, June 10 2015
 - NeuroBioTheory Seminar FIAS, Frankfurt, Germany, Dec 16 2014
 - Univ. of Electro-Communications, Tokyo, Shigeru Tanaka Lab, July 14 2014
 - Osaka University, Osaka, Japan, Nobuhiko Yamamoto Lab, July 11 2014
 - Osaka University, Osaka, Japan, Ichiro Fujita Lab, July 11 2014
 - Kyushu University, Fukuoka, Japan, Tsuyoshi Okamoto Lab, July 8 2014
 - Kyushu University, Fukuoka, Japan, Kenichi Ohki Lab, July 7 2014
 - Max Planck Campus Göttingen, Germany: Campus Seminar, May 28 2014
 - University Göttingen, Göttingen, 13th Göttingen Philosophical Colloquium with David Chalmers: 'Unconscious Neuroscience', May 4, 2014
 - Columbia University, NY: Columbia Neurotheory Seminar, March 14, 2014
 - Rutgers University, New Brunswick: The Seminar in Physics, March 11 2014
 - Technion University, Haifa, Israel, Shy Shoham Lab, Aug 8 2013
 - SUNY Center of Optometry, NY, USA, Jose Manuel Alonso Lab, March 7 2013